SEISMIC RESPONSE OF SHALLOW UNDERGROUND STRUCTURES IN DENSE URBAN ENVIRONMENTS

by

Kenneth M. Gillis

B.S. Mechanical Engineering, University of Colorado Boulder, 2005

M.S. Civil Engineering, University of Colorado Boulder, 2012

A thesis submitted to the

Faculty of the Graduate School of the

University of Colorado in partial fulfillment

of the requirements for the degree of

Doctor of Philosophy

Department of Civil, Environmental, and Architectural Engineering

2015

This thesis entitled:
SEISMIC RESPONSE OF SHALLOW UNDERGROUND STRUCTURES IN DENSE URBAN ENVIRONMENTS
written by Kenneth M. Gillis
has been approved for the Department of Civil, Environmental, and Architectural Engineering

_____
Dr. Shideh Dashti

_____
Dr. Abbie Liel

_____
Dr. Dobroslav Znidarcic

_____
Dr. Youssef Hashash

_____
Dr. Dan Wilson

Date _____

The final copy of this thesis has been examined by the signatories, and we find that both the content and the form meet acceptable presentation standards of scholarly work in the above mentioned discipline.

Gillis, Kenneth M. (Ph.D., Civil Engineering)

SEISMIC RESPONSE OF SHALLOW UNDERGROUND STRUCTURES IN DENSE URBAN ENVIRONMENTS

Thesis directed by Prof. Shideh Dashti

Shallow underground structures used for public transportation are a key component of sustainable cities. In dense urban environments, underground structures are often built near tall buildings. Although such buildings have the potential to alter ground motions in their vicinity and transmit significant forces to adjacent underground structures during earthquakes, these impacts are not well understood. Centrifuge tests were performed to evaluate seismic interactions between an underground structure, soil, and an adjacent mid- to high-rise building. The seismic response of a braced, temporary excavation and a permanent, cut-and-cover box structure in medium dense, dry sand is measured independently first and then when adjacent to mid and highrise buildings. The data from these tests serve two purposes: first, to better understand seismic soil-structure-underground structure-interaction (SSUSI), and second, to calibrate and improve numerical models.

In each centrifuge experiment, the seismic performance of the underground structure was investigated in terms of key design parameters, such as seismic lateral earth pressures, racking displacements, and bending moments using tactile pressure sensors, linear potentiometers, accelerometers, and strain gauges. Centrifuge measurements indicate that both tunnel and excavation racking versus flexibility ratios followed the expected patterns when compared to the available design procedures for an isolated underground structure (e.g., NCHRP 611). The experimental results also indicate that the presence of an adjacent mid to highrise building

slightly reduces racking displacements of the underground structure, but increases seismic lateral earth pressures. Bending moments along the excavation walls and axial forces on the struts are also shown to notably increase with the presence of an adjacent tall building. The dynamic lateral thrust acting on the sides of the underground structures is shown to roughly follow the adjacent building's base shear in amplitude and frequency content. Based on the observed results, mechanisms of interaction among the tall building, soil, and an adjacent permanent or temporary underground structure are explored in terms of: 1) the tall building's inertial forces, 2) the foundation's kinematic constraints, and 3) the building's added confinement.

Dedication

To my brother, Thomas, who has worked so hard toward his goal of becoming a firefighter.

Acknowledgements

I want to begin by thanking my parents and brother for their support throughout graduate school. My mom, Betsy, traveled to Davis to see the final experiment. My dad, Ed, flew to Colorado to see the defense presentation, thank you!

Thank you Professor Shideh Dashti, (my research advisor), for the opportunity to be a part of this project and for luring me into the area of geotechnical earthquake engineering through your class. I appreciate all of your support and guidance throughout this project. Your attention to detail, centrifuge testing expertise, and passion for geotechnical earthquake engineering raised the quality of each experiment. I don't know anyone else who works harder for the things they believe in. I appreciate your openness and willingness to talk about topics unrelated to research when it was necessary, too.

A big thank you to Professor Youssef Hashash and his students, Maria Ines Romero Arduz and Michael Musgrove at the University of Illinois, Urbana-Champaign, who contributed extensively to the design of the centrifuge experiments and the development of finite element models of the centrifuge experiments. Professor Hashash, thank you for all of your guidance and input over the course of this project.

I'm extremely grateful to the professors that made studying geotechnical engineering at CU so enjoyable. Dr. Znidarcic, thanks for outlining what graduate school would look like for someone coming back after some time away, and for instructing me in Geotechnical Engineering 2 over the summer. Also, thank you for serving on both my comprehensive and defense committees and for letting your passion for this profession shine through in your courses and advice. Professor John McCartney, your presence at CU is missed! Thank you for the encouragement and support when I was considering the PhD, and for serving on my

comprehensive committee. Thanks for being so active with the Geo-Institute student group, and for encouraging students to compete in the geo-challenge events at the Geo-Congress conferences, and helping find funding to do so! Also thanks for letting me and others know about scholarship opportunities and writing letters of recommendation. Thanks to Professor Abbie Liel for being available as a resource throughout the project, serving on my comprehensive and defense committees, and for providing detailed feedback of my dissertation draft. Your depth of knowledge in the area of structural earthquake engineering helped raise many important research questions and offered a unique and valuable perspective, thanks!

I can't imagine doing my PhD without the friends I made at CU. Over the course of a PhD, you see friends come and go, but Erik, CJ, and Melissa have been there since the beginning. Thanks for all the good times at the Geo-Congress conferences, around campus and in Boulder, and for being supportive friends. Zana, thanks for all the sound life coaching advice through the years and for being an excellent friend and office mate. Thanks to Majid Ghayoomi, who was one of the first people who exposed me to centrifuge research. I'm grateful to all my friends at CU through the years; you have made this journey possible, meaningful and fun.

This project would not have been possible without the help of a few students. Huge thanks go out to Christina Jones for her work in the final part of the project and for organizing large amounts of experimental data on NeesHub. Thank for your commitment, high energy, and focus in this project. Also, thanks for being such a solid friend! Tiago Gonzales, thanks for all the good times and your hard work in Boulder and Davis! Thanks to Xiao Fu for helping me prepare for the 2013 tests, and to Devon McLay, who was a huge help during the first summer at Davis as I was acclimating to the experimental phase of the project.

The staff at the Center for Geotechnical Modeling at UC Davis are amazing! Thank you Dan Wilson for teaching me about data acquisition, helping guide the early stages of the experiments, and being a resource even when I wasn't in Davis. Also, thank you for serving on my defense committee and providing feedback that really helped strengthen the dissertation. Thanks to Mark Stringer for explaining how many of the instruments worked and for setting up Matlab codes to convert the centrifuge binary files. Thanks to Jenny Chen, Lars Peterson, Anatoliy Ganchenko, and Peter Rojas for all the help and making my time at the centrifuge so much fun. "What are we doing for lunch?!" is a saying I will miss! I can't thank Chad Justice enough for all of his hard work and friendship! Also, thanks to Riky and Sam, and Mohammad, Jackee, Kaitlyn for being such great friends and making each summer so memorable! Mike Gomez, thanks for the education in bender elements. I owe thanks to Daniel Cimini and Chad Sugiyama for their support during model construction. Thanks to Professor Ross Boulanger for being so welcoming into the centrifuge facility and Professor Bruce Kutter for being available to talk about the research. I'm so grateful to have met and been exposed to so many fabulous, big hearted people in Davis. Your perspectives on life and science were always refreshing and stimulating.

Thank you Martin Walker at Arup, San Francisco, for consistently participating in the research update meetings and for offering your perspective as a practicing engineer. Also, thank you to Ramin Motamed, who was involved in the early stages of the project while he worked with Arup, San Francisco.

I'm grateful to both CTL Thompson and Golder Associates for exposing me to an array of geotechnical work. Thanks to Stuart Thompson at CTL Thompson for taking a chance on me and for everyone else there who I learned from and laughed with. Thanks to Dave O'Sadnick

and Matt Barrett for giving me the opportunity to work in the soils lab at Golder with Rob and Patrick!

In the life chapter previous to graduate school, I worked in New Orleans rebuilding homes destroyed by Hurricane Katrina. A shout out to the entire Prytania crew, plus Amanda, Ross, Liz, Katy, and Pete for such a good time and all the love. I was inspired and empowered by the work we did together.

I want to acknowledge Hushmand Associates, Inc. and the Los Angeles Department of Water and Power (LADWP) for providing partial funding towards the purchase of tactile pressure sensors. This work is supported by the NSF under Grant No. 11-34968 and by the Department of Civil, Environmental, and Architectural Engineering at the University of Colorado Boulder through a Doctoral Assistantship for Completion of Dissertation. Any opinions, findings, and conclusions or recommendations expressed in this material are those of the authors and do not necessarily reflect the views of the NSF.

CONTENTS

TABLES

FIGURES

Chapter 1

1 INTRODUCTION

Shallow underground structures used for public transportation are a key component of sustainable cities. The underground transportation infrastructure is often built near tall buildings with multistory basements. Although such buildings have the potential to alter ground motions in their vicinity and transmit forces to adjacent underground structures during earthquakes, these impacts are not well understood. This research involves a series of centrifuge tests to produce, for the first time, well-documented model "case histories" of the response of shallow underground structures near tall buildings under realistic confinement and loading conditions. The data from these tests serve two purposes: first, to better understand seismic soil-structure-underground structure-interaction (SSUSI), and second, to calibrate and improve numerical models that are used in design. The seismic response of a braced, temporary excavation and a permanent, cut-and-cover box structure in medium dense, dry sand are measured independently first and then when adjacent to mid to highrise buildings.

The centrifuge testing component of this project was primarily performed at the Center for Geotechnical Modeling at the University of California, Davis (UCD-CGM). The first two experiments, named T-No Bldg and E-No Bldg represent the baseline experiments in a series of six tests, to examine the seismic response of a cut-and-cover box structure and an open, braced excavation in medium-dense, dry sand (relative density of 55%), respectively when in isolation

(no adjacent buildings present). In the next pair of tests, T-Midrise and E-Midrise, each underground structure is placed in close proximity of a midrise building representing a 13-story structure. The final two experiments, T-Highrise and E-Highrise evaluate the response of each underground structure adjacent to a highrise building model. The buildings are designed to represent the dimensions and key dynamic properties (e.g., modal frequencies, base shear, and moment when possible) of a typical mid to highrise steel-frame structure in California. A sequence of six ground motions was applied to the base of the model container in each experiment. Each ground motion in the sequence provided unique characteristics in terms of intensity, duration, and frequency content, in order to evaluate the relative importance and impact of these properties on the response of the soil-structure system.

In each centrifuge experiment, the seismic performance of each underground structure was investigated with and without an adjacent building in terms of key design parameters, such as seismic lateral earth pressures, racking displacements, bending strains and moments using tactile pressure sensors, linear potentiometers, accelerometers, and strain gauges. Seismic racking, which is an important performance parameter, is defined for both a permanent box structure and a temporary excavation as the lateral transient displacement of the top of the structure with respect to its base, assuming a linear deformation pattern. Total (static and dynamic) earth pressures were measured by tactile pressure sensors mounted on both walls of each underground structure. A dynamic calibration methodology was developed for these sensors as a part of this research, in order to characterize their frequency-dependent response and compensate for the loss of pressure amplitude at high frequencies (Dashti et al. 2012; Gillis 2013; Gillis et al. 2015).

Experimental results showed that racking displacements of the permanent box structure and temporary braced excavation reduced slightly when an adjacent tall building was present, despite

larger dynamic lateral earth pressures recorded on both walls of both structures. A tall building with a deep basement appeared to slightly restrain lateral displacements in the surrounding soil and an adjacent underground structure. The permanent box structure deflected in a roughly symmetric manner in all tests, while the temporary excavation deflected (or racked) more on the free-side compared to the building side, even though the walls were connected via struts. Dynamic bending strains did not change notably on the permanent box structure with the addition of an adjacent tall building (in line with racking observations), whereas they were amplified on the excavation. Considerably larger static and dynamic bending strains along the excavation walls and larger axial forces on the struts imposed by an adjacent building indicate an increased demand as well as increased deflections along the excavation walls that were not captured solely by looking at racking displacements. Therefore, racking, although useful, may not be sufficient in evaluating the performance of braced excavations that do not deform linearly. Further, these experimental results point to the importance of taking into account the adjacent structures in the design and analysis of more flexible shallow underground structures.

The conclusions made in this dissertation are purely based on centrifuge experimental results with a limited number of structures and relatively simple model configurations, in order to evaluate SSUSI fundamentally. The results may not be generalized at this time. Parallel numerical simulations of centrifuge experiments, which are currently underway by the research team at the University of Illinois, Urbana Champaign (UIUC), will be combined with experimental observations to better evaluate the underlying mechanisms and interactions for a wider range of structures and more realistic soil conditions, in order to provide design recommendations.

Chapter 2 of this dissertation provides an overview of previous research on the seismic response of shallow underground structures, the current state of practice for the design of these underground structures, and the existing gaps in knowledge. Chapter 3 describes the design and setup of the centrifuge model experiments. In particular, since the experimental component of this research employed the tallest structures tested in centrifuge to date, the considerations and approximations necessary in their design, fabrication, and testing are intended as one of the key contributions of this research. Chapters 4 and 5 present the key results from the centrifuge experiments involving the permanent box structure and temporary excavation, respectively. Lastly, Chapter 6 summarizes the key conclusions and recommendations based on centrifuge experimental results.

Chapter 2

2 LITERATURE REVIEW

2.1 Background

Determining the seismic demand is a key component of the seismic design of any underground structure. In dense, urban environments, the seismic demand is, in turn, influenced by the presence of an adjacent building. Hence, a reliable evaluation of the nonlinear interactions between the responses of soil, the buried underground structure, and an adjacent building is necessary for safe design. This interaction is what we refer to in this proposal as seismic soil-structure-underground structure-interaction (SSUSI).

(a) (b)

Figure 2.1.1. Examples of underground structures in dense urban environments: (a) rendering of the Los Angeles metro's below-ground station next to the Bonaventure Hotel; (b) rendering of the Transbay Transit Center through downtown San Francisco (courtesy of L.A. Metro and the Transbay Transit Center, respectively).

2.2 State of Practice in the Seismic Design of Shallow Box Structures

The seismic design of underground structures has not received adequate attention in the past, because they typically perform well in earthquakes. However, the Daikai subway station in Kobe, Japan collapsed during the 1995 Hyogoken-Nambu Earthquake. This event was the first modern underground structure failure due to seismic loading, rather than ground instability (Hashash et al., 2001). The 1989 Loma Prieta and 1994 Northridge Earthquakes in California did not cause any significant damage to either the Alameda Tubes in the San Francisco Bay Area or the Los Angeles Metro, respectively. These earthquakes caused horizontal ground shaking that ranged between 0.1 to 0.25 g. It is expected that more damage to the underground infrastructure will result from stronger future earthquakes that are expected in major US cities (e.g., San Francisco, Los Angeles, Seattle, and Portland).

The seismic response of a buried box structure is controlled by the surrounding soil (Wang 1993; Wu and Penzien 1994; Hashash et al. 2001; Arango 2008). Underground structures may be affected by earthquakes in two ways: (1) ground shaking; and (2) ground failure through mechanisms like liquefaction, slope instability, and fault movement. Underground structures affected by ground shaking are the focus of this research. Four major factors influence the extent of shaking induced damage to a buried box structure: (1) the shape, dimensions, and depth of the structure; (2) the properties of the soil or rock surrounding the structure; (3) the underground structure stiffness; and (4) the characteristics of ground shaking (Hashash et al. 2001).

The seismic design of underground structures is unique in that its focus is less on the inertial response of the independent structure and more on the deformation of the surrounding soil and its interaction with the structure. Okamoto et al. (1973) showed that the seismic response

of an immersed tube tunnel was primarily controlled by soil response (shaking and deformations) and less by the inertial properties of the tunnel.

Owen and Scholl (1981) showed that ground shaking may lead to three different types of deformation in underground structures: (1) axial compression and extension; (2) longitudinal bending; and (3) ovaling/racking (Figure 2.1.1). Axial compression and extension of underground structures occur when an earthquake causes ground movements in the axis parallel to the length of the tunnel. Longitudinal bending occurs when an earthquake causes components of ground shaking that run perpendicular to the longitudinal axis of the tunnel. Ovaling and racking deformations occur when shear waves propagate approximately normal to the tunnel axis causing the cross-section of a tunnel structure to deform. Transverse shear waves transmit the greatest proportion of an earthquake's energy to underground structures (Hashash et al. 2001). Hence, racking deformations of an underground box structure caused by transverse shear waves are the type of deformation studied in this research. This type of wave can affect the cross section of the tunnel; often a plane strain perspective is taken when investigating underground structure racking deformation.

The seismic analysis and design of shallow, underground box structures, as outlined by Hashash et al. (2010), involves the following steps: (1) defining the seismic hazard; (2) developing the seismic performance criteria; (3) selection of seismic input motions; (4) 1-D site response analysis; and (5) soil-structure interaction analysis. Each step is discussed in the following subsections.

2.2.1 Seismic Hazard Analysis

The first step in the seismic design of any structure is to evaluate the earthquake hazard at the specific site of interest: identify the seismic sources, define ground motion parameters, and

compute the ground motion parameters (often the 5%-damped acceleration response spectrum, Sa (T)) at the site due to each seismic source using an attenuation relationship. The tectonic environment, properties of the surrounding faults (e.g., mechanism, rupture dimensions, and activity level), and distance to site need to be considered. The seismic hazard may be defined deterministically (i.e., deterministic seismic hazard analysis or DSHA) or probabilistically (i.e., probabilistic seismic hazard analysis or PSHA). Kramer (1996) provides more details into various seismic hazard analysis methods. At this stage, the ground motion parameters (e.g., Sa(T)) are often defined at an equivalent rock outcrop site.

2.2.2 Seismic Performance Criteria

A seismic performance criterion is needed to define how a structure should perform when subject to different earthquake motion levels. The Operating Basis Earthquake (OBE) is defined as the level of earthquake shaking that is expected to occur during the lifetime of a structure at a given site. The Maximum Credible Earthquake (MDE) is defined as the maximum level of earthquake shaking that may occur at the site within the known geologic framework (Kramer 1996). Both of these design earthquakes are defined by the DSHA process. Different design ground motions will subject the underground structure to different shaking characteristics (e.g., in terms of intensity, frequency content, and duration). Structures are expected to withstand an OBE with minimal damage, and an MCE without collapse.

2.2.3 Input Ground Motions

A suite of seven ground motions are typically selected for each of the design earthquake levels, to conduct site response and soil-structure interaction (SSI) analyses. The motions are selected to match the target design response spectra. It is important to select ground motions that contain

similar characteristics as those of the controlling earthquake event. These include amplitude, frequency content, duration, and near-fault effects. For longer box structures, ground motion incoherency effects need to be included as well. Ground motion incoherency is caused by (a) scattering and extended source effects, (b) wave passage, and (c) local site effects (Abrahamson et al. 1991; Hao, 1989; Tsai and Hashash 2010). For shorter box structures, scattering and extended source effects are generally negligible. Wave passage effects are modeled by delaying the arrival time of the ground motion along the length of the box structure. Local site analysis should include any significant variation in soil conditions at a given site (Hashash et al. 2010).

Researchers have studied the influence of ground motion characteristics on the seismic performance of underground structures. Hashash et al. (2010) reported that shaking direction and duration as well as the frequency and amplitude of velocity pulses due to near-fault Forward Directivity (FD) effects greatly influence the response of underground box structures. Liu and Song (2005) investigated the seismic response of large underground structures subject to both horizontal and vertical shaking using fully coupled, dynamic Finite Element (FE) analyses. Their results showed that the inclusion of vertical motions had a significant effect on the underground structure. Cilingir and Madabhushi (2011) performed both FE analyses and centrifuge testing to evaluate the influence of 1-D ground motion parameters (e.g., intensity, duration, and frequency content) on a circular tunnel. It was found that PGA was the most important factor affecting tunnel deformations. However, in their centrifuge testing, a rigid container was used with DUXSEAL absorbing container boundaries, which did not allow for proper deformations to be simulated in the free-field soil. Dashti et al. (2010) showed through a centrifuge experiments that Shaking Intensity Rate (SIR) has a significant effect on seismically-induced ground settlements and damage to building structures. SIR effectively quantifies the rate of earthquake energy

buildup, and is defined as I_{A5-75} / D_{5-75}, where I_{A5-75} is the change in Arias Intensity from its 5% to 75% value, and D_{5-75} is the corresponding duration. There is a clear need to better understand how various ground motion parameters affect underground structures in terms of the key design parameters of interest: racking displacements, seismic lateral earth pressures, and bending moments.

2.2.4 Site Response Analysis

Site conditions affect how seismic waves travel through the soil, and hence the amplitude and frequency content of the motion applied to the structure. It is common to perform a one dimensional (1-D) site response analysis (Idriss 1990; Matasovic 1993; Hashash et al. 2010), to evaluate the influence of local site conditions on each of the selected outcropping rock motions. A 1-D site response analysis is often performed to assess:

1. The free-field racking deformations at elevations corresponding to the top and bottom of the box structure (maximum relative lateral displacement).
2. The input ground motions at the level of the structure, which are needed for a dynamic SSI analysis.
3. The effective strain in the free-field and the strain compatible free-field soil properties.
4. Liquefaction and ground failure potential.

Site response is typically analyzed through an equivalent-linear, frequency-domain, wave propagation method (e.g., SHAKE or DEEPSOIL) or a nonlinear, time-domain approach. The equivalent-linear, wave propagation method is easy to use, well calibrated, and therefore more common. Nonlinear methods require more input parameters, validation, and more expertise and time. A nonlinear site response analysis is recommended when simulating site response under moderate to strong levels of shaking leading to more soil nonlinearities and permanent

deformations, in addition to softer soil conditions. The following steps are taken in a 1-D, equivalent-linear site response analysis (Hashash et al. 2010):

1. *Idealized Soil Profile:* An idealized soil profile is generated using knowledge about the site stratigraphy. Site conditions may be gathered through a field or laboratory investigation.
2. *Soil Model Parameters:* Soil parameters needed for the site response analysis include: the depth to bedrock, an idealized shear wave velocity (or G_{max}) profile, stress history, and unit weight. Modulus reduction and damping curves for each soil layer may be found directly through laboratory testing or indirectly using the published empirical observations (Darendeli, 2001; Vucetic and Dobry, 1991). Empirical curves should check the implied shear strength, friction angles, and any rate dependency effects (Hashash et al. 2010).
3. *Input Ground Motions:* A suite of ground motions selected to match the target, outcropping rock, design spectra will be used as input to the site response analysis. Some processing such as baseline correction may be needed to minimize drift of calculated displacements.
4. *Site Response Analysis and Results:* A 1-D site response analysis is then conducted using the equivalent-linear model parameters (from step 2), and the following results are recorded at a minimum:
    a. Racking displacement of the free-field at elevations corresponding to the height of the box structure from strain time histories.
    b. Strain compatible shear modulus and damping ratios.
    c. Maximum shear strain, shear stress, and PGA profiles.

The results of the site response analysis may be used to calculate the seismic response of an underground box structure and to evaluate the potential for ground failure (e.g., liquefaction).

2.2.5 Transverse Soil-Structure Interaction Analysis

Overview

The goal of a soil-structure interaction (SSI) analysis is to evaluate the transverse deformation of a box structure due to the deformation of the surrounding soil. The seismic design of shallow, cut-and-cover, rectangular, box structures requires consideration of SSI for two main reasons. First, the geometry of box structures is less efficient than circular tunnels for supporting static loads; therefore walls are constructed to be much thicker than for circular structures. This leads to an increased structure stiffness that is less tolerant to distortion. Increased stiffness of the structure compared to the surrounding soil amplifies SSI effects. Second, at shallow depths, the soil typically displaces more during shaking due to: (1) less soil stiffness from decreased overburden pressure, and (2) site amplification effects. In addition to deformations, lateral earth pressures under the design earthquake motions need to be evaluated to ensure safe seismic design. An accurate estimation of lateral earth pressures requires consideration of the seismic interactions between soil and structure. Closed-form solutions from circular tunnel analyses are not easily adaptable to box structures because of geometric variability. Therefore, alternatives are needed for the seismic design of shallow, box structures, as summarized below.

Simplified Frame Analysis

Through a series of dynamic, finite element analyses, Wang (1993) proposed a simple method for the seismic design of underground rectangular box structures, referred to as the *Simplified Frame Analysis Model*. This pseudo-static method calculates transverse racking of the box structure by using information about the surrounding soil, which is in turn the output of a 1-D

site response analysis. Free-field shear strains at elevations corresponding to the top and bottom of the tunnel provide free-field racking displacements. The strain compatible shear modulus is used to estimate the soil stiffness. These parameters paired with racking stiffness and geometric properties of the structure are used to calculate the racking displacement of the tunnel through the use of design charts that were developed using dynamic, finite element analyses performed by Wang (1993). More details of each step of this design procedure are explained below.

Although factors such as the embedment depth, structure geometry, and input earthquake motion all play critical roles in the response of the soil-structure system, a primary factor is the relative shear stiffness between the soil and the structure it displaces (Wang 1993). This measure of relative stiffness is referred to as the Flexibility Ratio (F), and is defined as:

$$F = \frac{G_M B}{K_S H} \qquad \text{Eq. 1}$$

where, G_M = mean, strain-compatible, shear modulus of the soil in the free-field, B = the width of the structure, K_S = the racking stiffness of the structure, and H = the height of the underground structure (see Figure 2.2.2). To calculate the racking stiffness of the structure, a lateral force is applied to the structure's roof (when pinned at its base), and the resulting lateral deflection is observed. The racking stiffness, K_S = force applied divided by the lateral displacement observed at the roof. If the flexibility ratio is less than one, the soil is softer than the structure, and vice versa for values greater than one. At the extremes, a flexibility ratio of zero implies infinite structure stiffness compared to soil and a flexibility ratio of infinity means the structure has no stiffness so that it moves with the deforming ground. Wang (1993) defined the Racking Ratio (R) as:

$$R = \frac{\Delta_{structure}}{\Delta_{free-field}} = \frac{\frac{\Delta_{structure}}{H}}{\frac{\Delta_{free-field}}{H}} = \frac{\gamma_{structure}}{\gamma_{free-field}} \quad \text{Eq. 2}$$

where, Δ = racking displacement and γ = shear strain, as shown in Figure 2.2.2 (Hashash et al. 2010). Wang (1993) calculated racking ratios using dynamic finite element analyses, which led to the development of recommended design charts (Figure 2.2.3). It was observed that circular tunnels typically deform about 10% more than square cross-section structures for a given flexibility ratio. Thus, the racking ratio of circular tunnel can be thought of as an upper bound approximation to box structure racking ratios for equivalent flexibility ratios.

Once the racking ratio has been found using the design charts, the racking displacement is imposed onto the box structure and its response analyzed. Wang (1993) suggests that the imposed racking displacement can be applied to the box structure either in the form of a concentrated force at the roof-wall joint or a triangular pressure distribution along one wall. Wang (1993) explains that for more shallow tunnels, the predominant external force from the soil should be applied as a normal earth pressure developed along the side walls because for shallower depths, there is less overburden pressure. For deeper tunnels, Wang (1993) recommends applying a pseudo-concentrated force at the roof-wall joint because for deeper tunnels, the main cause of racking comes from a shear force on the exterior surface of the roof. In general, this simplified method makes quick computations of racking possible, which can be useful for design, but limiting by assuming a roughly linear racking displacement profile in the soil, as shown in Figure 2.2.2.

Direct Dynamic Transverse SSI Analysis

Wang (1993) introduced the *Simplified Frame Analysis Model* for box structures described above as a practical seismic design method, which is an alternative to dynamic numerical simulations of the soil-structure model that are often complex and not practical for conventional design purposes. However, a dynamic, transverse SSI analysis more carefully considers the properties of each soil sub-layer and its coupled interaction with a buried structure, to find structural racking as well as other key design parameters, such as the induced lateral earth pressures (static and dynamic). Each soil layer is assigned properties that match the idealized soil profile in the site response analysis. Additionally, the dynamic numerical analysis considers the box structure directly along with the soil. In this way, the simulation can directly output racking displacements of the box structure and the free-field. Soil behavior is simulated using equivalent-linear properties. For more sensitive projects, soil nonlinearity may also be incorporated by using nonlinear soil constitutive models. Figure 2.2.5 is used by Hashash et al. (2010) to demonstrate and summarize how the dynamic SSI analysis approach works for box structures. In this figure, the free-field is located 4.5 times the width of the box structure away from the structure and the soil layers are more finely discretized.

Dynamic soil-structure interaction (SSI) analyses may be performed using the lumped mass/stiffness, finite element, or finite difference methods. In finite element and difference methods, the underground structure and surrounding soil is spatially discretized or the surrounding soil is treated as springs. Examples of the available programs for this type of analysis include: FLUSH (Lysmer et al., 1975), ANSYS-III (Oughourlian and Powell, 1982), SASSI (Lysmer et al., 1991), FLAC^{3D} (Itasca, 1995), and ABAQUS (Hibbitt et al., 1999).

Alternate SSI Analysis Methods

Two other types of SSI analyses, though not as common in current practice, may be performed to evaluate the seismic response of underground box structures. The first is the *Free-Field Racking Method*, in which one imposes deformations calculated in the free-field directly onto the box structure to evaluate its response. In the second method, one estimates seismic lateral earth pressures from the surrounding soil and applies them to the box structure to evaluate structural deformations.

The *Free-Field Racking Method* works well when the soil strata is stiff or for low intensity ground shaking during which soil remains primarily elastic. Most underground structures that are designed properly for static loading can support ground deformations that result from these conditions. This SSI method is not recommended for softer soils or high intensity ground motions, where excessive free-field distortions can lead to large and unrealistic structural deformations. The *Free-Field Racking Method* was presented by Kuesel (1969) for the seismic design of the San Francisco Bart subway stations. Also, Monsees and Merritt (1991) applied Kuesel's method to evaluate the response of rectangular frame structures of the LA Metro.

2.2.6 Seismic Design of Temporary Underground Structures

Temporary braced excavations are used to provide the space required for the construction of permanent cut-and-cover box structures. In a seismically active area, these structures must be designed to withstand some level of ground shaking. The level of shaking used for the design of these temporary structures is often lower than that of a permanent box structure, due to their relatively shorter life. Either pseudo-static or dynamic SSI analysis methods may be used in the design of a temporary braced excavation to evaluate racking displacements, in a similar manner as discussed previously for permanent structures. However, a dynamic SSI analysis is preferred

in this case due to a lack of soil cover. Figure 2.2.6 shows a schematic drawing of the racking response of a temporary braced excavation. The seismic response of temporary braced excavations has not been evaluated experimentally in the past, in order to validate the available simplified procedures and advanced numerical tools.

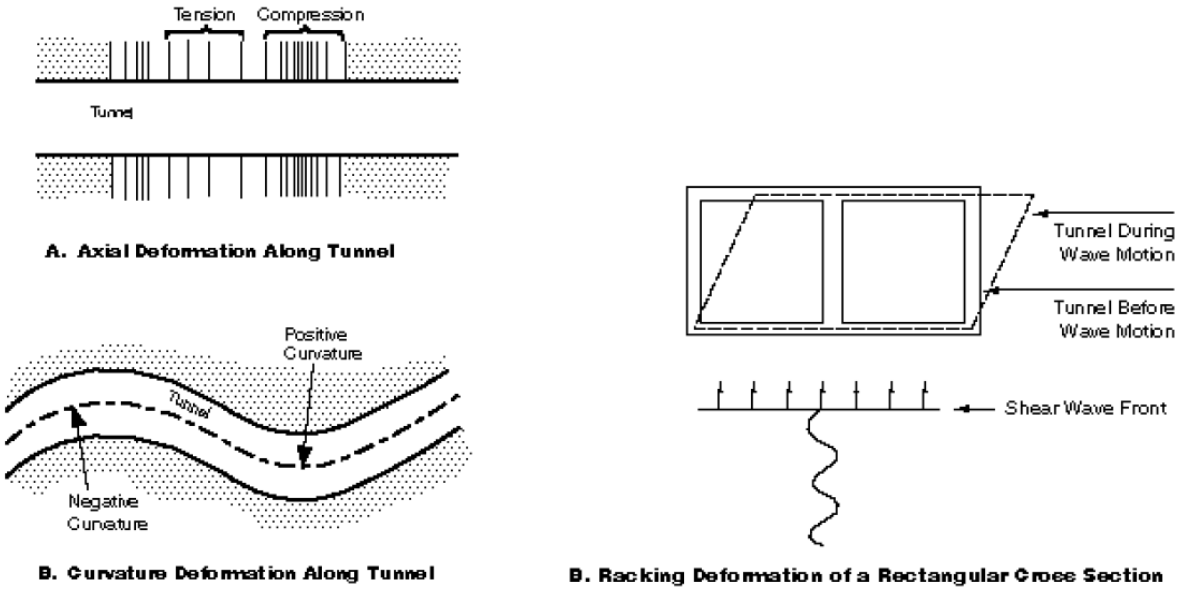

Figure 2.2.1. Different types of underground box structure deformation due to ground shaking (Owen and Scholl 1981).

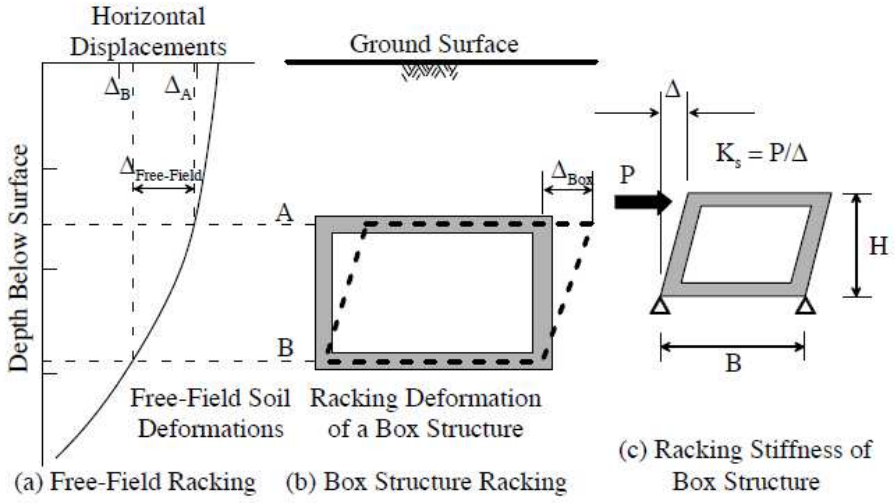

Figure 2.2.2. Graphical demonstration of how to obtain: (a) free-field racking; (b) racking of a permanent box structure; and (c) racking stiffness of a box structure (Hashash et al. 2010).

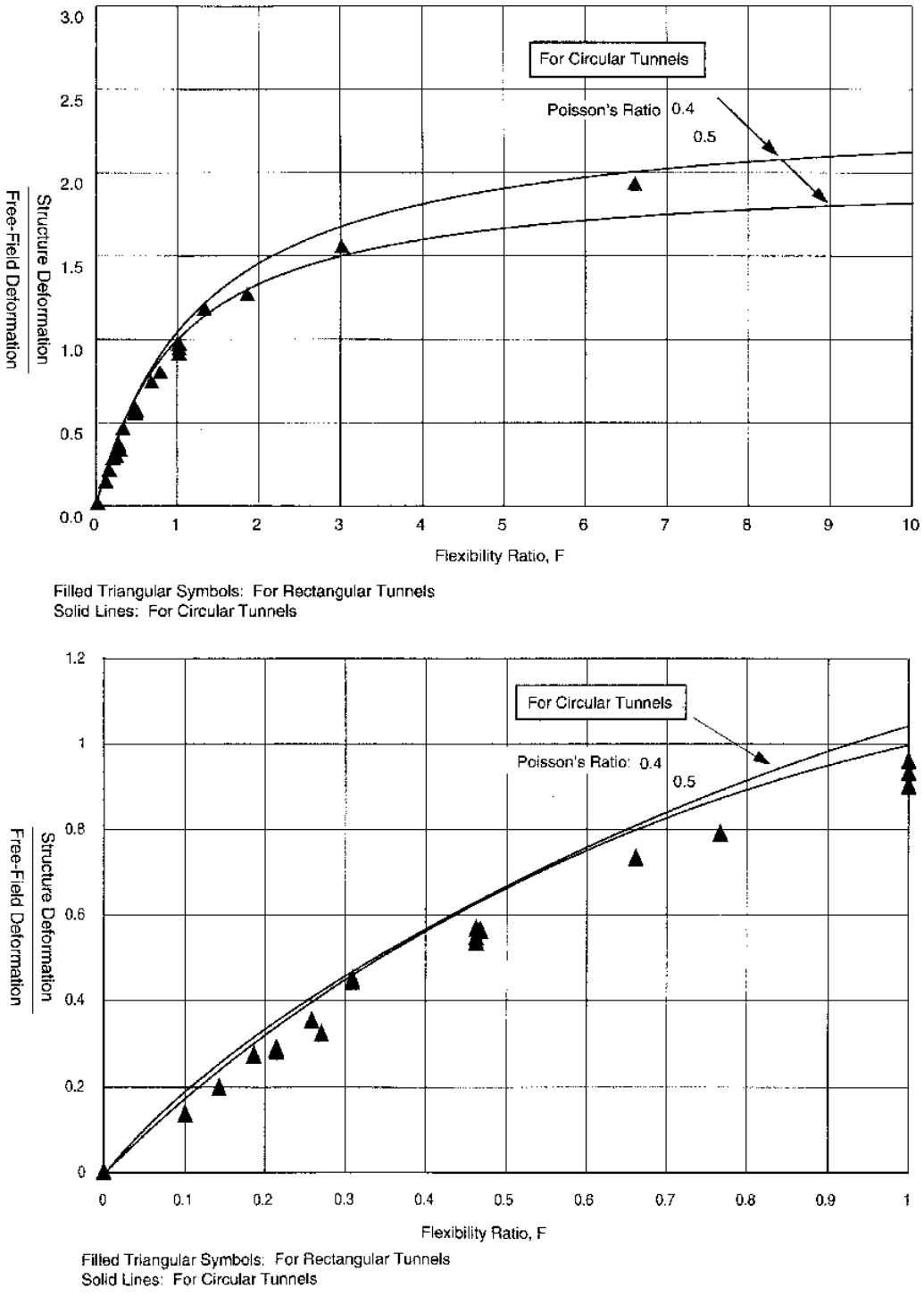

Figure 2.2.3. Racking versus flexibility ratios (R versus F) obtained from dynamic finite element SSI analyses performed on rectangular and circular tunnels (Wang 1993).

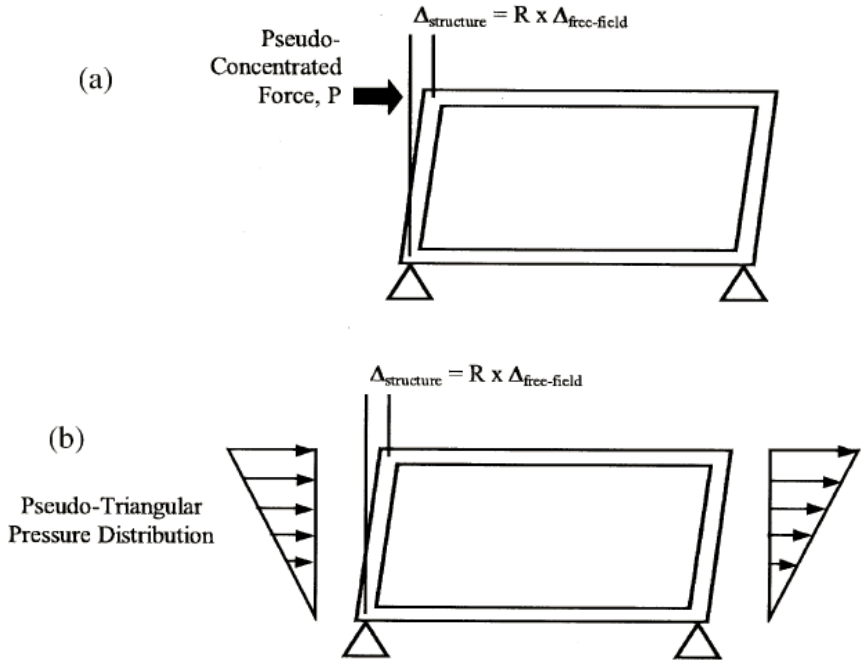

Figure 2.2.4. Simplified frame analyses : (a) pseudo-concentrated force at roof-wall joint for deeper tunnels; and (b) pseudo-triangular wall pressure distribution for shallow tunnels (Wang 1993).

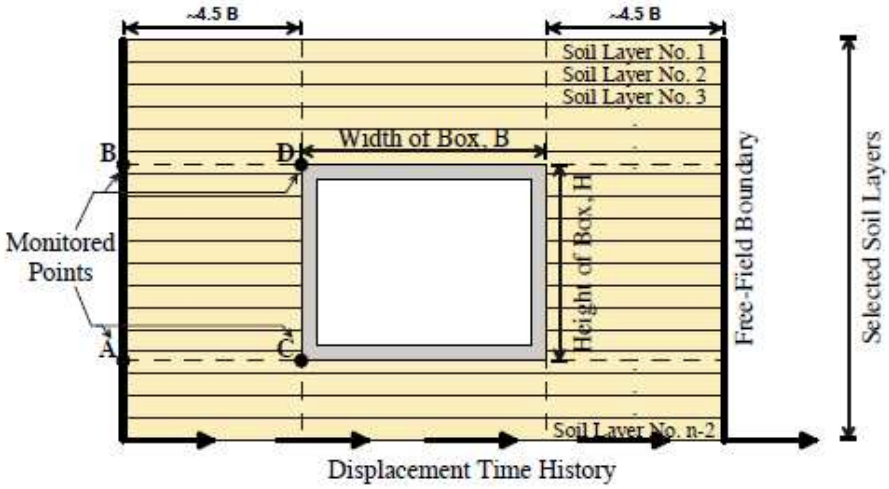

Figure 2.2.5. Schematic of a dynamic SSI analysis on a permanent box structure (Hashash et al. 2010).

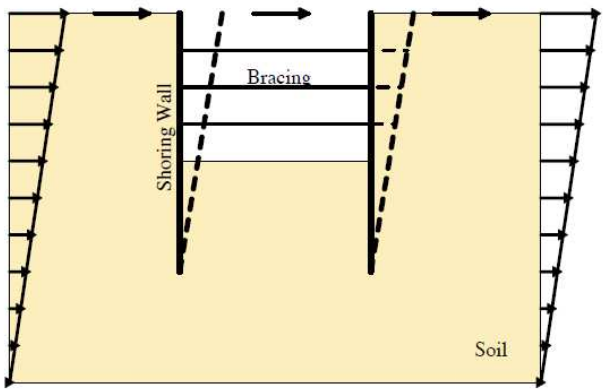

Figure 2.2.6. Schematic of racking deformations of a temporary braced excavation (Hashash et al. 2010).

2.3 Insight from Selected Analytical and Numerical Studies

2.3.1 Seismic Lateral Earth Pressures and Racking Displacements

One of the oldest and most common procedures for estimating seismic lateral earth pressures on retaining walls is the Mononobe-Okabe (M-O) pseudo-static method, which is based on work by Okabe (1926) and Mononobe and Matsuo (1929). This method relies on the properties of the backfill soil and shaking intensity to calculate seismic lateral earth pressures assuming adequate wall movements to generate active conditions (yielding walls). This method may not be applicable to a class of stiffer, rectangular, underground box structures, which do not deform enough to generate active conditions in the backfill soil. Seed and Whitman (1970) later investigated the effects of varying various parameters, such as soil and wall friction angle, slope of backfill, and the magnitude of acceleration, on seismic earth pressures obtained from the M-O method. Based on experimental observations, Seed and Whitman (1970) proposed that total thrust be applied at a height of 0.6 times the wall height, and that total maximum lateral earth pressures be split into static and dynamic components.

Wood (1973) developed a theoretical method of estimating dynamic lateral earth pressures for non-displacing, rigid walls. This method produced results that were typically 1.5 to 2.0 times greater than the M-O method. Underground, transportation box structures are not perfectly rigid and are expected to experience some deformation. Therefore Wood's (1973) method is also not applicable to this class of underground structures and may lead to excessive pressures.

Among many researchers, Gazetas et al. (2004) performed finite element analyses (FEA) on four different types of retaining wall systems to investigate the magnitude and distribution of seismic earth pressures. The ground motions used in these models had a PGA of 0.4g and were of relatively short duration. Both linear and nonlinear soil models were used in the analyses. Gazetas et al. (2004) discovered that L-shaped, reinforced concrete walls experienced dynamic earth pressures less than those predicted by the M-O method. For pre-stressed anchor pile or diaphragm walls, earth pressures were in most cases less than M-O, due to the structure's higher flexibility. This observation was especially true for the upper half of the wall. Gazetas et al. (2004) also found that the addition of severe simultaneous vertical accelerations had no significant effect on the wall's dynamic lateral earth pressures or sliding displacements at the base of the wall.

Ostadan (2005) introduced a method based on elastic wave propagation using SASSI finite element code to calculate dynamic earth pressures on rigid basement walls fixed at their base retaining an infinite, uniform elastic soil layer. The natural frequency of the soil column adjacent to the wall was determined as a controlling factor for the maximum soil pressure. Ostadan (2005) developed a simplified method consisting of: 1) obtaining the 5% damped response spectra at the base of the wall using a 1-D site response analysis method: 2) determining the value of spectral acceleration at the fundamental frequency of the soil column; and 3) using the Ostadan (2005)

equations to obtain the dynamic earth pressure profile. The dynamic soil properties and soil nonlinearity were indirectly incorporated in the method through 1-D site response analyses used to obtain the response spectra at the base of the wall. The simplified method was verified with SASSI for a variety of ground motions. The maximum pressure from this method is predicted at the top of the wall, because the highest amplification occurs at the ground surface. The simplified method compared well with Wood (1973) but was greater than M-O's method.

Brandenberg et al. (2015) analytically studied seismic earth pressures on retaining walls. They provided a framework for understanding earth pressures on retaining walls by breaking them into two components of inertial and kinematic. The authors proposed that seismic earth pressures arising from kinematic interaction is highly influenced by the ratio of the wavelength of vertically propagating shear waves to the structure's wall height. This kinematic interaction based on the principles of wave propagation and SSI explains the difference between observations made Ostadan (2005) and other researchers on seismic earth pressures. The authors noted that inertial interactions between soil and structures may be the primary source of dynamic earth pressures and that these inertial demands should be evaluated separately from the kinematic type.

Through dynamic finite element analyses of soil-underground structure models, Wang (1993) found that flexibility ratio (F) had the most significant influence on structural racking displacements with respect to those in the free-field (racking ratio). These analyses were done on a homogeneous soil profile, but they can also be applied to multi-layered soil strata. Figure 2.2.3 shows their estimated racking ratios as a function of the flexibility ratio obtained from dynamic finite element analyses on rectangular and circular underground structures.

Hashash et al. (2010) performed a series of pseudo-static and dynamic SSI analyses for single and double box structures in both soft and stiff soils using fourteen ground motions spectrally matched to a target response spectrum. Both equivalent-linear and nonlinear site response analysis results were used in their SSI analyses. Figure 2.3.1 shows their estimated response of two different box structures with different soil types. The solid line is the recommended relationship between racking and flexibility ratio proposed in the NCHRP 611 report, which is based on Wang (1993). Each group of points represents the behavior of a structure in a specific soil type; each point in a data cluster represents a specific ground motion. Hashash et al. (2010) found that pseudo-static and dynamic analyses provided similar results for cases when the flexibility ratio (F) is less than one (i.e., when the soil was very soft compared to the structure). For cases when a box structure was buried in moderately stiff soils (4<F<9), the dynamic analyses showed more scatter and higher racking ratios than the pseudo-static method. The results in this case plotted above the NCHRP 611 line. For structures in stiff soils (10<F<13), Hashash et al. (2010) found that dynamic analysis results produced slightly lower racking ratios than the pseudo-static method; the results in this case fell below the NCHRP 611 line. From these dynamic analyses, it was observed that the flexibility ratio may significantly vary even for a single structure in a uniform soil profile, subject to a specific earthquake shaking intensity. The conclusions and results presented in this section are from numerical simulations. These results need to be validated against well-documented case histories or physical model studies under controlled conditions.

2.3.2 Influence of an Adjacent Structure

Previous numerical studies have shown the significance of the interaction between soil, foundation, and structure (SFSI) on the seismic response of the underlying soil both in terms of

shaking and settlements (e.g., Stewart et al. 1999; Pecker and Pender 2000; Martin and Lam 2000; Pitilakis et al. 2004; Dashti et al. 2010; Mason et al. 2010; Ghayoomi and Dashti 2013). Comparatively, far less research has been performed on the interaction between soil and multiple adjacent structures, i.e., structure-soil-structure-interaction (SSSI).

Isbiliroglu et al. (2014) performed numerical simulations of idealized building clusters on representative, non-liquefiable sites and their coupling effects during earthquakes. They arranged building models in clusters consisting of N x N buildings, where N = 1, 3, 5, and 9. Their results showed that ground motions change noticeably in and around building clusters. The motion experienced at the foundation of structures and surrounding soil was shown to be strongly affected by site conditions, individual SSI, and collective SSSI effects (e.g., Fig. 8). In general, SSSI effects were shown to amplify for a larger number of buildings and smaller separations. The interaction among building clusters and underground structures was beyond the scope of their study.

Choy (2011) developed a wave attenuation prediction model based on forced-mass vibration testing of a model structure using centrifuge tests. The predictive model is used to estimate accelerations at other building sites at specific distances away, given material and geometric damping. In the field, Mucciarelli et al. (2003), Gallipoli et al. (2006), and Ditommaso et al. (2010) applied lateral loads to existing, constructed buildings and then removed these loads to observe their vibration. They concluded that the shaking of a building affects site response. This is especially true when the site and building have similar periods. They also showed that factors such as soil type, the characteristics of seismic waves, and the arrangement and type of buildings within a city all affect how buildings influence one another during an earthquake.

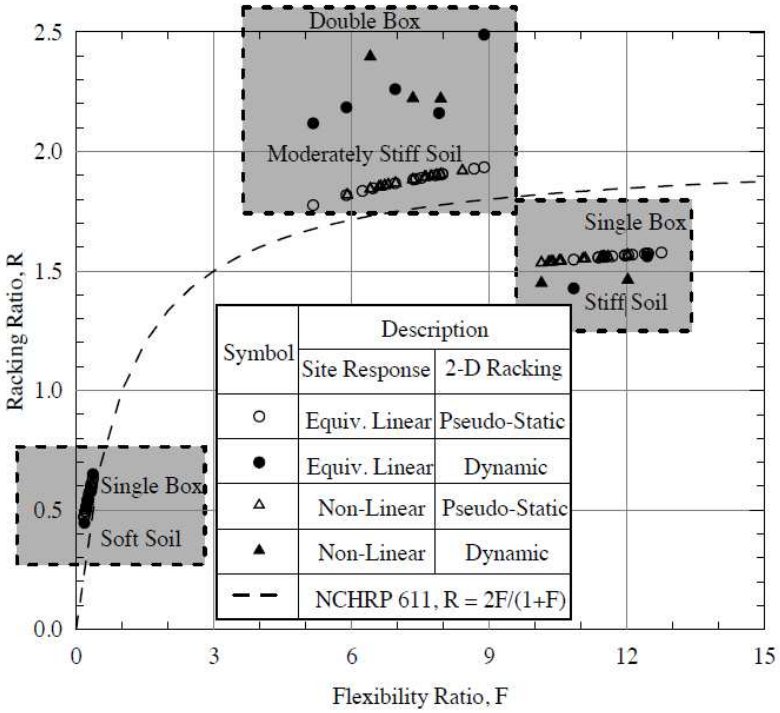

Figure 2.3.1. Pseudo-static and dynamic SSI analysis results for a single and double box structures (Hashash 2010).

2.4 Insight from Selected Experimental Studies

2.4.1 Seismic Lateral Earth Pressures and Racking Deformations

Stadler (1996) performed 14 centrifuge experiments to study the response of retaining walls subject to seismic loading and found that total lateral earth pressures were approximately triangular. The dynamic increment of lateral pressure ranged from a rectangular to triangular in shape. Stadler (1996) found that the M-O method over-predicted the experimental results for all cases, but especially the pressures on more flexible structures.

Al Atik (2008) performed two dynamic centrifuge experiments to study the distribution and magnitude of seismic lateral earth pressures on cantilever wall structures as wells as the general seismic response of a retaining wall. Strain gauges, tactile pressure sensors, and force-sensing bolts were used in the centrifuge tests to measure dynamic wall moments and seismic lateral

earth pressures. It was observed that the maximum dynamic earth pressures increase monotonically with depth and can be approximated as a triangular distribution similar to static earth pressures, thus indicating that the resultant force should be applied at 1/3 of the height of the wall from its base (0.33 H). This is important because it significantly reduces the magnitude of seismic moments compared to the Seed-Whitman's recommendation. Another critical observation was that the maximum dynamic inertial force and maximum dynamic earth pressures did not occur at the same time. Therefore, dynamic lateral earth pressures measured were typically 65% of those predicted by the M-O method. By comparing the calculated seismic coefficient of earth pressures and the PGA of soil surface, it was recommended that seismic earth pressures be ignored for cantilever retaining walls at PGA values of less than 0.4g.

Building on the work of Al Atik (2008), Mikola (2012) performed two centrifuge experiments using the same U-shaped cantilever walls, except that two levels of bracing struts instrumented with load cells were placed in between the walls of each U-shaped cantilever wall system. Also, a free-standing cantilever wall was tested in the second test. Lateral earth pressures on the walls of all structures were measured directly by tactile pressure sensors and by double differentiating bending moments from strain gauges. Experimental results showed that the dynamic earth pressure distributions did not take on an "inverted triangle" shape as derived by Seed and Whitman (1970). The Seed and Whitman theory did, however, provide an upper-bound estimate of dynamic earth pressures on U-shaped, braced and non-braced cantilever wall systems. Another important finding was that the stiff, embedded, braced retaining systems did not experience a noteworthy increase in seismic lateral earth pressures compared to a cantilever structure with a fixed base. Therefore, Sitar et al. (2012) did not recommend using Wood's (1973) method for these types of relatively stiff or constrained retaining wall systems. Similar to

Al Atik (2008) and others, it was observed that the resultant seismic lateral thrust acted at approximately 1/3 the height of the wall from its base for these types of structures.

Tsinidis et al. (2013) performed a series of centrifuge tests to evaluate the seismic performance of rectangular tunnels embedded in dry sand. Finite element analyses were also performed using ABAQUS. Both numerical and experimental results showed that horizontal accelerations were greater at higher elevations on the tunnel wall and that the tunnel experienced rocking motions during shaking. Dynamic earth pressure increments measured at the bottom of the wall were greater at the wall's mid-height, which was believed to be due to a stiffer wall section due to the presence of the wall-base slab joint. Measured dynamic bending moments and earth pressures followed the same trends. Also, large residual earth pressures and bending moments were observed after each shake due to cumulative strains during shaking.

Luu (2013) performed a large scale, 1g shake table experiment to evaluate the seismic behavior of underground structures in soft, dry sand. Underground structures consisted of two vertical shafts connected by a tunnel. Seismic lateral earth pressures were measured on one of the vertical shafts and showed that seismic lateral earth pressures are highly acceleration-dependent. Also, dynamic earth pressures followed a triangular pressure distribution on these structures, increasing with depth. The recommended location of the resultant seismic force was observed to be range from about 0.4 to 0.44 of the shaft's height, above its base. The M-O theory did not match seismic lateral earth pressures measured at small acceleration levels. The M-O method showed a good fit to the distribution and magnitude of earth pressures when accelerations reached 0.3-0.4 g, but over predicted seismic, lateral earth pressures for accelerations levels greater than 0.4 g. A reliable and direct experimental evaluation of the distribution of seismic lateral earth pressures on a range of underground structures with different backfill soils is still

lacking, which is a necessary step to validate our advanced numerical methods and design procedures.

Ozkan et al. (2013) performed a series of centrifuge tests to evaluate soil-structure interaction near underground box culverts in dry sand subject to harmonic motions. The main objectives of this study were to investigate the deformation of a box structure with varying stiffness values with respect to the free-field soil as well as seismic lateral earth pressures. An elevation view drawing of their testing configuration is shown in Figure 2.4.1. Three different model tunnels were built with different sidewall thicknesses (Figure 2.4.2). Maximum racking displacements on these structures were compared with theoretical values of racking based on relationships proposed by Penzien (2000). Model 1 racking displacements were overestimated by Penzien's relationship, while Models 2 and 3 were underestimated.

2.4.2 Influence of an Adjacent Structure

Mason (2011) performed three centrifuge experiments to evaluate how adjacent buildings influence one another during shaking (e.g., Figure 2.4.3). In this study, models representing prototype 3- and 9-story moment resisting frame structures with basement were placed in dry, dense sand. This study showed experimentally that when isolated, basement accelerations were reduced compared to the free-field surface-level motions, particularly at higher frequencies, due to embedment effects and kinematic interaction, as expected. Importantly, he found that a deeply embedded basement reduces the displacement and rotation of an adjacent structure as compared to the case where the building is not adjacent to a structure with an embedded basement. Also, Mason (2011) showed that as a taller, heavier building rocked and settled, the footings of an adjacent building experienced uplift.

In line with Mason's (2011) experimental observations of potentially significant structure-soil-structure-interaction (SSSI) effects, previous analyses have shown that shallow underground structures may be greatly influenced by the transfer of energy from an adjacent tall superstructure. Buildings, especially when taller and heavier with higher base shear and moment, are expected to influence the ground motions in the vicinity of their foundation as well as soil displacements. Hence, they are expected to apply significant forces to an adjacent underground structure. However, the influence of these forces on the performance of the underground structure in terms of the key design parameters (e.g., racking displacements or seismic earth pressures) is not clearly understood. To meet this need, a Japanese team led by Professor Towhata and supported by Japan's E-Defense, is investigating the seismic response of a set of tunnels, vertical shafts, and adjacent structures using the E-Defense shaking table facility (Figure 2.4.4). The study was deemed too complex to yield clear results on its own at the 2010 E-Defense meeting in Japan. Therefore, a simplified and more focused study of an underground structure, soil, and an adjacent superstructure was judged necessary to complement experiments taking place in Japan, which was the motivation behind this research and the grant obtained from the National Science Foundation supporting this work.

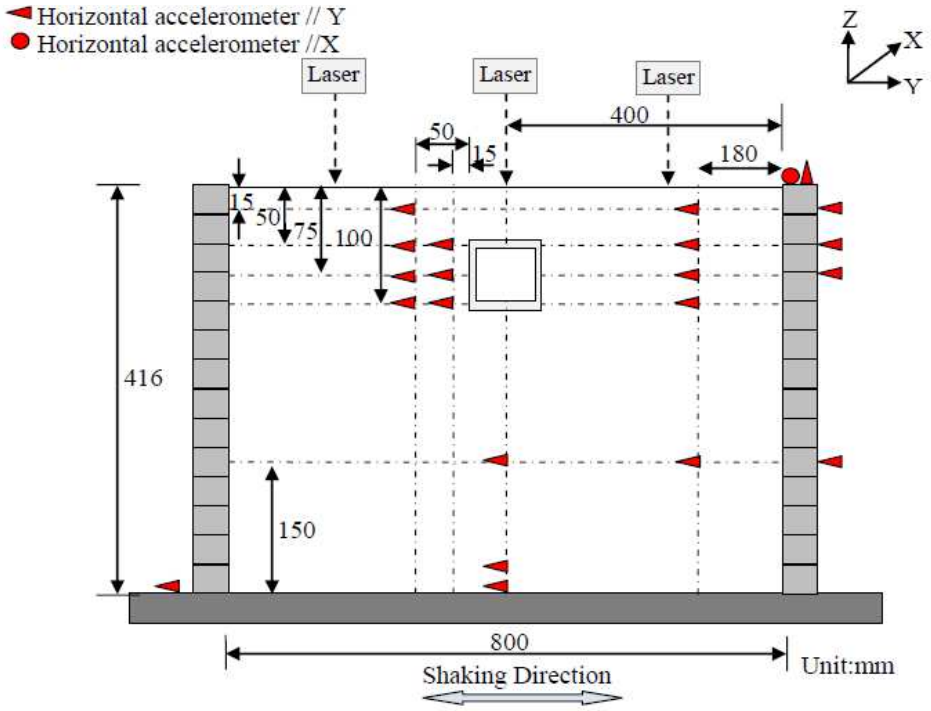

Figure 2.4.1. Elevation view of instrumentation layout of centrifuge tests on model culverts (Ozkan et al. 2013).

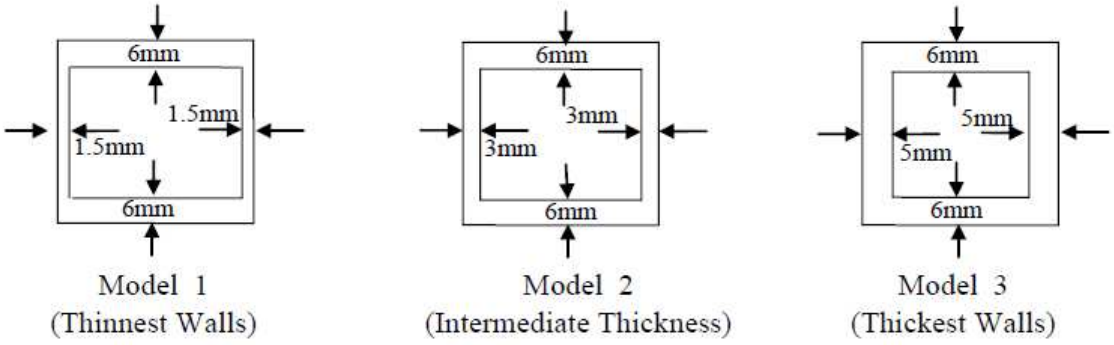

Figure 2.4.2. Three different model culverts used in centrifuge tests (Ozkan et al. 2013).

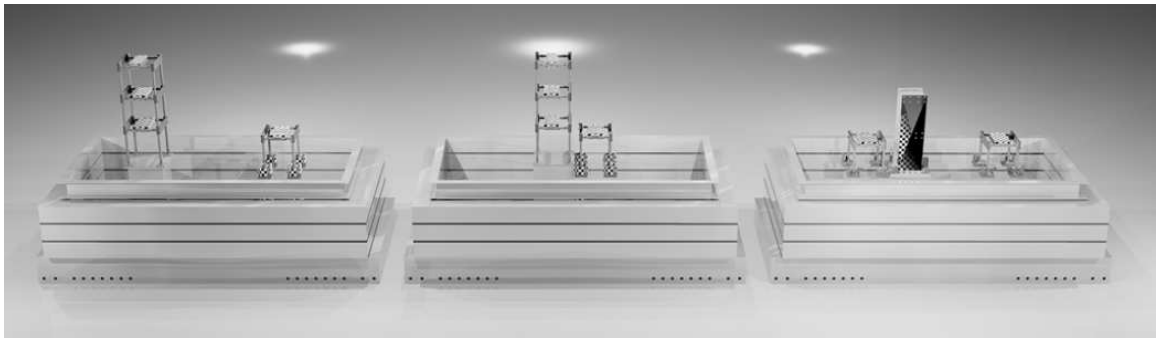

Figure 2.4.3. Experimental centrifuge series performed by Ben Mason to learn about SFSI (Mason 2011).

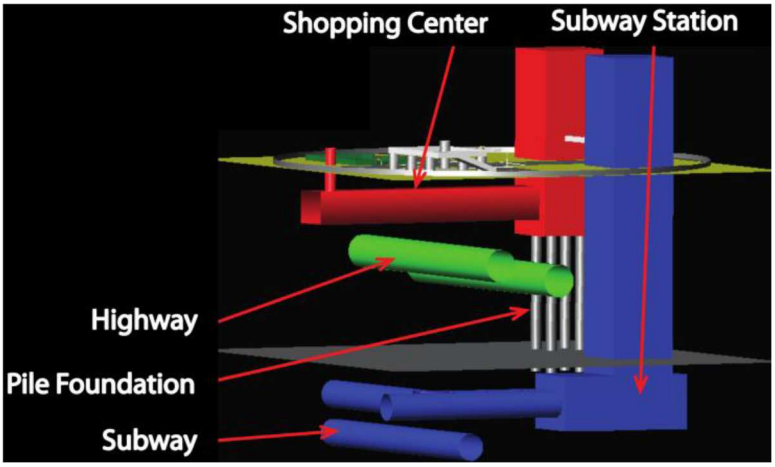

Figure 2.4.4. Japanese E-Defense supported research to investigate the SFSI of a set of tunnels, vertical shafts, and adjacent buildings (Kawamata 2010).

2.5 Summary

The current state of practice for the seismic design of underground box structures near tall buildings is primarily based on simplified procedures or numerical tools that have not been validated adequately against physical model studies. The seismic analysis of permanent or temporary underground box structures and the proper estimation of transverse racking displacements require a clear definition of the seismic demand and the seismic performance objectives. Defining the seismic demand, in turn, requires an adequate understanding of the influence of earthquake motion characteristics on the performance of the box structure. In dense

urban environments, it also requires a reliable evaluation of the interaction between the nonlinear responses of soil and the buried underground structure with an adjacent tall building. There are currently significant uncertainties in both areas:

- The influence of the embedment, geometry, and dynamic properties of an adjacent building on the demand imposed on shallow underground structures of different flexibilities during realistic earthquake motions has previously not been studied experimentally. This has led to a lack of well-calibrated analytical tools to capture seismic SSUSI in urban areas.
- Ground motion characteristics, such as the direction and duration of shaking, frequency content, energy rate, and near-fault Forward Directivity effects are expected to influence the response of underground box structures. Their influence and relative importance, however, is not understood adequately as is necessary in the validation of the numerical procedures.

To address the existing shortcomings in the state of knowledge and practice, this research aims to produce a series of well-documented model "case histories" under realistic loading conditions through centrifuge testing. The data from these tests will provide insight into SSUSI and will be used to calibrate and improve numerical models. The research plan summarized in this document is intended to serve as a key step toward a performance-based earthquake design of critical infrastructure.

Chapter 3

3 EXPERIMENTAL DESIGN OF CENTRIFUGE TESTS

3.1 Centrifuge Testing Plan

Figure 3.1.1 shows a schematic drawing of the centrifuge testing plan in this study. All centrifuge tests were conducted at the UC Davis Center for Geotechnical Modeling (UCD-CGM). Experiments T-No Bldg and E-No Bldg were designed to evaluate the individual response of a model tunnel and braced excavation in dry, medium dense sand subject to a series of ground motions. These tests served as the baseline experiments with no adjacent building present. In the subsequent tests (T-Midrise, E-Midrise, T-Highrise, and E-Highrise), the tunnel and braced excavation were each separately placed near a model mid to highrise building. Key experimental measurements included racking deformations of the box structure in relation to the soil in free-field, settlement patterns across the container, and seismic lateral earth pressures and bending moments on the walls of the underground structures. It was also critical to measure building base shear, bending moments on the basement walls, and the moment-rotation behavior of the beam and column fuses during different scenario earthquakes. In this chapter, we will discuss the limits or constraints of dynamic centrifuge modeling, instrumentation challenges, and the considerations needed to design and simulate the key components of tall buildings and their effects on shallow underground structures.

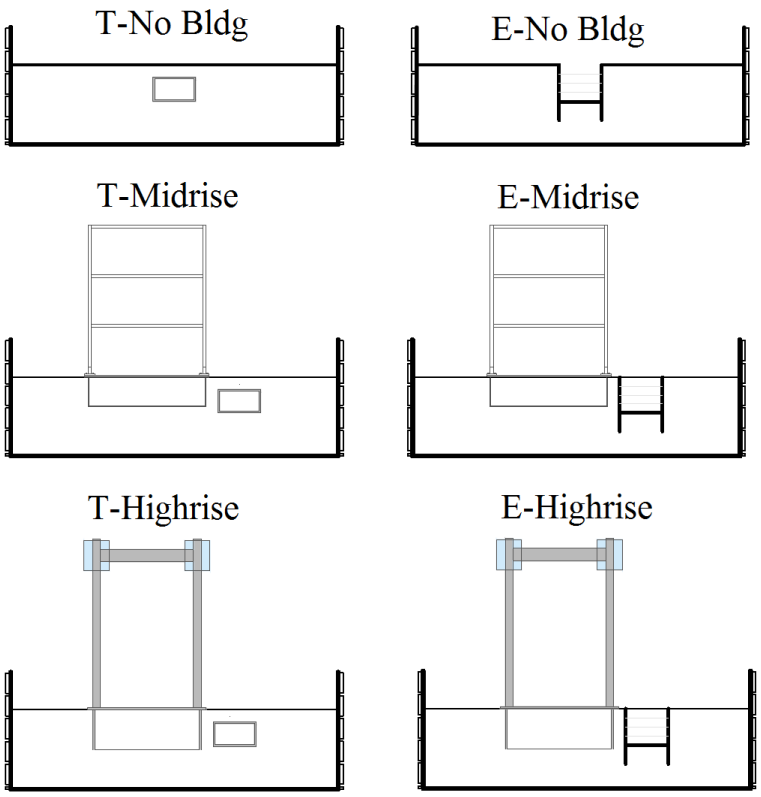

Figure 3.1.1. Schematic drawings of the centrifuge testing plan.

3.2 Selection of Centrifuge Container

The large flexible-shear-beam (FSB) container made of aluminum and rubber frames at the UCD-CGM facility was selected in this study because of its lower lateral stiffness that is representative of a soil layer in its softened state, reducing boundary effects. Although the low lateral stiffness (i.e., low fundamental frequency) of an FSB container is particularly advantages in modeling a liquefiable soil deposit, it is also used when modeling a stiffer soil specimen, because it does not add to the lateral resistance of the system. In comparison with laminar containers that also have a low lateral stiffness, the FSB container is particularly advantageous in simulating the dynamic response of complex soil-structure systems in centrifuge because of their simple and continuous boundaries. In laminar containers, special care is required to prevent soil

(and water if saturated) from penetrating into the gaps between the frames, which is not necessary in an FSB container.

A centrifugal acceleration of 65 g was selected to provide the desired prototype dimensions. Increasing the centrifugal acceleration further would allow for the simulation of larger (and more realistic) prototype model structures, but at the cost of increased weight applied on the shaking table in flight that would affect its performance.

The large size of the FSB model container (inside dimensions: 107 L x 51 W x 38 H m in prototype scale) allowed for the simulation of a 38 m-thick soil deposit in prototype scale if filled to top of the fifth ring and spun to 65g. However, to increase the available height above the soil surface for the tall buildings, soil was only pluviated up to a part of the forth container ring, thus, simulating the response of a 26 m-thick deposit in prototype scale. Further, because experiments T-Midrise, T-Highrise, E-Midrise, and E-Highrise were asymmetric, it was important to place a counter balance weight at the base of the container to minimize rocking tendencies. The amount and location of the added weight were determined in each experiment to balance moments with respect to the center of the container base.

3.3 Soil Properties

3.3.1 Soil Selection and Preparation Method

Dry, uniform, medium dense Nevada Sand was selected to provide a simplified soil stratum from which basic observations of seismic soil-structure-underground structure-interaction (SSUSI) could be made and to limit the changes in soil relative density and dynamic properties after each earthquake motion. It was recognized that the selected soil profile would not provide insight on SSUSI in soft soils nor on the influence of soil liquefaction on the response and interaction of the

system. The objective here was to undertake a fundamental study with a relatively simple configuration of structures and soil conditions. This is a necessary and fundamental step before additional complexities can be studied. Future research can build on the advances made through this work to investigate the response of other configurations of structures, soils, and yet other loading conditions. Fine, uniform, Nevada Sand (D_{50} =0.14 mm, C_u=2.07, e_{min}=0.53, e_{max}=0.9, G_s=2.66) was dry pluviated into the container to achieve a relative density of 55 +/- 5%. Pluviation was stopped and the soil surface leveled with a vacuum at the elevations corresponding to instrumentation or a structure.

3.3.2 Measurement of Soil Properties

Due to the critical importance of free-field soil properties in numerical simulations, four different methods were employed at UCD-CGM to measure soil properties in flight at locations away from both model structures and container boundaries. These methods consisted of: 1) a miniature cone penetration test (CPT); 2) bender element tests; 3) application of a small-amplitude, high frequency sinusoidal motion; and 4) acceleration recordings of centrifuge ambient vibrations. These procedures and their measurements are discussed in more detail by Jones (2015). Bender elements and ambient recordings were collected before each ground motion, whereas the CPT was only performed before the first ground motion. The high frequency sine waves were recorded before each motion of T-Highrise and E-Highrise. Figure 3.3.1 through Figure 3.3.6 provide the detailed instrumentation layouts for all experiments, showing the elevation-view location of strain gauges, linear potentiometers, bender elements, and accelerometers. Figure 3.3.7 shows a picture of T-Highrise after model construction with all instrumentation in place. Creating a true “free-field” condition was not possible in these experiments due to the inherent boundary effects in a tight space, particularly when a model

building was present. In each test, however, the "far-field" instrumentation array placed half-way in between a model structure and container boundaries was approximated as "free-field" in that test. These far-field measurements obtained from different experiments were compared with each other and with 1-D nonlinear and equivalent-linear site response analyses before making any conclusions about free-field soil response (Romero et al. under review).

A miniature cone available at UCD-CGM (Figure 3.3.8a) was used to measure tip resistance and side friction with depth in the free-field in each test prior to shaking. These values were then converted to equivalent shear wave velocities with depth using correlations applicable to young, dry, medium-dense sand. The correlations proposed by Piratheepan (2002) and Baldi et al. (1989) provided the lower and upper bound V_s profiles from the cone. Bender element pairs (sender and receiver) were placed at two depths in the free-field and under the buildings (e.g., Figure 3.3.3, Figure 3.3.6, and Figure 3.3.8b). All bender element pairs were triggered separately prior to each motion, and the wave arrival time at each receiver divided by its distance from the corresponding transmitter provided a direct measure of soil's small-strain shear wave velocity (V_s) at that depth and location. Figure 3.3.9 shows the range of V_s values obtained by two bender element pairs at depths of 8m and 21.3m in the free-field prior to different motions in T-Highrise, showing an expected trend of soil densification initially, which plateaued after the third motion.

Applying a small-amplitude, high frequency (PGA = 0.05 g; f = 500 Hz) sinusoidal motion to the base excited the model specimen at small strain levels. A high frequency motion was selected to avoid resonance and excessive motion amplification. This small amplitude motion also served as an opportunity to check the performance of the instruments and the data acquisition system prior to the application of earthquake motions. The actual base motion that

was achieved consisted of a range of frequencies (as opposed to a clean sinusoidal wave only having content at 500 Hz). Settlements were monitored across the container to ensure no soil densification occurred. An array of free-field accelerometers recorded wave propagation through soil during this motion. The frequency-dependent transfer function (TF) of accelerations recorded at the soil surface to container base was used to obtain the average fundamental frequency of the free-field soil column at small strains (f_{so}), which was then converted to an average $\overline{V_s}$ value (e.g., $\overline{V_s}$ = 4H.f_{so}, where H is the total thickness of the soil column). The average wave arrival time and travel distance from base to soil surface was also used to independently obtain the $\overline{V_s}$. Together, the frequency-domain TF and time-domain arrival time approaches provided a range of $\overline{V_s}$ values from the high frequency sinusoidal base motion.

Lastly, data was recorded by free-field accelerometer arrays under centrifuge ambient vibrations (with no applied shake table motion), which itself contained content at a range of frequencies at small strains. The TF of surface to base accelerations was used again to obtain the small strain, average f_{so} of the free-field soil column and hence, soil's $\overline{V_s}$. In this case, using the travel-time approach was not easy with such small acceleration recordings. Figure 3.3.10 shows the TF of surface to base accelerations obtained from the small-amplitude sine wave and ambient recordings in T-Highrise and the values of average soil fundamental frequency (f_{so}) corresponding to the peak TF. These methods only provide an average value of shear wave velocity ($\overline{V_s}$) for the soil column as opposed to a V_s profile with depth provided by the cone or bender elements.

These four methods of direct and indirect V_s measurement were compared with empirically obtained V_s profiles (e.g., Seed and Idriss 1970; Bardet 1993; Jamiolkowski et al. 1991; Menq 2003; Hardin and Drnevich 1972) based on the properties of Nevada Sand at D_r = 55%. Figure

3.3.11 compares the profiles and average values of V_s in the free-field obtained experimentally and empirically during T-Highrise prior to shaking. Generally, lower values of V_s were obtained indirectly from CPT measurements compared to other methods in every experiment. This is likely due to the large-strain nature of cone penetration tests. Similarly, the low amplitude sine-wave method tended to provide slightly lower estimates of $\overline{V_s}$ compared to ambient recordings and bender elements, likely due a slightly larger induced shear strains with the sinusoidal base motion. Ambient vibration and bender element results, which were judged most appropriate for obtaining small-strain soil properties, compared well with the upper bound empirical equations of V_s in all tests (e.g., Seed and Idriss 1970 and Jamiolkowski et al. 1991).

Table 3.3.1. Properties of the suite of selected base ground motions.

Event	Station	PGA (g)	PGV (cm/s)	PGD (cm)	I_a (m/s)	$D_{5\text{-}95}$ (s)	T_p (s)
Northridge 1994	Newhall - WPC	0.43	87.7	55.1	1.5	6.6	2.2
Loma Prieta 1989	Santa Cruz - L. Obs.	0.41	21.2	6.8	2.0	9.7	0.2
Landers 1992	Joshua Tree	0.28	42.7	15.7	2.3	26.1	0.7
Chi Chi 1999	TCU078	0.45	39.5	31.3	5.8	25.9	0.6
Landers 1992	Lucerne	0.72	142.9	254.2	7.0	13.1	3.7
Kobe 1995	Takatori	0.68	169.5	45.1	8.1	9.9	1.2
Loma Prieta 1989	Los Gatos	0.3	32.5	30.3	1.9	4.3	1.1

Table 3.3.2. Properties of the achieved base motions (shown in the sequence they were applied in each experiment).

Source Event	Source Station	PGA (g)	PGV (cm/s)	PGD (cm)	I_a (m/s)	$D_{5\text{-}95}$ (s)	T_p (s)
Northridge 1994	Newhall - WPC	0.46	49.4	12.1	1.0	6.2	2.2
Loma Prieta 1989	Santa Cruz - L. Obs.	0.1	10.5	0.6	0.1	11.3	0.6
Landers 1992	Joshua Tree	0.25	21.8	4.4	1.8	27.5	0.7
Chi Chi 1999	TCU078	0.34	26.9	5.0	2.5	26.8	0.7
Landers 1992	Lucerne	0.38	32.6	6.8	1.0	9.6	0.7
Kobe 1995	Takatori	0.45	52.8	16.2	3.4	11.6	1.3
Northridge 1994	Newhall - WPC	0.49	56.6	16.0	1.4	9.1	2.2
Loma Prieta 1989	Los Gatos	0.04	9.2	3.1	0.0	8.0	4.1
Loma Prieta 1989	Los Gatos	0.07	18.0	6.3	0.1	8.1	4.1

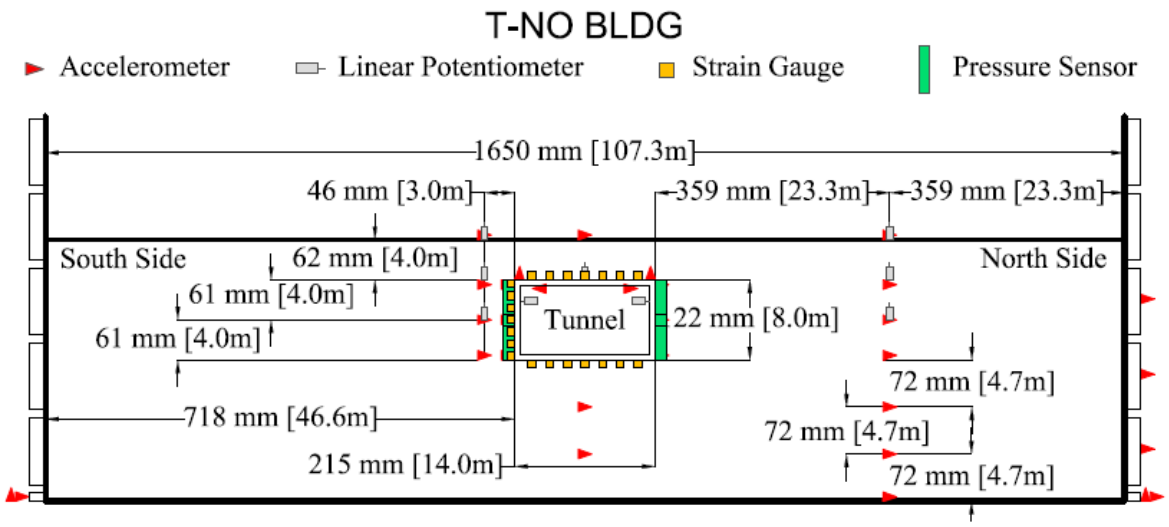

Figure 3.3.1. T-No Bldg instrumentation layout shown in elevation view (dimensions shown in model scale).

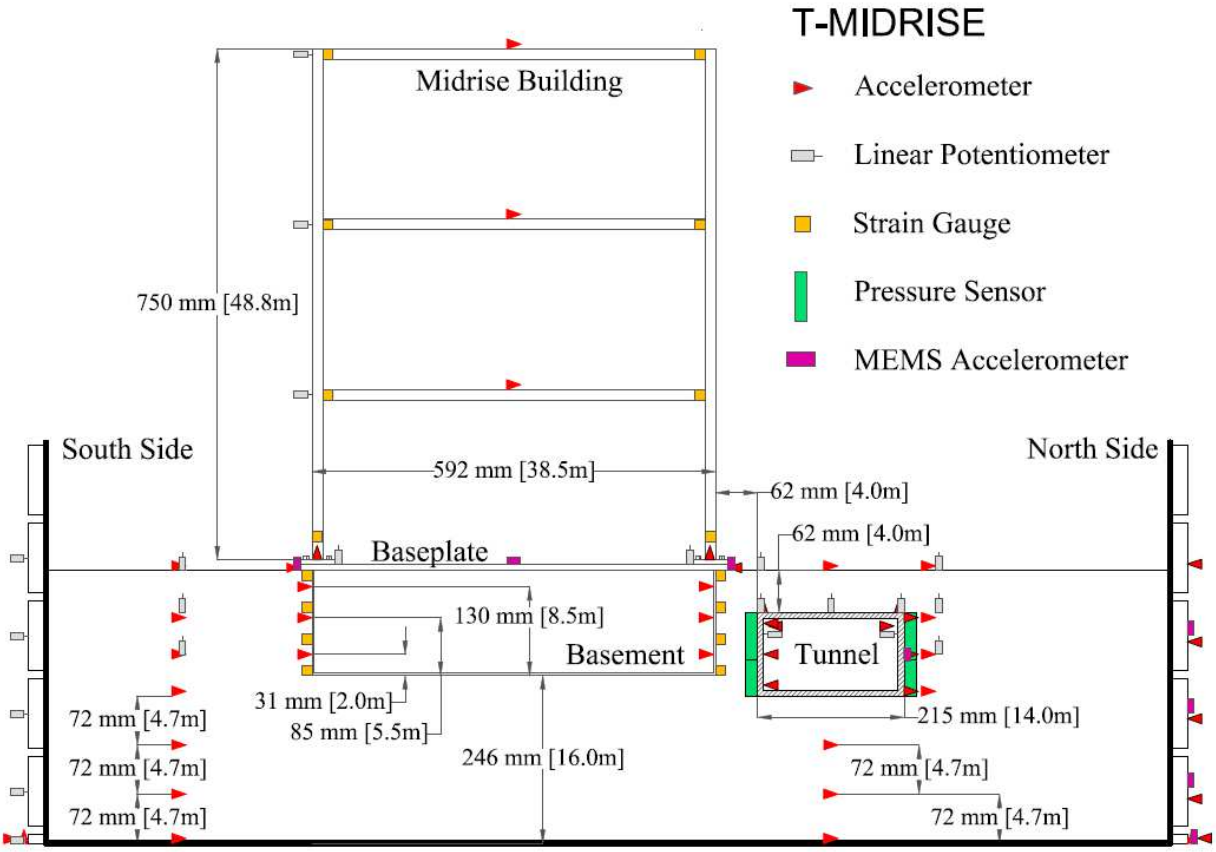

Figure 3.3.2. T-Midrise instrumentation layout shown in elevation view (dimensions shown in model scale).

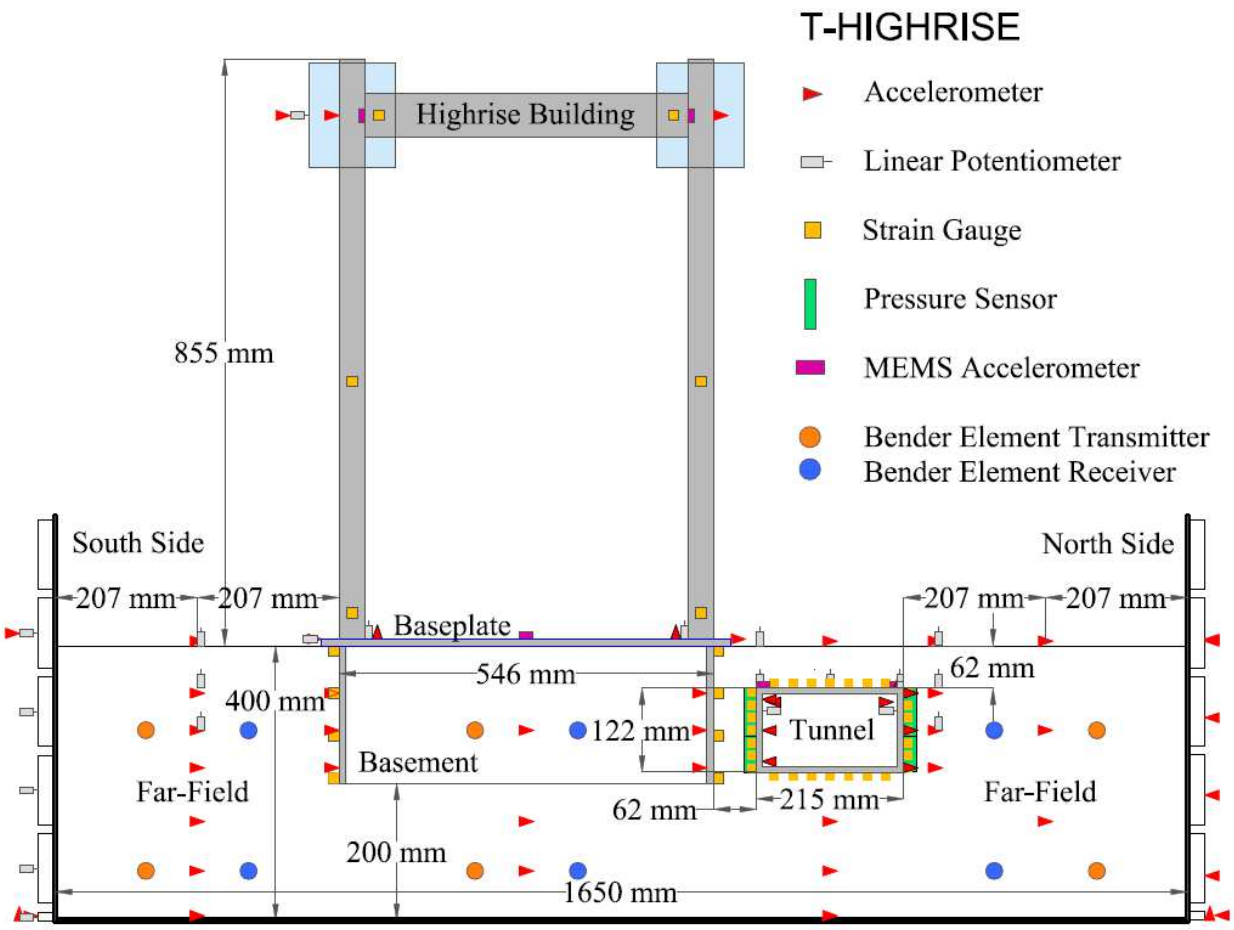

Figure 3.3.3. T-Highrise instrumentation layout shown in elevation view (dimensions shown in model scale).

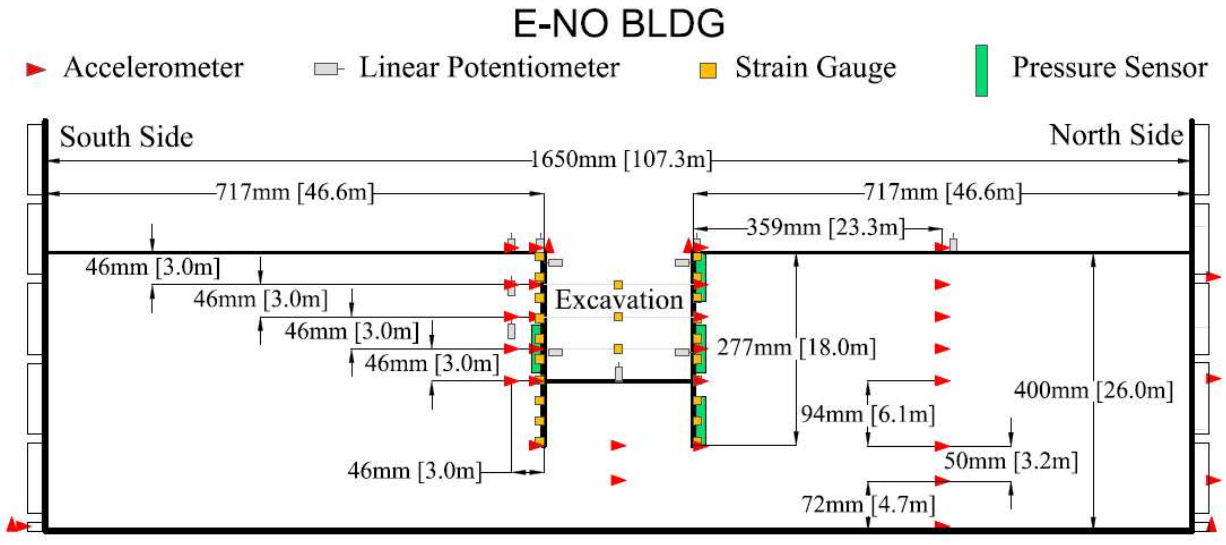

Figure 3.3.4. E-No Bldg instrumentation layout shown in elevation view (dimensions shown in model scale).

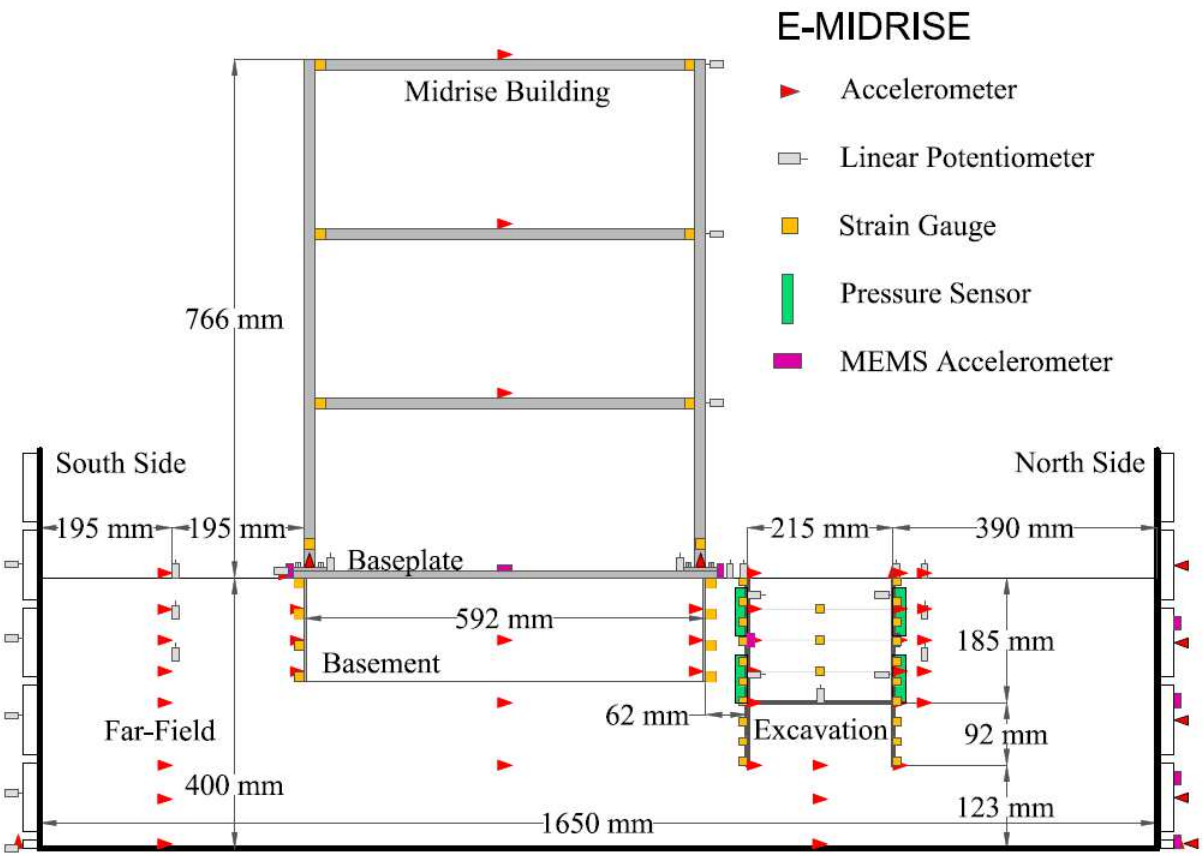

Figure 3.3.5. E-Midrise instrumentation layout shown in elevation view (dimensions shown in model scale).

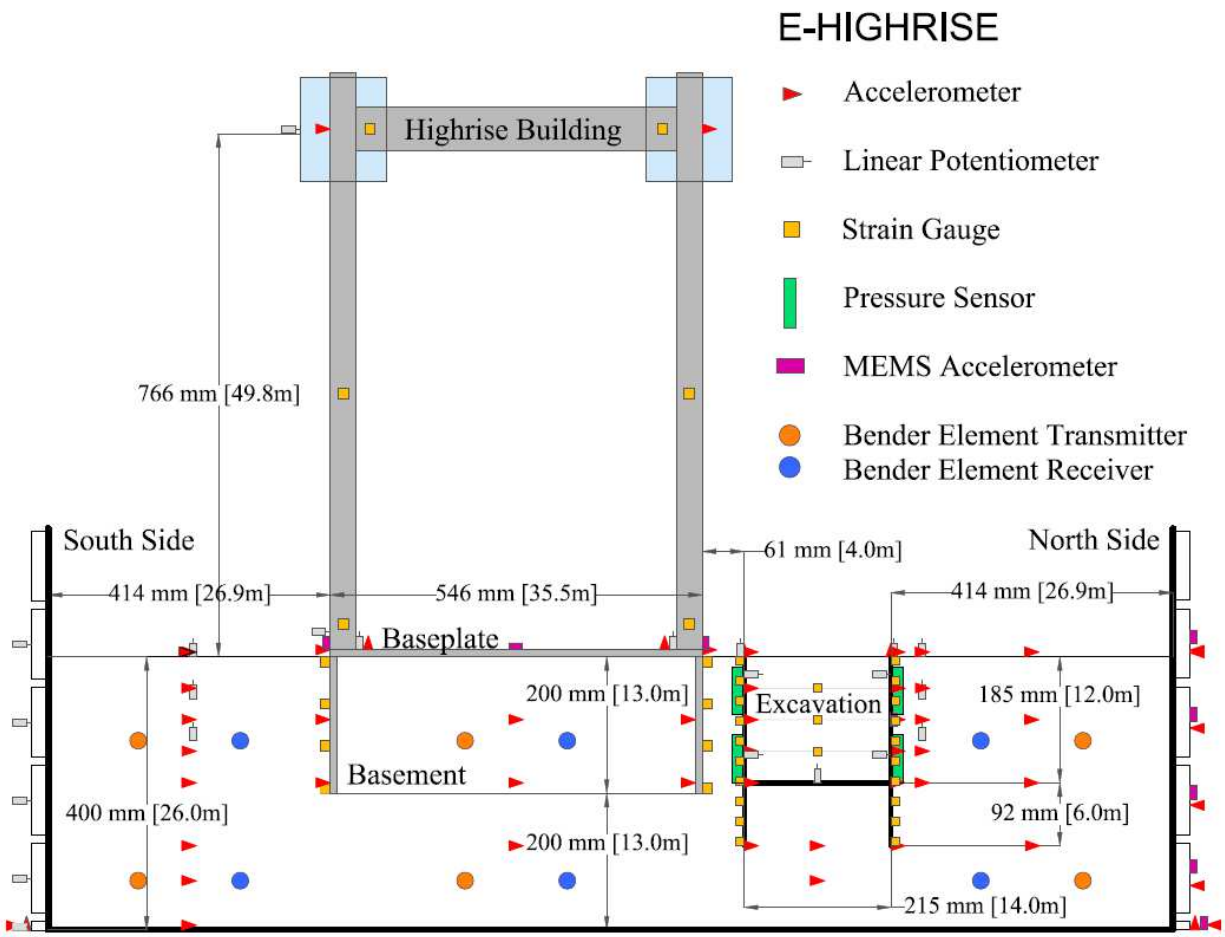

Figure 3.3.6. E-Highrise instrumentation layout shown in elevation view (dimensions shown in model scale).

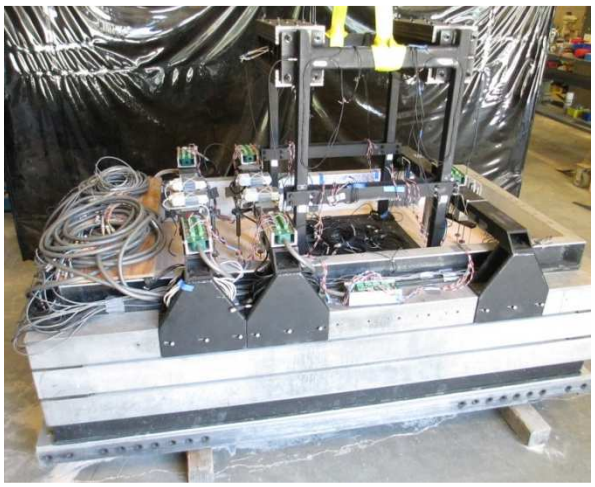

Figure 3.3.7. T-Highrise after model construction.

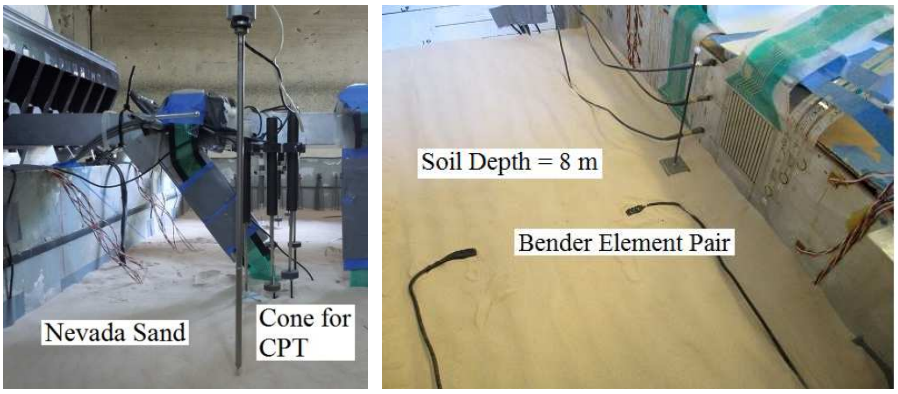

(a) (b)

Figure 3.3.8. Instrumentation used to measure soil properties: (a) cone penetration test; and (b) bender elements.

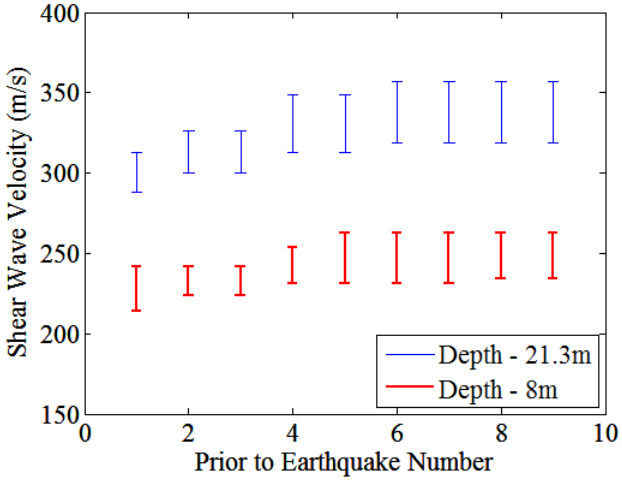

Figure 3.3.9. Range of shear wave velocities as recorded by two bender element pairs before different ground motions in T-Highrise (Jones 2015).

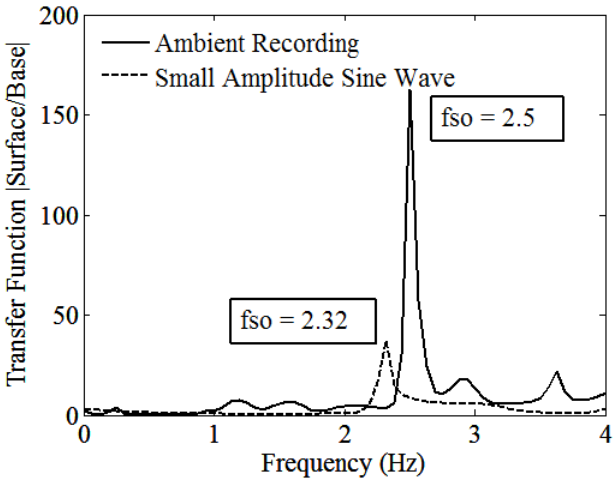

Figure 3.3.10. Transfer function used to find the modal frequency of the entire soil column using the ambient and sine wave methods.

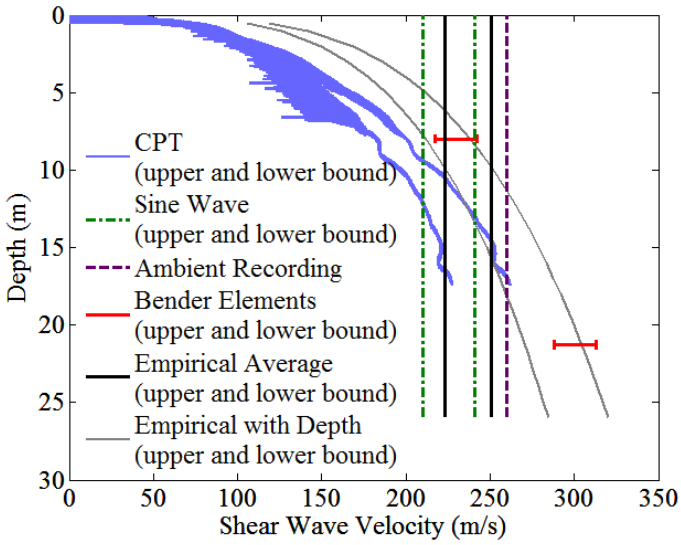

Figure 3.3.11. Measuring soil properties in the free-field (Jones 2015).

3.4 Base Motions

3.4.1 Selection of Desired Base Motions

The *desired* motion is the ideal record that is selected based on an acceptable earthquake motion selection procedure (Mason 2011). In this study, a suite of *desired* earthquake motions were selected not for a specific site, but to cover a range of amplitudes, frequency contents, and

durations. The goal was to study the influence of ground motion characteristics on the response of the soil-structure-underground structure system. The properties of *desired* base motions are summarized in Table 3.3.1, as obtained from the Pacific Earthquake Engineering Research (PEER) center's database.

3.4.2 Influence of Shaker-Container-Soil-Structure System on the Achieved Base Motions

The shake table at UCD-CGM is controlled by servo-hydraulic actuators. The dynamic properties of the shaker-model system in relation to the properties of the command signal can significantly influence the characteristics of the *achieved* base motion – actual accelerations produced by the shake table. As such, the *desired* base motions are often different from those *achieved*. The desired motions were first converted to model scale units (in both acceleration and time) and filtered to make sure large displacements beyond the shaker's stroke were removed as well as permanent displacements. Subsequently, modal frequencies of the centrifuge system were filtered out of the motion to avoid resonance and damage. A high-pass, fifth-order, acausal Butterworth filter at a corner frequency of 10 Hz (in model scale) was used to limit displacements and to remove energy at the first mode of the centrifuge (near 5 Hz). Further, frequencies between 14 to 24 Hz and 95 to 115 Hz, which corresponded to the higher modes of the centrifuge, were removed (similar to Mason 2011). Lastly, a low-pass filter with a corner frequency of 400 Hz was used to remove the content beyond the shake table's controllable bandwidth. The resulting acceleration time history was then numerically double integrated to obtain the *command* signal, which is the relative displacement between the shake table and the reaction mass (centrifuge bucket floor). A general purpose transfer function developed by UCD-CGM (Mason 2011) was then applied to the *command* signal to boost its high-frequency content and improve the match between the *achieved* and *desired* base motions.

Because the *command* signals had little to no content at frequencies below 10 Hz and between 14-24 Hz in model scale (periods greater than 6.5 s and between 2.7 and 4.6 s in prototype scale at 65g) due to filtering, they were not going to excite the highrise building near its fundamental period of approximately 4.3-4.9 s, as described in later sections. Subsequently, in T-Highrise and E-Highrise, two scaled and processed *command* signals obtained from the Los Gatos recording of the 1989 Loma Prieta earthquake were selected from the existing library of motions at UCD-CGM and added to the previously selected records, because they were processed to produce small motions in periods near 4-5 s without damaging the shaker or centrifuge.

The *achieved* motions at UCD-CGM were recorded by accelerometers mounted on the shake table and base of the container. Table 3.3.2 presents the properties of the achieved motions in T-No Bldg, and Figure 3.4.1 compares their 5%-damped spectral accelerations, Fourier amplitude spectra, and Arias Intensity time histories. Figure 3.4.2 shows the transfer functions (TF) of the *achieved* to *desired* accelerations in T-No Bldg. In most cases, the *achieved* motions were de-amplified greatly compared to those *desired*, particularly in frequencies ranging from 3 to 10 Hz in prototype scale. In terms of the peak ground acceleration (PGA), the *achieved* Loma Prieta, Lucerne, and Kobe motions were significantly de-amplified compared to the *desired* motions. The TFs are not shown for the two Los Gatos motions in Figure 3.4.2, because these motions were processed and altered by UCD-CGM specifically to achieve high-period content. Hence, their comparison with the originally selected, *desired* record was not meaningful.

The presence of the midrise and highrise buildings and different underground structures affected the weight and natural frequency of the container-soil-structure system, and hence the

shaker's performance. The container model system weight varied from 15.9 to 18.7 kN in different experiments at a centrifugal acceleration of 65g. As a result, the achieved motions were expected to vary to some degree from test to test. Figure 3.4.3 compares the 5% damped spectral accelerations, Fourier amplitude spectra, and Arias Intensity time histories of the achieved base motions in six different tests during a representative motion (Northridge), showing a reasonable match.

The repeatability of the *achieved* base motions and their dependence on the dynamic properties of the model may be quantified by the coefficient of variation (COV) of the recorded base accelerations in different tests. The COV of a given dataset is defined as the ratio of the mean of that dataset to its standard deviation (i.e., $COV = \sigma/\mu$). Here, the dataset of interest is the base acceleration measured in different tests, which varies with time. Therefore, a COV may be calculated for each motion as a function of time or frequency, characterizing that motion's repeatability among different experiments. Figure 3.4.4 shows the COV of Fourier amplitude spectra of different base motions achieved in six different experiments. Overall, the COV values were reasonably low in the frequency range of interest (from approximately 0.5 to 5 Hz in prototype scale corresponding to 32.5 to 325 Hz in model scale), but tended to increase slightly at higher frequencies that are more difficult to produce by the shake table under increased gravity.

3.4.3 Ground Motions used in the Design of Structures

Prior to the primary experiments at UCD-CGM (Fig. 1), a preliminary centrifuge test was conducted at the University of Colorado Boulder (CUB) centrifuge facility simulating free-field soil conditions with no structures present. The goal was to experimentally simulate 1-D site response without the interference of the structural models, to properly calibrate numerical

simulations of soil response that were subsequently used in the design of structures. The results obtained from this preliminary test and their comparison with different site response analysis procedures were detailed by Romero et al. (under review). A motion-specific and iterative shake table calibration procedure was conducted at CUB following the procedure described by Mason (2011), instead of applying a general-purpose transfer function to all command signals (as was done at UCD-CGM due to a higher cost). Therefore, the *achieved* base motions at CUB were closer to the *desired* records both in terms of spectral accelerations and Arias Intensity time histories. The base motions *achieved* at the CUB facility and the free-field acceleration and lateral displacement recordings at different depths were used in the subsequent design of both permanent and temporary box structures to be used in the primary experiments at UCD-CGM.

The base motions *achieved* at UCD-CGM during the primary experiments were considerably different from those *desired* as well as those *achieved* at the CUB facility. As a result, following the first two primary baseline experiments, T-No Bldg and E-No Bldg, the corresponding base motions at UCD-CGM were used to anticipate the seismic performance of the midrise and highrise building models in the subsequent tests (T-Midrise, E-Midrise, T-Highrise, E-Highrise).

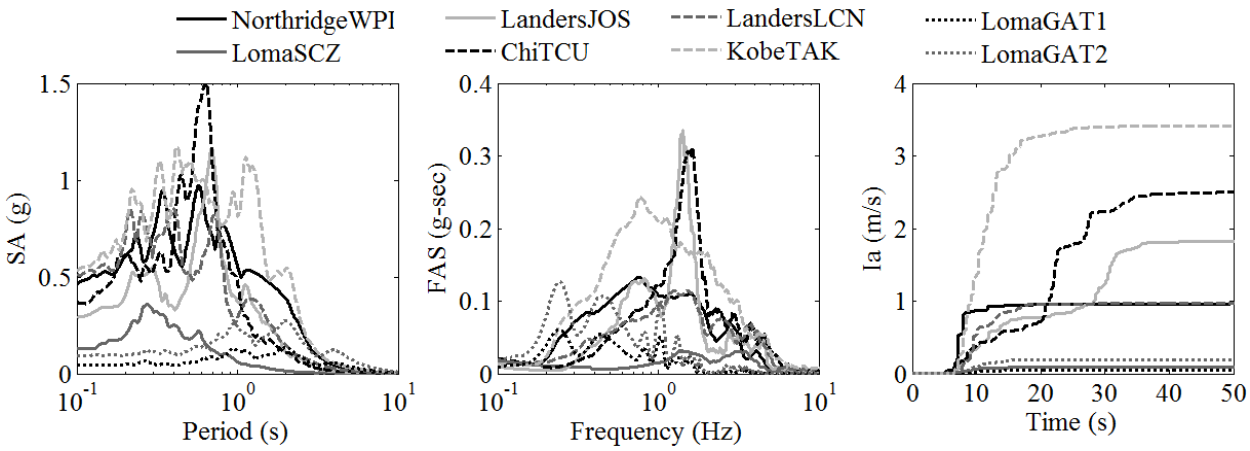

Figure 3.4.1. 5%-damped acceleration response spectra, Fourier amplitude spectra, and Arias Intensity time histories of the achieved base motions in T-No Bldg.

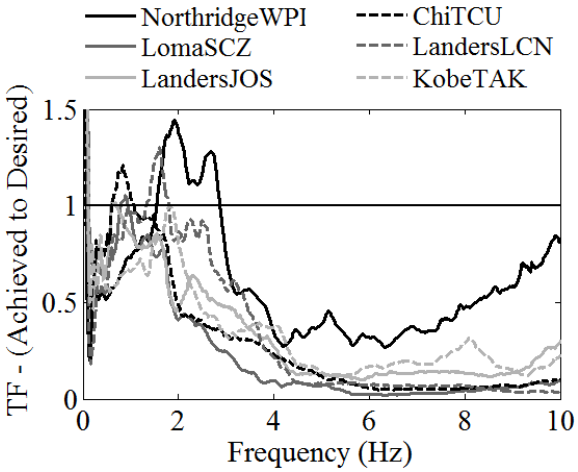

Figure 3.4.2. Transfer functions of achieved to desired ground motions in T-No Bldg.

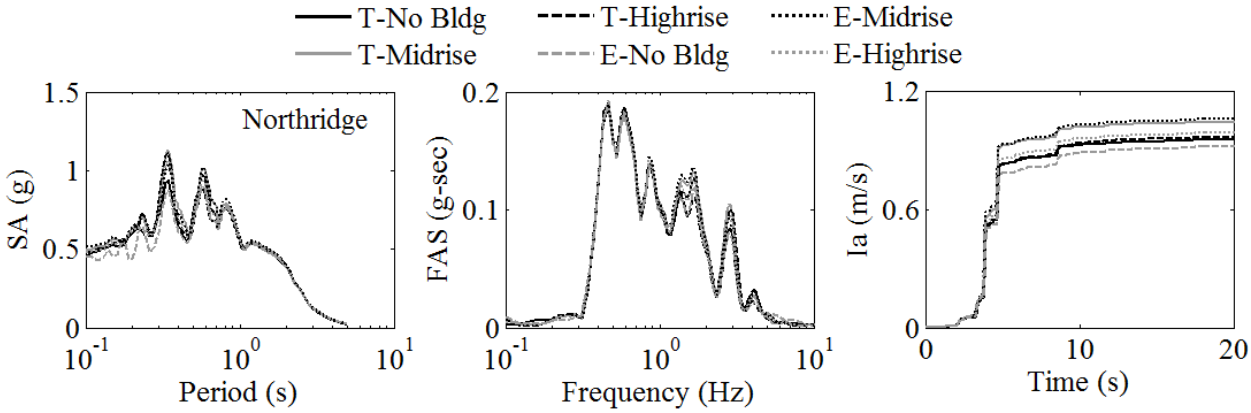

Figure 3.4.3. Comparison of 5%-damped spectral accelerations, Fourier amplitude spectra, and Arias Intensity time histories achieved during the NorthridgeWPI motion in six different experiments.

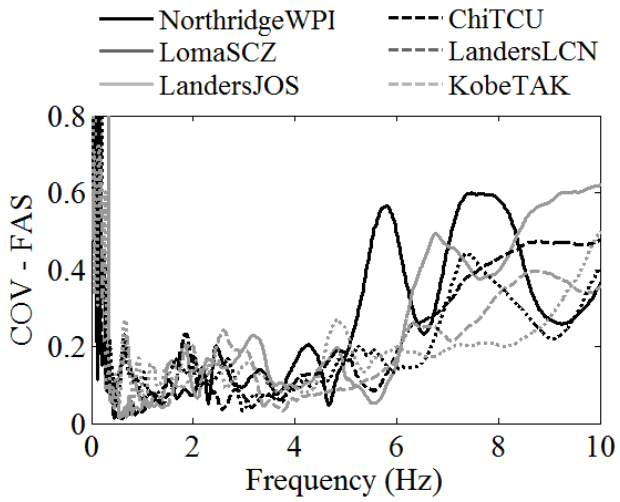

Figure 3.4.4. Coefficient of Variation (COV) of Fourier amplitude spectra during six experiments for different motions.

3.5 Modeling of Shallow Underground Structures

3.5.1 Design Approach

3.5.1.1 Permanent Box Structure

A parametric study was undertaken to select the size and stiffness of a realistic permanent box structure in prototype scale units. Six different structures were considered representative of a transportation tunnel, as shown in Figure 3.5.1. The goal was to select a box structure that would undergo similar and slightly larger racking displacements compared to the free-field soil (Racking Ratios or *R* values of approximately 1 to 1.5), while satisfying the constraints of a limited centrifuge container. It was preferred to select a single box structure with the smallest realistic dimensions to increase the separation between structures and container boundaries and hence, minimize boundary effects, particularly in later tests with the addition of an adjacent large building.

The racking displacement and stiffness of different box structure options were estimated and compared with those of the soil in free-field based on the NCHRP 611 guideline. 1-D site

response analyses were first performed to evaluate the deformation and shear stiffness of the free-field soil during each motion. Multi-degree-of-freedom (MDOF), lumped mass, 1-D site response analyses were conducted in DEEPSOIL (Phillips and Hashash 2009) using equivalent-linear and nonlinear soil models. Subsequently, finite element analyses of the free-field site response were conducted in OpenSees using the nonlinear, Pressure-Dependent-Multi-Yield (PDMY) soil model (Elgamal 2002; Yang 2000), as detailed by Romero et al. (under review). Table 3.5.1 and Table 3.5.2 summarize the soil model parameters used in these 1-D site response analyses and Figure 3.5.2 and Figure 3.5.3 show the V_s profile, modulus reduction curves, and damping curves used in the DEEPSOIL analyses. Accelerometer recordings during the preliminary free-field centrifuge test at CUB were also used to experimentally evaluate site response in the free-field. In this way, free-field racking displacements corresponding to the elevation of each box structure option shown in Figure 3.5.1 were estimated during each ground motion from equivalent-linear and nonlinear DEEPSOIL analyses, nonlinear OpenSees analyses, and actual centrifuge measurements. Figure 3.5.1 presents the maximum free-field racking displacements obtained from either of the three types of site response analyses and the CUB centrifuge test recordings for each motion and structure height option.

To estimate the peak racking displacement of the box structures based on the NCHRP 611 guidelines, the flexibility ratio (F) needed to be calculated as $F = (G_m.B)/(K_s.H)$, where G_m is the strain-compatible shear modulus of soil in the free-field, B is the width of the box structure, K_s is the racking stiffness of the structure, and H is the structure height. To estimate G_m, the equivalent shear strain (γ_{eq}) was needed in the free-field. The maximum free-field soil shear strain (γ_{max}) was estimated during each motion by dividing the corresponding maximum racking displacement by the structure height. The small-strain, maximum soil shear modulus (G_{max}) was

then estimated at the depth corresponding to the mid-height of each structure option using the average of empirical relations proposed by Seed and Idriss (1970), Bardet (1993), Jamiolkowski et al. (1991), Menq (2003), and Hardin and Drnevich (1972). The median modulus reduction curve proposed by Darendeli (2001) at that depth was adopted and corrected for the implied shear strength of soil, as detailed by Romero et al. (under review) and shown in Figure 3.5.3. The equivalent, free-field, shear strain ($\gamma_{eq} = 0.65\gamma_{max}$) was subsequently estimated during each motion, which was used together with G_{max} to obtain G_m from the corrected modulus reduction curve.

The racking stiffness of each box structure option was estimated through 2-D frame analyses with a known horizontal load applied to the roof of the frame, keeping the base nodes fixed from displacement but not rotation (NCHRP 611). The ratio of roof lateral load to displacement was subsequently used to obtain the racking stiffness (K_s) of each structure option. The Flexibility Ratio (F) could then be calculated. Having F and the maximum free-field racking displacement in Figure 3.5.1 ($max|\Delta_{FF}|$), the racking ratio ($R = (max|\Delta_{structure}|) / (max|\Delta_{FF}|)$) was estimated based on the NCHRP 611 guideline, $R = 2F/(1+F)$. The maximum racking of the structure ($max|\Delta_{structure}|$) could then be obtained for each structure option and ground motion, as shown in Figure 3.5.1.

Box structure Option 4 provided racking ratios of near 0.9 to 1.6, while simultaneously having the smallest realistic dimensions to help maximize separation with the centrifuge container. Figure 3.5.4 shows the R versus F values estimated for structure Option 4 during different motions based on free-field deformations obtained from equivalent-linear and nonlinear site response analyses and CUB accelerometer recordings.

The box structure Option 4 was designed based on the material properties of reinforced concrete. Aluminum is often used to fabricate a small scale model instead of reinforced concrete because of its similar unit weight and easier fabrication. However, the equivalent section thickness of aluminum had to be calculated to keep the racking stiffness (K_s) of the box structure the same as target structure Option 4. Table 3.5.3 summarizes the properties of the box structure as originally designed and simplified for centrifuge testing in prototype scale units. The dimensions of the equivalent aluminum structure were converted to model scale units (at 65g) for fabrication. The racking stiffness of the fabricated model box structure was subsequently experimentally measured by fixing its base, applying a known load to the roof, and measuring the lateral displacement. Table 3.5.3 provides the estimated racking stiffness of the centrifuge model structure obtained both analytically and experimentally, which were in good agreement.

Later during the primary centrifuge experiments conducted at UCD-CGM, the accelerometer recordings in the free-field (e.g., shown in Figure 3.3.1) were double integrated to obtain the maximum free-field racking displacement ($\max|\Delta_{FF}|$) corresponding to the elevation of the box structure during each motion. Accelerometer recordings on the roof and base of the box structure were similarly used to obtain the peak structural racking ($max|\Delta_{structure}|$). These values that were actually recorded in T-No Bldg are presented in Figure 3.5.1 in comparison with those estimated during design. Both free-field and structural racking displacements measured were smaller than those estimated during design because of significantly weaker base motions achieved in the UCD-CGM centrifuge tests compared to those at CUB, as previously discussed. However, the trends were similar to those expected, and the *R* values were close to design.

3.5.1.2 Temporary Excavation

A target temporary braced excavation was first designed in accordance with FHWA-IF-99-015. 2-D finite element analyses were performed in Plaxis to evaluate the stability of the temporary excavation under static and seismic loads with and without an adjacent highrise building. Table 3.5.4 summarizes the hardening soil model parameters used in the 2-D finite element analyses of the temporary excavation. At the design stage, the presence of an adjacent building was simulated only as an added overburden pressure of 658 kPa on a massless plate (corresponding to a 50-story building). Although in reality, temporary excavations in seismic regions are often designed for a lower level earthquake scenario, the same suite of acceleration time histories used to design the permanent box structure were implemented in its design (i.e., the same base accelerations measured in the CUB centrifuge test).

Figure 3.5.5 shows an example base acceleration time history used as input to the Plaxis2D model (KobeTAK). Figure 3.5.6 shows the maximum relative lateral deflection of the two excavation walls estimated during the KobeTAK motion with and without the presence of an adjacent building. The maximum absolute bending moments and shear forces along the walls and the maximum axial forces on the struts were checked against their corresponding design strength values (AISC 2006), to ensure stability. As shown in

Figure 3.5.7 and summarized in Table 3.5.5, for the original excavation design with a horizontal strut spacing of 4m, the strength values were exceeded under dynamic loading. Therefore, the horizontal strut spacing was reduced to 2m for the target excavation to ensure a minimum FS of 2 under all conditions considered.

This target braced excavation was, however, designed based on the properties of steel soldier piles and steel tube struts (as summarized in Table 3.5.6). Equivalent aluminum wall sections and aluminum tube struts were selected for the centrifuge model to provide the same

equivalent racking stiffness (K_s) as the designed target braced excavation, while using the available wall and strut section properties to avoid costly custom design fees, and simultaneously increasing horizontal strut spacing to a practical level in centrifuge allowing for instrumentation and wiring. Table 3.5.5 summarizes the minimum factors of safety (FS) calculated on the walls and struts of the simplified centrifuge model design under static and dynamic conditions, with and without the adjacent building present. The minimum FS against wall shear dropped below 1.0 under dynamic loading based on the CUB motions, as shown in Table 3.5.5. However, since immediately following T-No Bldg, base motions were known to be significantly weaker at the UCD-CGM facility compared to those used in design (CUB motions), the estimated FS values were judged to be acceptable.

3.5.2 Model Fabrication and Testing

The simplified permanent box structure model was constructed using four aluminum plates, each with a wall thickness of 8.8 mm. The roof and floor sections were welded to the inside upper and lower corners of the wall plates to provide fixed connections. After the box structure was built, its racking stiffness (K_s) was evaluated experimentally by clamping the base of the structure and applying a lateral load at the top of the wall. The applied lateral load divided by the measured lateral displacement at the roof provided an experimental measure of K_s, which was then compared with the design value obtained from a frame analysis. The experimental value of K_s after model calibration was less than the design value, likely due to incomplete penetration of welding across the wall thickness. Therefore, small angle aluminum sections were glued to the four inside corners of the box structure covering its full length, in order to increase K_s. Table 3.5.3 shows that the experimentally obtained value of $K_s \approx 26.6$ MN/m/m after this

modification compared well with the design value of 25 MN/m/m. Figure 3.6.5b shows a picture of the model permanent box structure after fabrication and instrumentation.

Fabrication of the temporary excavation was more challenging than the permanent box structure due to additional components that needed to be held together during model preparation and the amount of instrumentation with limited space. The final design specified 36 struts that needed to be length adjustable for model construction. Also, a pin connection between the excavation wall and the struts was required, as the struts were intended to serve only as axially loaded elements. Figure 3.5.8b shows the excavation wall with the bracing struts installed after model construction. Each strut was constructed using a hollow aluminum tube with an insert at both ends that could be adjustable in length. Each inserts was constructed using a thread, a steel acorn nut, and two lock nuts. The acorn nut connected the strut to the excavation wall. The excavation walls were machined with small round indents at the location of the struts, to provide a ball (strut) and socket (indent) type connection that would allow rotation (see Figure 3.5.8b). Model construction was time consuming for the excavation tests, since after soil pluviation each strut needed to be placed into position, length adjusted, and then the lock nuts tightened to prevent the strut length from changing during the test.

3.5.3 Instrumentation Design

Racking displacement of the tunnel and free-field soil during shaking in addition to seismic lateral earth pressures on the walls of underground structures were critical parameters to measure reliably in centrifuge. Other important measurements were accelerations at key locations within the soil and structure, bending moment distributions on the walls, axial strains on the excavation struts, and settlement patterns across the model after each motion.

Four primary types of sensors were employed on the two underground structures: accelerometers, linear potentiometers (LPs), strain gauges, and tactile pressure sensors. Analog cameras were also used to monitor the experiment and the movement of the cone penetration device into soil before and after testing. Miniature ICP accelerometers with a 100 g capacity were placed horizontally (in the direction of shaking) within the soil in the free-field and near-field, on the tunnel walls, LP holders, container frames, and the shake table. Double integration of these accelerations could also provide transient lateral displacement time histories at different locations. Vertical accelerometers were placed on the tunnel and container base at the two ends to monitor their rocking potential.

LPs were used to measure settlements in the free-field and near-field at different elevations as well as the tunnel. Racking displacement of the permanent box structure was measured directly by four LPs that were mounted on a bracket attached to the bottom of the tunnel, as shown in Figure 3.5.9a. In this way, LPs provided direct measurements of the lateral displacement of the roof of the tunnel with respect to its base. Horizontal LPs were placed at the top and bottom of the braced excavation, which were connected to longer holders attached from the top to the instrumentation rack, as shown in Figure 3.5.9. These longer LP holders were reinforced to minimize their independent vibration and bending. To monitor the independent movement of LP holders, accelerometers were placed next to the LP, as shown in Figure 3.5.9. In some cases, these accelerometers indicated a small degree of independent vibration, which affected the LP recordings of lateral displacement. As such, in cases where no permanent displacement was expected or measured, transient displacements obtained indirectly from accelerometers were judged more reliable than direct LP measurements.

Tactile pressure sensors (manufactured by Tekscan Inc.) were used to measure static and dynamic lateral earth pressures on the tunnel walls. Tactile pressure sensors are flexible, thin sheets containing a matrix of sensels (sensors), allowing them to measure pressure distributions without soil arching effects. The sensor model 9500 was used, which contained a 14 by 14 matrix of sensels, a shown in Figure 3.5.8a. This sensor was selected due to its high sampling rate capability (e.g., 4000 samples/sec/sensel) to avoid under-sampling in the high frequency environment of the centrifuge. These sensors require proper static and dynamic calibration, conditioning, and equilibration before they can be used reliably in dynamic centrifuge modeling (detailed by Dashti et al. 2012 and Gillis et al. 2015). Tactile pressure sensors are equipped with a separate data acquisition system and software. Hence their recordings must be synchronized with other instrumental recordings manually after the test.

Strain gauges were placed around the tunnel and excavation walls in two arrays in a half-bridge configuration. Each array was placed 16 cm away from the center of the underground structure along its length (or along container width), shown in Figure 3.5.8a. Bending strains were key measurements on underground structures to indirectly obtain static and dynamic bending moments and lateral earth pressures, when possible. Since a reliable measurement of lateral earth pressures is difficult in centrifuge and topic of ongoing research, having an indirect measurement strategy was critical. Strain gauges were also installed on four strut arrays inside temporary excavations in a full-bridge configuration to measure static and dynamic axial strains and hence, axial forces acting on struts. This was a critical measurement both for evaluating the response of struts, and also for indirectly obtaining lateral earth pressures on the excavation walls.

Table 3.5.1. Soil parameters used in equivalent-linear and nonlinear site response analyses in DEEPSOIL performed by the research team at UIUC.

Variable	Value	Units
Soil Unit Weight	15.4	kN/m^3
Shear Wave Velocity	As shown in Figure 3.5.2	m/sec
Modulus Reduction Curve	As shown in Figure 3.5.3a	-
Damping Curve	As shown in Figure 3.5.3b	%

Table 3.5.2. Pressure Dependent Multi-Yield (PDMY) constitutive model parameters (Elgamal 2002; Yang 2000) used in nonlinear site response analyses in OpenSees performed by the research team at UIUC.

Variable	Value	Units
Mass density	1.56	Mg/m^3
Ref. shear modulus, G_r	8.29e4	kN/m^2
Ref. mean confinement, p'_r	80	kN/m^2
Poisson's ratio	0.31	---
Ref. bulk modulus, B_r	1.91e5	kN/m^2
Confinement dependence coefficient, d	0.5	---
Friction angle, ϕ	33	°
Peak shear strain, γ_{max}	10	%
Number of Yield surfaces	20	---
Phase transformation angle	26.5	°
Initial void ratio	0.692	---
Contraction parameter	0.05	---
Dilation parameters	d_1=0.6 / d_2=2	---
Liquefaction induced strain constants	0	---

Table 3.5.3. Properties of the designed target single-box tunnel compared to the simplified centrifuge model tunnel (prototype scale).

	Design Properties	Centrifuge Model Properties
Height (m)	8	8
Width (m)	14	14
Wall Thickness (m)	0.8	0.57
Material Type	Reinforced Concrete	6061 Aluminum
Density (kg/m^3)	2400	2700
Young's Modulus	2.50E+07	6.89E+07
Poisson's Ratio	0.2	0.33
Racking Stiffness (MN/m/m)	25 (frame anal.)	25 (frame anal.), 26.6 (experiment)

Table 3.5.4. Hardening soil model parameters used in 2-D finite element analyses of temporary excavation under dynamic conditions using Plaxis2D performed by the research team at UIUC.

Soil Model:	Hardening Soil	ψ:	3
Soil Type:	Nevada Sand	$K_{o\,nc}$:	0.46
e:	0.692	K_o:	0.46
γ_t (kN/m^3):	15.342	Poisson's ratio:	0.32
ϕ' (^{o}):	33	m:	0.5
OCR:	1	v_{ur}:	0.2
c':	0	R_f:	0.9

Table 3.5.5. Factors of safety obtained for the temporary excavation under static and dynamic conditions (results from analyses performed by the research team at UIUC).

		Wall bending moment		Wall shear force		Struts axial force	
Original Design (inadequate horiz. strut spacing = 4m)	Simulation	Static	Dynamic	Static	Dynamic	Static	Dynamic
	Excavation only	14	1	7	1	7	0.9
	Excavation and building	4	0.9	2	0.5	4	0.6
Final Simplified Centrifuge Design (horiz. strut spacing = 4.2m)	Simulation	Static	Dynamic	Static	Dynamic	Static	Dynamic
	Excavation only	6	1.2	3	0.8	8	1.2
	Excavation and building	6	1.5	3	0.7	8	1.3

Table 3.5.6. Properties of the designed target temporary excavation compared to the simplified centrifuge model excavation (prototype scale).

	Design Properties	Centrifuge Model Properties
Height (m)	18 (6 embedded)	18 (6 embedded)
Width (m)	14	14
Material Type	Steel	6061 Al.
Wall Beams	W27x178 (horiz. spacing: 1.5 m)	0.41m thick plate
Struts	HSS14x0.625 (spacing: 2m horiz.; 2-3-3m vert. from top)	OD-0.41m, ID-0.39m (spacing: 4.2m horiz.; 3-3-3m vert. from top)
Density (kg/m^3)	7800	2700
Young's Mod. (kPa)	2.50E+07	6.89E+07
Poisson's Ratio	0.28	0.33
Racking Stiffness (MN/m/m)	2.0 (Anal. Solution)	1.5 (FEM)

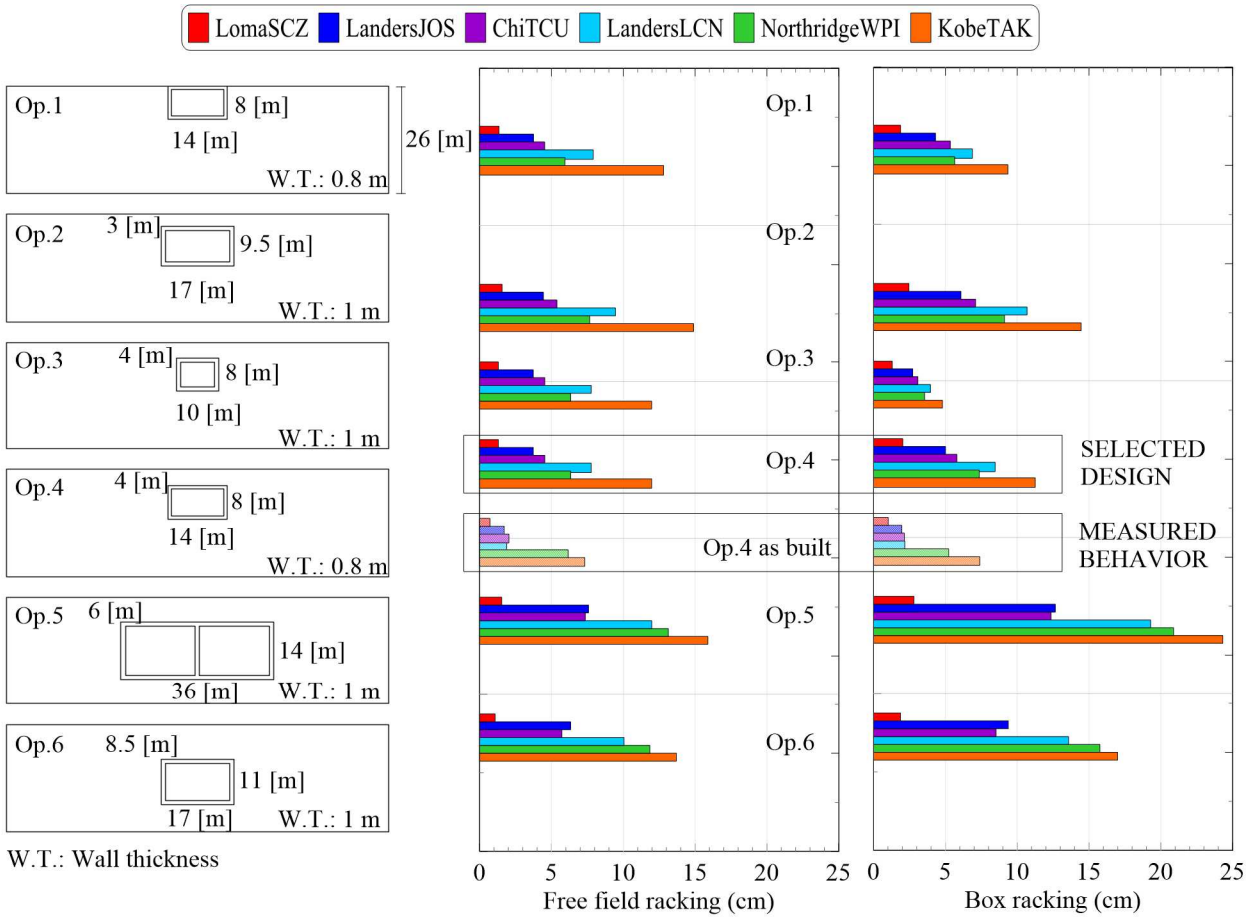

Original design (Op.1 to 6): Max{OpenSees, Deepsoil Nonlinear, Deepsoil Eq. Linear, Centrifuge CU Boulder}
Measured behavior (Op.4 as built): Max{T-NoBldg Free field and Box Centrifuge measurements}
NOTE: Original design input motions (expected) differ from measured input motions (achieved)
Original design box racking stiffness differs from built box racking stiffness

Figure 3.5.1: Design process for the permanent box structure based on the maximum free-field and box racking displacements for the six cut-and-cover box structures analyzed according to the NCHRP 611 procedure compared with the measured behavior in T-No Bldg (analyses performed by the research team at UIUC).

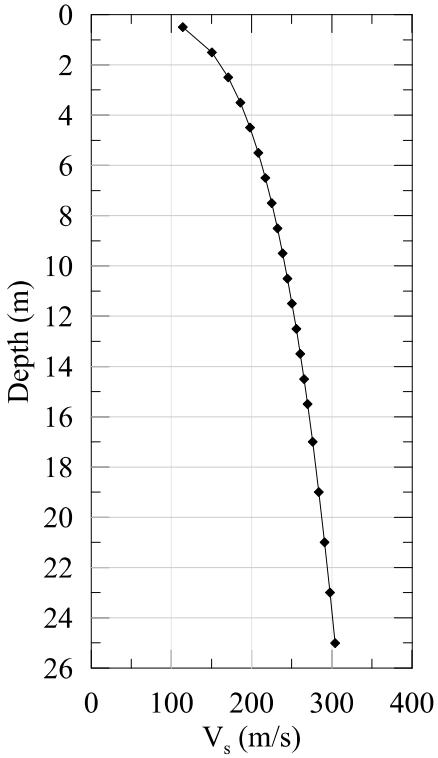

Figure 3.5.2. Shear wave velocity profile used in the DEEPSOIL analyses performed by the research team at UIUC.

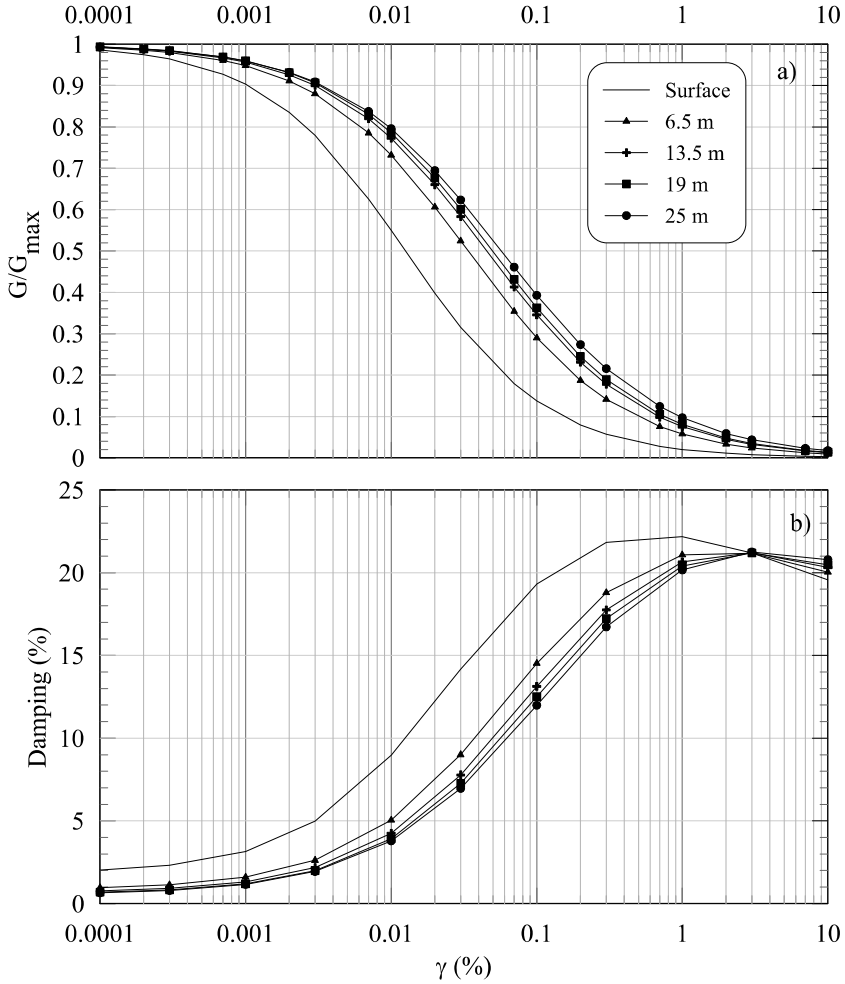

Figure 3.5.3. Modulus reduction (a) and damping curves (b) used in the DEEPSOIL analyses performed by the research team at UIUC.

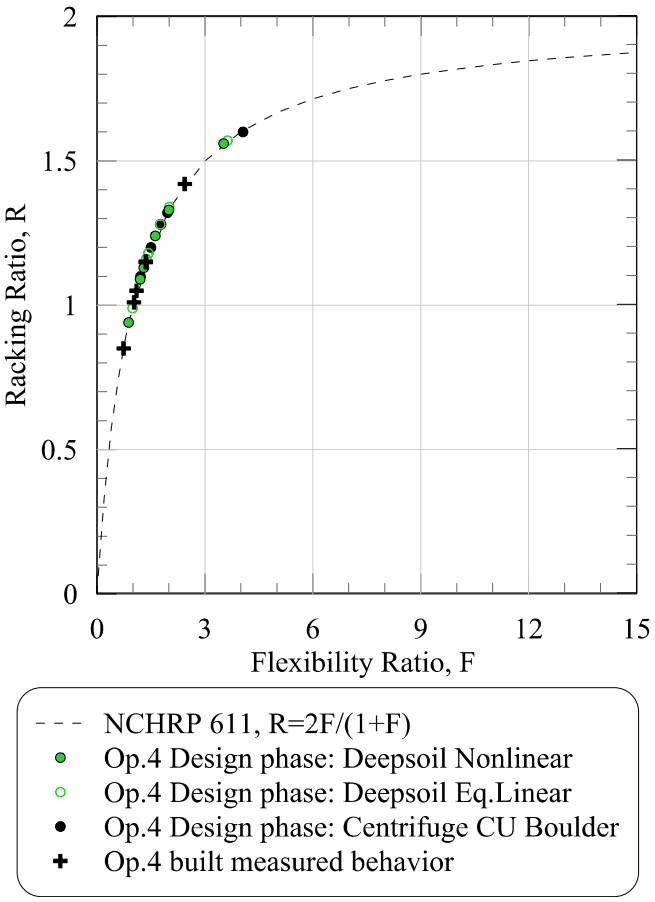

Figure 3.5.4. Racking vs. flexibility ratio for the selected design (Single box: 14mx8m, cover 4m, thickness 0.8m) using different methods to account for G_m of the free-field soil compared with the NCHRP611 guideline (analyses performed by the research team at UIUC).

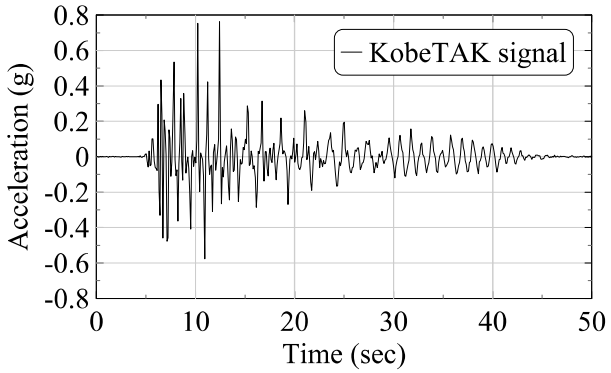

Figure 3.5.5. The KobeTAK base motion recorded in the CUB centrifuge test used as input to Plaxis2D dynamic analyses (performed by the research team at UIUC) for the design of temporary braced excavation.

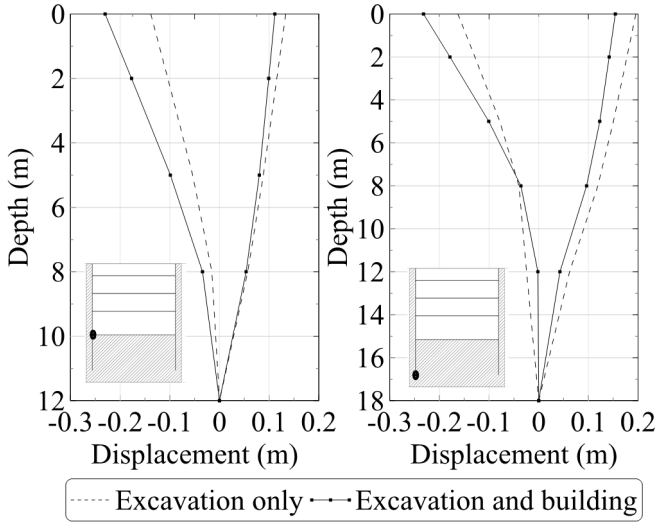

Figure 3.5.6. Maximum and minimum lateral displacement profiles of the two excavation walls during the KobeTAK motion with and without the adjacent highrise building (left: with respect to the bottom of the excavation; and right: with respect to the bottom of the wall). Analyses were performed by the research team at UIUC.

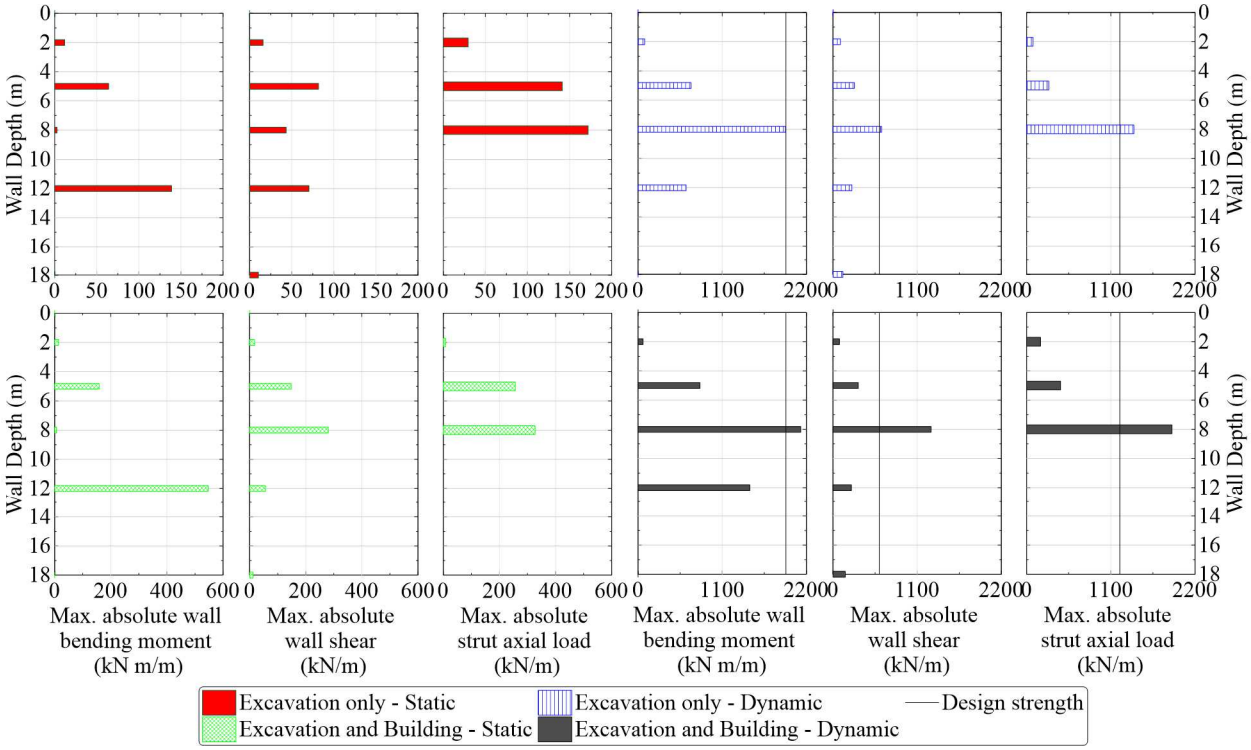

Figure 3.5.7. Maximum absolute forces on the excavation wall and struts under static and dynamic conditions computed in the Plaxis2D finite element simulations performed by the research team at UIUC for the original design compared with the corresponding design strengths.

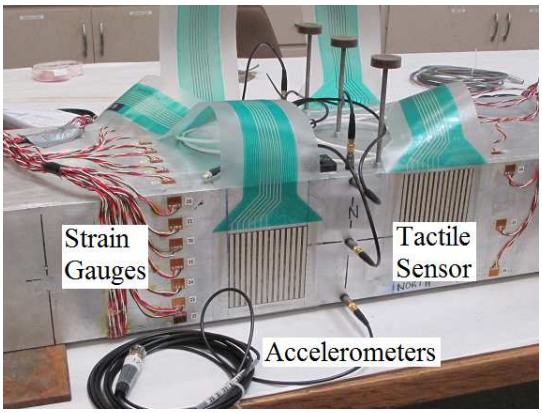

(a)

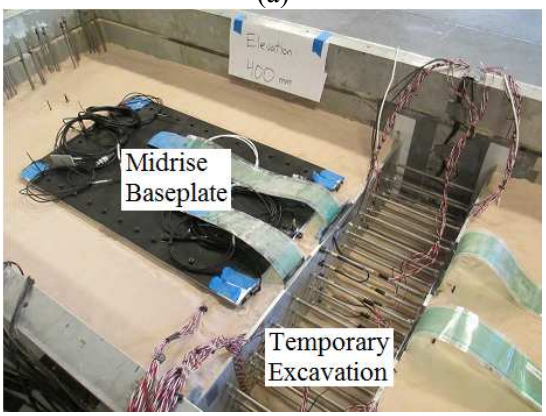

(b)

Figure 3.5.8. Underground structures fabricated for testing: (a) permanent box structure and its instrumentation before placed in the model container; (b) temporary excavation after model construction with struts and sensors placed in T-Midrise.

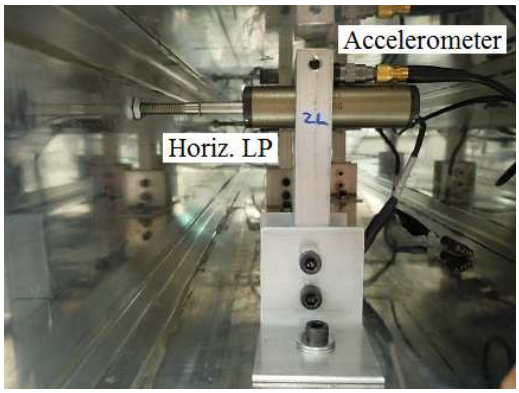

(a)

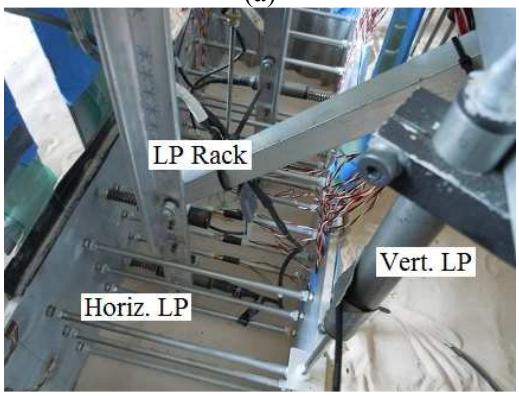

(b)

Figure 3.5.9. Measuring racking deformations directly with horizontally placed linear potentiometers (LPs): (a) inside the permanent box structure; (b) temporary excavation.

3.6 Modeling of Tall Buildings

3.6.1 Design Approach

3.6.1.1 Midrise Building

To design a realistic midrise building that can withstand seismic loading, the fundamental period, modal shapes, footprint dimensions, height, and seismic weight of a range of typical buildings in Los Angeles and San Francisco, California were evaluated, while considering the centrifuge container size limitations. Since at the time the midrise building was designed, the first two baseline experiments, T-No Bldg and E-No Bldg, were already completed, the actual achieved base motions at UCD-CGM were available. Therefore, the container base and free-field soil surface accelerometer recordings could be used to anticipate the building's seismic performance.

Steel and reinforced concrete, moment resisting frame (SMRF and RCMF), 13 to 15 story structures with 1 to 2 story basements were found common in Los Angeles and San Francisco with total seismic weights ranging from about 39,000 to 135,000 kN, corresponding to seismic weight densities of 7.13 kN/m^2/story for RCMF and 3.5 to 3.81 kN/m^2/story for SMRF buildings (as summarized in Table 3.6.1). The ASCE 7-10 shear demands on these buildings were then compared with those induced if subject to the ground motions measured in T-No Bldg at the container base and far-field soil surface. The shear demands obtained from ASCE7-10 for a building in Los Angeles controlled the design for a midrise SMRF building.

A 13-story, SMRF building was selected as the target midrise building for this study with a seismic weight density of 3.5 (kN/m^2/story) and footprint dimensions of 38.5 m x 22.5 m in prototype scale. This model represented the largest and heaviest structure tested at UCD-CGM to date. For practical reasons, the midrise building was simplified as a 3-DOF system for centrifuge modeling to capture its three primary modes of vibration. The seismic shear load demand per floor was subsequently estimated for the selected structure based on ASCE 7-10 in Los Angeles. Detailed properties and dimensions of the centrifuge midrise building are summarized in Table 3.6.1 both in prototype and model scale units.

To design the structural elements and fuses, static pushover and modal analyses were performed in OpenSees v.2.4.3. Fuses, which are areas with a reduced cross section, were strategically designed on the beam and column ends to control the frame's inelastic deformations. The geometry of the fuses controls the inelastic response of the structure. The properties of columns and fuses were varied, producing different natural periods, as shown for the three models considered in Figure 3.6.1. Model II was selected with first three modal periods of 3.02, 0.85, and 0.43 s in prototype scale, as it complied with ASCE 7-10 design requirements

in terms of allowable base shear and drift and it provided a fundamental period close to target. The type of fuses selected on the beam and column ends of the centrifuge midrise building are shown in Figure 3.6.2 in model scale. Because the precise, inelastic behavior of the model building was not the topic of investigation in this research, the moment-rotation behavior of the selected fuses were not investigated experimentally or numerically during design. But they were measured during the experiments.

3.6.1.2 Highrise Building

The goal was to design a tall structure that had realistic dimensions and key dynamic properties, complied with the latest seismic design requirements in California, and simultaneously satisfied centrifuge container and overhead space limitations. No centrifuge experiment had been performed on a highrise model structure prior to T-Highrise and E-Highrise by other researchers. Hence, its design process and considerations for centrifuge modeling is one of the intended contributions of this research.

The Tall Building Initiative (TBI) Task 12 Final Report (Moehle et al. 2011) presented the results of dynamic time history analyses on selected tall buildings in San Francisco, CA. = Concrete core SMRF building models 2B and 2C in this report were selected as the target highrise buildings of interest in this study. These models had 42 stories, 4 stories of basement, footprint dimensions of 69 m x 69m for the building and 33m x 33m for the core, a seismic weight of 453,719 kN, a fundamental period of approximately 4.3 to 4.9 s, and an average horizontal shear demand of 47,738 kN when subject to 7 motions matching the MCE target response spectra (Moehle et al. 2011). Figure 3.6.3 compares the MCE target response spectrum used in the TBI report with the response spectra of the motions recorded at the far-field soil surface in each of the two baseline experiments (T-No Bldg and E-No Bldg). At the

fundamental period of the target highrise building (approximately 4 s), the largest expected horizontal base shear demand in centrifuge (i.e., 22,000 kN) was approximately 46% of the TBI demand (47,000 kN), as shown in Figure 3.6.3.

Static pushover analyses were performed in OpenSees and SAP2000 to design a simplified structure that simulated the key dynamic properties of the target highrise building, while sacrificing other properties to satisfy the centrifuge size limitations. The target building footprint dimensions of 69m x 69m could not fit within the centrifuge container at the selected level of centrifugal acceleration (65g). Therefore, the target core footprint dimensions of 33m x 33m were selected instead for the entire building. The overhead height available in centrifuge also did not allow a proper simulation of the building's center of gravity and hence, its seismic moments and rocking tendencies. However, the total seismic weight and fundamental period of the target building could be simulated, which were expected to strongly influence SSUSI and hence, the response of an adjacent underground structure.

A simplified single-degree-of-freedom (SDOF) system was designed to simulate only the fundamental period, weight, and shear capacity of the target highrise building. Higher modes could not be simulated effectively in a scaled model and were therefore sacrificed. Figure 3.6.4a presents the first series of pushover analyses in OpenSees to select the properties of a simplified SDOF structure. Model IV had a fundamental period near the target value of 4s, while simultaneously satisfying the shear capacity requirements in TBI. Figure 3.6.4b compares the static pushover analyses performed on the final design (Option IV) using OpenSees and SAP2000. The horizontal base shear causing initial yielding of the structure was estimated at 61,000 kN (shown in Figure 3.6.4b), while the largest expected horizontal base shear demand in centrifuge was 22,000 kN. Therefore, this structure was expected to respond in its linear elastic

range in centrifuge for the achieved series of ground motions, because of its high fundamental period. As a result, fuses were removed from the beams and columns to simplify the design.

Static structural analyses were performed in AISC 360-05 and SAP2000 to check and ensure adequate static factors of safety of beams and columns under 65g of centrifugal acceleration against axial, shear, and bending yield. The final design was verified by changing the element's geometric transformation in OpenSees, as shown in Figure 3.6.5c. The P-delta effect was also implemented in the final design, showing no significant change in the behavior of the structure for the expected range of roof displacements. Table 3.6.1 presents the final properties of the simplified SDOF model structure representing some key properties of the target highrise building in centrifuge both in prototype and model scale.

3.6.1.3 Basement Walls

The basement of both midrise and highrise buildings was designed as a box open at the bottom and filled with the test soil. The building was connected to the basement through a diaphragm or base plate at the ground level (as shown in Figure 3.6.5), which transferred the weight and shear loads from the building to the perimeter basement walls and from there to the soil and adjacent underground structure. The inclusion of a realistic, empty basement would significantly reduce the confining pressure under the building, particularly for the 4-story basement of the highrise structure. This would reduce the influence of the adjacent building on the seismic performance of a box structure and their interactions. Our goal in these fundamental experiments was to maximize the building's influence, in order to provide a more clear understanding of the underlying mechanisms of interaction. Further, in many cases, mid to highrise buildings are placed on pile foundations instead of a multistory basement. In end, to maximize the inertial influence of the adjacent building without introducing the complexities of deep foundations, it

was decided to include soil in the basement, even though it would lead to an unrealistic apparent condition. The subsequent numerical simulations of the centrifuge experiments would similarly include soil inside the basements.

The basement walls that were surrounded by soil inside and outside needed to be designed with proper stiffness and height to withstand lateral earth pressures and protect the superstructure against sliding and overturning under static and seismic conditions. These walls were analyzed in SAP2000 using shell elements and aluminum properties. The stability of the soil-basement-superstructure system was evaluated for both buildings under two critical loading conditions: 1) sliding and overturning about the building base plate; 2) sliding and overturning about the bottom of the basement walls.

In the first set of analyses that excluded the inertia of the embedded soil inside basement, the driving forces included the inertia of the superstructure, base plate, and basement walls, as well as active static, and dynamic lateral earth pressures acting on the two basement walls in the direction of shaking. The resisting forces included the sliding resistance force at the bottom of the base plate due to the weight of the structure and passive static earth pressures acting on one basement wall only (because of the presence of the tunnel next to the other wall). In the second set of analyses, the driving forces included the inertia of the superstructure, base plate, basement walls, and embedded soil in basement as well as the active earth pressures acting on one wall only (since the entire basement and soil inside was treated as a single moving mass in this case). The resisting forces included the sliding resistance at the bottom of the basement from the weight of the superstructure-basement-soil system. No passive earth pressures were taken into account in this scenario due to the presence of the tunnel. The basement wall section thickness and height were designed for each building model to reach a minimum FS of 2 in either condition

and ensure static and seismic stability of the entire system. Basement properties are summarized in Table 3.6.1 in prototype and model scale.

3.6.2 Model Fabrication and Testing

In fabricating the simplified midrise building model, steel and aluminum plates were ordered in a fashion that was mindful of the fabrication process so that machining time could be minimized. Once all of the structure components were machined, the structure was bolted together and tested. The modal frequencies of the structure were experimentally obtained by fixing the base of the structure and using a hammer to excite the structure into free vibration. The three modal frequencies obtained experimentally were in close agreement with the design values, as summarized in Table 3.6.1.

The simplified highrise building model was the heaviest single structure ever tested at the UC Davis CGM. As a result, the design of the columns, beams, and the top mass as well as the selection of base motion to excite this building went through several iterations by the research team and centrifuge staff. One challenge during fabrication was a practical strategy for placing 150 kg (at 1g) of mass to the top story without altering the frame's intended stiffness and deformation pattern. The original design of the top floor mass included large steel plates at the top and bottom of the cross beams. This design would limit rotation of the top floor and add unwanted stiffness to the building. In the final design, eight smaller steel plates were placed at the top and bottom of each individual cross beam, as shown in Figure 3.3.3 and Figure 3.6.5b. Once the design was finalized, materials were ordered. After fabrication, using a hammer impact test, the structure was found to be more flexible than intended (higher fundamental period than design). This was likely due to over-welding of the column connections to the base plate. The building model was then modified by using adjustable cross bracing to achieve a higher effective

stiffness and the design fundamental frequency (summarized inTable 3.5.3). The cross braces were bolted into place once the design natural frequency was achieved.

All fasteners on the structure were of the highest grade to minimize the possibility for any sort of bolt or nut failure during testing. Loading the highrise superstructure onto the centrifuge model was done using an overhead crane positioned above the centrifuge bucket. The highrise superstructure was installed on the model after it had been loaded onto the centrifuge shake table, in order to prevent damage to the model during transportation. Safety straps were attached to each corner of the building top floor to catch or restrain the structure if tipping or component failure was to occur during testing.

3.6.3 Instrumentation Design

In this research, it was critical to measure building base shear, inter-story drift, and moment-rotation behavior of columns and beams at fuse locations (if applicable) during different earthquake events in addition to bending strains and accelerations on the basement walls. Building base shear was indirectly evaluated through the recordings of accelerometers on structural masses and base plate (see Figure 3.3.2) multiplied by the corresponding masses. Permanent and transient inter-story drifts were measured directly by horizontal LPs placed on each structural mass and base plate, which were connected to LP holders attached to an external rack (as shown in Figure 3.6.6). Due to the large height of our model buildings, however, the LP holders could move independently at times, even though they were reinforced. Since the permanent drift of both buildings was expected to be minimum (they were designed not to yield), accelerometers were judged more reliable to indirectly obtain transient inter-story drift through double-integration (similar to the approach taken in estimating the racking displacement of underground structures). Lastly, to evaluate the moment-rotation behavior at fuse locations,

half-bridge strain gauges were placed in the middle of each fuse, as shown in Figure 3.6.7. The data from strain gauges and accelerometers could be used to obtain rotation and moment time histories at fuse locations.

Table 3.6.1. Properties of midrise and highrise buildings as designed and simplified for centrifuge modeling.

	Design Properties Target Range	Centrifuge Model Properties		Design Properties Target Range	Centrifuge Model Properties	
		Prototype Dimensions	Model Dimensions N=65		Prototype Dimensions	Model Dimensions N=65
Number of Stories	13 to 15	13 simulated with 3 masses	3 mass system	42	42 simulated with 1 mass	1 mass system
Subterranean Levels	1 to 2	1	1	4	4	4
Seismic Structural System	RCMF or SMRF [1]	SMRF	SMRF	Concrete core with SMRF	SMRF	SMRF
Height Above Ground (m)	50 to 70	48.75 [2]	0.75 [2]	142	48.75 [2]	0.75 [2]
Depth below Ground (m)	4.5 to 6.5	4.25	0.065	13	13	0.2
Footprint Dim. (m x m)	23x59 / 53x53 / 38.5x22.5	38.5 x 22.5 [2]	0.592 x 0.346 [2]	Bldg: 69 x 69; Core: 33 x 33	33 x 33	0.508 x 0.508
Seismic Weight Density (kN/m^2/story)	RCMF: 7.13; SMRF: 3.5 to 3.81	3.5	-	Bldg. footprint: 2.27; Core footprint: 9.92	9.92	-
Weight of Superstructure (kN)	42,860 to 125,743	39,414	0.192	453,719	453,719	1.77
Fundamental Periods (sec)	RC: 2.6-2.7; SMRF: 3.03/1.08/0.65; 1.69/0.56/0.32	3.02/0.85/0.43 [3]	3.35/0.84/0.43 [5]	4.28 to 4.93	4.03	-
Base Shear (kN)	V_y/W = 0.088 to 0.094	Demand: 3,510; Yield: 3,510 [3]	-	Demand: 47,738	Yield: 57,858[4]	-
Max. Drift Ratio (m)	0.44 to 0.52	0.15 [3]		N.A.	N.A.	N.A.
Overturning Moment (kN-m)	Yield: 188,584 to 827,389	Demand: 167,602; Yield: 167,602	-	Demand: 1,057,538	Yielding: 2,820,580[4]	-
Column and Beam Model Sections	N.A.	N.A.	HSS 5/8" x 5/8" x 1/16"	N.A.	N.A.	HSS 3/2 x 3/2 x 1/8"
Basement Wall Sections (m)	N.A.	H= 10m, Th.= 0.2m	H= 154mm Th.= 3.2mm	N.A.	H= 200mm Th.= 9.5mm	H = 13m Th.= 0.6m

NOTE: [1] RCMF: Reinforced Concrete Moment Frame, SMRF: Steel Moment Resisting Frame;
[2] Due to centrifuge size limitations;
[3] Estimated using a 2D OpenSees model to meet seismic demand and allowable drift requirements from ASCE7-10 for the building properties selected;
[4] Estimated using a 2D OpenSees model to the demands estimated for the prototype building;
[5] Found experimentally using a hammer impact test; [6] Not provided in the literature found.

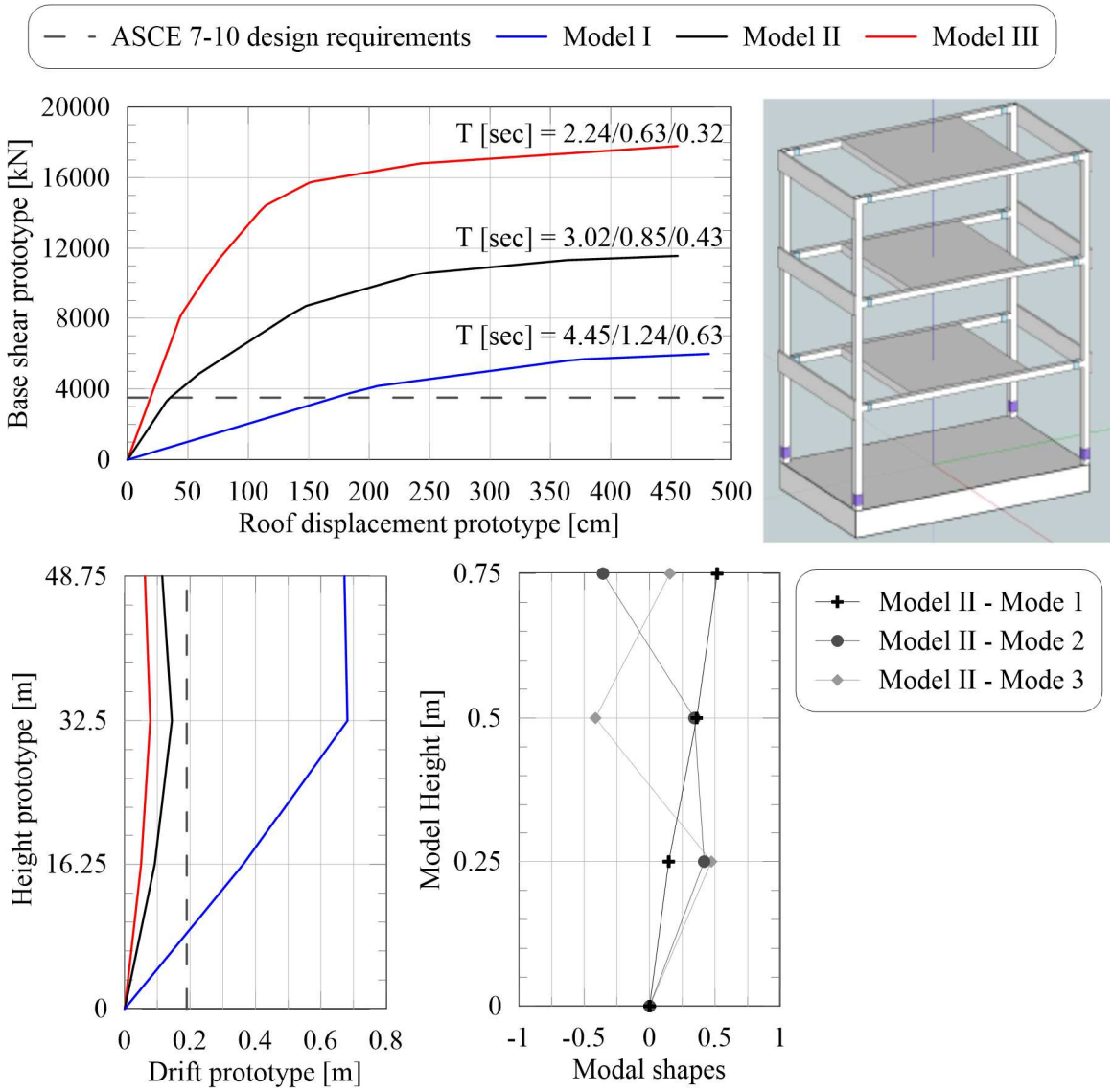

Figure 3.6.1. Static pushover analysis and modal analysis results for three midrise building model options in OpenSees to select the structural properties of a midrise building model for centrifuge testing. Analyses were performed by the research team at UIUC.

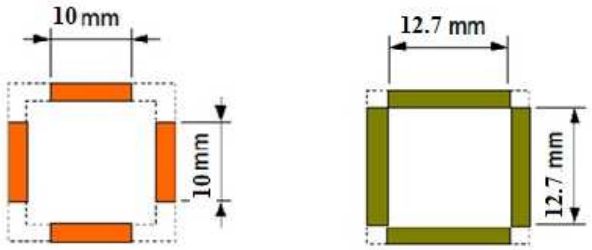

Beam fuse; Length: 12.7 mm

Column fuse; Length: 25.4 mm

Figure 3.6.2: Fuses designed on the beams and columns of the midrise structure.

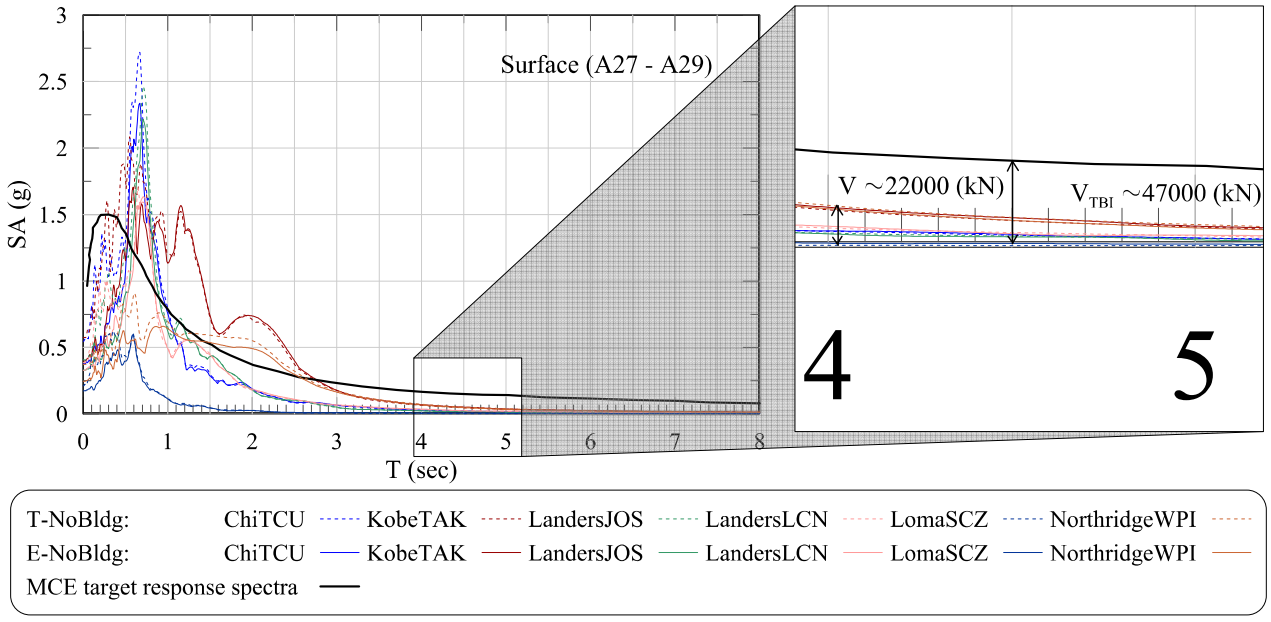

Figure 3.6.3. Measured acceleration response spectra (5% damped) at the soil surface in the free-field in T-No Bldg and E-No Bldg compared with the TBI MCE level target acceleration response spectrum.

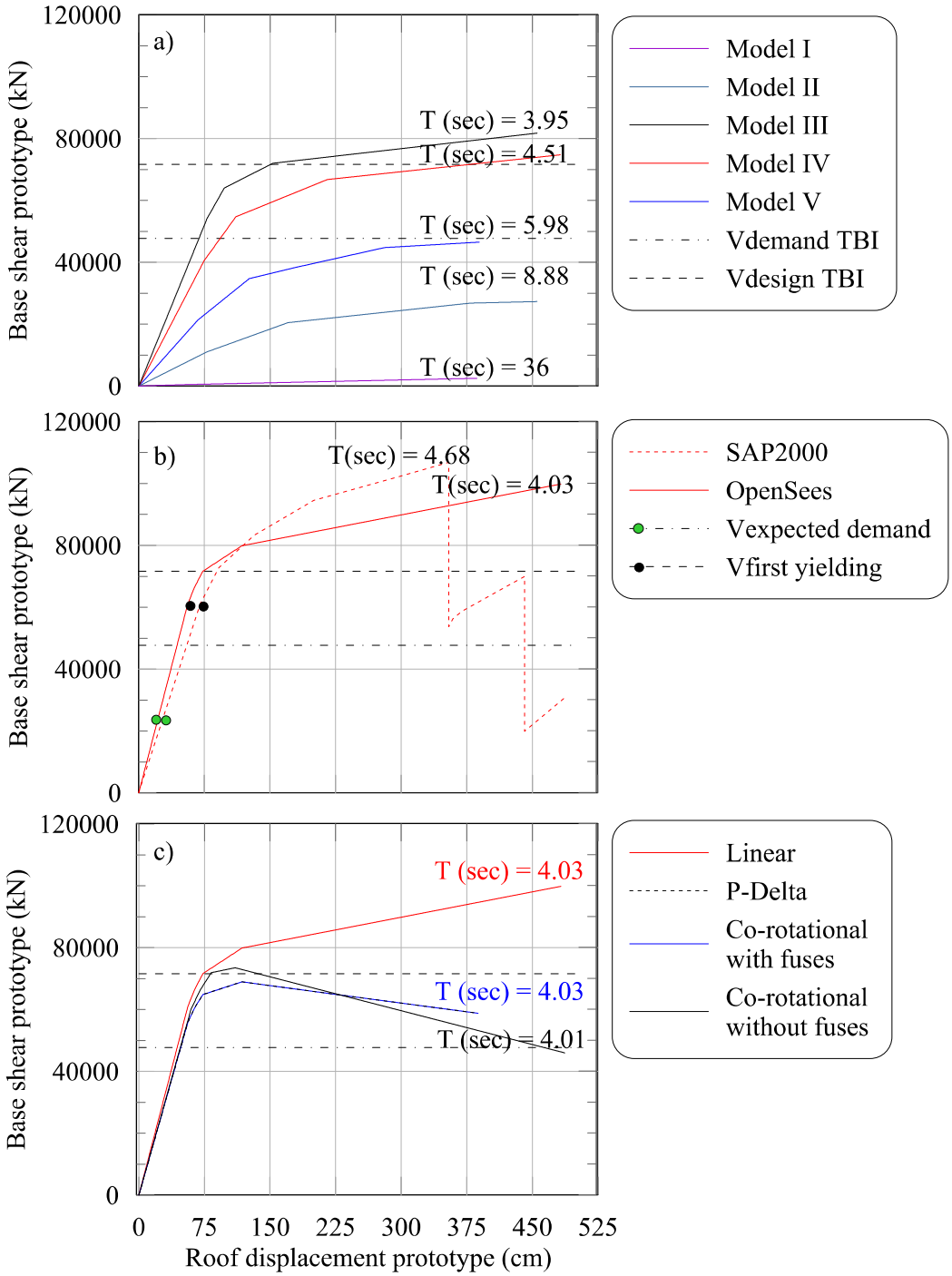

Figure 3.6.4. Pushover analysis results for the highrise building model design: a) OpenSees first set of analyses to achieve target parameters (Model IV); b) comparison of results from OpenSees and SAP2000 for the final design; c) verification of the final design by varying the element's geometric transformation in OpenSees. Analyses were performed by the research team at UIUC.

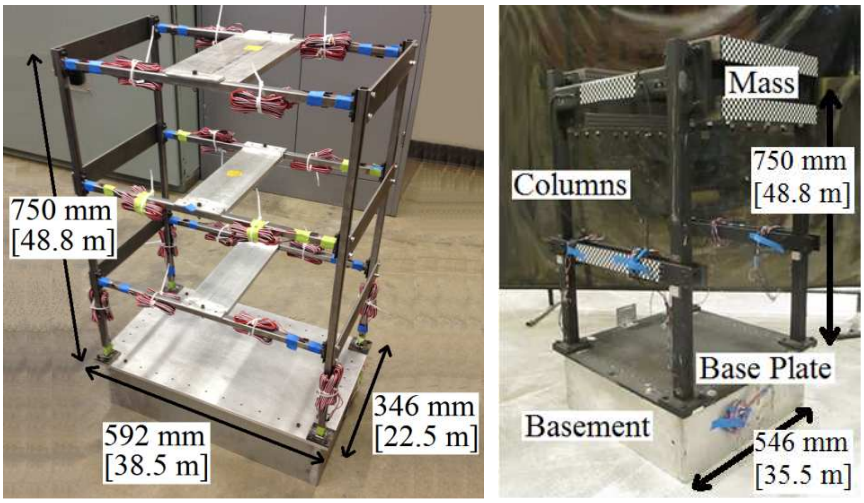

(a) (b)

Figure 3.6.5. Photographs showing the finished: (a) midrise and; (b) highrise building models used in centrifuge. Dimensions shown in both model and prototype scale.

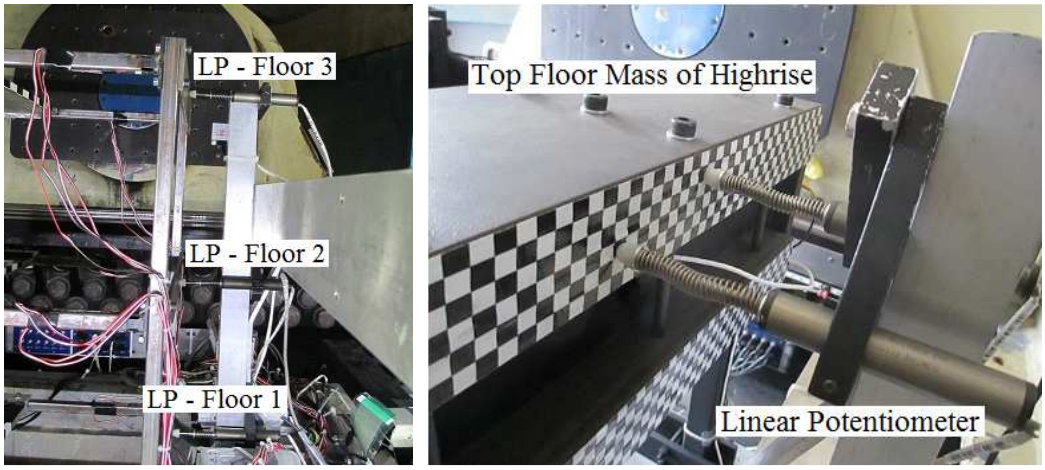

(a) (b)

Figure 3.6.6. LP measurement of lateral displacements on each story of: (a) midrise; and (b) highrise building models in centrifuge.

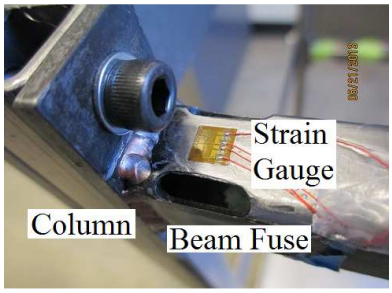

Figure 3.6.7. Midrise beam fuse and placement of a strain gauge in half bridge configuration.

Chapter 4

4 RESULTS – UNDERGROUND BOX STRUCTURE

4.1 Overview

This chapter presents the results from three centrifuge tests involving the tunnel: T-No Bldg, T-Midrise, and T-Highrise. Results from these tests are presented and compared in terms of acceleration and displacement in the far-field and near-field as well as strain and pressure on the underground box structure.

4.2 Accelerations

4.2.1 Selection of a Representative Base Accelerometer

In each centrifuge experiment, a number of accelerometers were positioned at the base of the centrifuge container to monitor the input motion and provide redundancy for this important measurement. Figure 4.2.1 shows the accelerometer layout in T-Midrise. Four accelerometers were located at the base of the container highlighted by the red boxes. Of these four accelerometers, one was selected as the representative base accelerometer after comparing their recordings with each other in a given experiment and across experiments.

To use T-Midrise as an example, accelerometers labeled as A01, A09, A49, and A52 in Figure 4.2.1 were all positioned at the base of the container. Two additional accelerometers were

located on the east and west sides of the shake table at the north end of the container. These accelerometers are labeled as STE and STW in Figure 4.2.1. Base acceleration time histories were first compared during the first ground motion, Northridge in Figure 4.2.2. The shake table east and west (STE, STW) accelerometers showed a small high-frequency content that did not exist in other recordings. Further, their amplitudes were slightly different from each other in every test, indicating a small amount of torsion experienced by the container. These accelerometers were bolted or glued to the shake table, and the high frequency response was likely the result of the bolt or glue connection.

In addition to acceleration time histories, the base accelerometer recordings were compared in terms of 5%-damped spectral accelerations, Fourier Amplitude Spectra, and Arias Intensity time histories for each of the tunnel tests, as shown by Figure 4.2.3. Results showed that the accelerometer located at the base of the container underneath the far-field array showed the most consistent results and compared well across experiments. Hence, this accelerometer was chosen as the reference base accelerometer in the following sections.

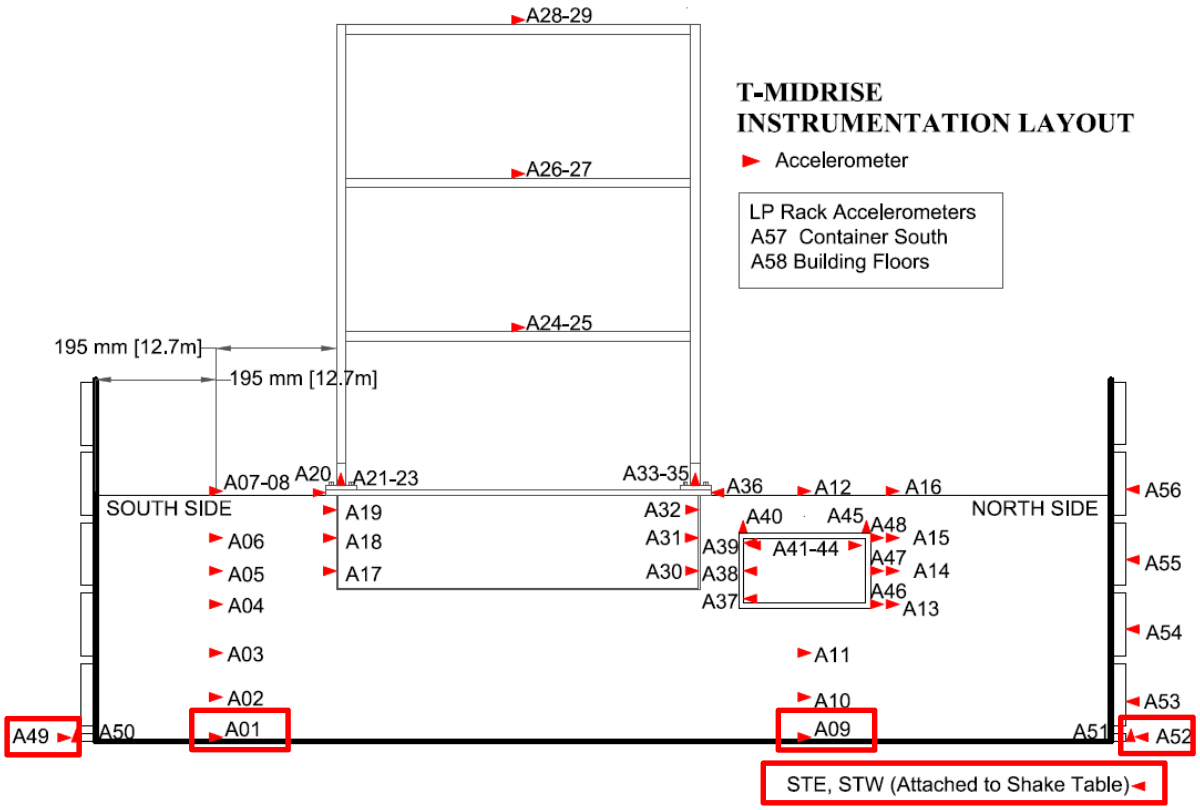

Figure 4.2.1. T-Midrise accelerometer instrumentation layout.

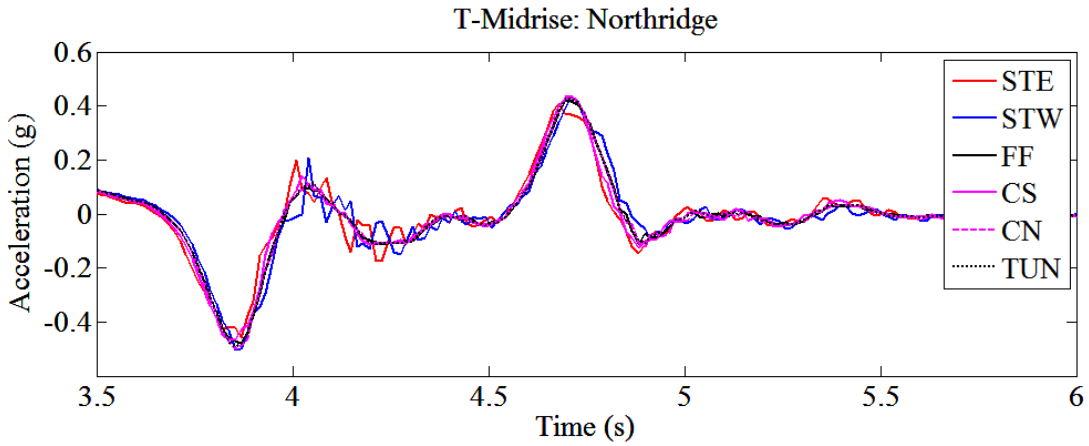

Figure 4.2.2. Comparison of base acceleration time histories of T-Midrise, Northridge motion.

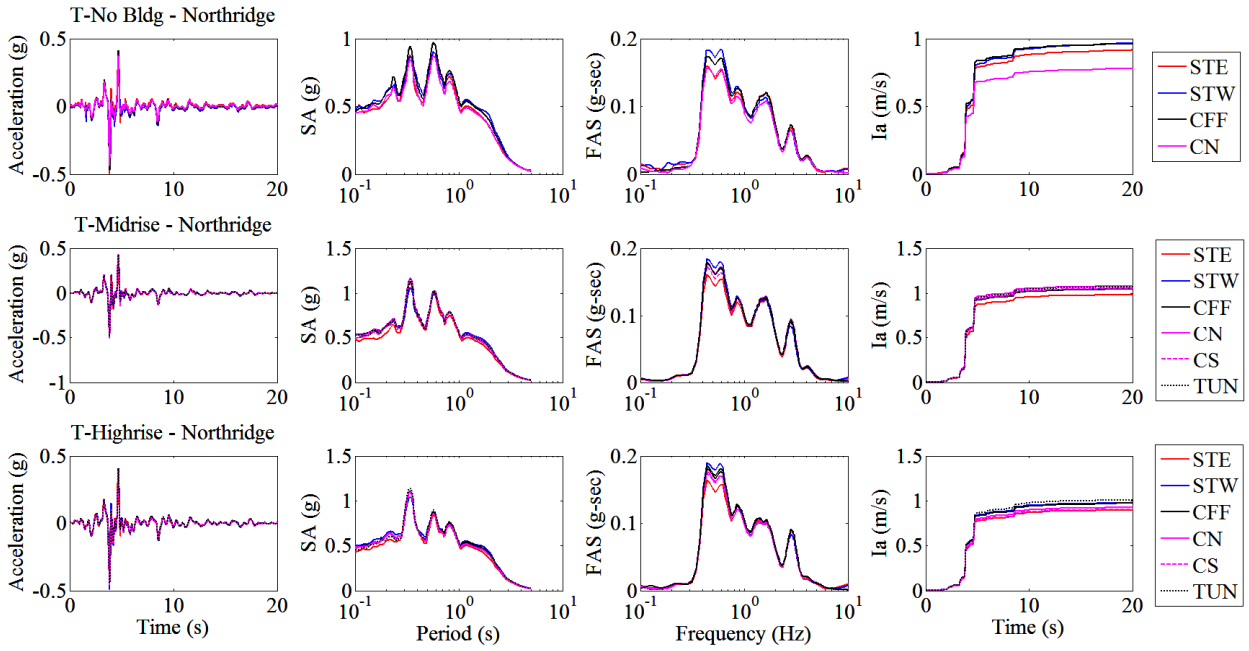

Figure 4.2.3. Base accelerometer comparison during the Northridge ground motion.

4.2.2 Base Acceleration Comparison

The achieved base accelerations from each experiment involving the tunnel were compared using three intensity measures, PGA, PGV, and PGD, to compare the energy input into the system during each ground motion. It's critical that the input base accelerations compare reasonably well, so that base level shaking is not a variable across experiments. Although each test had significantly different weights (seeFigure 3.4.4.

Table 4.2.1), the shake table produced similar ground motions among the three different experiments in the frequency range of interest, as shown in Figure 4.2.4 and Figure 3.4.4.

Table 4.2.1. Weight of the model container-soil-structure system in each tunnel experiment.

Experiment	Model Weight (lbs)	Model Weight (N)
T-No Bldg	3646	16218
T-Midrise	3734	16610
T-Highrise	4209	18723

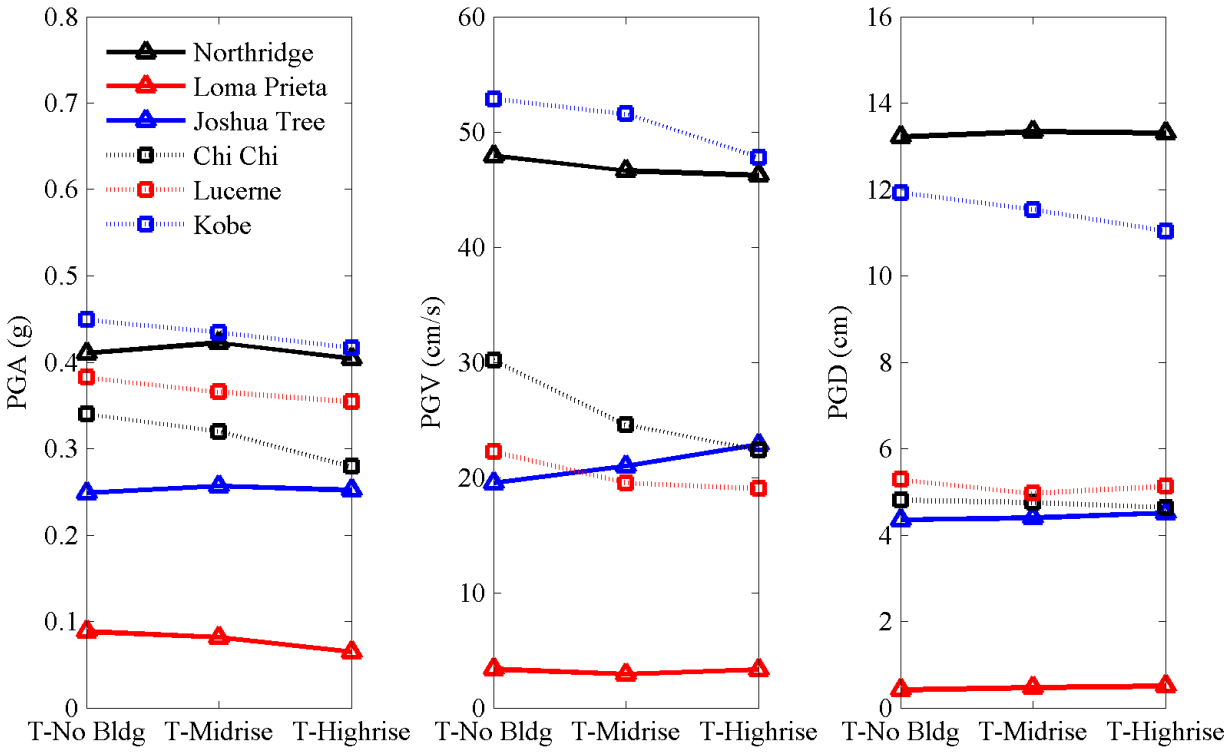

Figure 4.2.4. Comparing tunnel experiment base accelerations in terms of PGA, PGV, and PGD.

4.2.3 Far-Field Accelerations

Each experiment contained a vertical array of accelerometers that were located halfway between the container boundaries and structures as shown in Figure 4.2.5, which were used to approximate soil response in the free-field. In this dissertation, these accelerometers are referred to as "far-field" arrays, as they are not true free-field but experimentally approximate free-field conditions to the extent possible within the space constrains of a centrifuge container. In the field, an ideal free-field condition would be one where no structures or boundary effects are present. The presence of structures can alter the response of the ground during an earthquake. When working within the limited space of the centrifuge container, it can be challenging to create a true free-field condition due to the presence of the boundaries or any structures, particularly when modeling tall buildings with a large contact area. By locating an accelerometer array halfway between the centrifuge container boundary and the structure in our

tests, the influence from structures or the container itself was reduced. The first experiment, T-No Bldg had no tall building and therefore the distance between the far-field accelerometer array, the container boundary, and the underground structure was the greatest at 359 mm (model scale) shown in Figure 4.2.5 and Table 4.2.2. The accelerometer array to structure or container minimum distance was reduced to 195 and 207 mm in T-Midrise and T-Highrise, respectively, as shown in Figure 4.2.6 and Figure 4.2.7, and listed in Table 4.2.2**.** The acceleration recordings from these far-field arrays were compared among the three tests and compared with 1-D site response analyses during each motion. Because the far-field array in T-No Bldg had the largest distance to a structure or boundary compared to other tests, this test was selected to approximate free-field conditions in all tests when evaluating the response of the permanent box structure with respect to soil. The base motions were compared among the three tests (as discussed in Section 4.2.1) to ensure they were similar in the frequency range of interest before using the T-No Bldg far-field array in all tests.

The next set of figures (Figure 4.2.8 through Figure 4.2.13) compare far-field accelerations in T-No Bldg, T-Midrise, and T-Highrise during different motions. Although, the T-No Bldg array was the most representative of free-field conditions, the accelerations are presented in all three tests here for comparison. These figures compare the time histories and Fourier amplitude spectra of accelerations in the three tunnel tests at different elevations. The figures also show the transfer function (TF) of far-field accelerations in T-Midrise or T-Highrise to T-No Bldg, to evaluate the impact of each building on far-field recordings at different frequencies. A TF value equal to 1.0 indicates no change, while a positive TF indicates amplification and a negative TF de-amplification of far-field accelerations at a given frequency due to the addition of a midrise or highrise building.

Some trends that can be identified from Figure 4.2.8 through Figure 4.2.13:

- The amplitude of the acceleration was amplified from base to surface during all ground motions considered in this study, which can be seen from looking at the columns labeled (a) and (b) in each figure.
- The frequency content of far-field accelerations varied slightly among the three tests in elevations above 14m during all motions in frequencies near 1 to 5 Hz. The response was particularly amplified in T-Highrise near 3 Hz. This pattern was likely due to the presence of the midrise (basement elevation of 16m) and highrise (basement elevation of 13m) buildings in the two tests, respectively.
- Overall, in most of the frequency range of interest (0.5 – 10 Hz), the TF of far-field acceleration recordings were close to 1.0, indicating a roughly similar response in the three tests across the frequency range of interest.

Table 4.2.2. The closest distance between the far-field accelerometer array and a structure or container boundary in different experiments.

Experiment	Free-Field Accelerometer Array Minimum Distance to Container Boundary or Structure
T-No Bldg	Prototype: 23.3 m [model: 359 mm]
E-No Bldg	23.3 m [359 mm]
T-Midrise	12.7 m [195 mm]
E-Midrise	12.7 m [195 mm]
T-Highrise	13.5 m [207 mm]
E-Highrise	13.5 m [207 mm]

Table 4.2.3. Far-field accelerometers used to represent free-field conditions in each test.

Test ID	Free-Field Accelerometers
T-No Bldg	A21 - A27
T-Midrise	A01 - A08
T-Highrise	A01 - A08, A20 - A22

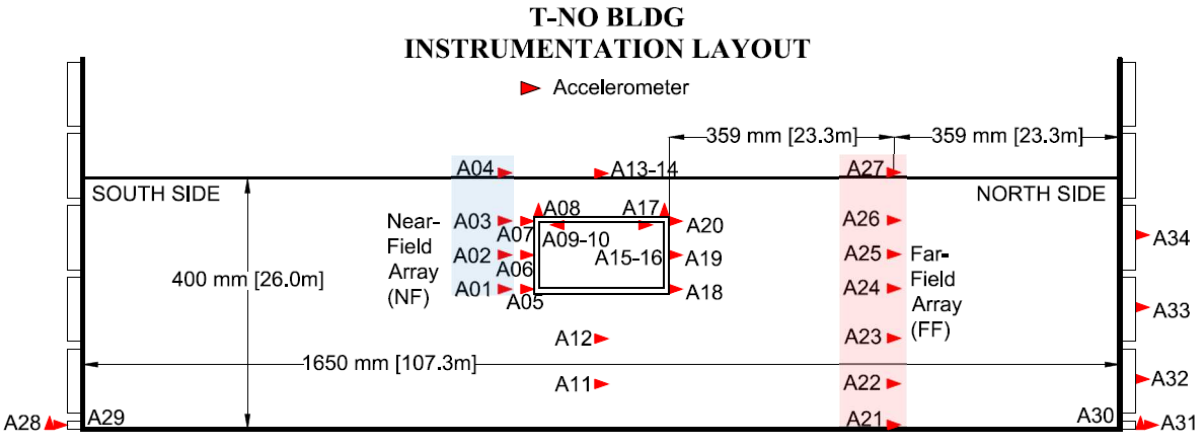

Figure 4.2.5. Elevation view of accelerometer layout in T-No Bldg.

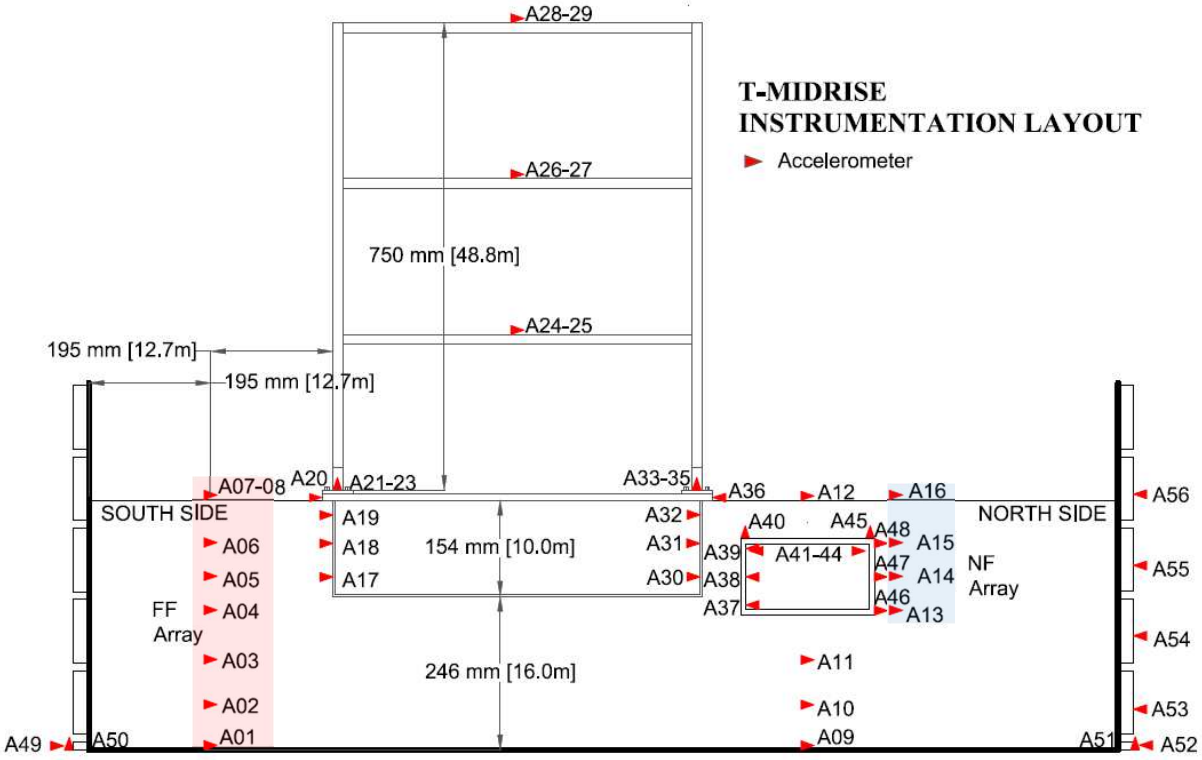

Figure 4.2.6. Elevation view of accelerometer layout in T-Midrise.

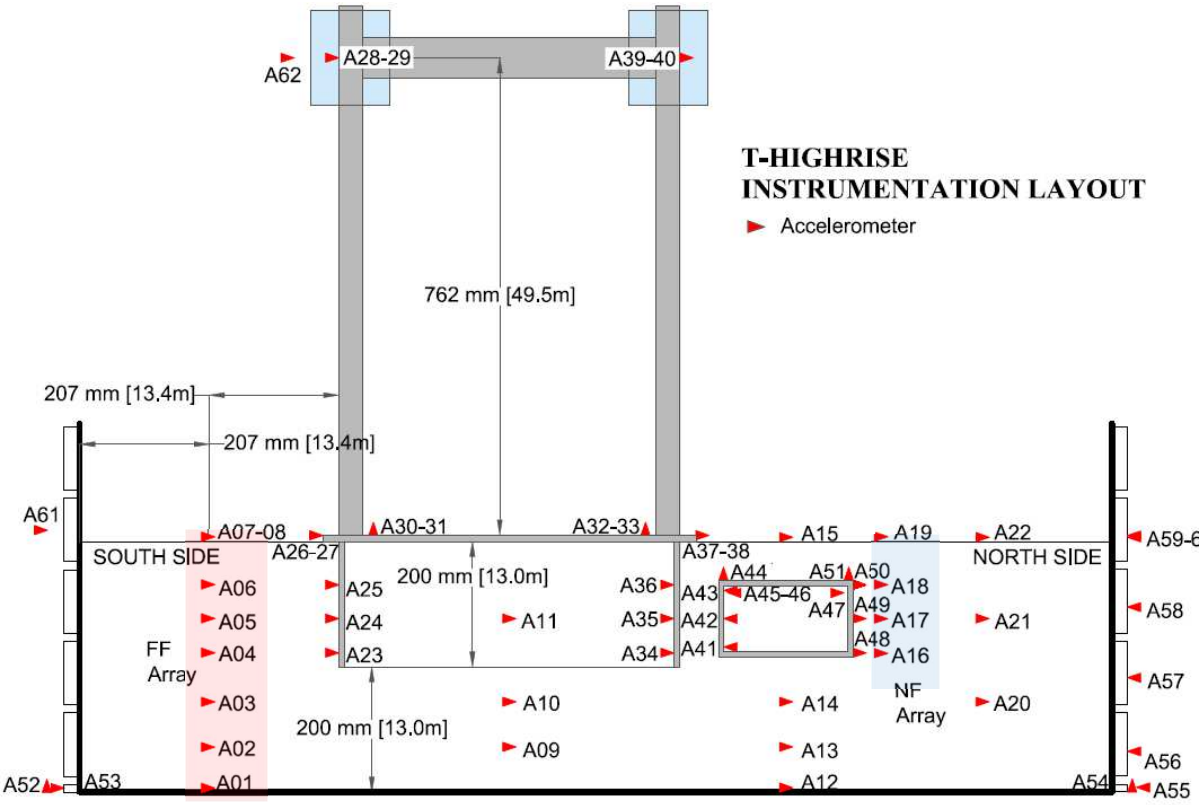

Figure 4.2.7. Elevation view of accelerometer layout in T-Highrise.

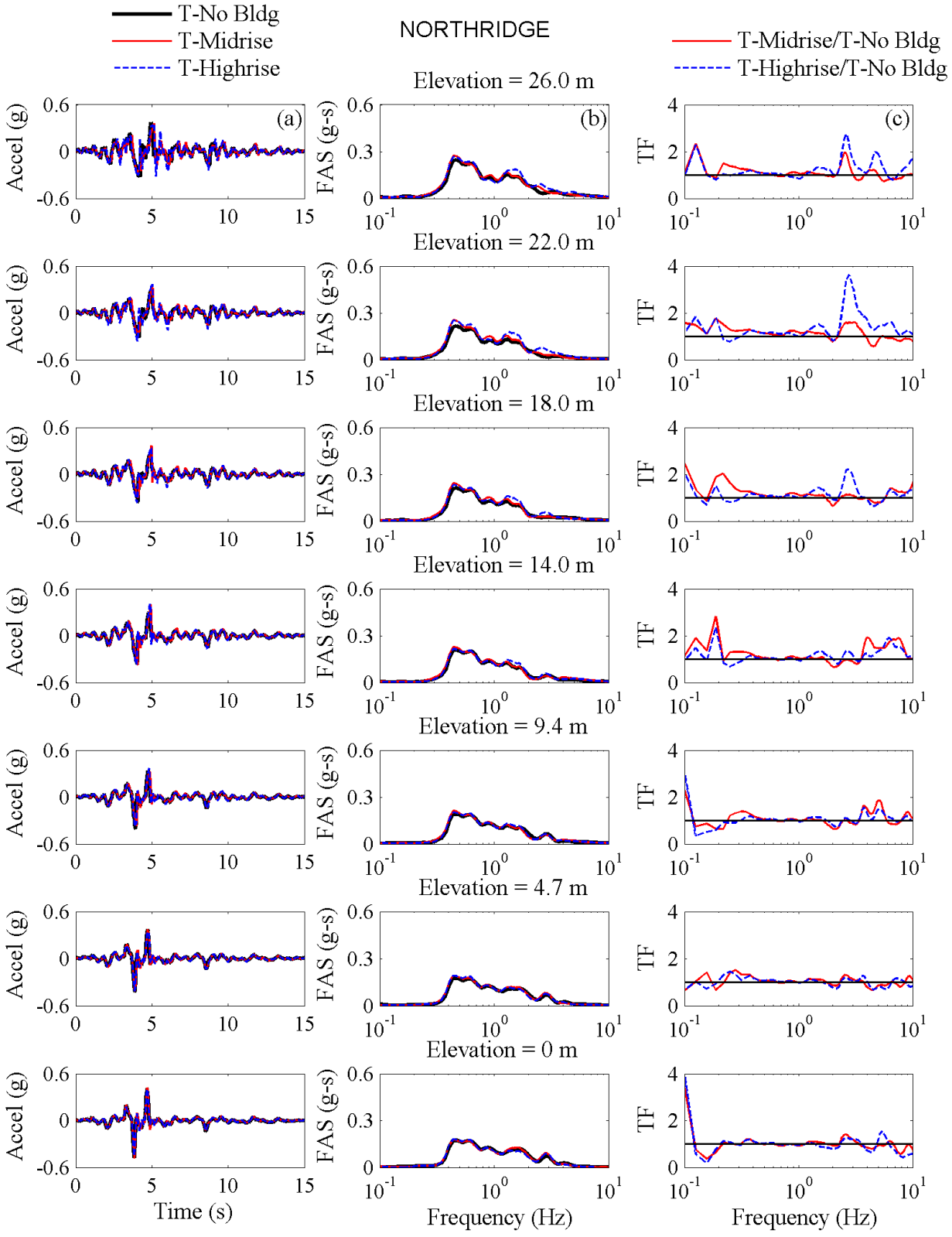

Figure 4.2.8. Northridge far-field acceleration response shown as (a) acceleration time histories; (b) Fourier amplitude spectra; and (c) transfer functions.

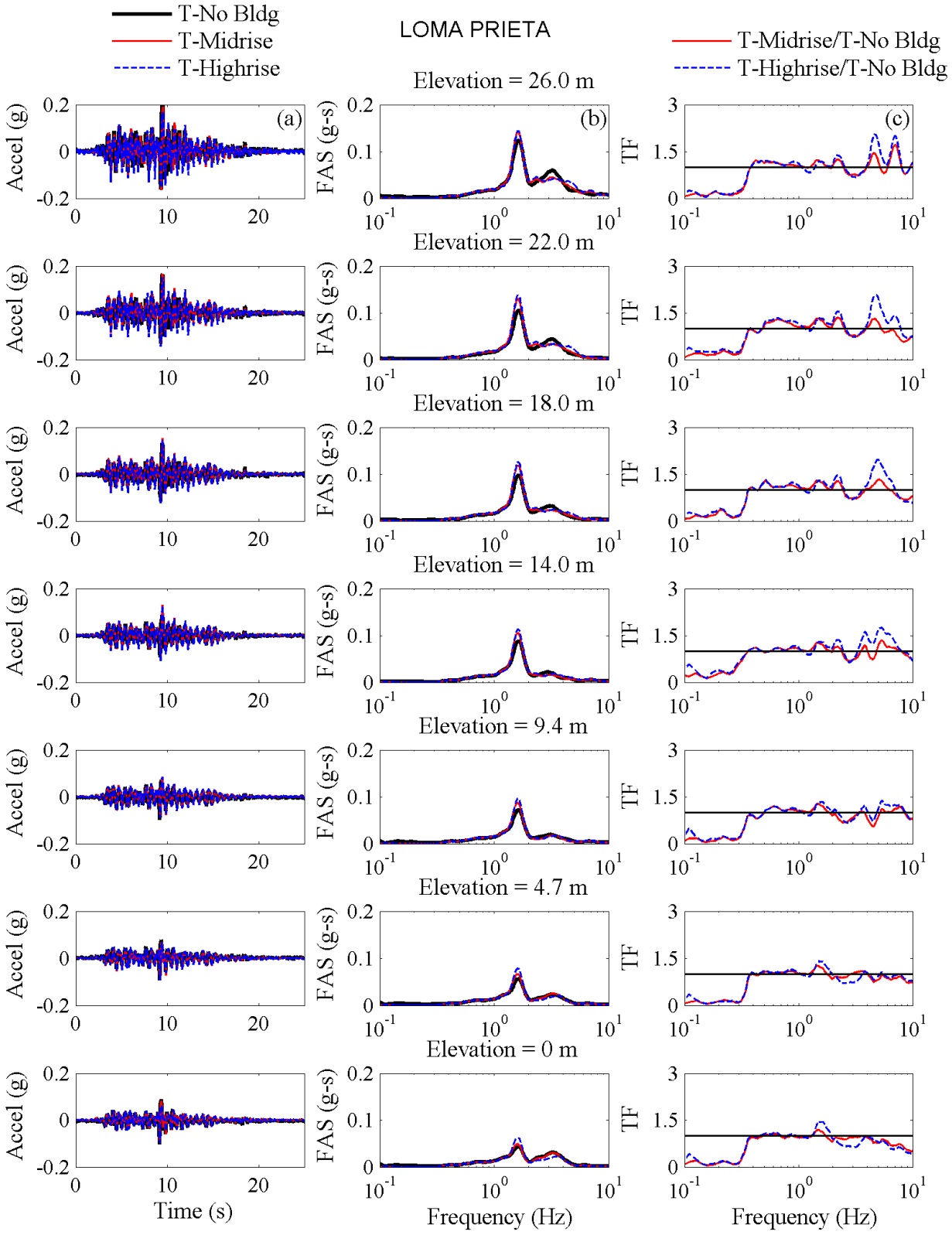

Figure 4.2.9. Loma Prieta far-field acceleration response shown as (a) acceleration time histories; (b) Fourier amplitude spectra; and (c) transfer functions.

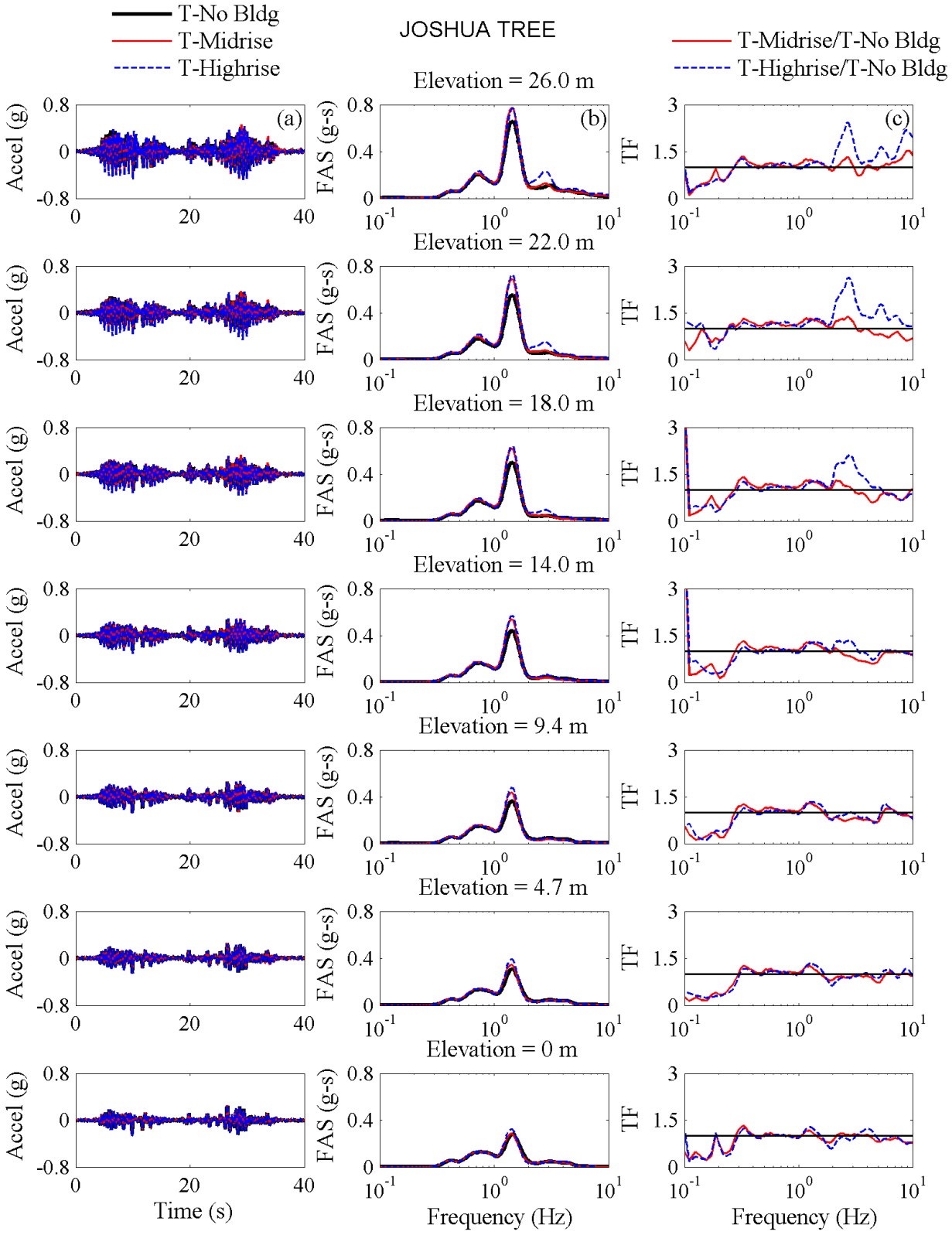

Figure 4.2.10. Joshua Tree far-field acceleration response shown as (a) acceleration time histories; (b) Fourier amplitude spectra; and (c) transfer functions.

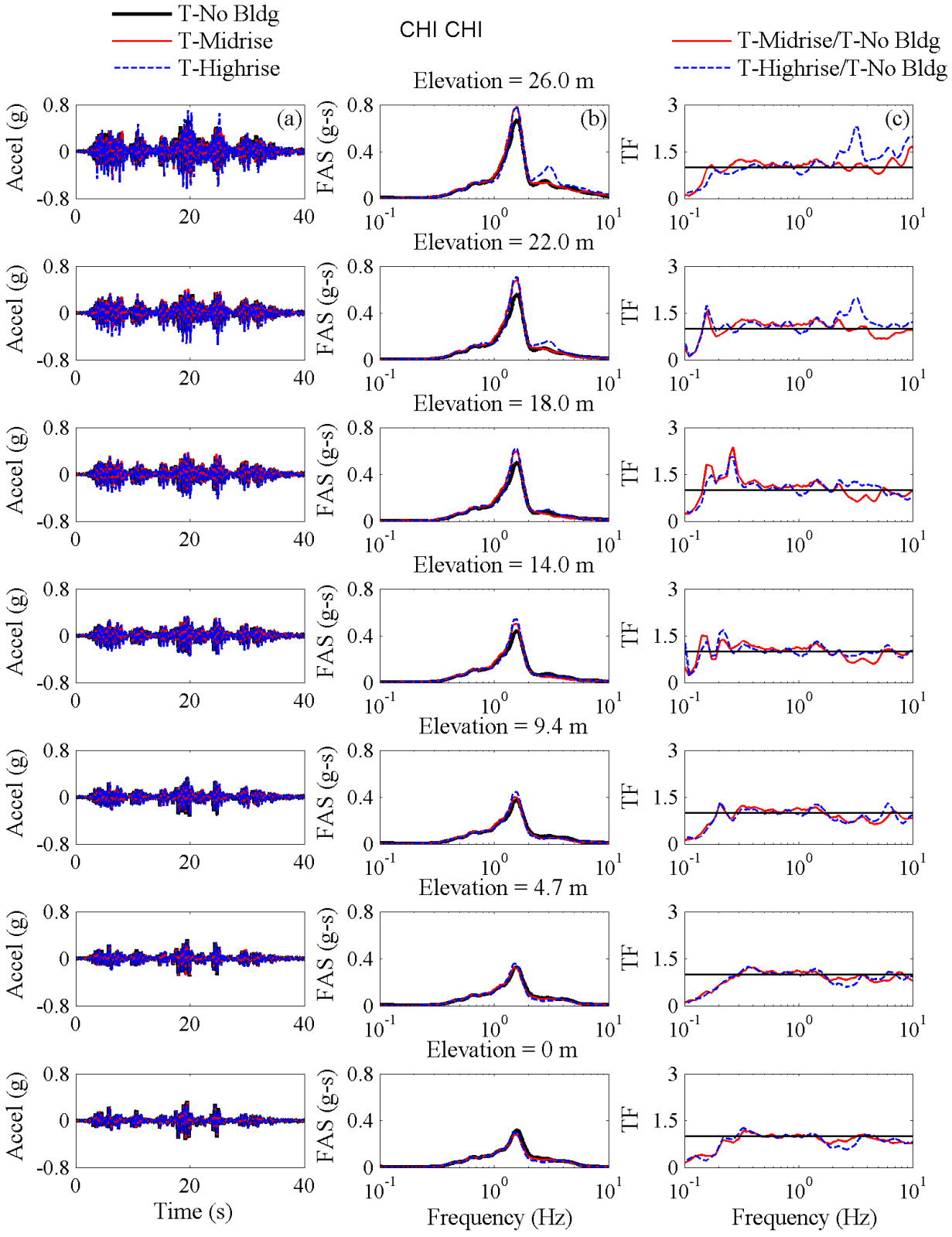

Figure 4.2.11. Chi Chi far-field acceleration response shown as (a) acceleration time histories; (b) Fourier amplitude spectra; and (c) transfer functions.

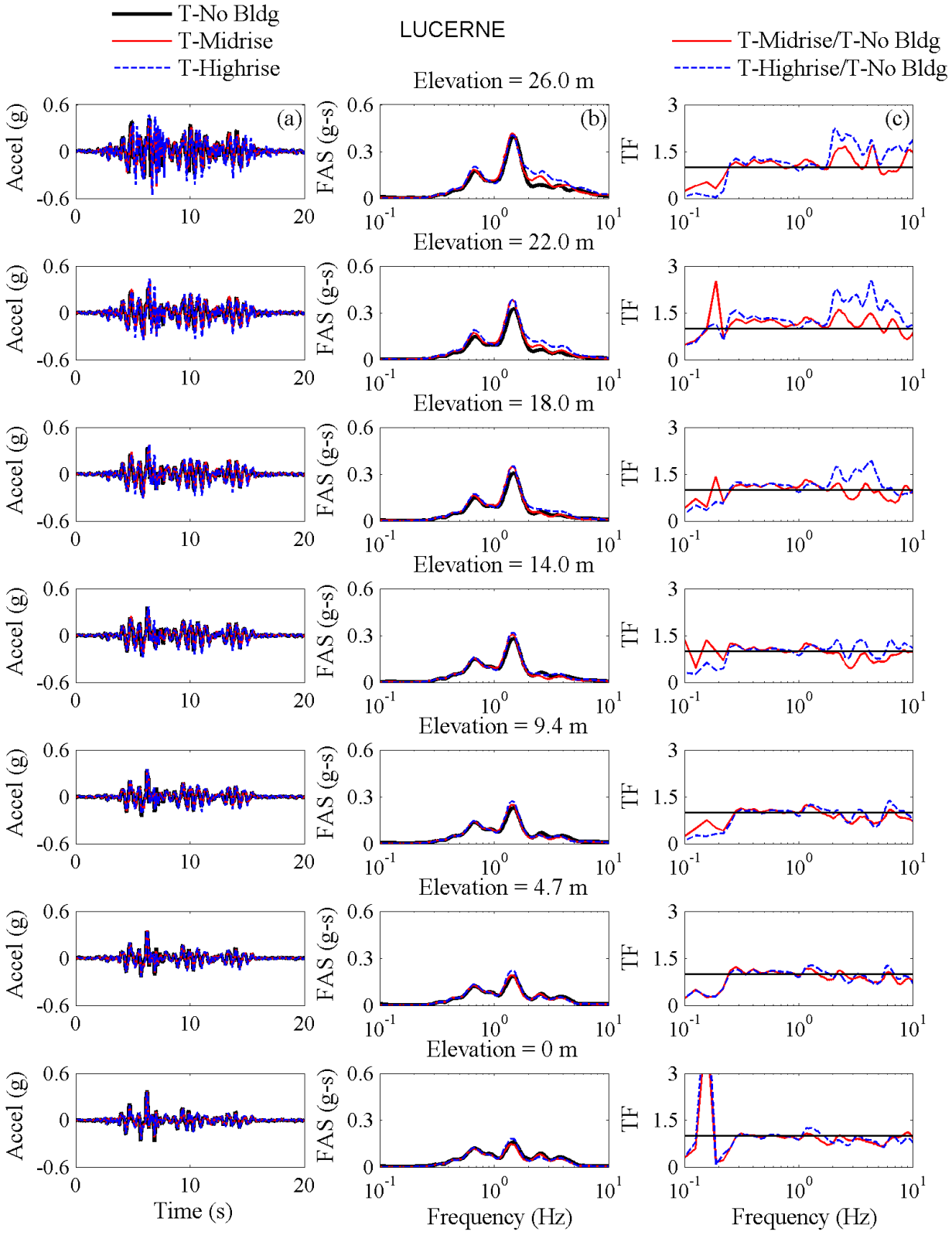

Figure 4.2.12. Lucerne far-field acceleration response shown as (a) acceleration time histories; (b) Fourier amplitude spectra; and (c) transfer functions.

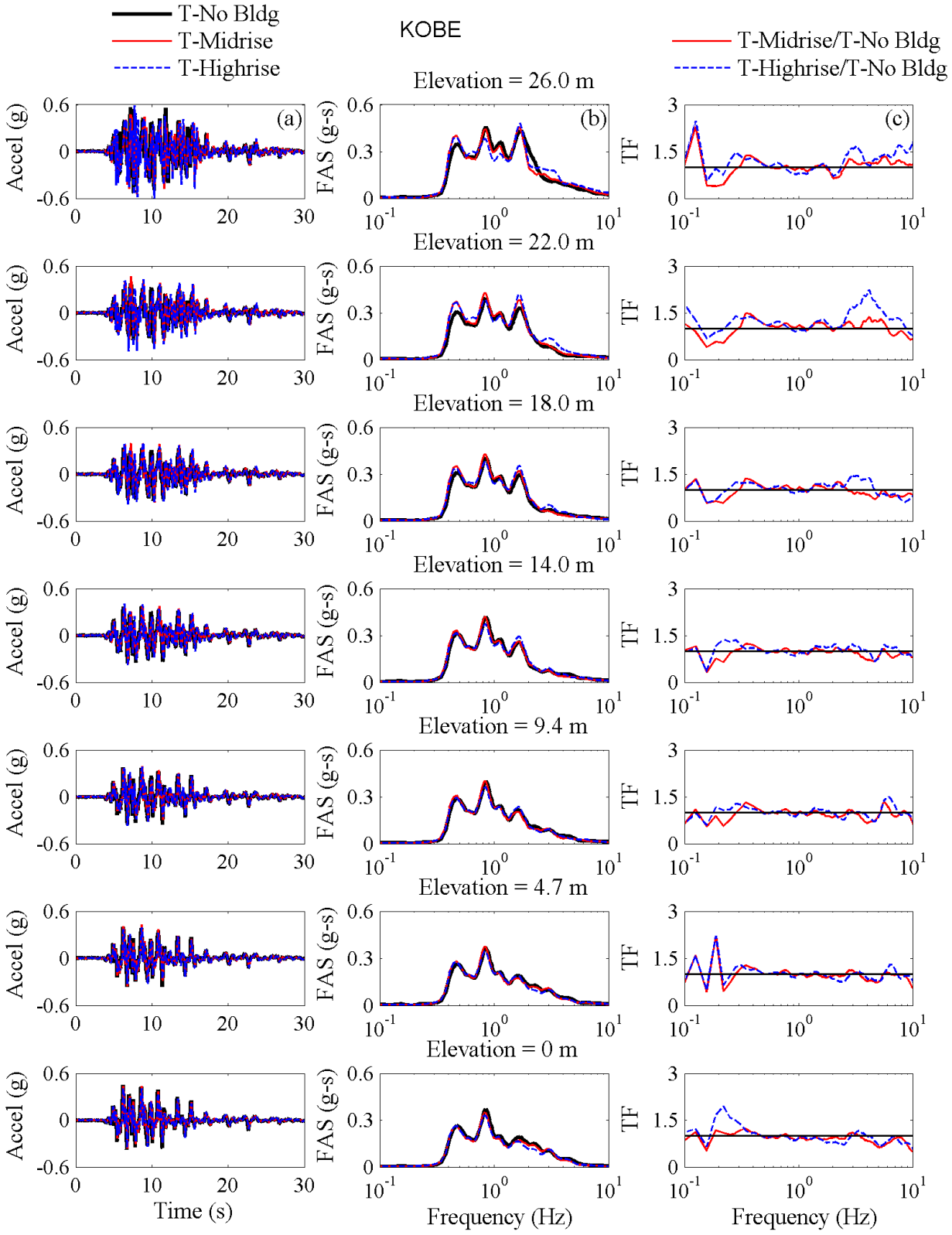

Figure 4.2.13. Kobe far-field acceleration response shown as (a) acceleration time histories; (b) Fourier amplitude spectra; and (c) transfer functions.

4.2.4 Near-Field Accelerations

In addition to a far-field array, each experiment contained an array of four accelerometers that were located inside the soil 3 m (prototype scale) laterally away from the tunnel, and placed on the opposite side from the tall building, if present. The near-field (NF) accelerometers measured the soil's response very close to the tunnel to evaluate any influence from the underground structure and the adjacent building. Table 4.2.4 shows the accelerometers used in the NF of each experiment.

A summary of the NF acceleration response for all experiments involving the permanent box structure is provided in Figure 4.2.14 through Figure 4.2.19. T-Midrise accelerometer A15 located at the elevation corresponding to the top of the tunnel malfunctioned and therefore is not shown in the following figures.

The acceleration time histories presented in Figure 4.2.14 through Figure 4.2.19 (a) show reasonable agreement among the three different experiments for all ground motions. The frequency content of each motion is expressed using Fourier amplitude spectra in the second column labeled (b) in Figure 4.2.14 through Figure 4.2.19. The third column, labeled (c), shows the transfer function or ratio of Fourier acceleration amplitudes in T-Midrise to T-No Bldg and T-Highrise to T-No Bldg to evaluate the change in near-field response due to the presence of a tall building.

The main observations are as follows:

- The amplitude of NF accelerations increased from the base toward the surface in each experiment (similar trend to far-field).
- The presence of the building did not significantly alter near-field accelerations in the frequency range of interest (i.e., the calculated TFs were near 1.0).

- Slight changes in near-field accelerations existed at frequencies greater than about 3Hz and smaller than 0.3Hz (sometimes amplification and sometimes de-amplification observed).

Table 4.2.4. Accelerometers used in each experiment in the near-field.

Test ID	Near-Field Accelerometers ID
T-No Bldg	A1 - A4
T-Midrise	A13 - A16
T-Highrise	A16 - A19

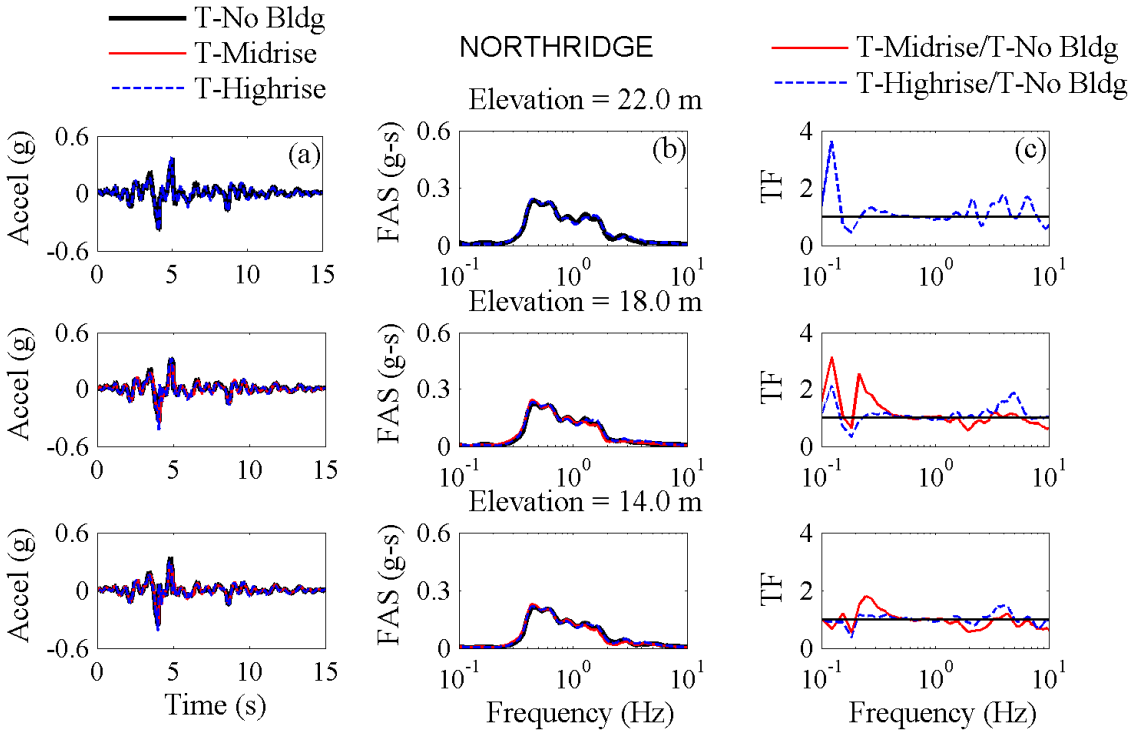

Figure 4.2.14 Northridge near-field acceleration response shown as (a) acceleration time histories; (b) Fourier amplitude spectra; and (c) transfer function.

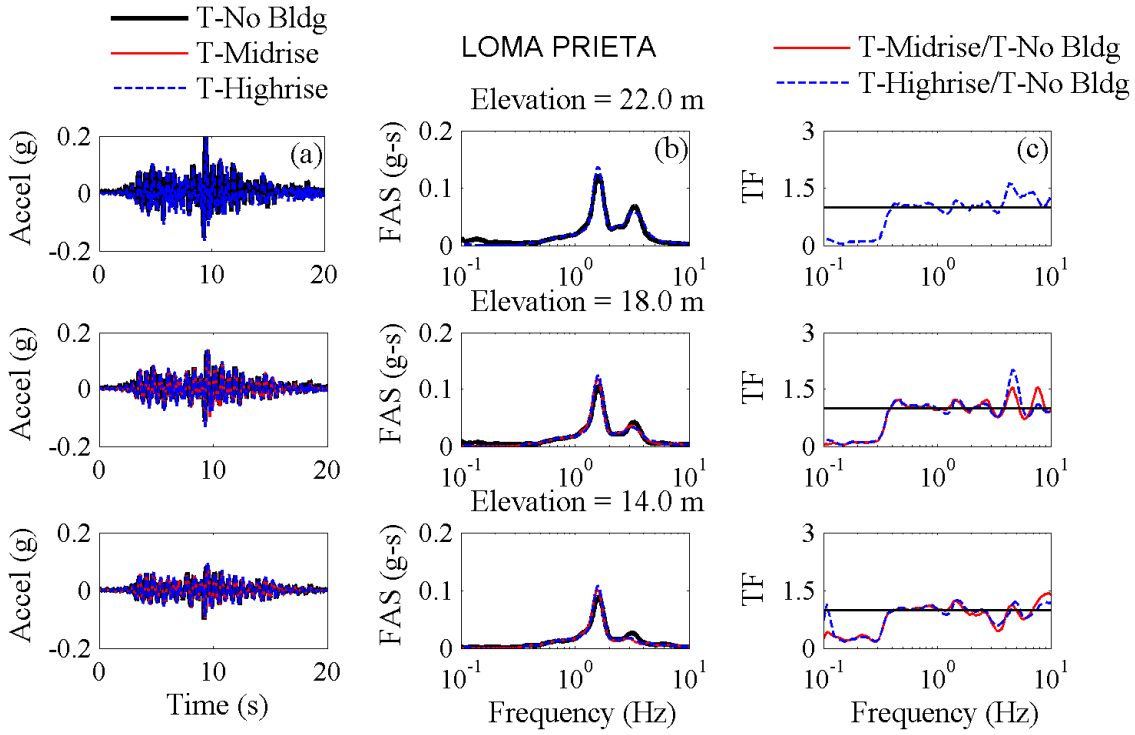

Figure 4.2.15 Loma Prieta near-field acceleration response shown as (a) acceleration time histories; (b) Fourier amplitude spectra; and (c) transfer functions.

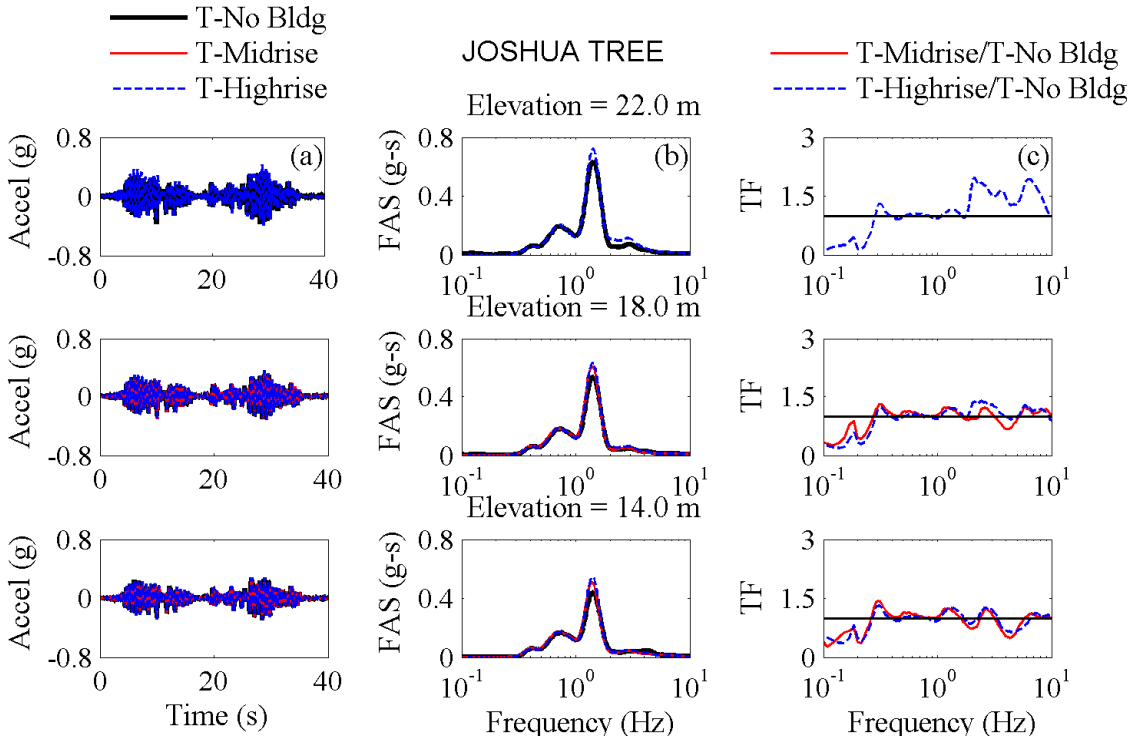

Figure 4.2.16 Joshua Tree near-field acceleration response shown as (a) acceleration time histories; (b) Fourier amplitude spectra; and (c) transfer functions.

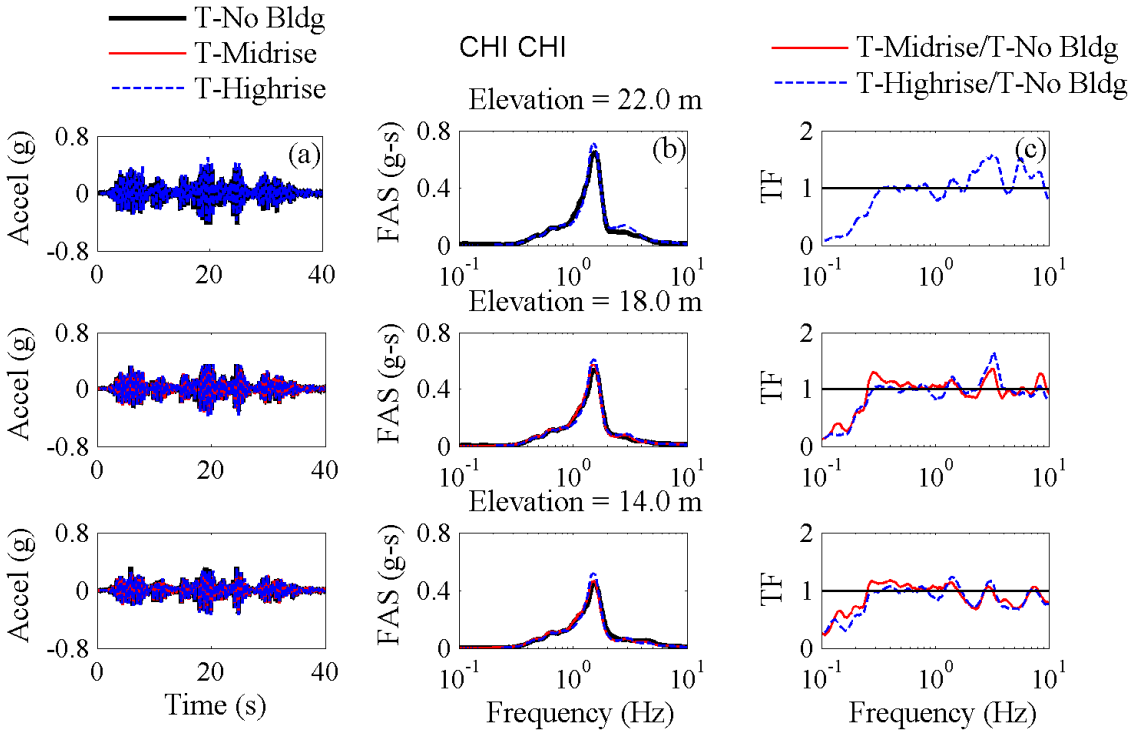

Figure 4.2.17 Chi Chi near-field acceleration response shown as (a) acceleration time histories; (b) Fourier amplitude spectra; and (c) transfer functions.

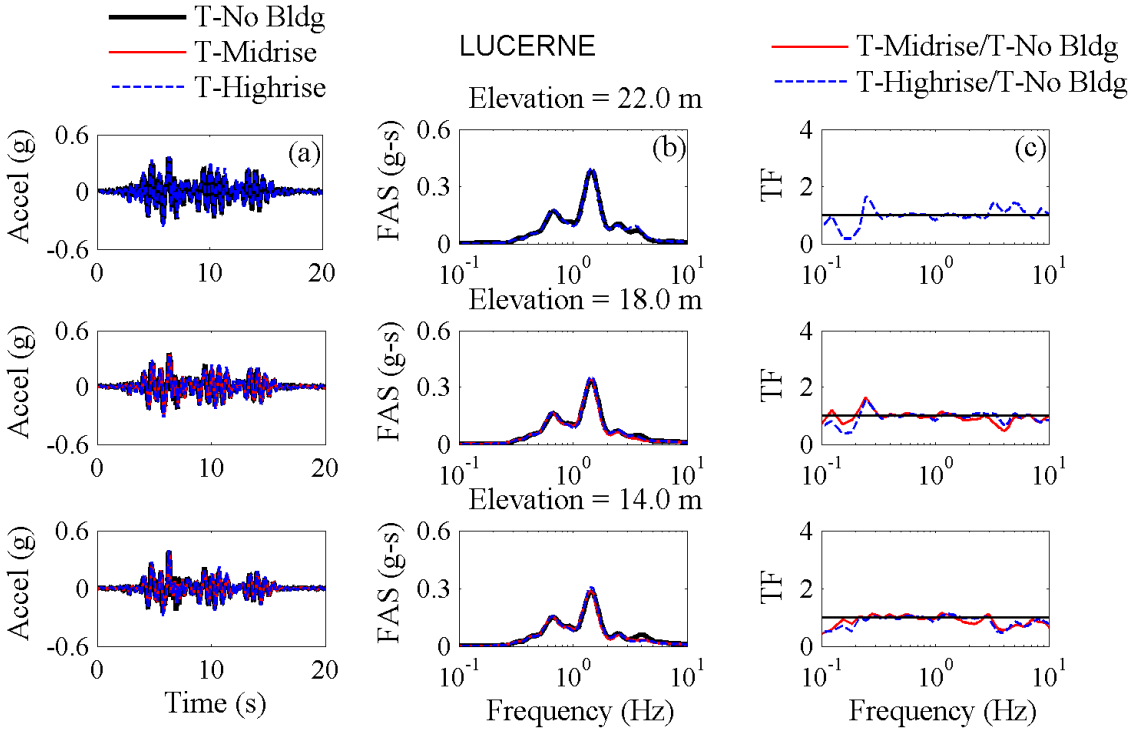

Figure 4.2.18 Lucerne near-field acceleration response shown as (a) acceleration time histories; (b) Fourier amplitude spectra; and (c) transfer functions.

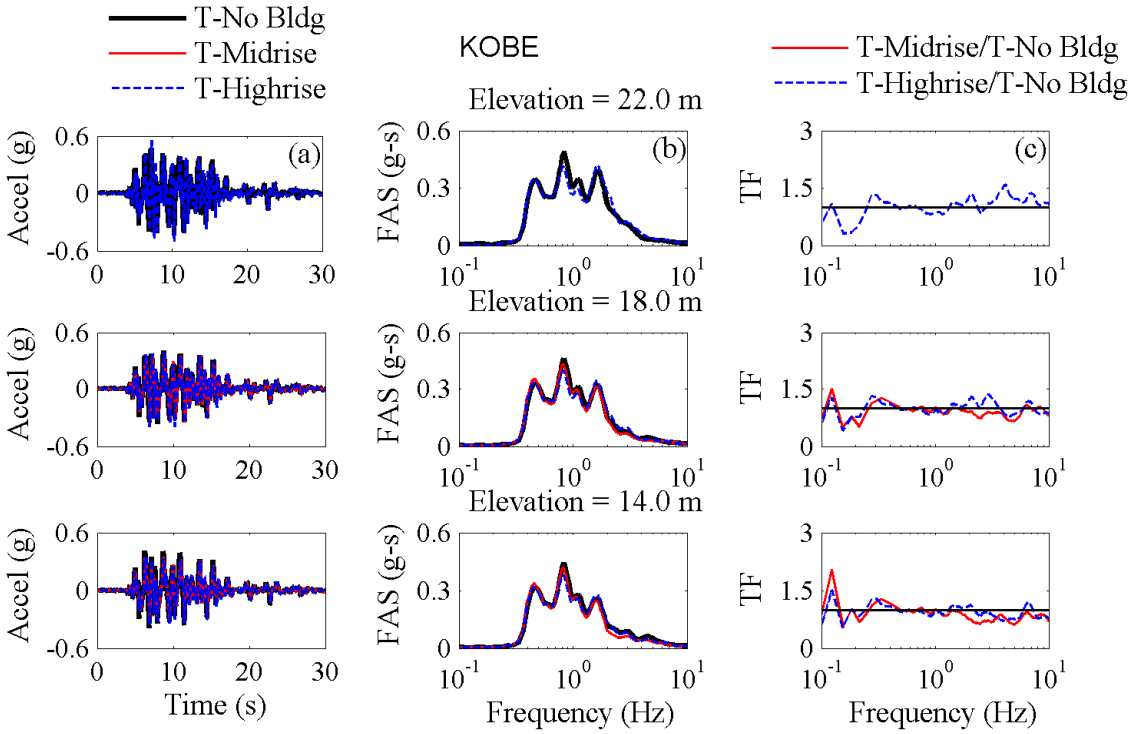

Figure 4.2.19 Kobe near-field acceleration response shown as (a) acceleration time histories; (b) Fourier amplitude spectra; and (c) transfer functions.

4.2.5 Tunnel Acceleration Response

The underground box structure had six horizontal accelerometers in each experiment placed centrally along the length of the tunnel as shown in Figure 4.2.20. The south and north walls each were instrumented with three accelerometers. Two vertically oriented accelerometers were also positioned on top of the tunnel to capture the rocking motion if present. Table 4.2.5 shows the tunnel accelerometer IDs in each test. There were three non-working accelerometers located on the tunnel in the three experiments, as summarized in Table 4.2.6. The data from these instruments are not included in the following group of figures.

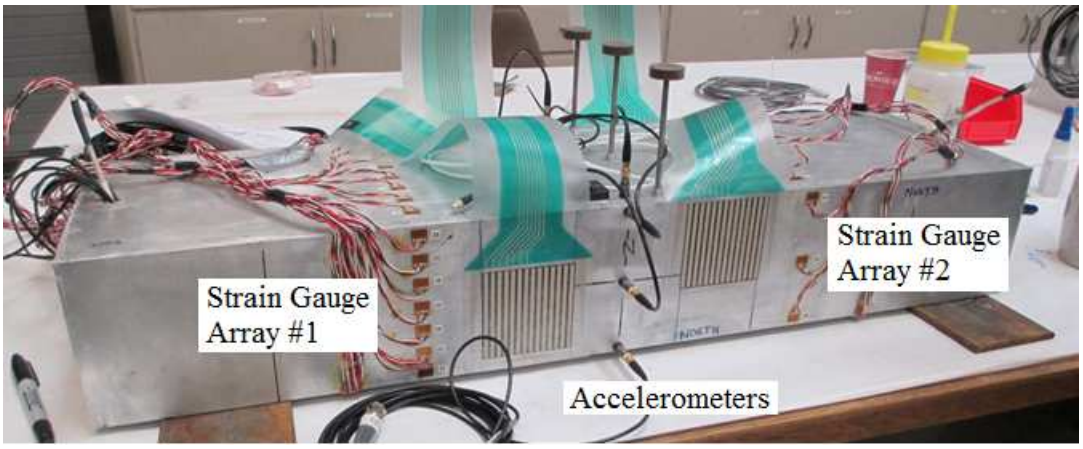

Figure 4.2.20.Model permanent box structure (tunnel) shown with instrumentation including accelerometers, strain gauges, and tactile pressure sensors.

Table 4.2.5. Tunnel accelerometer IDs used in each experiment.

Test ID	S. Tunnel Wall Accelerometers	N. Tunnel Wall Accelerometers
T-No Bldg	A5 - A7	A18 - A20
T-Midrise	A37 - A39	A46 - A48
T-Highrise	A41 - A43	A48 - A50

Table 4.2.6. List of non-working accelerometers placed on the permanent box structure during the tunnel experiments.

Test ID	Non-Working Accelerometers
T-No Bldg	A6, A19
T-Midrise	A48
T-Highrise	N/A

The following trends were found from the following set of figures:

- The acceleration response of the tunnel was generally similar among the three tests in both time and frequency domains (particularly in frequencies ranging from about 0.3 to 3 Hz).
- Generally, the presence of an adjacent midrise or highrise building slightly de-amplified accelerations along the tunnel walls at frequencies of less than approximately 0.3 Hz. However, the accelerations at those same frequencies were amplified during the Northridge and Kobe motions near the top of the box structure.

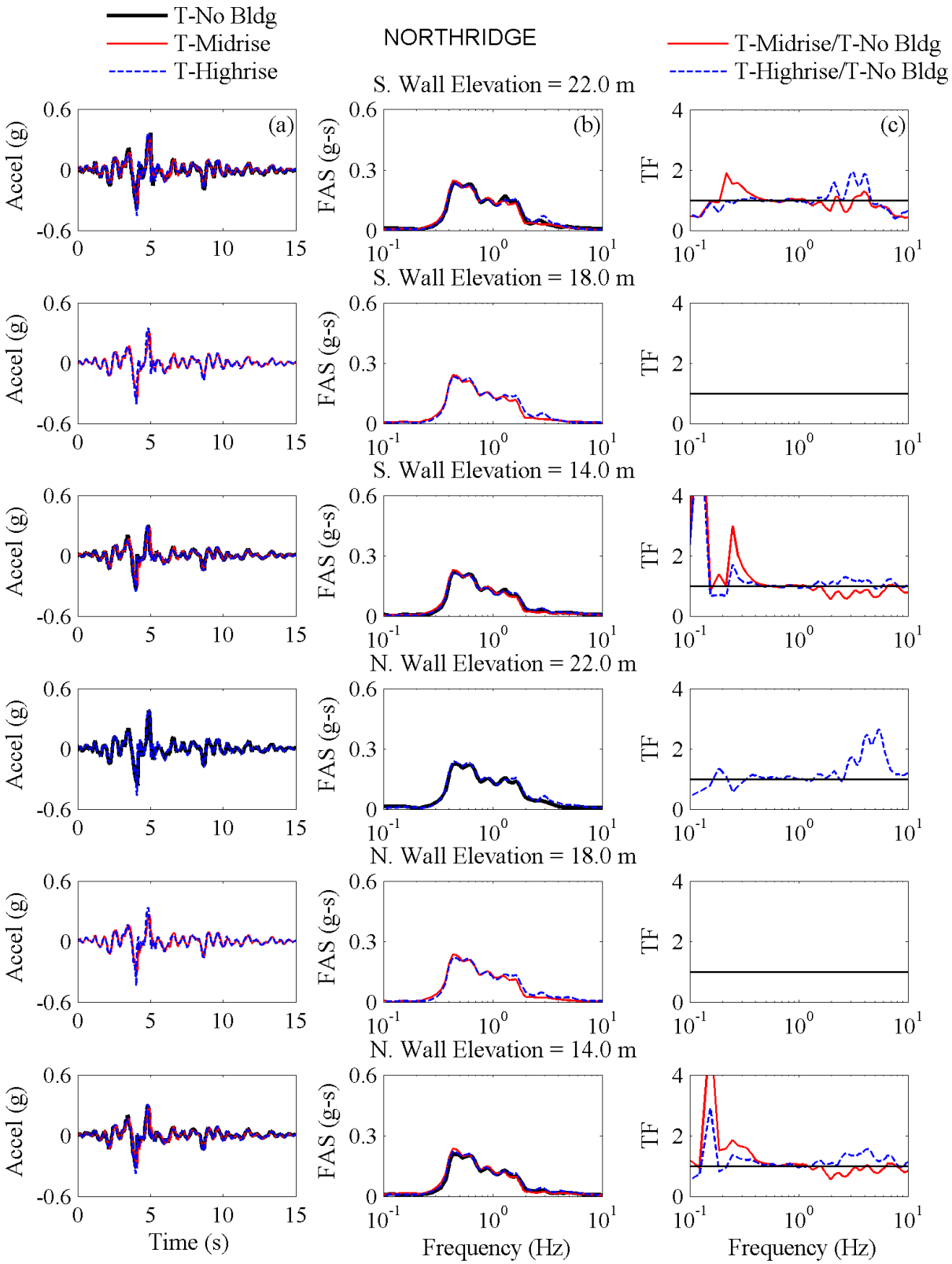

Figure 4.2.21. Northridge tunnel acceleration response shown as (a) acceleration time histories; (b) Fourier amplitude spectra; and (c) transfer function.

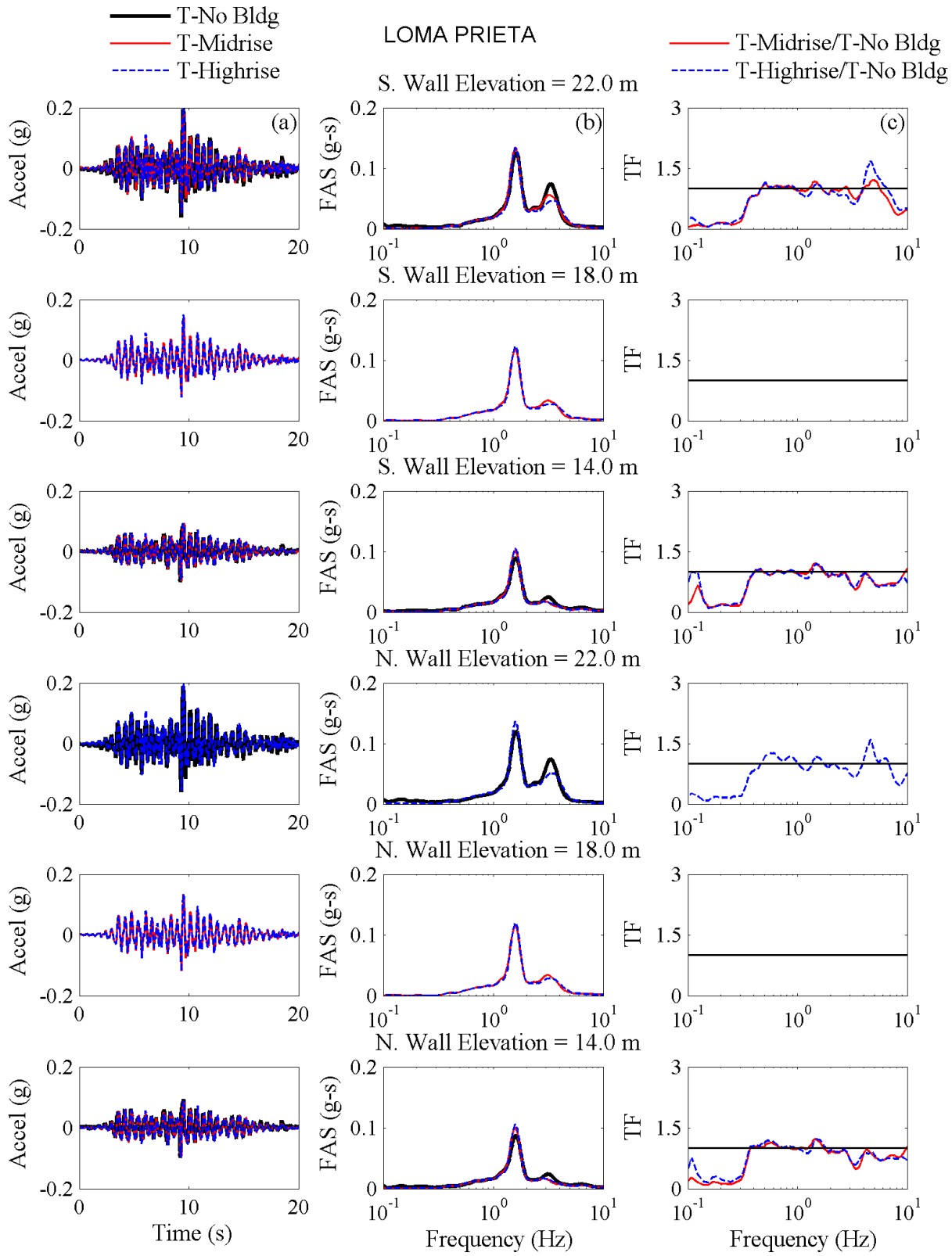

Figure 4.2.22. Loma Prieta tunnel acceleration response shown as (a) acceleration time histories; (b) Fourier amplitude spectra; and (c) transfer function.

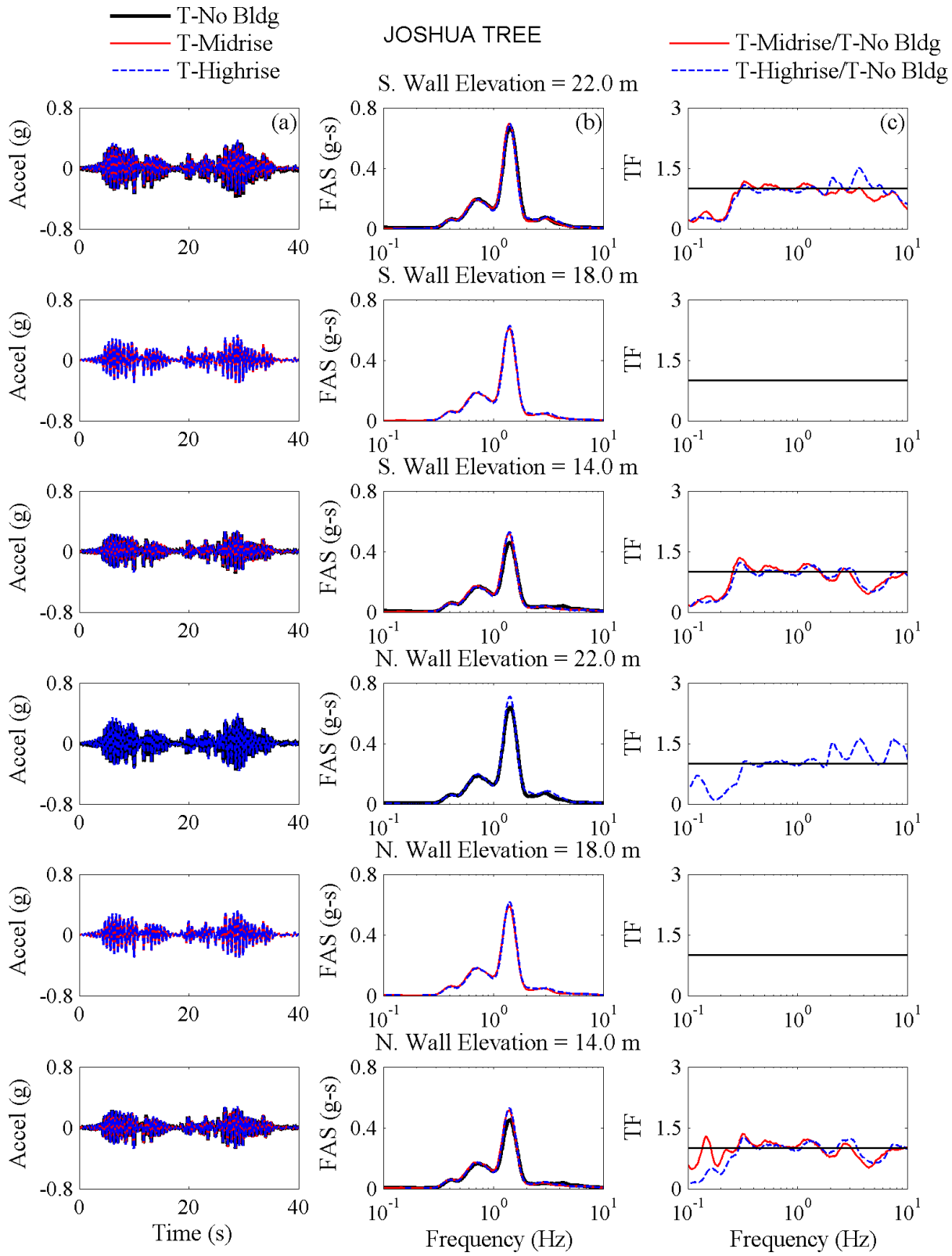

Figure 4.2.23. Joshua Tree tunnel acceleration response shown as (a) acceleration time histories; (b) Fourier amplitude spectra; and (c) transfer function.

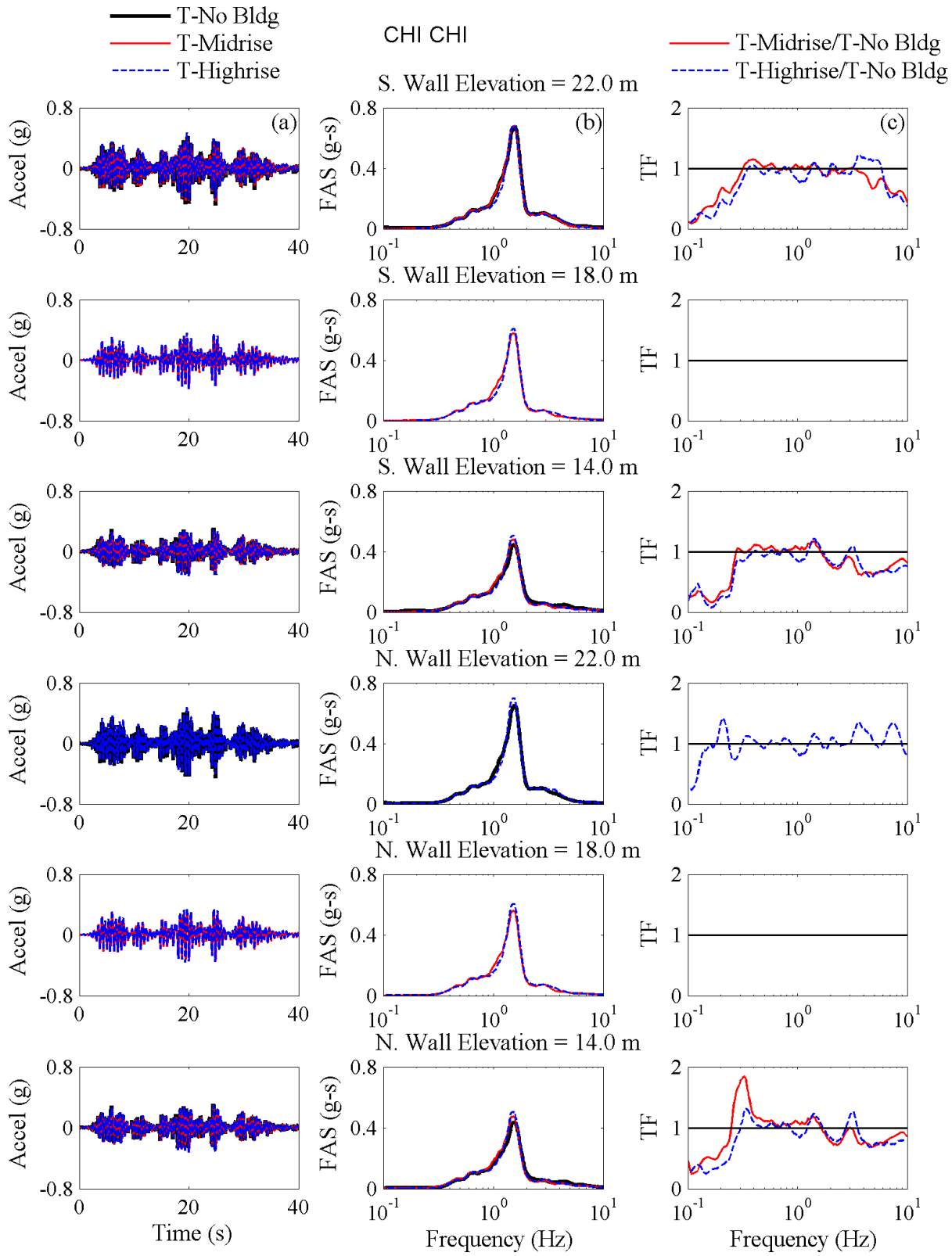

Figure 4.2.24. Chi Chi tunnel acceleration response shown as (a) acceleration time histories; (b) Fourier amplitude spectra; and (c) transfer function.

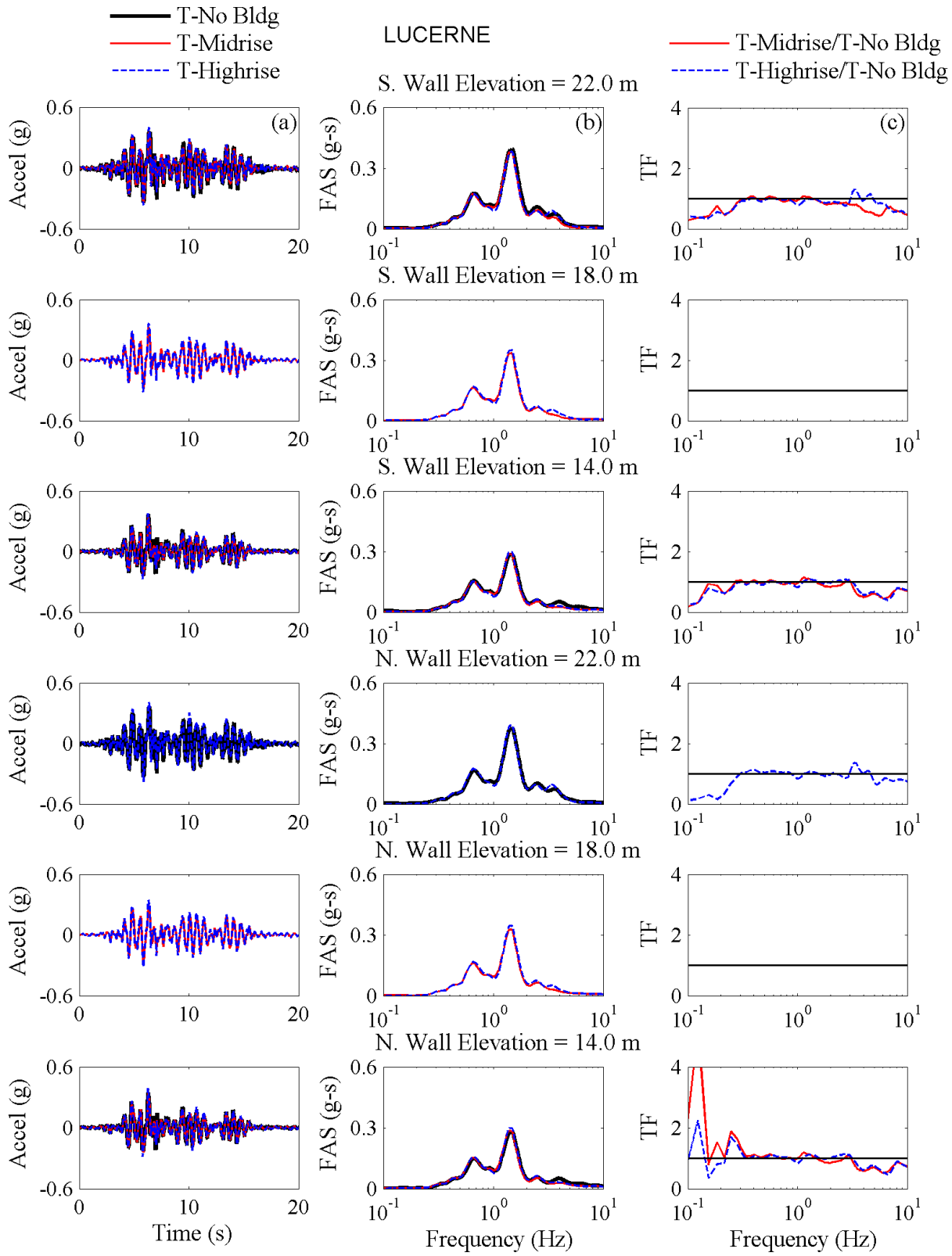

Figure 4.2.25. Lucerne tunnel acceleration response shown as (a) acceleration time histories; (b) Fourier amplitude spectra; and (c) transfer function.

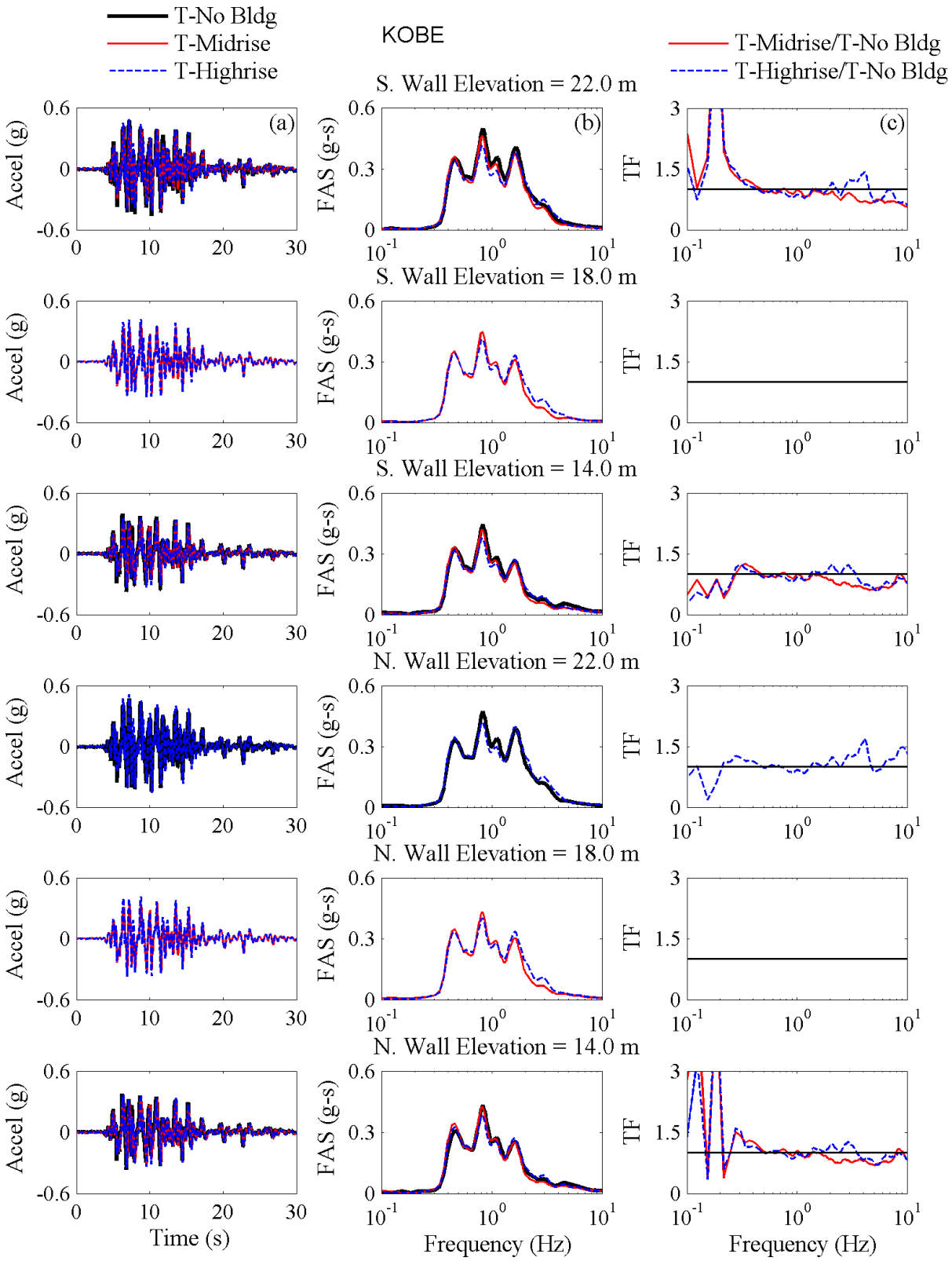

Figure 4.2.26. Kobe tunnel acceleration response shown as (a) acceleration time histories; (b) Fourier amplitude spectra; and (c) transfer function.

4.3 Lateral Displacements

Maximum lateral displacement of the underground structure and the surrounding soil was evaluated and compared to gain an understanding of how the tall buildings' presence influenced the displacement response of the underground structure-soil-building system during each shaking event. These displacements were calculated by filtering and then double integrating the recordings of accelerometers.

4.3.1 Displacement in the NF Soil

Maximum lateral displacements in the soil surrounding the underground structure were compared among experiments to observe how the presence of the tall buildings influenced the near-field (NF) lateral displacements. Figure 4.3.1 shows a zoomed-in instrumentation layout of T-Highrise showing the accelerometers used to calculate displacement at each elevation in that test. The NF accelerometer arrays were placed at the same distance from the tunnel in all three tests: 3m on the free side and 4m on the building side. Table 4.3.1 lists the accelerometers used at each elevation to calculate lateral displacements of the NF soil surrounding the tunnel. Two NF arrays were considered: 1) 3m horizontally away from the excavation on its free (north) side; 2) 4m horizontally away from the tunnel on its building (south) side. These arrays are referred to as "NF Free Side" and "NF Bldg Side", respectively. There were only two accelerometers on the highrise building's basement at elevations corresponding to the other experiments for comparison. Because there was no tall building in T-No Bldg, the NF Free Side and Bldg Side accelerations were taken from the NF accelerometer array, and therefore were the same. The presence of the basement was observed to reduce peak lateral displacements in the NF compared to T-No Bldg in most cases, particularly on the building side near the surface, which was expected due to its kinematic constraints.

Table 4.3.1. Accelerometers used to calculate lateral displacements in the NF.

	NF Free Side			NF Bldg. Side		
Elevation (m)	T-No Bldg	T-Midrise	T-Highrise	T-No Bldg	T-Midrise	T-Highrise
14	A01	A13	A16	A01	NA	A34
18	A02	A14	A17	A02	A30	A35
22	A03	A15	A18	A03	A31	A36
26	A04	A16	A19	A04	A36	A37

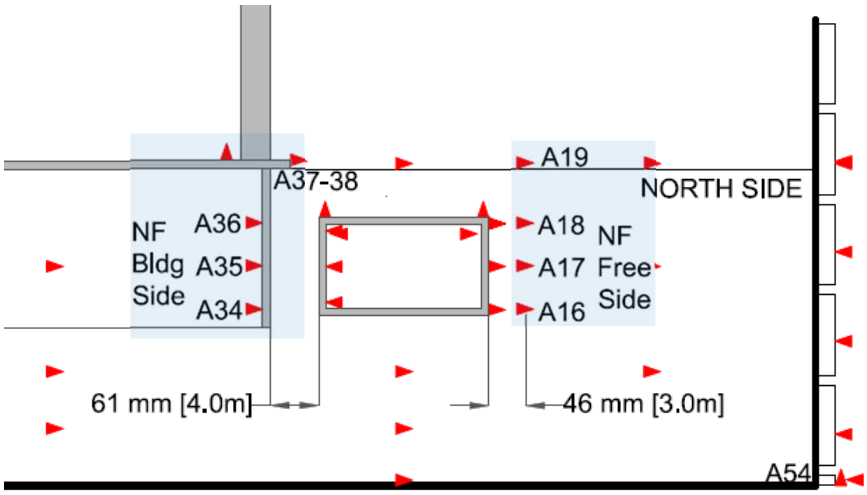

Figure 4.3.1. Accelerometers used for T-Highrise lateral displacement calculations in the NF.

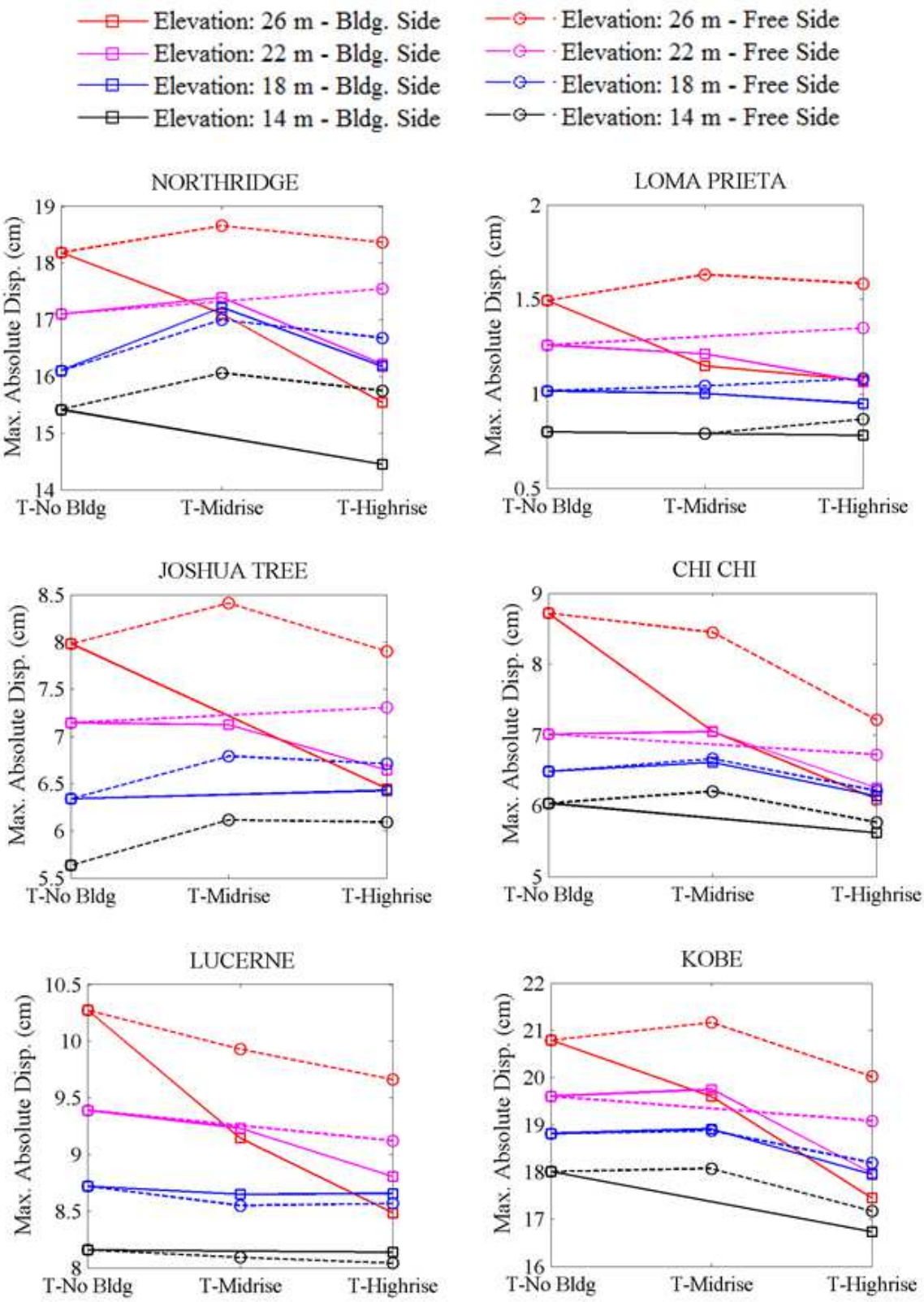

Figure 4.3.2. Comparing near-field (NF) soil maximum lateral displacements on the free side and building side of the underground box structure.

4.3.2 Displacement of the Box Structure

The maximum transient average lateral displacement along the tunnel's two wall in each experiment is shown in Figure 4.3.3. The average wall displacement was obtained by averaging the lateral displacement at the top and bottom of the corresponding tunnel wall (both obtained from double integrating accelerometer recordings), since the middle accelerometer malfunctioned in a number of tests. It is shown that the maximum lateral displacement of the tunnel walls did not change significantly from one experiment to the other. Therefore, the presence of an adjacent tall building did not influence the maximum amount of average transient lateral displacement on the tunnel walls during these tests.

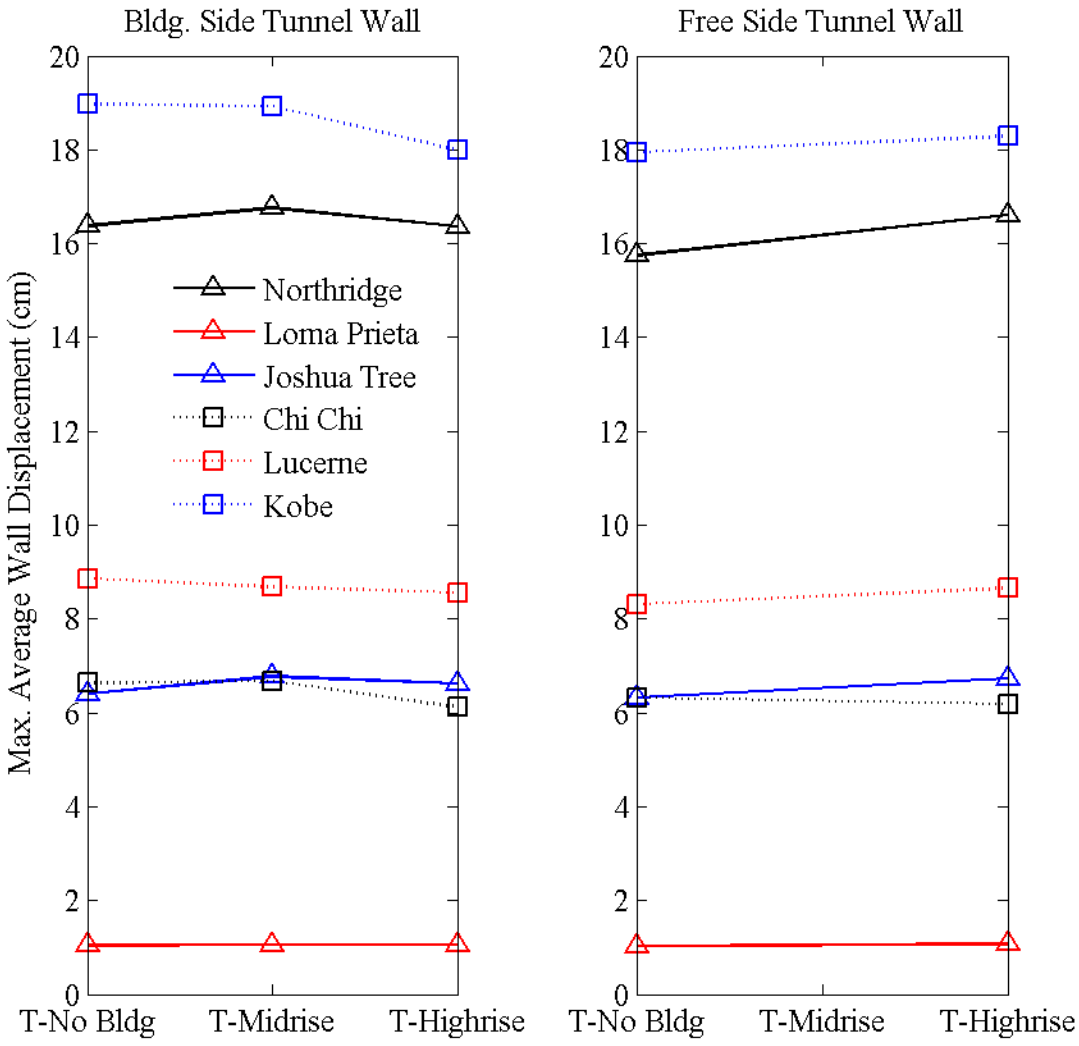

Figure 4.3.3. Maximum absolute lateral displacement of the tunnel walls.

4.3.3 Racking Displacement of the Box Structure

One of the most important measurement objectives in these centrifuge tests was the translational distortion of the box structure due to earthquake loading, or its racking displacement, compared to that of the soil away from the structures (in the far-field). Racking displacement is the relative translational displacement between the roof and floor that occurs during an earthquake as seismic waves propagate toward the surface (reference Chapter 2 for more information on racking displacements). In order to measure tunnel racking displacements, accelerometers located on the

upper and lower tunnel walls were first filtered using a 7th order band-pass Butterworth filter with corner frequencies of 0.3 and 30 Hz. The tunnel accelerometers used in each test are listed in Table 4.3.2. The filtered accelerometer data was then double integrated to obtain displacement time histories at the top and bottom of the tunnel wall. Racking displacement time histories were calculated as the difference between the displacement time histories at the top and bottom of the tunnel. The same process was performed to calculate racking displacements in the far-field soil. Although double integrating an accelerometer record to obtain displacement is not direct and removes any permanent displacement, the accelerometers were considered more reliable for measuring transient displacements compared to direct measurements with LPs, because the LP holders at times indicated independent vibration.

The next group of figures (Figure 4.3.4 through Figure 4.3.9) compare racking displacements measured on two sides of the tunnel and in the far-field soil during all earthquakes. There was a non-working accelerometer on the north tunnel wall during the T-Midrise experiment, the recordings of which are excluded. The Fourier amplitude spectra of theses time series are also shown in each figure to evaluate the frequency content of racking. The transfer function of the Fourier amplitude spectra of T-Midrise to T-No Bldg and T-Highrise to T-No Bldg helps evaluate the influence of an adjacent building on racking deformations at different frequencies. For easier comparison, maximum racking displacements are also compared on the two tunnel walls among the three tests in Figure 4.3.10.

Key observations from these figures are as follows:

- Racking displacements were consistent on the two sides of the tunnel in both time and frequency domains.

- Tunnel racking reduced slightly in T-Midrise and T-Highrise compared to T-No Bldg during most ground motions. The Fourier amplitude spectra (FAS) of tunnel racking showed a reduction in amplitude due to the presence of an adjacent building for most of the frequency range of interest (0.5 to 3 Hz). The transfer functions also highlight the slight de-amplification of tunnel racking in T-Midrise and T-Highrise compared to T-No Bldg at lower frequencies.
- The presence of the building affected racking displacements in the far-field. With the exception of the Loma Prieta motion (weakest motion), racking displacements increased in the far-field of the corresponding test with the addition of a midrise and then a highrise building, particularly in frequencies ranging from about 0.6 to 0.8 Hz. The building seemed to push the soil in the far-field to deform more.

Table 4.3.2. Accelerometers used in the calculation of racking displacements.

Test ID	S. Wall Racking Accels.	N. Wall Racking Accels.	Far-Field Racking Accels.
T-No Bldg	A01, A03	A18, A20	A24, A26
T-Midrise	A37, A39	A46, A48	A04, A06
T-Highrise	A41, A43	A48, A50	A04, A06

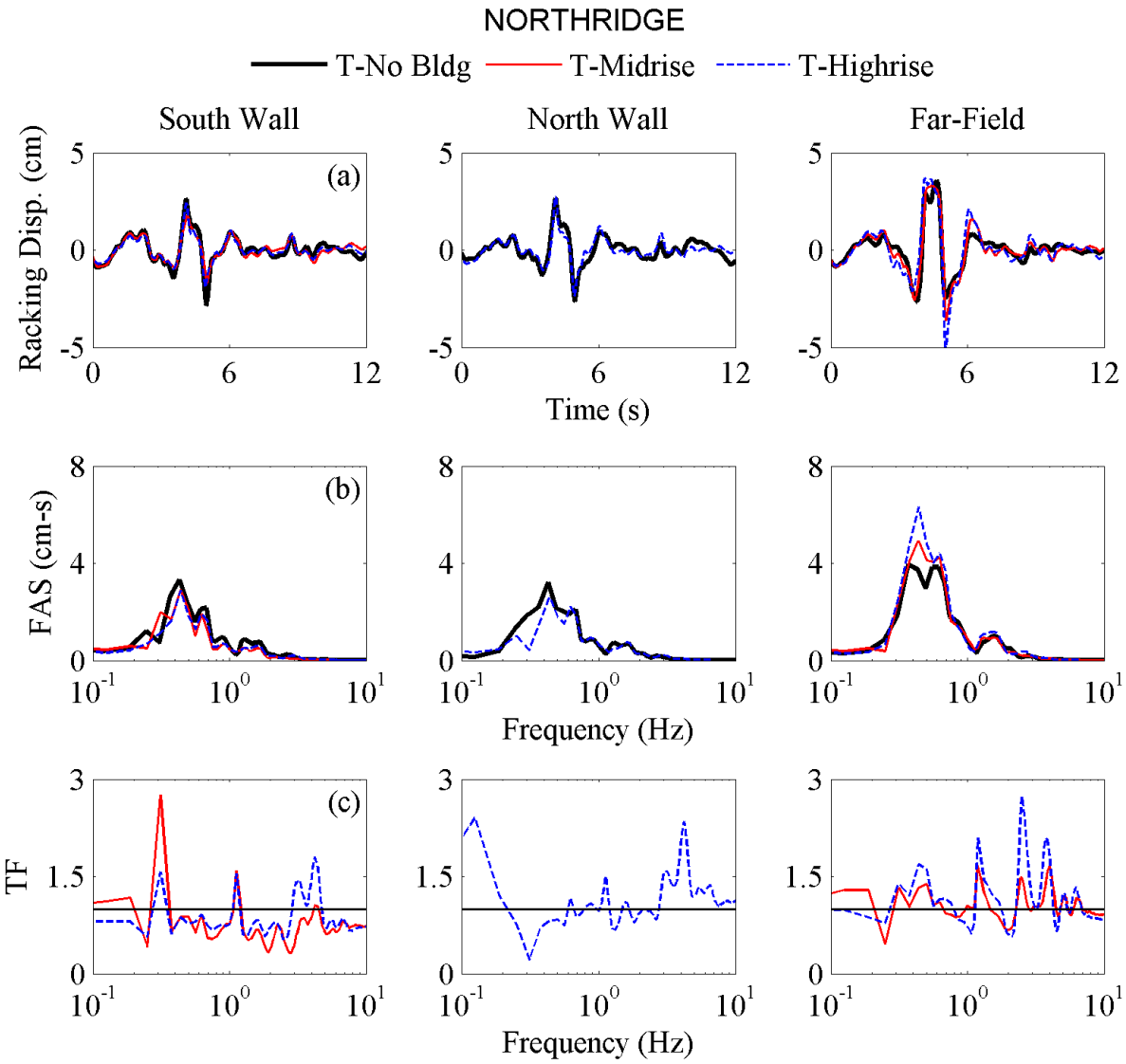

Figure 4.3.4. Northridge tunnel and far-field racking displacements in the time and frequency domains.

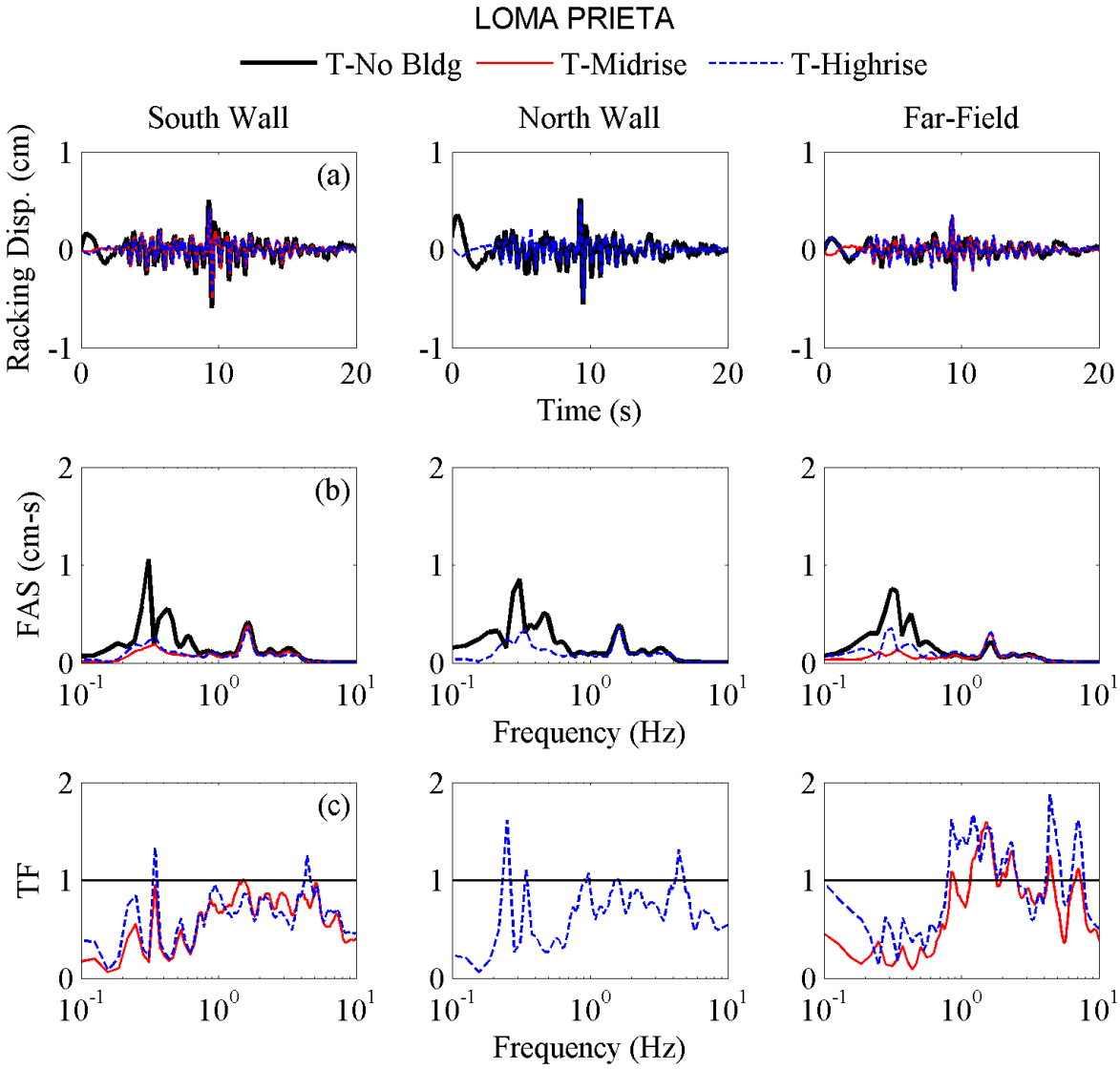

Figure 4.3.5. Loma Prieta tunnel and free-field racking displacements in the time and frequency domains.

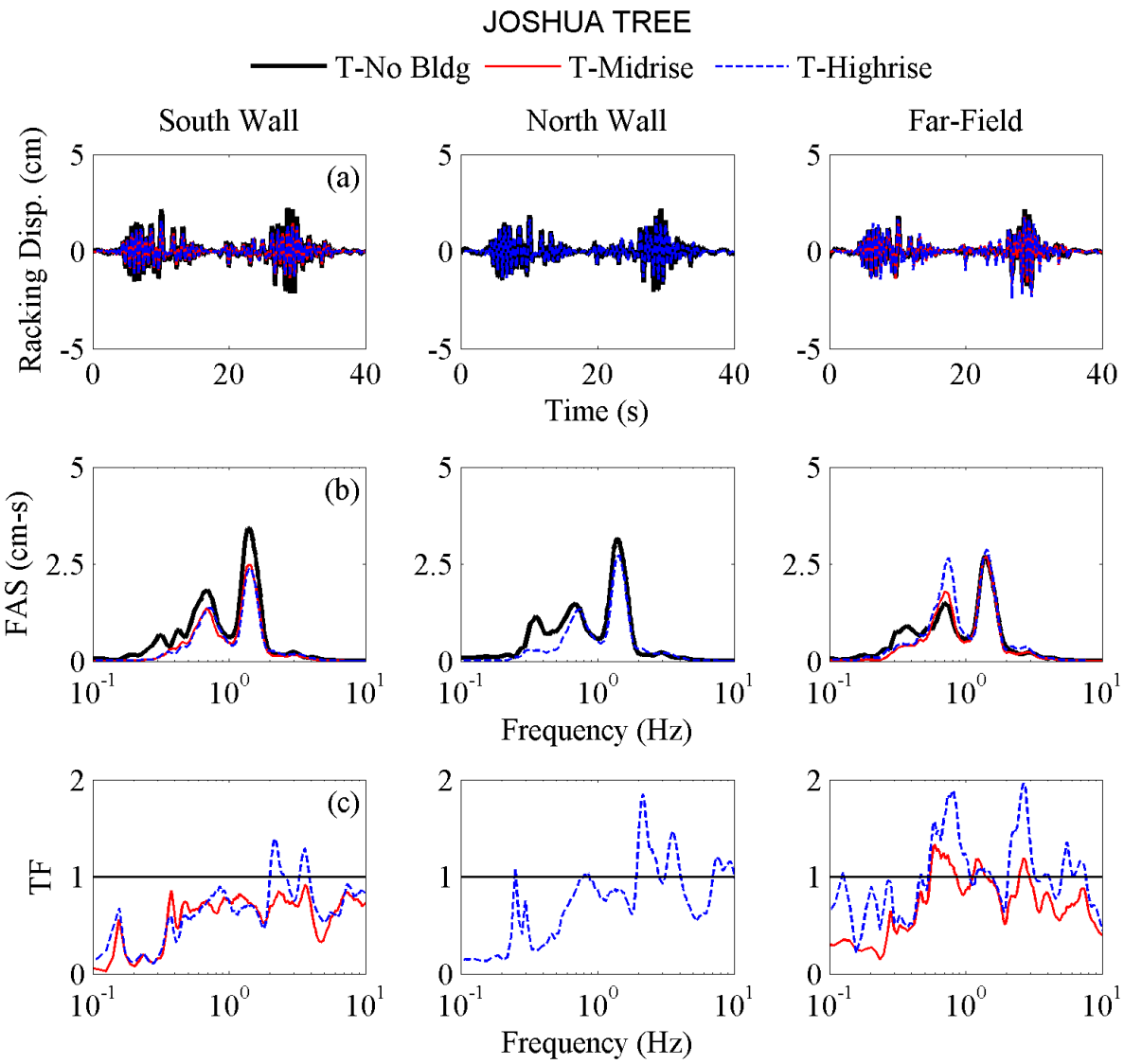

Figure 4.3.6. Joshua tree tunnel and free-field racking displacements in the time and frequency domains.

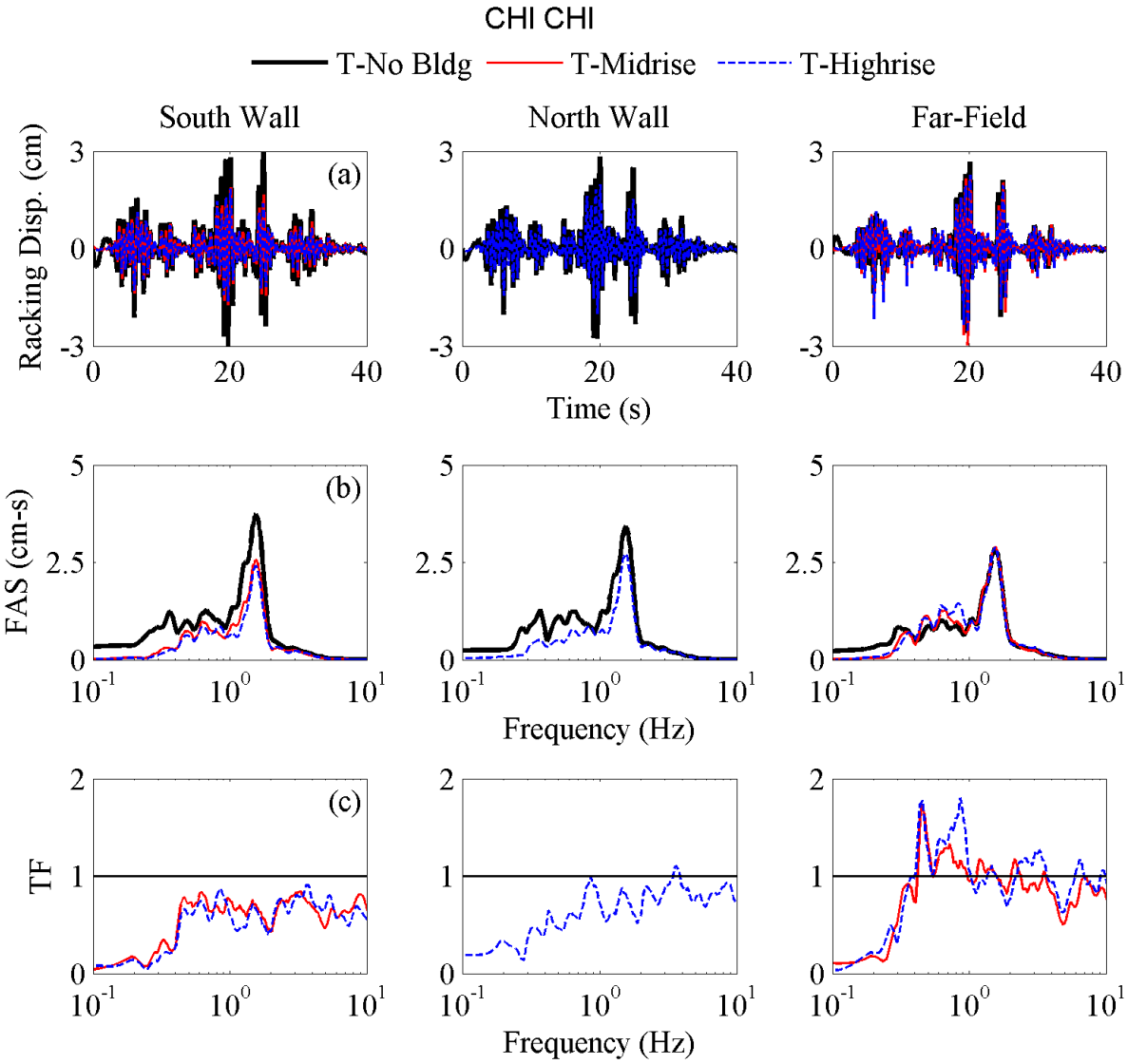

Figure 4.3.7. Chi Chi tunnel and free-field racking displacements in the time and frequency domains.

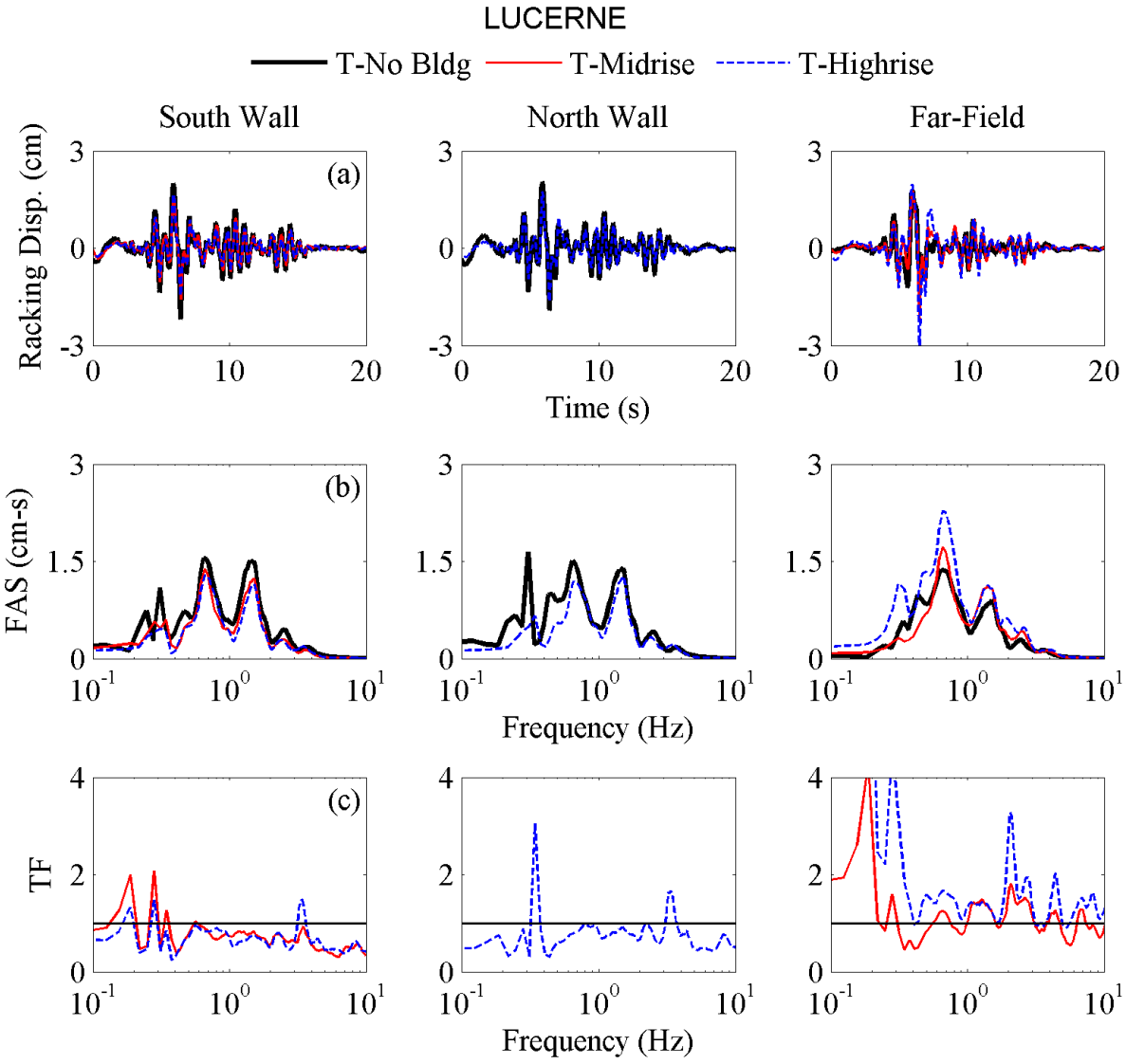

Figure 4.3.8. Lucerne tunnel and free-field racking displacements in the time and frequency domains.

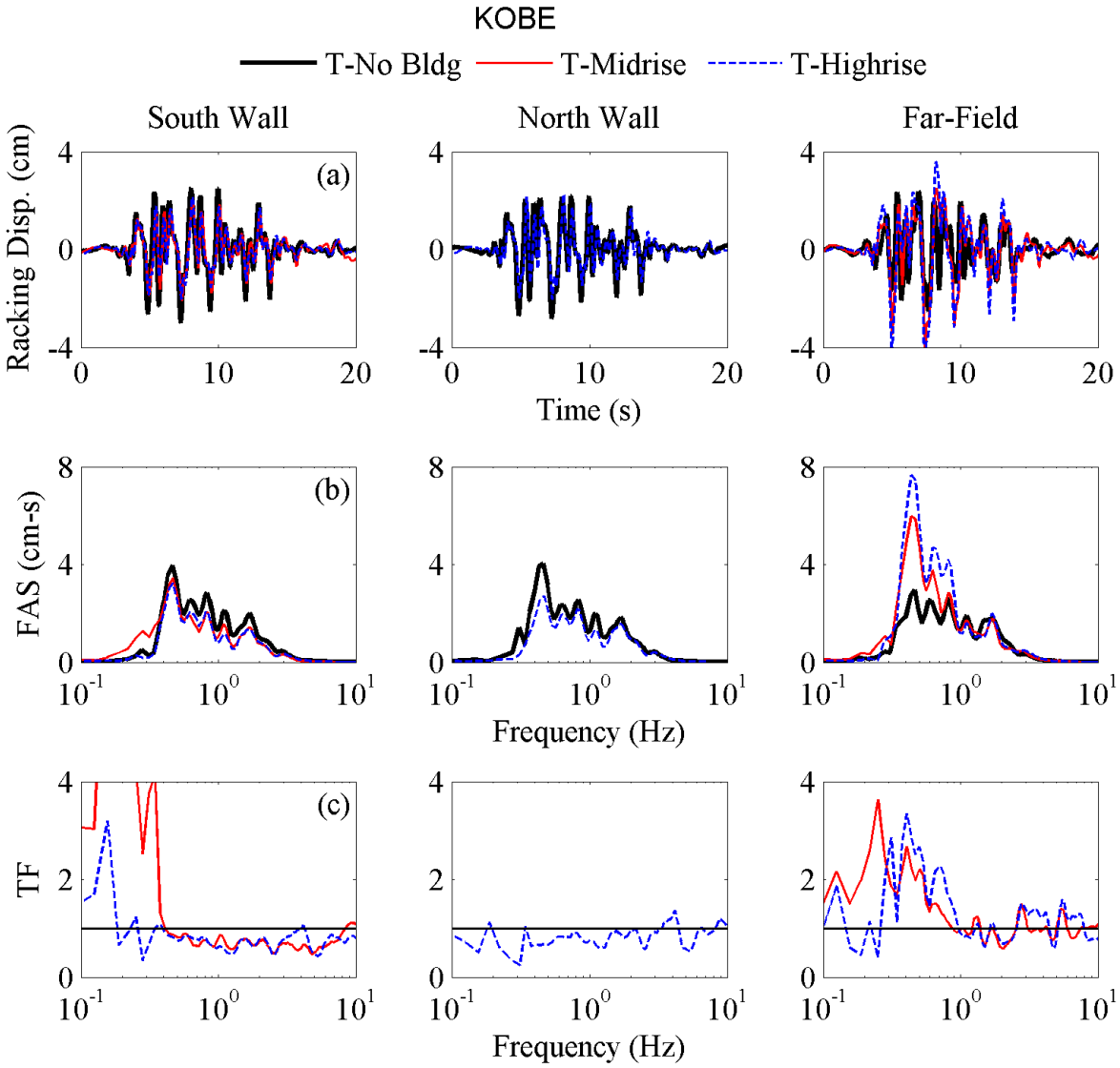

Figure 4.3.9. Kobe tunnel and free-field racking displacements in the time and frequency domains.

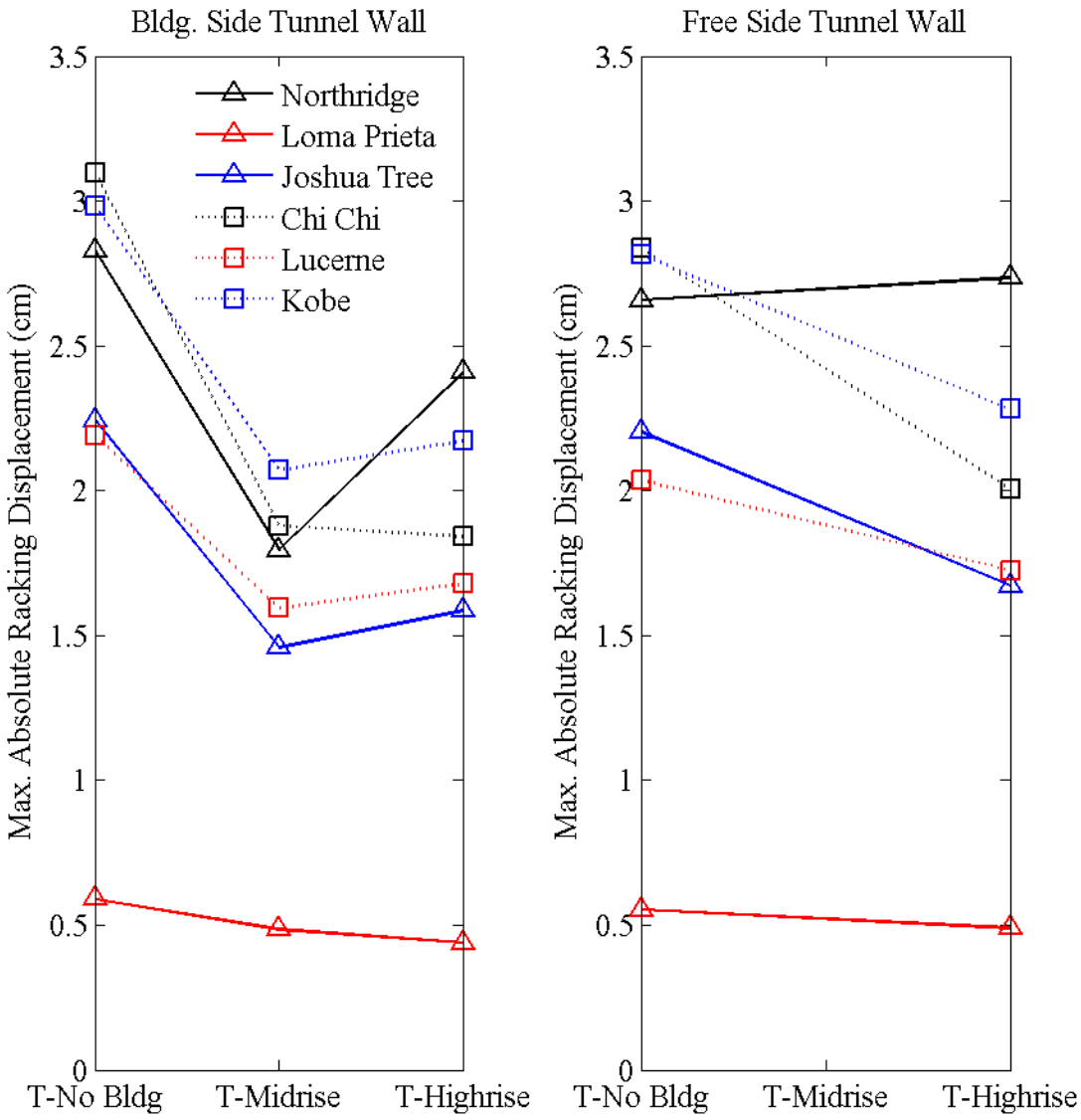

Figure 4.3.10. Maximum tunnel wall racking dispalcements.

4.3.4 Racking Versus Flexibility Ratios

A primary factor that influences the racking deformation of a box structure is the relative shear stiffness of the buried structure compared to the surrounding soil (Hashash et al. 2010; Anderson et al. 2008). This measure of relative stiffness is referred to as the Flexibility Ratio (F), defined as $(G_m B)/K_S H$, where G_m is the strain-compatible shear modulus of the soil in the free-field, B is the width of the structure, K_S is the racking stiffness of the structure, and H is the height of the

underground structure. More information about Flexibility Ratio can be found in Section 2.2.5. To estimate G_m experimentally, the equivalent shear strain (γ_{eq}) was needed in the far-field soil in T-No Bldg that roughly represented "free-field" conditions. The shear strain in the far-field was estimated during each shake from the far-field accelerometer array in T-No Bldg, which had the greatest separation from structures and container boundaries.

The far-field racking time history was calculated over the height of the underground structure, and the maximum shear strain (γ_{max}) was obtained for each event. The effective strain ($0.65.\gamma_{max}$) was then used to obtain the G_m/G_{max} value from several shear modulus reduction curves. Darendeli's (2001) shear modulus reduction curve at the overburden pressure of the mid-height of the underground structure was strength-corrected (Romero Arduz – under review) based on two different shear wave velocity profiles: 1) Seed and Idriss (1970), which was the upper bound of the available empirical relations; 2) average of the available empirical relations: Seed and Idriss (1970), Bardet (1993), Menq (2003), Jamiolkowski et al (1991), and Hardin and Drnevich (1972) (Eq 4.3-1 through Eq 4.3-5, respectively). The value of $K_{2,max}$ was assumed to be 45 in EQ1; C_u= 2.07 and $D_{50}$was taken as 0.144 mm in EQ4 (Cooper Lab tests on Nevada Sand); and Hardin and Drenevich's relation (EQ5) uses imperial units. This provided two median, strength-corrected Darendeli (2001) shear modulus reduction curves. Their median and median +/- 1 standard deviation curves were also used to obtain six values of G_m/G_{max} (Figure 4.3.11). These values were un-normalized using the corresponding G_{max} relation (from the corresponding V_s profile assumed in each case), to obtain a range of values for the strain-compatible, shear modulus (G_m) of soil in the far-field.

$$V_s = \sqrt{\frac{1000K_{2,max}(\sigma'_m)\text{^}0.5}{\rho}} \quad \text{Eq 4.3-1}$$

$$V_s = \sqrt{\frac{625\frac{1}{e^{1.3}}OCR^k P_a^{0.5}(\sigma'_m)^{0.5}}{\rho}} \quad \text{Eq 4.3-2}$$

$$V_s = \sqrt{\frac{8811\frac{(1.935 - e)^2}{1+e}(\sigma'_m)\text{^}0.5}{\rho}} \quad \textbf{Eq 4.3-3}$$

$$V_s = \sqrt{\frac{67100(C_u)^{-0.2}(e^{-1-\left(\left(\frac{D_{50}}{20}\right)^{0.75}\right)\left(\frac{\sigma'_m}{P_a}\right)^{0.48(C_u)^{0.09}}}}{\rho}} \quad \textbf{Eq 4.3-4}$$

$$V_s = \sqrt{\frac{2630 * (2.17 - e)^2 * (\sigma'_m)\text{^}0.5}{(1+e) * \rho}} \quad \textbf{Eq 4.3-5}$$

To calculate the racking stiffness of the box structure experimentally, a lateral force was applied to the structure's roof (when fixed from movement at its base), and the resulting lateral deflection was measured. In this way, the racking stiffness, K_S, was experimentally obtained as the force applied divided by the lateral displacement observed at the roof (more information can be found in Section 3.5). Subsequently, a range of Flexibility Ratios (F) values could be estimated for each motion in each test, and its median and standard deviation calculated.

The racking ratio (R) was estimated as the ratio of the maximum racking displacement measured on the underground box structure to that of the far-field soil during each motion and experiment. Again, in calculating R, far-field racking displacements were obtained from T-No Bldg in all cases, which was judged to be less affected by structures and container boundaries.

The relationship between R and F according to the NCHRP 611 guideline (Anderson et al. 2008), which is based on the results of dynamic finite element analyses, is presented in Figure

4.3.12 (more information provided in Chapter 2). This figure also shows the R versus F values obtained during each tunnel experiment for all six motions. A range of values for F are shown based on the different empirical methods used to modify Darendeli's modulus reduction curves (Figure 4.3.11). Figure 4.3.12 shows that values of R versus F followed the NCHRP 611 guideline closely in T-No Bldg, and a slight reduction in R was observed during all motions with the addition of a midrise and a highrise structure.

Racking deformations characterize the seismic performance of the tunnel due to earthquake loading. The slight reduction in racking deformations or lack of amplification of racking on the underground box structure in T-Midrise and T-Highrise has important implications: that an adjacent mid- to highrise building does not worsen the seismic performance of a permanent box structure in terms of racking.

The presence of the tall buildings may have acted to "anchor" the ground during shaking due to the embedded basement as well as the pressure of the superstructure. Mason (2011) observed similar trends on the behavior of a lowrise building adjacent to a midrise structure in centrifuge. Their experimental results indicated that the presence of a nine-story building with an embedded basement next to a three-story, shallow founded structure restrained or reduced its rotation and settlement. However, the response of the lowrise building on isolated (untied) spread footings became asymmetric, which increased the demand on columns. In the experiments presented in this study, since the two tunnel walls were connected via the base and roof (rigid connection), the wall response did not become asymmetric, and the distortion of the roof with respect to the base (racking) generally reduced, slightly improving the tunnel's performance. It must be noted that these observations only apply to the type of structure and soil investigated here.

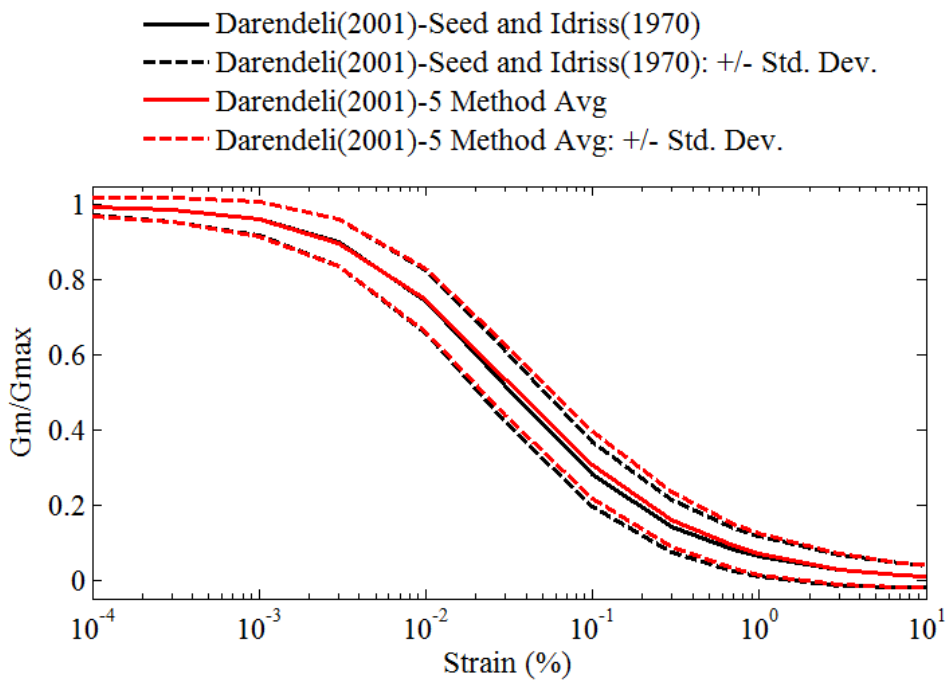

Figure 4.3.11. Strength-corrected modulus reduction curves used to find a range of equivalent G_m values in the free-field.

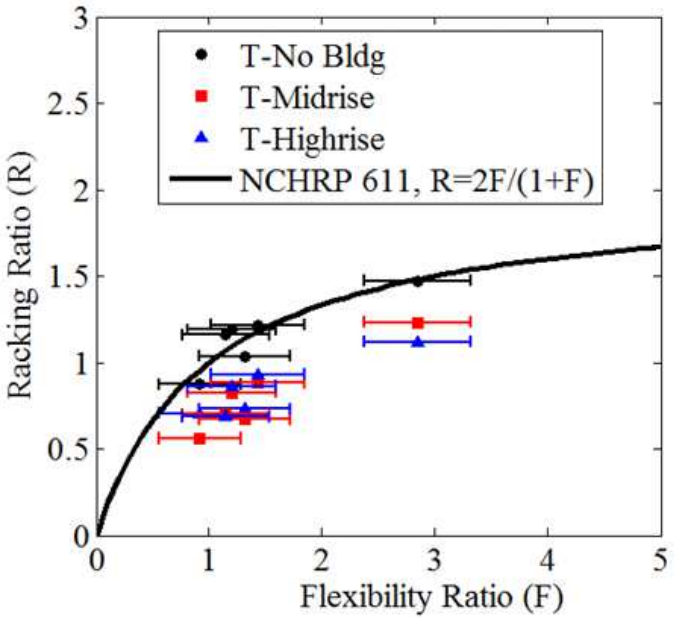

Figure 4.3.12. Racking versus Flexibility Ratios (R versus F) obtained experimentally compared to the NCHRP 611 guidelines. Far-field racking obtained from T-No Bldg.

4.4 Bending Strains

Strain gauges were placed around the tunnel in two arrays in a half-bridge configuration (Figure 4.4.1 through Figure 4.4.4). The goal of these instruments was to measure bending strains around the perimeter of the underground structure during shaking, so that the tunnel's bending strains and corresponding bending moments could be compared among the three experiments.

4.4.1 Measurement Challenges

During the experiments involving the permanent box structure and an adjacent tall building, strain gauge measurements showed a significant degree of slow drift, making their static recordings unreliable. Drift of the strain gauge could have been caused by loose connections, faulty hardware, or an incorrect data acquisition (DAQ) setting. The following figures show the "slow data" for seven strain gauges located on the south wall of the tunnel. Slow data references recordings on all instruments at a rate of 1 sample per second (sps), which was run throughout the centrifuge tests in parallel to fast data recordings during the motions. In Figure 4.4.5, the six ground motions in T-No Bldg can be recognized in the slow data by small, rapid changes in strain readings. The centrifuge spin down began after 4000 seconds. As shown in Figure 4.4.5 and Figure 4.4.6, in T-Midrise and T-Highrise, the strain gauge measurements showed a large degree of drift throughout the tests. The large drift made it difficult to reliably evaluate static bending strains around the tunnel in these particular experiments. However, due to the short time of shaking, the dynamic increment of strain was obtained with more confidence.

In addition to strain gauge drift, some strain gauges recorded no data or went out of range. Table 4.4.1 provides a list of non-working strain gauges on the tunnel in each of the three tests. Results are not presented for the malfunctioning strain gauges. Further, static measurements are

not presented on the tunnels because of the large degree of drift, but dynamic measurements are presented and discussed below.

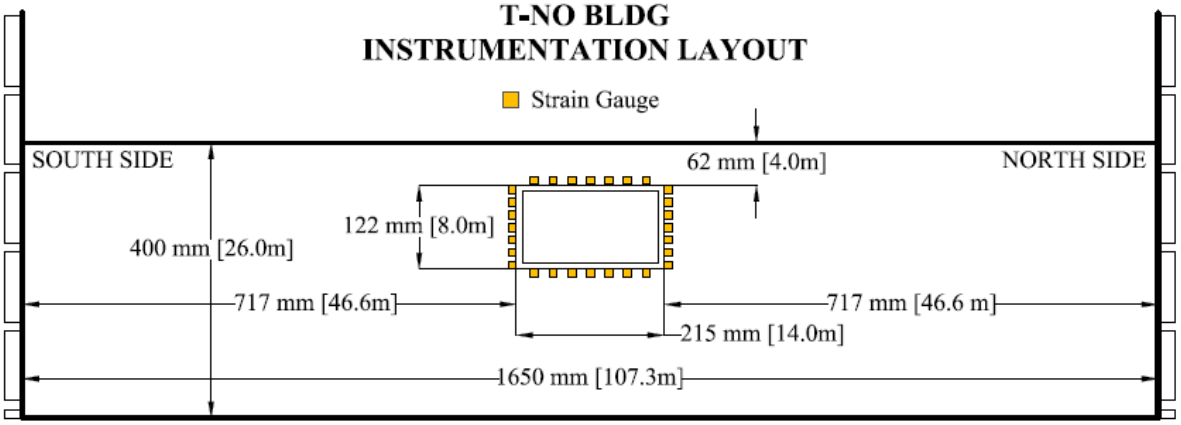

Figure 4.4.1. T-No Bldg elevation view of tunnel strain gauges.

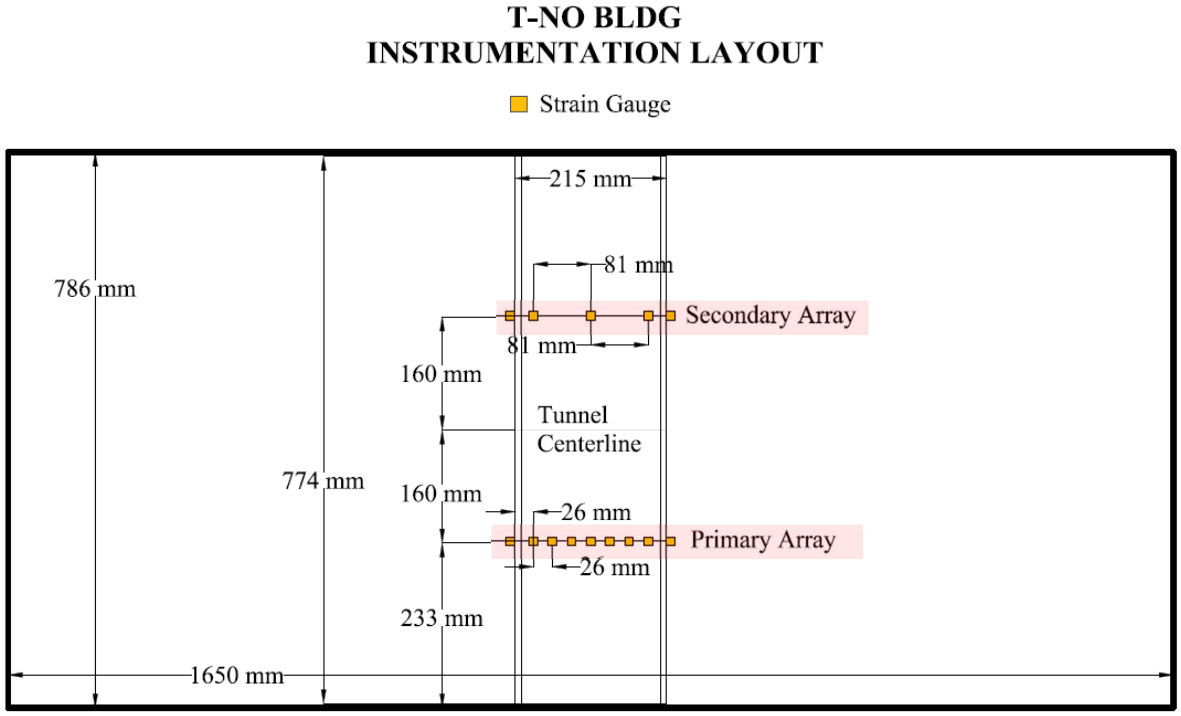

Figure 4.4.2. T-No Bldg plan view of tunnel strain gauges.

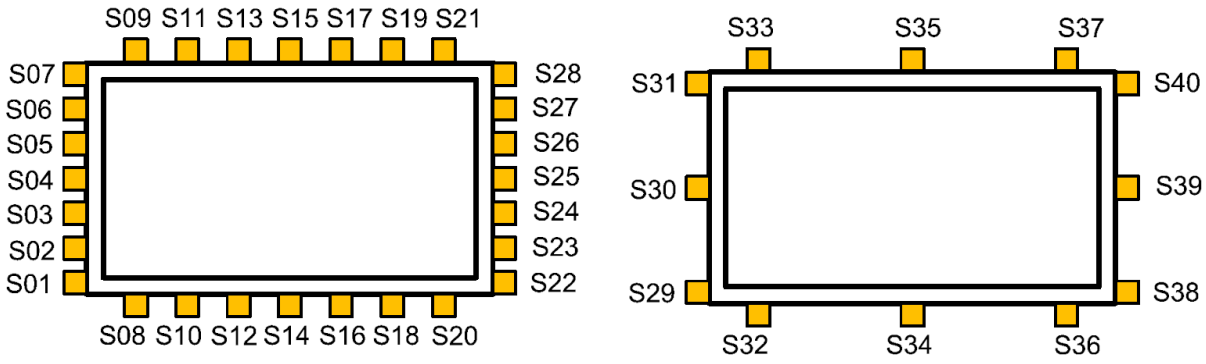

(a) (b)

Figure 4.4.3. Elevation view of tunnel strain gauges, (a) primary array; and (b) secondary array.

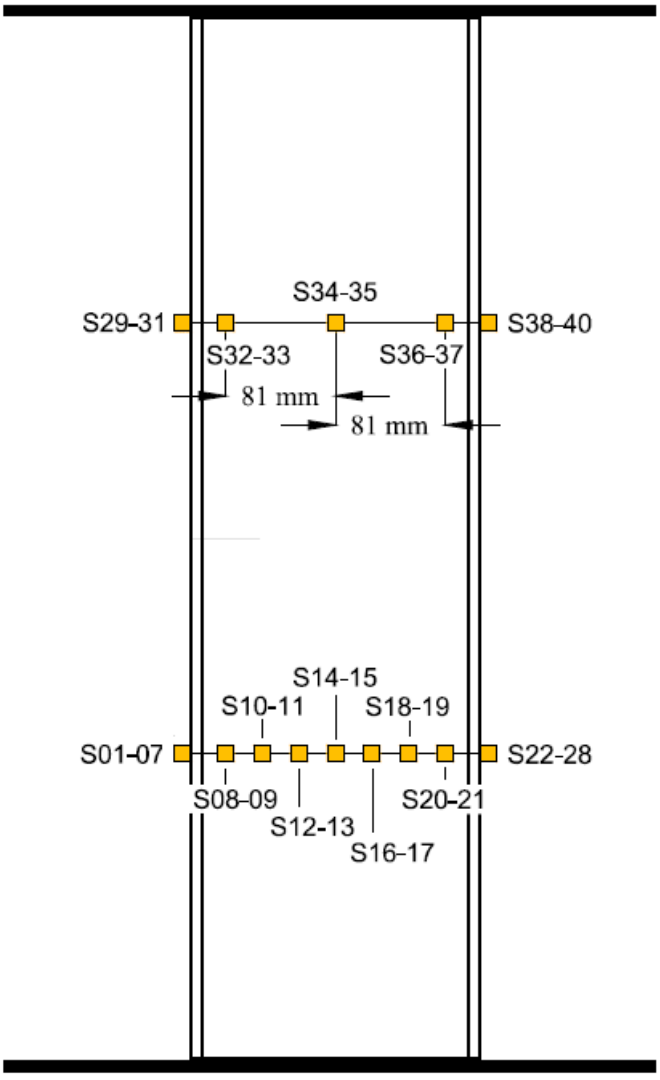

Figure 4.4.4. Numbering and layout of tunnel strain gauges (SGs) in plan view.

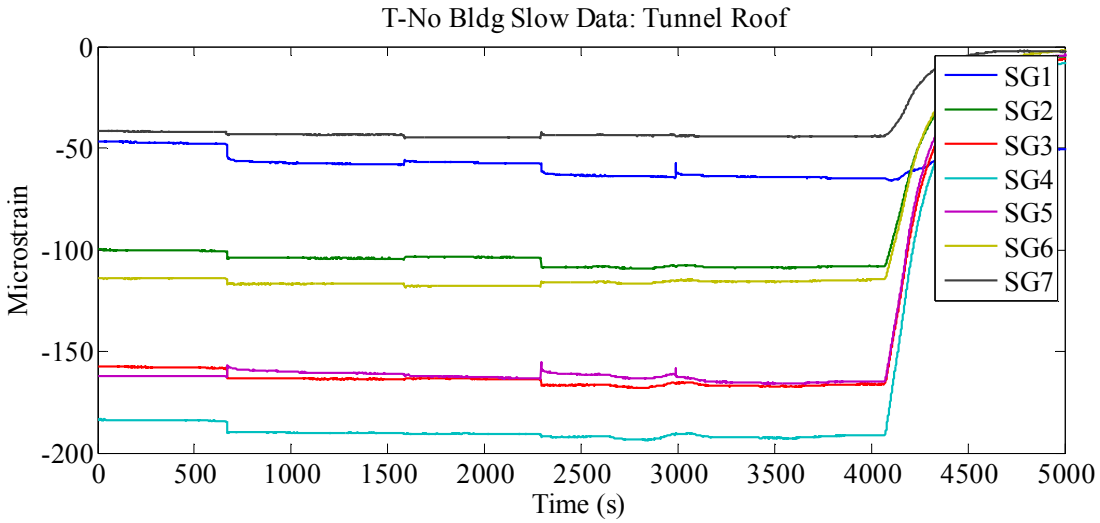

Figure 4.4.5. T-No Bldg slow data recorded by the strain gauges on the south wall of the tunnel in T-No Bldg.

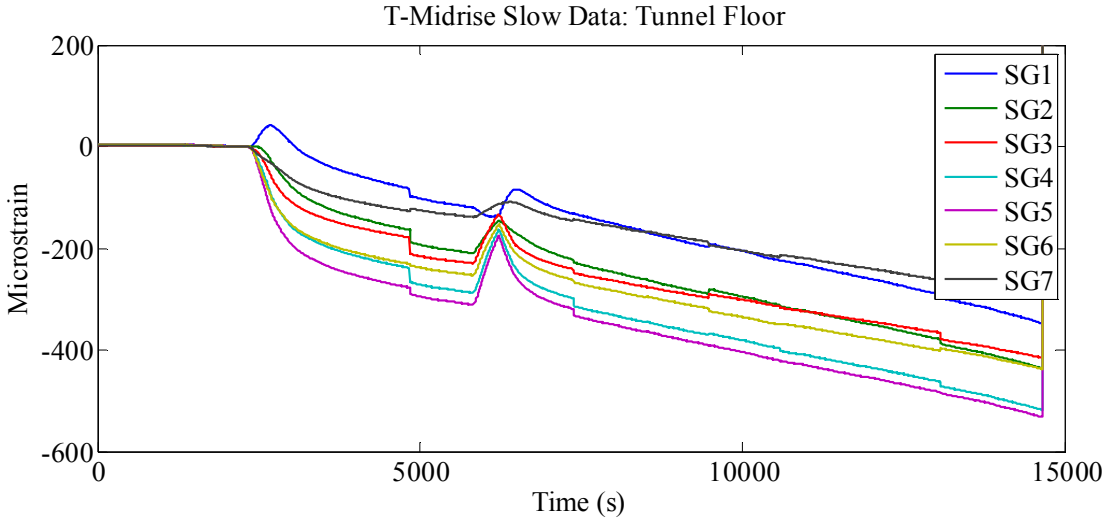

Figure 4.4.6. T-Midrise slow data recorded by the strain gauges on the south wall of the tunnel in T-Midrise.

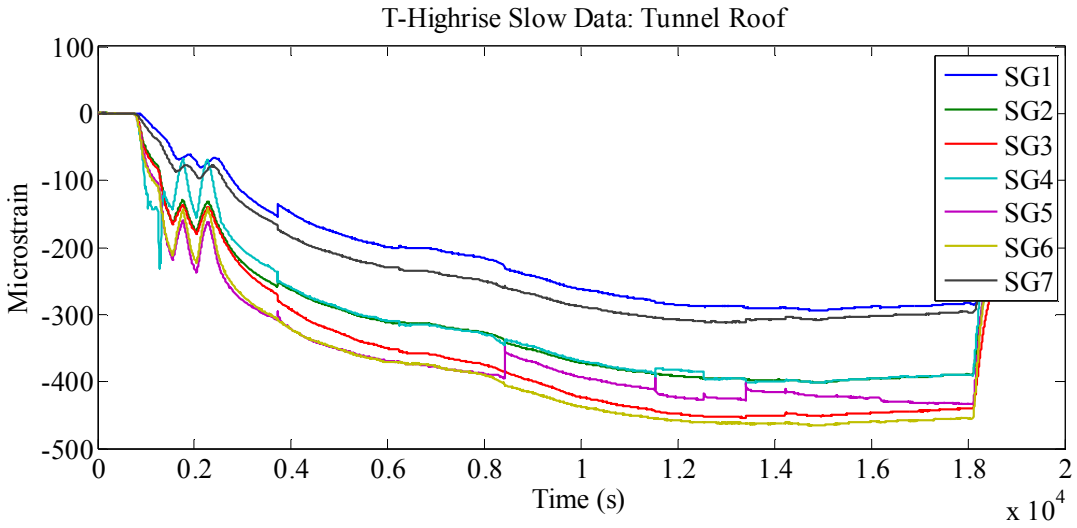

Figure 4.4.7. T-Highrise slow data recorded by the strain gauges on the south wall of the tunnel in T-Highrise.

Table 4.4.1. List of known non-working strain gauge in the three tunnel tests.

Experiment	Non-Working Strain Gauges						
T-No Bldg	3	9					
T-Midrise	23	24					
T-Highrise	15	16	17	23	25	27	28

4.4.2 Dynamic Bending Strains and Moments on the Tunnel

The following set of figures (Figure 4.4.8 through Figure 4.4.13) show the dynamic recordings obtained from strain gauges expressed in terms of bending moments in prototype scale. The bending moment was calculated using the section properties of the tunnel (i.e. wall thickness, length, and modulus of elasticity). The second moment of inertia about the neutral axis (I_x) of the tunnel was calculated per unit length (1m in prototype scale) in the horizontal direction perpendicular to shaking. "y" is the distance from the neutral axis to the outside edge of the beam or in this case, half the beam thickness. All calculations are performed in the prototype scale. Knowing the aluminum tunnel stayed within its elastic limits, the bending stress was calculated using the measured bending strains and the material's Young's modulus of elasticity:

$$\sigma = \frac{My}{I_x} \quad \rightarrow \quad M = \frac{\sigma I_x}{y} \qquad \text{Eq. 4.4-1}$$

It was assumed that all strains recorded by the strain gauges were mainly due to bending, and not axial deformation.

The following figures show the dynamic increment of bending moment on the tunnel walls, floor, and roof during six ground motions in each experiment involving the permanent box structure (T-No Bldg, T-Midrise, and T-Highrise). Dynamic bending moments are shown at one instance of time. For the tunnel walls, results are presented at the time of maximum dynamic moment recorded on that wall (when one strain gauge recorded maximum dynamic strain). The same procedure was followed for the tunnel roof and floor.

The following trends can be seen from the following figures:

- In general, dynamic bending moment profiles around the perimeter of the tunnel were roughly similar in the three tests, showing a relatively negligible effect due to the presence of the adjacent midrise or highrise building on the tunnel's bending.
- The greatest dynamic bending moments were recorded at the corners of the floor and roof sections. The largest floor dynamic moments were recorded in T-No Bldg compared to the other tests for almost all ground motions. This shows a slight reduction in dynamic bending strains due to the presence of the adjacent structure, which was consistent with racking deformation patterns discussed in the previous section.

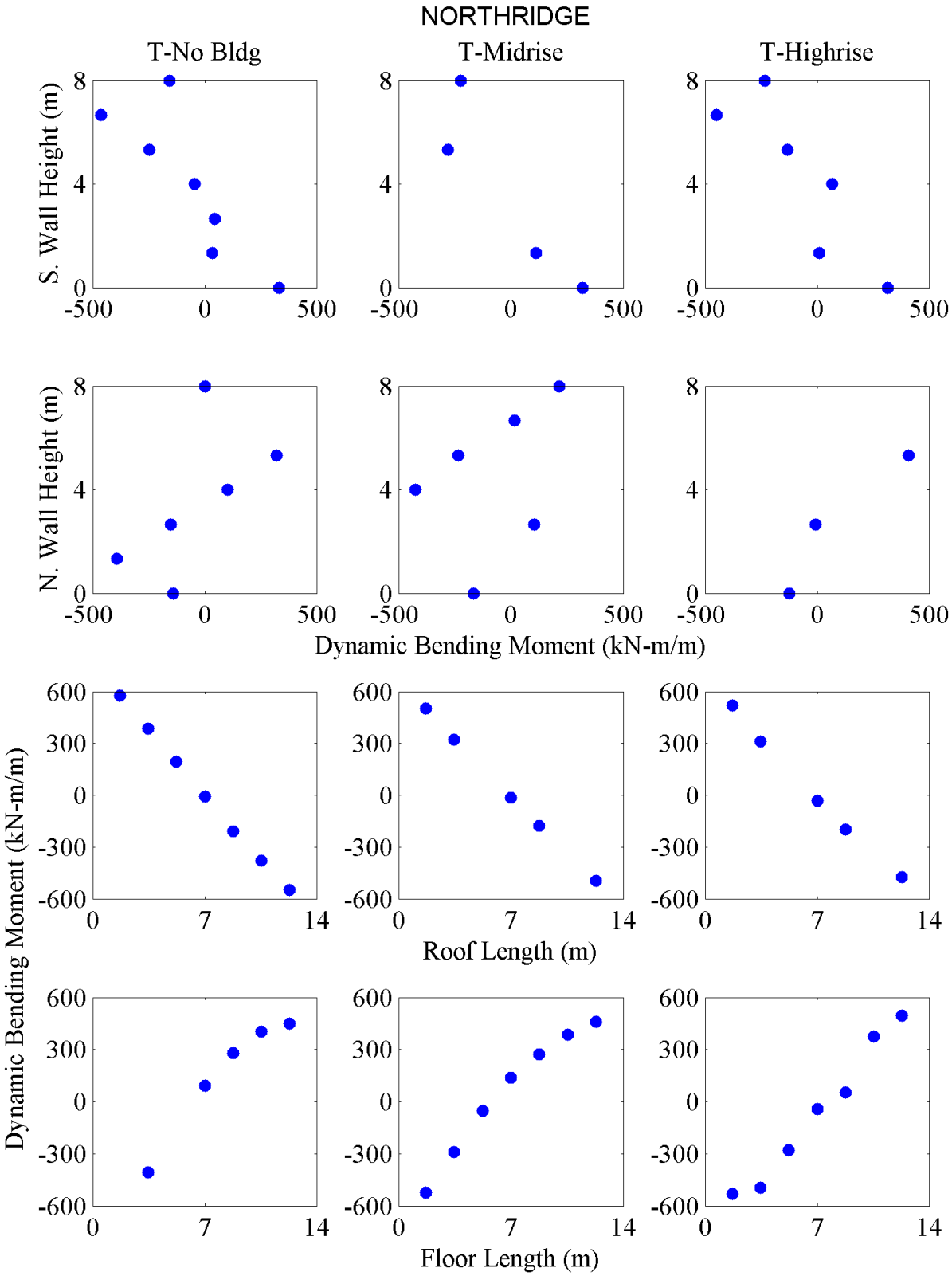

Figure 4.4.8. Dynamic bending moments shown on the south and north tunnel walls, roof, and floor at the time of maximum moment on that wall during the Northridge motion.

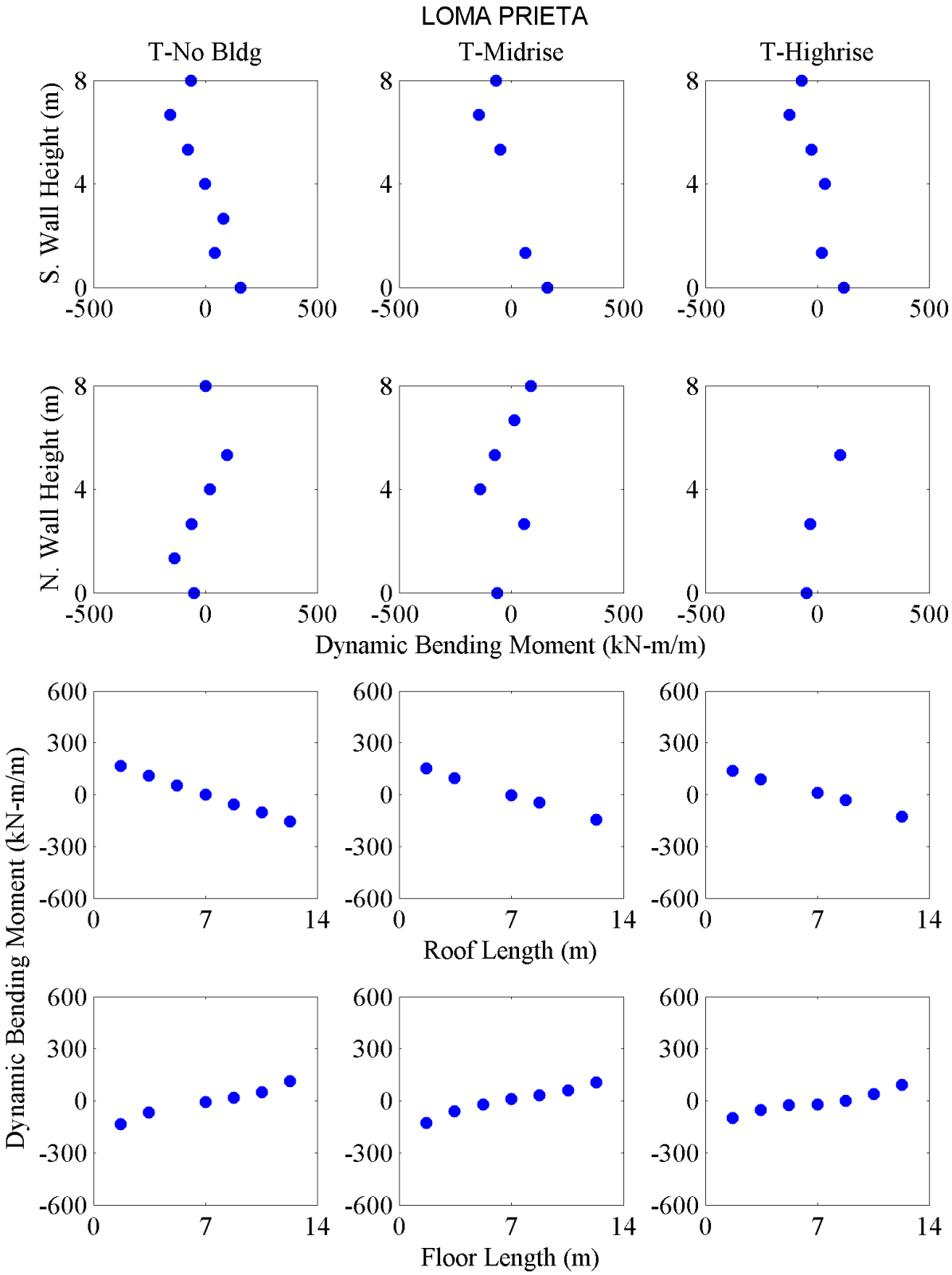

Figure 4.4.9. Dynamic bending moments shown on the south and north tunnel walls, roof, and floor at the time of maximum moment on that wall during the Loma Prieta motion.

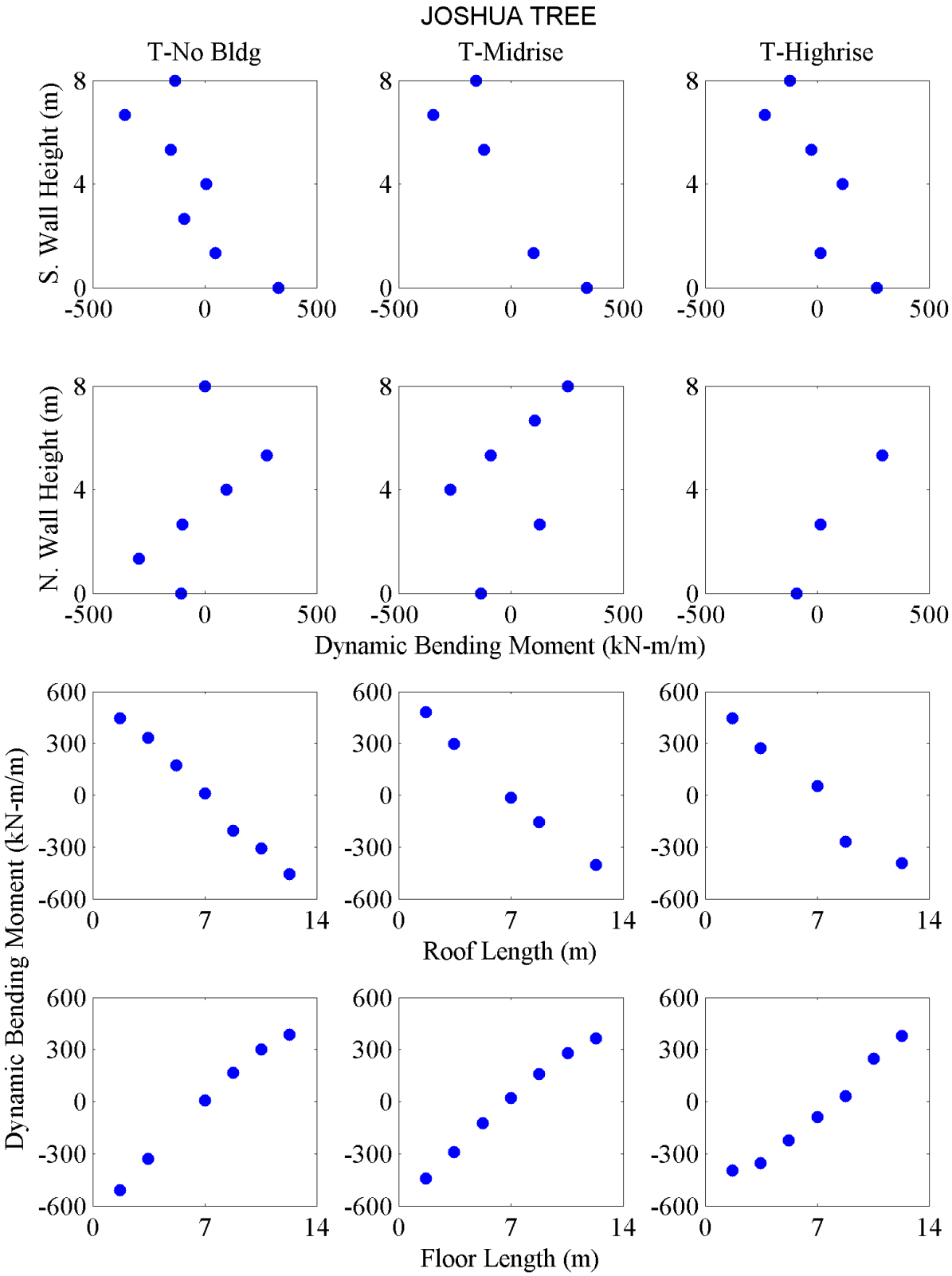

Figure 4.4.10. Dynamic bending moments shown on the south and north tunnel walls, roof, and floor at the time of maximum moment on that wall during the Joshua Tree motion.

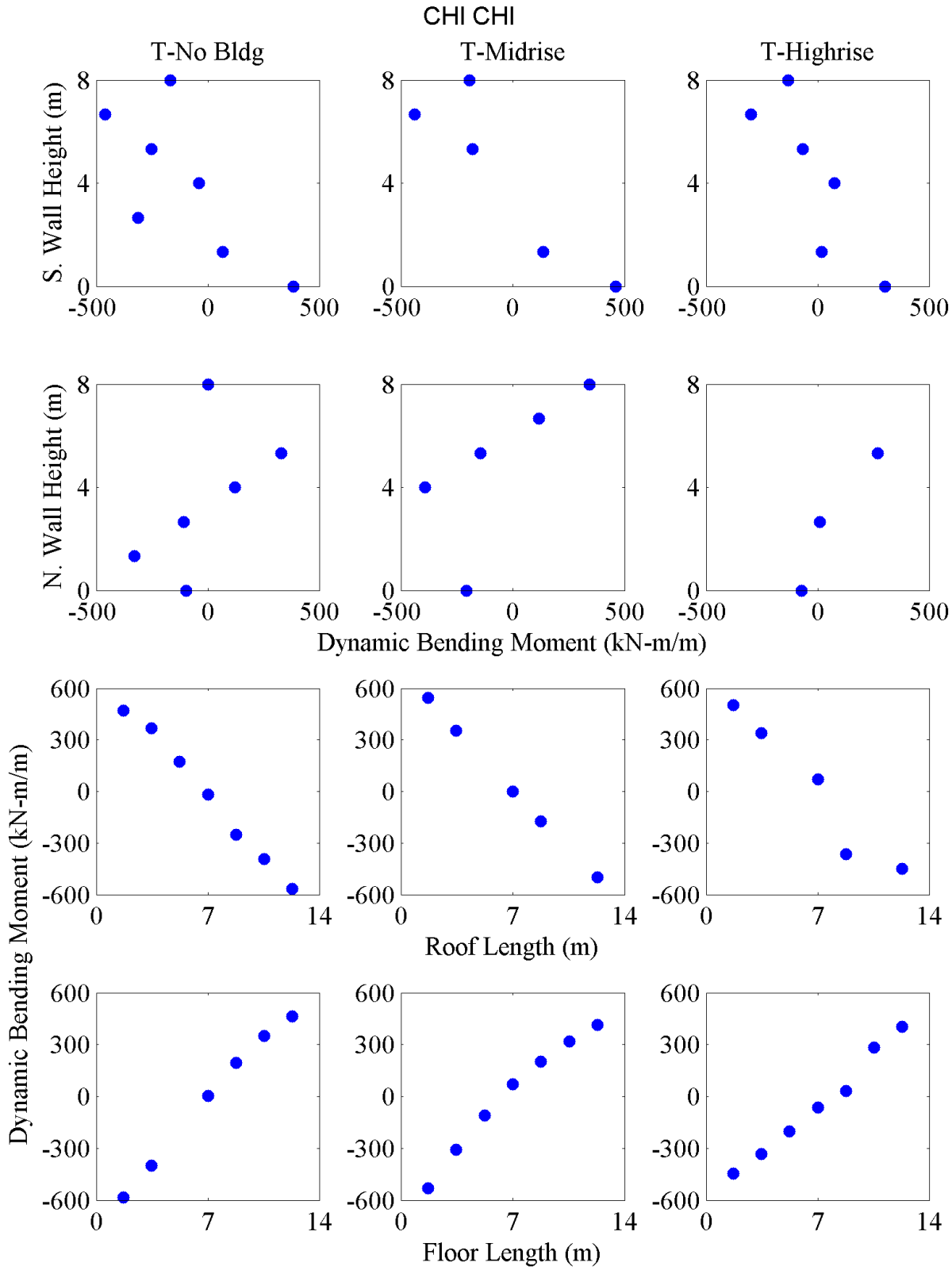

Figure 4.4.11. Dynamic bending moments shown on the south and north tunnel walls, roof, and floor at the time of maximum moment on that wall during the Chi Chi motion.

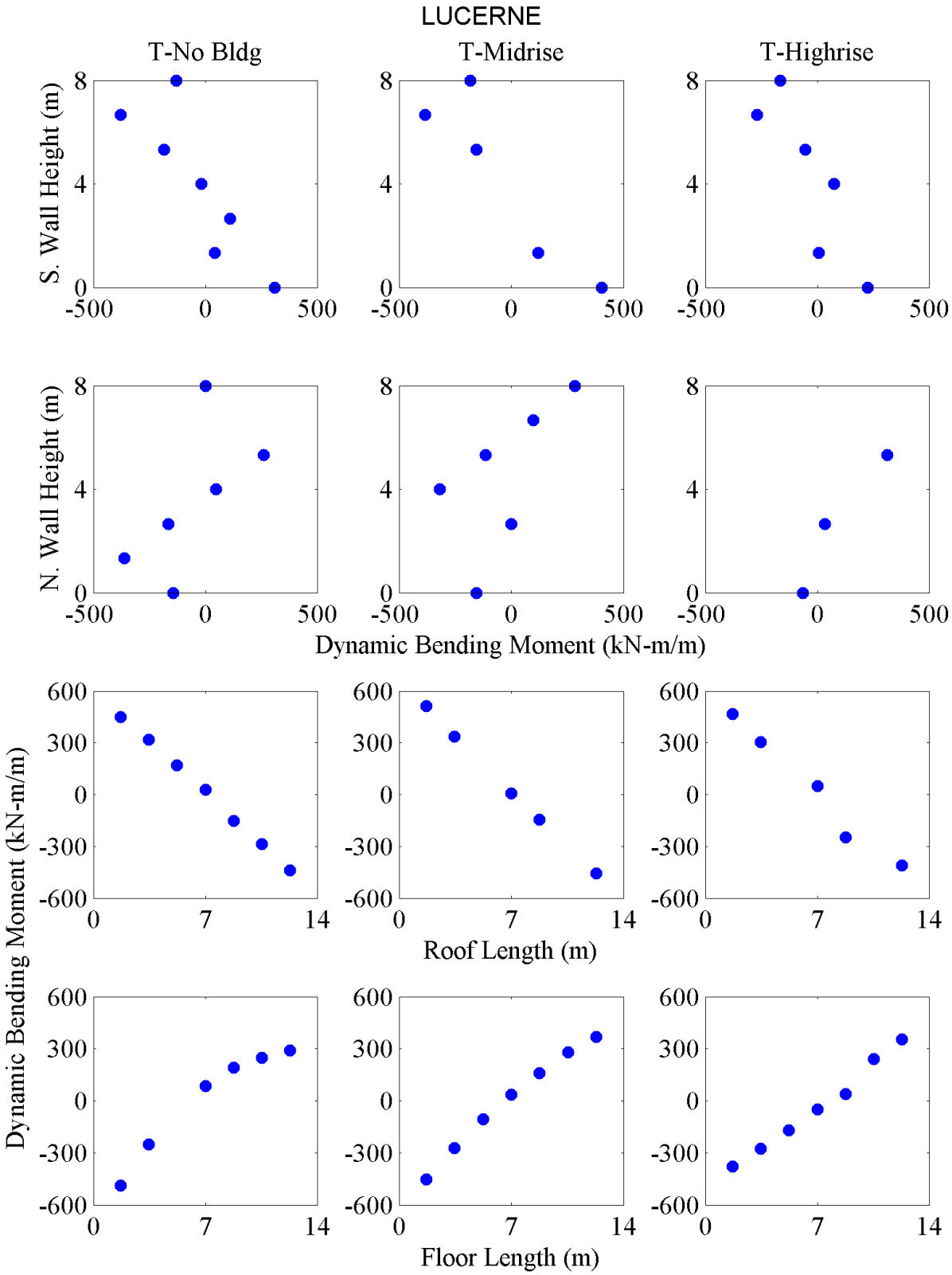

Figure 4.4.12. Dynamic bending moments shown on the south and north tunnel walls, roof, and floor at the time of maximum moment on that wall during the Lucerne motion.

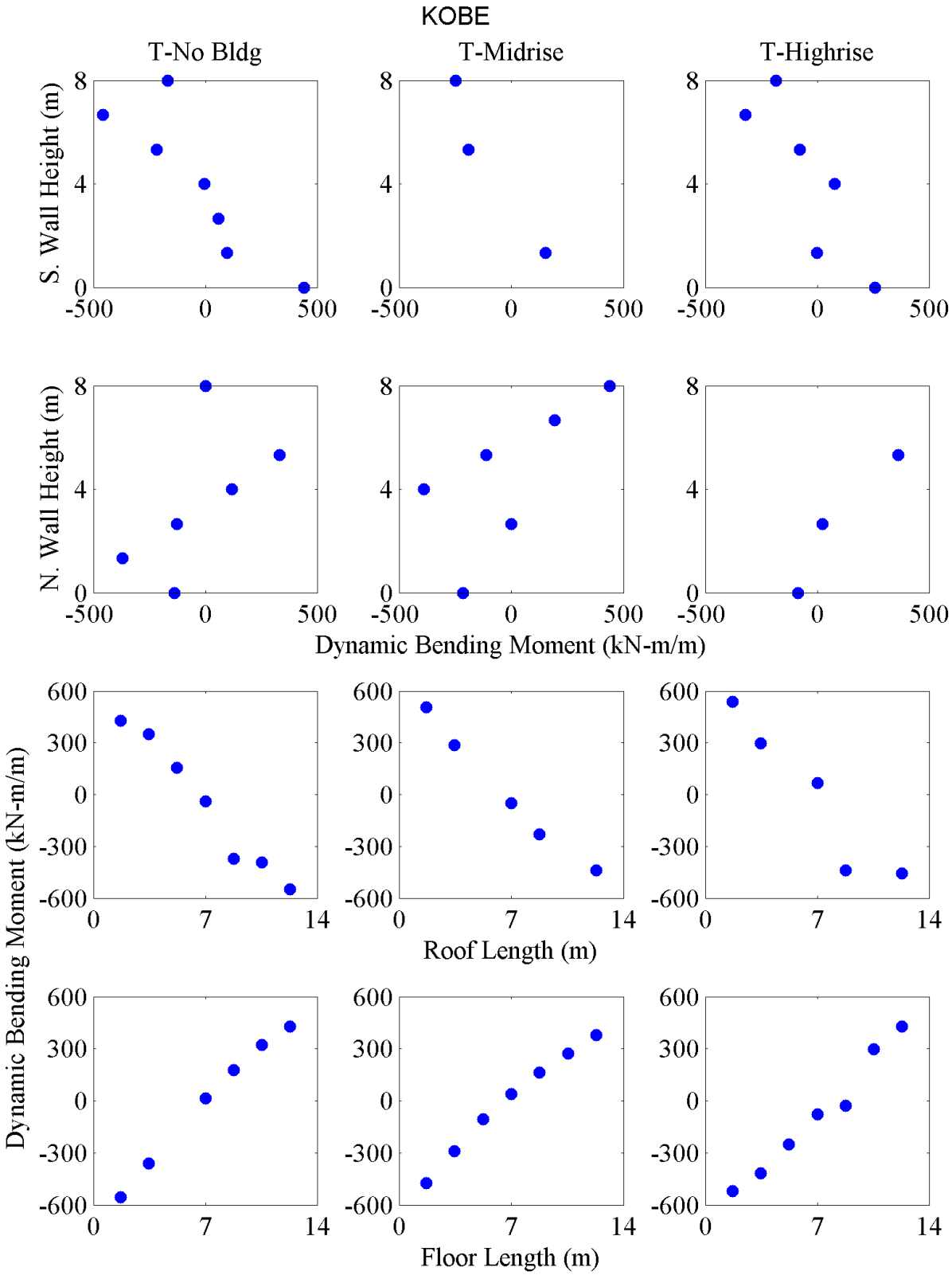

Figure 4.4.13. Dynamic bending moments shown on the south and north tunnel walls, roof, and floor at the time of maximum moment on that wall during the Kobe motion.

4.5 Lateral Earth Pressures

Lateral earth pressures were measured on the tunnel walls using tactile pressure sensors. The pressure sensors were conditioned, equilibrated, and statically and dynamically calibrated using methods outlined in Dashti et al. 2012, Gillis et al. 2013, and Dasti et al. 2015. All tunnel experiments used four tactile pressure sensors, two on each side of the tunnel (Figure 4.5.1).

The lateral thrust acting on the tunnel was calculated by integrating the data from the tactile pressure sensors along the tunnel wall. To calculate thrust, a single pressure profile was first established at each instance of time by averaging pressure measurements from two sensors where they overlapped, as shown in Figure 4.5.1 and Figure 4.5.2.

The pressure profile measured by the tactile sensors only extended from 4.5 to 11 m depth as shown by Figure 4.5.3, whereas the top and bottom of the tunnel were at 4 and 12 m depth. The best fit to the pressure profile data at each instance of time was extrapolated to the top and bottom of the tunnel to cover its full height, before integrating the profile to obtain thrust.

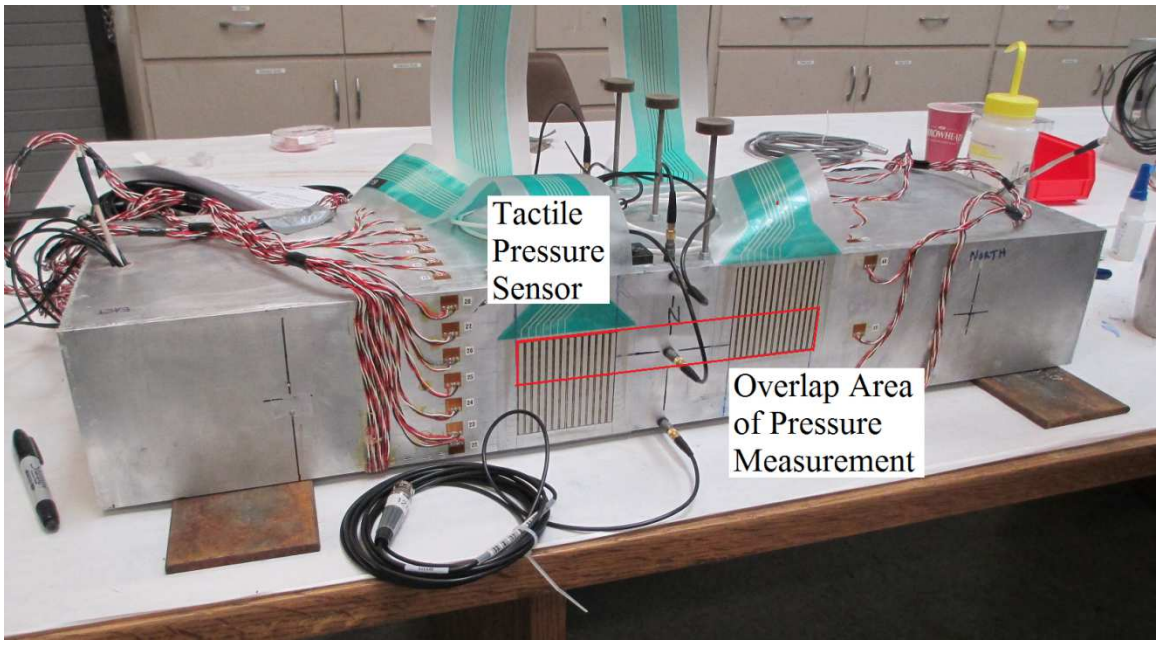

Figure 4.5.1. Tunnel with tactile pressure sensors during model preparation.

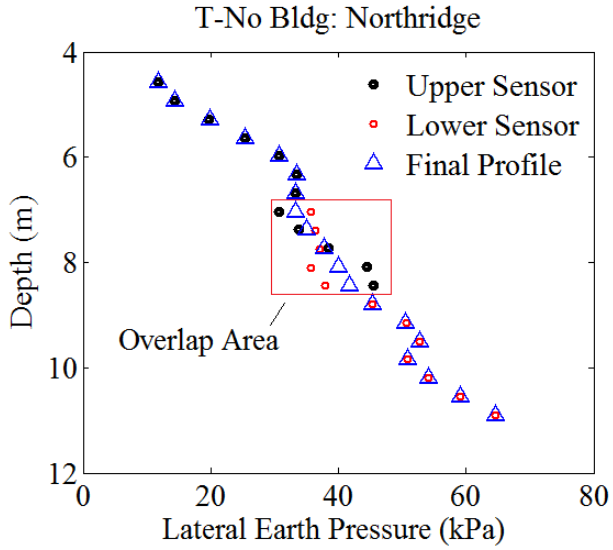

Figure 4.5.2. Static pressure recordings obtained from two tactile sensors on the tunnel wall in T-No Bldg.

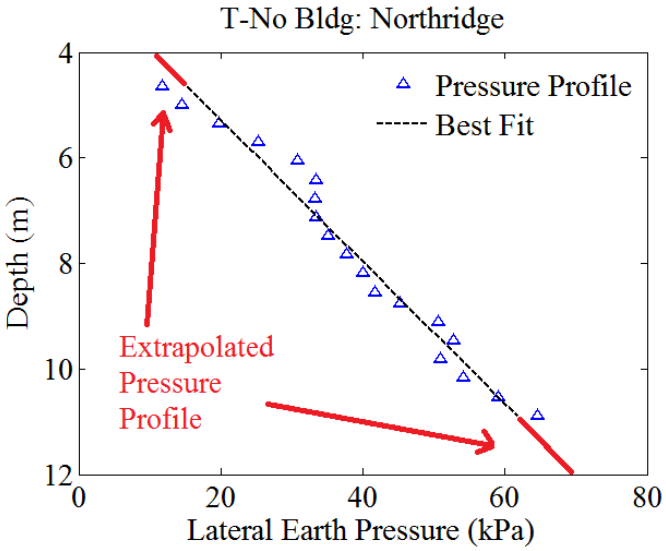

Figure 4.5.3. Extrapolating the pressure profile to cover the entire height of the tunnel.

4.5.1 Pressure Measurement Challenges

In the first experiment, T-No Bldg, two tactile pressure sensors on the north side of the tunnel malfunctioned before the first ground motion, as their stems ripped due to the air turbulence in the centrifuge. The two remaining pressure sensors collected data during the Northridge, Loma Prieta, Joshua Tree, and Chi Chi ground motions before they stopped working. Therefore, lateral earth pressures were not measured during the final two ground motions in T-No Bldg: Lucerne and Kobe.

The pressure and thrust time histories obtained on each wall were filtered to reduce noise present in the tactile sensor recordings. This noise was especially pronounced in T-Highrise, where higher capacity sensors were employed in the anticipation of higher lateral earth pressure being transferred from the heavier structure. An acausal, fifth order, bandpass Butterworth filter was used with corner frequencies of 0.1 and 10 Hz in T-No Bldg and T-Midrise. A more aggressive filter was required to reduce the noise of the high capacity sensors in T-Highrse to a reasonable level: 0.1 and 5 Hz. Generally, very little pressure content was present in frequencies

beyond 5 Hz (in prototype scale) in all experiments. Therefore, the more aggressive filtering required in T-Highrise was not anticipated to affect actual pressure recordings significantly. However, the lower signal to noise ratio (SNR) of these sensors used in T-Highrise (on the building side) affected the reliability of their measurements.

Generally, there is a significant degree of uncertainty associated with earth pressure measurements in centrifuge. This is a difficult measurement and a topic of on-going research. Further, the reliability of tactile sensors is highly influenced by air-trap in the sensor or its stem internally as well as local inhomogeneities in the contact soil. Even though these tactile sensors were carefully de-aired, conditioned, equilibrated, statically and dynamically calibrated, and filtered, these inherent uncertainties must be kept in mind before drawing definite conclusions on pressure patterns purely from these sensors. It is critical to compare the overall observations from tactile sensors with those from strain gauges and accelerometers in parallel to evaluate the impact of the adjacent structure more holistically both in terms of forces and deformations (as discussed in more detail in Section 4.6).

4.5.2 Dynamic Earth Pressures and Thrust

Figure 4.5.5 through Figure 4.5.7show the dynamic thrust time histories on the tunnel walls during the three tunnel experiments during a few representative motions. In addition to comparing the amplitude of dynamic thrust on the two walls, these figures enable comparing the timing of thrust peaks and valleys on the two sides of the wall in a given test. For comparison, the recorded thrust in T-No Bldg is also presented to show the change in the magnitude of thrust with the addition of a new building.

The dynamic thrust was greater during all ground motions in T-Midrise on the building side compared to the free side, but the thrust was approximately similar on the two sides in T-

Highrise in most cases and sometimes smaller on the building side. As noted previously, the low sensitivity tactile sensors used on the building side of the tunnel in T-Highrise had a lower resolution and SNR. Therefore, they may have underestimated the amplitude of pressure on the building side. For this reason, results from the building side pressure sensors of T-Highrise will be not be presented in this section, in order not to misleading imply a reduction in pressure on the building side of the tunnel. In a few motions when the sensors on both walls performed well with an adequate SNR, the dynamic thrusts on the two walls appeared to be roughly similar. The free-side sensors, as a result, will be presented in T-Highrise in place of the building side, as they are expected to be a better representation of the pressure on both sides, due to their higher resolution.

Figure 4.5.8 through Figure 4.5.12 show the dynamic lateral thrust time histories in T-No Bldg, T-Midrise, and T-Highrise. The south or building side is presented in T-No Bldg and T-Midrise, and the free side is presented in T-Highrise. The maximum dynamic thrust and its corresponding time is identified in each figure. The "time of maximum thrust" in these figures corresponds to the time at which maximum positive dynamic thrust was recorded, because this is when the tunnel experienced lateral earth pressures greater than static.

The second row of Figure 4.5.8 to Figure 4.5.12 presents the static and total (static and dynamic) lateral earth pressures on both sides of the wall at the time of maximum thrust. In T-No Bldg, one side of the wall is presented only because two pressure sensors on the other wall malfunctioned. Theoretical static earth pressure profiles under active and at-rest conditions expected for this soil are plotted as well for comparison. Using equations Eq. 4.5-1 and Eq. 4.5-2, K_a and K_o values were calculated as 0.29 and 0.46, assuming a friction angle (ϕ') of 33^{o}for Nevada Sand at a relative density of about 55% (Prevost 1993).

$$K_o = 1 - \sin(\emptyset') \qquad \textbf{Eq. 4.5-1}$$

$$K_a = \frac{1 - \sin(\emptyset')}{1 + \sin(\emptyset')} \qquad \textbf{Eq. 4.5-2}$$

The third row in Figure 4.5.8 - Figure 4.5.12 presents the dynamic increment of lateral earth pressures (i.e., total pressure – static) at the time of maximum dynamic thrust as identified in the top row in each experiment involving the underground box structure during different motions. Theoretical profiles of active and at-rest lateral earth pressure are again presented for comparison.

The following trends were observed in Figure 4.5.8 through Figure 4.5.12:

- The static profiles of lateral earth pressure measured by tactile sensors typically fell between theoretically expected active and at-rest lateral earth pressures.
- Total earth pressures at the time of maximum thrust acting on the tunnel in T-No Bldg were typically within the expected static range of pressure, meaning that dynamic earth pressures were not significant on this type of structure during the ground motions considered. This observation is in line with previous centrifuge experiments (e.g., Al Atik 2008 and Mikola 2012) and case histories on the seismic response of underground structures.
- The amplitude of dynamic earth pressure and thrust increased on both sides of the tunnel in T-Midrise and T-Highrise compared to T-No Bldg. The trends in pressure distributions were, however, roughly similar in T-Midrise and T-Highrise in most cases.
- In both T-Midrise and T-Highrise, the increase in thrust on the two sides of the tunnel was not in phase during the Northridge record, which was more pulse like. In other motions, the

thrust was more in phase on the two sides. The in-phase nature of the increased dynamic thrust on the two sides of the tunnel may be partly responsible for the reduction in its dynamic racking displacements when the tall buildings were present. When the thrust on two walls was not in phase (e.g., during the Northridge motion), a small degree of amplification in racking was observed on the free side of the tunnel.

- In most cases (with the exception of Northridge), dynamic earth pressures at the time of maximum thrust were greater at shallower depths in T-Midrise and T-Highrise compared to T-No Bldg due to the effect of the adjacent building (showing an inverse triangular shape).

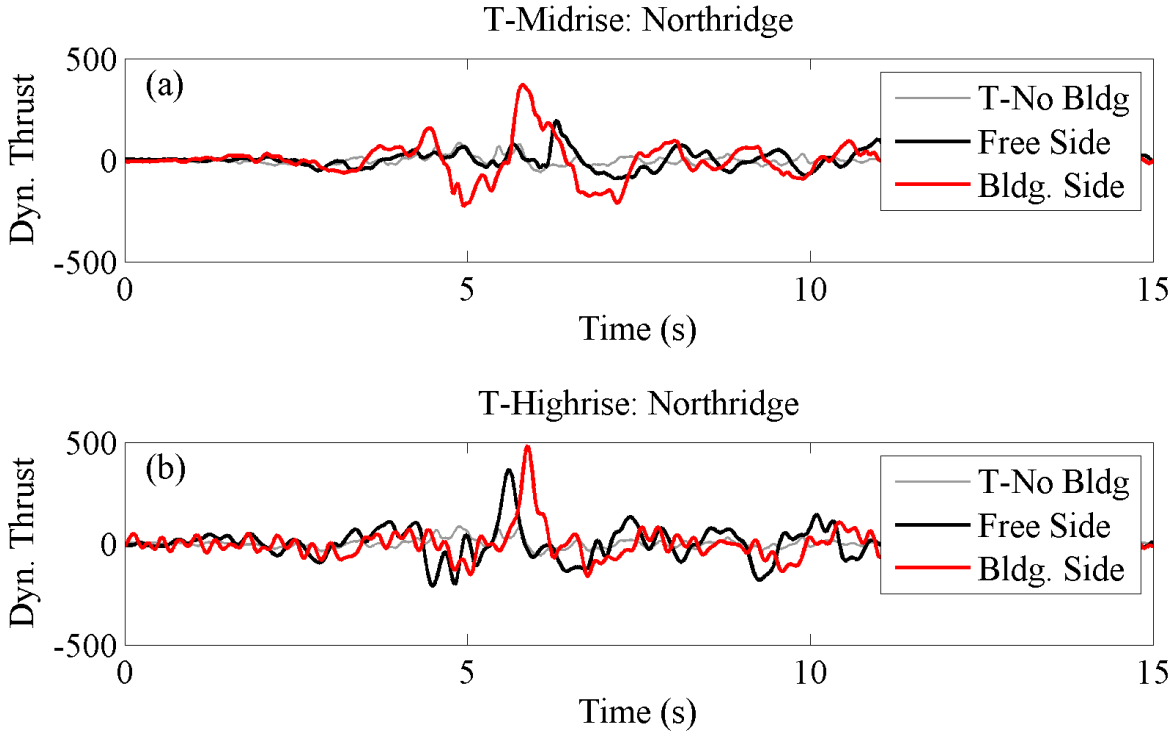

Figure 4.5.4. Dynamic thrust time histories on the two sides of the wall in: (a) T-Midrise; (b) T-Highrise compared to the thrust in T-No Bldg.

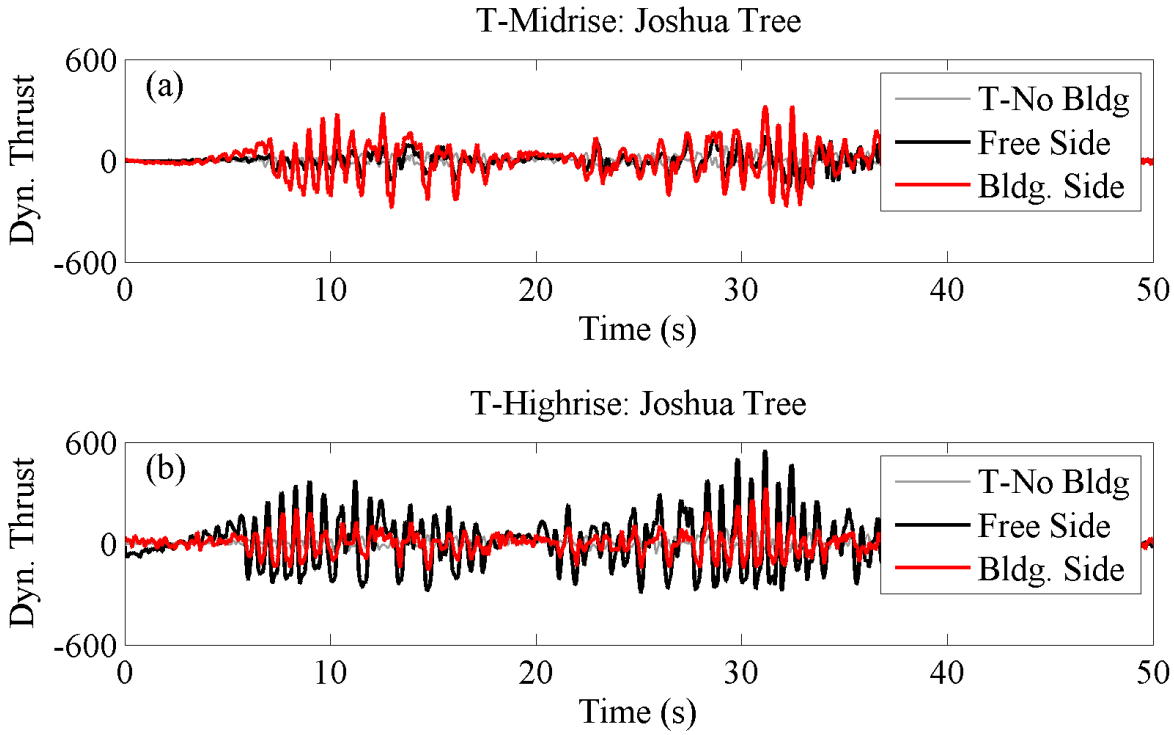

Figure 4.5.5. Dynamic thrust time histories on the two sides of the wall in: (a) T-Midrise; (b) T-Highrise compared to the thrust in T-No Bldg.

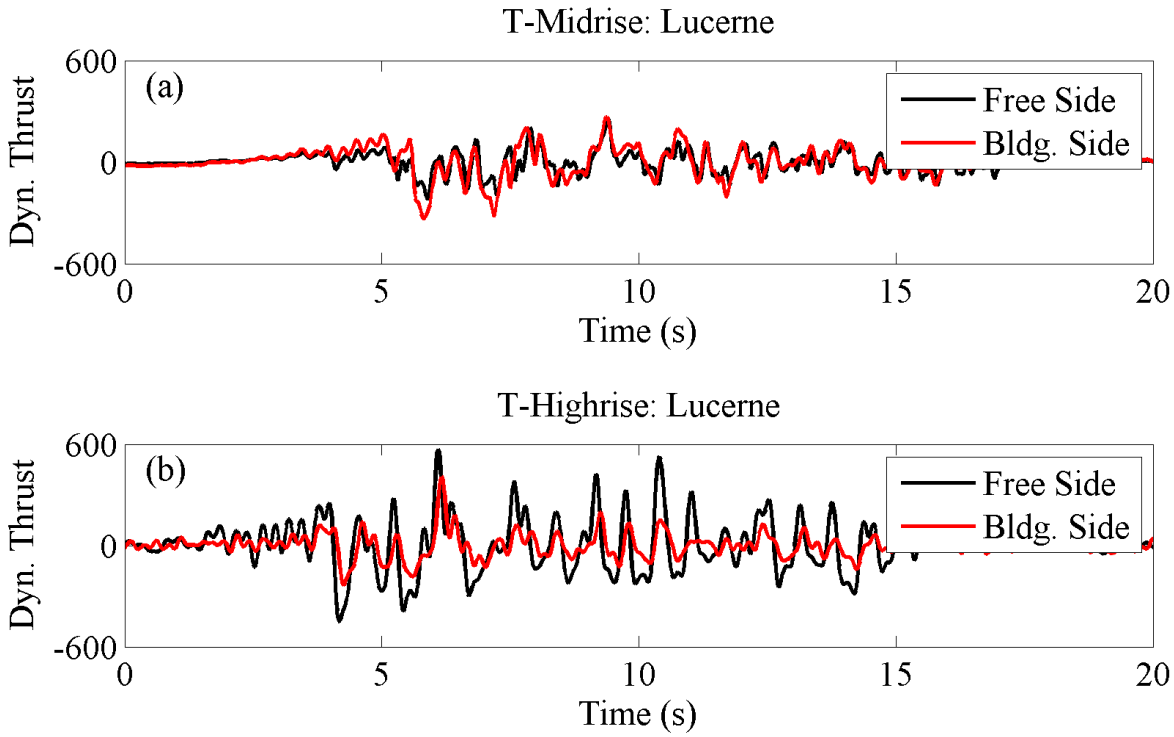

Figure 4.5.6. Dynamic thrust time histories on the two sides of the wall in: (a) T-Midrise; (b) T-Highrise compared to the thrust in T-No Bldg.

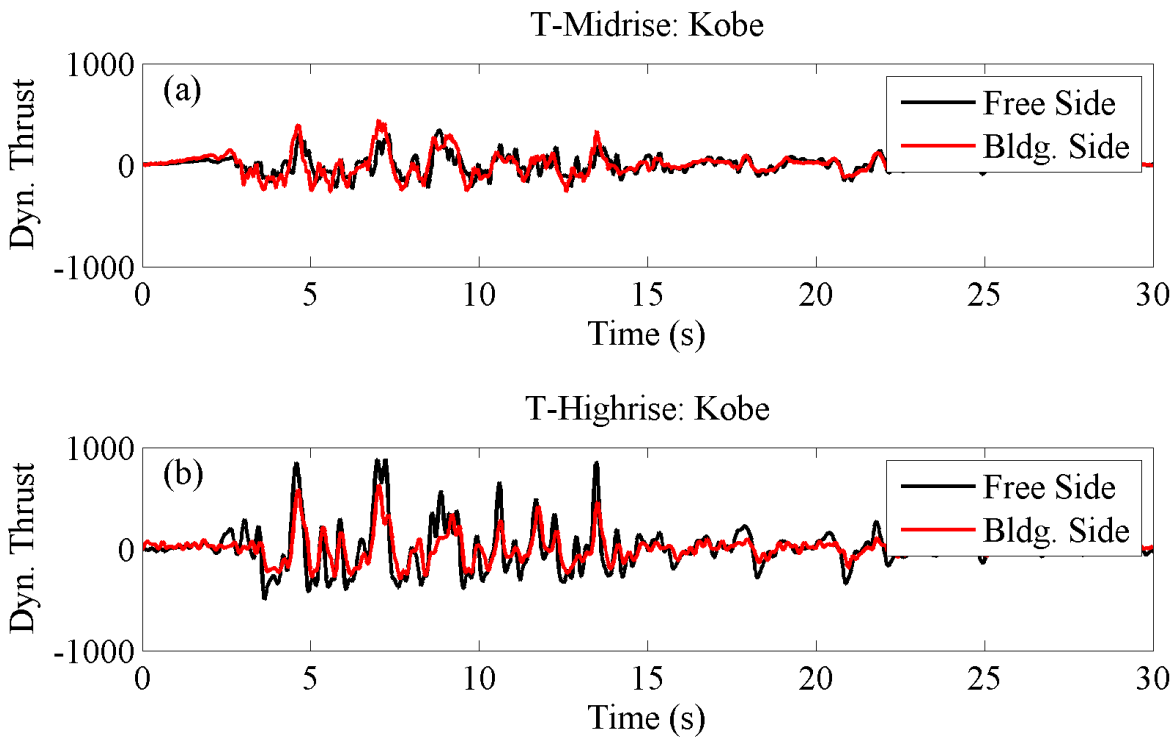

Figure 4.5.7. Dynamic thrust time histories on the two sides of the wall in: (a) T-Midrise; (b) T-Highrise compared to the thrust in T-No Bldg.

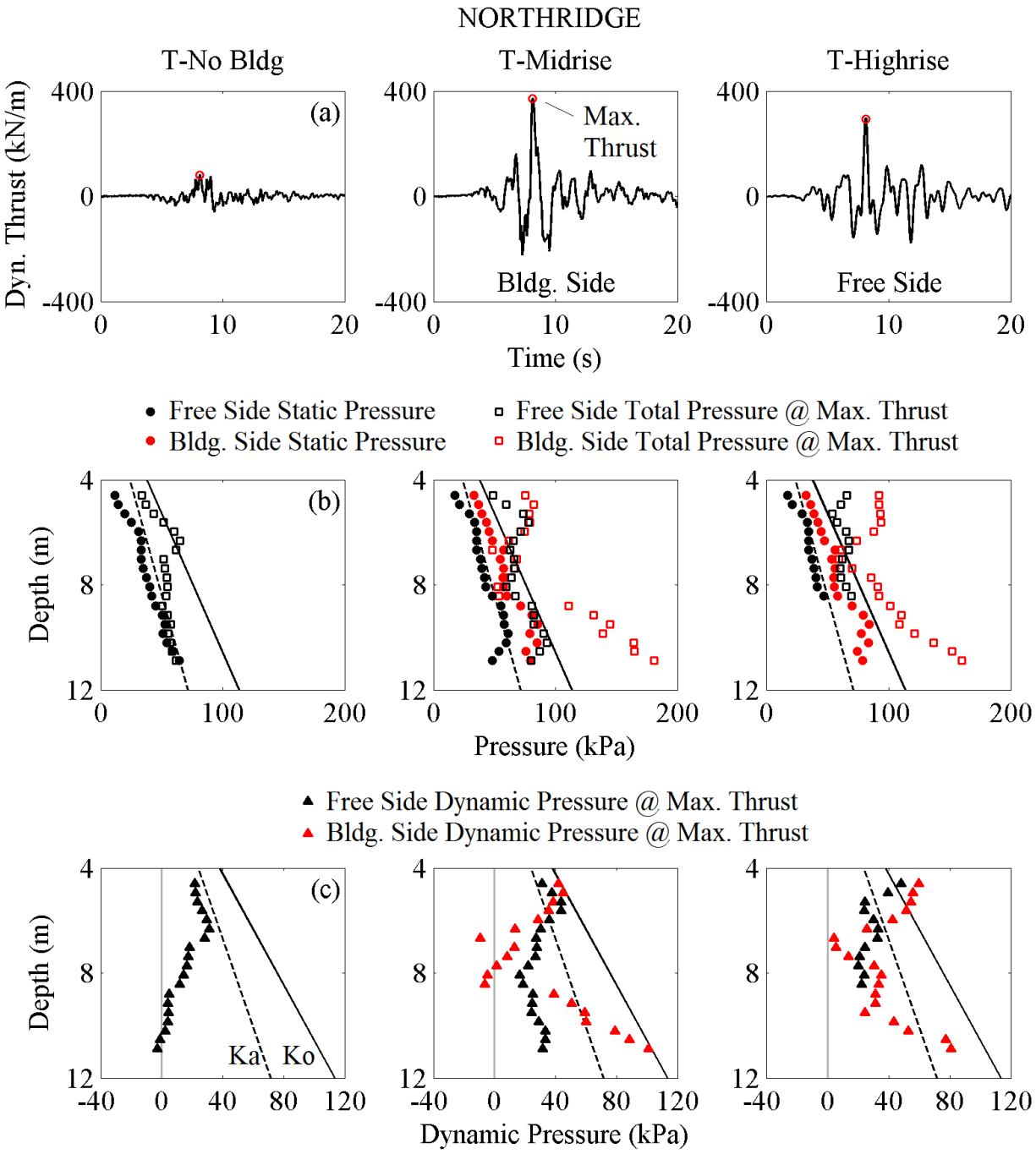

Figure 4.5.8. Northridge lateral earth pressure results presented as (a) dynamic increment of thrust time history; (b) initial static and maximum total pressure at the moment of maximum thrust; and (c) the dynamic increment of lateral earth pressure at the moment of maximum thrust.

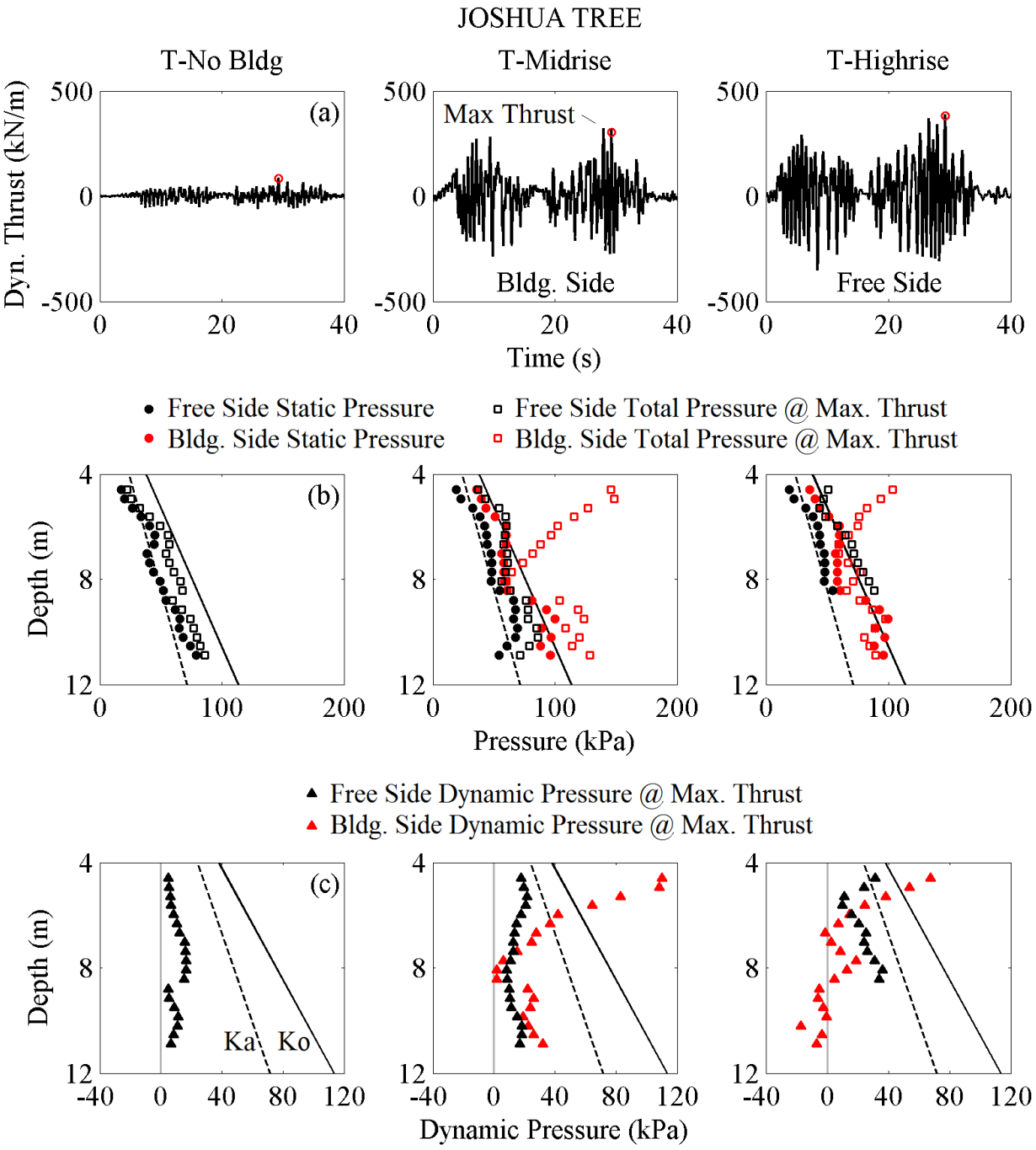

Figure 4.5.9. Joshua Tree lateral earth pressure results presented as (a) dynamic increment of thrust time history; (b) initial static and maximum total pressure at the moment of maximum thrust; and (c) the dynamic increment of lateral earth pressure at the moment of maximum thrust.

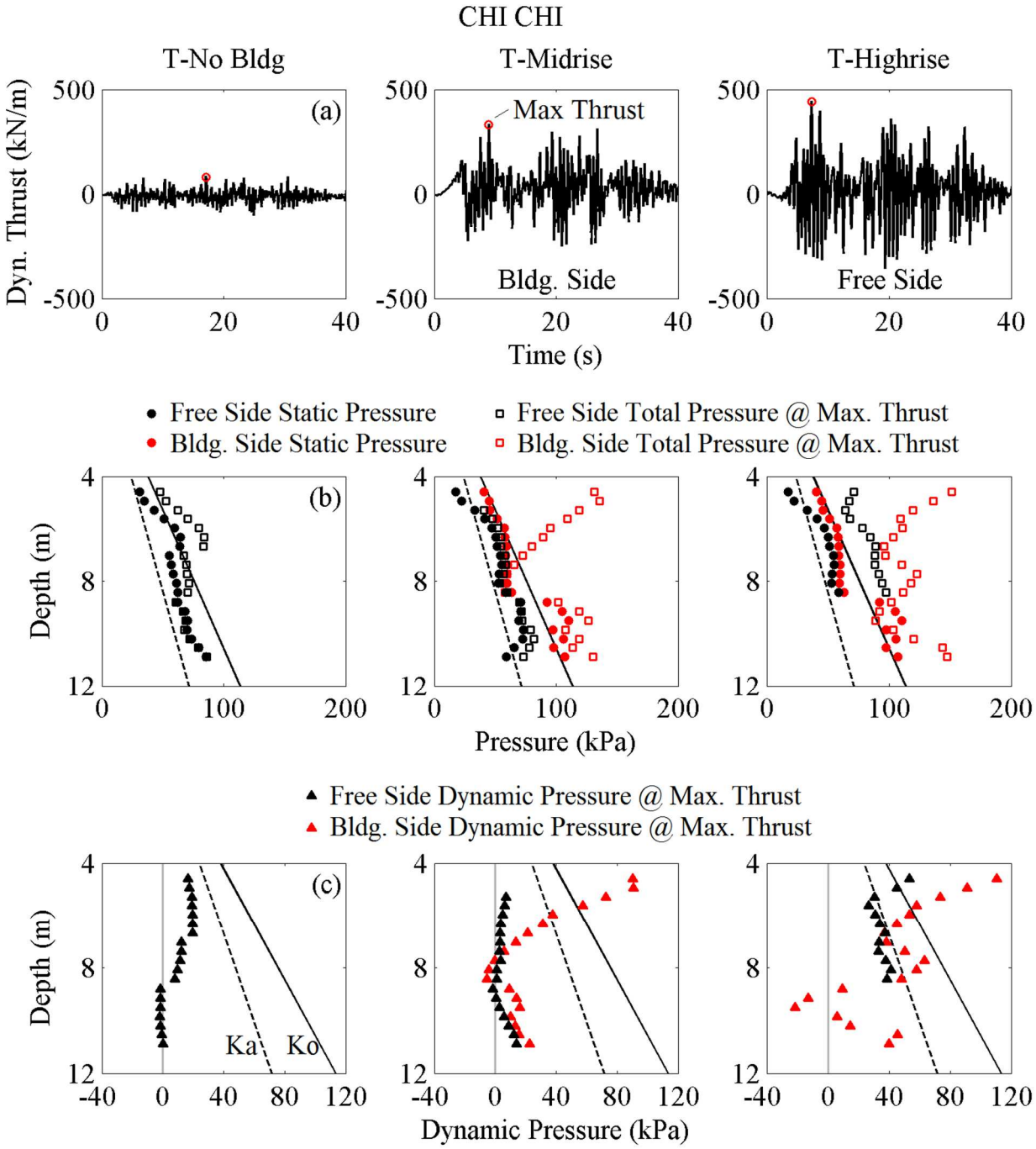

Figure 4.5.10. Chi Chi lateral earth pressure results presented as (a) dynamic increment of thrust time history; (b) initial static and maximum total pressure at the moment of maximum thrust; and (c) the dynamic increment of lateral earth pressure at the moment of maximum thrust.

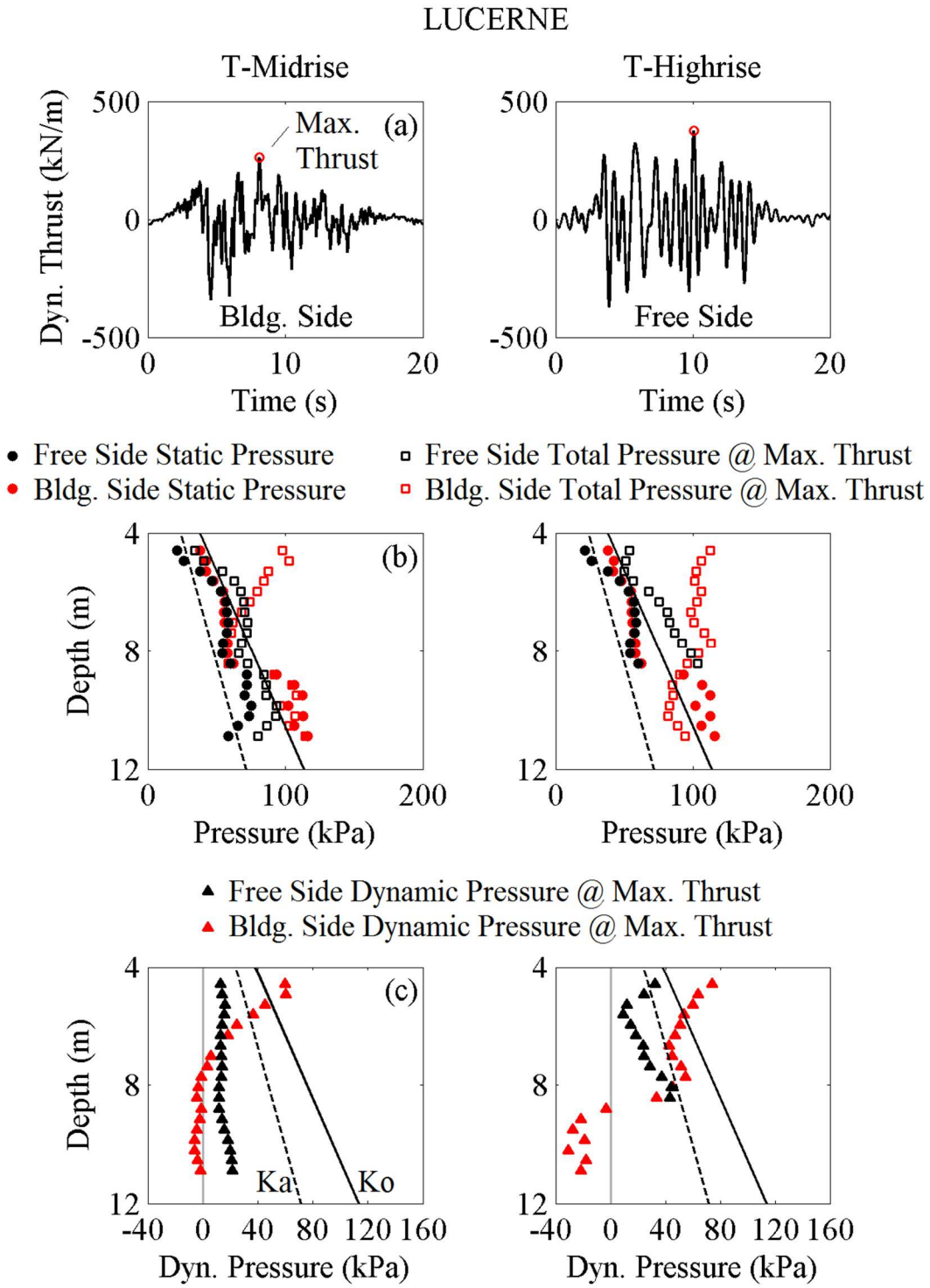

Figure 4.5.11. Lucerne lateral earth pressure results presented as (a) dynamic increment of thrust time history; (b) initial static and maximum total pressure at the moment of maximum thrust; and (c) the dynamic increment of lateral earth pressure at the moment of maximum thrust. Note: T-No Bldg is not presented during this motion due to instrument failure.

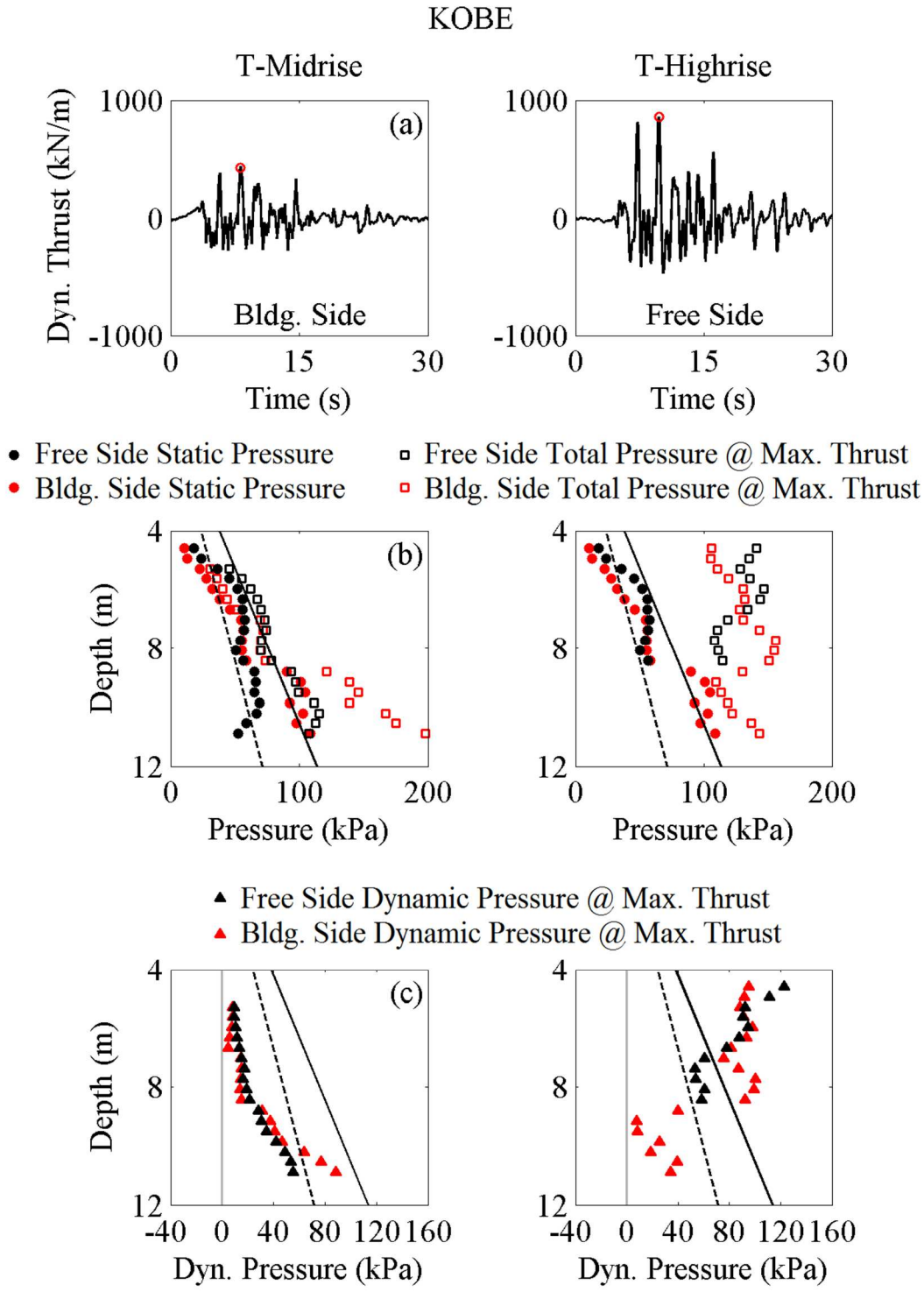

Figure 4.5.12. Kobe lateral earth pressure results presented as (a) dynamic increment of thrust time history; (b) initial static and maximum total pressure at the moment of maximum thrust; and (c) the dynamic increment of lateral earth pressure at the moment of maximum thrust. Note: T-No Bldg is not presented during this motion due to instrument failure.

4.6 Discussion and Comparison of Results

In this chapter, results from various instruments have been presented with the goal of better understanding how the presence of an adjacent midrise and highrise structure influenced the seismic performance of an underground box structure in a more holistic manner, both in terms of deflections and forces.

A slight reduction of tunnel racking was observed when an adjacent midrise or highrise building was present as compared to when the tunnel was in isolation. Also, the dynamic lateral displacements de-amplified on the basement wall at shallow depths compared to the case with no building (at the same distance from the tunnel and same elevation). This suggests that the tall buildings acted to "anchor" the ground during shaking, most likely because of both kinematic effects (embedment of the basement walls) and inertial effects dominated by the dynamic properties of the tall buildings (high natural periods compared to the predominant period of the motion). Thus, the presence of the tall buildings seems to have slightly confined the tunnel by limiting the lateral displacements in the surrounding soil and therefore the tunnel. The dynamic bending strains generally confirmed a similar pattern in these structures.

The tactile pressure sensors recorded significantly larger lateral dynamic earth pressures on both tunnel walls during T-Midrise and T-Highrise compared to T-No Bldg, particularly at shallow depths in most cases. The higher dynamic thrusts may be attributed to the base shear transferred to the soil and adjacent underground structure from the superstructure, which will be investigated in detail in this section.

The increase in dynamic lateral earth pressures on the tunnel did not translate into increased tunnel racking displacements or overall deflections, which seems at first contradictory. The timing of the dynamic thrust experienced on the two walls likely played a major role in the

observed trends of increased pressure and slightly reduced racking. During most ground motions, the dynamic thrust in T-Midrise and T-Highrise on the two walls of the tunnel was in phase (increased and decreased together), which may have been responsible for the reduction in overall racking distortions (Figure 4.5.8 through Figure 4.5.12).

4.6.1 Dynamic Bending Moments and Racking Displacements

Four strain gauges located at the corners of the tunnel were used to evaluate tunnel distortion and racking displacements in parallel among the three tunnel tests. Strain gauges located at the corners of the tunnel were selected here because the peak bending moment in the tunnel often occurred at these locations during shaking. The locations of the four gauges used to measure tunnel distortion are shown in Figure 4.6.1. Strain Gauge (SG) 9 malfunctioned in T-No Bldg, therefore SG 11 was used in its place.

Figure 4.6.2 through Figure 4.6.13 compare the tunnel racking displacements with the dynamic bending moments at the tunnel corners. Two figures are shown for each ground motion, one on the south (building side) wall, and one on the north (free side) wall. It should be noted that tunnel racking displacement measurements are a more systematic measure of average tunnel distortion than dynamic bending moments measured by one strain gauge that measures deflection locally. However, this comparison enabled a secondary evaluation of the impact of an adjacent building on the overall deformation and performance of the permanent box structure.

The following trends were observed from the racking displacement and dynamic bending moment comparisons:

- T-Midrise produced the largest dynamic bending moment and racking in the tunnel during the Northridge and Kobe motions. The dynamic bending moments measured at the corners of the tunnel seemed to be a function of the frequency content of the ground motion. When the

ground motion had a smaller predominant frequency (e.g., Northridge and Kobe), the tunnel showed more distortion in T-Midrise at lower frequencies. This is likely due to the ground motion's predominant frequency being closer to the fundamental frequency of the midrise structure amplifying the superstructure displacements, shear forces, and moments induced onto the soil and adjacent box structure.

- T-Highrise consistently showed the least racking displacement and dynamic bending moments among the three experiments in the frequency range of interest (0.5 to 5 Hz).
- Generally, the frequency contents of dynamic moments were similar to those of racking deformations on the tunnel, with the exception of lower frequency contents that were sometimes present in racking and not picked up by strain gauges.
- During the Joshua Tree, Chi Chi, and Lucerne motions, T-Midrise dynamic bending moments were similar and sometimes greater than those of T-No Bldg at frequencies less than 1 Hz. At higher frequencies, both racking and bending moments were greatest in T-No Bldg compared to other tests.

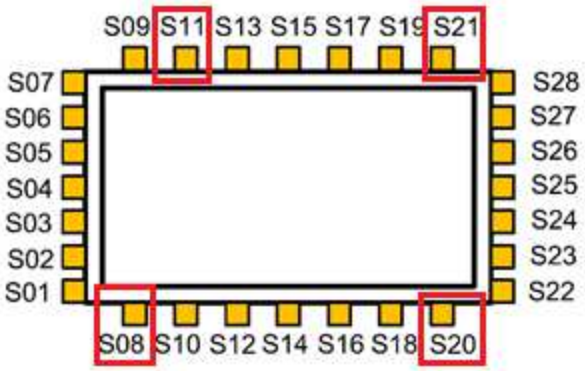

Figure 4.6.1. Tunnel strain gauges used to investigate localized deflections.

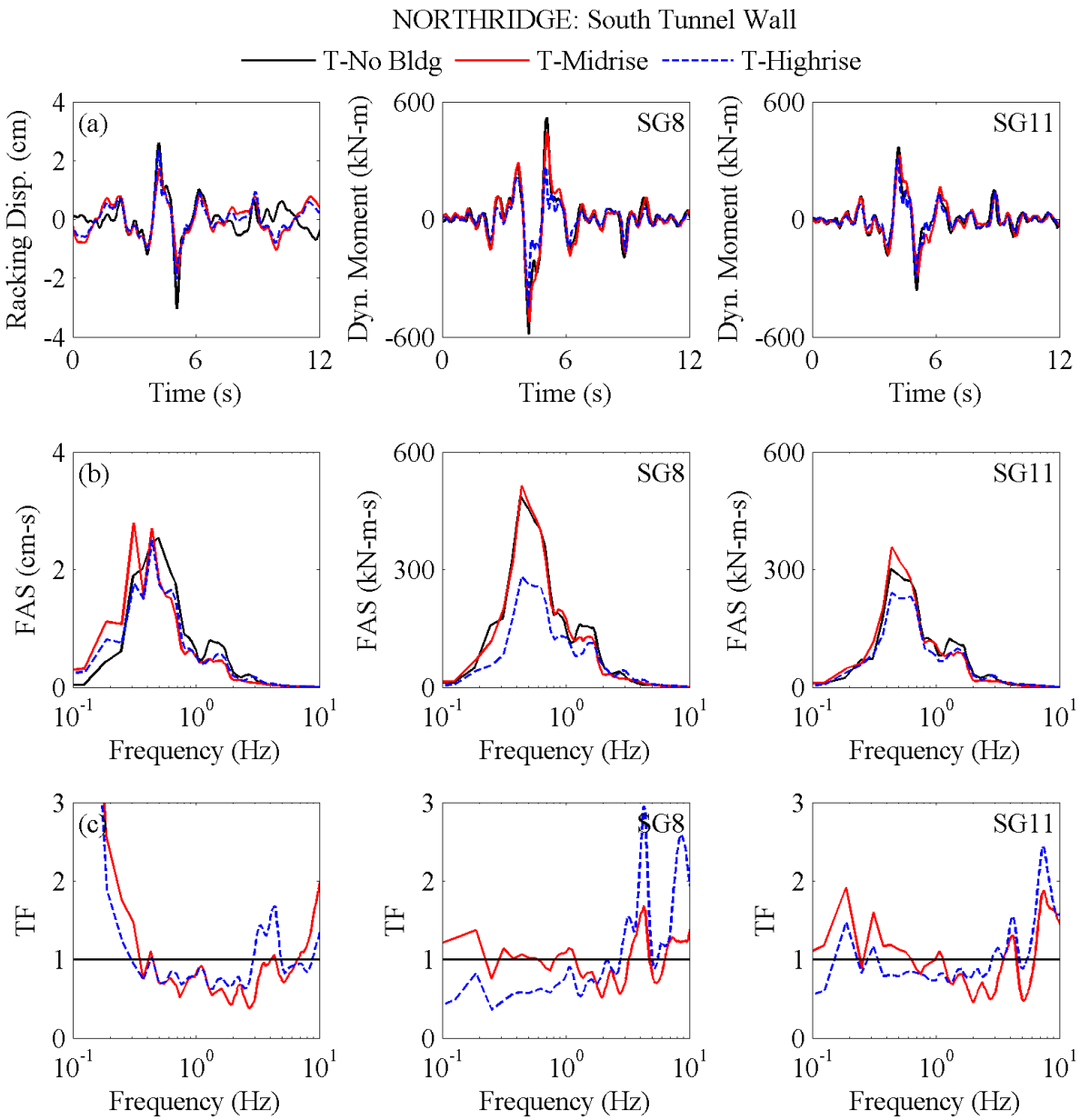

Figure 4.6.2. South tunnel wall racking displacement and tunnel corner bending moment comparison shown using: (a) time histories; (b) Fourier amplitude spectra, and (c) transfer functions of Fourier amplitude spectra.

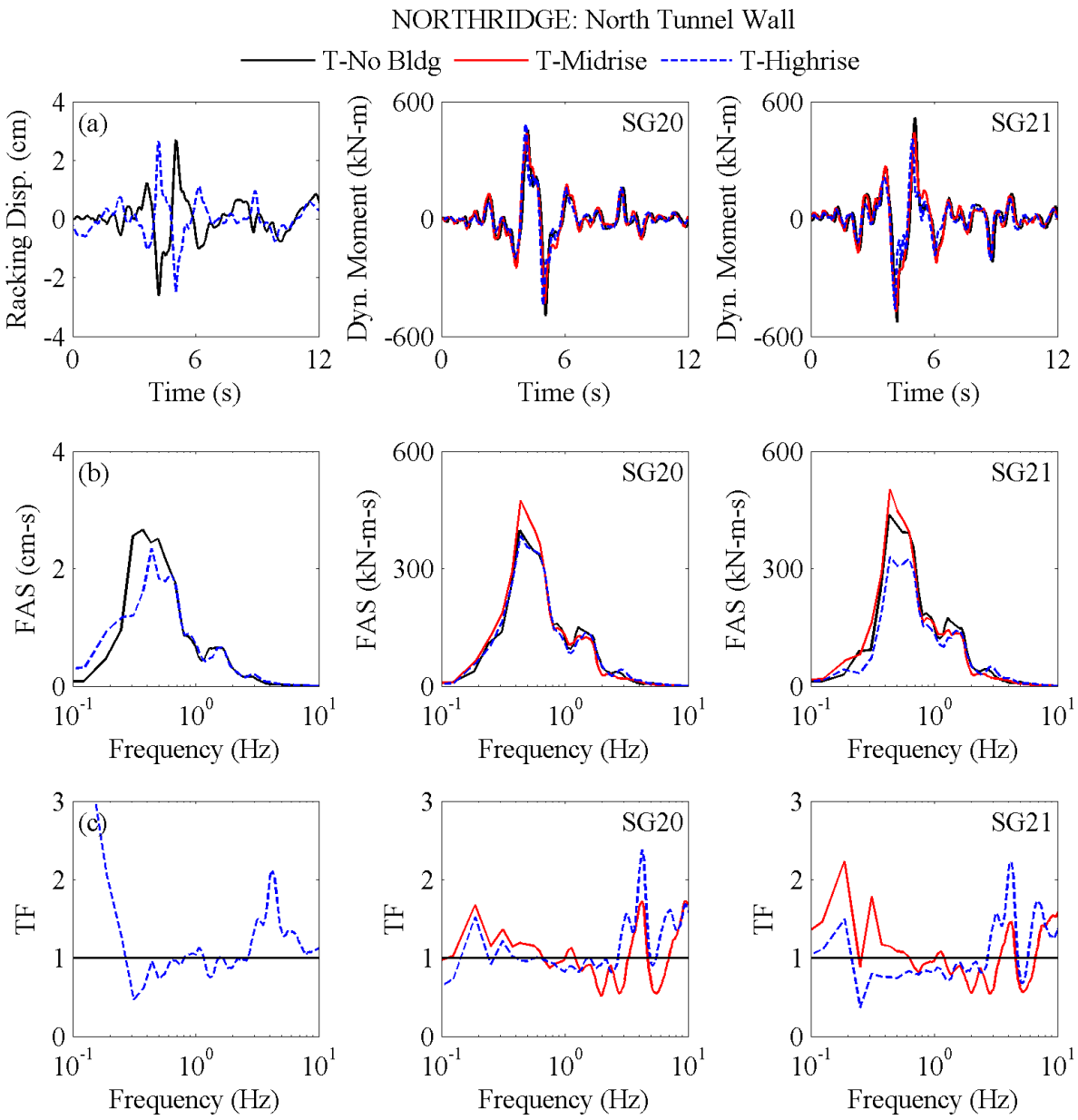

Figure 4.6.3. North tunnel wall racking displacement and tunnel corner bending moment comparison shown using: (a) time histories; (b) Fourier amplitude spectra, and (c) transfer functions of Fourier amplitude spectra.

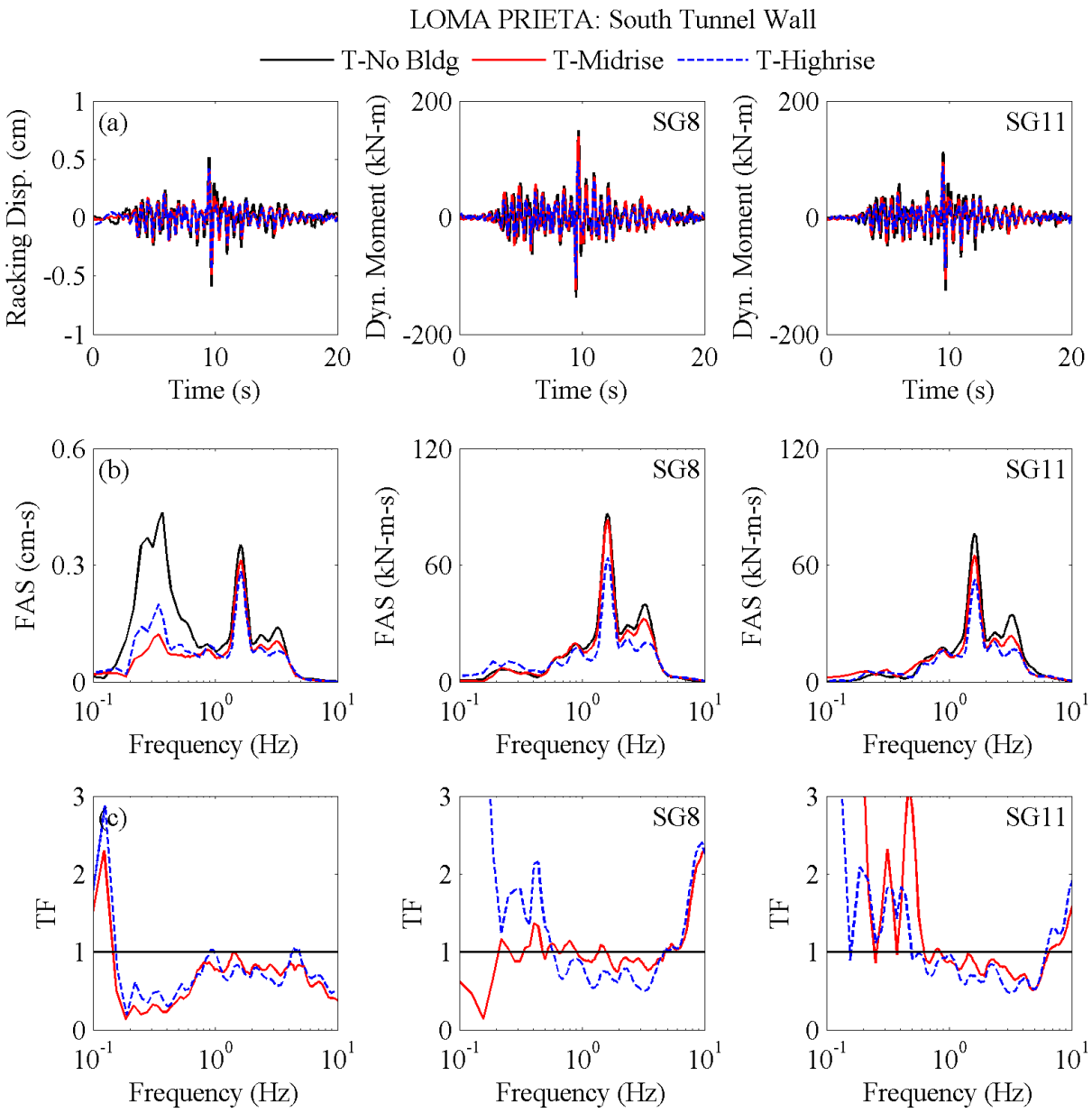

Figure 4.6.4. South tunnel wall racking displacement and tunnel corner bending moment comparison shown using: (a) time histories; (b) Fourier amplitude spectra, and (c) transfer functions of Fourier amplitude spectra.

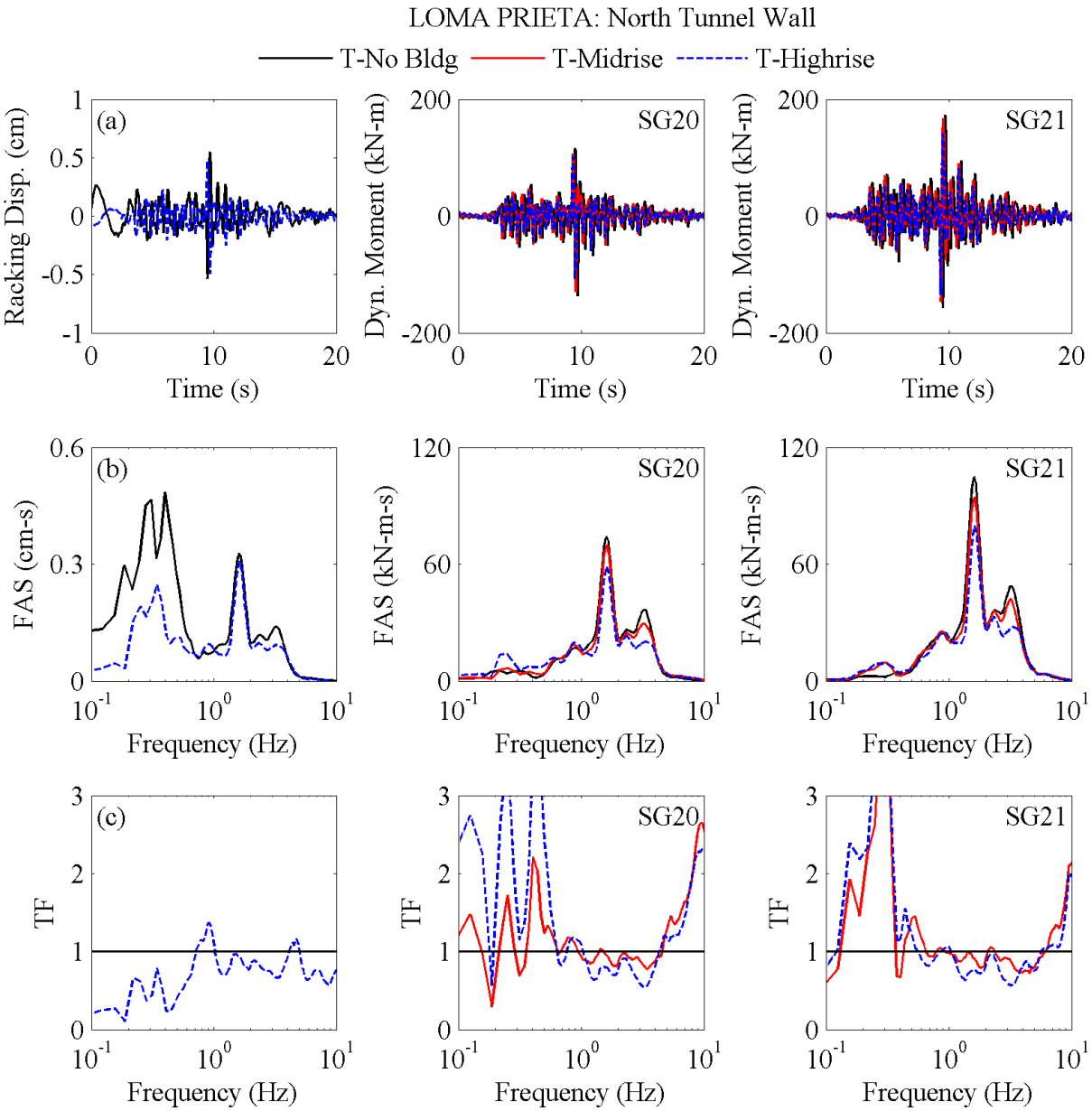

Figure 4.6.5. North tunnel wall racking displacement and tunnel corner bending moment comparison shown using: (a) time histories; (b) Fourier amplitude spectra, and (c) transfer functions of Fourier amplitude spectra.

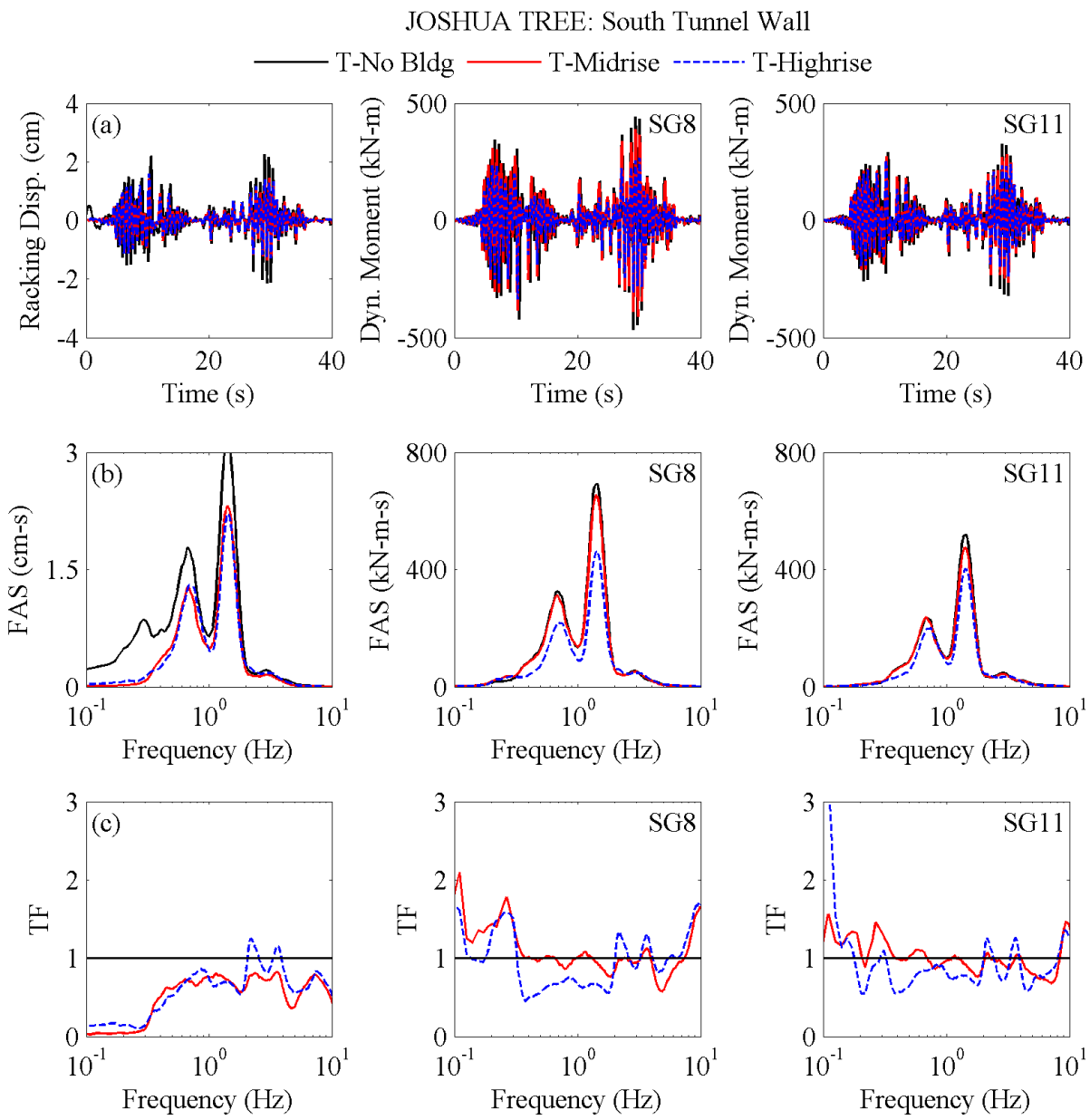

Figure 4.6.6. South tunnel wall racking displacement and tunnel corner bending moment comparison shown using: (a) time histories; (b) Fourier amplitude spectra, and (c) transfer functions of Fourier amplitude spectra.

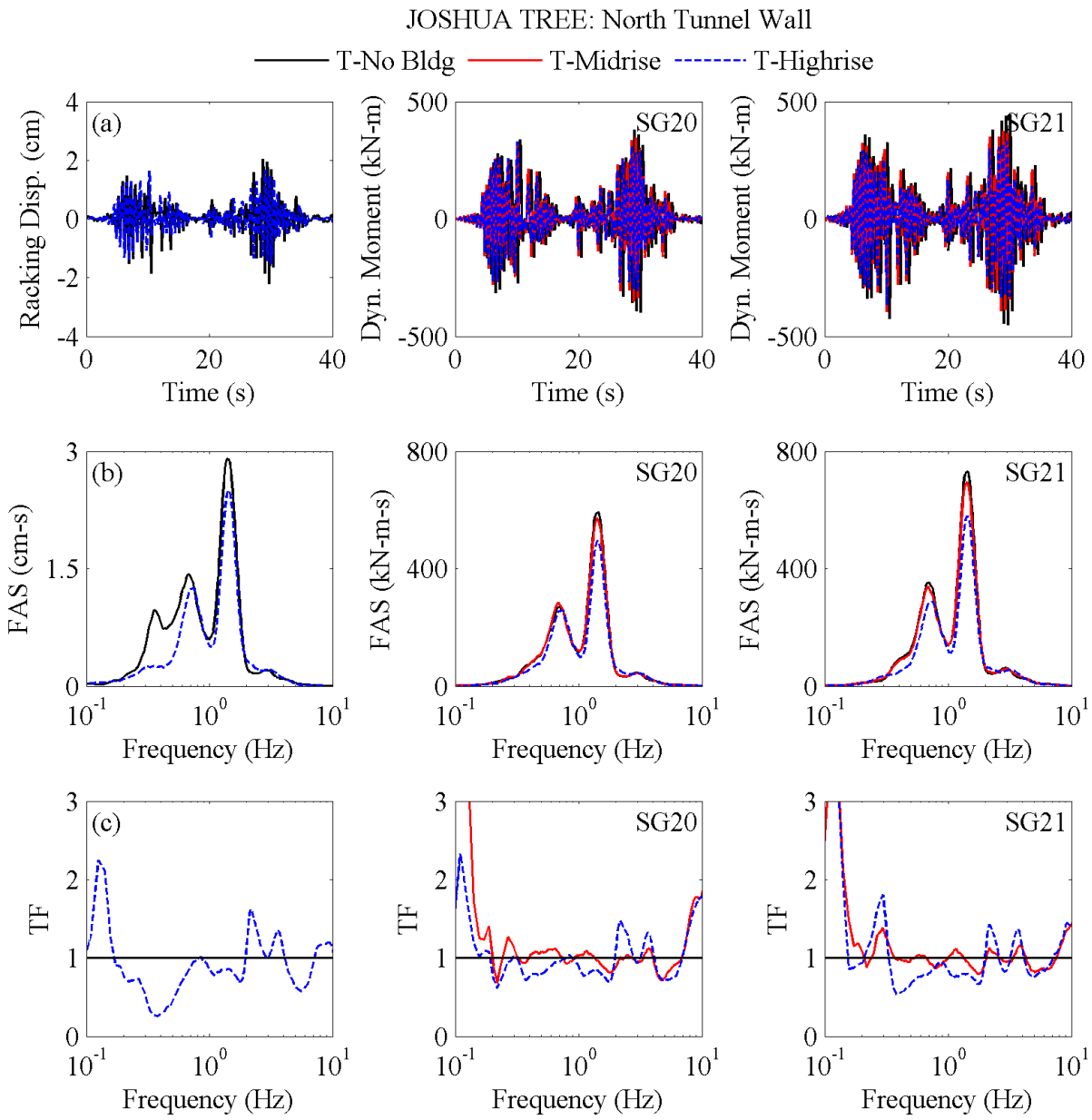

Figure 4.6.7. North tunnel wall racking displacement and tunnel corner bending moment comparison shown using: (a) time histories; (b) Fourier amplitude spectra, and (c) transfer functions of Fourier amplitude spectra.

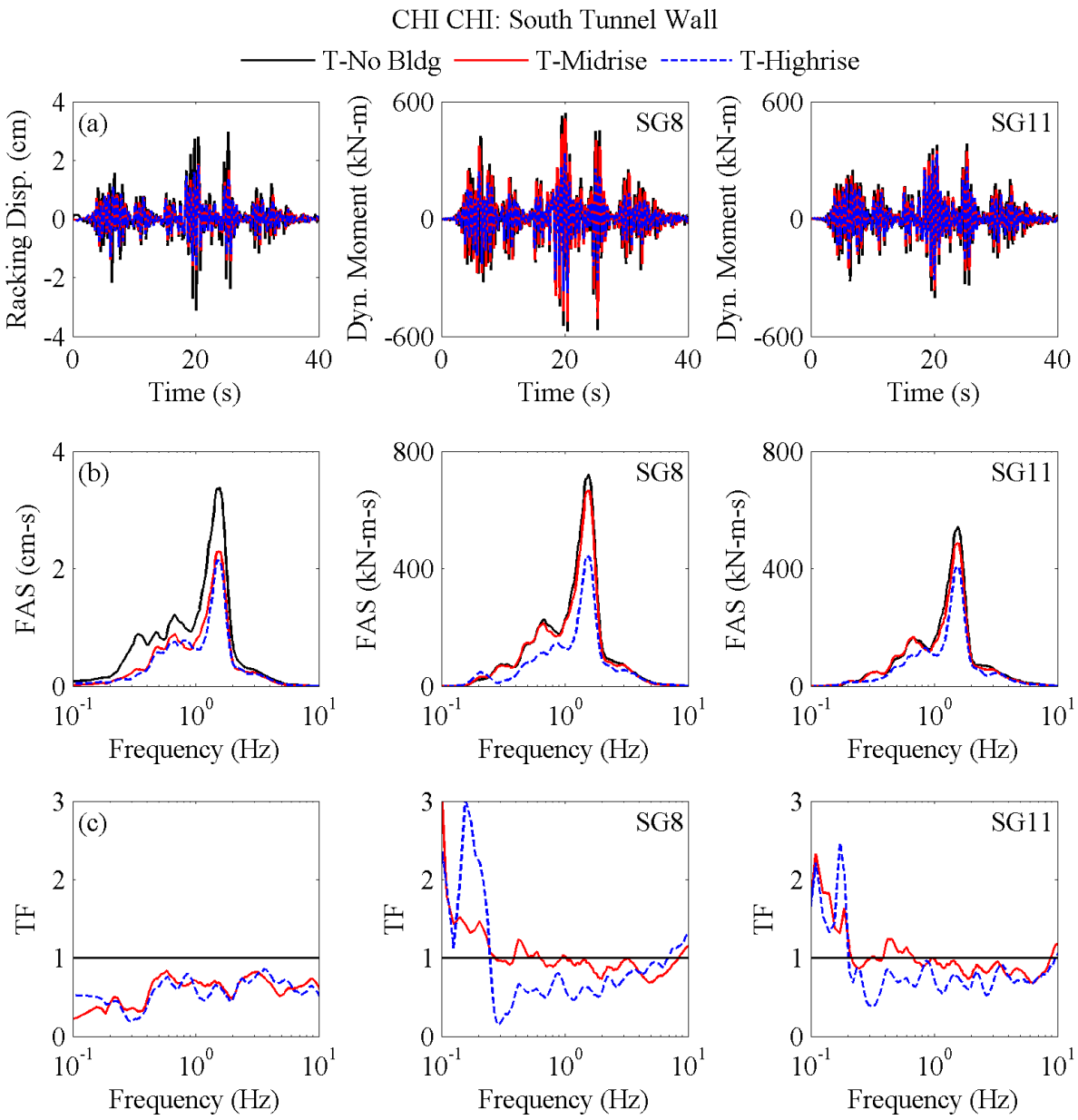

Figure 4.6.8. South tunnel wall racking displacement and tunnel corner bending moment comparison shown using: (a) time histories; (b) Fourier amplitude spectra, and (c) transfer unctions of Fourier amplitude spectra.

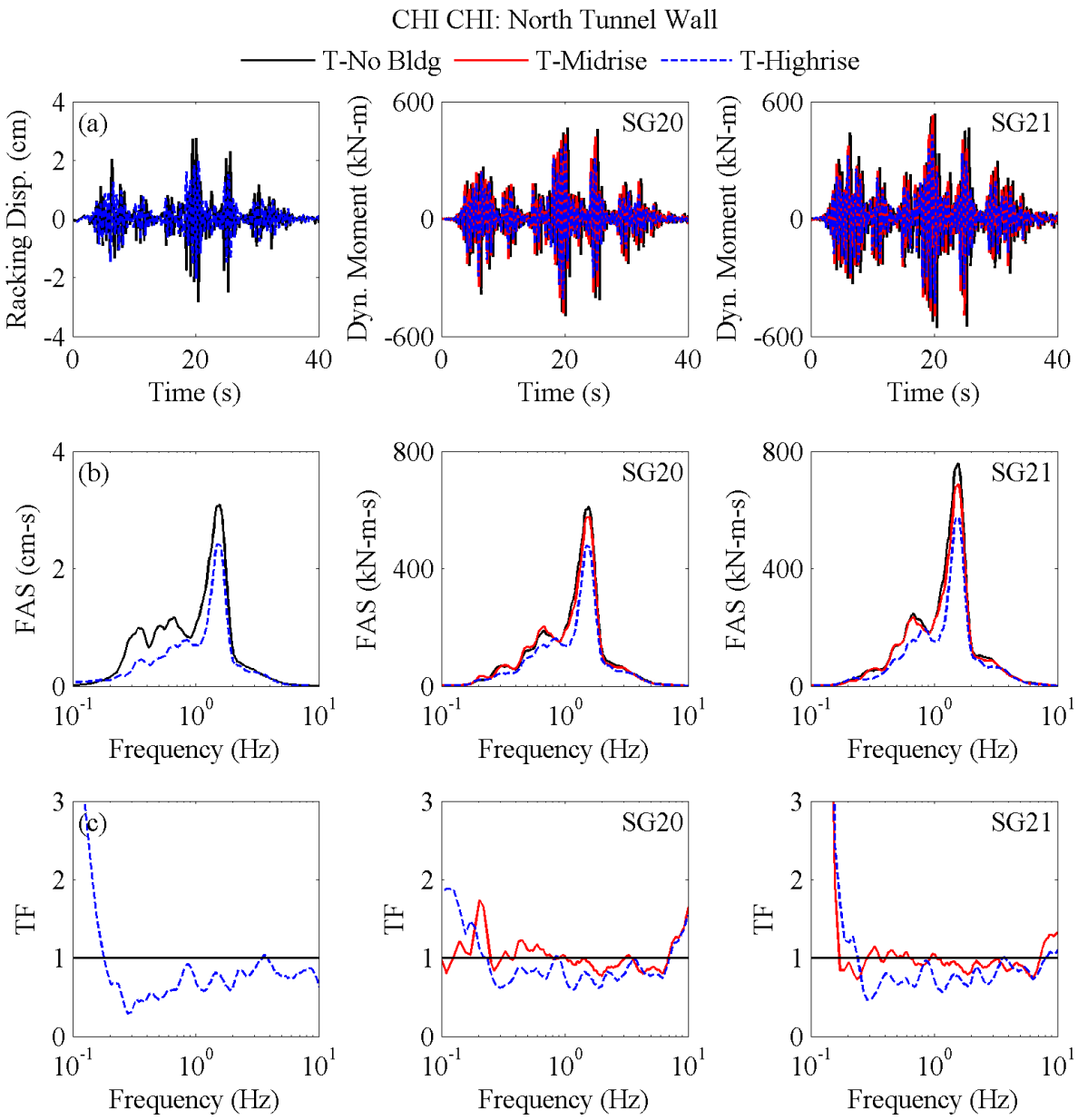

Figure 4.6.9. North tunnel wall racking displacement and tunnel corner bending moment comparison shown using: (a) time histories; (b) Fourier amplitude spectra, and (c) transfer functions of Fourier amplitude spectra.

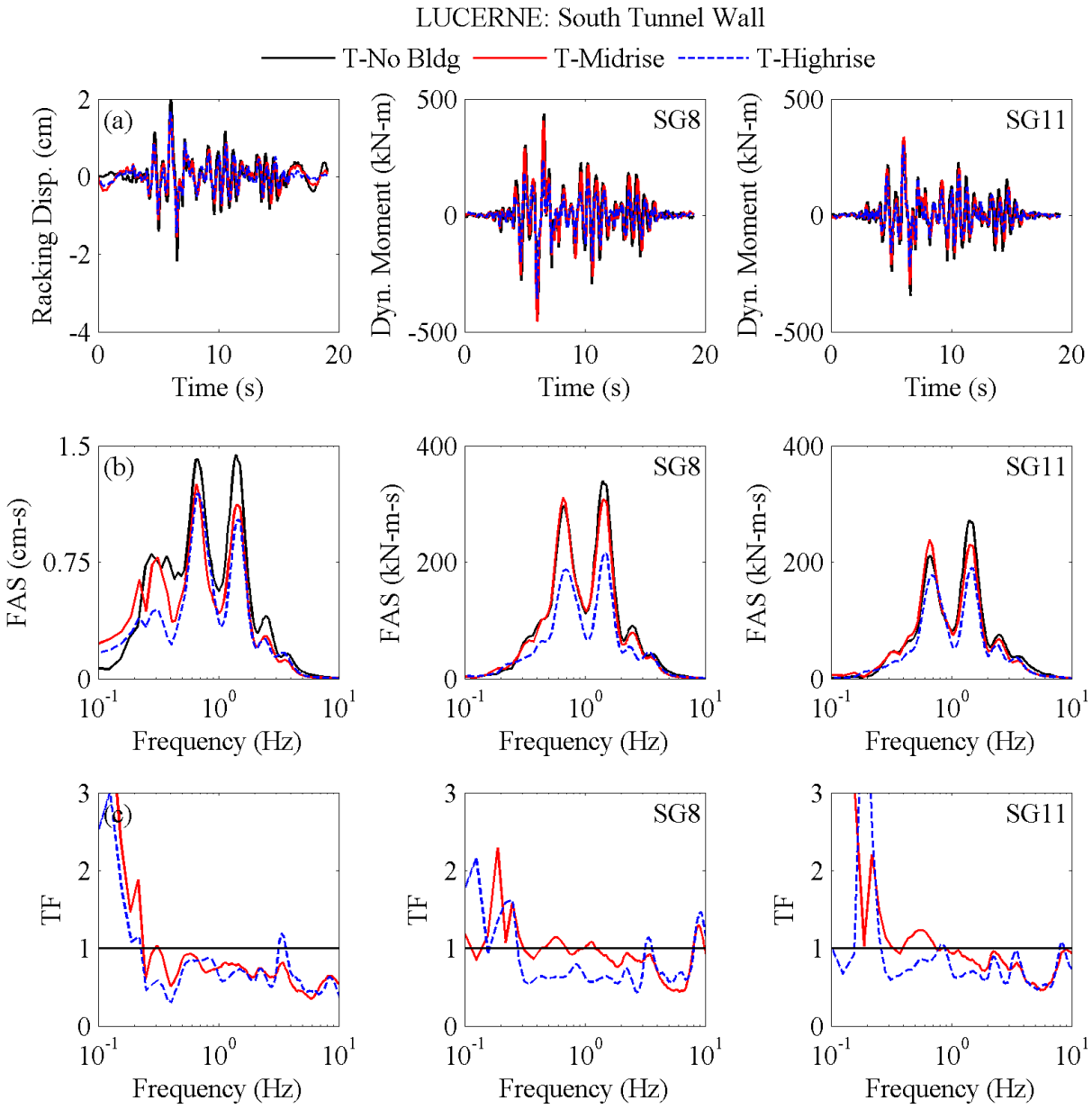

Figure 4.6.10. South tunnel wall racking displacement and tunnel corner bending moment comparison shown using: (a) time histories; (b) Fourier amplitude spectra, and (c) transfer functions of Fourier amplitude spectra.

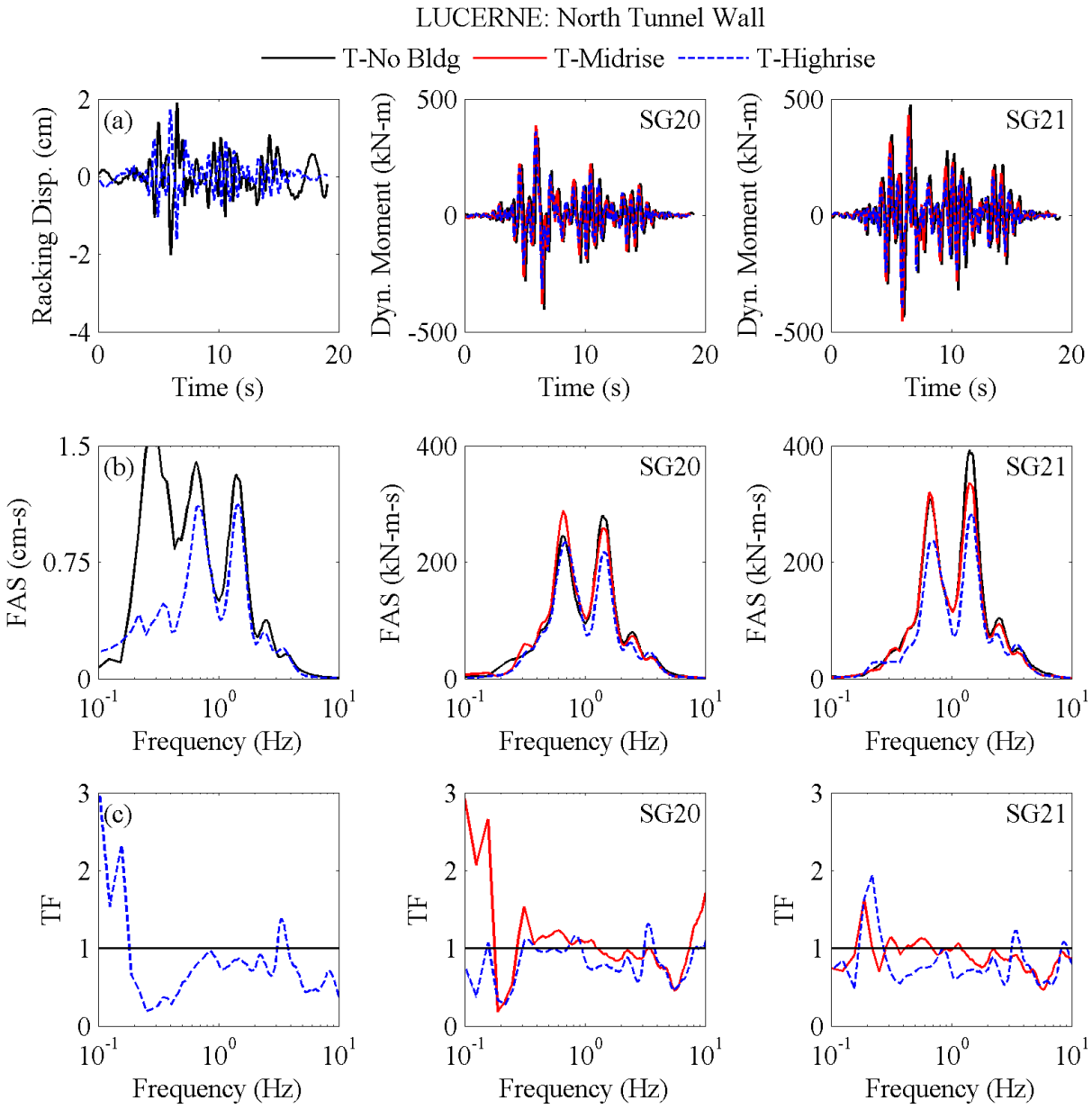

Figure 4.6.11. North tunnel wall racking displacement and tunnel corner bending moment comparison shown using: (a) time histories; (b) Fourier amplitude spectra, and (c) transfer functions of Fourier amplitude spectra.

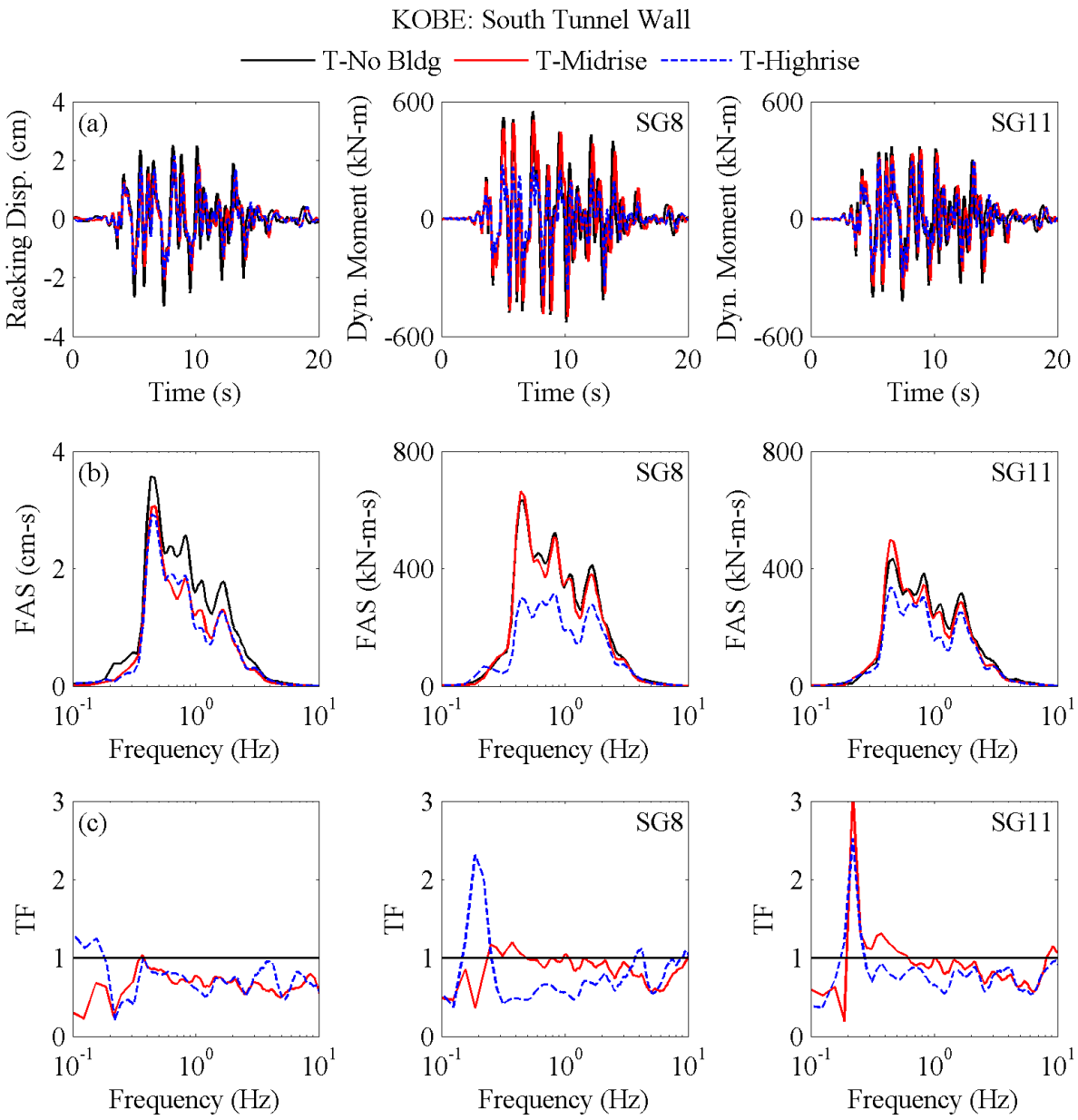

Figure 4.6.12. South tunnel wall racking displacement and tunnel corner bending moment comparison shown using: (a) time histories; (b) Fourier amplitude spectra, and (c) transfer functions of Fourier amplitude spectra.

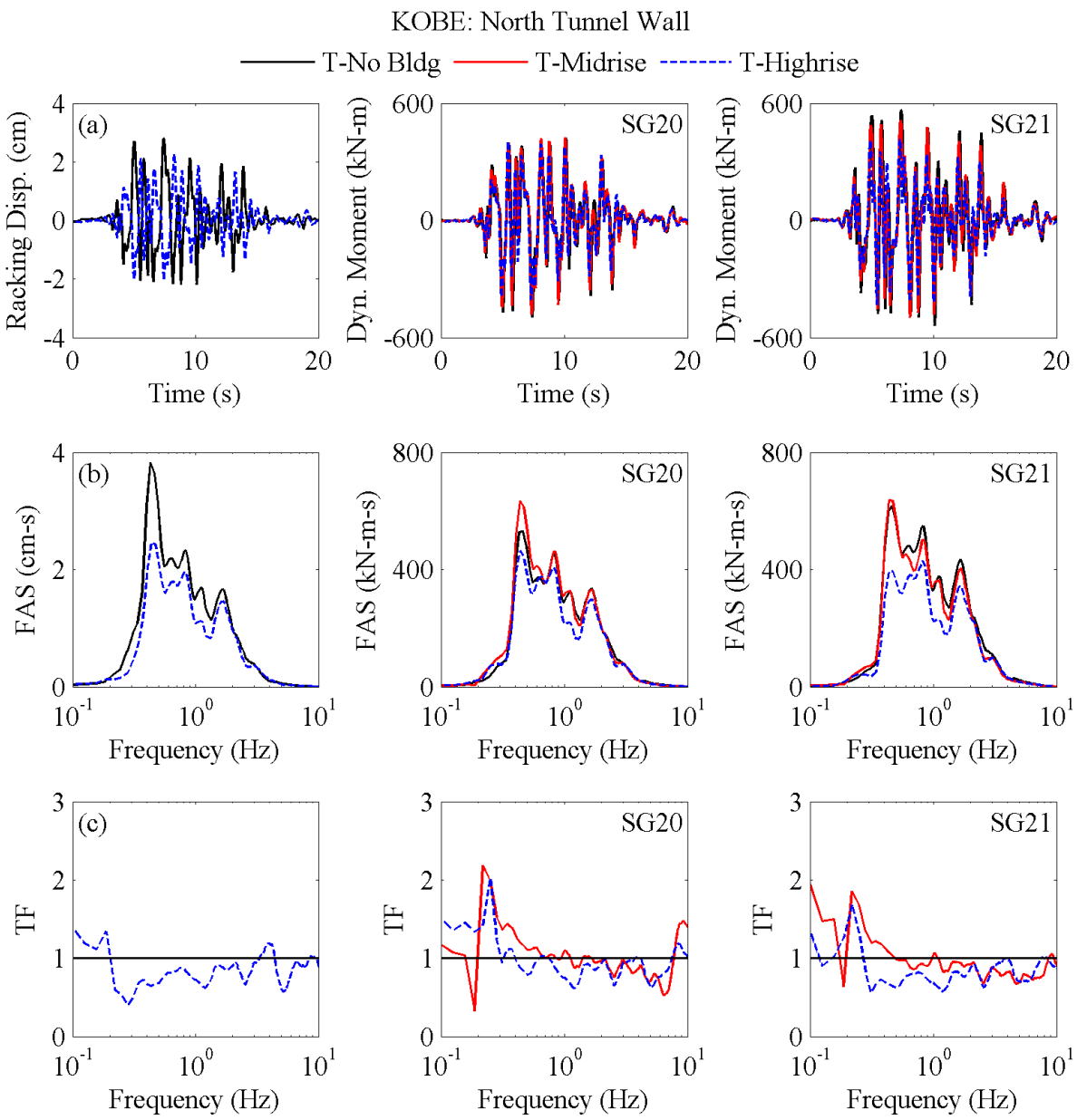

Figure 4.6.13. North tunnel wall racking displacement and tunnel corner bending moment comparison shown using: (a) time histories; (b) Fourier amplitude spectra, and (c) transfer functions of Fourier amplitude spectra.

4.6.2 Dynamic Thrust and Building Base Shear

Seismic forces induced by the adjacent superstructure were expected to significantly influence the dynamic thrust experienced on the tunnel (both walls). One way to measure these induced forces from the building is through its base shear. The following figures compare the dynamic thrust measured on the two walls in each experiment with the base shear force from the adjacent midrise or highrise building. The building base shear was computed as the sum of the shear forces from each floor of the structure and the base plate (i.e., product of acceleration time history measured on each floor and its corresponding mass).

Dynamic thrust time histories as interpreted from the tactile pressure sensors were not recorded with the same data acquisition system as other sensors. Therefore the two sets of data presented here were aligned manually. Alignment to the main data acquisition system was performed using data from a given row of pressure sensor and strain gauge at the same depth on the tunnel, with the assumption that strain and pressure would be roughly synchronous. However, the uncertainties in the timing of these measurements arising from their manual synchronization must be kept in mind.

It is shown that the amplitude of building base shear and thrust measured on the tunnel walls is comparable. It is worth noting that the building base shear doesn't include the mass of the basement walls or the soil within the skirt basement section. In addition to a comparison of time histories, the Fourier amplitude spectra of the dynamic thrust and base shear are reported as well, to compare their frequency contents. It appears that in most motions (other than Loma, which was very low in intensity), overall the dynamic thrust on both walls compared well with the base shear of the adjacent building in both time and frequency domains. The comparisons generally improve on the building side of the tunnel.

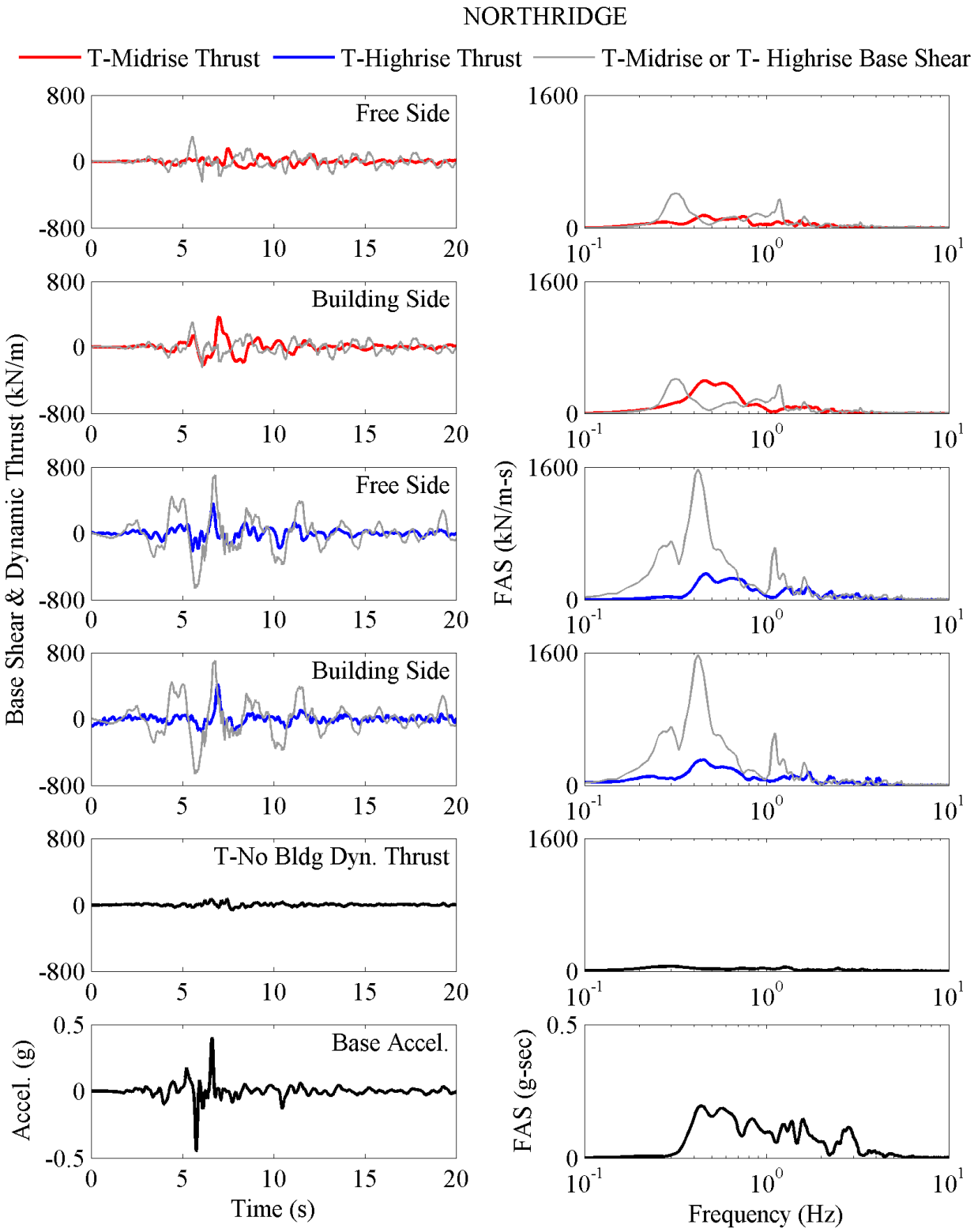

Figure 4.6.14. Dynamic lateral thrust on the tunnel compared with base shear from the tall building.

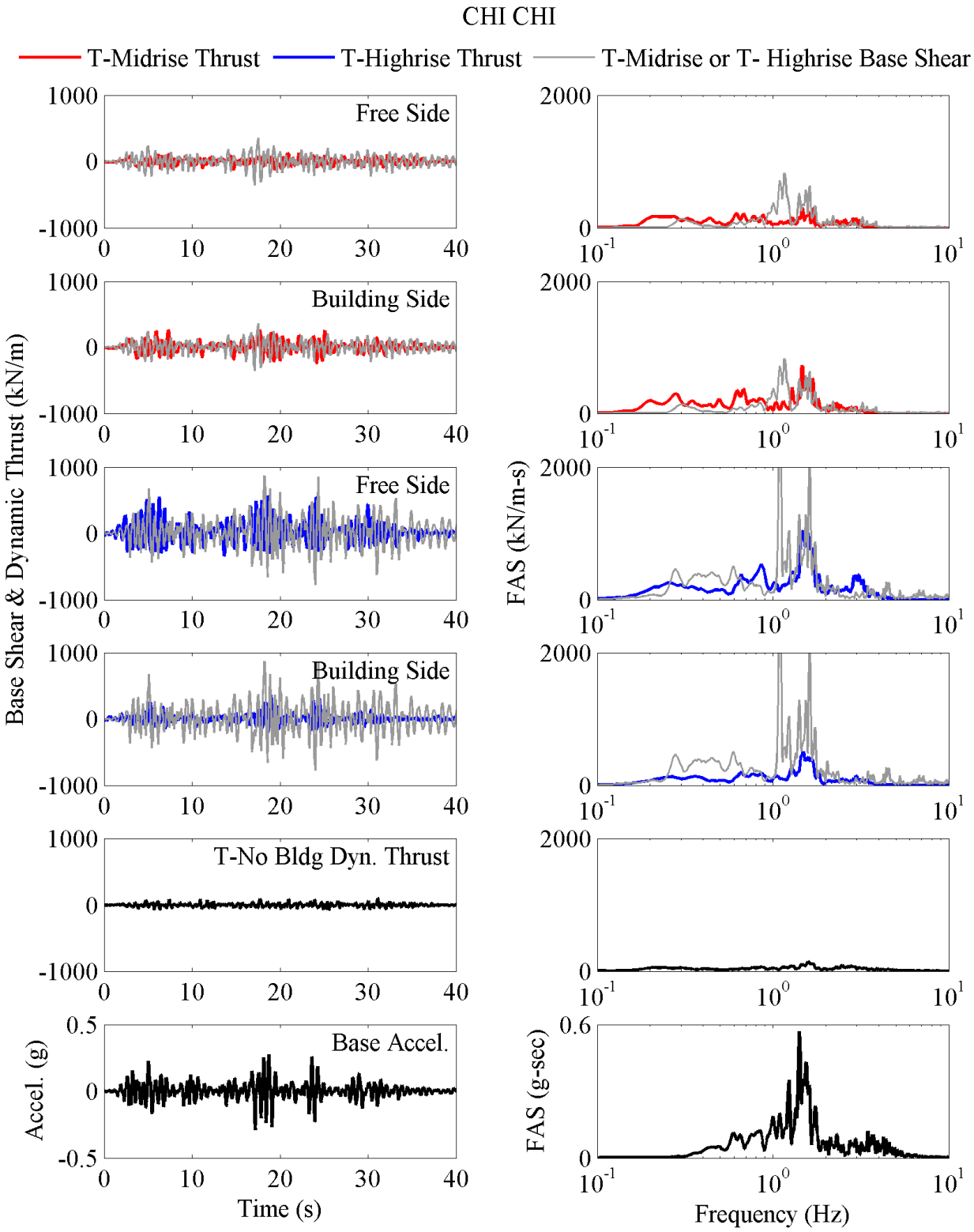

Figure 4.6.15. Dynamic lateral thrust on the tunnel compared with base shear from the tall building.

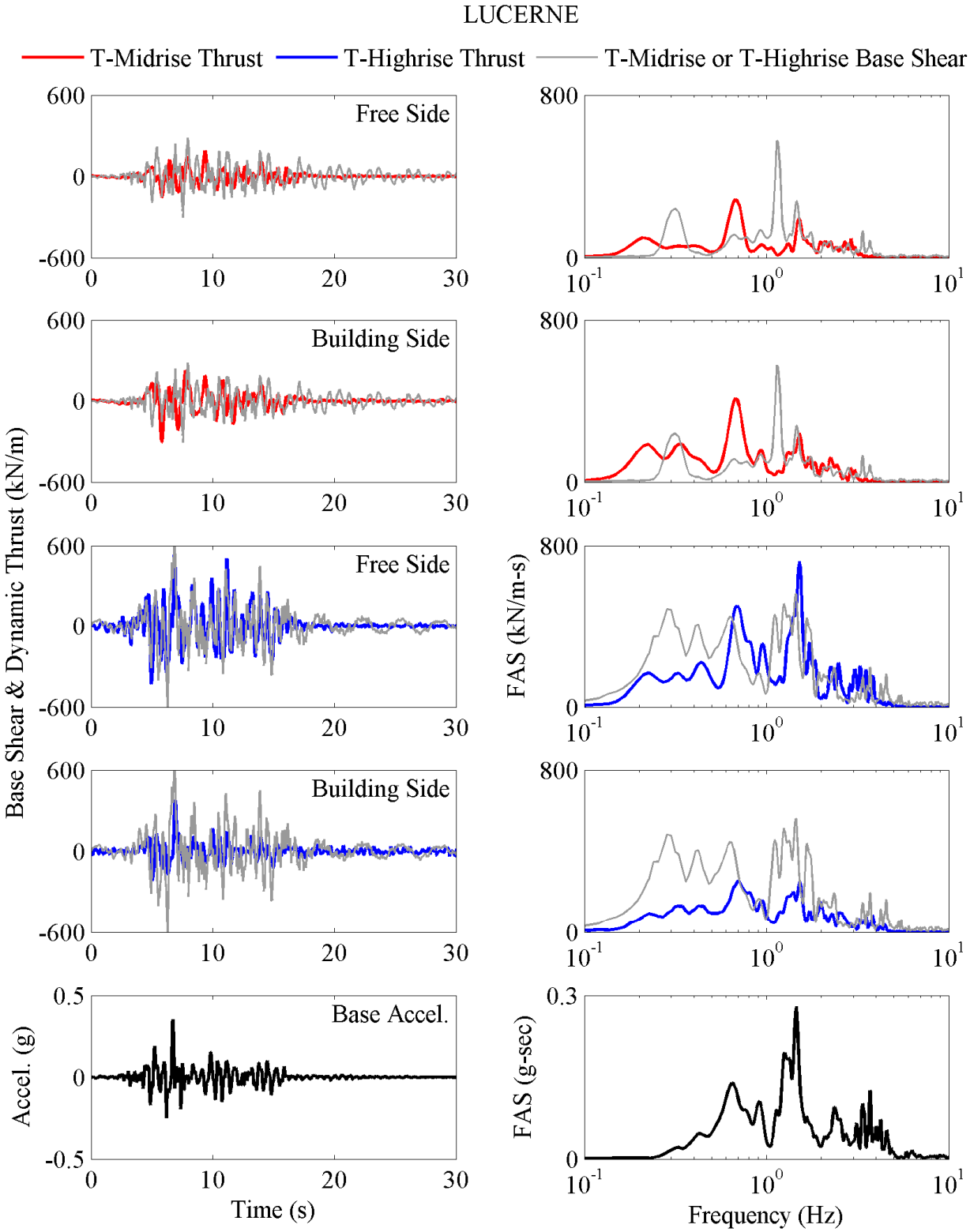

Figure 4.6.16. Dynamic lateral thrust on the tunnel compared with base shear from the tall building.

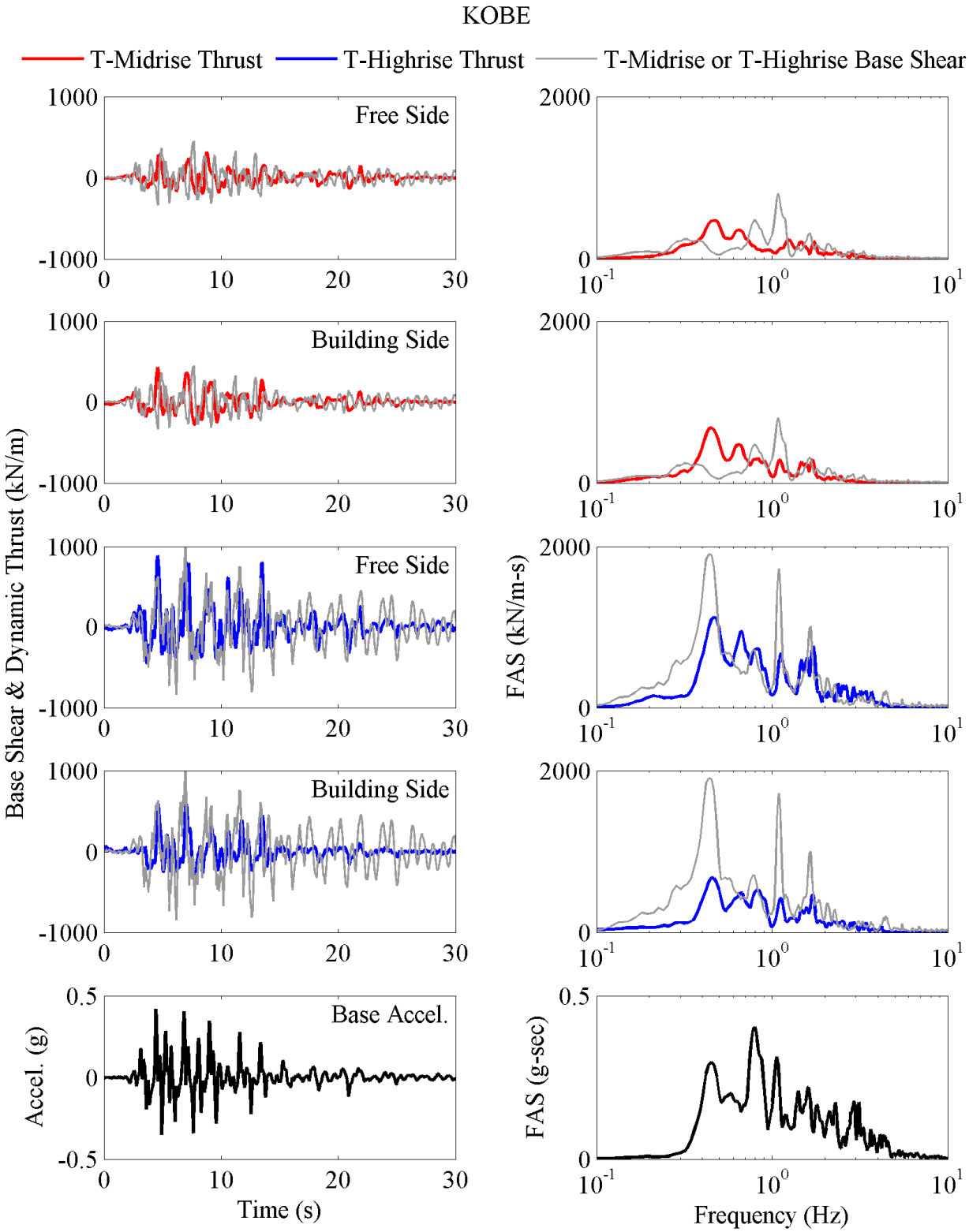

Figure 4.6.17. Dynamic lateral thrust on the tunnel compared with base shear from the tall building.

4.6.3 Dynamic Thrust and Relative Displacement

The following set of figures compare dynamic thrust on the building side of the tunnel with the relative displacement between the tunnel and basement of the midrise and highrise structures for a few representative ground motions. Accelerometers located at the mid-height of the tunnel and the corresponding elevation of the adjacent basement were double integrated to obtain displacements, and their difference used to obtain relative displacement. A positive relative displacement indicates an increased gap between the tunnel and the basement during earthquake loading. No thrust is reported for T-No Bldg during the final two ground motions, Lucerne and Kobe, as the tactile pressure sensors malfunctioned before these motions. Displacements at the base of the container are also shown in each figure for reference.

Based on the manual synchronization of thrust and relative displacement, it can be seen that when the distance between the structures was a minimum, the dynamic thrust often immediately followed with a maximum. Also, the frequency content between relative displacement and dynamic thrust is similar, especially for the ground motions later in the testing sequence.

The relative displacement between the tunnel and the building correlate strongly with the thrust recorded on the building side tunnel wall. These two quantities do not have similar amplitudes or units of measure, but the frequency content is similar. As was mentioned, the frequency content of relative displacement between the structure and thrust seemed to be more related during the later shakes. This could be due to a densification of the soil between the structures, resulting in a more efficient transfer of seismic loads between the structures through a better packed backfill soil.

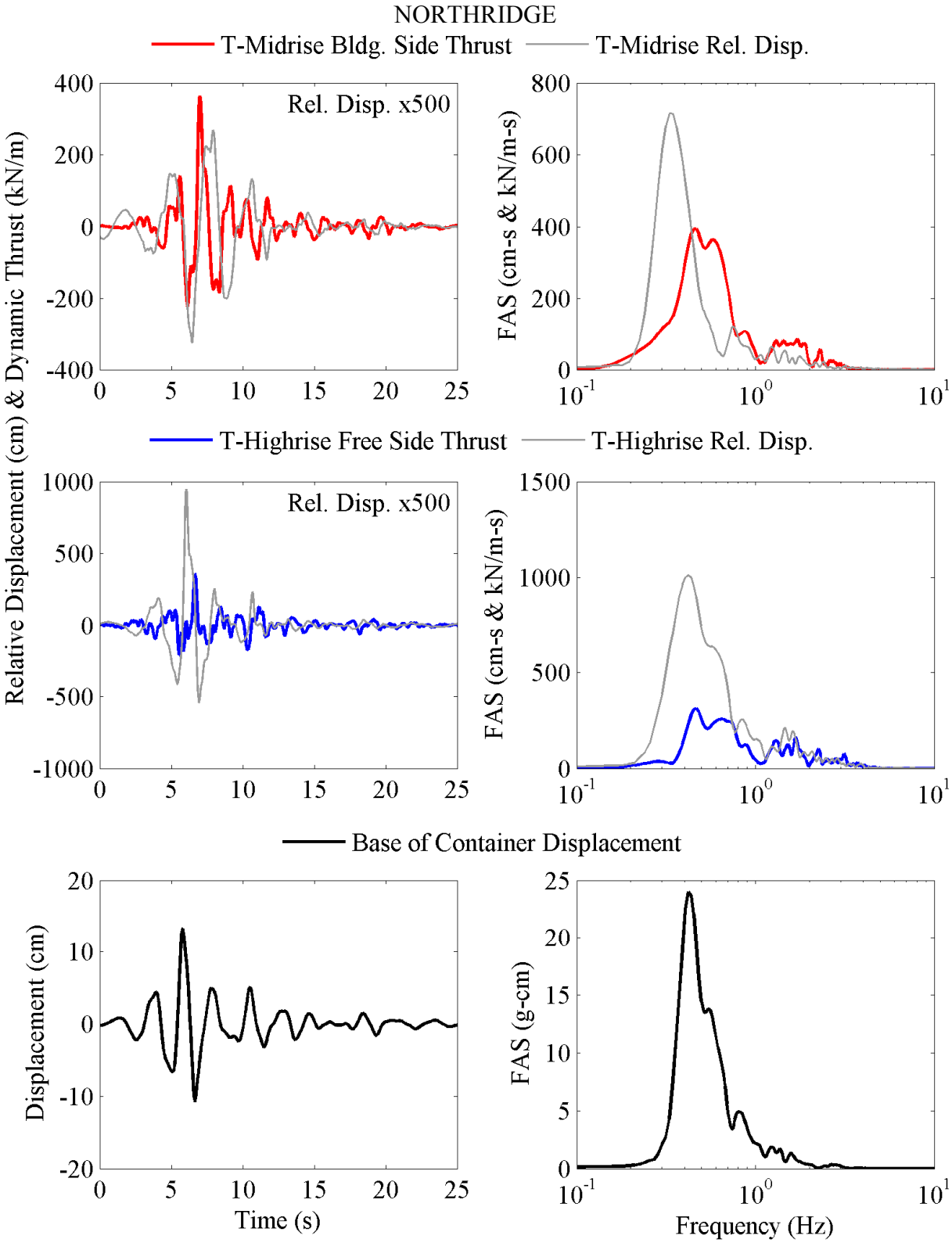

Figure 4.6.18. Dynamic tunnel thrust compared with the distance between the underground structure and the tall building's basement.

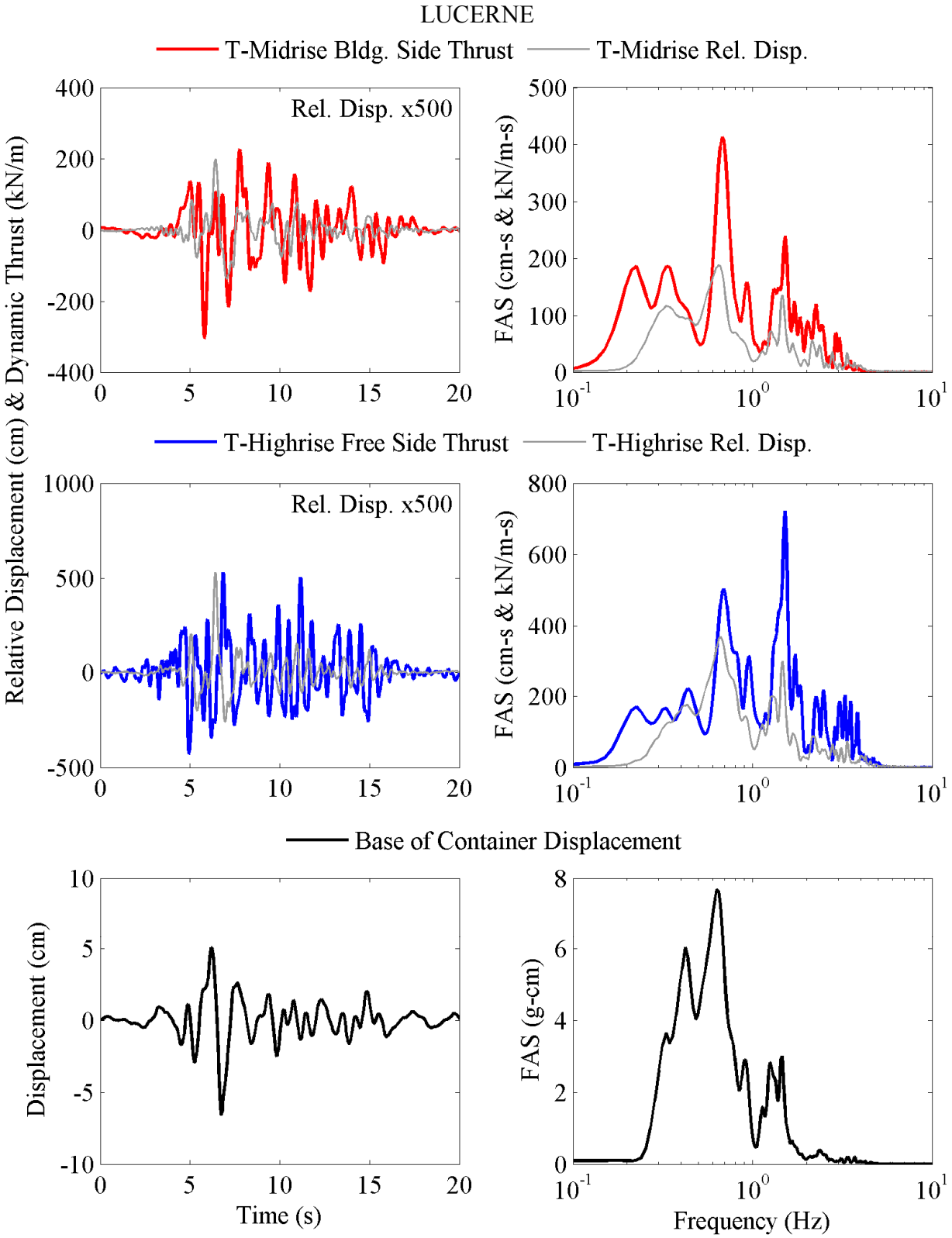

Figure 4.6.19. Dynamic tunnel thrust compared with the distance between the underground structure and the tall building's basement.

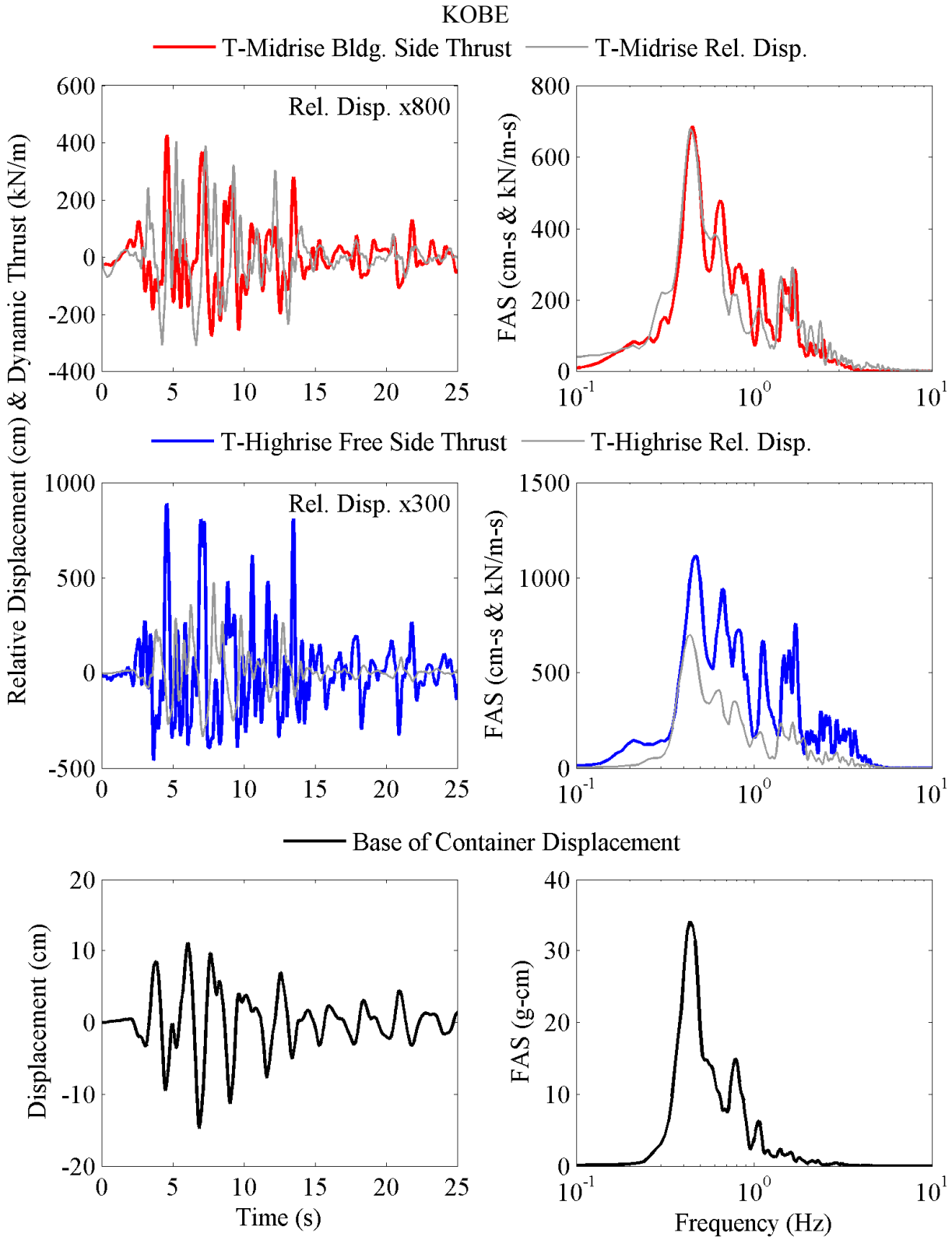

Figure 4.6.20. Dynamic tunnel thrust compared with the distance between the underground structure and the tall building's basement.

4.6.4 Dynamic Thrust and Tunnel Racking Displacements

Figure 4.6.21 through Figure 4.6.25 compare the dynamic thrust on the building side of the tunnel and the dynamic racking displacements recorded on the tunnel in time and frequency domains. Racking displacements, as discussed previously, were obtained from double integrating accelerometers on the roof and base of the tunnel and taking the difference of the two. The time history and frequency contents of racking displacements and dynamic thrust on the tunnel were remarkably similar in shape and content. However, it was observed that a greater lateral dynamic thrust doesn't necessarily translate into larger tunnel racking displacements, as mentioned previously.

Based on the manual synchronization performed between the tactile pressure sensor and accelerometer data, the values of dynamic thrust and racking were plotted against one another in Figure 4.6.26 through Figure 4.6.28, Insightful information may be gleamed from this style of plotting in terms of the timing and amplitude of maxima. The plots indicate that the maximum values of racking and dynamic thrust occurred primarily within one loop during the Northridge motion that was pulse-like. In other motions, more values near the maximum occurred during more cycles. Further, the loops became vertically longer and horizontally narrower going from T-No Bldg to T-Midrise and T-Highrse, clearly showing an increase in dynamic thrust and a slight decrease in tunnel racking with the presence of an adjacent building.

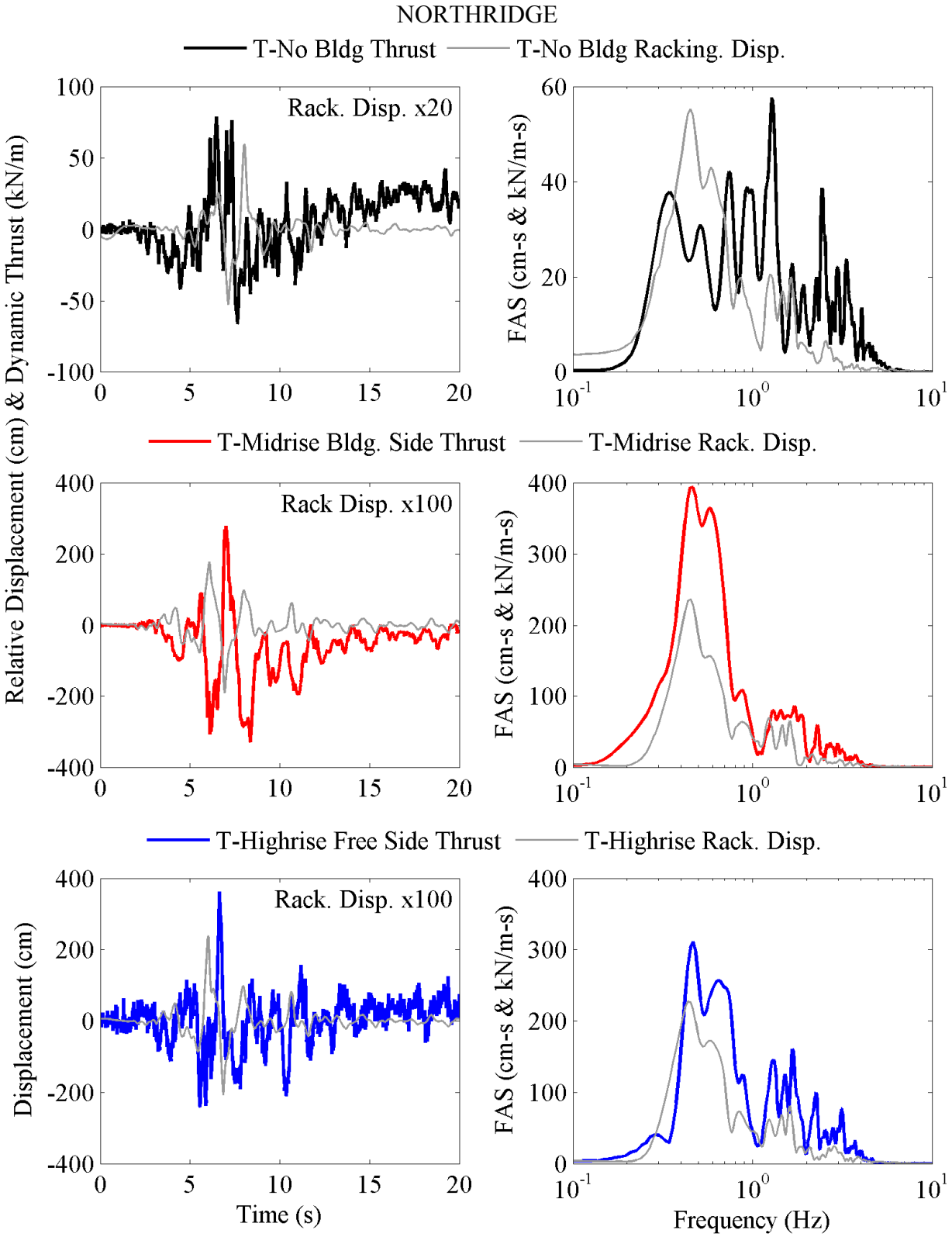

Figure 4.6.21. Dynamic lateral thrust compared with tunnel racking displacement.

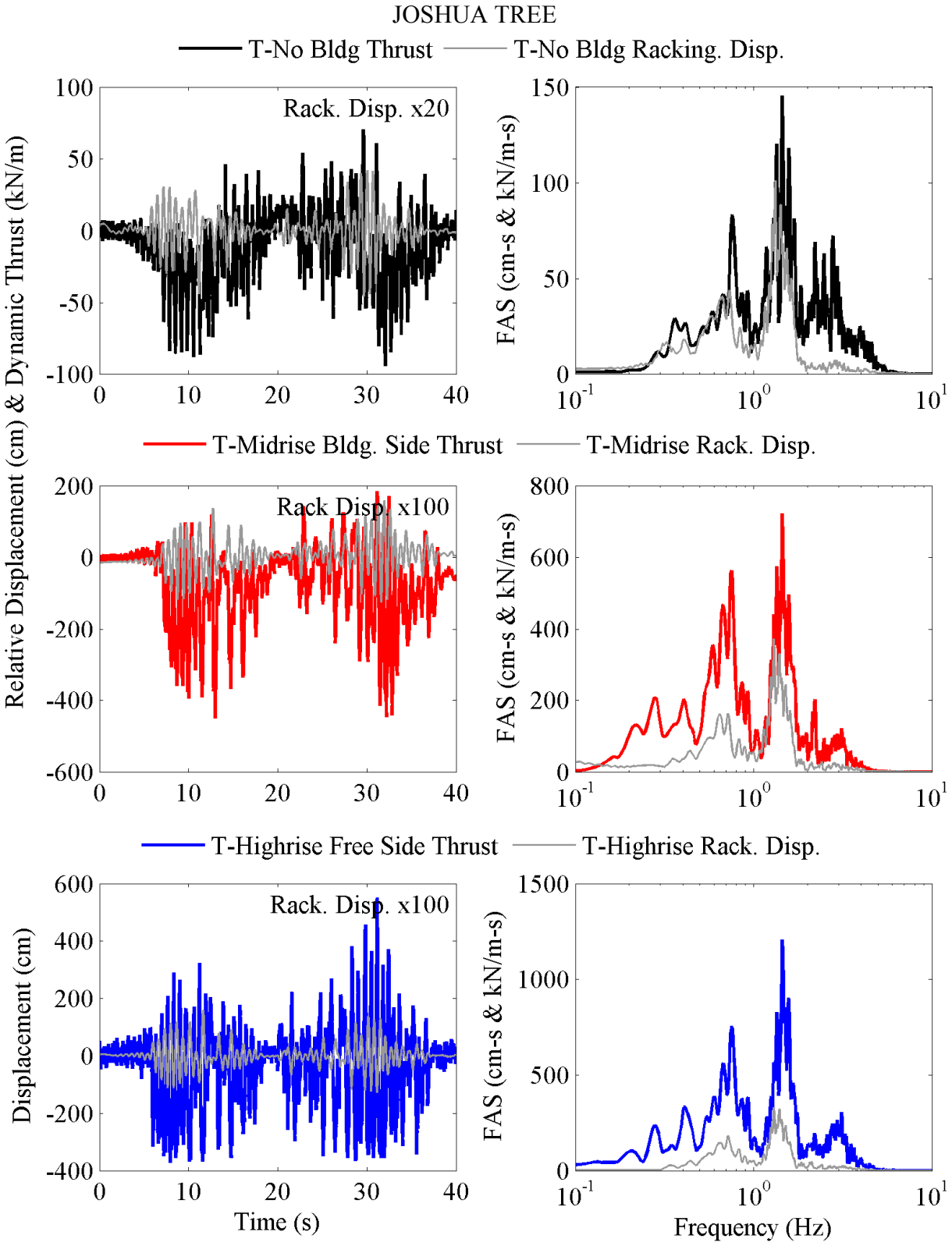

Figure 4.6.22. Dynamic lateral thrust compared with tunnel racking displacement.

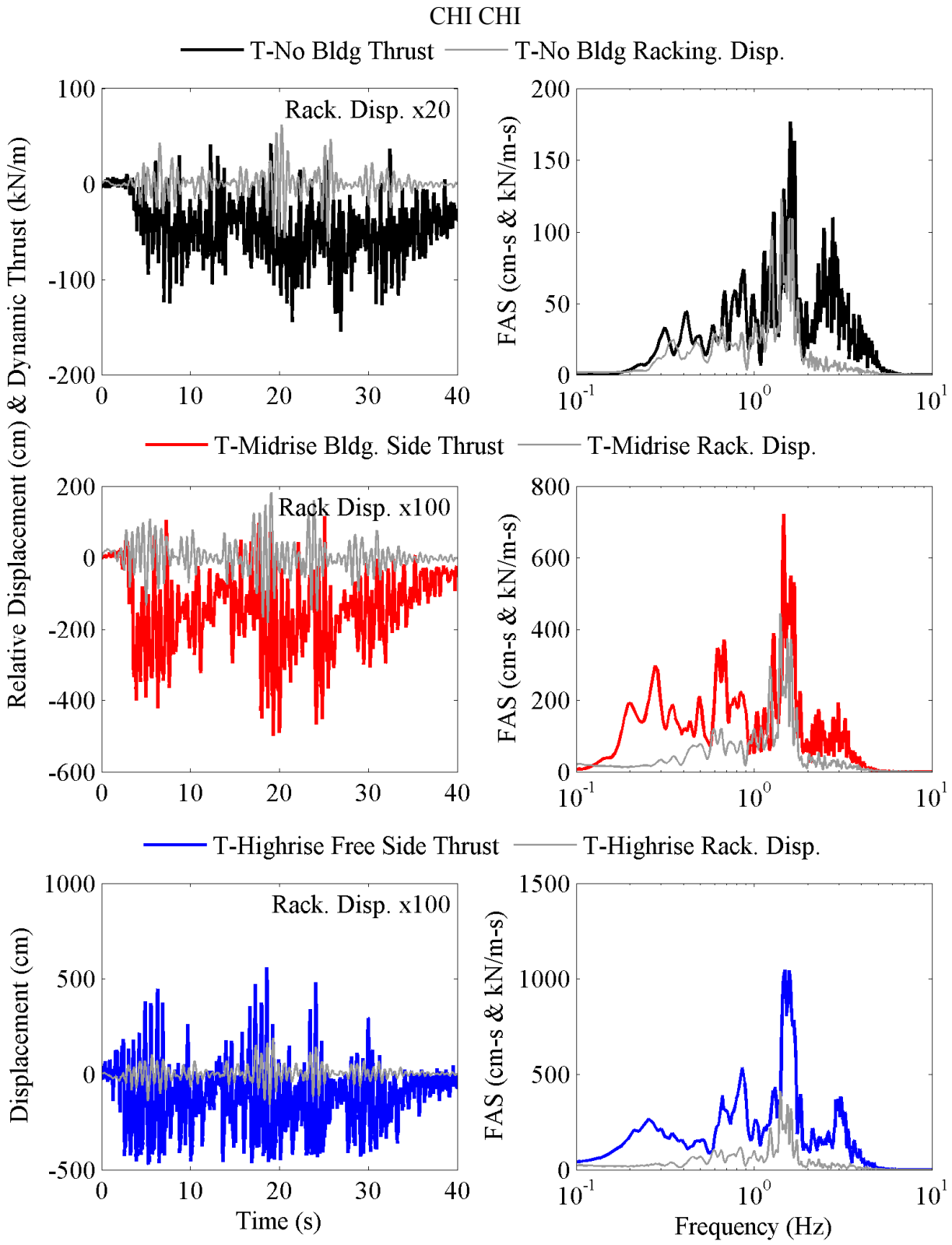

Figure 4.6.23. Dynamic lateral thrust compared with tunnel racking displacement.

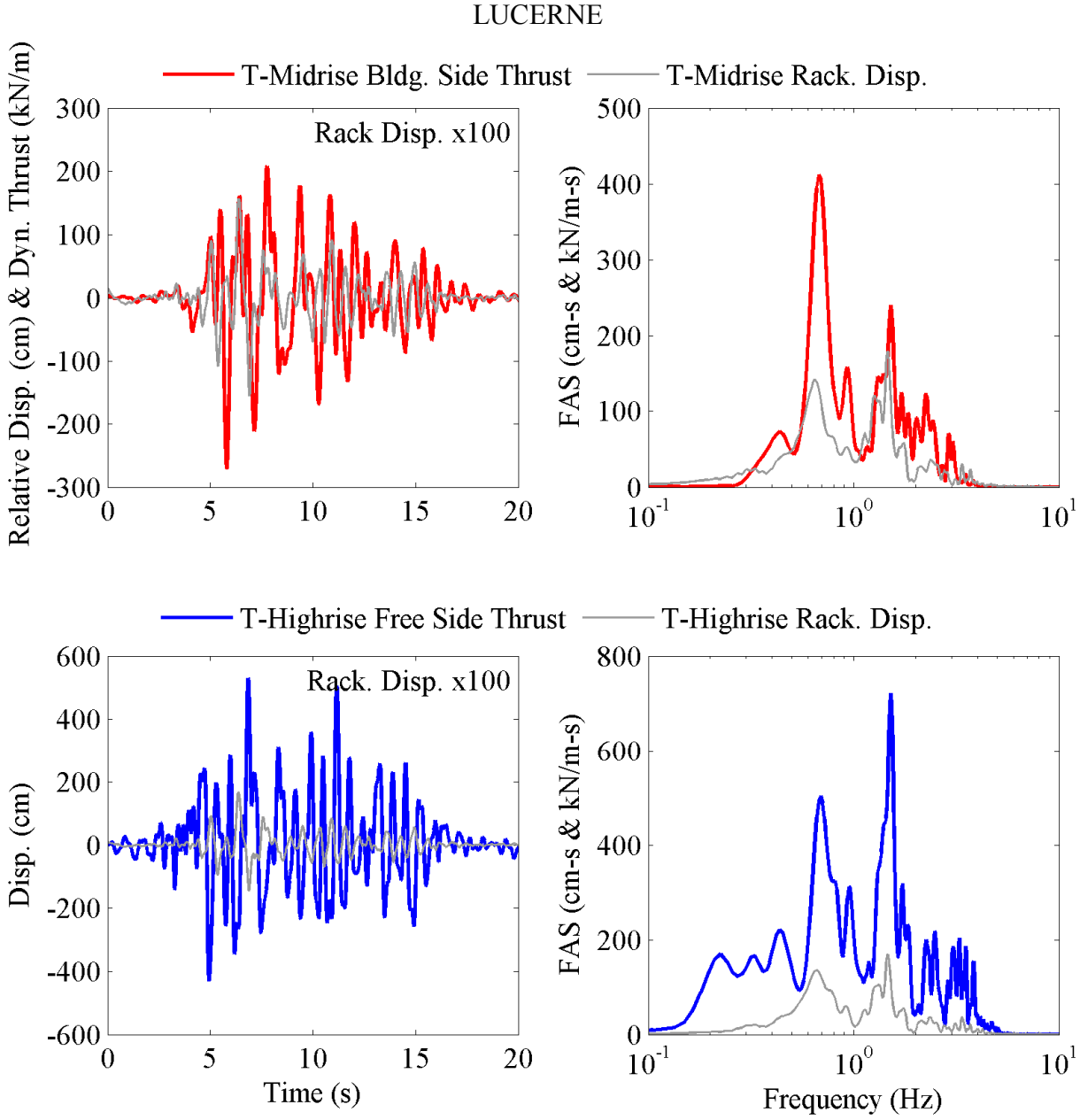

Figure 4.6.24. Dynamic lateral thrust compared with tunnel racking displacement.

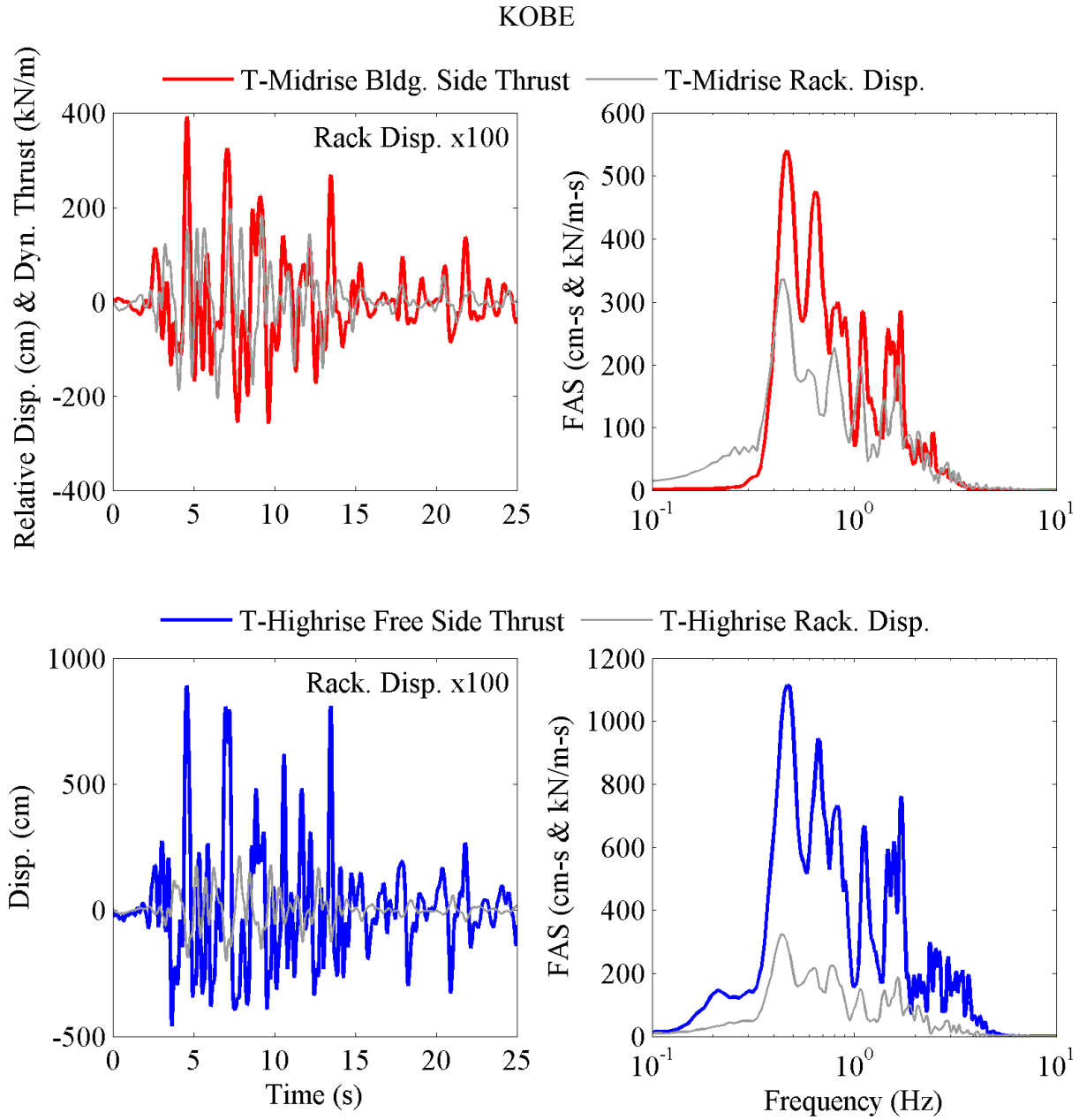

Figure 4.6.25. Dynamic lateral thrust compared with tunnel racking displacement.

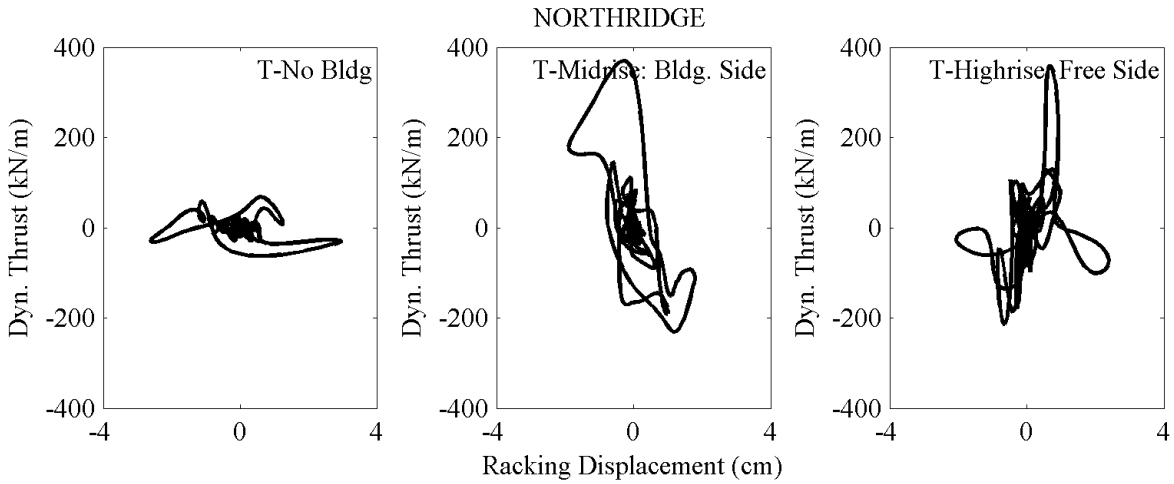

Figure 4.6.26. Dynamic thrust versus racking displacement time history loops.

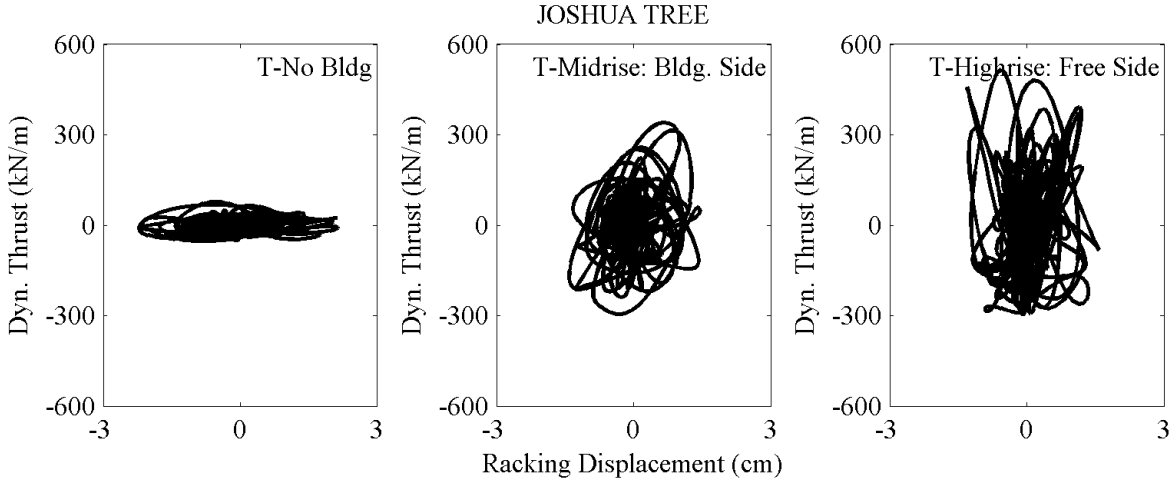

Figure 4.6.27. Dynamic thrust versus racking displacement time history loops.

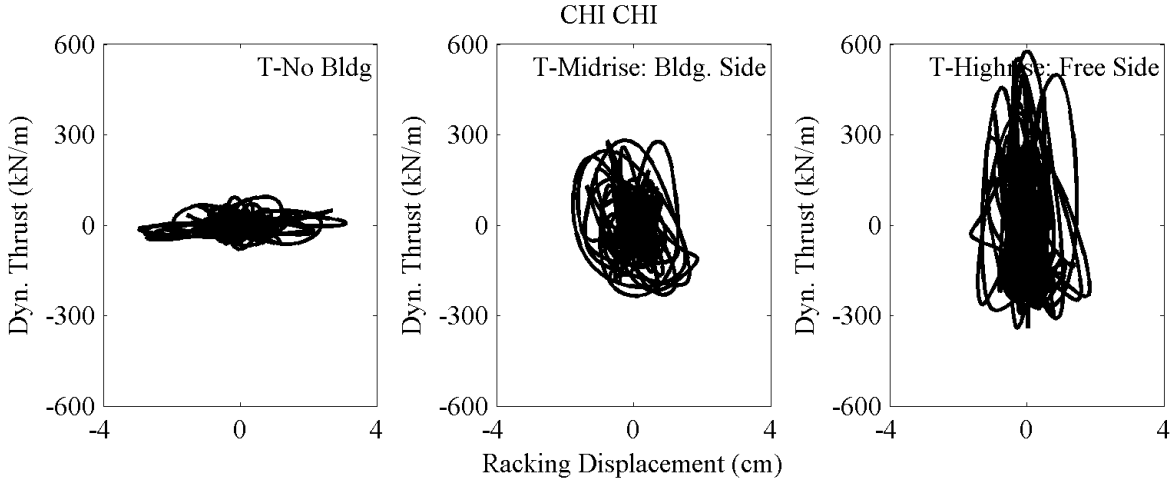

Figure 4.6.28. Dynamic thrust versus racking displacement time history loops.

4.6.5 Dynamic Thrust and Bending Moments

Similar to the loops presented in the previous section, the dynamic thrust and dynamic bending moments are plotted together in this section, and their timing and amplitudes are compared during different experiments and a few representative motions. The dynamic bending moments were measured using Strain Gauge 8 (Figure 4.6.1). The observations were consistent those of thrust versus racking. Generally, the addition of an adjacent tall building increased dynamic thrust but slightly reduced bending strains and moments on the tunnel and hence, its deflection.

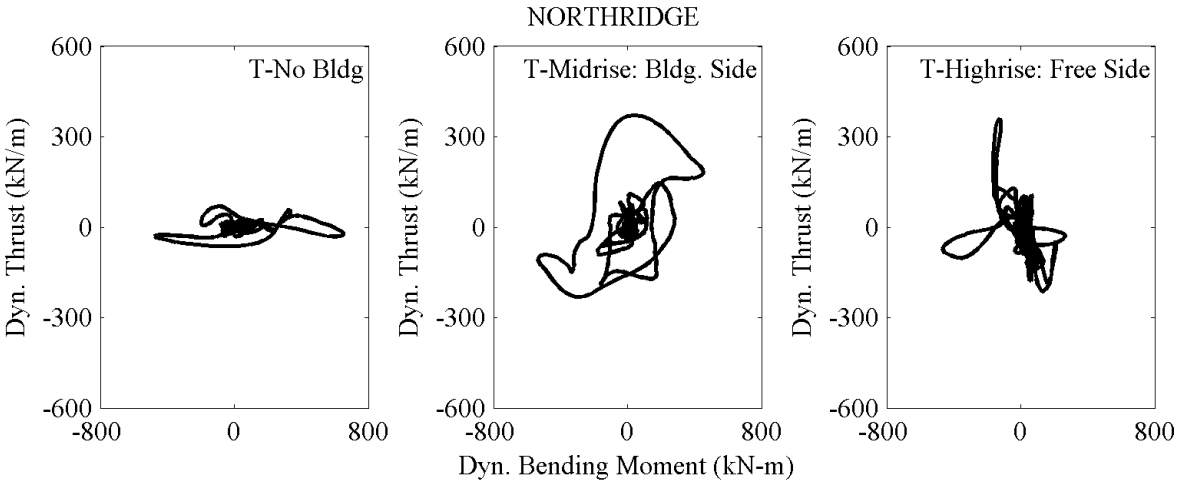

Figure 4.6.29. Dynamic thrust versus dynamic bending moment at SG8, time history loops.

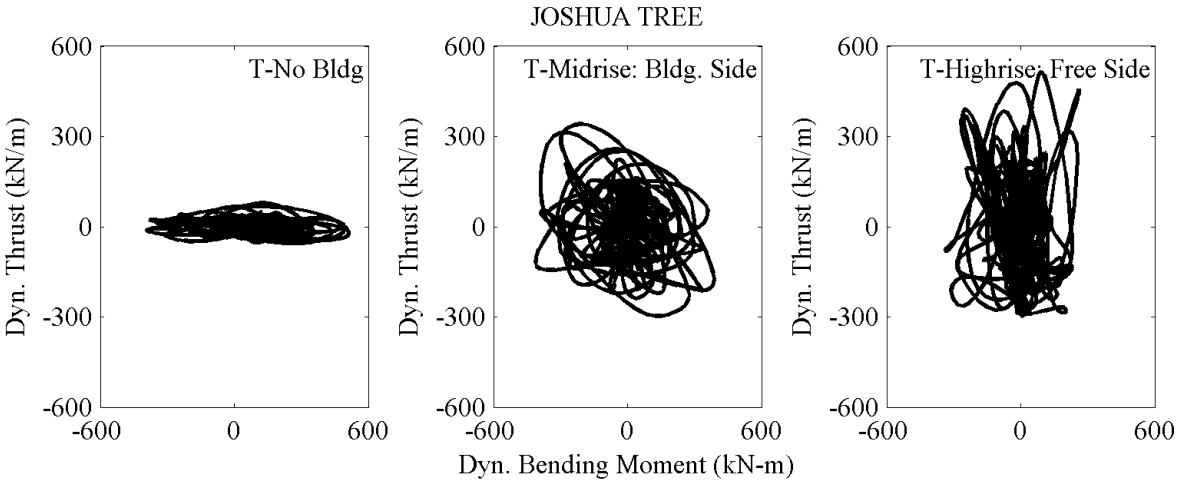

Figure 4.6.30. Dynamic thrust versus dynamic bending moment at SG8, time history loops.

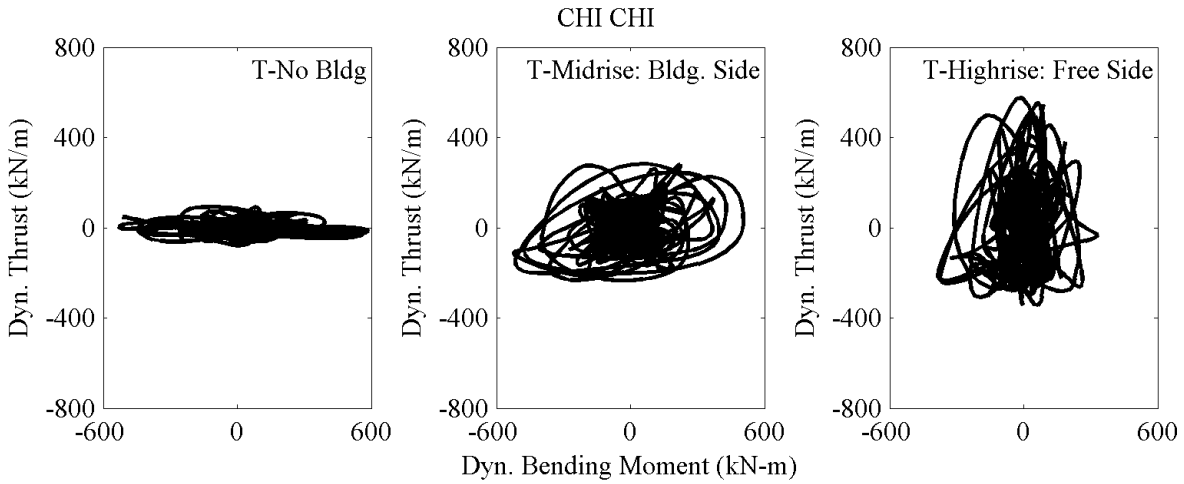

Figure 4.6.31. Dynamic thrust versus dynamic bending moment SG8, time history loops.

4.6.6 Tunnel Racking Displacement vs Ground Motion Intensity Parameters

The racking displacement of the box structure was plotted against different measures of ground motion intensity and frequency content. The best correlation was found between tunnel racking displacement and peak ground acceleration (PGA) of the base motion.

Table 4.6.1.T-No Bldg achieved base motion intensity parameters.

Ground Motion	PGA (g)	PGV (cm/s)	PGD (cm)
Northridge	0.41	47.9	13.2
Loma	0.09	3.3	0.4
Joshua Tree	0.25	19.5	4.4
Chi Chi	0.34	30.1	4.8
Lucerne	0.38	22.2	5.3
Kobe	0.45	52.8	11.9

Table 4.6.2. Maximum absolute value of racking displacement measured on the permanent box structure.

	Max. Absolute Racking Disp. (cm)		
Ground Motion	T-No Bldg	T-Midrise	T-Highrise
Northridge	2.98	1.91	2.41
Loma	0.59	0.49	0.44
Joshua Tree	2.25	1.46	1.59
Chi Chi	3.11	1.88	1.84
Lucerne	2.17	1.57	1.66
Kobe	3.00	2.07	2.17

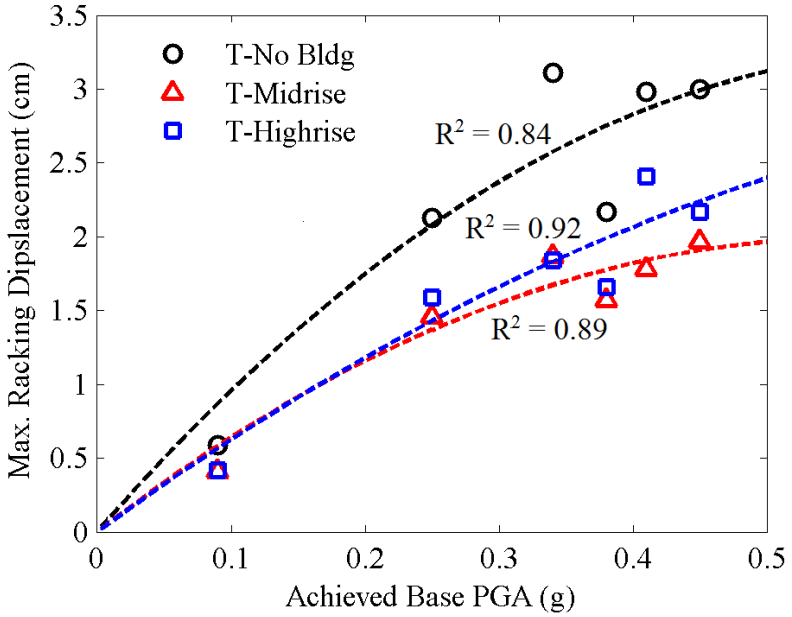

Figure 4.6.32. Maximum absolute racking displacement on the permanent box structure versus the PGA of base motion.

Chapter 5

5 RESULTS – TEMPORARY BRACED EXCAVATION

5.1 Overview

This chapter presents the results from three centrifuge tests involving the temporary braced excavation, E-No Bldg, E-Midrise, and E-Highrise. Results from these tests are presented and compared in terms of accelerations, displacements, strain, and pressure in the far-field and near-field.

5.2 Accelerations

5.2.1 Selection of a Representative Base Accelerometer

Similar to the underground box structure experiments, the braced excavation contained a number of accelerometers positioned at the base of the centrifuge container. Figure 5.2-1 shows the accelerometer layout in E-Midrise. Three accelerometers were located at the base of the container highlighted by the red boxes. Of these accelerometers, one was selected as the representative base accelerometer for the following sections and in parallel numerical simulations. This selection was done by comparing the recordings of all base accelerometers with each other in a given experiment and across experiments.

To use E-Midrise as an example for the comparisons made for each experiment, accelerometers labeled as A01, A13, and A56 in Figure 5.2-1 were positioned at the base of the container. Two additional accelerometers were located on the east and west side of the shake table at the north end of the container. These accelerometers are labeled as STE and STW in Figure 5.2-1. Base acceleration time histories were first compared during the first ground motion, Northridge, in Figure 5.2-2. Similar to the tunnel experiments, the shake table east and west (STE and STW) accelerometers showed a small high-frequency content that appeared to be noise, most likely due to their rigid bolted or glued connection to the shake table.

In addition to acceleration time histories, the base accelerometer recordings were compared in terms of 5%-damped spectral accelerations, Fourier Amplitude Spectra, and Arias Intensity time histories for each of the tunnel tests, as shown by Figure 4.2.3. Results showed that the accelerometer located at the base of the container underneath the far-field array showed the most consistent results and compared well across experiments. Hence, this accelerometer was chosen as the reference base accelerometer in the following sections.

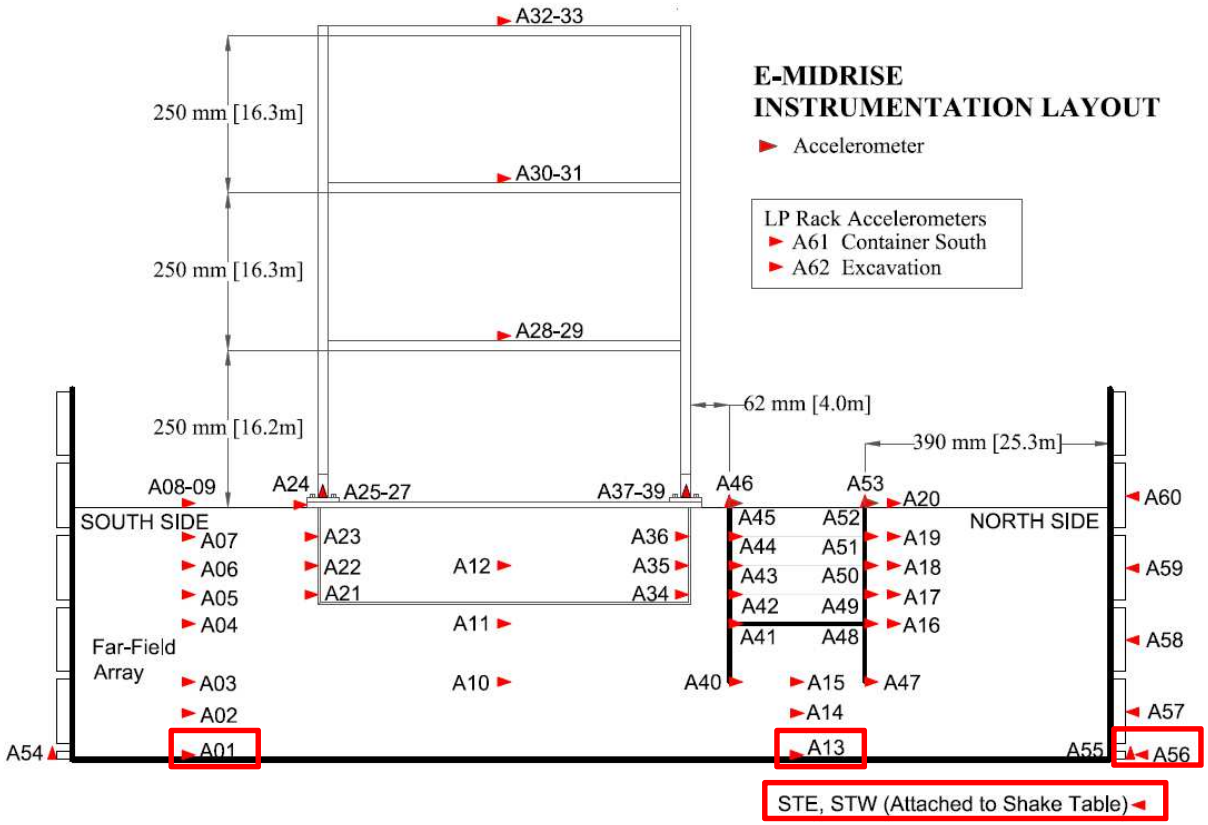

Figure 5.2-1. E-Midrise accelerometer instrumentation layout.

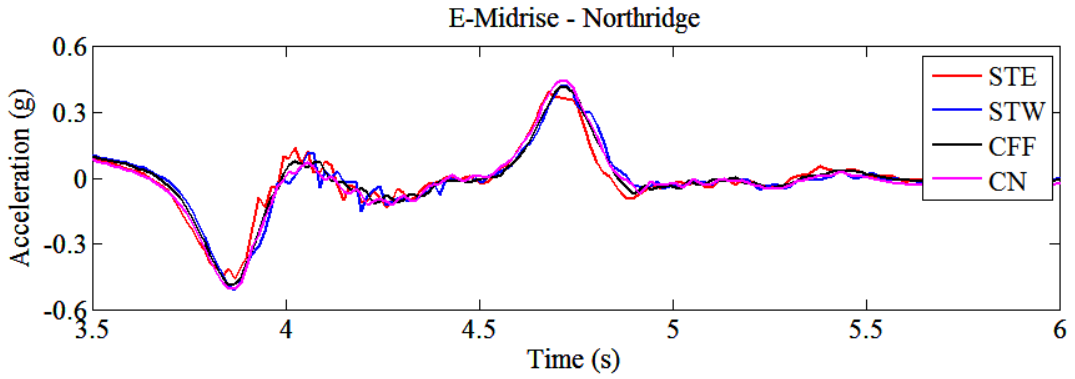

Figure 5.2-2. Comparison of base acceleration time histories of E-Midrise, Northridge motion.

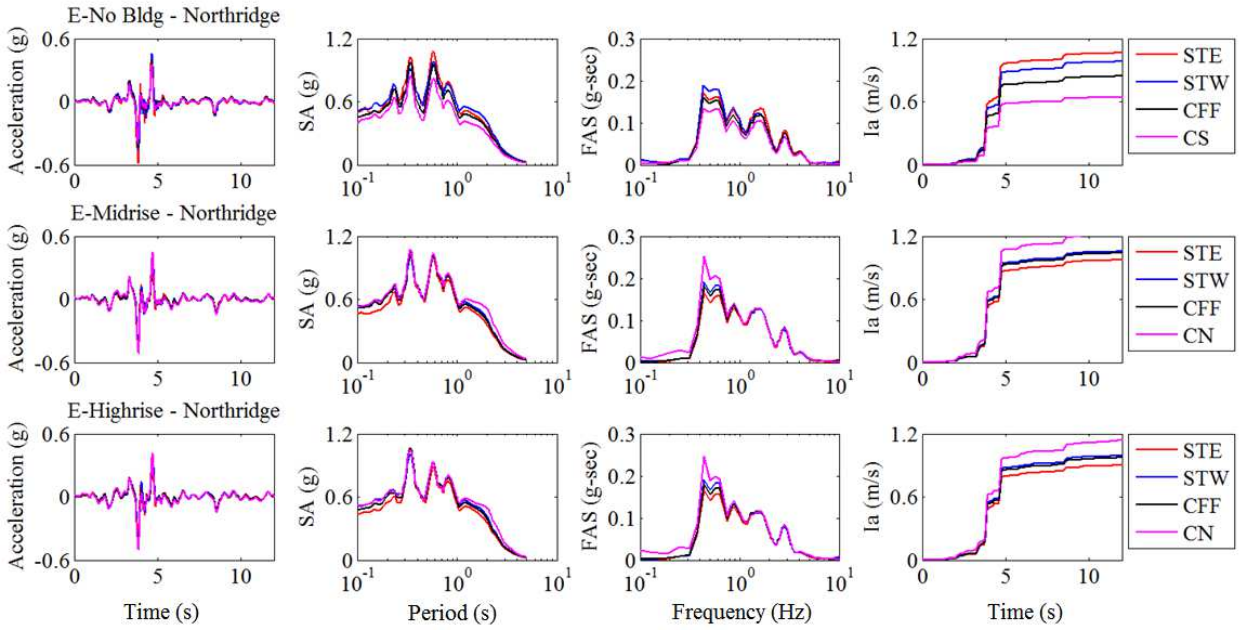

Figure 5.2-3. Base accelerometer comparison during the Northridge ground motion.

5.2.2 Base Acceleration Comparison

The achieved base accelerations from each experiment involving the excavation were compared using three intensity measures: PGA, PGV, and PGD as shown in Figure 5.2-4. Each experiment had a different weight due to the different structures used (see Table 5.2.1). Despite these differences in weight, the achieved base accelerations compared well.

Table 5.2.1. Weight of each excavation experiment.

Experiment	Model Weight (lbs)	Model Weight (N)
E-No Bldg	3576	15907
E-Highrise	3704	16476
E-Highrise	4180	18594

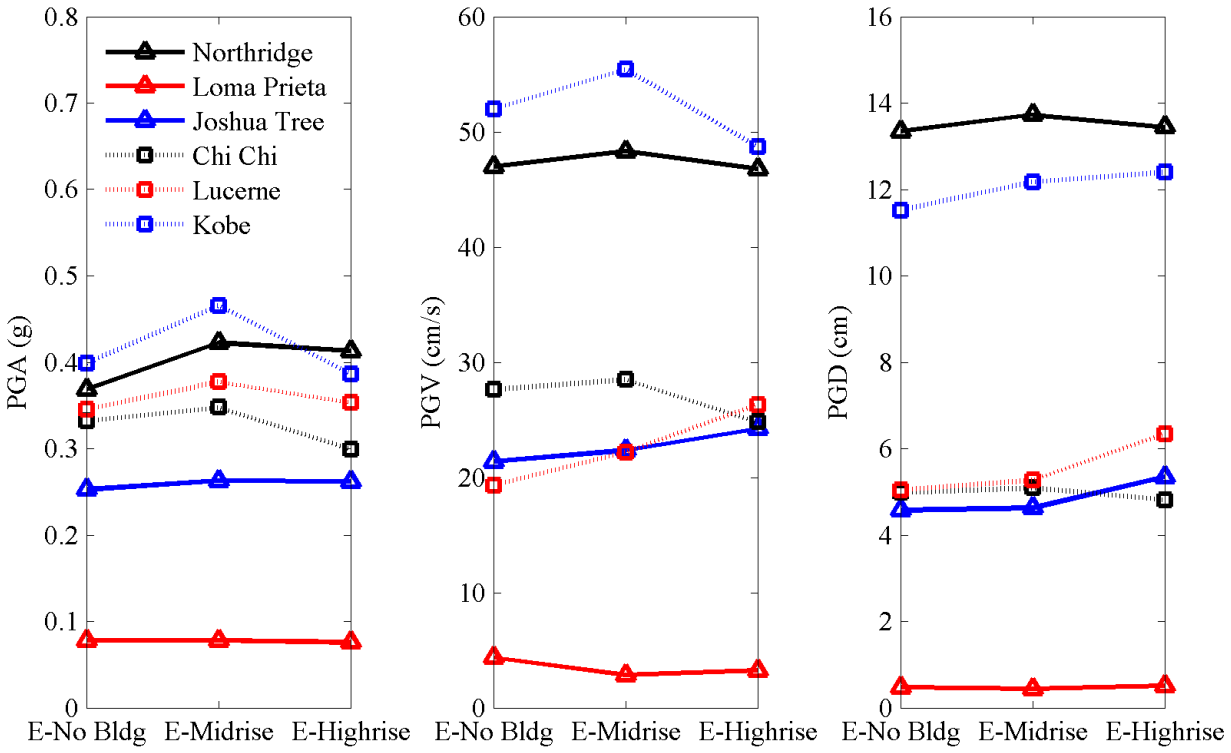

Figure 5.2-4. Comparing excavation experiments base accelerations in terms of PGA, PGV, and PGD.

5.2.3 Far-Field Accelerations

Similar to the experiments involving the underground box structure, the excavation experiments (E-No Bldg, E-Midrise, and E-Highrise) also employed a vertical array of accelerometers halfway between container boundaries and structures as shown in Figure 5.2-5, which were used to approximate soil response in the free-field. These accelerometer arrays will be referred to as "far-field" because an ideal free-field measurement could not be achieved in the centrifuge container.

The spacing between the far-field array and the nearest container or structure boundaries was similar to the tunnel experiments. E-No Bldg had the greatest far-field spacing because only the excavation was present. Therefore, the far-field accelerometer array from E-No Bldg was selected to approximate free-field conditions in all excavation tests when evaluating the response

of the temporary braced excavation with respect to soil. The acceleration recordings from these far-field arrays were compared among the three tests and compared with 1-D site response analyses during each motion (as detailed by Romero Arduz et al. under review).

The next set of figures (Figure 5.2-8 through Figure 5.2-13) compare the acceleration response of the far-field arrays in E-No Bldg, E-Midrise, and E-Highrise during different motions. Although, the E-No Bldg array was the most representative of free-field conditions, the far-field accelerations are presented in all three tests here for comparison. These figures compare the time histories and Fourier amplitude spectra of far-field acceleration in the three tunnel tests at different elevations. The figures also show the transfer function (TF) of far-field accelerations in E-Midrise or E-Highrise to E-No Bldg, to evaluate the impact of each building on far-field recordings at different frequencies. A TF value equal to 1 indicates no change, while a positive TF indicates amplification and a negative TF de-amplification of far-field acceleration at a given elevation due to the addition of a midrise or highrise building.

Some trends that can be identified from Figure 5.2-8 through Figure 5.2-13:

- Acceleration amplification was observed from the base toward the soil surface in the far-field in all experiments.
- Overall, the far-field response of E-Midrise and E-Highrise was amplified compared to E-No Bldg, particularly at higher elevations and higher frequencies. More amplification was observed in E-Highrise compared to E-Midrise. Hence, the weight and proximity of the superstructure influenced the response of far-field soil in these experiments.

Table 5.2.2.Far-field accelerometers used to represent free-field conditions in each test.

Test ID	Far-Field Accelerometers
E-No Bldg	A22 – A29
E-Midrise	A01 - A09
E-Highrise	A01 - A09

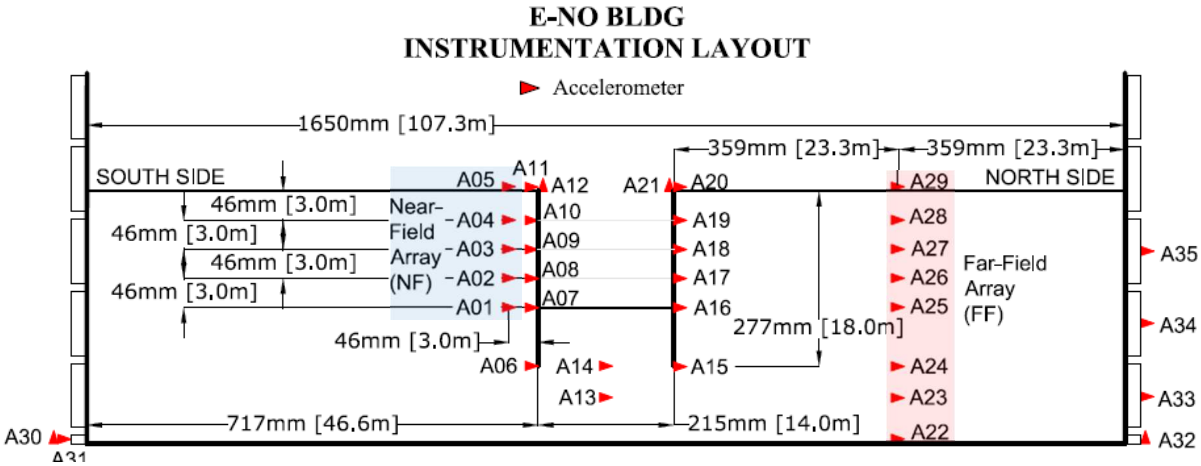

Figure 5.2-5. Elevation view of accelerometer layout for E-No Bldg.

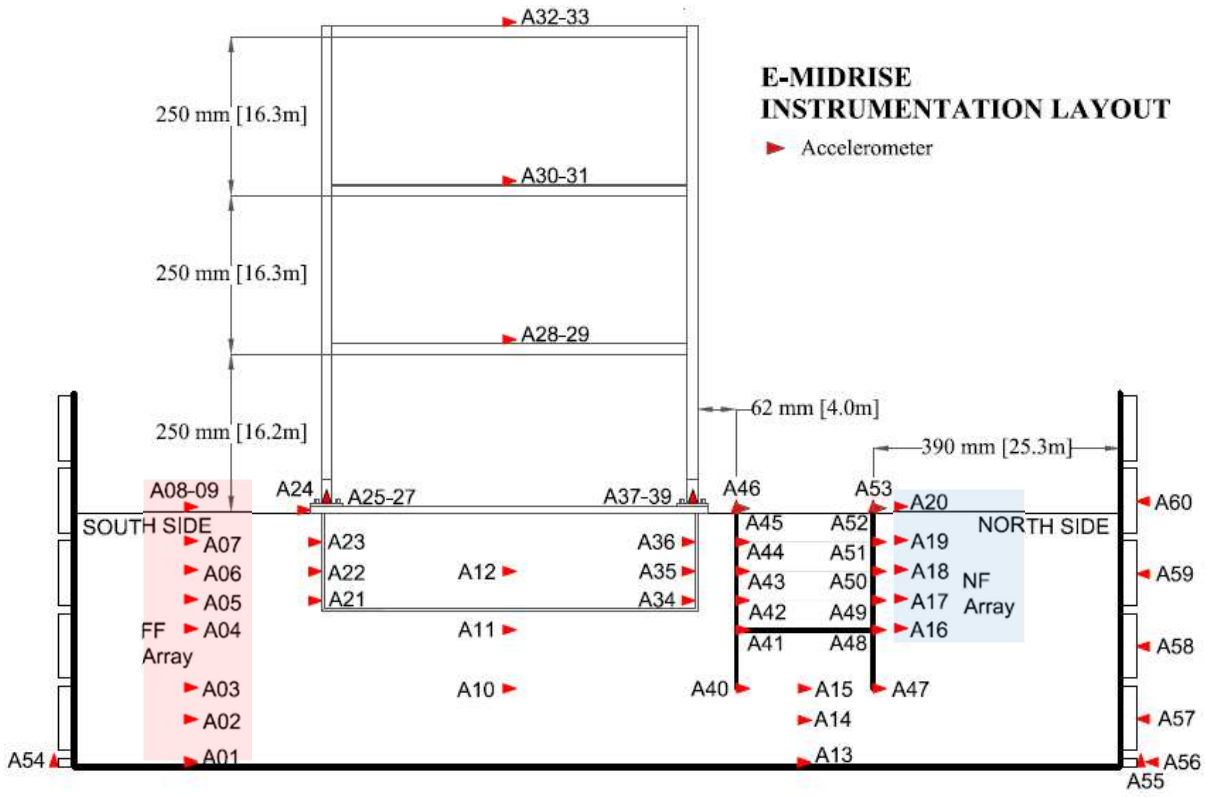

Figure 5.2-6. Elevation view of accelerometer layout of E-Midrise.

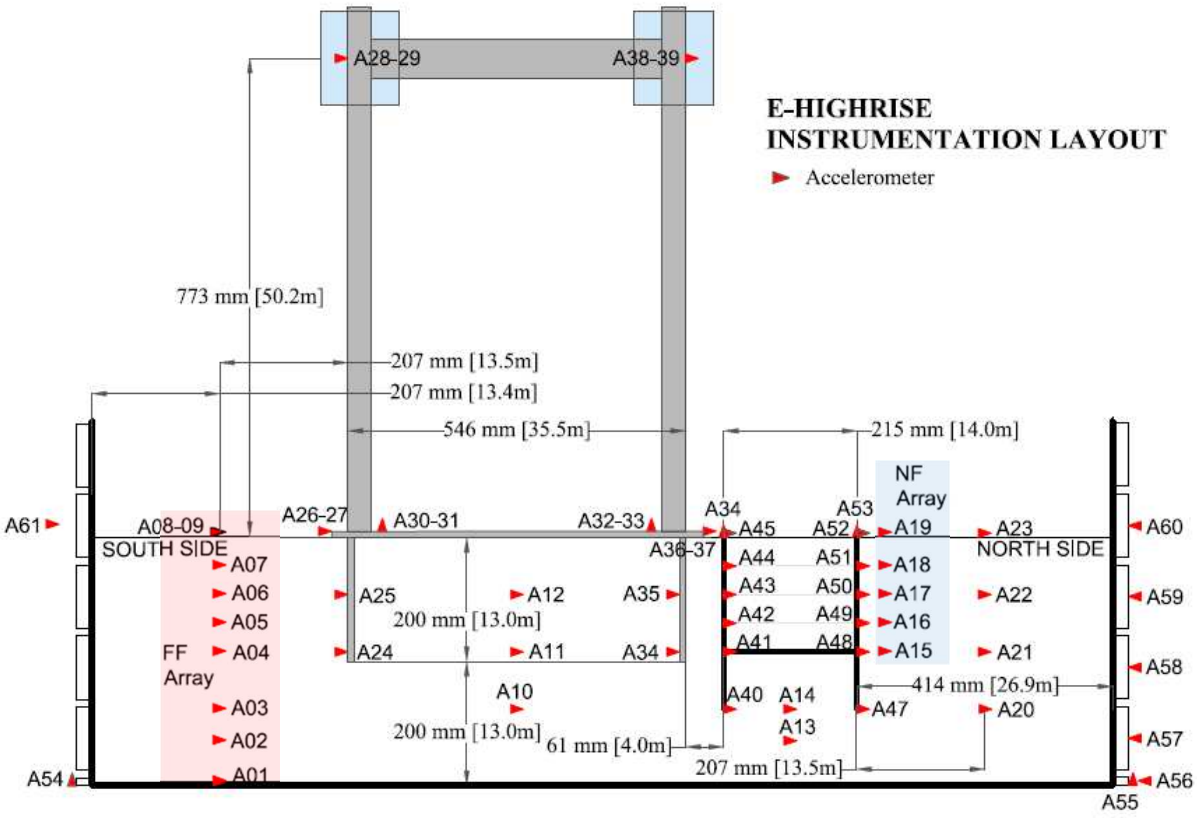

Figure 5.2-7. Elevation view of accelerometer layout of E-Highrise.

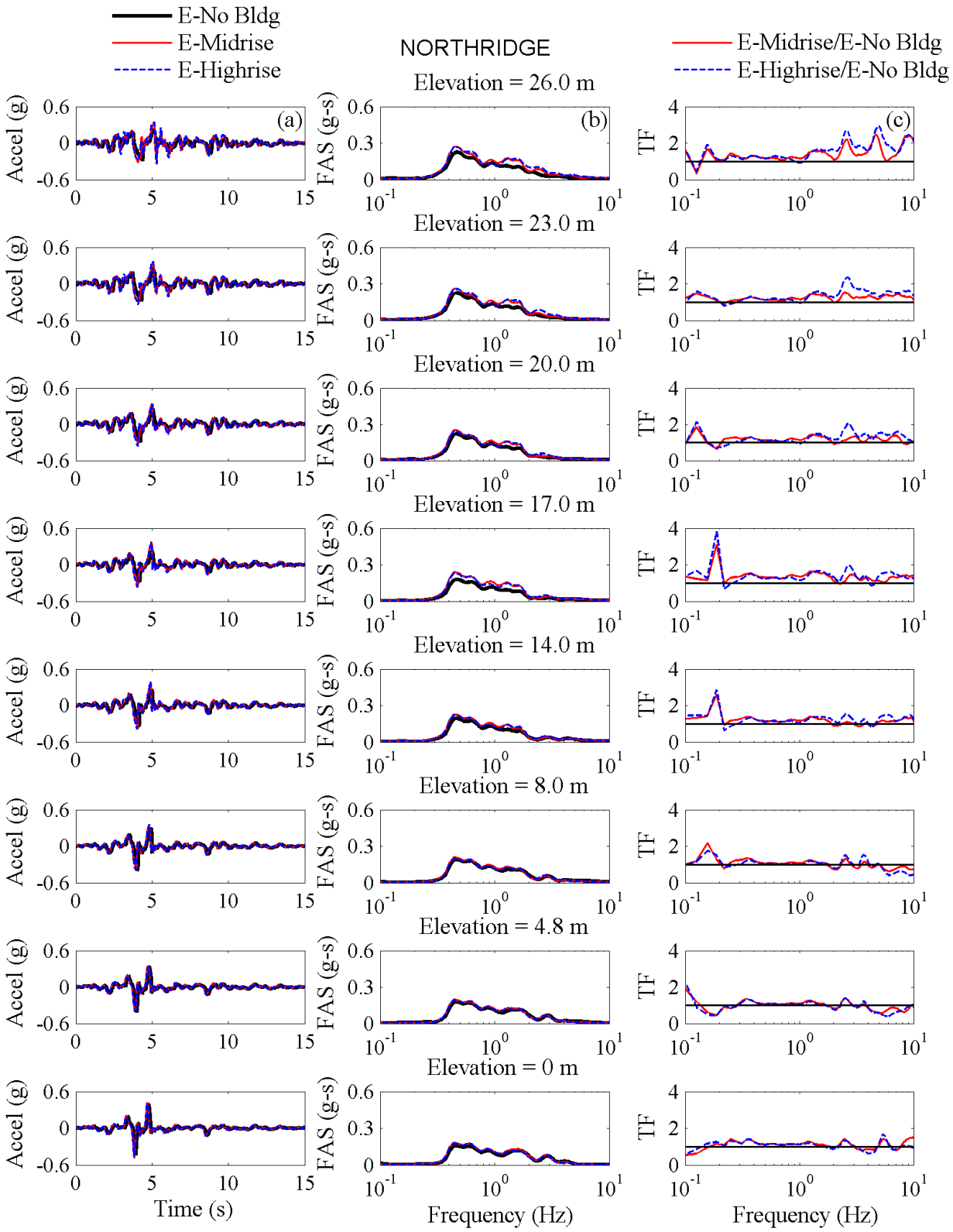

Figure 5.2-8. Northridge free-field acceleration response shown as (a) acceleration time histories; (b) Fourier amplitude spectra; and (c) transfer functions.

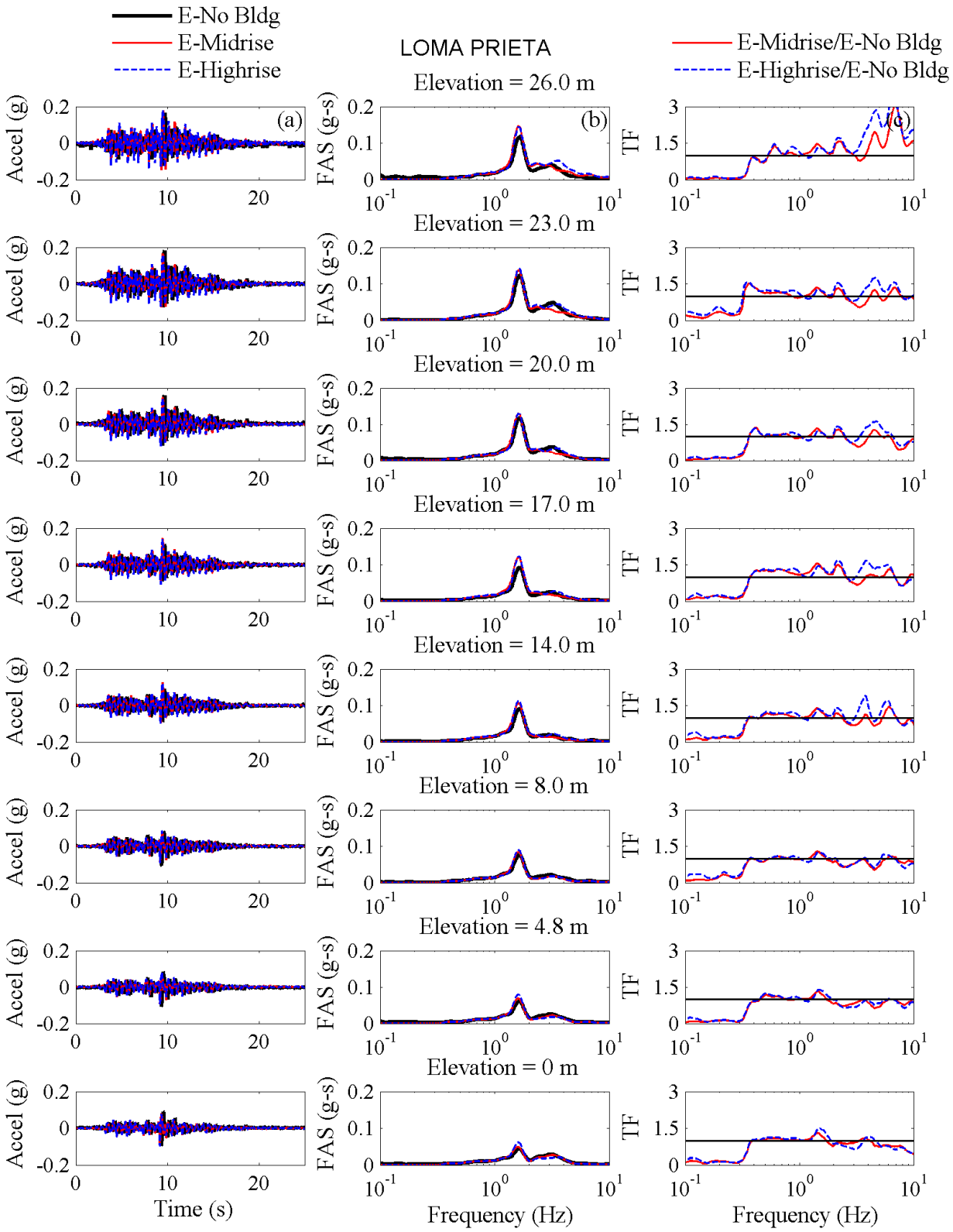

Figure 5.2-9. Loma Prieta free-field acceleration response shown as (a) acceleration time histories; (b) Fourier amplitude spectra; and (c) transfer functions.

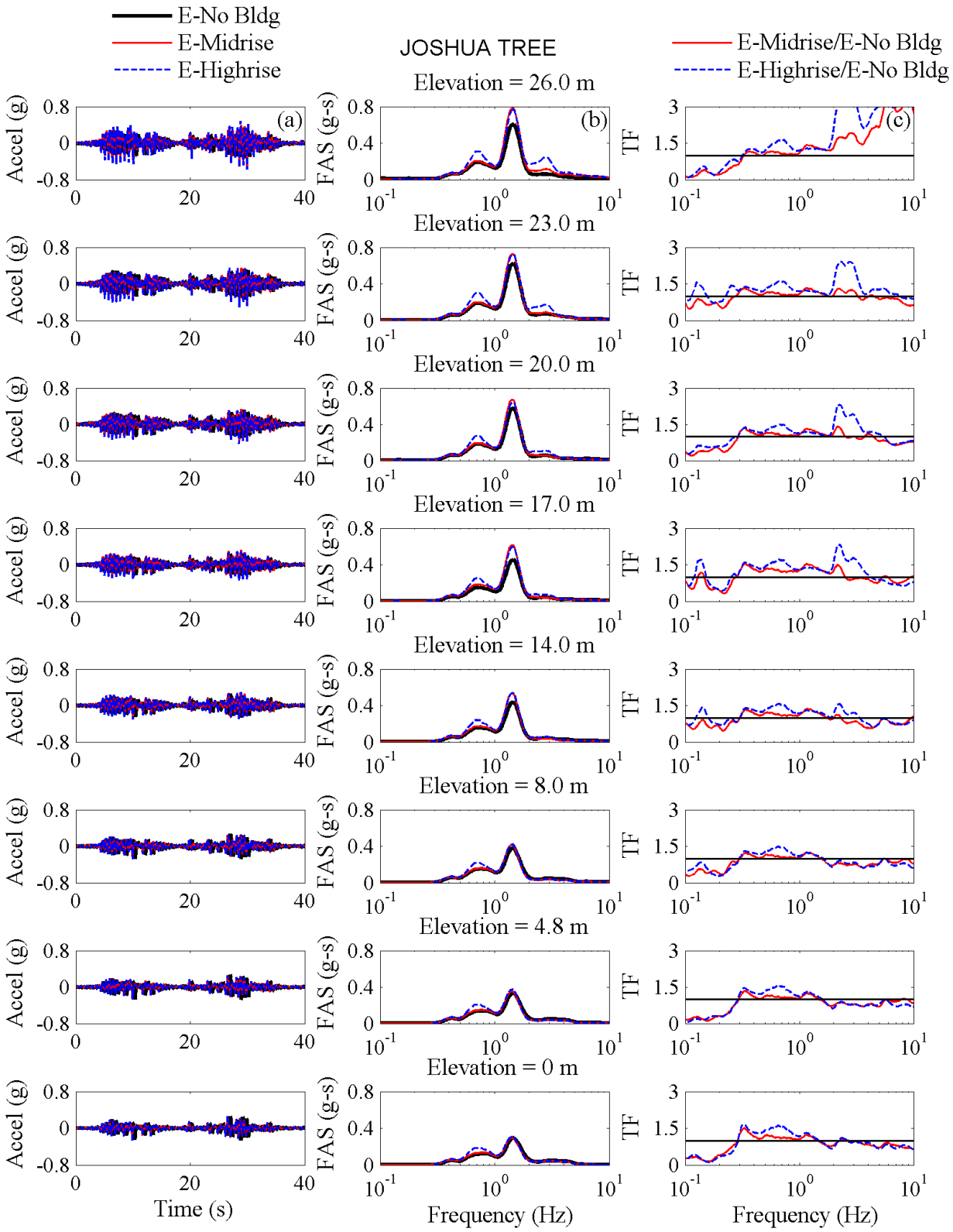

Figure 5.2-10. Joshua Tree free-field acceleration response shown as (a) acceleration time histories; (b) Fourier amplitude spectra; and (c) transfer functions.

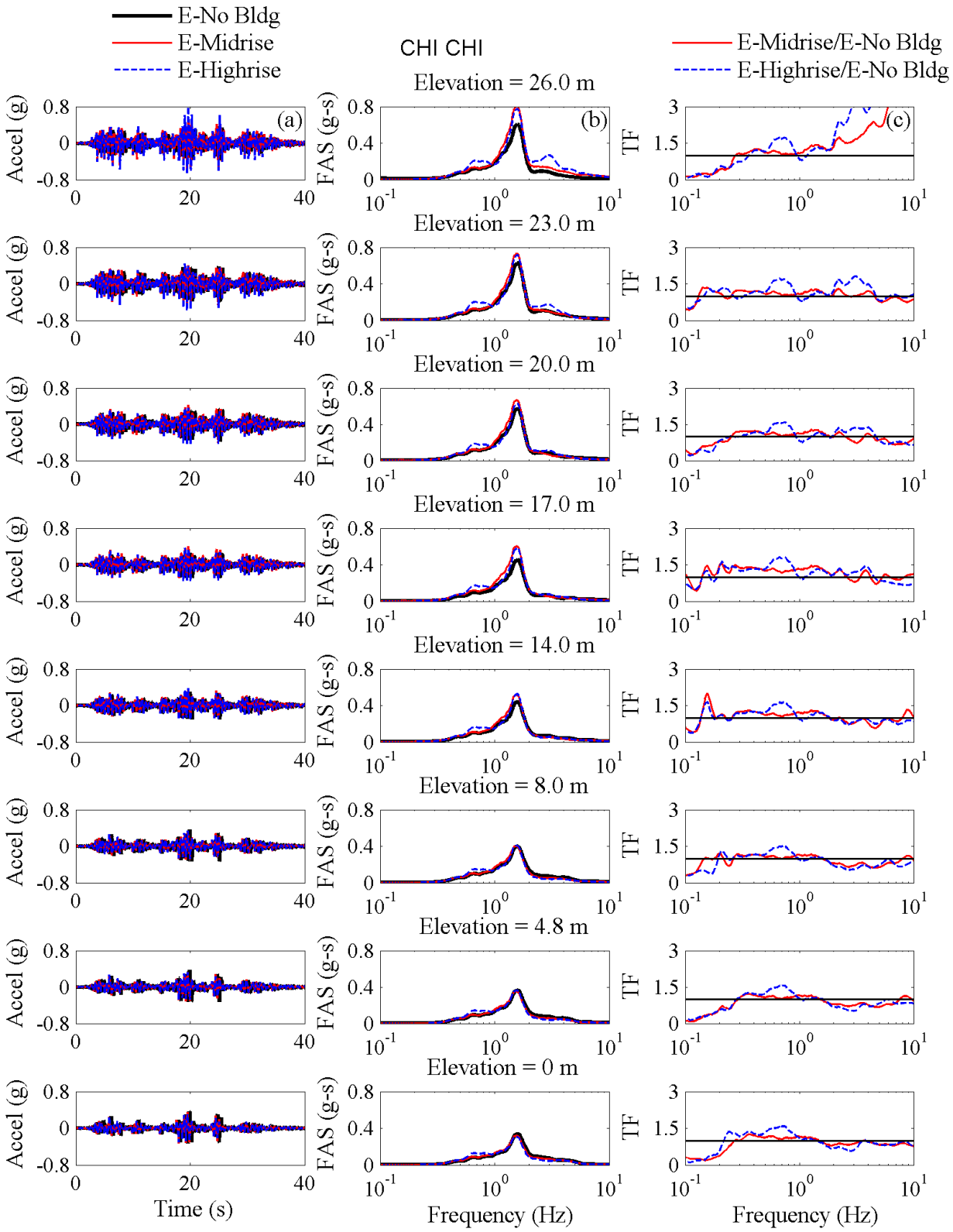

Figure 5.2-11. Chi Chi free-field acceleration response shown as (a) acceleration time histories; (b) Fourier amplitude spectra; and (c) transfer functions.

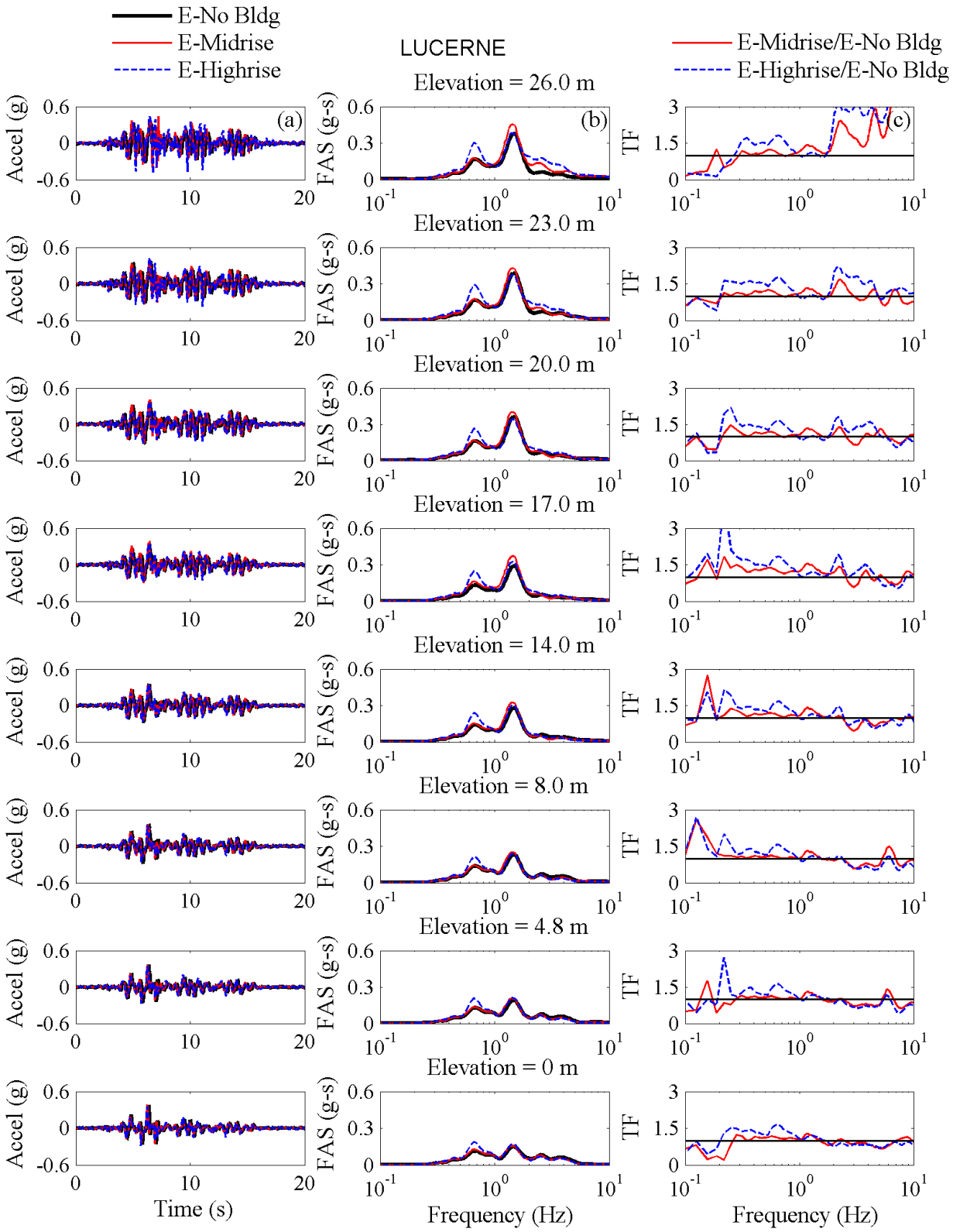

Figure 5.2-12. Lucerne free-field acceleration response shown as (a) acceleration time histories; (b) Fourier amplitude spectra; and (c) transfer functions.

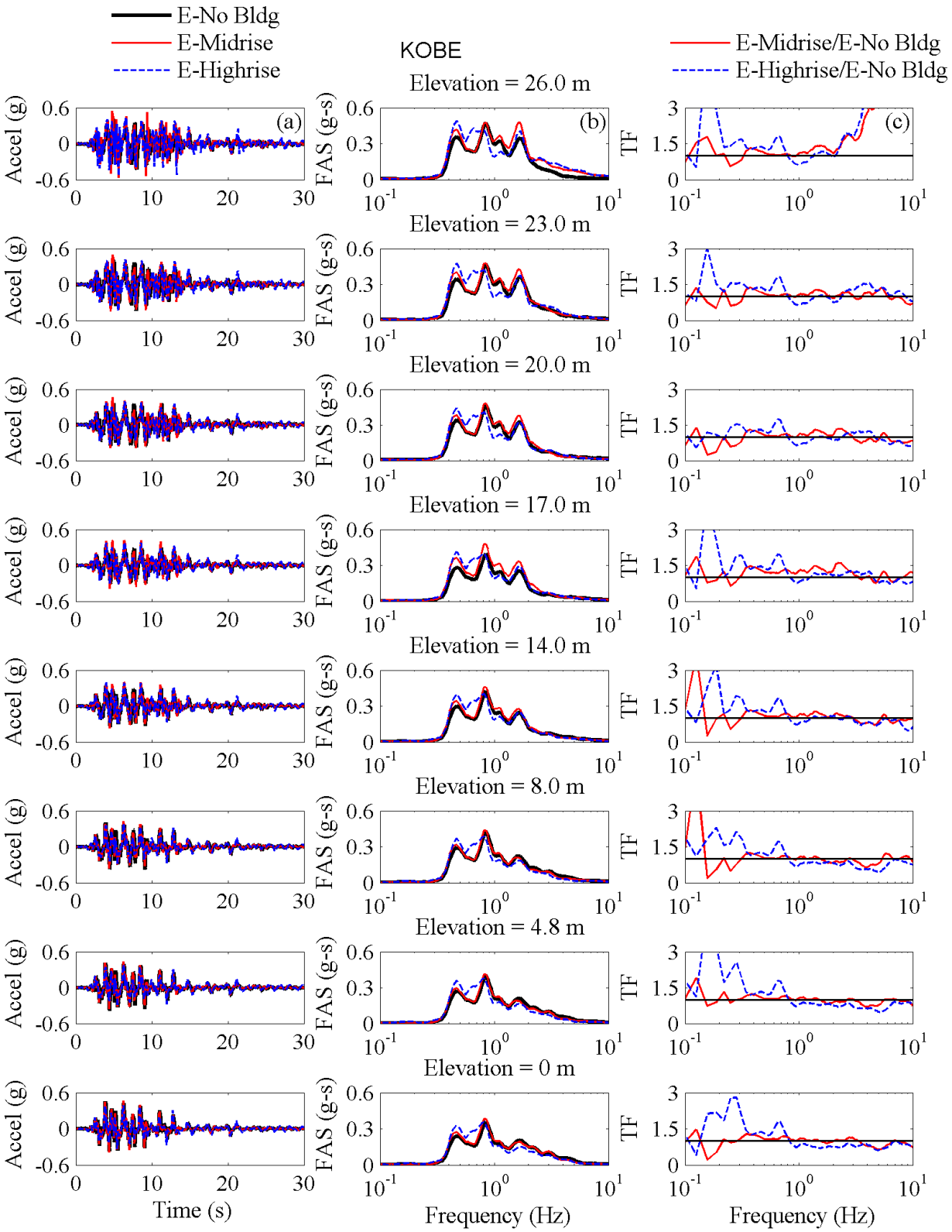

Figure 5.2-13. Kobe free-field acceleration response shown as (a) acceleration time histories; (b) Fourier amplitude spectra; and (c) transfer functions.

5.2.4 Near-Field Accelerations

In addition to the far-field array, each experiment involving the braced excavation contained an array of five accelerometers located in the sand 3 m (prototype scale) horizontally away from the excavation, and placed on the opposite side from the tall building if present. The near-field (NF) accelerometers measured the soil's response very close to the braced excavation to evaluate any influence from the underground structure and the adjacent building. Table 5.2.3 shows the accelerometers used in the NF of each experiment. These accelerometers are also shown in Section 5.2.3.

The next set of figures (Figure 5.2-14 through Figure 5.2-19) compare the acceleration response of the near-field arrays of E-No Bldg, E-Midrise, and E-Highrise during different motions. These figures compare the time histories and Fourier amplitude spectra of near-field accelerations in the three excavation experiments at different elevations. The figures also show the transfer function (TF) of near-field accelerations in E-Midrise or E-Highrise to E-No Bldg.

The key observations were as follows:

- E-Midrise and E-Highrise NF accelerations were often amplified compared to E-No Bldg at higher frequencies (greater than about 2 Hz) and de-amplified at lower frequencies (less than about 0.2 Hz). Deformations are more controlled by lower frequency motions. Hence, the presence of the buildings likely de-amplified NF displacements (as will be discussed in more detail in the next section).
- The influence of the highrise building on NF accelerations was greater than the midrise building (more amplification or more de-amplification was observed in E-Highrise compared to E-Midrise).

- The results indicate that the presence of a heavy building adjacent to the excavation influences NF accelerations even on the opposite side where no building was present.

Table 5.2.3. Accelerometers used in each experiment in the near-field.

Test ID	Near-Field Accelerometers ID
E-No Bldg	A1 - A5
E-Midrise	A16 -A20
E-Highrise	A15 - A19

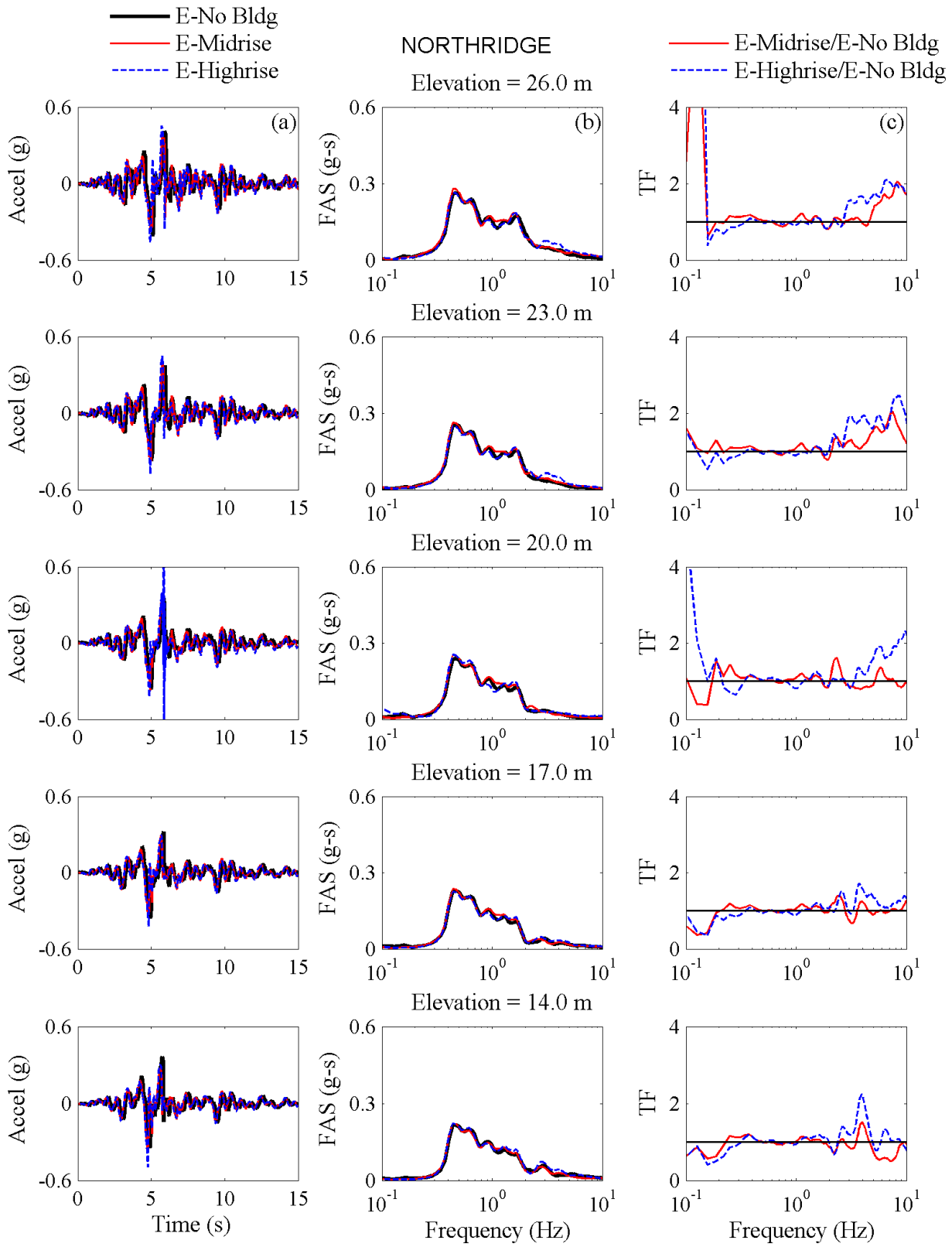

Figure 5.2-14. Northridge near-field acceleration response shown as (a) acceleration time histories; (b) Fourier amplitude spectra; and (c) transfer function.

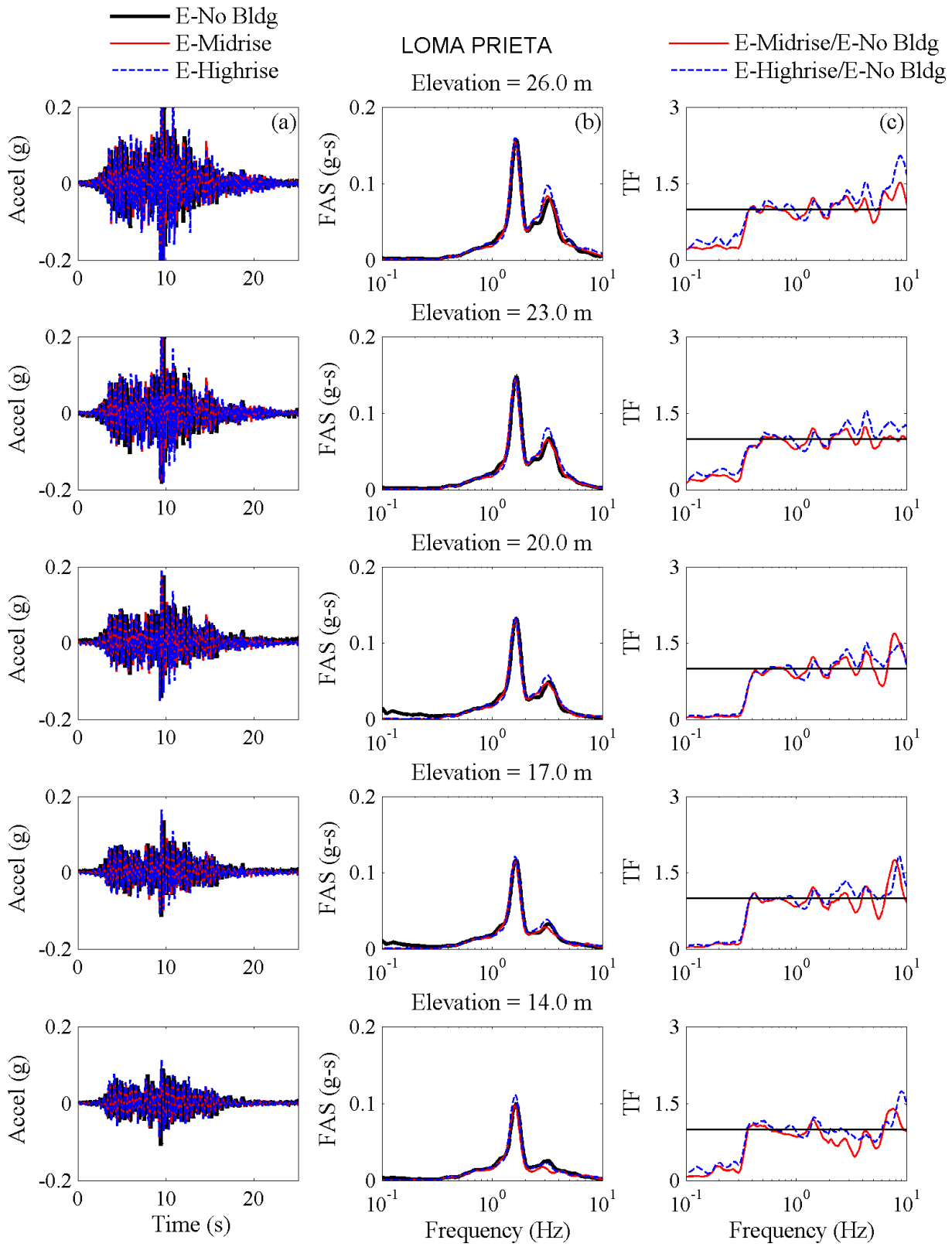

Figure 5.2-15. Loma Prieta near-field acceleration response shown as (a) acceleration time histories; (b) Fourier amplitude spectra; and (c) transfer functions.

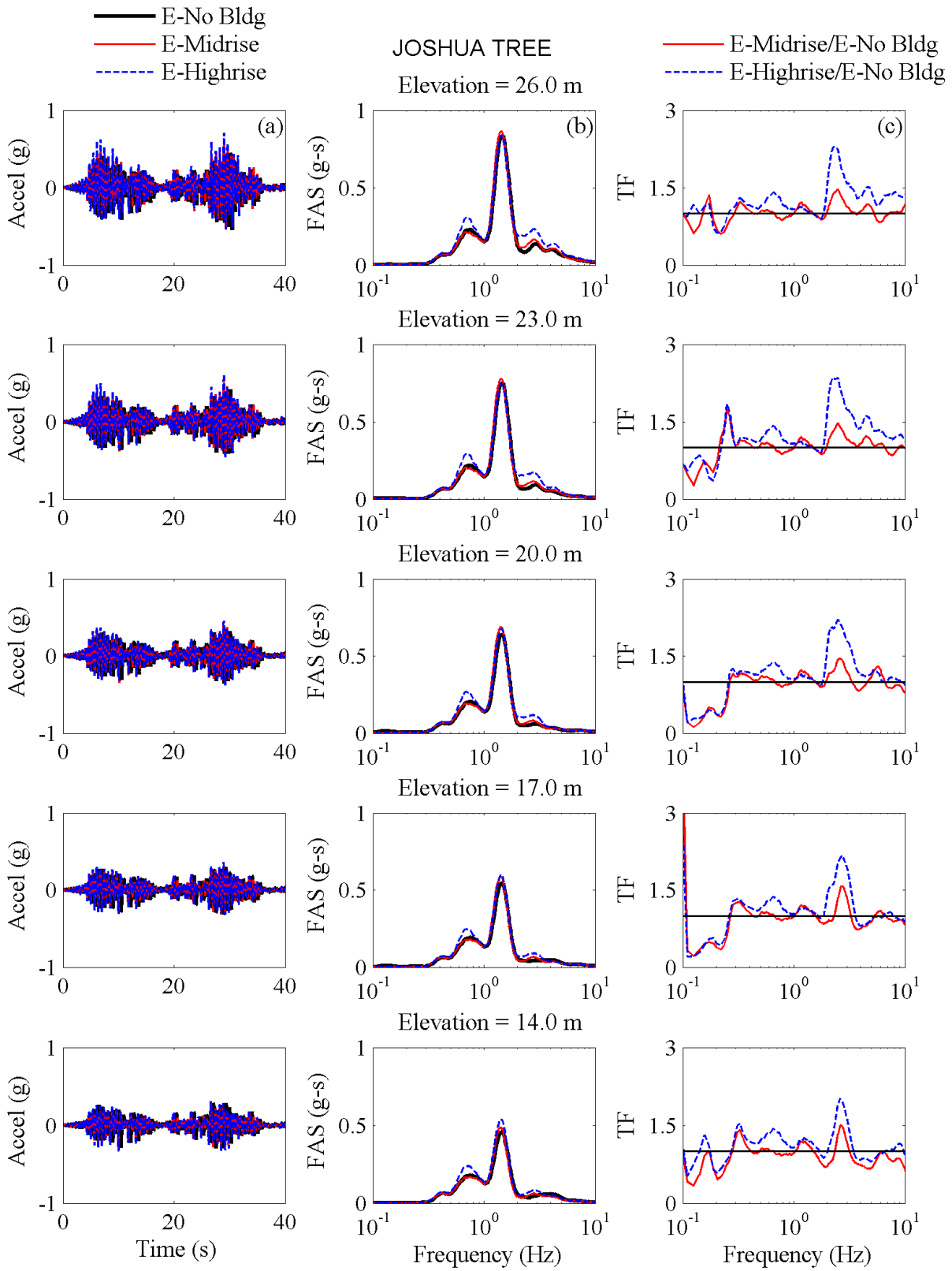

Figure 5.2-16. Joshua Tree near-field acceleration response shown as (a) acceleration time histories; (b) Fourier amplitude spectra; and (c) transfer functions.

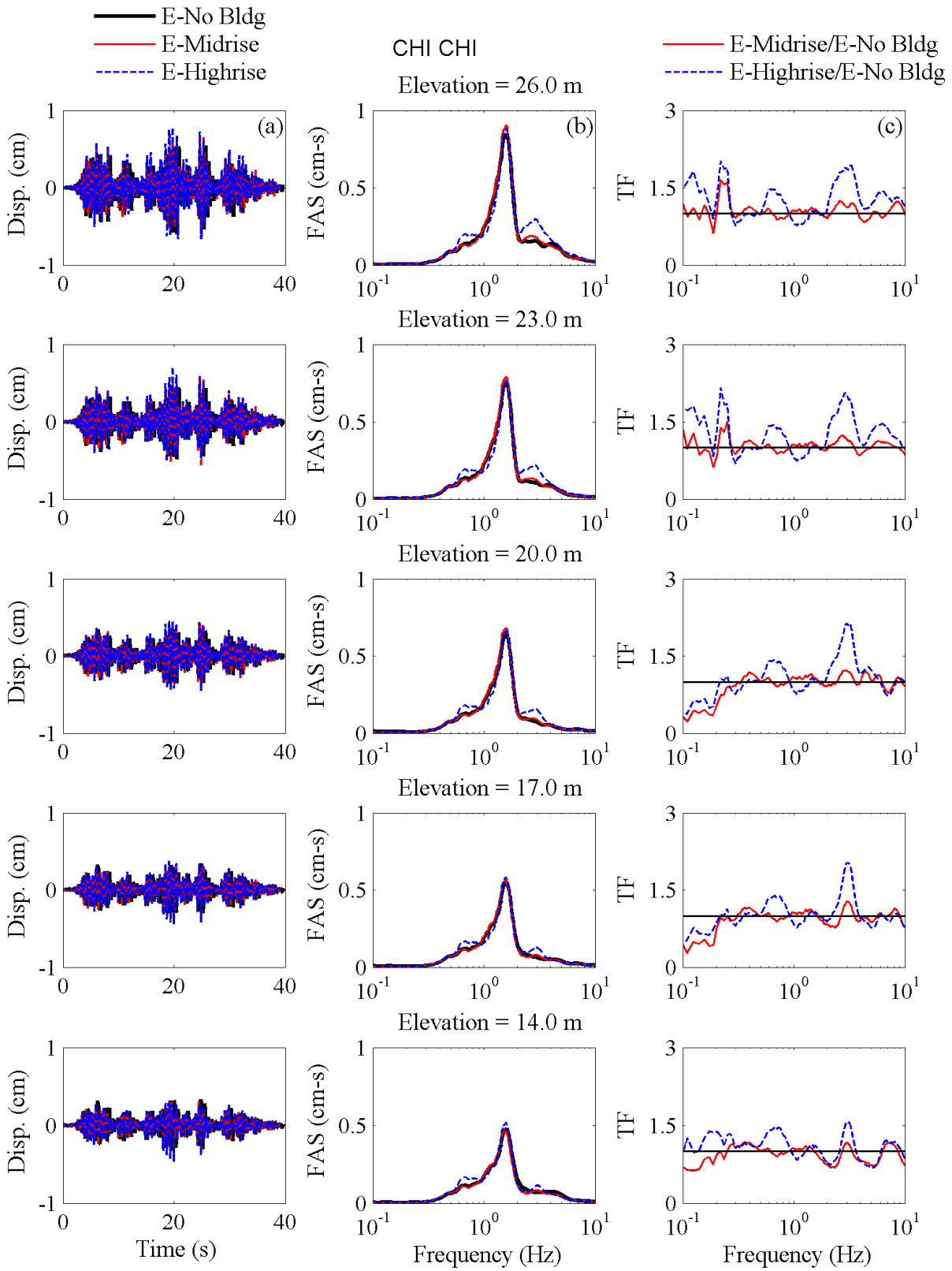

Figure 5.2-17. Chi Chi near-field acceleration response shown as (a) acceleration time histories; (b) Fourier amplitude spectra; and (c) transfer functions.

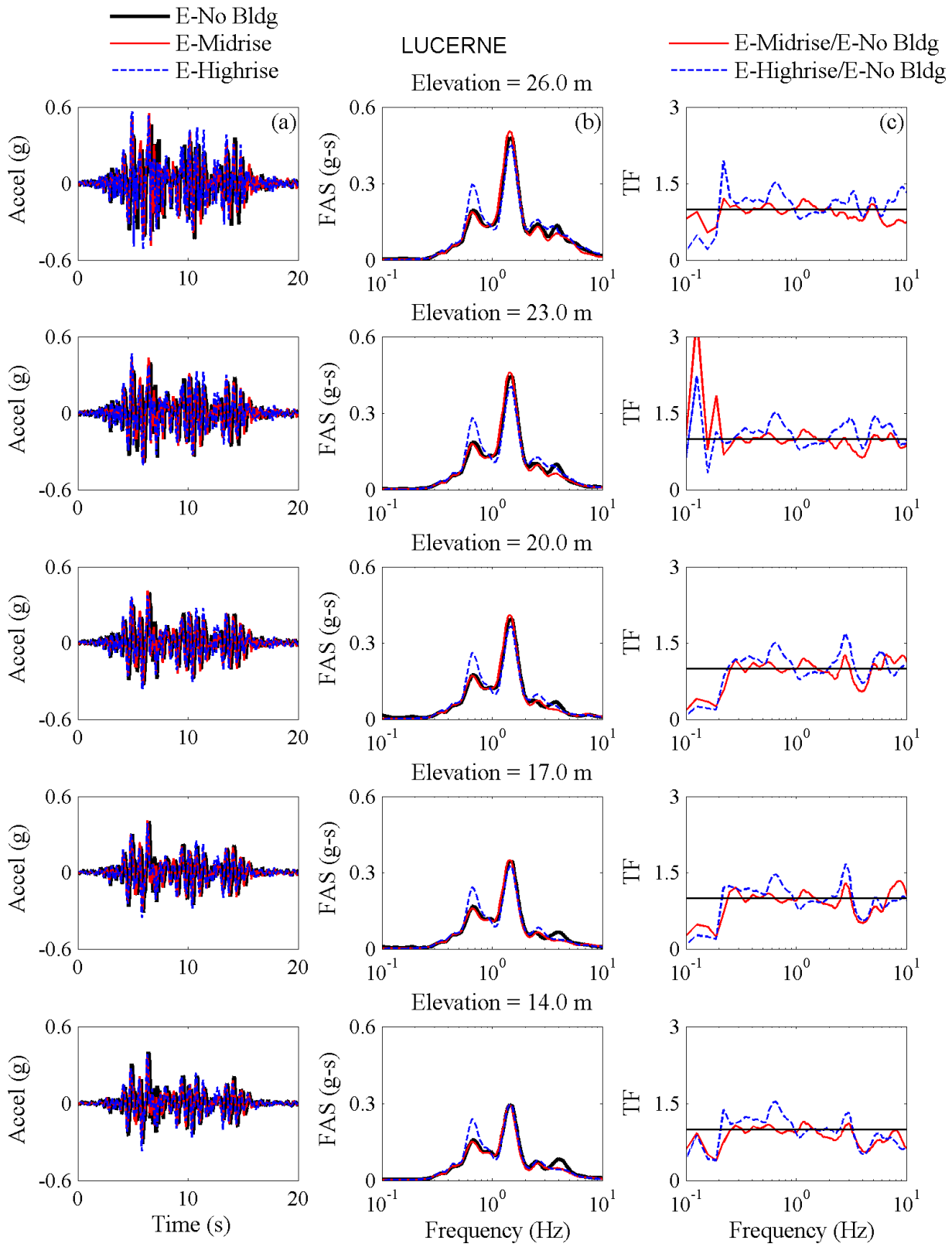

Figure 5.2-18. Lucerne near-field acceleration response shown as (a) acceleration time histories; (b) Fourier amplitude spectra; and (c) transfer functions.

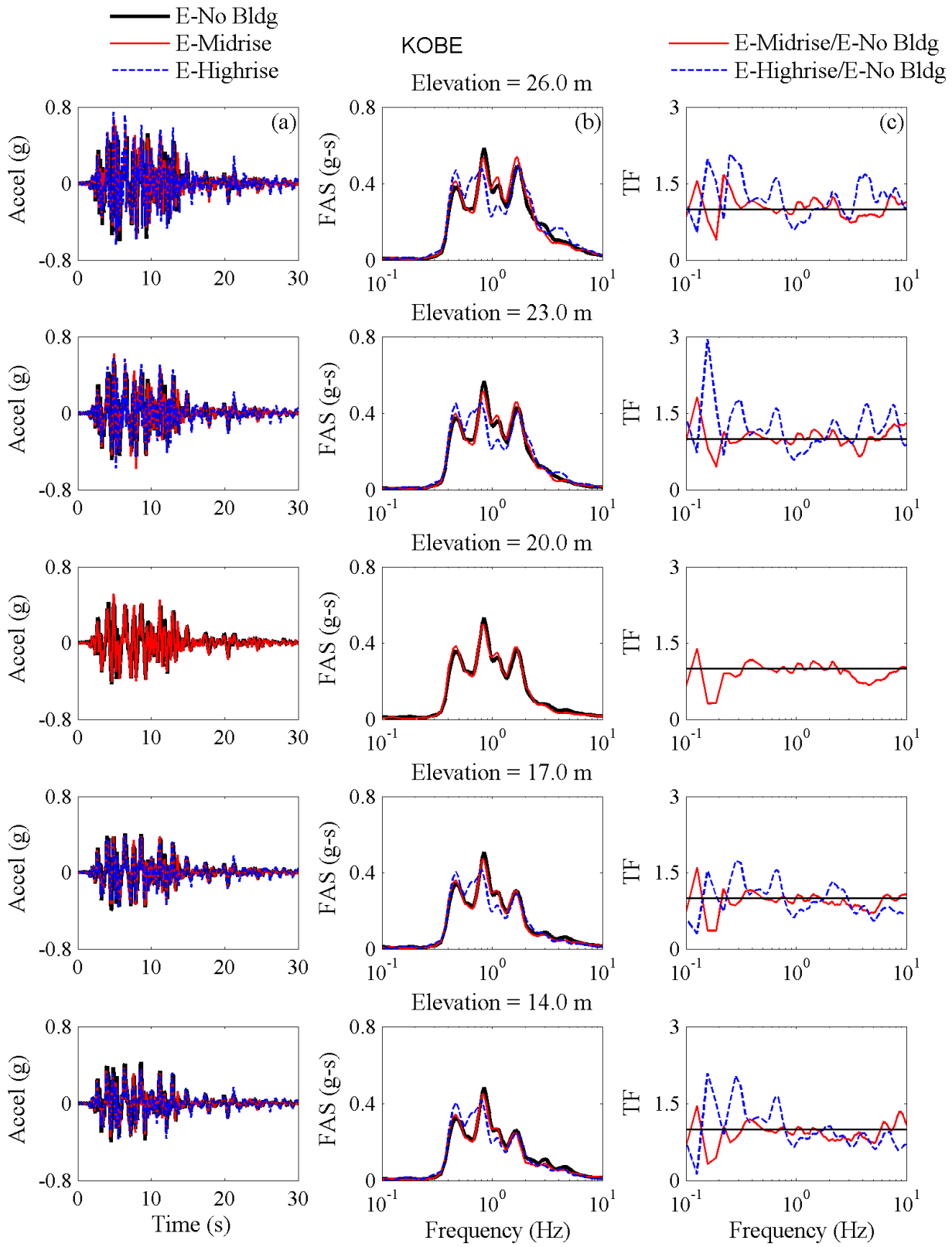

Figure 5.2-19. Kobe near-field acceleration response shown as (a) acceleration time histories; (b) Fourier amplitude spectra; and (c) transfer functions.

5.2.5 Excavation Acceleration Response

The walls of the temporary braced excavation had six horizontal accelerometers placed at various elevations corresponding to the experiments involving the permanent box structure. These accelerometers were placed centrally along the length of the tunnel, as shown in Figure 5.2-20. Table 5.2.4 summarizes the excavation accelerometer IDs in each test. Non-working accelerometers located on the excavation walls in the three experiments are listed in Table 5.2.5 by elevation, the recordings of which are not included in the following figures (Figure 5.2-21 through Figure 5.2-32).

E-Midrise and E-Highrise exhibited an amplification of accelerations on both excavation walls in frequencies greater than about 2 Hz and a de-amplification in frequencies of less than about 0.3 Hz, particularly at higher elevations. Therefore, the presence of the adjacent building influenced the acceleration of the temporary excavation differently at different frequencies.

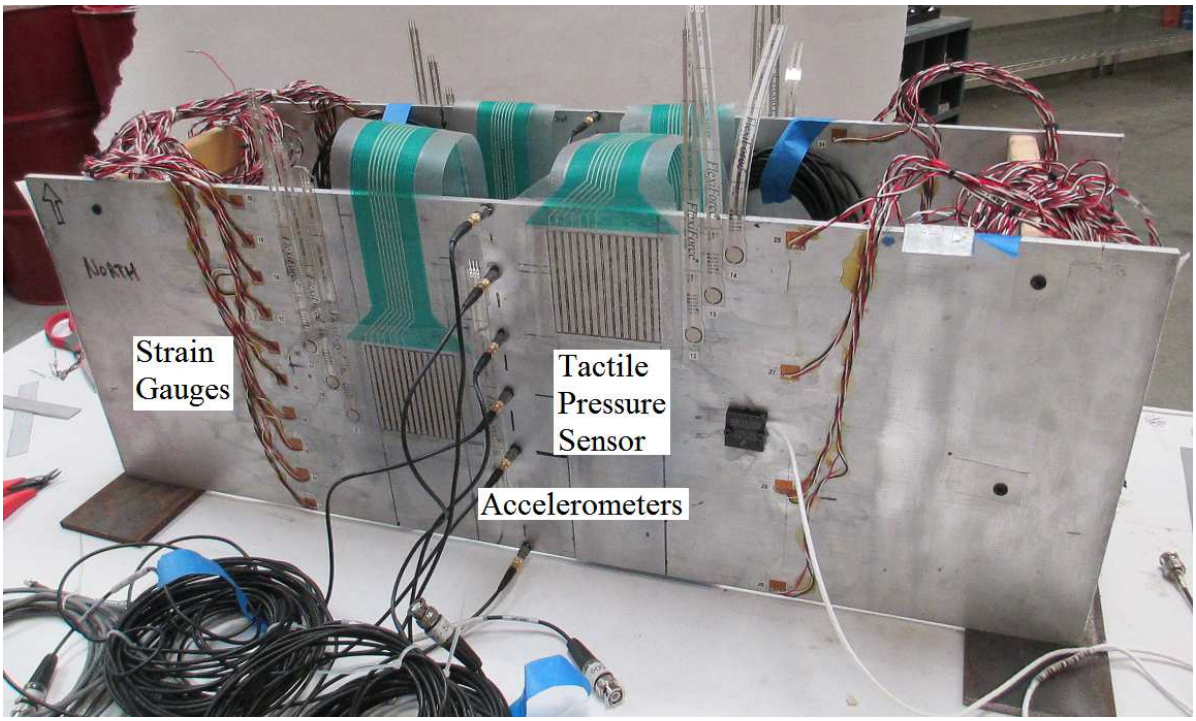

Figure 5.2-20. Model temporary braced excavation shown with instrumentation including accelerometers, strain gauges, and tactile pressure sensors.

Table 5.2.4. Excavation wall accelerometer IDs used in each excavation test.

Test ID	S. Tunnel Wall Accelerometers	N. Tunnel Wall Accelerometers
T-No Bldg	A6 – A11	A15 - A20
T-Midrise	A40 – A45	A47 – A52
T-Highrise	A40 - A45	A47 - A52

Table 5.2.5. List of non-working accelerometers placed on the excavation walls during E-No Bldg, E-Midrise, and E-Highrise.

Ground Motion	S. Wall Elevation (m)			N. Wall Elevation (m)		
	E-No Bldg	E-Midrise	E-Highrise	E-No Bldg	E-Midrise	E-Highrise
Northridge	17, 20	8,17		14	20	20
Loma Prieta	20	17				
Joshua Tree	20,23	17			8	20
Chi Chi	20	14, 17	14		20	20
Lucerne	20	14,17	14			20
Kobe	20	14,17	14		26	20

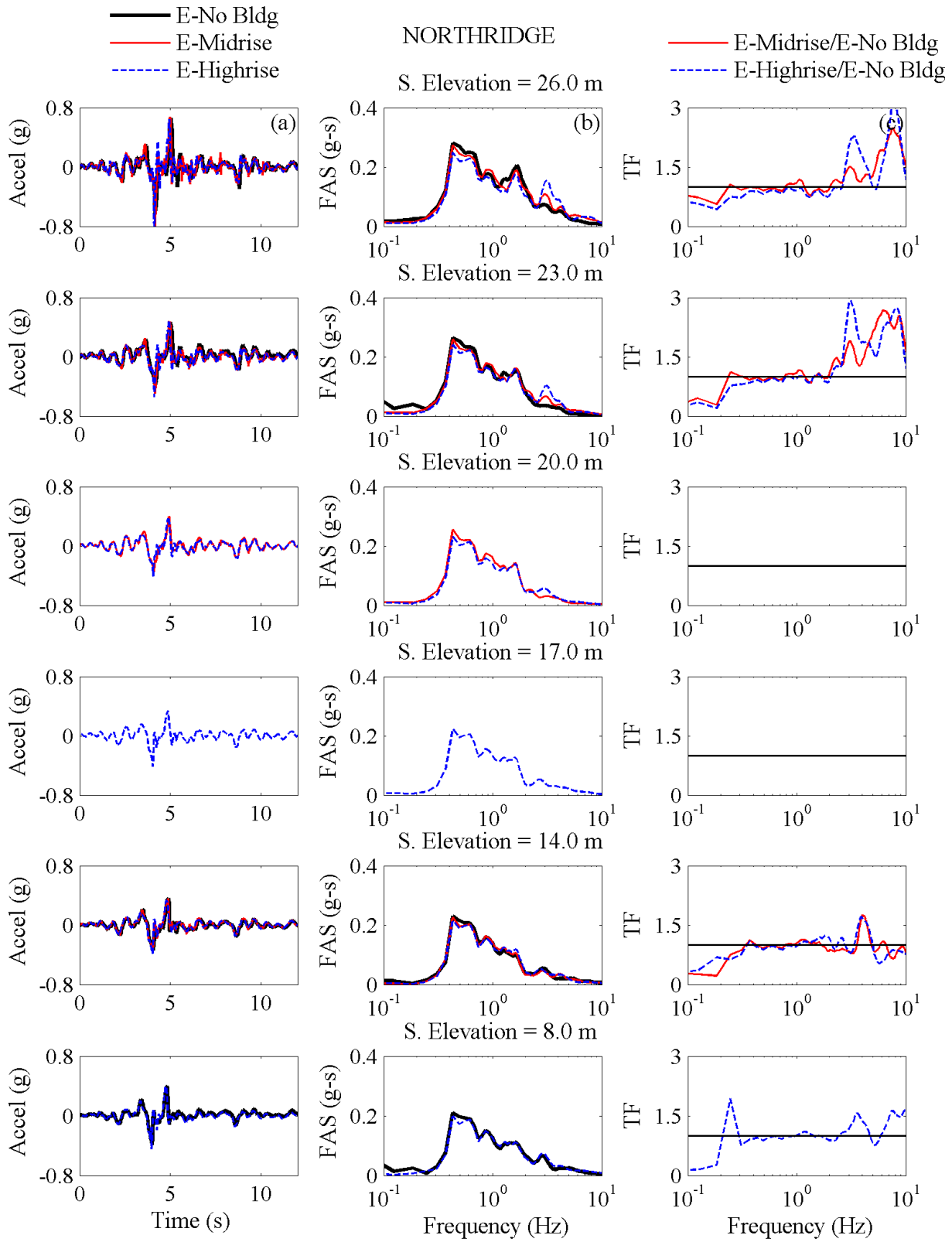

Figure 5.2-21. Northridge south wall excavation acceleration response shown as: (a) acceleration time histories; (b) Fourier amplitude spectra; and (c) transfer function.

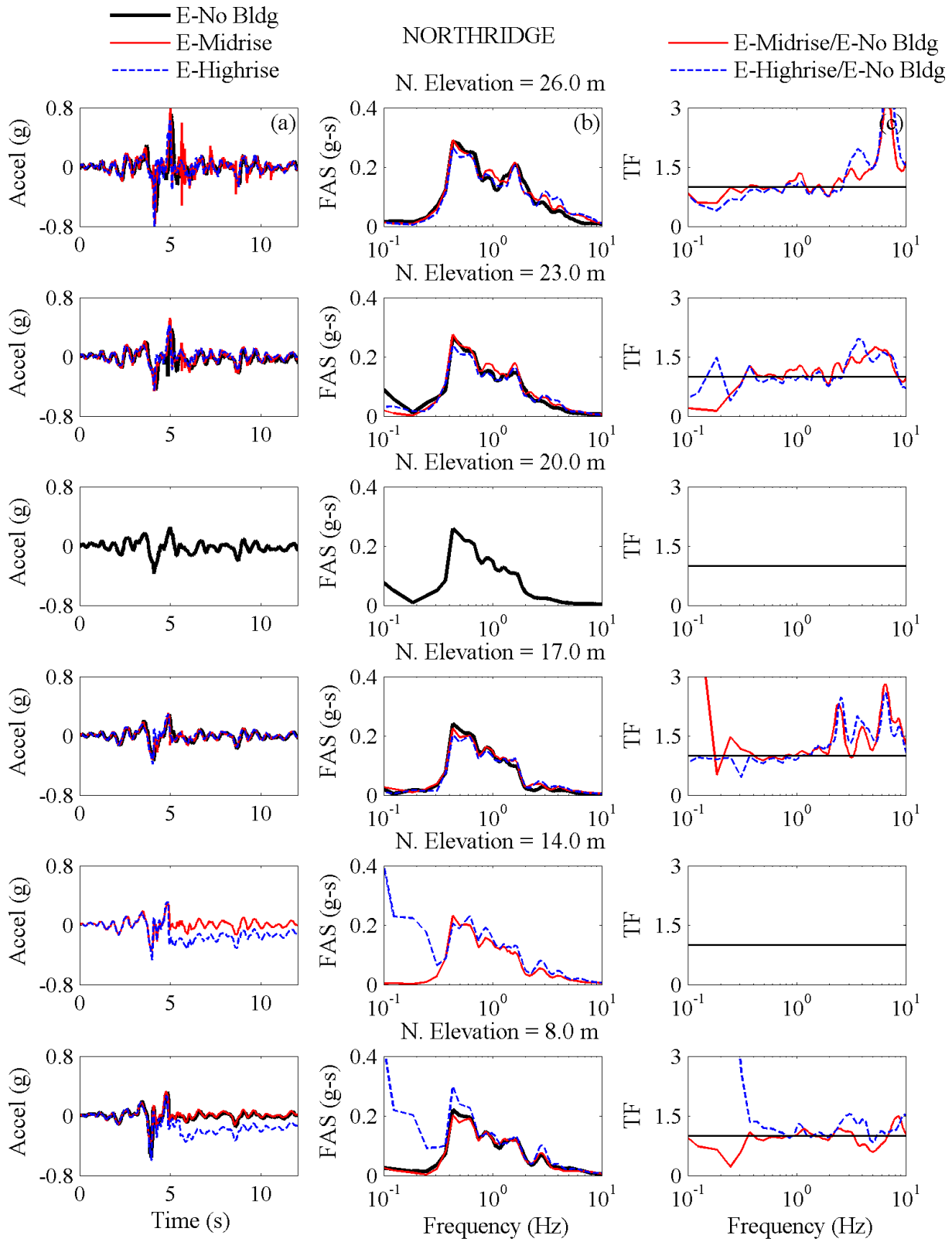

Figure 5.2-22. Northridge north wall excavation acceleration response shown as (a) acceleration time histories; (b) Fourier amplitude spectra; and (c) transfer function.

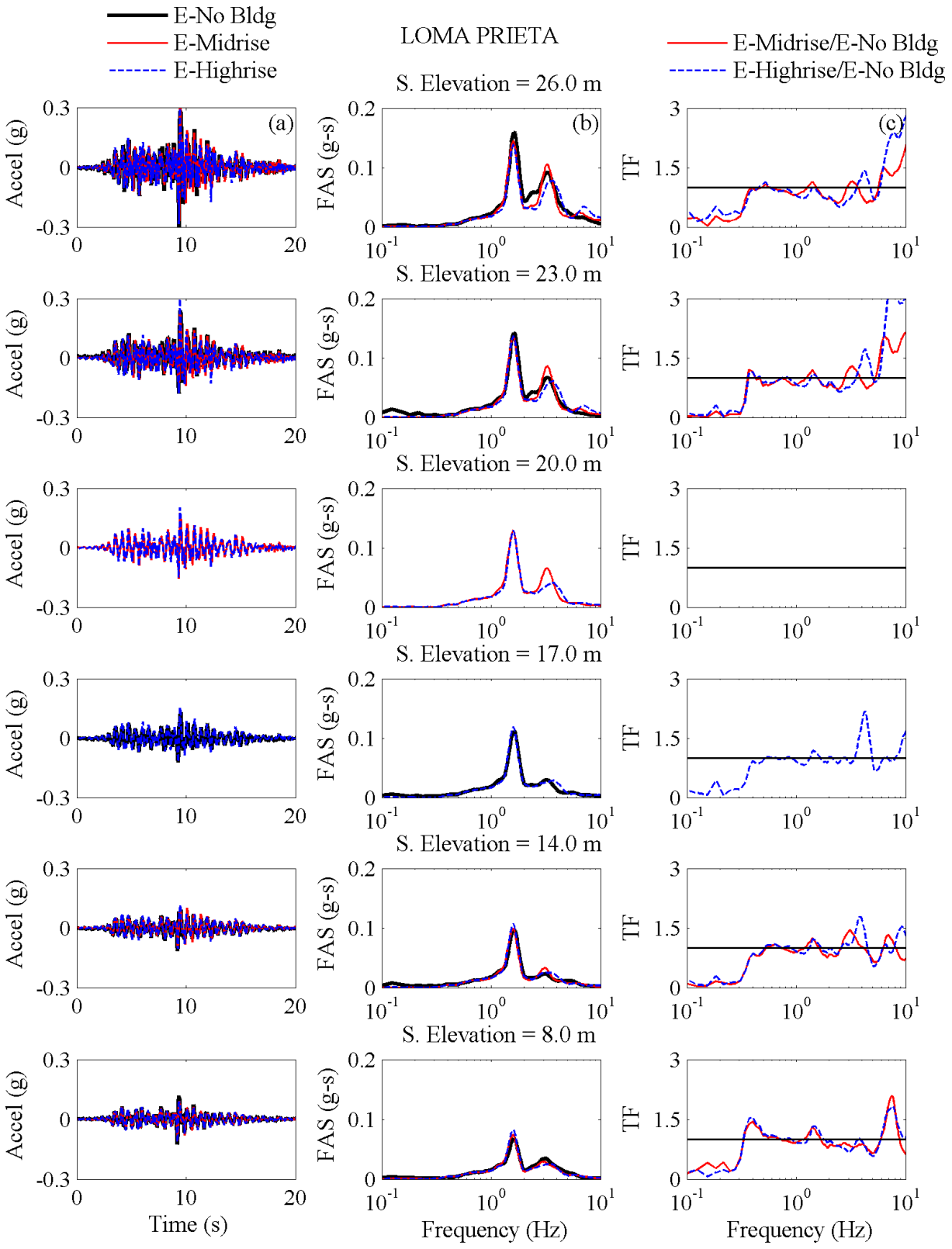

Figure 5.2-23. Loma Prieta south wall excavation acceleration response shown as (a) acceleration time histories; (b) Fourier amplitude spectra; and (c) transfer function.

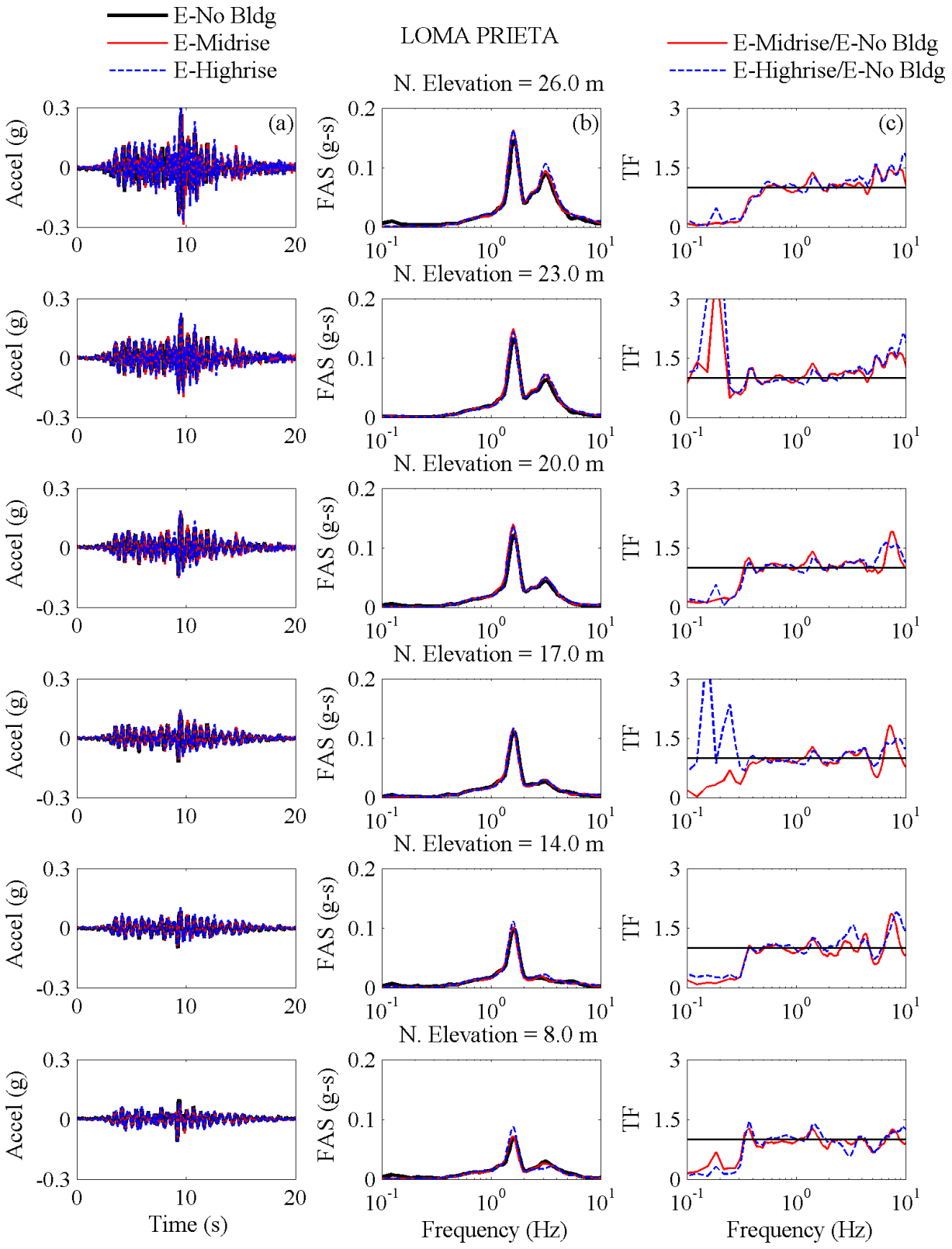

Figure 5.2-24. Loma Prieta north wall excavation acceleration response shown as (a) acceleration time histories; (b) Fourier amplitude spectra; and (c) transfer function.

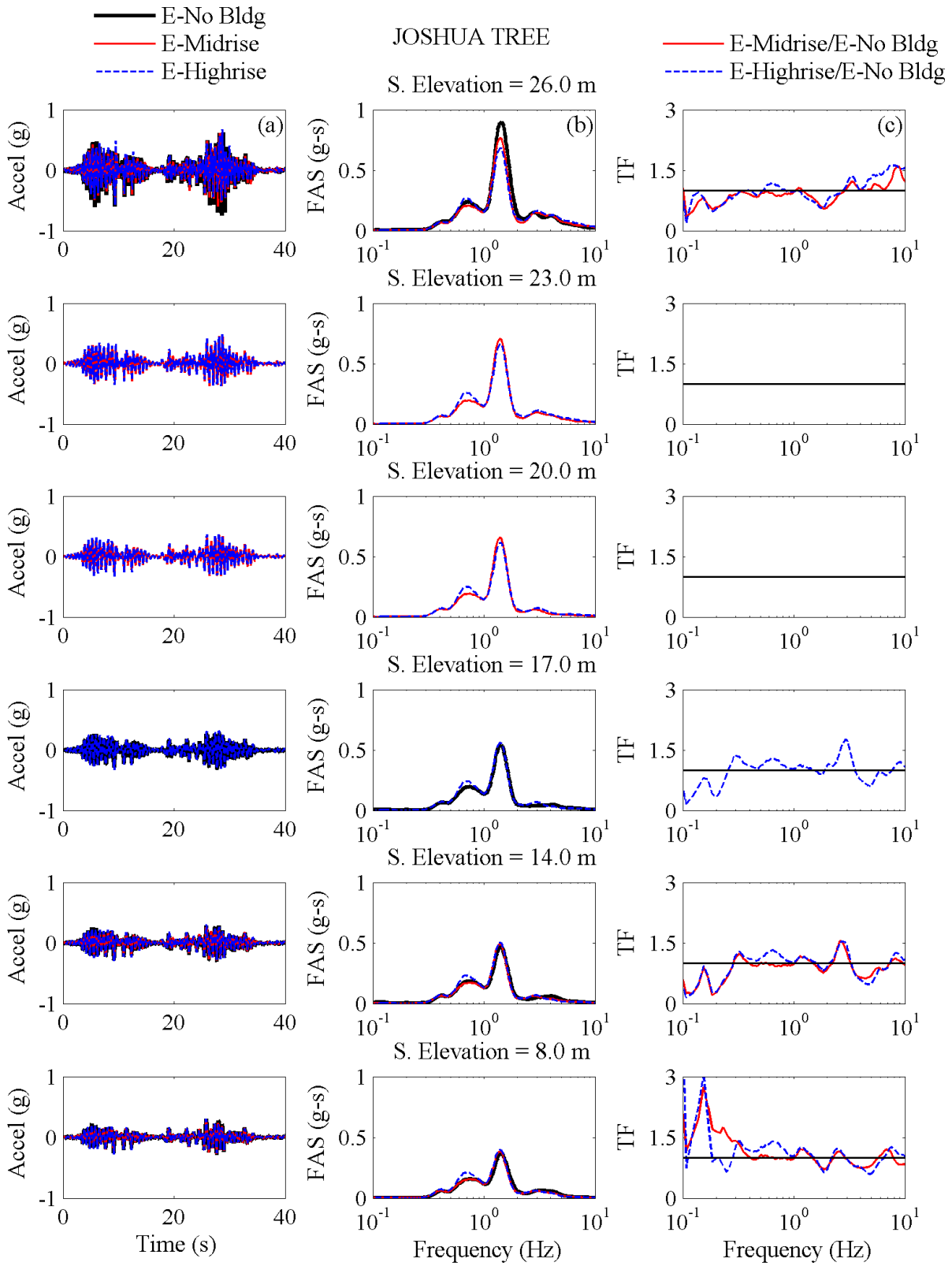

Figure 5.2-25. Joshua Tree south wall excavation acceleration response shown as (a) acceleration time histories; (b) Fourier amplitude spectra; and (c) transfer function.

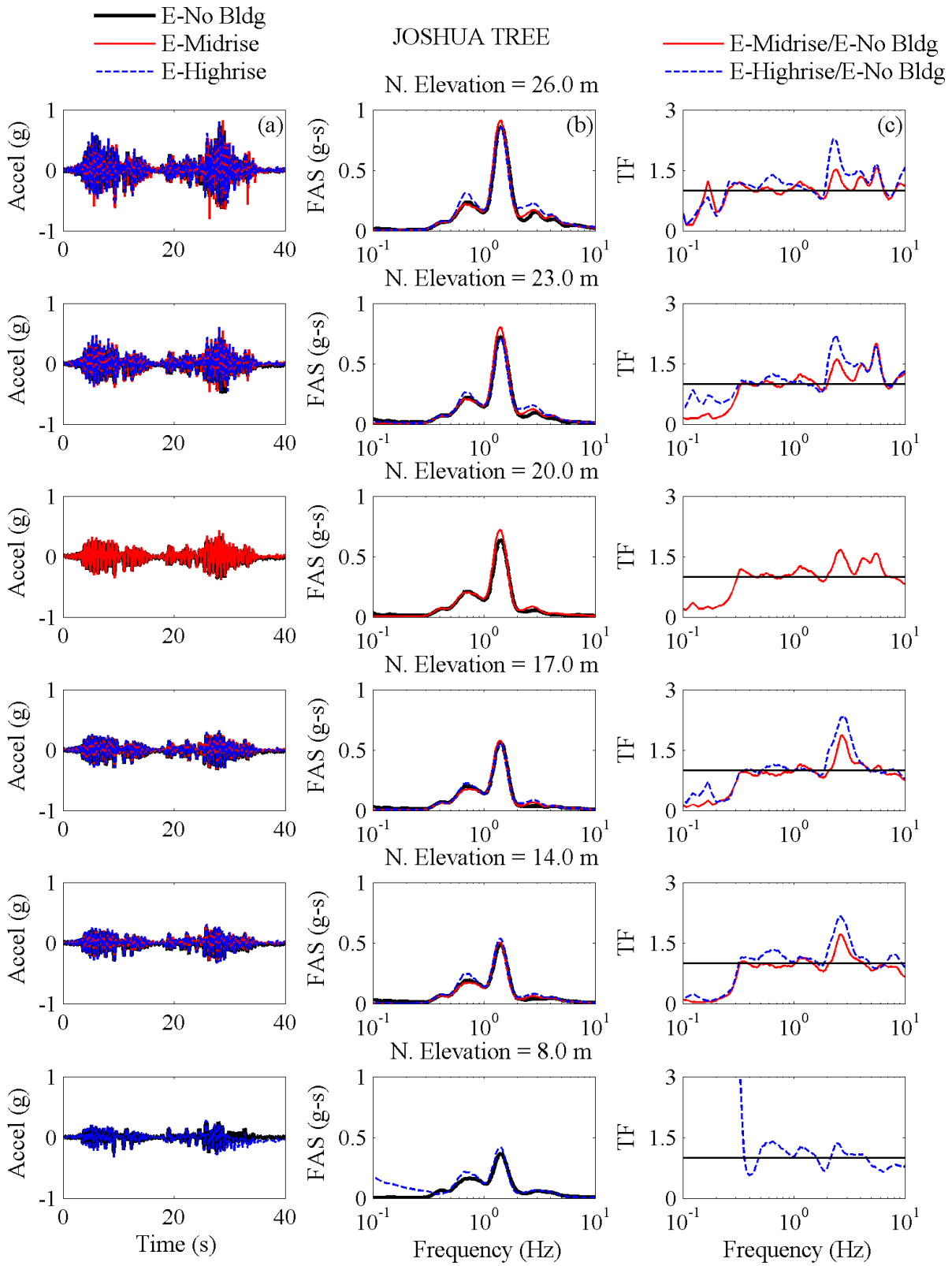

Figure 5.2-26.Joshua Tree north wall excavation acceleration response shown as (a) acceleration time histories; (b) Fourier amplitude spectra; and (c) transfer function.

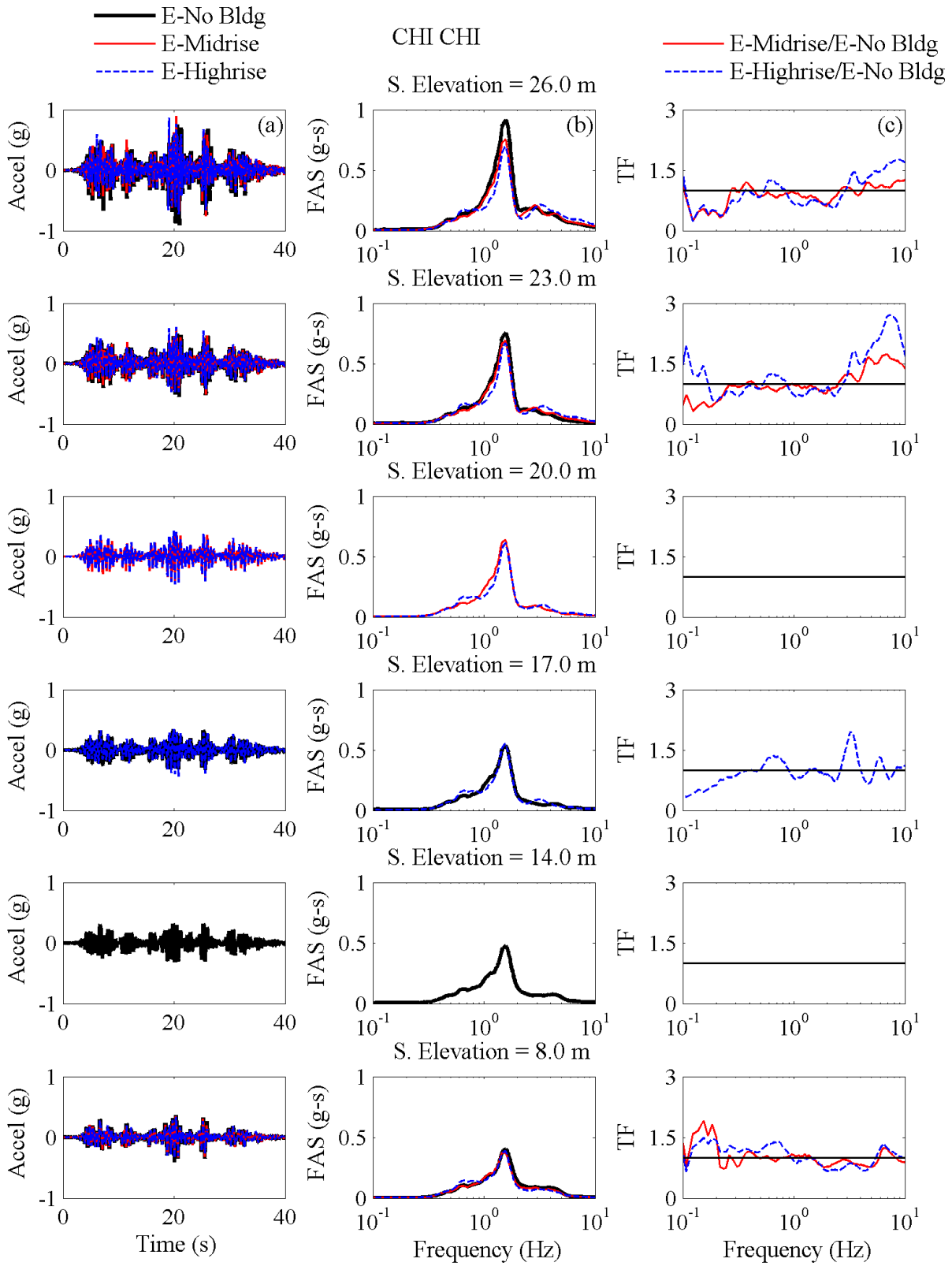

Figure 5.2-27. Chi Chi south wall excavation acceleration response shown as (a) acceleration time histories; (b) Fourier amplitude spectra; and (c) transfer function.

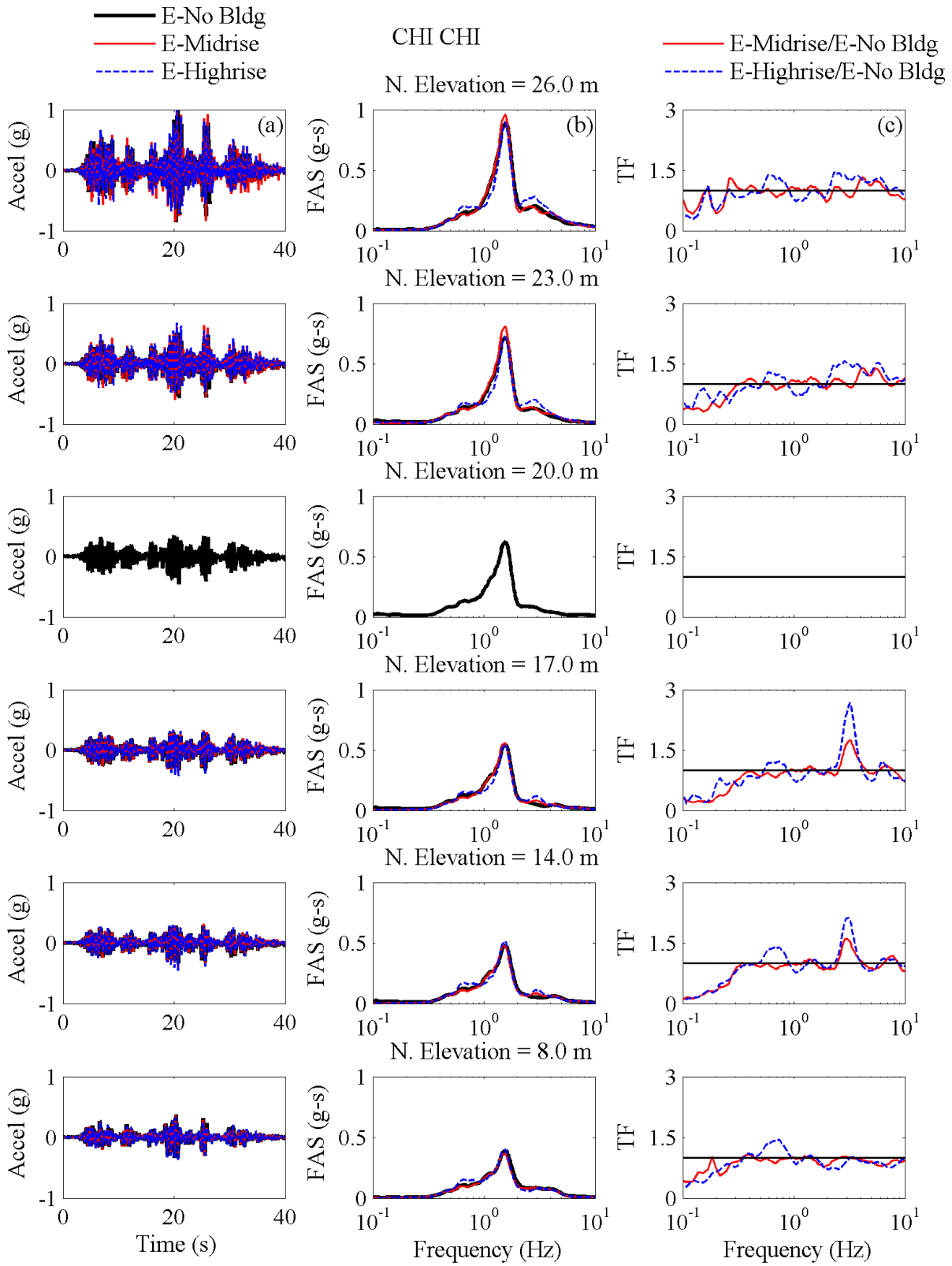

Figure 5.2-28. Chi Chi north wall excavation acceleration response shown as (a) acceleration time histories; (b) Fourier amplitude spectra; and (c) transfer function.

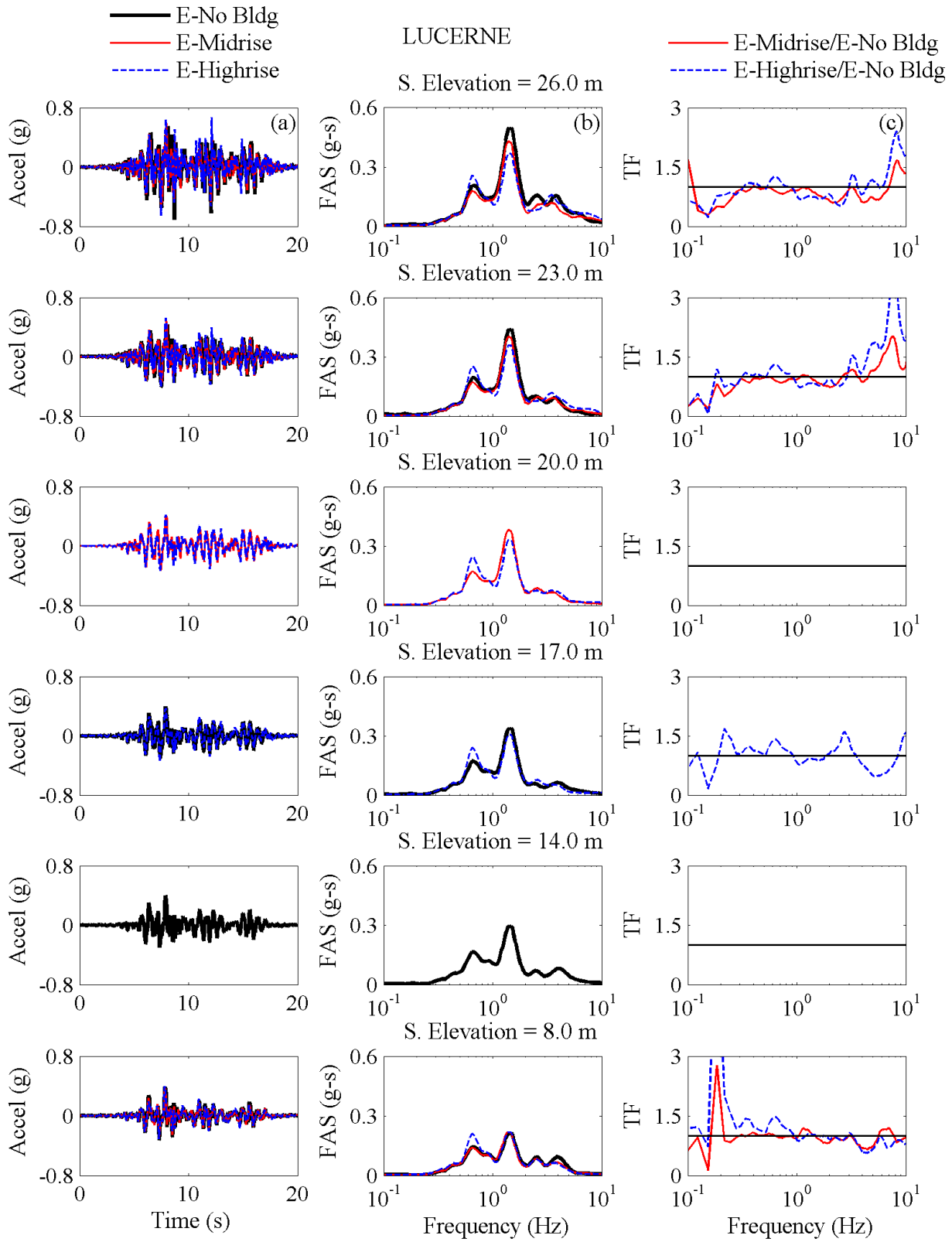

Figure 5.2-29. Lucerne south wall excavation acceleration response shown as (a) acceleration time histories; (b) Fourier amplitude spectra; and (c) transfer function.

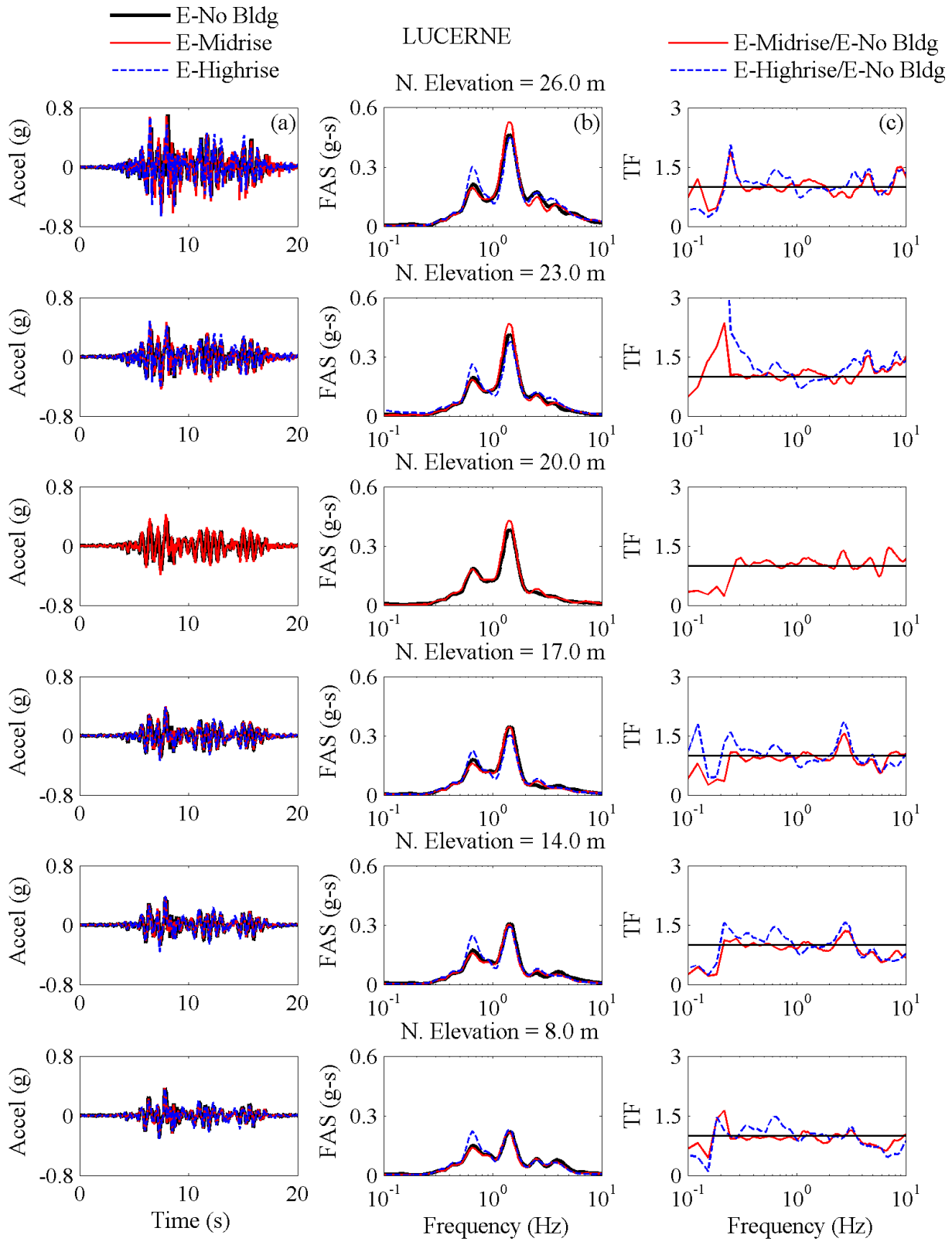

Figure 5.2-30. Lucerne north wall excavation acceleration response shown as (a) acceleration time histories; (b) Fourier amplitude spectra; and (c) transfer function.

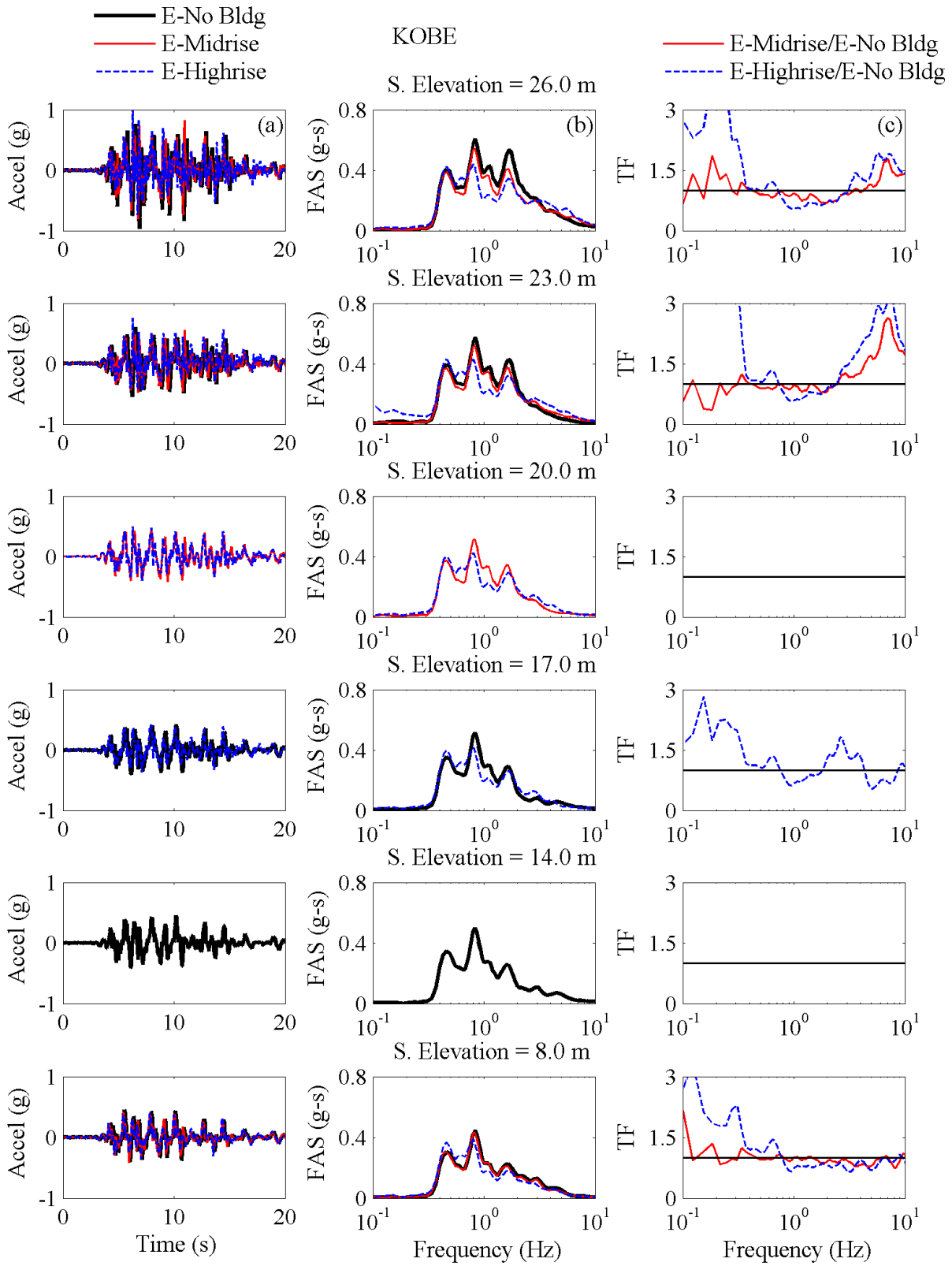

Figure 5.2-31. Kobe south wall excavation acceleration response shown as (a) acceleration time histories; (b) Fourier amplitude spectra; and (c) transfer function.

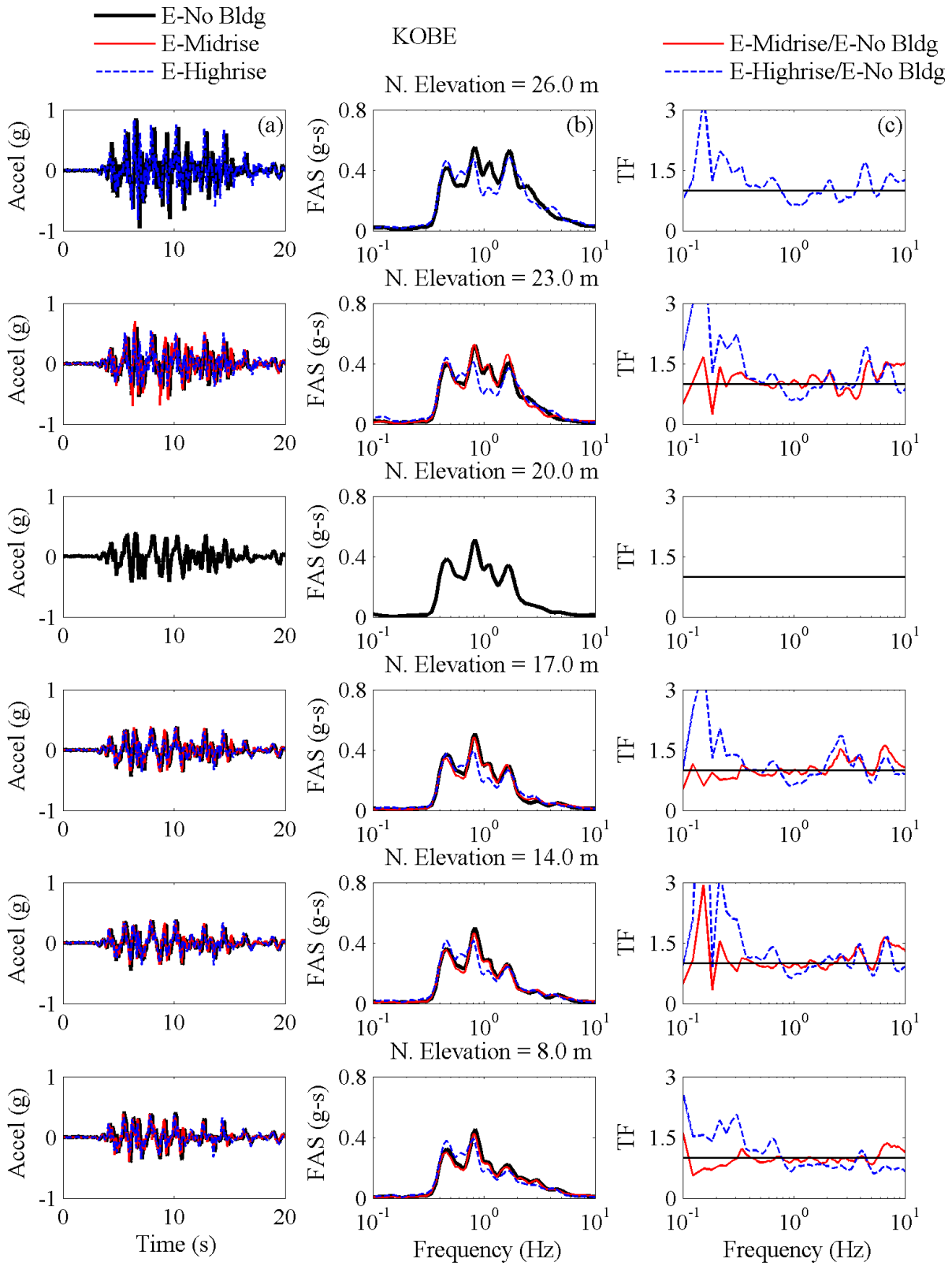

Figure 5.2-32. Kobe north wall excavation acceleration response shown as (a) acceleration time histories; (b) Fourier amplitude spectra; and (c) transfer function.

5.3 Lateral Displacements

The lateral displacement of the braced excavation and its surrounding soil was evaluated and compared among the three excavation tests to gain an understanding of the impact of tall buildings on the displacement response of the underground structure-soil-building system during each shaking event. These displacements were calculated by filtering and then double-integrating accelerometer recordings.

5.3.1 Displacement in the NF Soil

Maximum lateral displacements in the NF soil surrounding the underground structure were first compared among the three excavation experiments to evaluate the influence of the all building's presence. Figure 4.3.1 shows a zoomed-in instrumentation layout of T-Highrise showing the accelerometers used to calculate displacement at each elevation in that test. Table 5.3.1 lists the accelerometers used at each elevation to calculate the maximum lateral displacement of the soil and structures surrounding the tunnel. Two NF arrays were considered: 1) 3m horizontally away from the excavation on its free (north) side; 2) 4m horizontally away from the excavation on its building (south) side. These arrays are referred to as "NF Free Side" and "NF Bldg Side", respectively. There were only two accelerometers on the highrise building's basement at elevations corresponding to the other experiments for comparison. Because there was no tall building in E-No Bldg, the NF Free Side and Bldg Side accelerations were taken from the NF accelerometer array, and therefore were the same.

In Figure 5.3-3 the maximum lateral displacements are compared in the NF Free Side and Bldg Side in the three excavation tests. These figures indicate that overall, the maximum lateral displacement did not change noticeably among the three tests, but the NF peak displacement at the surface (elevation 26m) on the Bldg Side often significantly decreased from E-No Bldg to E-

Midrise and to E-Highrise. Further, during one motion (Lucerne), peak displacements increased consistently on both sides with the addition of the tall buildings at all elevations other than surface (26m on Bldg side).

Table 5.3.1.Accelerometers used to calculate maximum lateral displacements in the NF Free Side and Bldg Side.

	NF Free Side			NF Bldg Side		
Elevation (m)	E-No Bldg	E-Midrise	E-Highrise	E-No Bldg	E-Midrise	E-Highrise
17	A02	A17	A16	A02	A34	**NA**
20	A03	A18	A17	A03	A35	A35
23	A04	A19	A18	A04	A36	**NA**
26	A05	A20	A19	A05	A37	A36

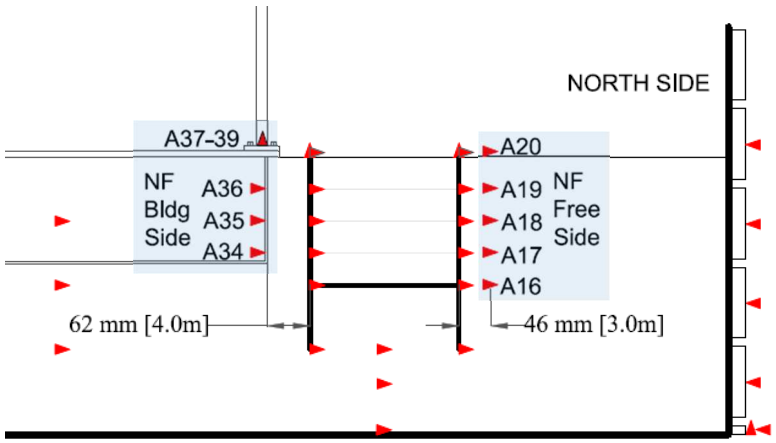

Figure 5.3-1Accelerometers used in E-Midrise to calculate maximum lateral displacements in the NF.

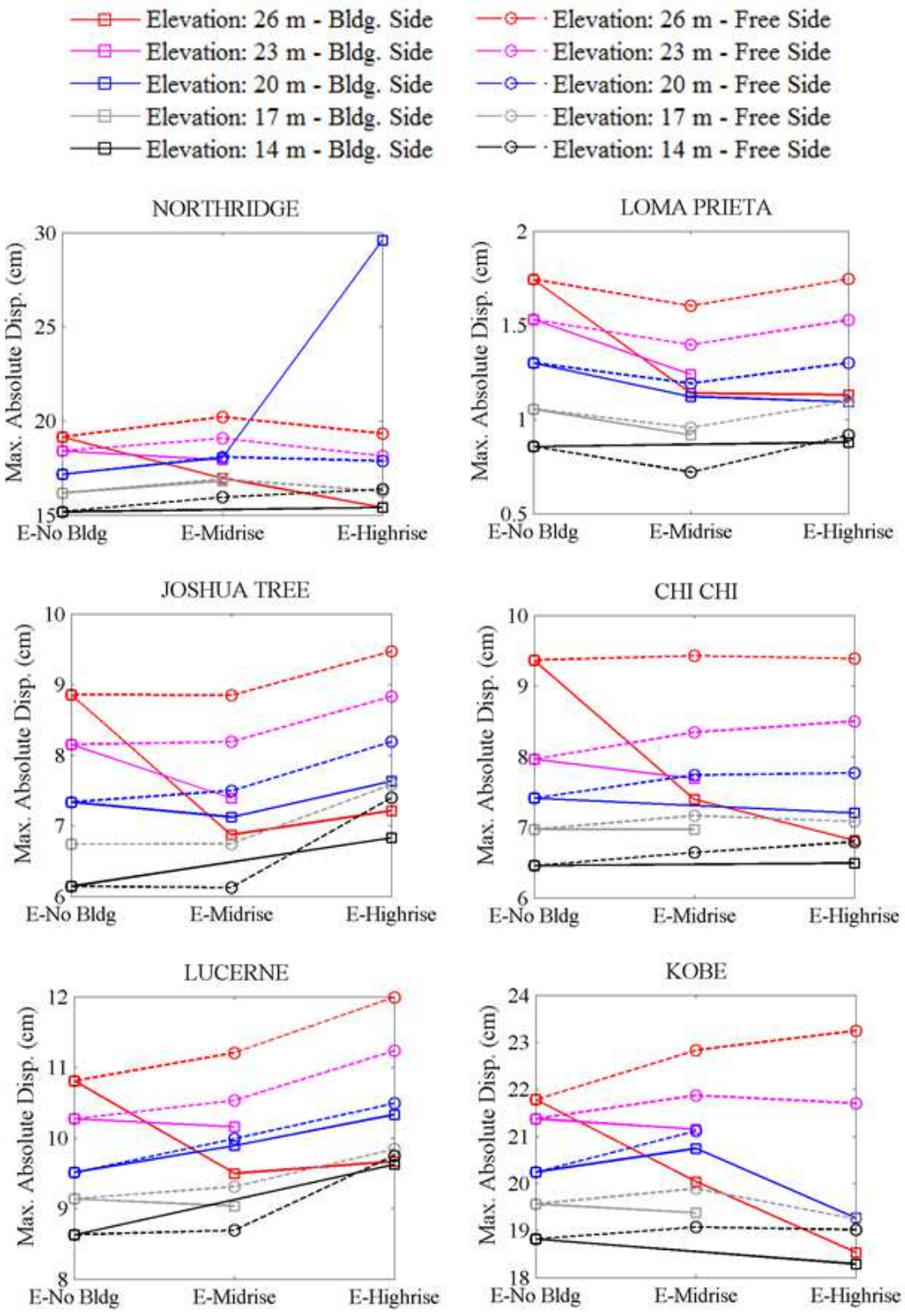

Figure 5.3-2. Comparing near-field (NF) soil maximum lateral displacements on the free side and building side of the temporary braced excavation walls.

5.3.2 Lateral Displacement of the Excavation Walls

The average lateral displacements were computed on each excavation wall by numerically integrating the lateral displacements obtained from accelerometers along the whole wall and dividing the value by the total wall height (18m) at each instance of time. In this way, one may obtain a time history of average wall displacements, which shows the overall dynamic movement of the whole wall in an absolute sense, as opposed to its relative deflection. The maximum average wall displacements are compared among the different tests on the two walls during different motions in Figure 5.3-3. There was no maximum reported for E-Midrise, Northridge motion on the building side wall or E-Midrise, Joshua Tree on the free side wall due to bad accelerometer data. Overall, the two walls moved roughly similarly in terms of average absolute displacement. However, the peak value of average wall displacement decreased slightly on both sides of the excavation with the addition of the adjacent mid to highrise building for the two most intense ground motions, Northridge and Kobe.

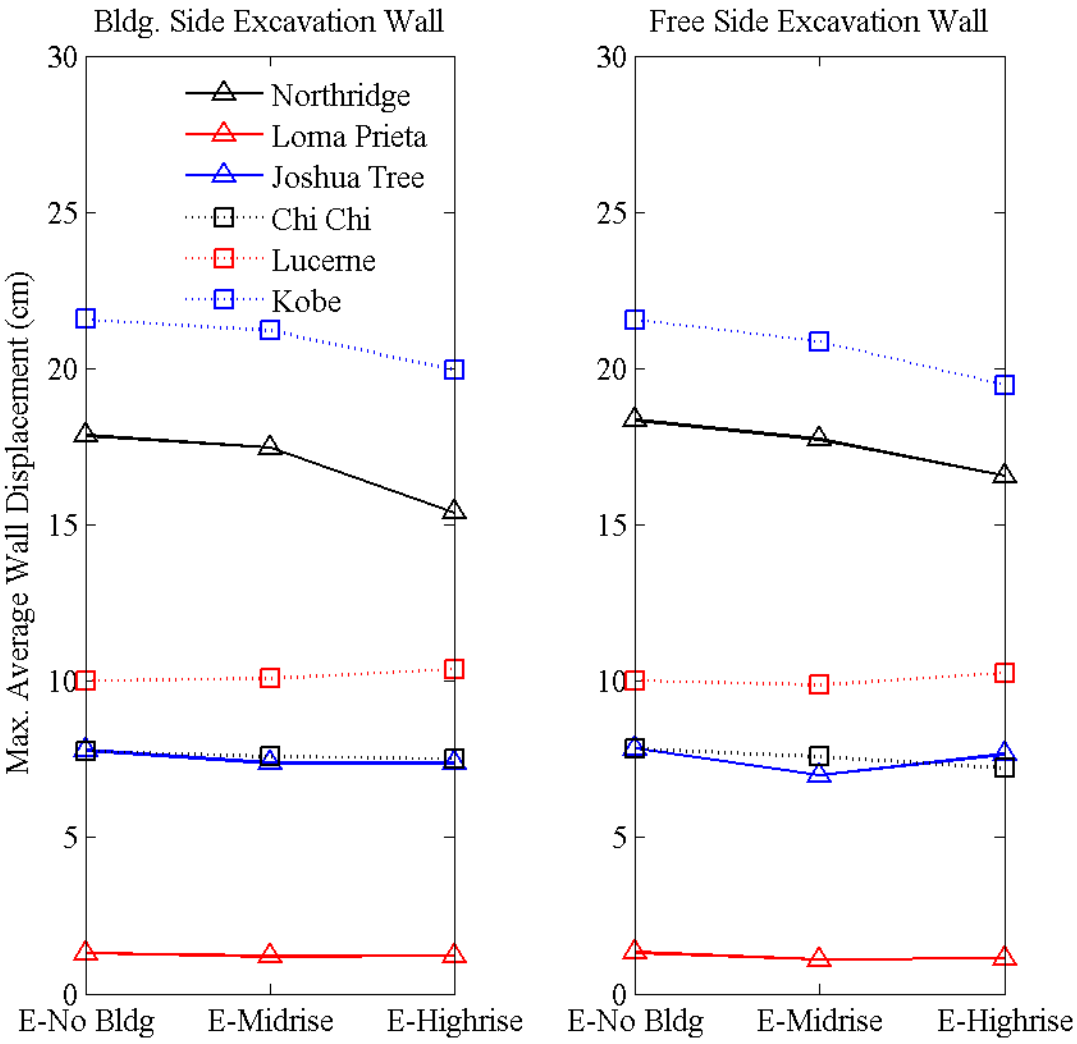

Figure 5.3-3. Maximum absolute lateral displacement of the excavation walls.

5.3.3 Racking Displacement of the Excavation Walls

As discussed previously, in addition to the average overall displacement of the underground structure, racking displacements are an important measure of the distortion of the structure during earthquake loading and hence, its performance. For the tunnel, racking displacement was estimated as the difference in the lateral displacement of the roof and the floor. For the braced excavation, racking displacement was calculated as the relative displacement of the top of each wall with respect to the base of the excavation (as opposed to the bottom of the corresponding

wall). The temporary excavation walls were more flexible and taller than the tunnel walls, and were therefore expected to deflect more. Also, unlike the stiff roof and base sections of the tunnel connecting the two side walls, the excavation walls were connected only with three rows of bracing struts, which were loaded in compression (Ch. 3). Therefore, the two excavation walls could show a more independent seismic response and deformation pattern compared to the walls of the permanent box structure.

In order to calculate racking displacements, accelerometers were first filtered using a 7^{th} order band-pass filter with corner frequencies of 0.3 and 30 Hz. The excavation wall accelerometers used in each test to calculate excavation racking are listed in Table 5.3.2. The filtered accelerometer data were then double integrated to obtain displacement time histories at the top of the wall and bottom of the excavation. Racking displacement time histories were calculated as the difference between the two. The same process was performed to calculate racking displacements in the far-field soil in these excavation tests.

There were a few non-working accelerometers on the excavation walls as listed in Table 5.2.5. Due to non-working sensors, the estimation of racking displacements was done using extrapolation when needed. For example, if the accelerometer at the bottom of the excavation was not working, which was the case for the south wall in E-Midrise, then the accelerometer above it on the corresponding wall was used in its place. The racking displacement calculated over the height of the working accelerometers was then extrapolated linearly to account for the full height of the wall above the excavation. Figure 5.3-4 shows the peak racking displacements recorded on the two excavation walls in each test and ground motion. Figure 5.3-5 through Figure 5.3-10 compare racking displacements in terms of time histories and Fourier amplitude spectra. The frequency-dependent transfer functions calculated by dividing the Fourier

amplitude of racking in E-Midrise to E-No Bldg and E-Highrise to E-No Bldg are also provided in these figures to evaluate the influence of an adjacent building on racking deformations at different frequencies.

Key observations from these figures are as follows:

- Peak racking displacements reduced slightly in E-Midrise and E-Highrise compared to E-No Bldg during most ground motions on both sides of the wall. Therefore, even though the peak average lateral wall displacements slightly increased, the racking, which is a simplistic measure of wall deflection (only comparing the displacement of top of the wall with respect to the base of excavation) reduced with the presence of the adjacent building.
- Peak racking displacements became asymmetric in the experiments involving an adjacent building: the free (or north) side of the excavation often experienced greater distortion compared to the building (or south) side, even though average displacements were similar.
- Comparison of the Fourier amplitude spectra (FAS) of tunnel racking showed a reduction in amplitude due to the presence of an adjacent building for most of the frequency range of interest (0.5 to 3 Hz).
- The presence of the building affected racking displacements in the far-field also. With the exception of the Loma Prieta motion (weakest motion), racking displacements increased in the far-field of the corresponding test with the addition of a midrise and then a highrise building, particularly in frequencies greater than about 2 Hz. The building seemed to push the soil in the far-field to deform more in most cases.

Table 5.3.2. Accelerometers used in calculation of racking displacements.

Test ID	S. Wall Racking Accels.	N. Wall Racking Accels.	Far-Field Racking Accels.
E-No Bldg	A7, A8, A10, A11	A16, A17, A19, A20	A25, A29
E-Midrise	A41 - A45	A48 - A52	A04, A08
E-Highrise	A41, A42, A45	A48, A52	A04, A06

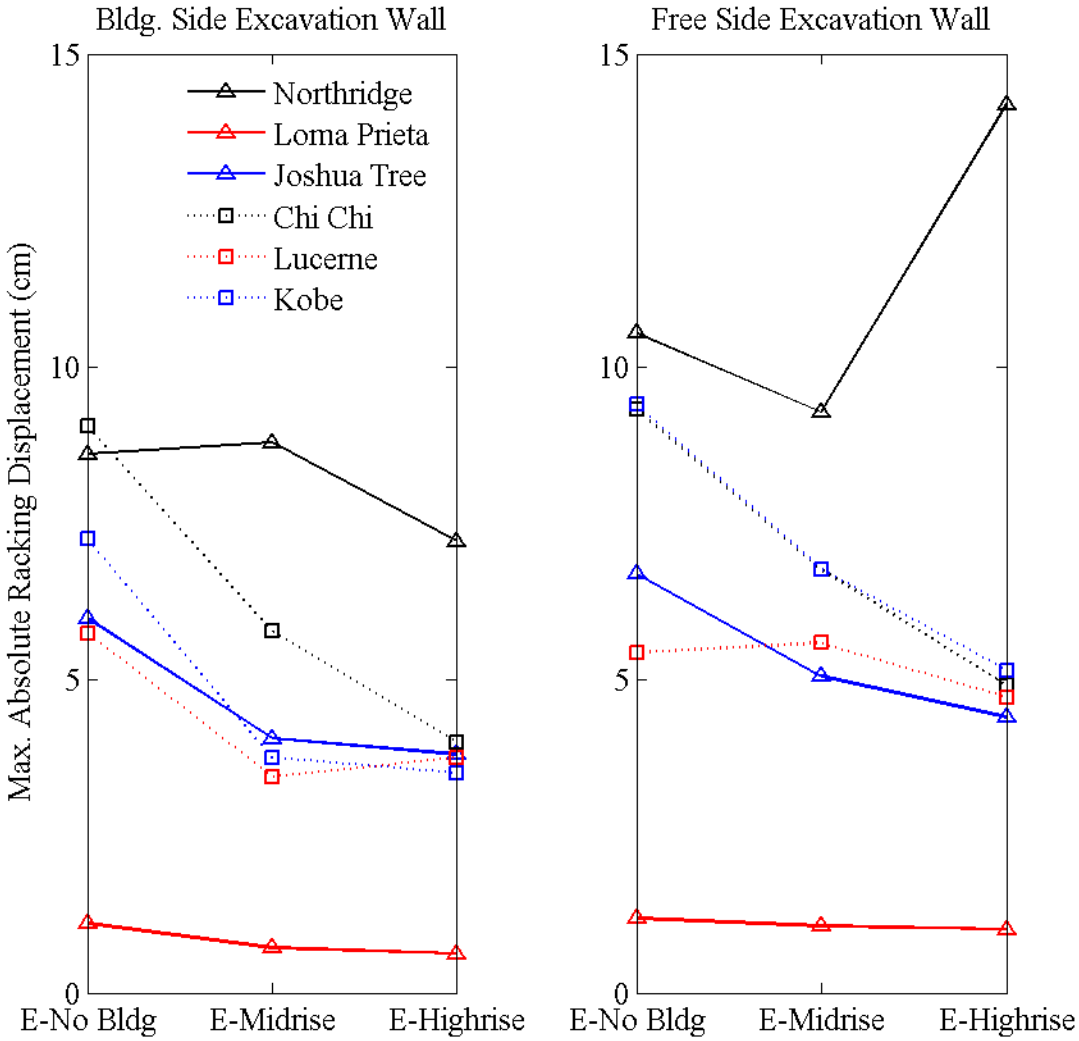

Figure 5.3-4. Maximum excavation wall racking dispalcements.

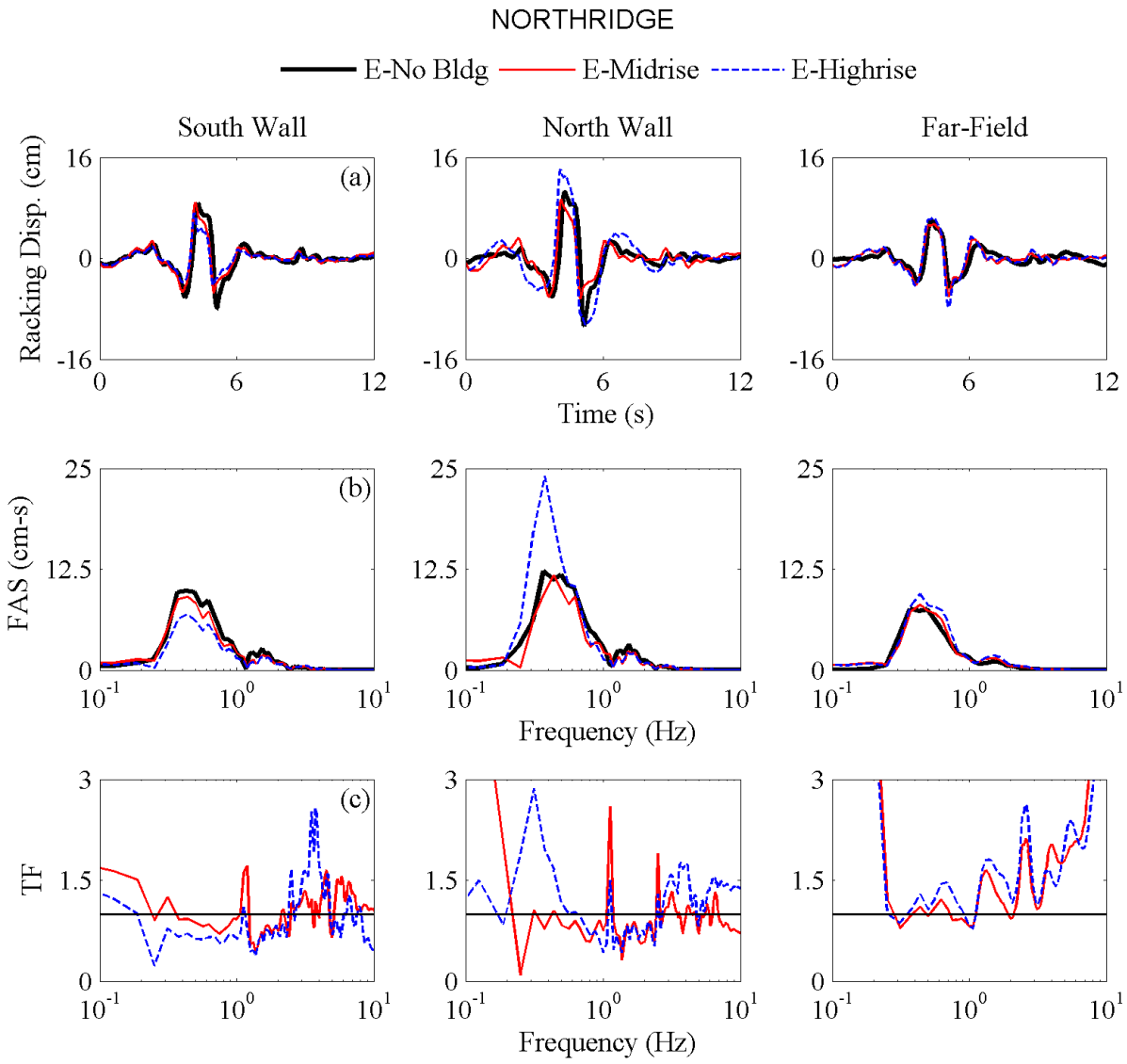

Figure 5.3-5. Northridge excavation and far-field racking displacements in the time and frequency domains.

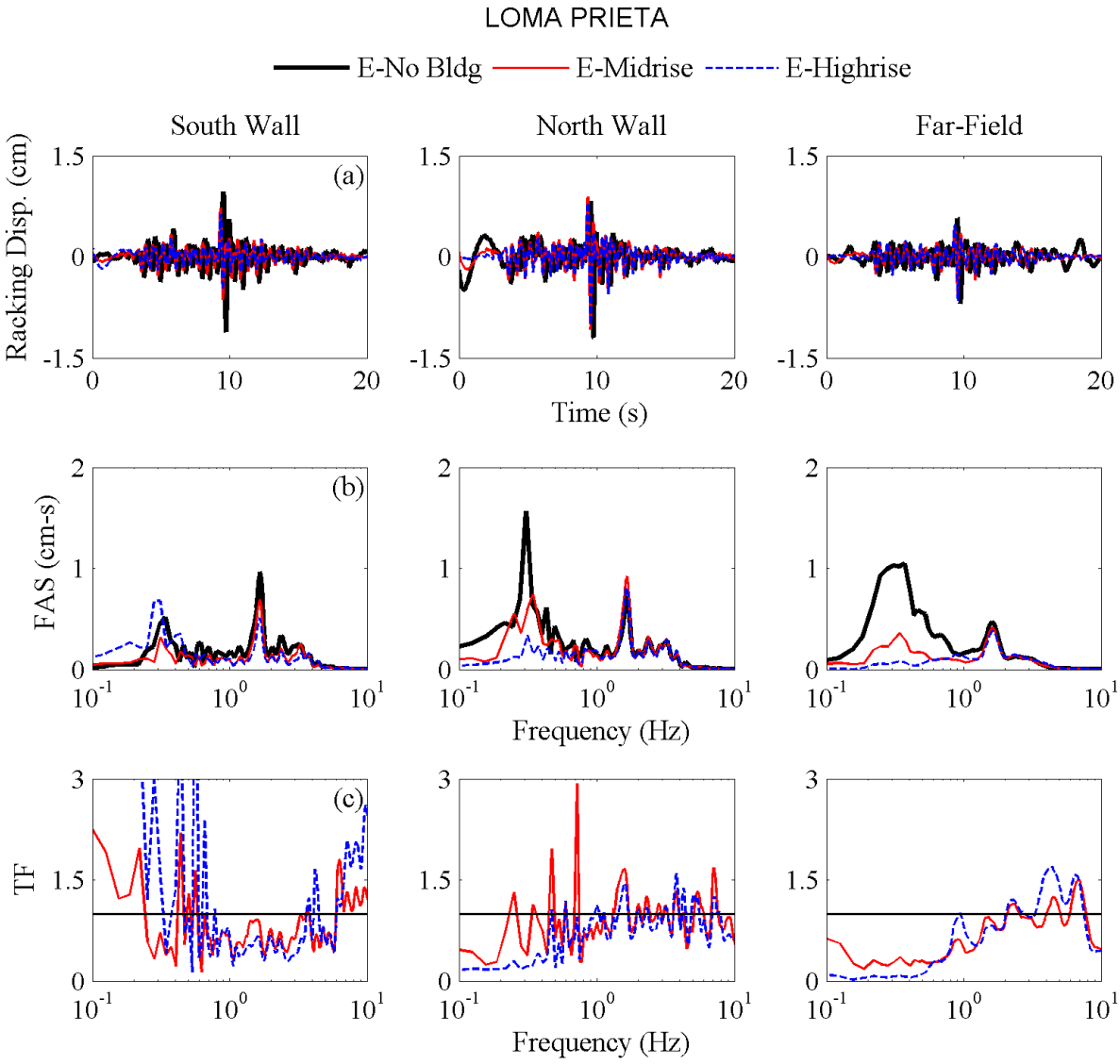

Figure 5.3-6. Loma Prieta excavation and free-field racking displacements in the time and frequency domains.

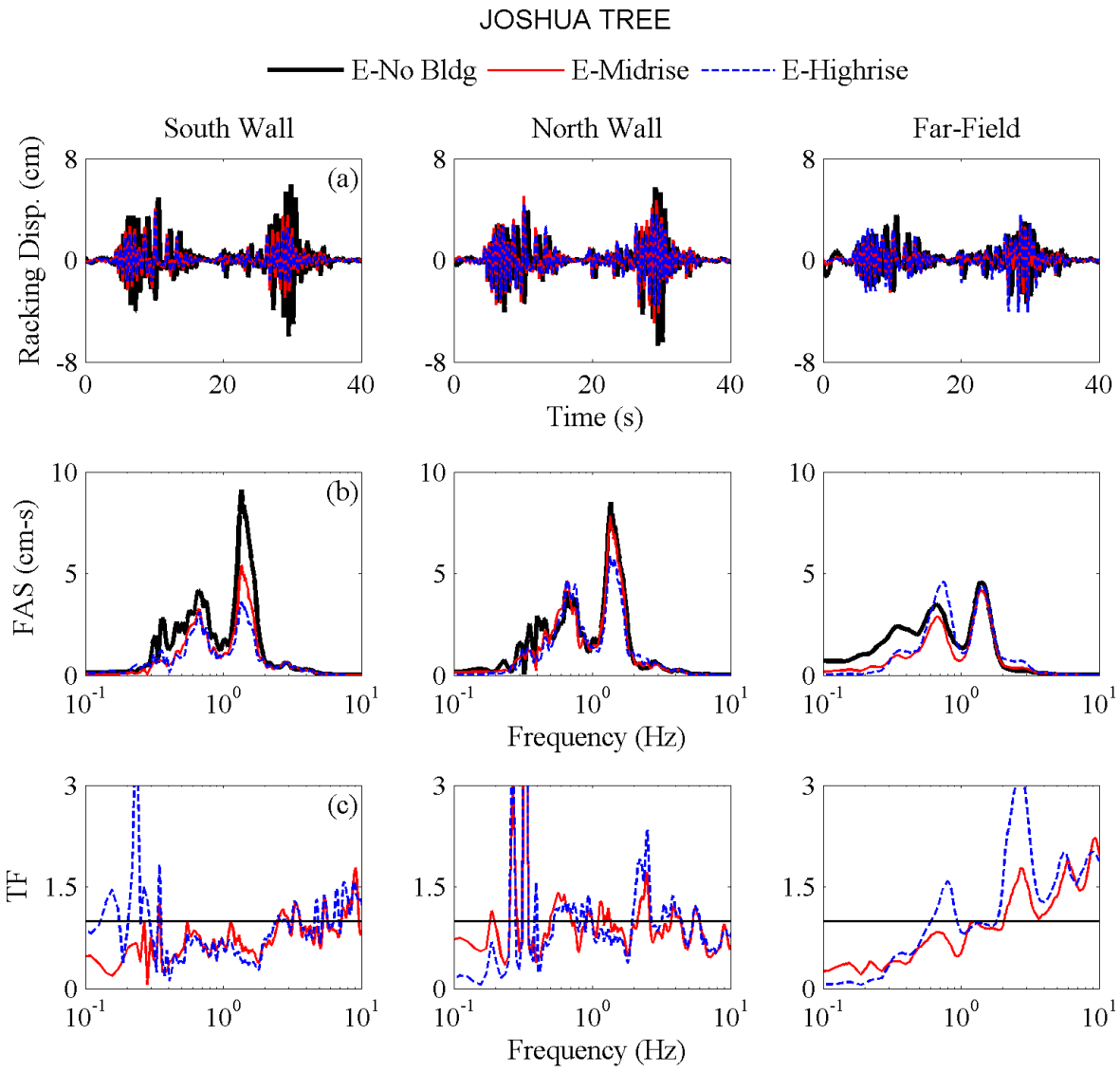

Figure 5.3-7. Joshua Tree excavation and free-field racking displacements in the time and frequency domains.

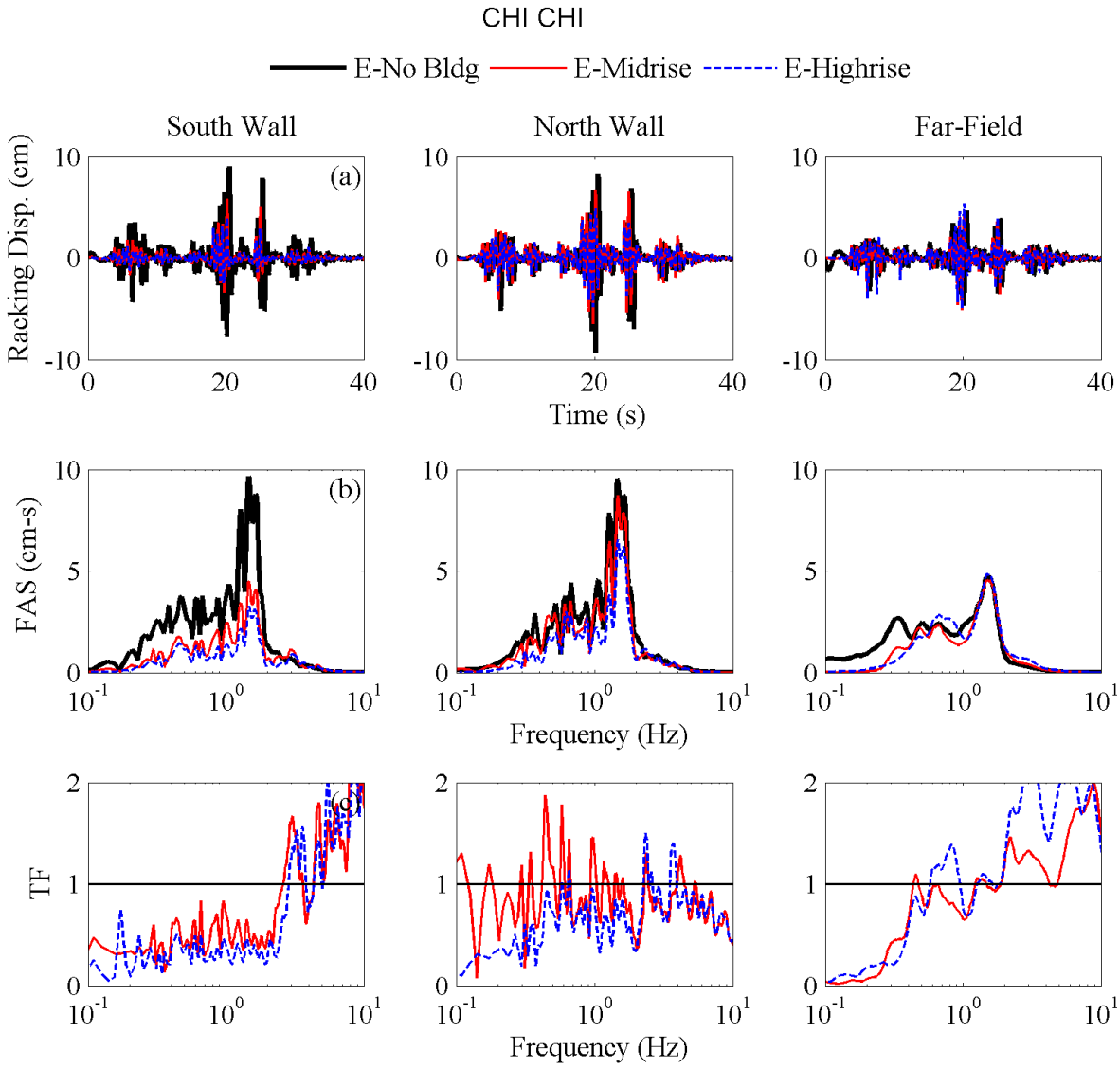

Figure 5.3-8. Chi Chi excavation and free-field racking displacements in the time and frequency domains.

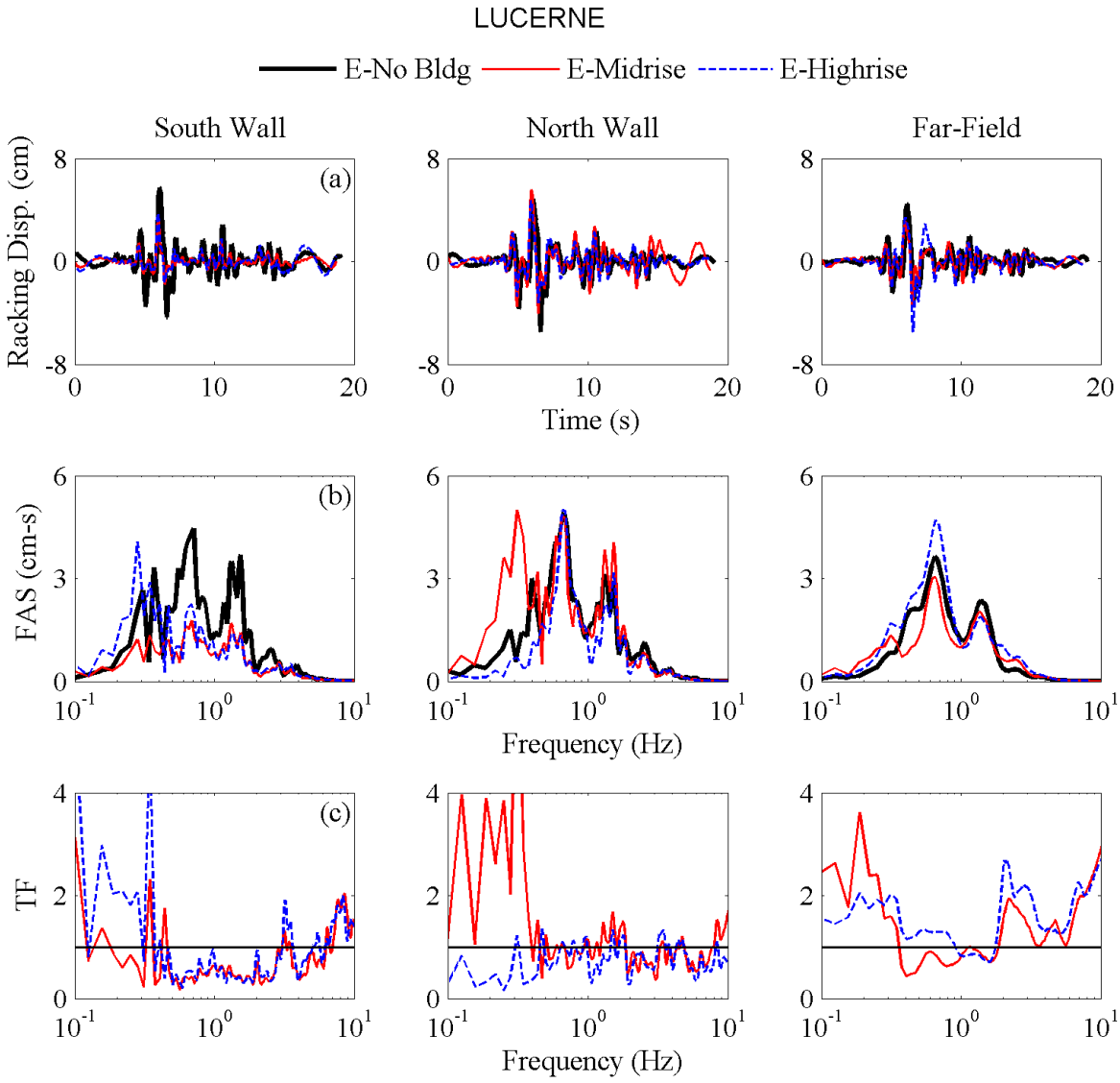

Figure 5.3-9. Lucerne excavation and free-field racking displacements in the time and frequency domains.

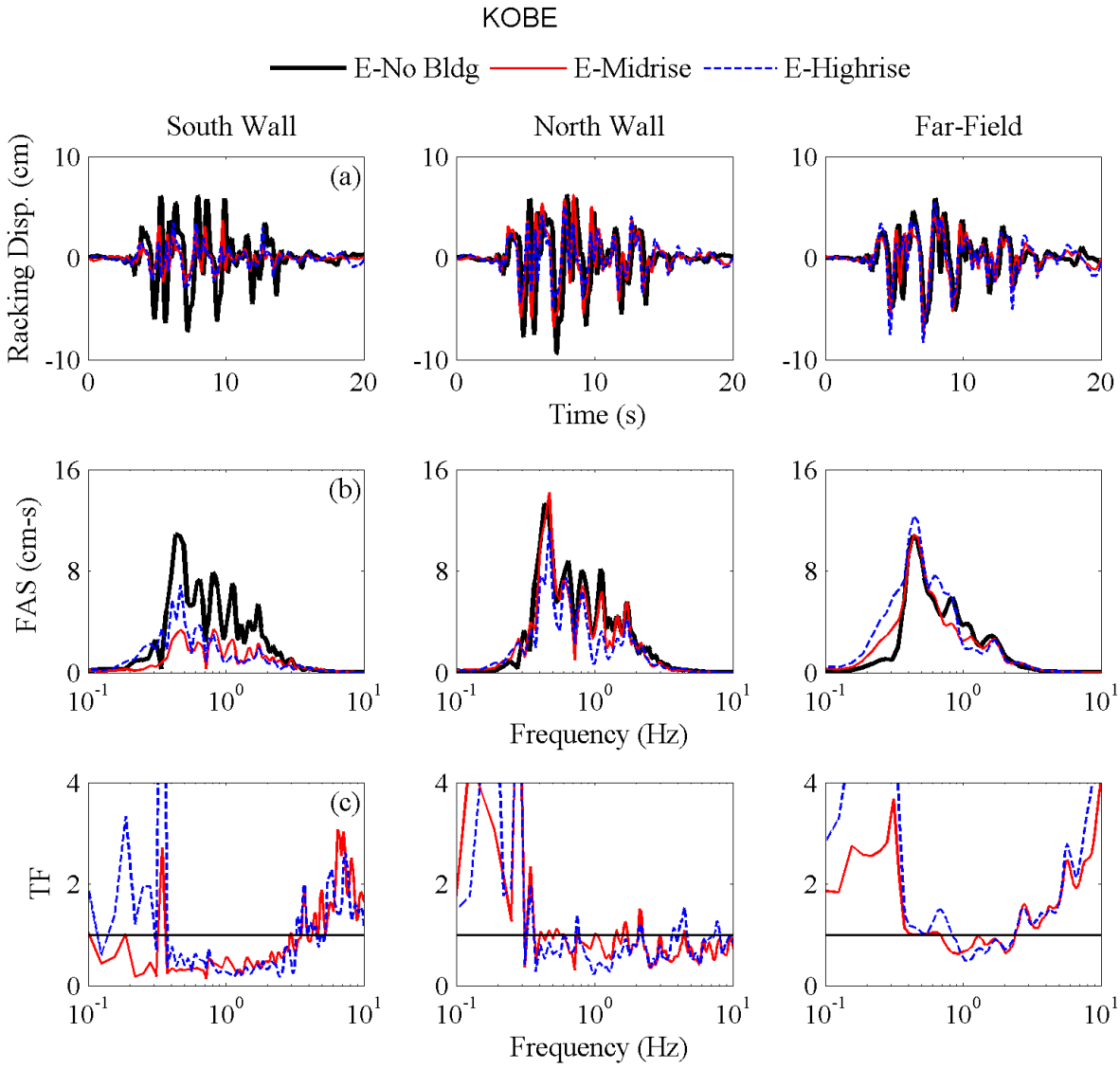

Figure 5.3-10. Kobe excavation and free-field racking displacements in the time and frequency domains.

5.3.4 Racking Versus Flexibility Ratio

The racking versus flexibility ratio values for the excavation walls were calculated in the same manner as they were for the tunnel structure as described in Section 4.3.3. To experimentally obtain the stiffness of the excavation walls alone, the walls were clamped to the edge of a sturdy table, and a known weight was suspended from the hanging edge of each plate and displacement

measured (Figure 5.3-11). Racking stiffness of the entire excavation (walls and struts included), however, was obtained numerically, which was then used in calculating the Flexibility Ratio (F).

The racking ratio (R) was estimated as the ratio of the maximum racking displacement measured on the excavation walls compared to that of the far-field soil during each motion and experiment. As shown previously, the presence of the buildings in E-Midrise and E-Highrise were observed to influence far-field racking displacements in the corresponding test. Therefore, in calculating R, far-field racking displacements were obtained from T-No Bldg in all cases, which was less affected by structures and container boundaries.

The relationship between R and F according to the NCHRP 611 guideline (Anderson et al. 2008), which is based on the results of dynamic finite element analyses, is presented in Figure 5.3-12 and Figure 5.3-13 (more information provided in Chapter 2). These figures also shows the R versus F values obtained during each excavation experiment during all six motions. A range of values for F are shown based on the different empirical methods used to modify Darendeli's modulus reduction curves, as discussed in the previous section. Figure 5.3-12 and Figure 5.3-13 show that values of R versus F followed the NCHRP 611 guideline closely in E-No Bldg, and a slight reduction in R was observed during all motions with the addition of a midrise and a highrise adjacent structure. These two figures also show the asymmetry of the excavation racking with the addition of an adjacent building.

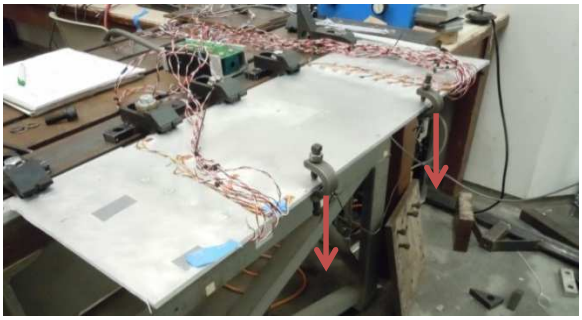

Figure 5.3-11. Experimentally testing the stiffness of the excavation walls alone (without struts).

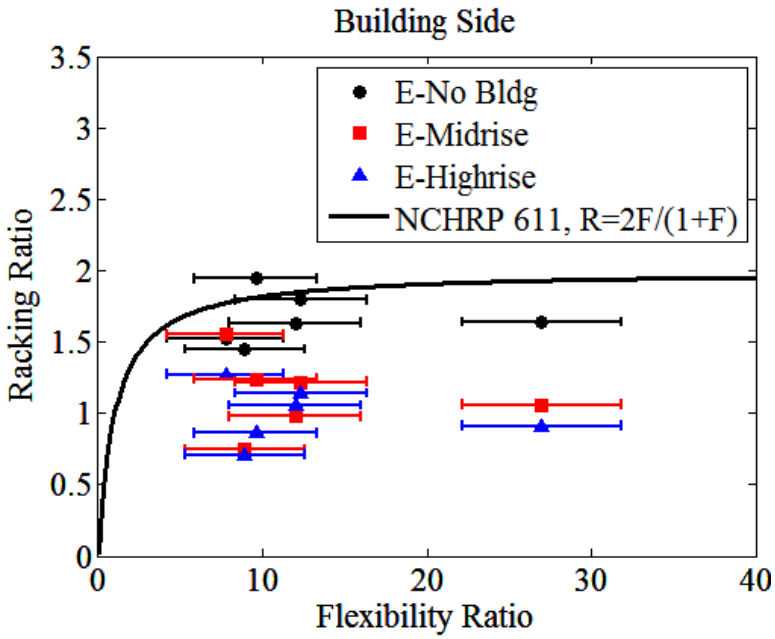

Figure 5.3-12. Excavation building side Racking versus Flexibility Ratios (R versus F) obtained experimentally compared to the NCHRP 611 guidelines. Far-field racking obtained from T-No Bldg.

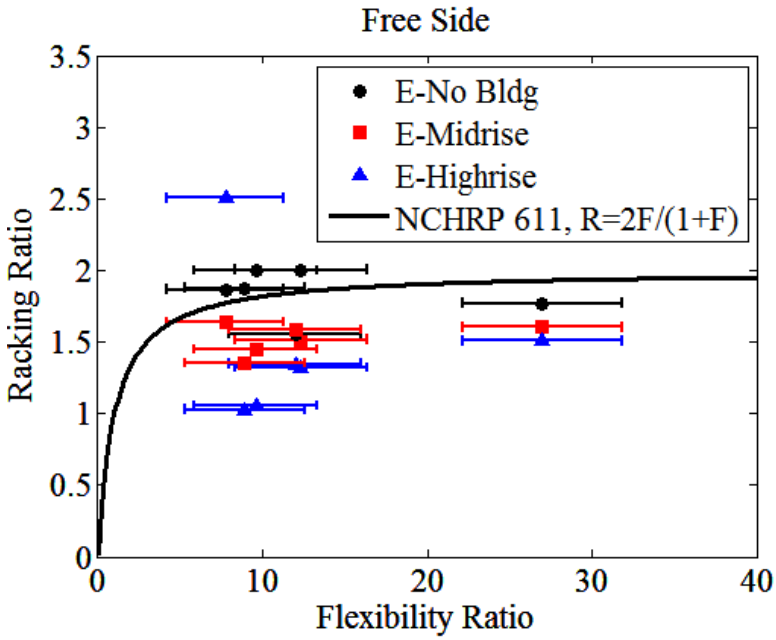

Figure 5.3-13. Excavation Free side Racking versus Flexibility Ratios (R versus F) obtained experimentally compared to the NCHRP 611 guidelines. Far-field racking obtained from T-No Bldg.

5.4 Excavation Bending and Strut Axial Strains

Strain gauges were placed on the excavation walls in two arrays and on centrally located excavation struts in a full-bridge configuration (Figure 4.4.1 through Figure 4.4.4). The goal of these instruments was to measure bending strains along the walls and axial strain in the struts during shaking, so that the excavation's strain response could be compared among the different experiments and motions.

5.4.1 Bending Strains and Moments on the Walls

Bending strains were obtained from strain gauges along the height of the excavation walls and expressed in terms of bending moments in prototype scale. The bending moment was calculated using the section properties of the excavation wall, i.e. wall thickness, length, and modulus of elasticity. The second moment of inertia about the neutral axis (I_x) of the excavation wall was calculated per unit length (1m in prototype scale) in the horizontal direction perpendicular to shaking. All calculations are performed in the prototype scale. The bending stress was calculated using the measured bending strains and the material's Young's modulus of elasticity, assuming that the walls stayed within their elastic range. It was assumed that all strains recorded by the strain gauges were purely due to bending, and not axial deformation. Figure 5.4-4 through Figure 5.4-9 show the initial static, total (static + dynamic), and dynamic increment of bending moments on the excavation walls during six ground motions in E-No Bldg, E-Midrise, and E-Highrise. Total and dynamic bending moments are shown at the instance of time when the maximum dynamic moment was recorded on that wall (when one strain gauge recorded maximum dynamic strain). Static moment profiles are presented in these tests, because the drift problem observed previously on the tunnel was not an issue here.

The following trends were identified from the following figures:

- Both static and dynamic bending moments increased significantly in E-Midrise and E-Highrise compared to E-No Bldg.
- In the later ground motions, Joshua Tree, Lucerne, and Kobe, the bending moment amplitudes were greater on the building (south) side of the excavation wall compared to the free (north) side.
- The increase in dynamic bending strains and moments with the addition of an adjacent tall building, particularly on the building side, did not translate into a larger wall deflection (as discussed in the previous section).

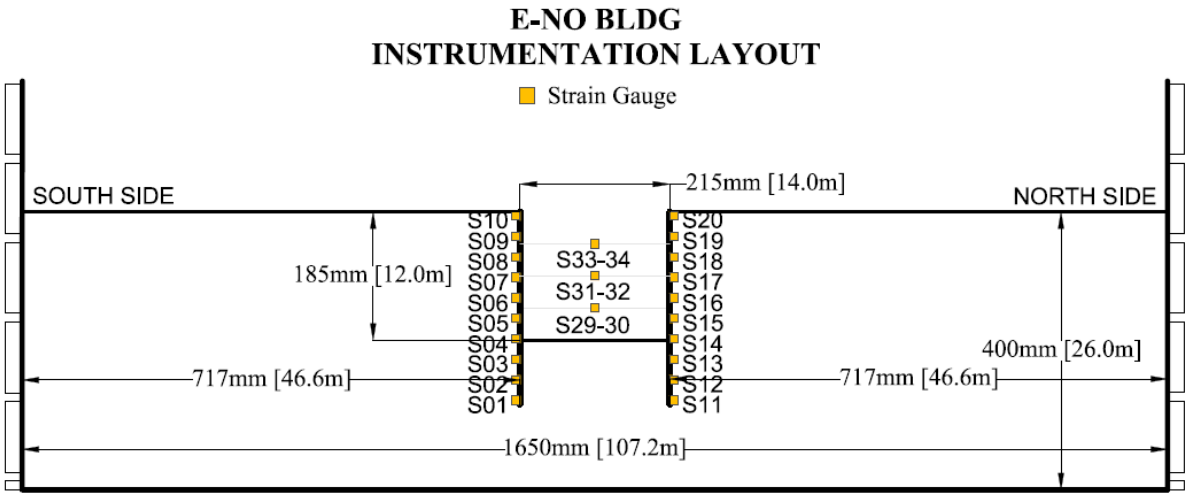

Figure 5.4-1. E-No Bldg elevation view of strain gauges mounted on the excavation walls and struts.

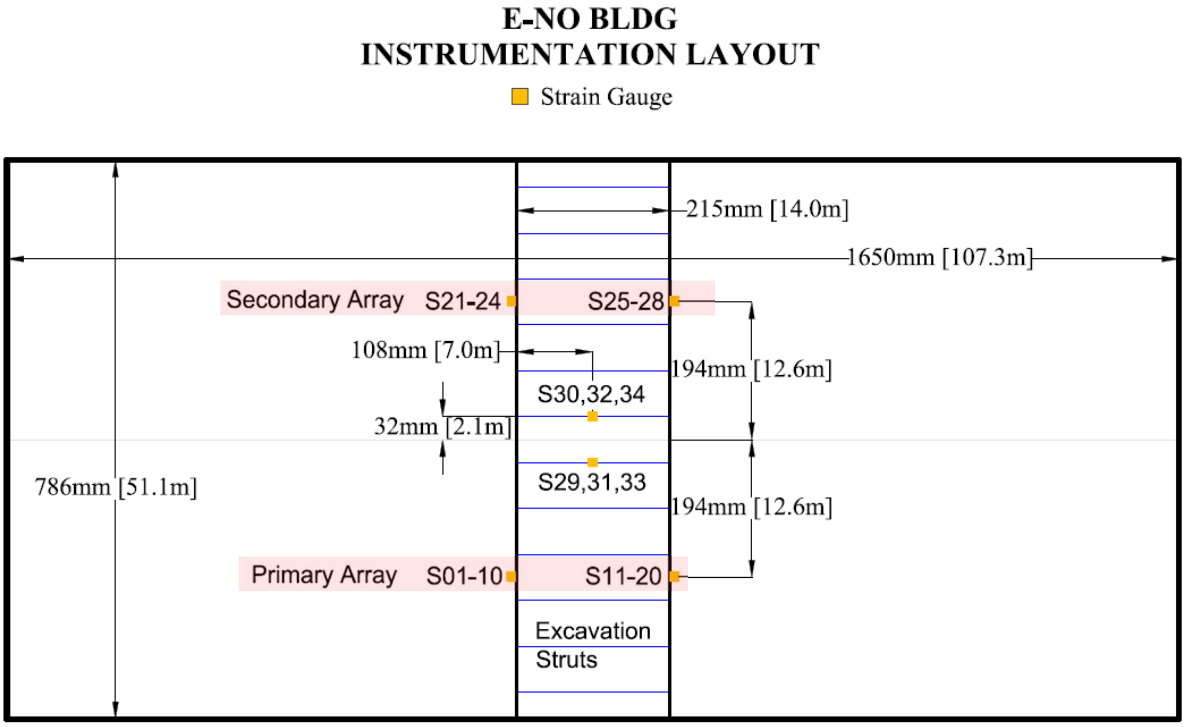

Figure 5.4-2. E-No Bldg plan view of strain gauges mounted on the excavation walls and struts.

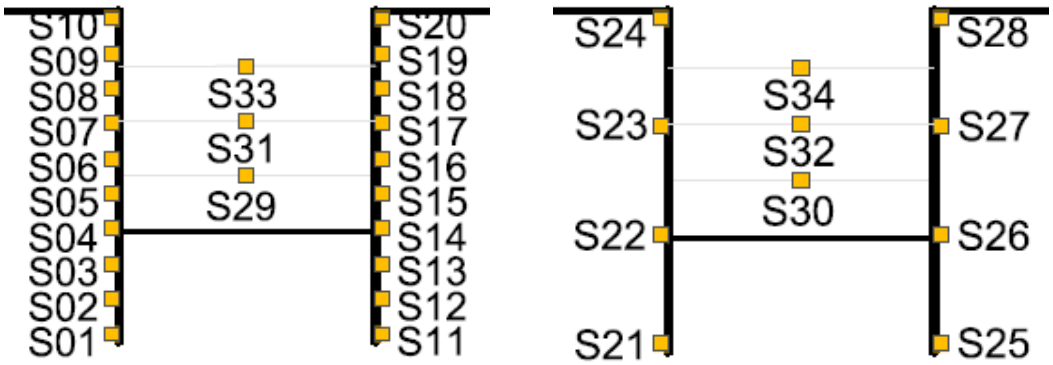

(a) (b)

Figure 5.4-3. Elevation view of excavation strain gauges: (a) primary array; and (b) secondary array.

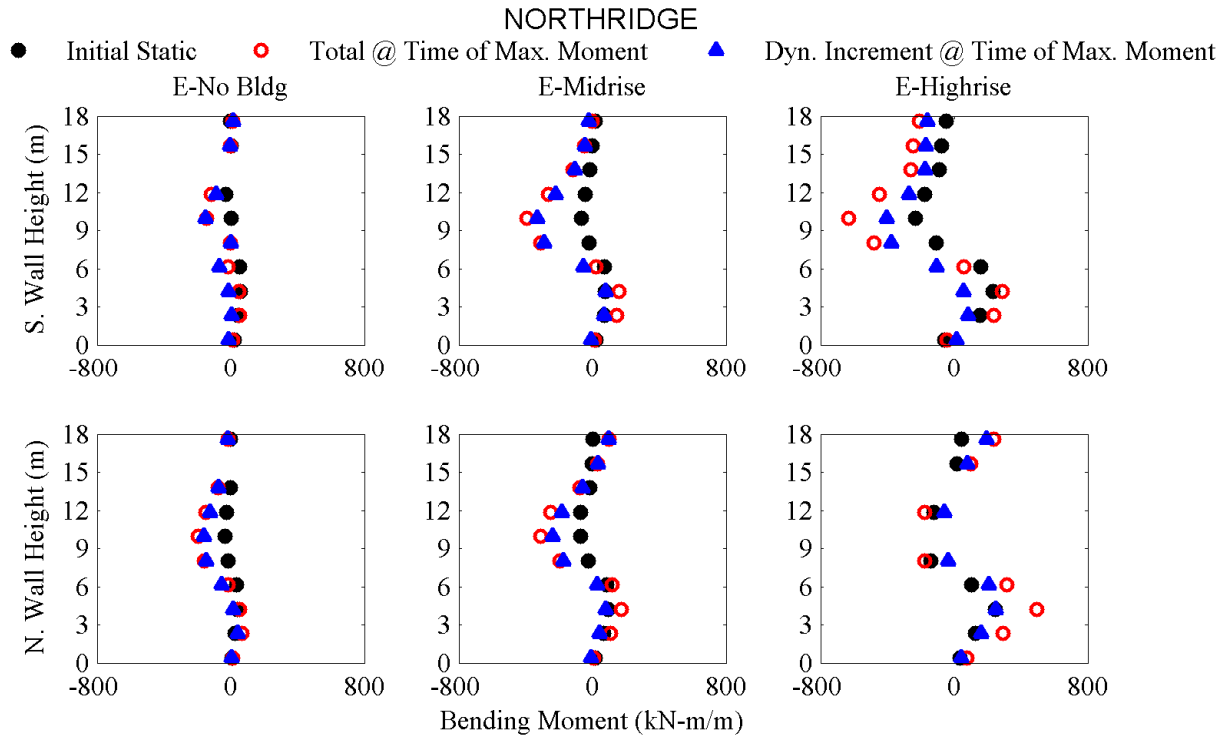

Figure 5.4-4. Initial static, total and dynamic bending moments shown on the south (bldg. side) and north (free side) excavation walls at the time of maximum moment on that wall.

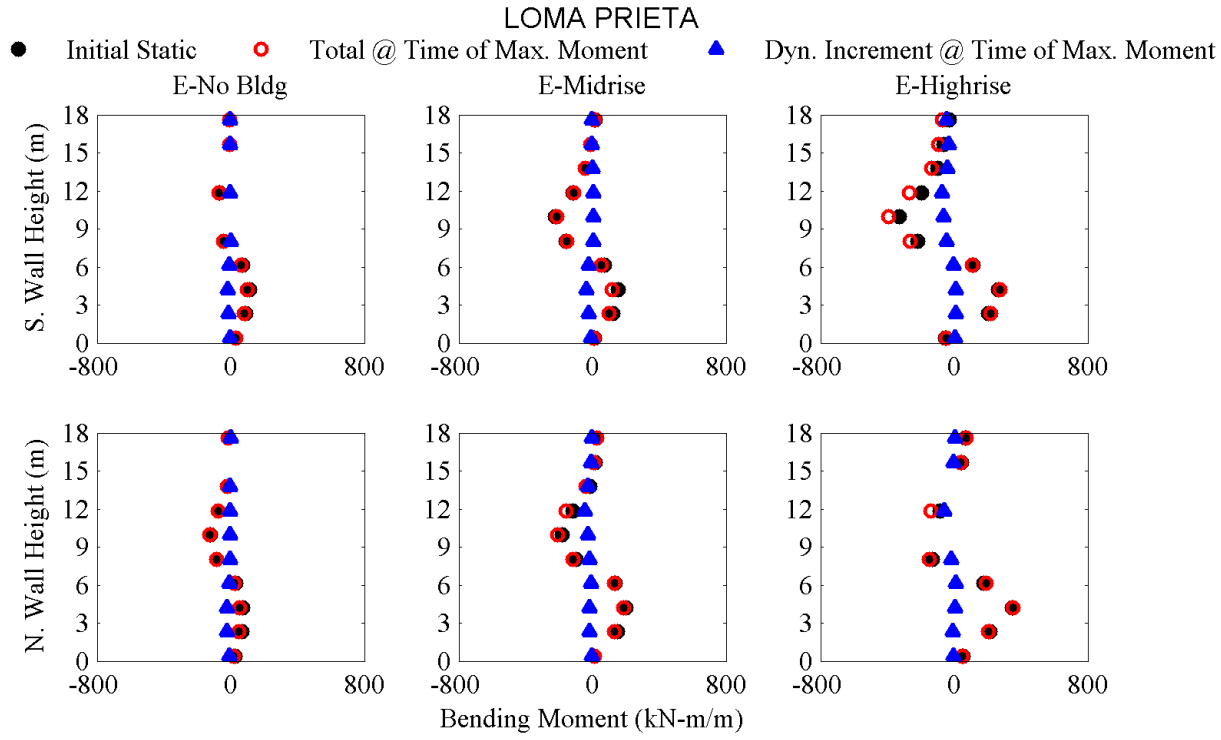

Figure 5.4-5. Initial static, total and dynamic bending moments shown on the south (bldg. side) and north (free side) excavation walls at the time of maximum moment on that wall.

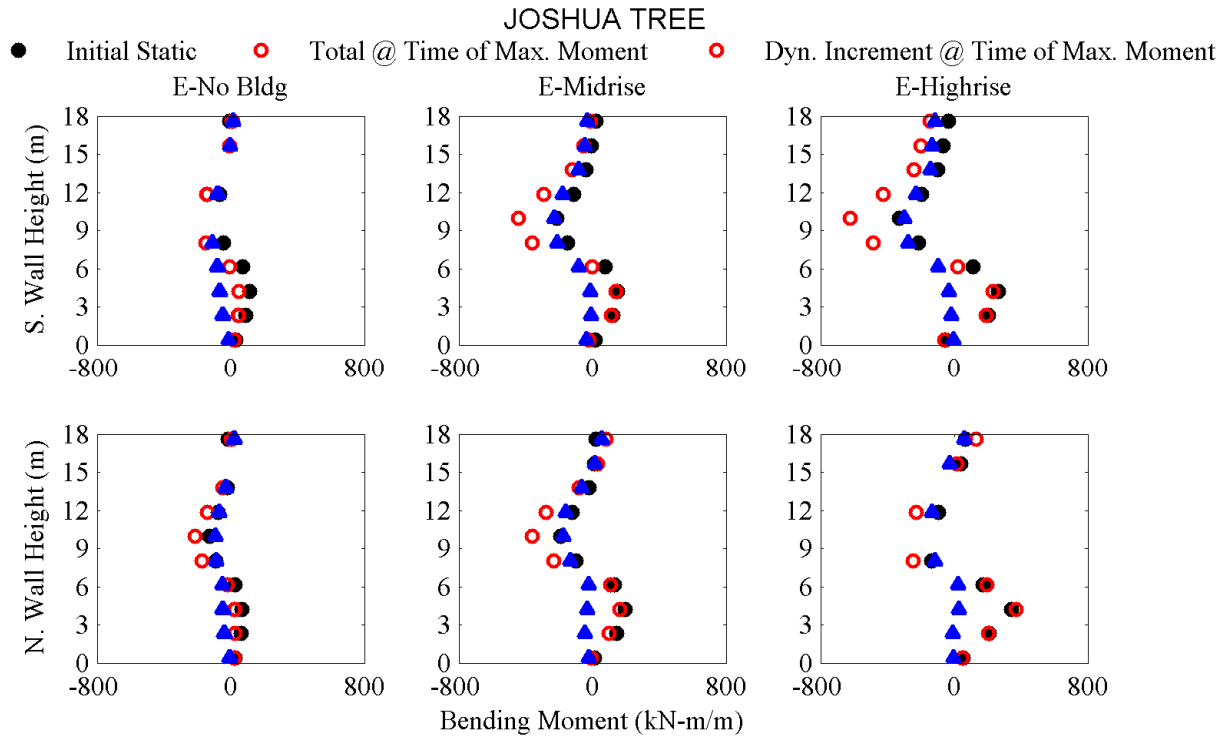

Figure 5.4-6. Initial static, total and dynamic bending moments shown on the south (bldg. side) and north (free side) excavation walls at the time of maximum moment on that wall.

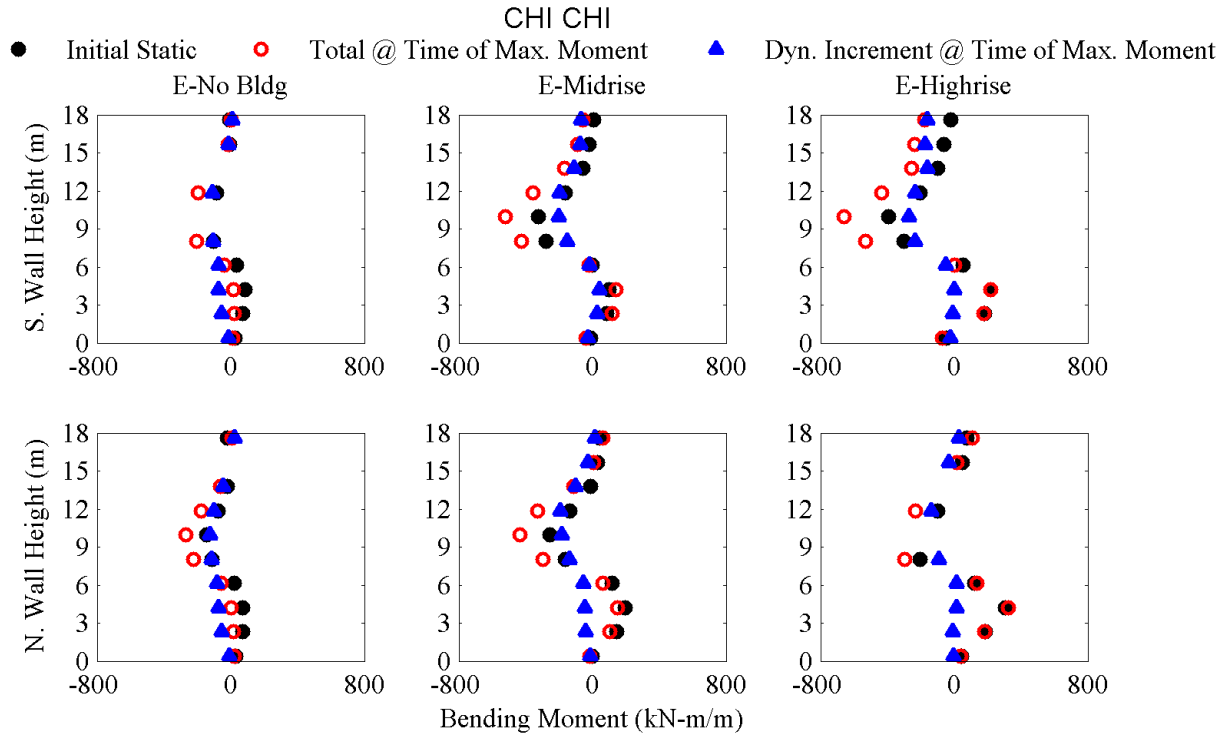

Figure 5.4-7. Initial static, total and dynamic bending moments shown on the south (bldg. side) and north (free side) excavation walls at the time of maximum moment on that wall.

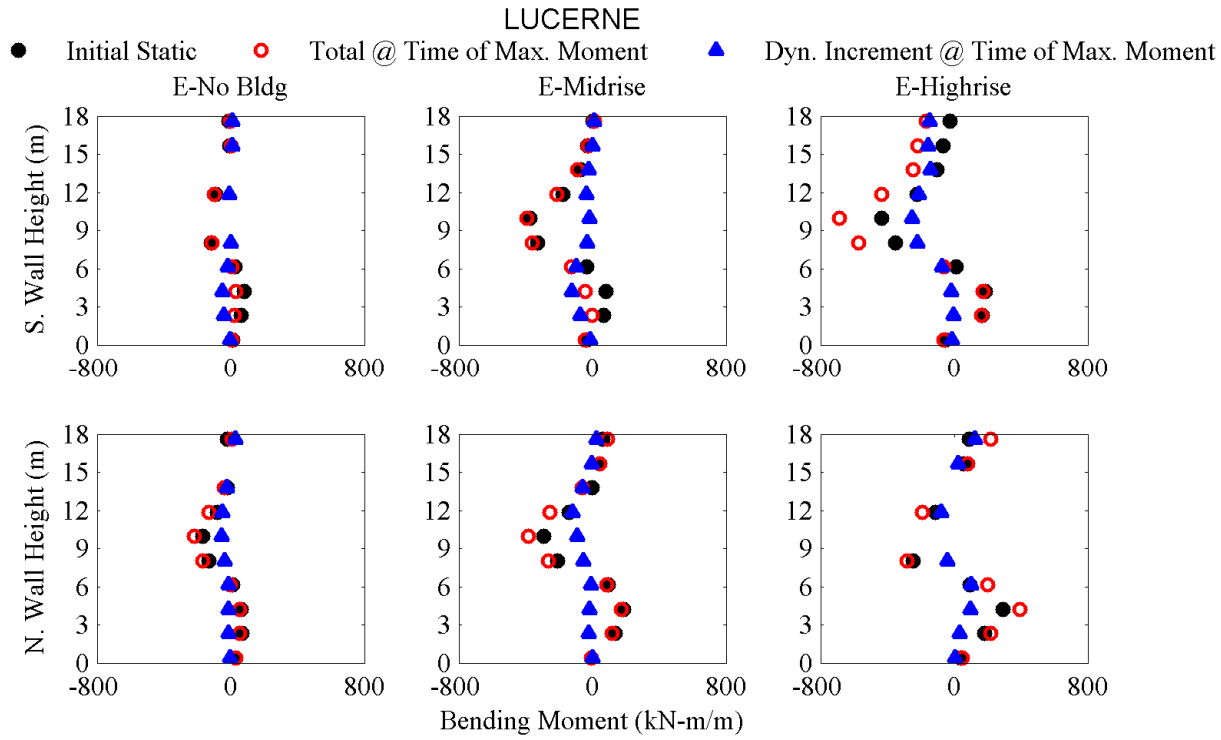

Figure 5.4-8. Initial static, total and dynamic bending moments shown on the south (bldg. side) and north (free side) excavation walls at the time of maximum moment on that wall.

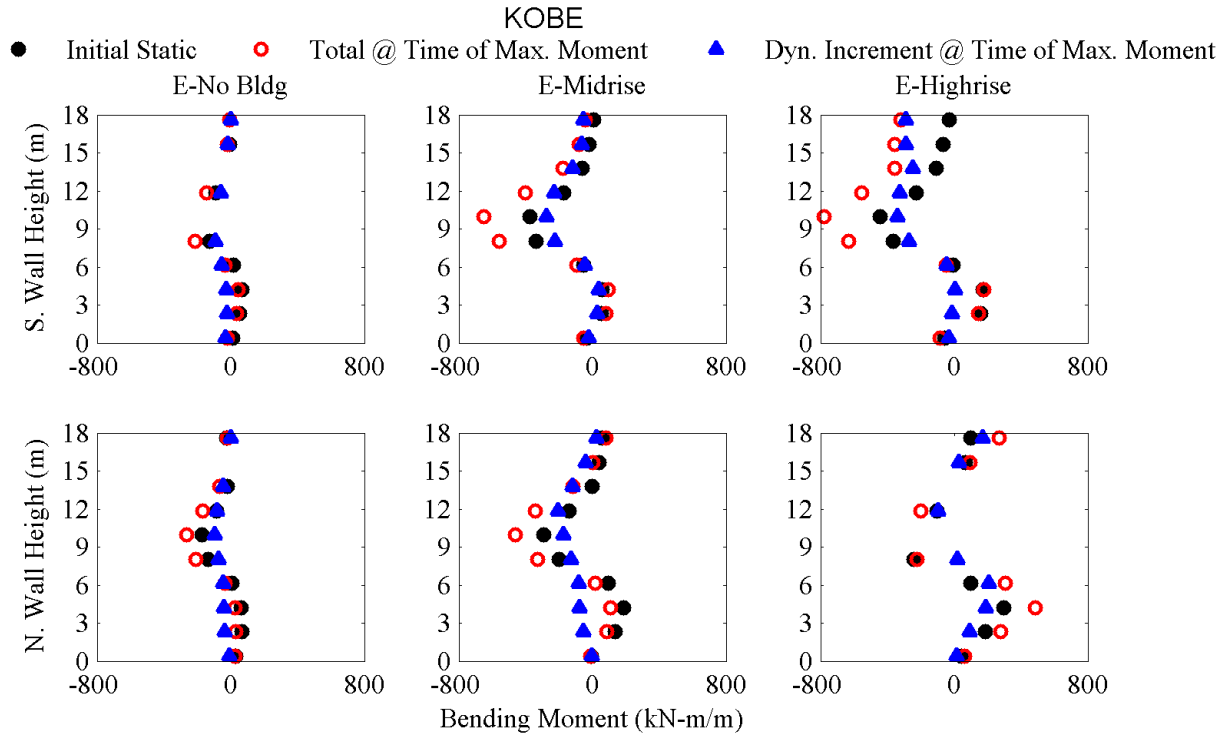

Figure 5.4-9. Initial static, total and dynamic bending moments shown on the south (bldg. side) and north (free side) excavation walls at the time of maximum moment on that wall.

5.4.2 Axial Forces on the Excavation Struts

Axial force time histories were computed from the axial strain measurements on the excavation struts during each shake and experiments: $Axial\ Force = E * A * \varepsilon$, where, E is the Young's Modulus, A is the cross sectional area of the hollow pipe strut, and ε is the measured axial strain in the strut . Axial forces recorded on the struts are compared between E-No Bldg and E-Highrse during three representative ground motions in Figure 5.4-10 and Figure 5.4-11. Figure 5.4-12 through Figure 5.4-17 present the same data shown in Figure 5.4-10 through Figure 5.4-11 using points of initial static, maximum total, and the dynamic increment of axial force in the struts for all ground motions. Unfortunately, data from the axial strain gauges did not save in E-Midrise, which are excluded from these figures. In general, greater static and dynamic axial forces were measured on struts at lower elevations in the excavation and in E-Highrise compared to E-No Bldg.

In summary, it was shown that racking deformations of the excavation walls reduced with the presence of an adjacent midrise or highrise building. The racking deformation patterns, however, became asymmetric with the addition of the adjacent tall building. The bending moment and axial force profiles presented in this section, on the other hand, show that the adjacent structure strongly amplified static and dynamic forces experienced on the excavation walls and struts. These results too point to an asymmetric distribution of bending moment: greater moments were observed on the building side of the excavation in E-Midrise and E-Highrise. The results show that despite the significant increase in static and seismic forces, the performance of the excavation as a whole did not get worse and in fact, deflections (measured by racking) slightly decreased.

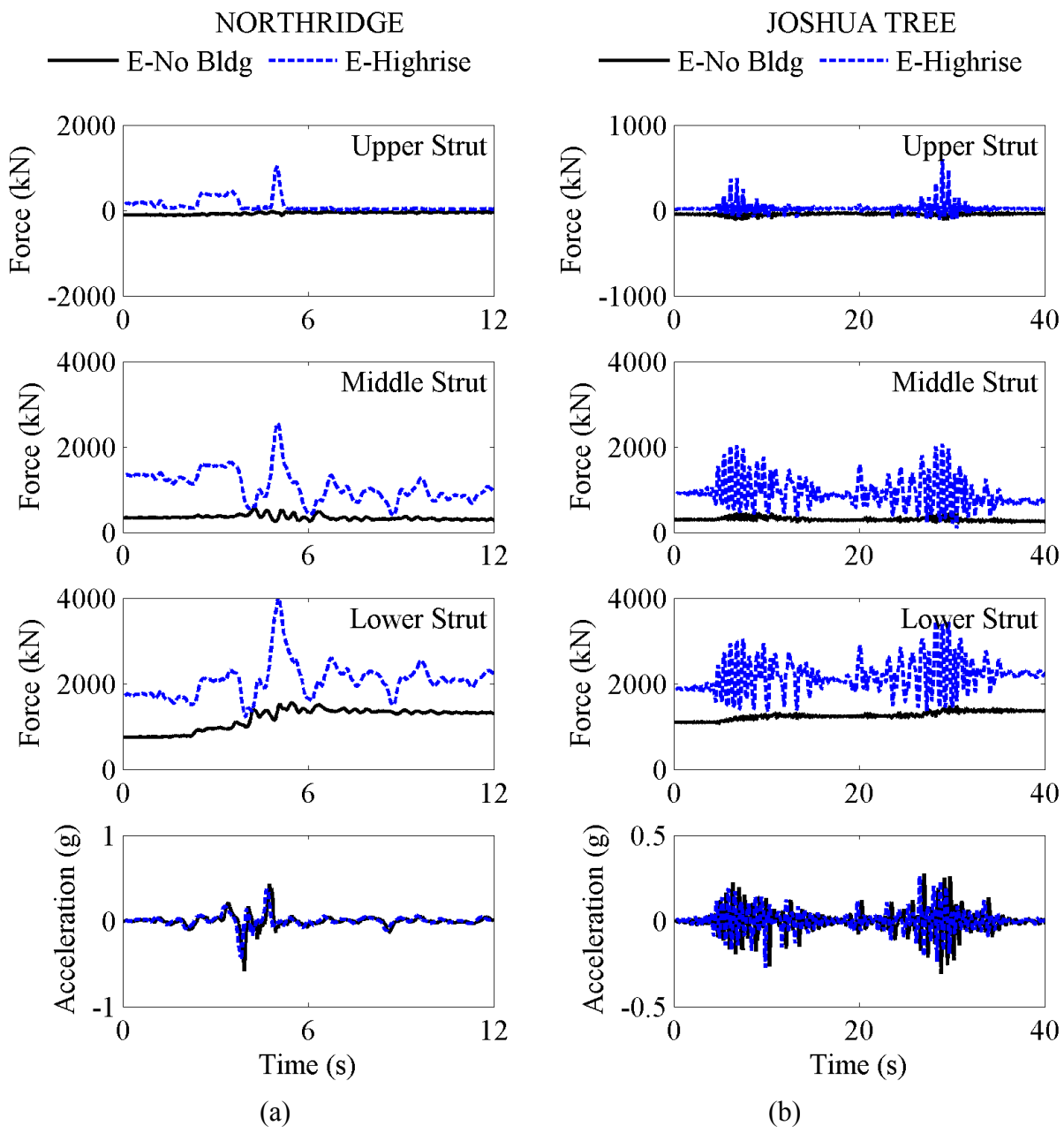

(a) (b)

Figure 5.4-10. Excavation strut axial force time histories in E-No Bldg and E-Highrise during the (a) Northridge; and (b) Joshua Tree motions.

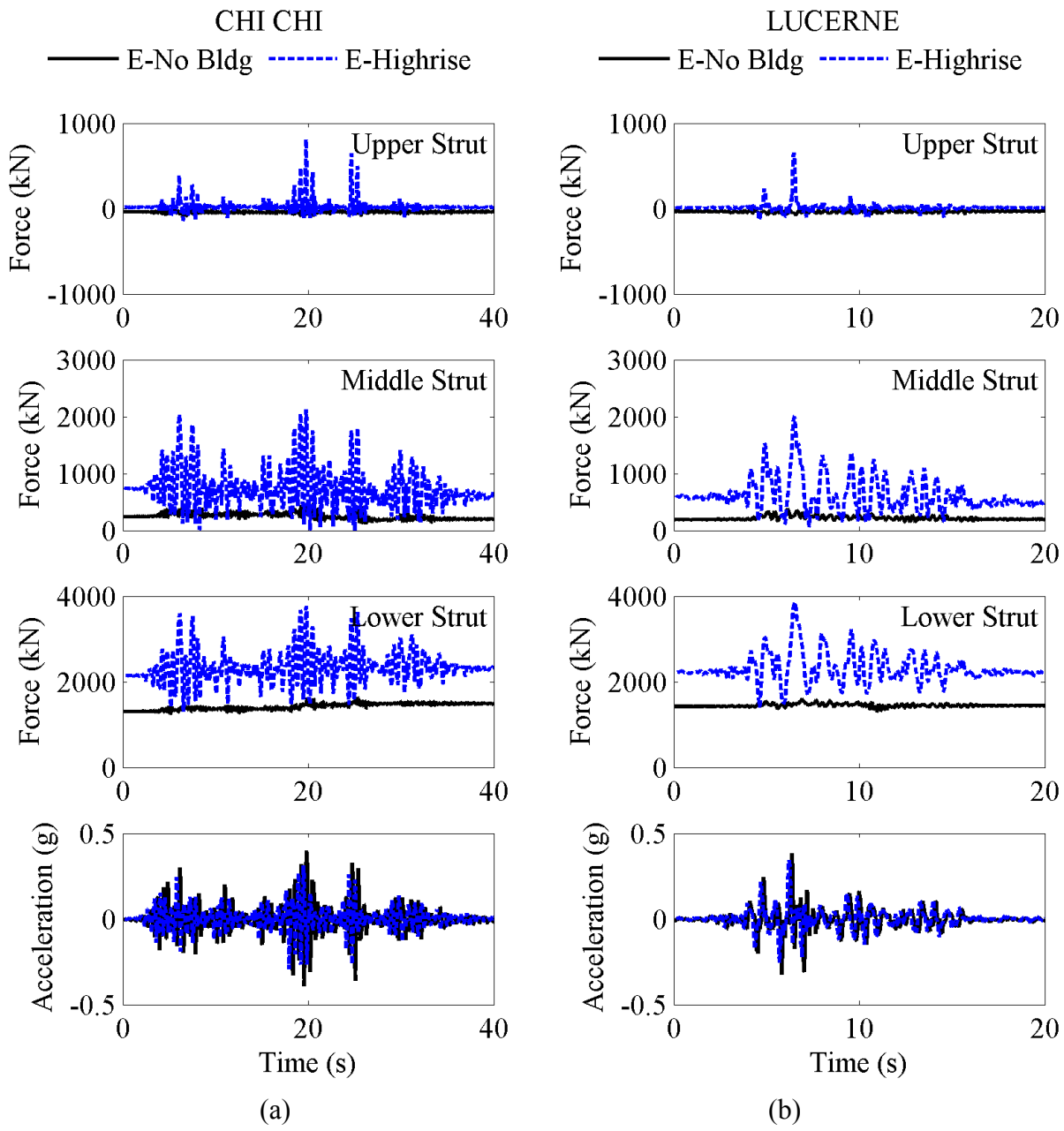

Figure 5.4-11. Excavation strut axial force time histories in E-No Bldg and E-Highrise during the (a) Chi Chi; and (b) Lucerne motions.

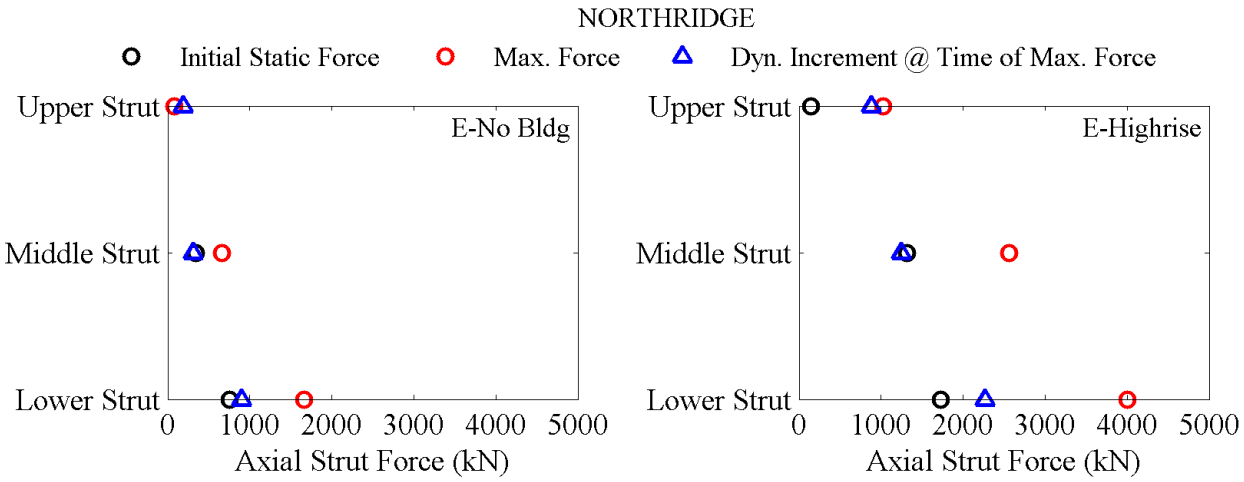

Figure 5.4-12. Initial, maximum and dynamic forces in the excavation struts.

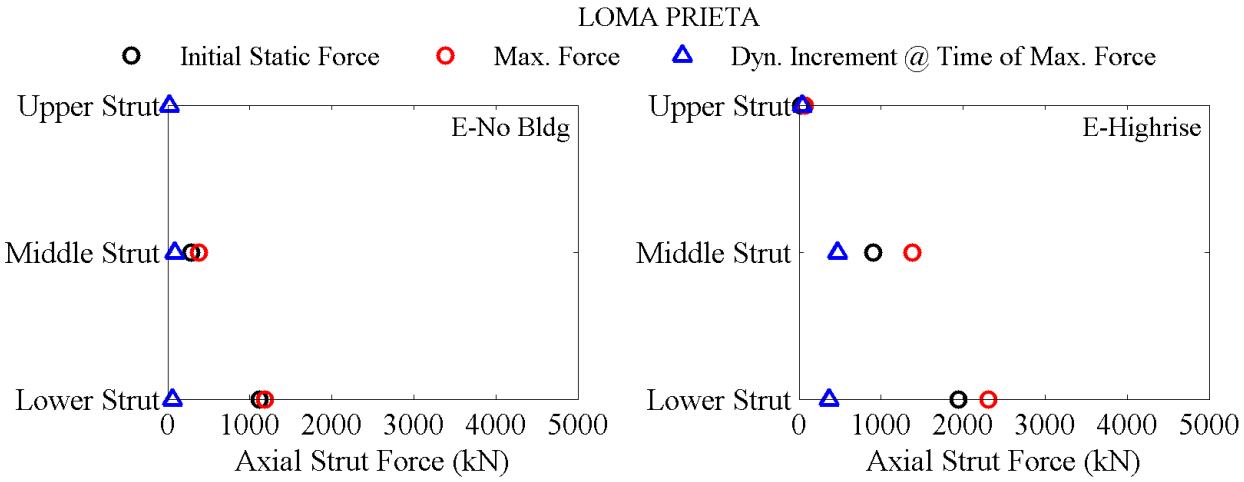

Figure 5.4-13. Initial, maximum and dynamic forces in the excavation struts.

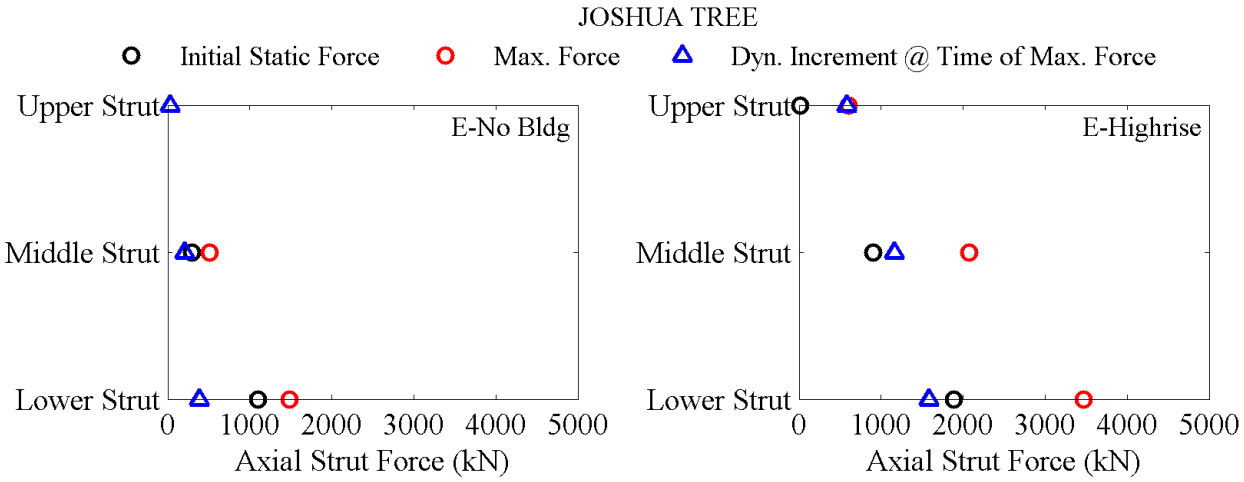

Figure 5.4-14. Initial, maximum and dynamic forces in the excavation struts.

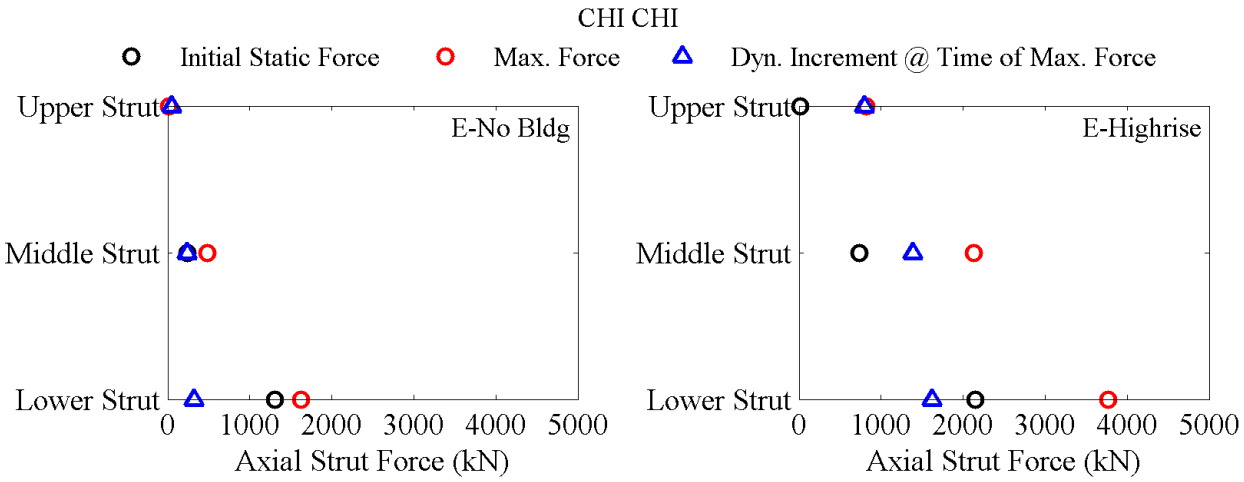

Figure 5.4-15. Initial, maximum and dynamic forces in the excavation struts.

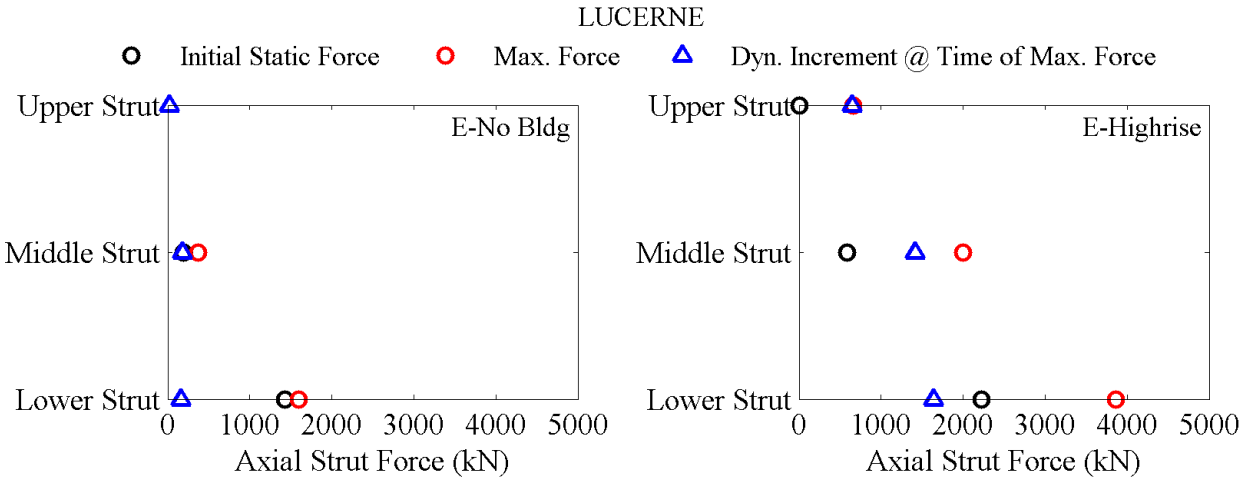

Figure 5.4-16. Initial, maximum and dynamic forces in the excavation struts.

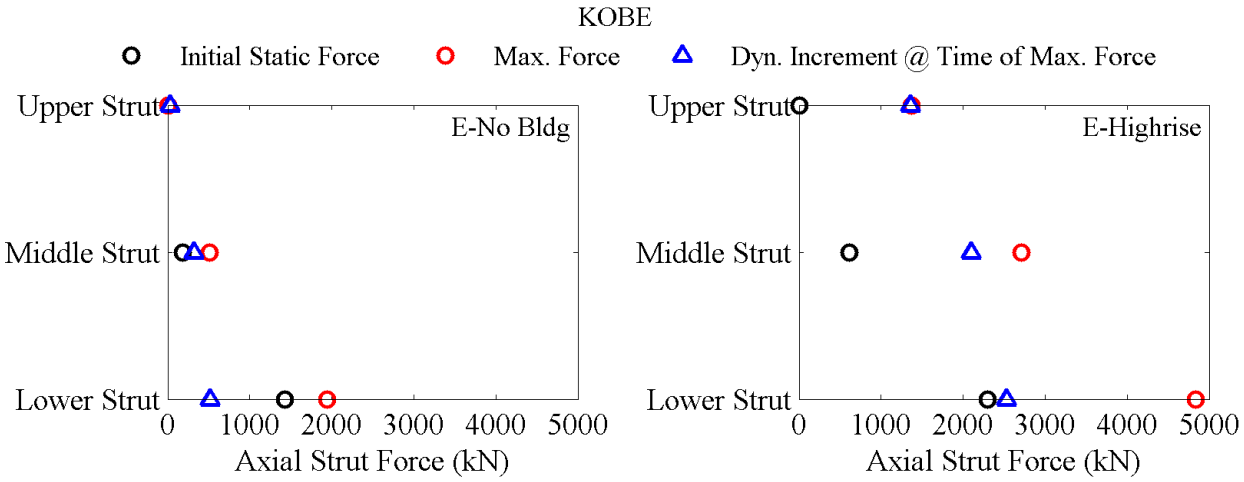

Figure 5.4-17. Initial, maximum and dynamic forces in the excavation struts.

5.5 Lateral Earth Pressures

5.5.1 Setup

Lateral earth pressures were measured on the excavation walls using tactile pressure sensors. The pressure sensors were conditioned, equilibrated, and statically and dynamically calibrated using methods outlined in Chapter 3. All excavation experiments used four tactile pressure sensors. In E-No Bldg, three pressure sensors were located on the north wall and one was placed on the south wall (Figure 5.5-1). For E-Midrise and E-Highrise, two sensors were affixed to each of the excavation walls (Figure 5.5-2). All sensors were located on the outside of each wall to measure the interaction between the wall and the backfill soil.

The lateral thrust acting on the excavation walls was calculated by integrating the data from tactile sensors along the wall above the base of the excavation only (since no pressure recordings were available below the excavation in the embedded area). Because the sensors did not cover the entire height of the wall, the pressure profile was extrapolated based on a linear fit of the pressure data to extend from the top to the base of the excavation before integrating the profile to obtain thrust.

5.5.2 Pressure Measurement Challenges

As mentioned previously, because of the low SNR of the high capacity tactile sensors used on the building side of E-Highrse, the recordings were less reliable in this case. Therefore, with the exception of an initial comparison of dynamic thrusts, the building side pressure profiles in E-Highrise will not be presented in this section, similar to T-Highrise. Instead, only the free side pressures will be presented, assuming that they are roughly similar on the building and free sides of the excavation.

5.5.3 Dynamic Earth Pressures and Thrust

Figure 4.5.4 shows the dynamic thrust time histories on the two sides of the excavation walls in E-Midrise and E-Highrise compared to the case with no building (E-No Bldg) during a representative motion (Northridge). This plot is presented because good recordings were obtained from both sides of the wall in E-Highrise. However, for many of the other motions of E-Highrise, noise from the building side sensor impaired the thrust measurement and therefore it was difficult to tell if dynamic thrust increased and decreased together on the two sides of the wall similar to the tunnel tests when the adjacent structure was present.

Figure 5.5-4 through Figure 5.5-9 show the dynamic lateral thrust time histories in E-No Bldg, E-Midrise, and T-Highrise during different motions. The south or building side is presented in E-Midrise, and the free side is presented in T-Highrise (due to its higher resolution and SNR). In E-No Bldg, the north wall side is presented only because the south wall only contained one pressure sensor. The maximum dynamic thrust and its corresponding time is identified in each figure. The "time of maximum thrust" in these figures corresponds to the time at which maximum positive dynamic thrust was recorded, because this is when the excavation experienced lateral earth pressures greater than static.

The second row of Figure 5.5-4 through Figure 5.5-9 presents the static and total (static and dynamic) lateral earth pressures on both sides of the wall at the time of maximum thrust. Theoretical static earth pressure profiles under active and at-rest conditions expected for this soil are plotted as well for comparison. Using equations Eq. 4.5-1 and Eq. 4.5-2, K_a and K_o values were calculated as 0.29 and 0.46, assuming a friction angle (ϕ') of 33^o for Nevada Sand at a relative density of about 55% (Prevost 1993).

Similar to the experiments with the tunnel, the dynamic thrusts were larger on both sides of the wall when the adjacent midrise or highrise buildings were present. This trend was consistent with the greater axial loads recorded on the struts (particularly lower struts) and larger bending moments along the excavation walls with the addition of an adjacent tall building, as discussed in the previous section. In many cases, the static and dynamic earth pressures reduced near the bottom of the excavation (below the lowest strut level), which is consistent with the literature on braced excavations.

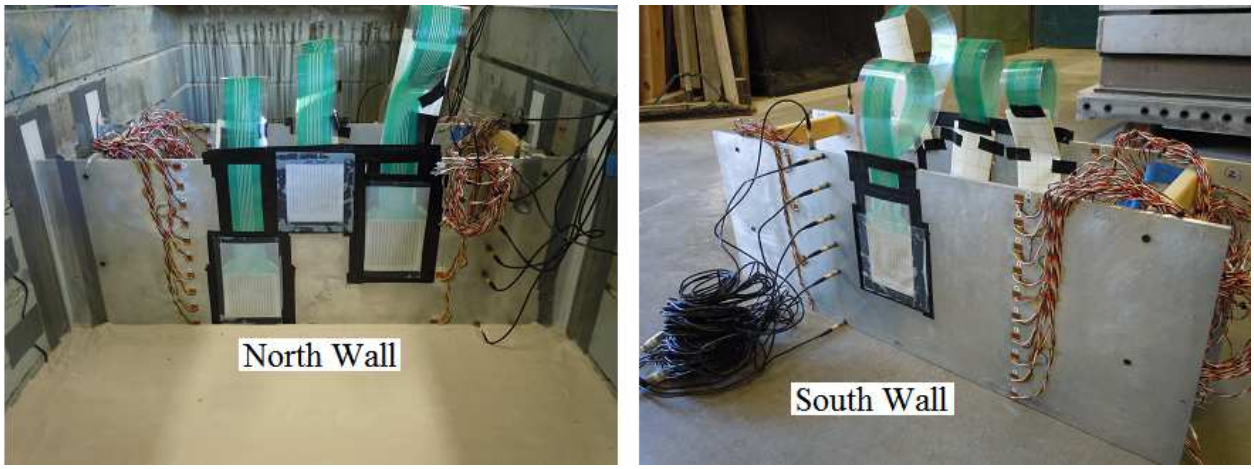

Figure 5.5-1. Tactile pressure sensors shown on the excavation walls in the E-No Bldg test.

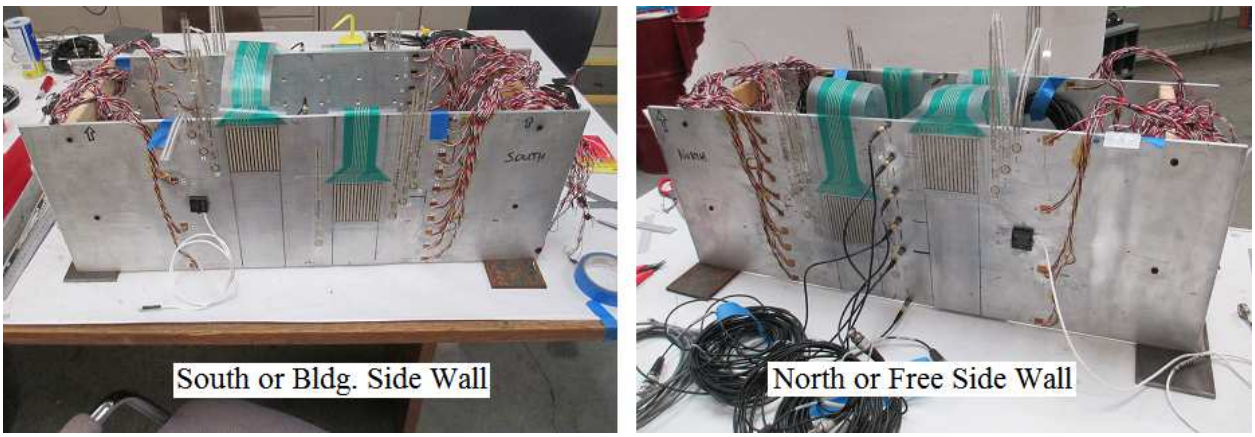

Figure 5.5-2. Excavation wall tactile pressure sensor locations in E-Midrise and E-Highrise.

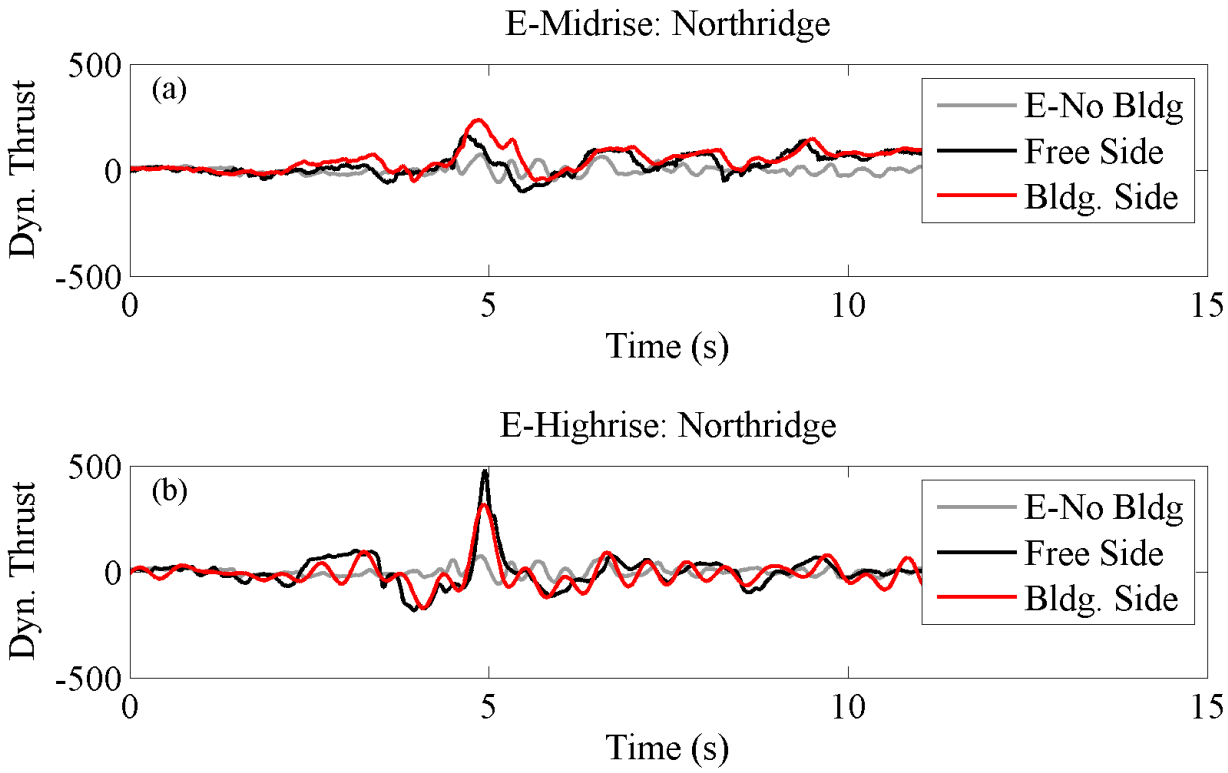

Figure 5.5-3. Dynamic thrust time histories on the two sides of the wall in: (a) E-Midrise; (b) E-Highrise compared to the thrust in T-No Bldg.

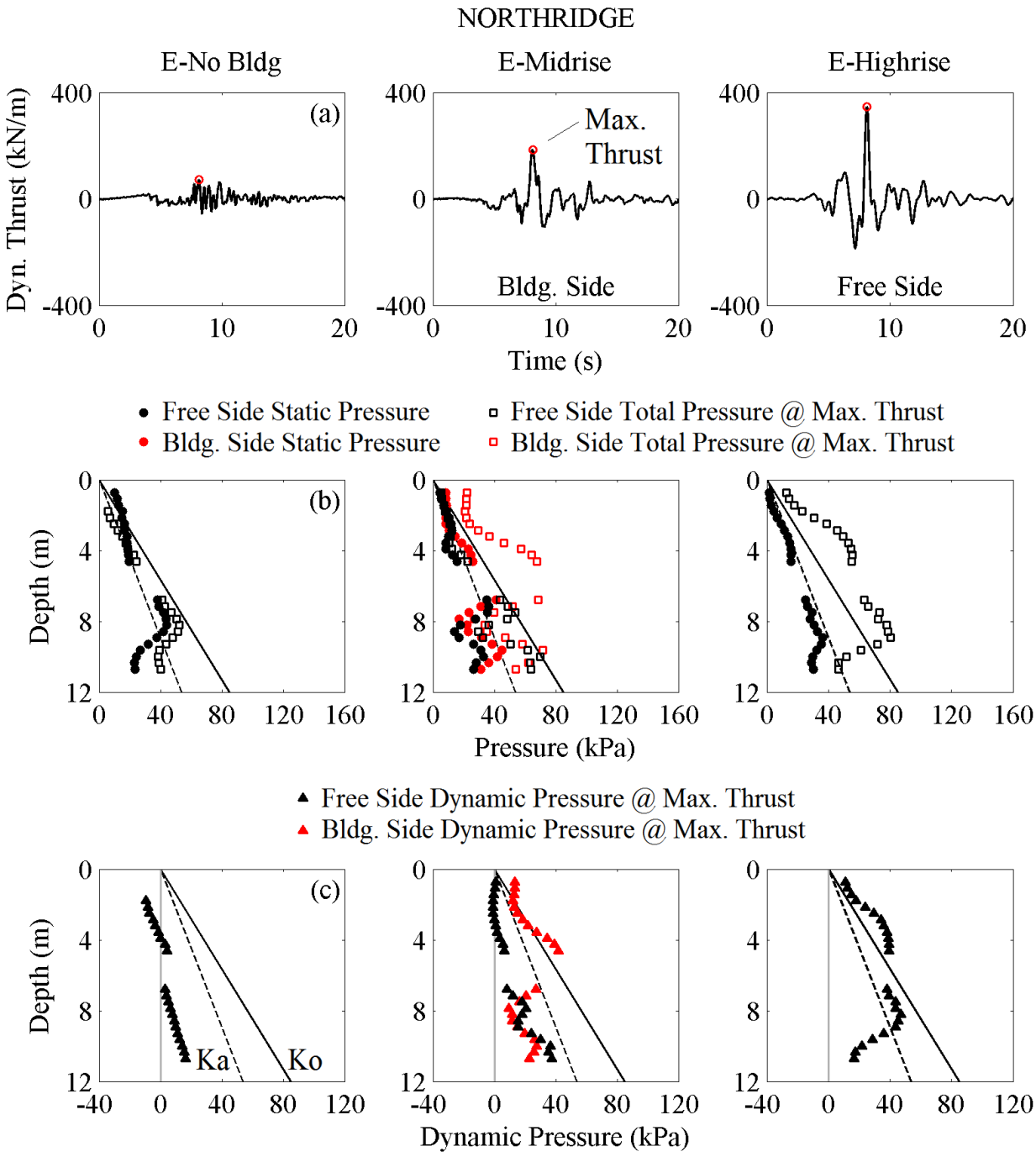

Figure 5.5-4. Northridge lateral earth pressure results presented as (a) dynamic increment of thrust time history; (b) initial static and maximum total pressure at the moment of maximum thrust; and (c) the dynamic increment of lateral earth pressure at the moment of maximum thrust.

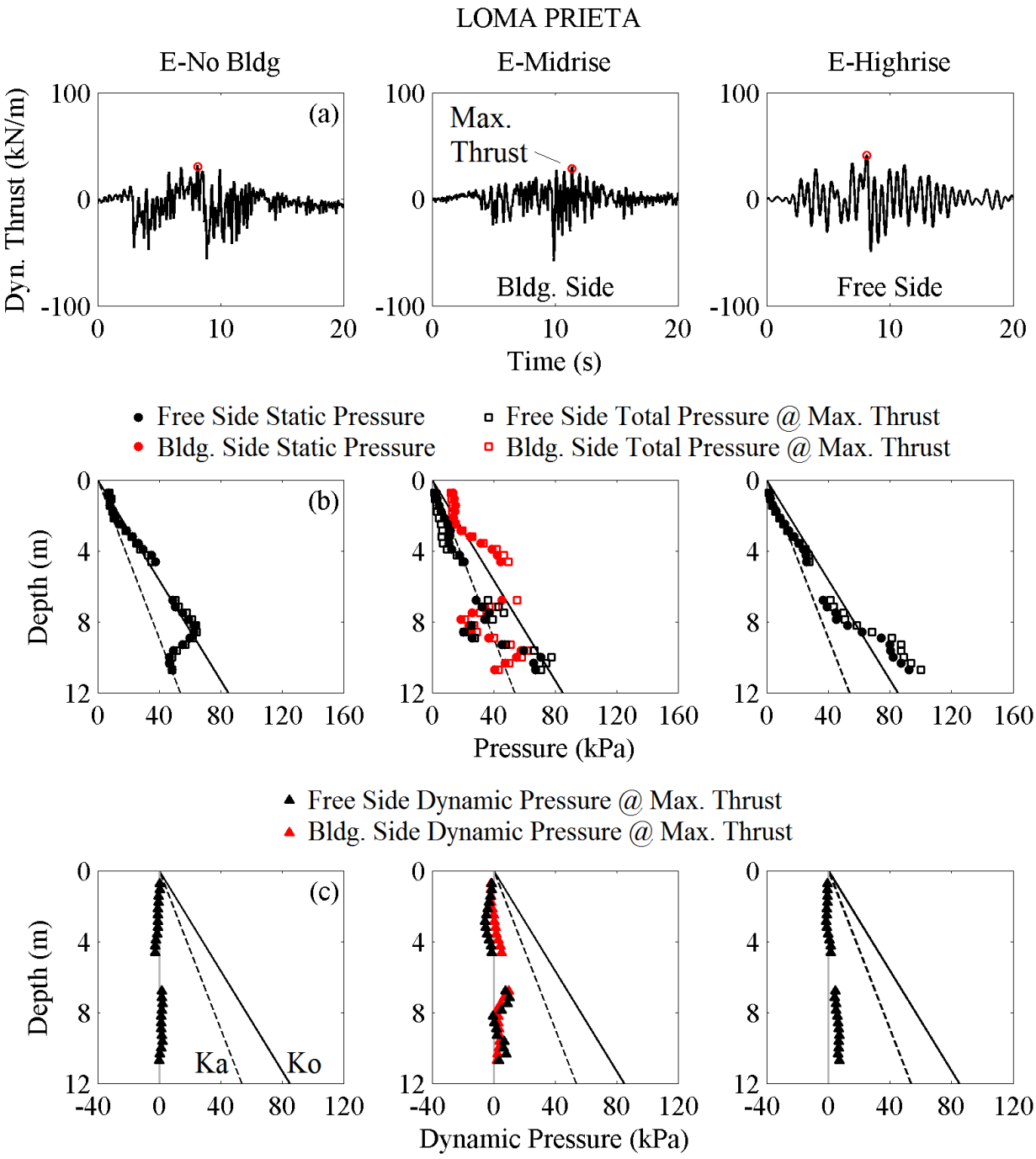

Figure 5.5-5. Loma Prieta lateral earth pressure results presented as (a) dynamic increment of thrust time history; (b) initial static and maximum total pressure at the moment of maximum thrust; and (c) the dynamic increment of lateral earth pressure at the moment of maximum thrust.

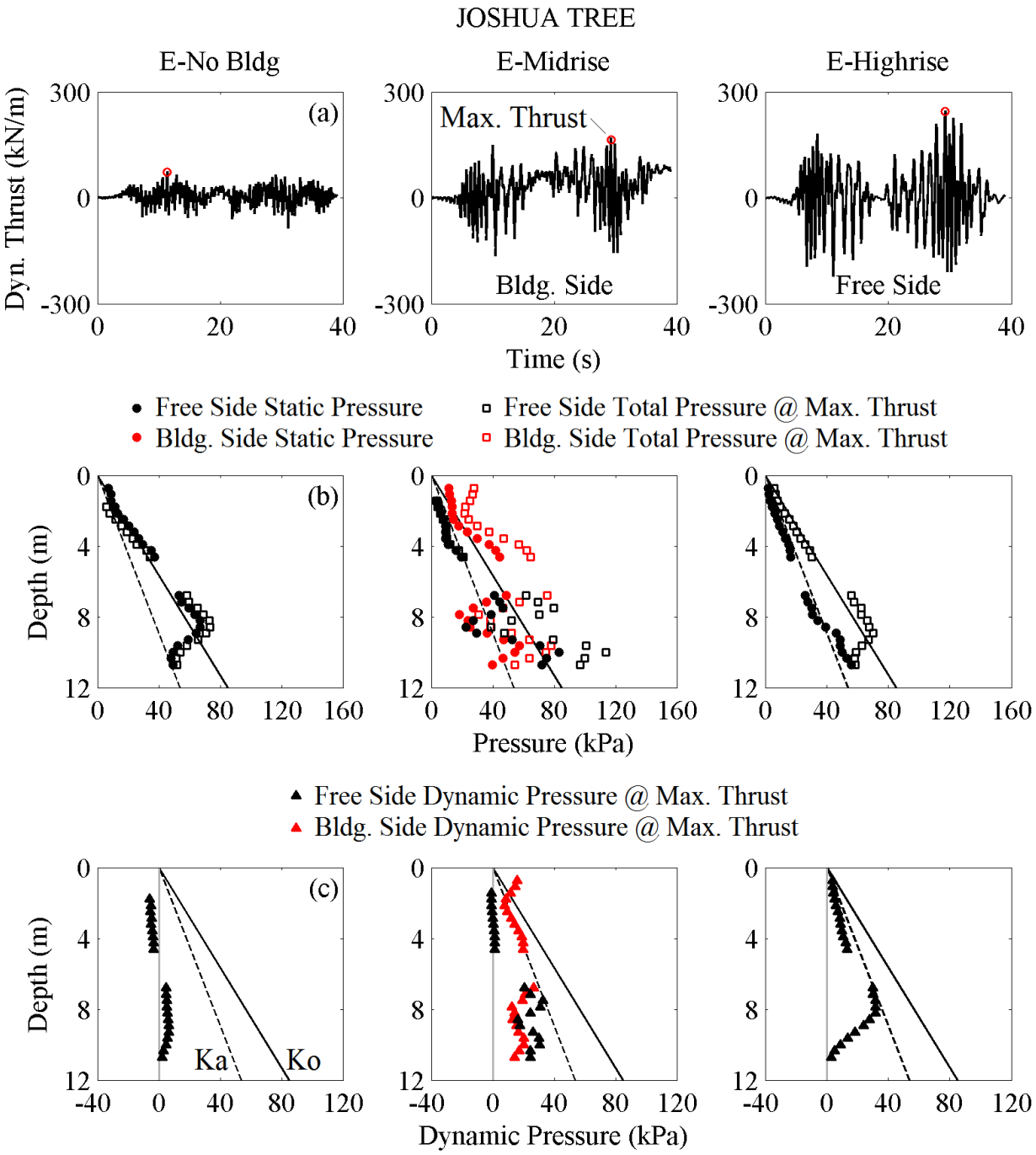

Figure 5.5-6. Joshua Tree lateral earth pressure results presented as (a) dynamic increment of thrust time history; (b) initial static and maximum total pressure at the moment of maximum thrust; and (c) the dynamic increment of lateral earth pressure at the moment of maximum thrust.

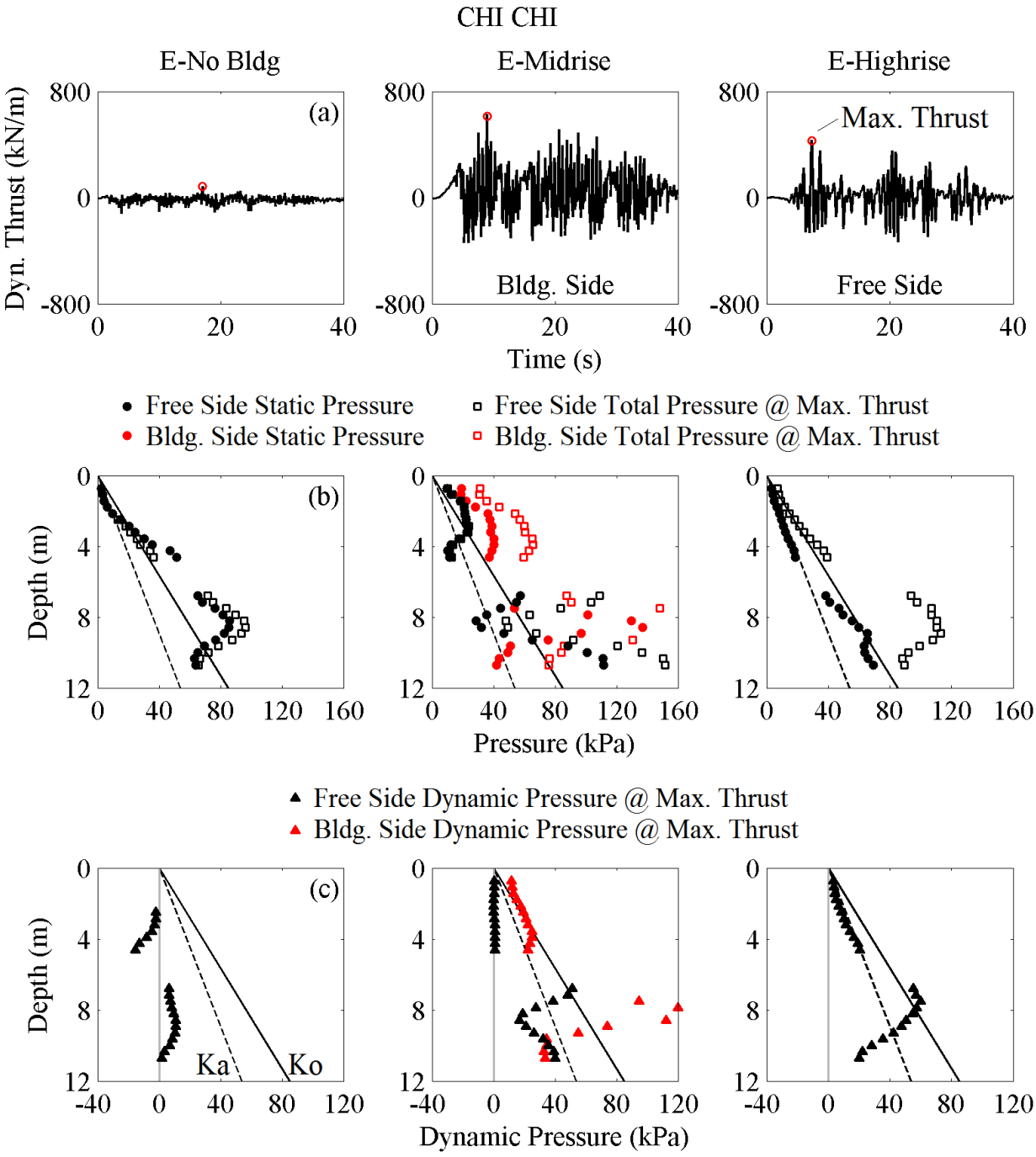

Figure 5.5-7. Chi Chi lateral earth pressure results presented as (a) dynamic increment of thrust time history; (b) initial static and maximum total pressure at the moment of maximum thrust; and (c) the dynamic increment of lateral earth pressure at the moment of maximum thrust.

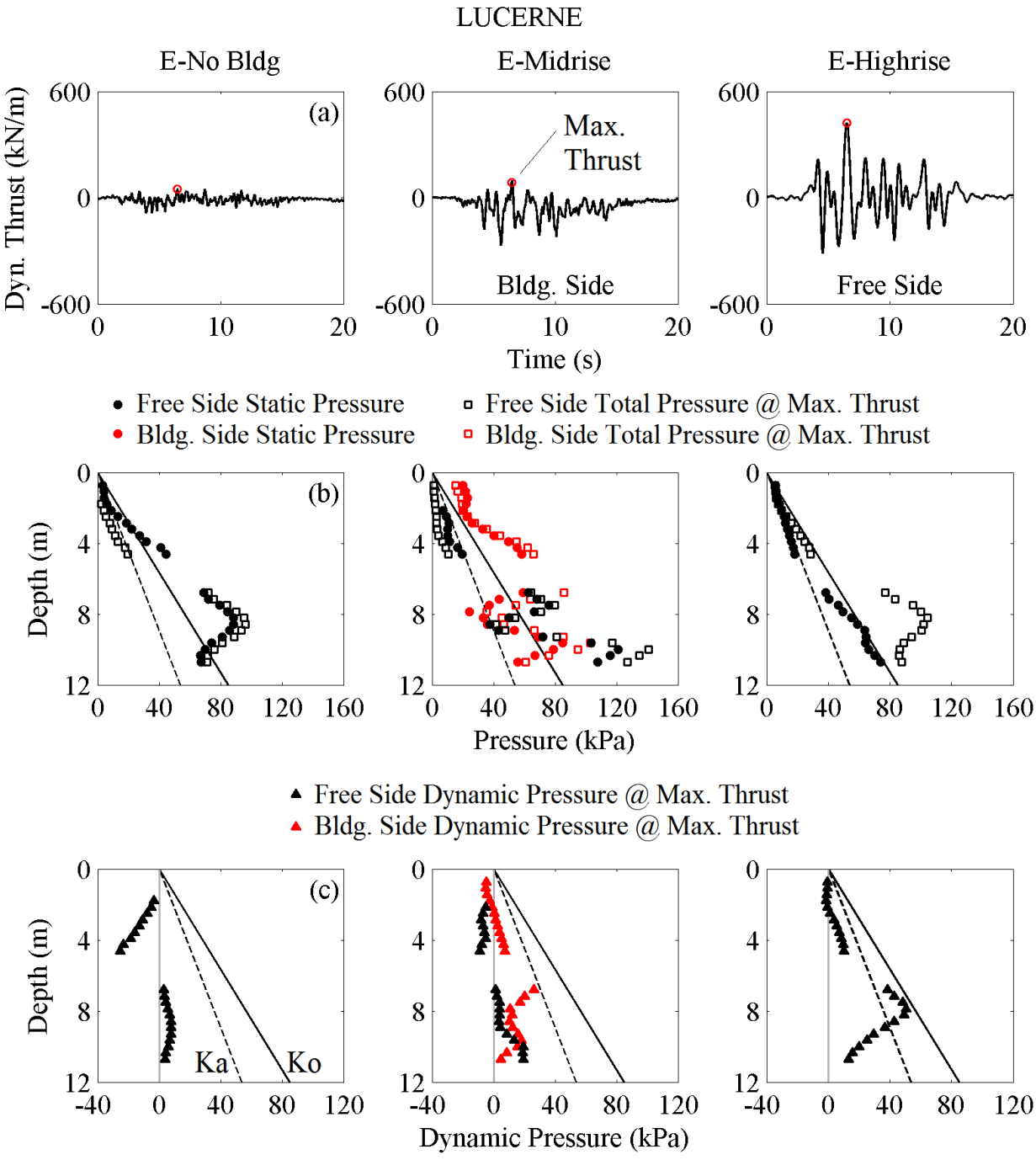

Figure 5.5-8. Lucerne lateral earth pressure results presented as (a) dynamic increment of thrust time history; (b) initial static and maximum total pressure at the moment of maximum thrust; and (c) the dynamic increment of lateral earth pressure at the moment of maximum thrust.

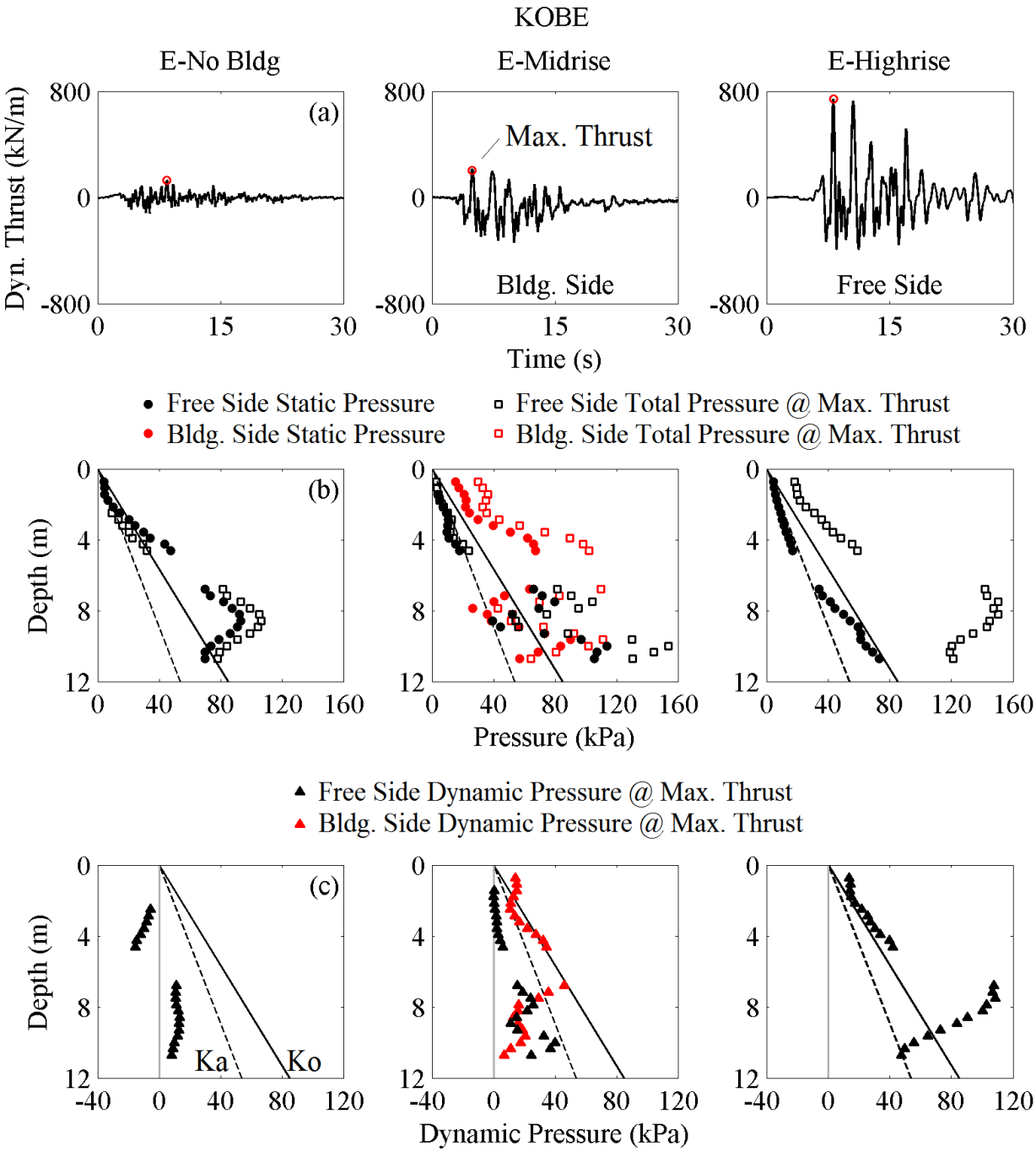

Figure 5.5-9. Kobe lateral earth pressure results presented as (a) dynamic increment of thrust time history; (b) initial static and maximum total pressure at the moment of maximum thrust; and (c) the dynamic increment of lateral earth pressure at the moment of maximum thrust.

5.6 Discussion and Comparison of Results

In this chapter, the results from various instruments were presented with the goal of better understanding how the presence of an adjacent midrise or highrise structure influenced the seismic response of a temporary braced excavation both in terms of deflections and forces.

5.6.1 Dynamic Thrust and Building Base Shear

Seismic forces induced by the adjacent superstructure were expected to influence the dynamic thrust experienced on both excavation walls in a similar manner to the tunnel. Base shear is one measure of these induced forces from the building. The following figures (Figure 5.6-1 and Figure 5.6-2) compare the dynamic thrust measured on the two walls in each experiment with the base shear force from the adjacent midrise or highrise building for two representative ground motions (i.e., Northridge and Chi Chi). The building base shear was computed as the sum of the shear forces from each floor of the structure and the base plate (i.e., sum of the product of acceleration time history on each floor and its corresponding mass). The following figures show that the amplitude of base shear on the adjacent building and dynamic thrust measured on the two excavation walls was comparable in both time and frequency domains, especially for the midrise experiment. It is worth noting that the building base shear does not include the mass of the basement walls nor the soil within the skirt basement.

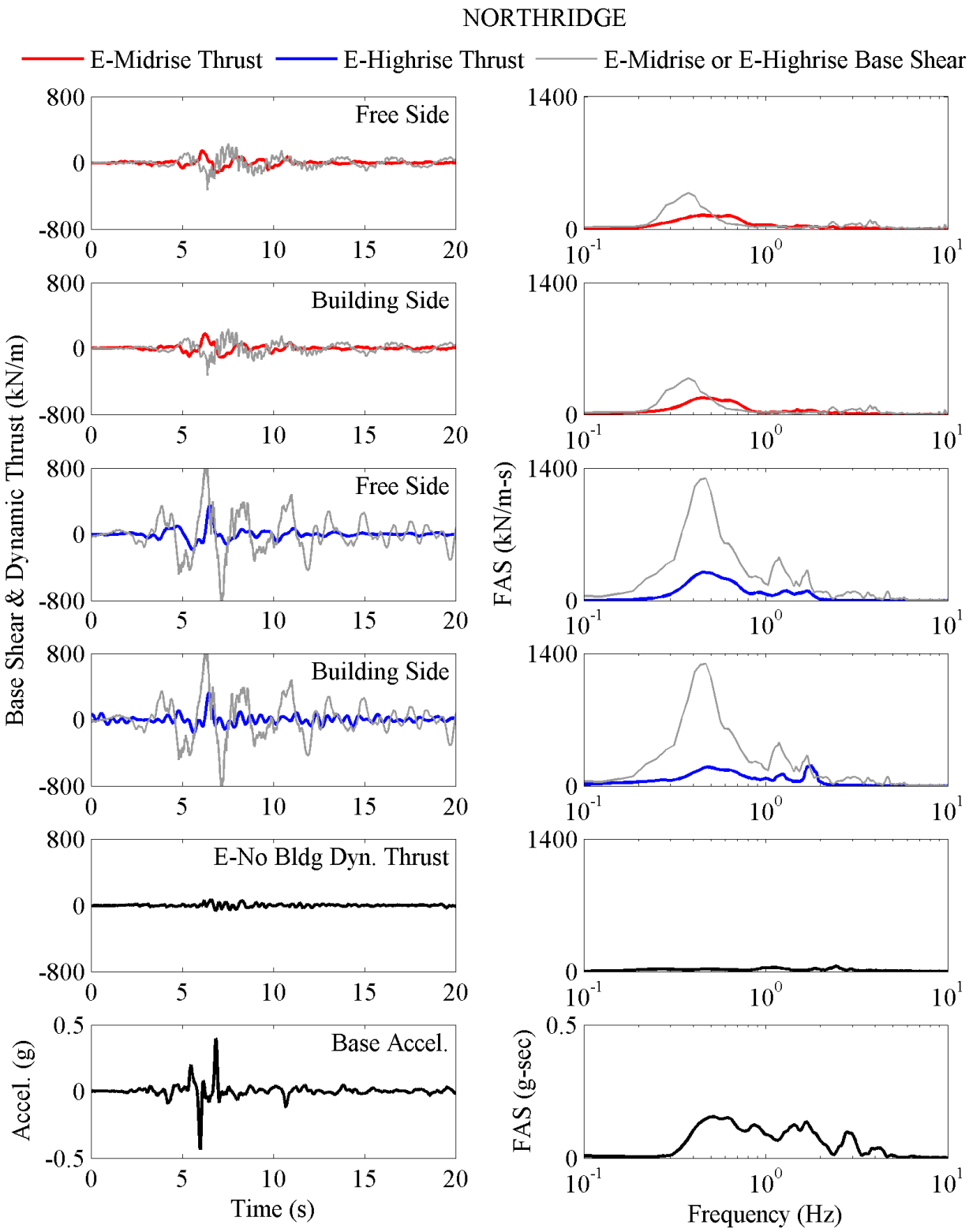

Figure 5.6-1. Dynamic lateral thrust on the excavation compared with base shear from the tall building.

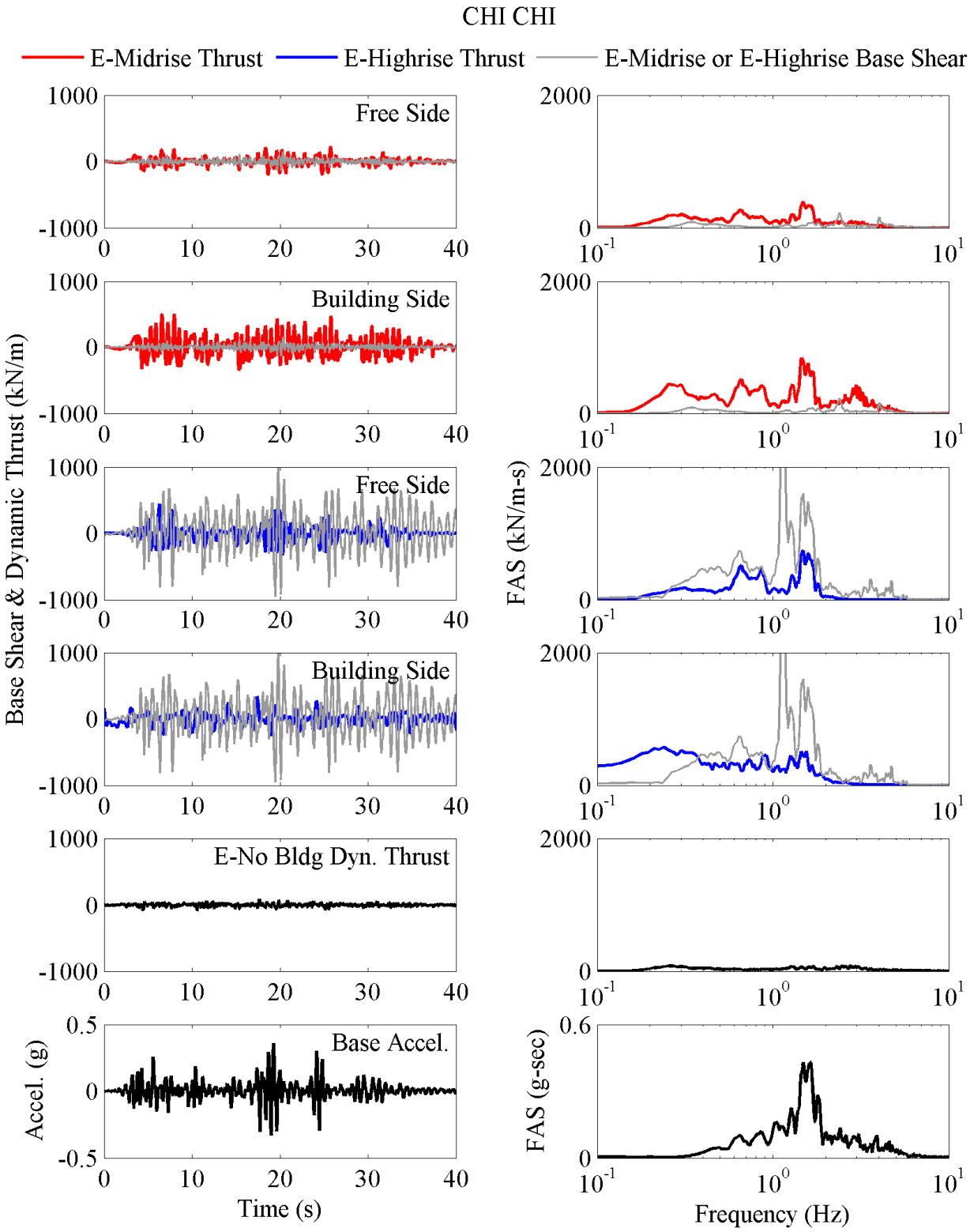

Figure 5.6-2. Dynamic lateral thrust on the excavation compared with base shear from the tall building.

5.6.2 Dynamic Thrust and Racking Displacements

Although racking displacement did not seem to fully capture the extend of wall deformation, it will be compared with thrust to see if there was a relationship between racking and dynamic thrust. As was mentioned in Chapter 4, data from the tactile sensors and the accelerometer data were manually synchronized using strain gauges (same DAQ system as accelerometers) from the excavation wall and thrust time histories. Figure 5.6-3 through Figure 5.6-8 compare dynamic thrust and racking displacement of the wall using loops. Note, the shape of the loop is dependent upon the quality of the manual synchronization of the two data sets. The loops show if maximum dynamic thrusts and racking displacements occur in one or many cycles. Generally, larger dynamic thrusts occur in the E-Midrise and E-Highrise tests. The E-No Bldg loops are generally the widest from left to right indicating the greatest amount of racking displacement.

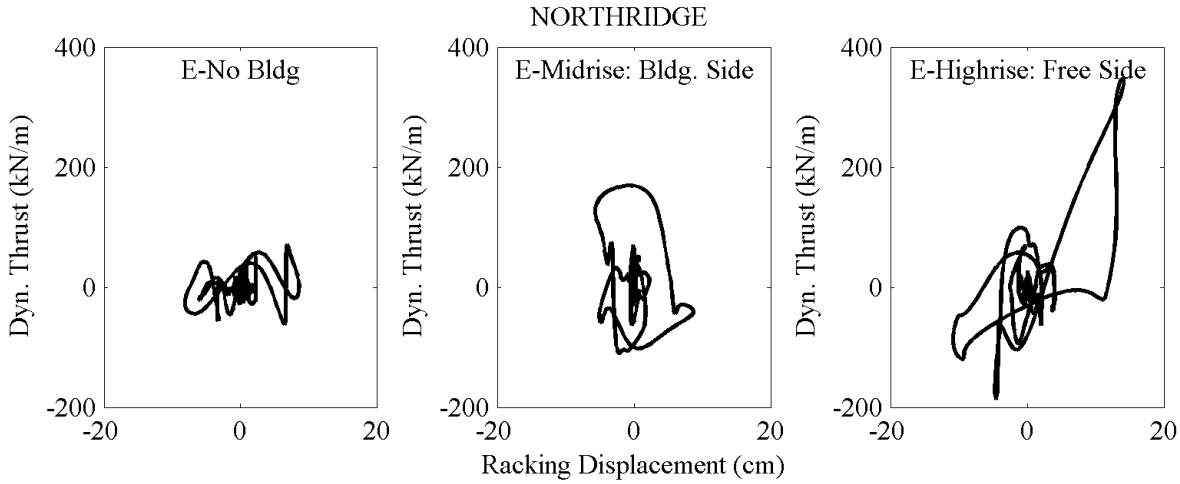

Figure 5.6-3. Dynamic thrust versus racking displacement loops.

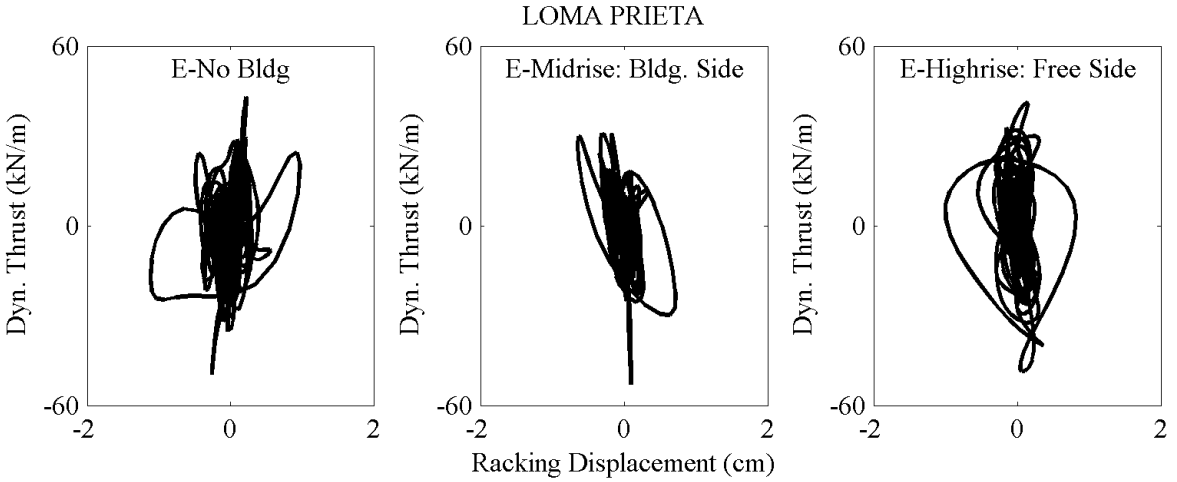

Figure 5.6-4. Dynamic thrust versus racking displacement loops.

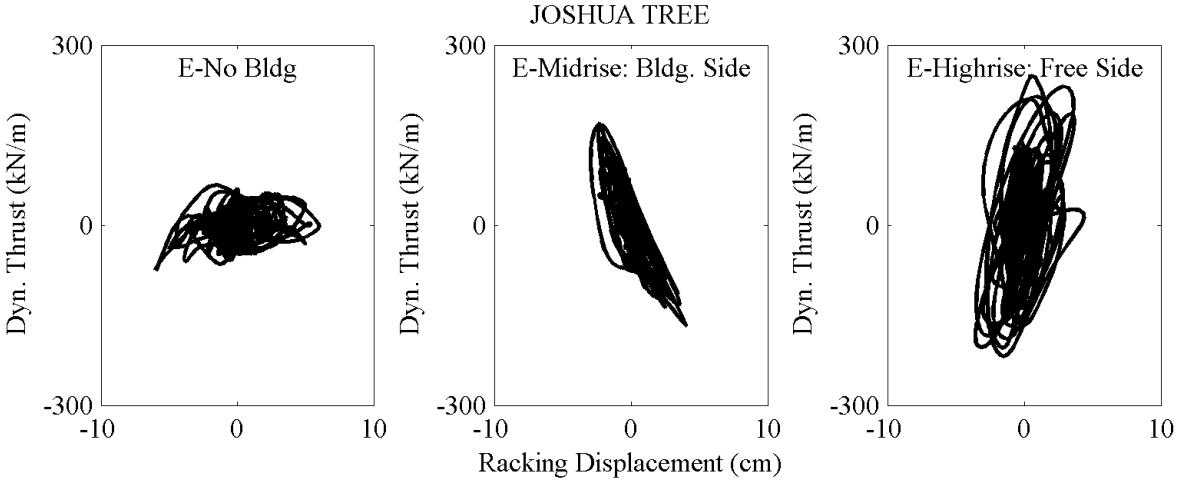

Figure 5.6-5. Dynamic thrust versus racking displacement loops.

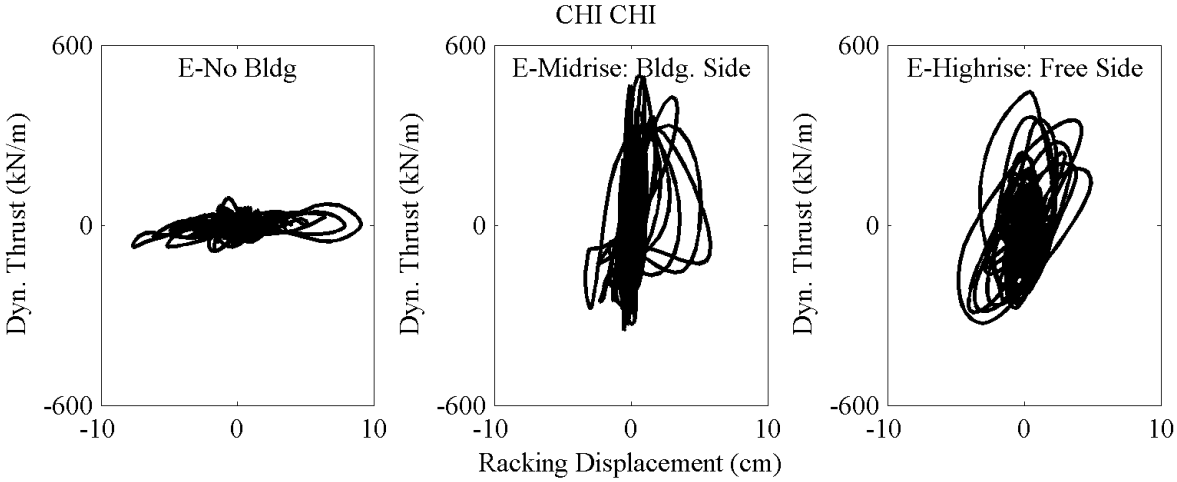

Figure 5.6-6. Dynamic thrust versus racking displacement loops.

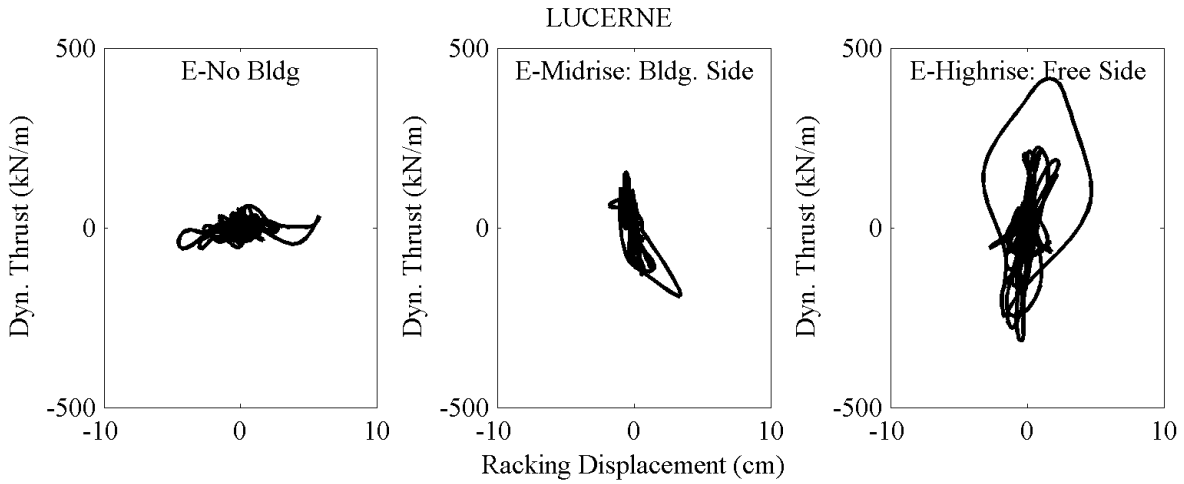

Figure 5.6-7. Dynamic thrust versus racking displacement loops.

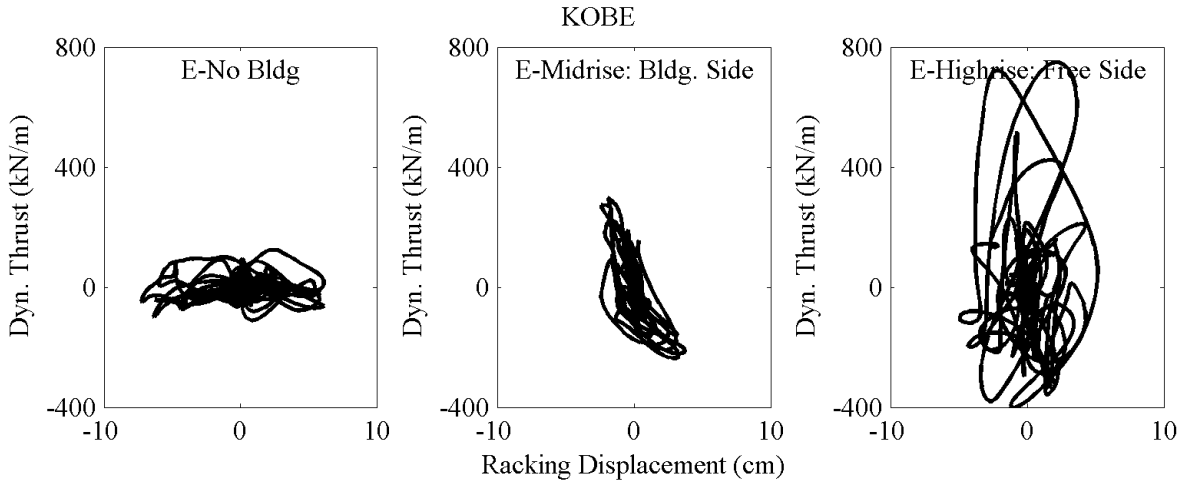

Figure 5.6-8. Dynamic thrust versus racking displacement loops.

5.6.3 Dynamic Thrust and Dynamic Bending Moments

Strain gauges at a depth of 8m on the excavation walls were selected, as they often recorded the highest dynamic bending moments on each wall, and their recordings were compared with the dynamic increment of thrust in both time and frequency domains (Figure 5.6-9 through Figure 5.6-11). The goal was to directly evaluate the relationship between dynamic thrust applied to the wall from the backfill soil with and without an adjacent structure and the resulting bending moments on the wall. In many cases, the FAS of dynamic thrust and bending moment

had similar forms with peaks at similar frequencies, indicating that the two responses were similar in their frequency content. Figure 5.6-12 through Figure 5.6-17 through show loops of dynamic thrust versus the bending moment from strain gauges at a depth of 8m on the wall. These loops show how the bending moment and thrust are related in terms of their timing and amplitude. The increase in dynamic thrust with the addition of a building was often also observed as an increase in dynamic bending moments at depth 8m, particularly on the free side of the excavation. In addition to looking at one individual strain gauge recording, the overall deflections along the two walls were shown to have amplified with the presence of an adjacent building in Section 5.4.1.

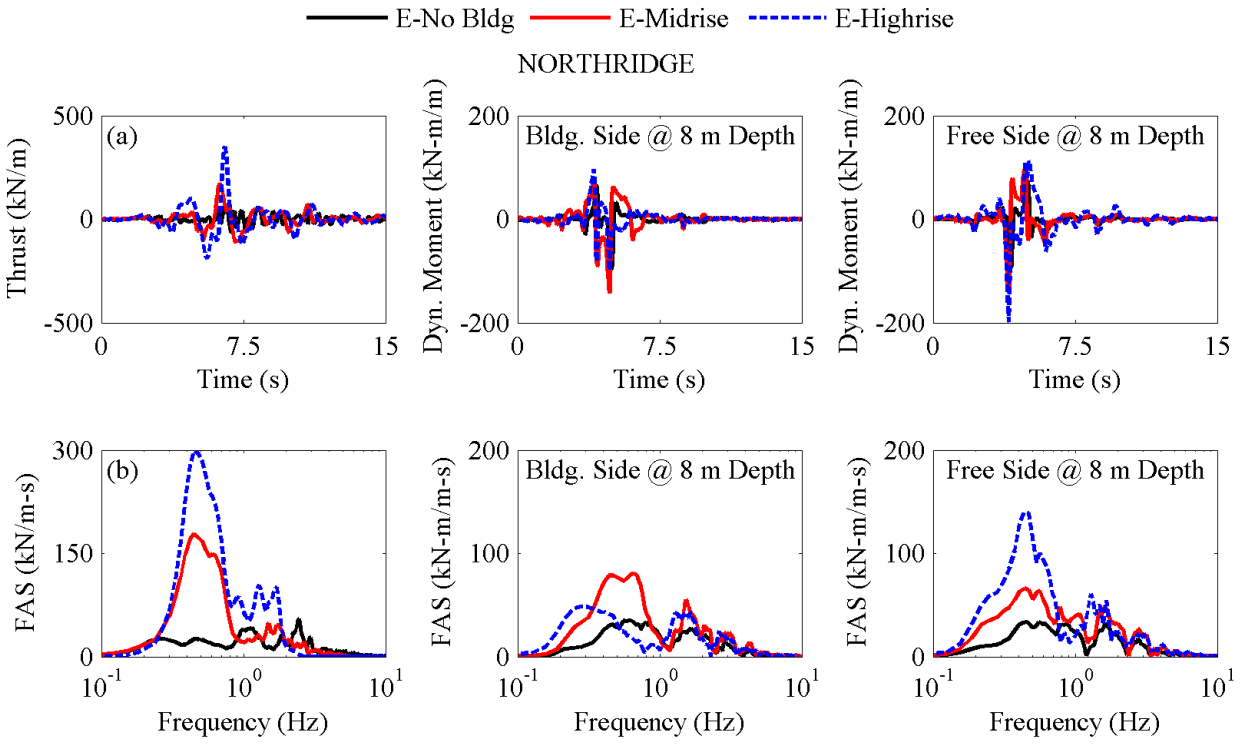

Figure 5.6-9. Dynamic thrust compared with dynamic bending moment at 8m depth on each excavation wall.

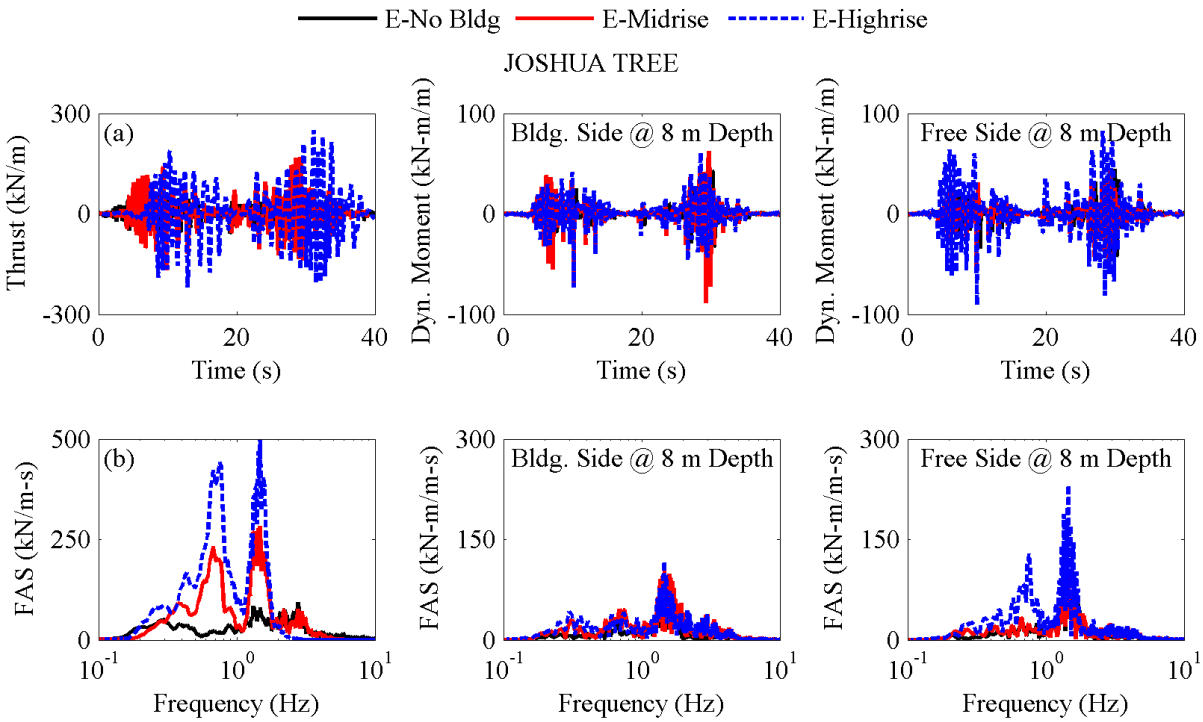

Figure 5.6-10. Dynamic thrust compared with dynamic bending moment at 8m depth on each excavation wall.

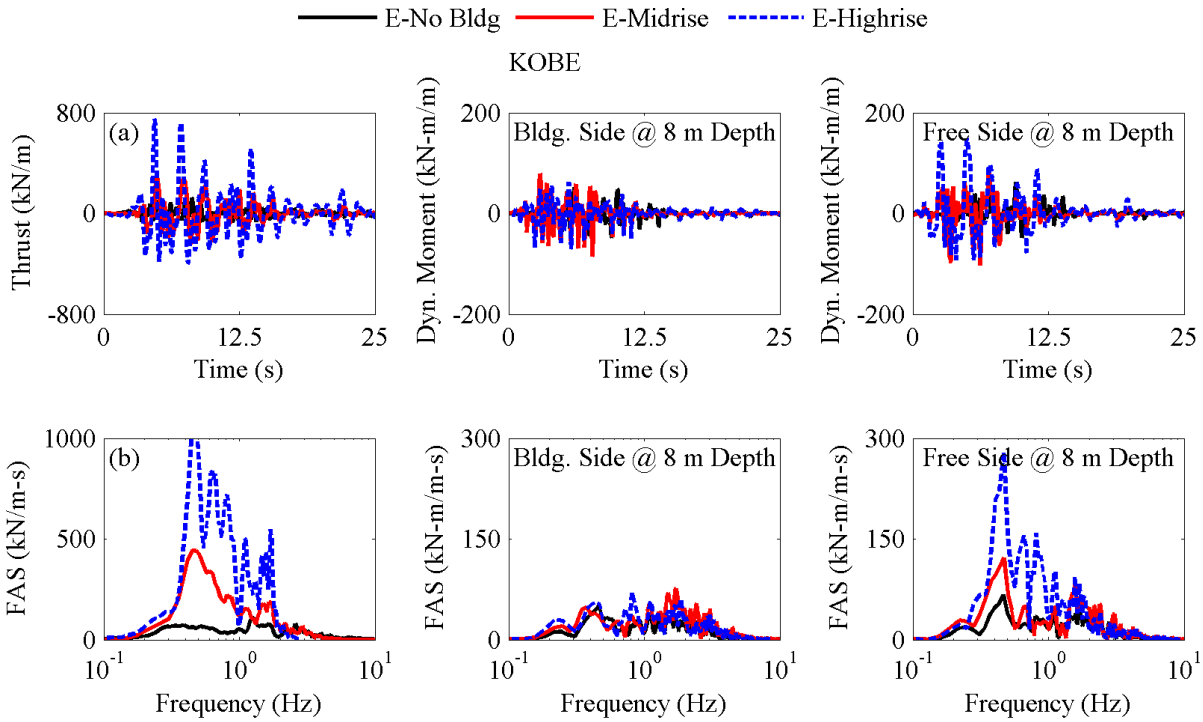

Figure 5.6-11. Dynamic thrust compared with dynamic bending moment at 8m depth on each excavation wall.

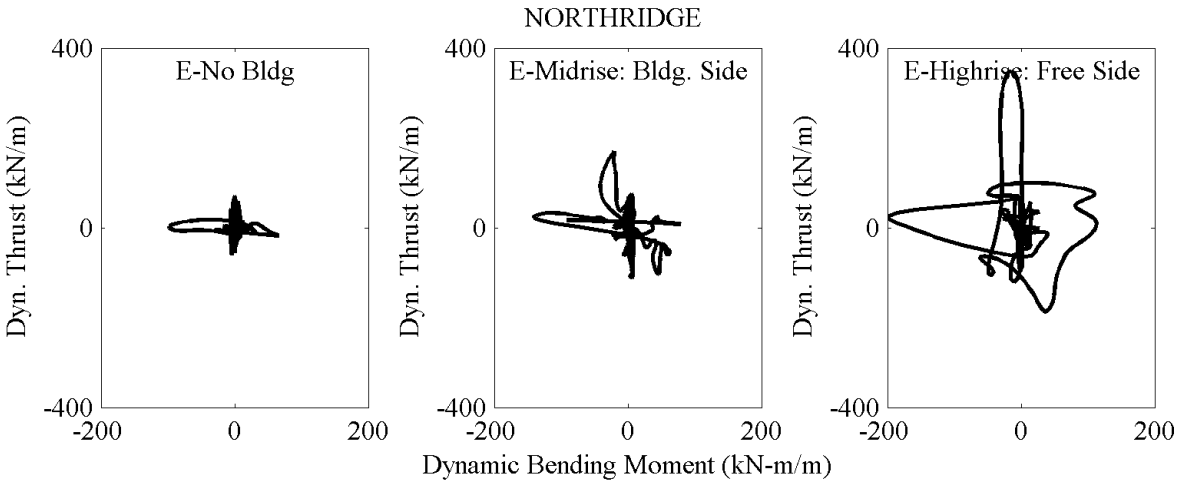

Figure 5.6-12. Dynamic thrust versus dynamic bending moment loops.

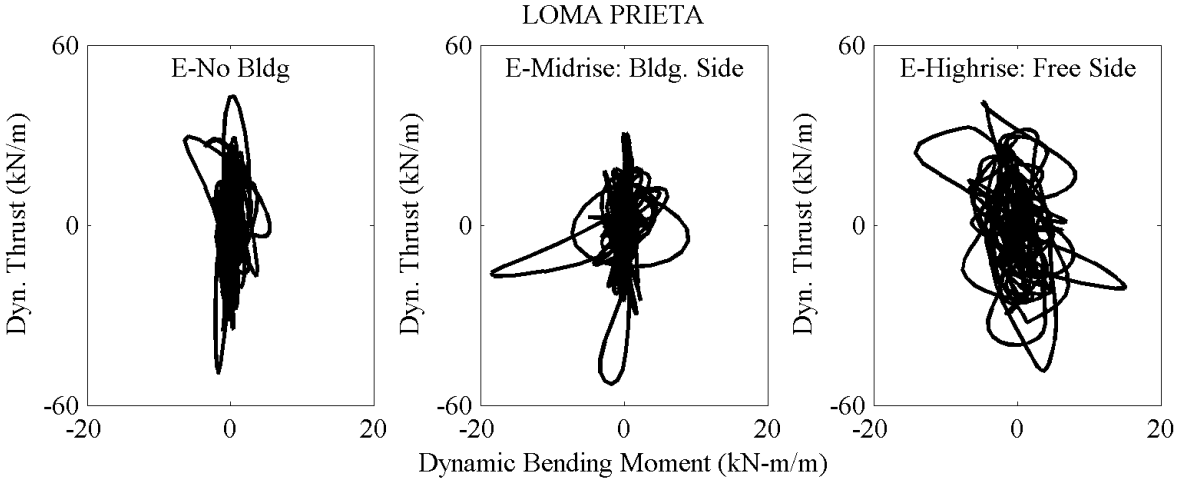

Figure 5.6-13. Dynamic thrust versus dynamic bending moment loops.

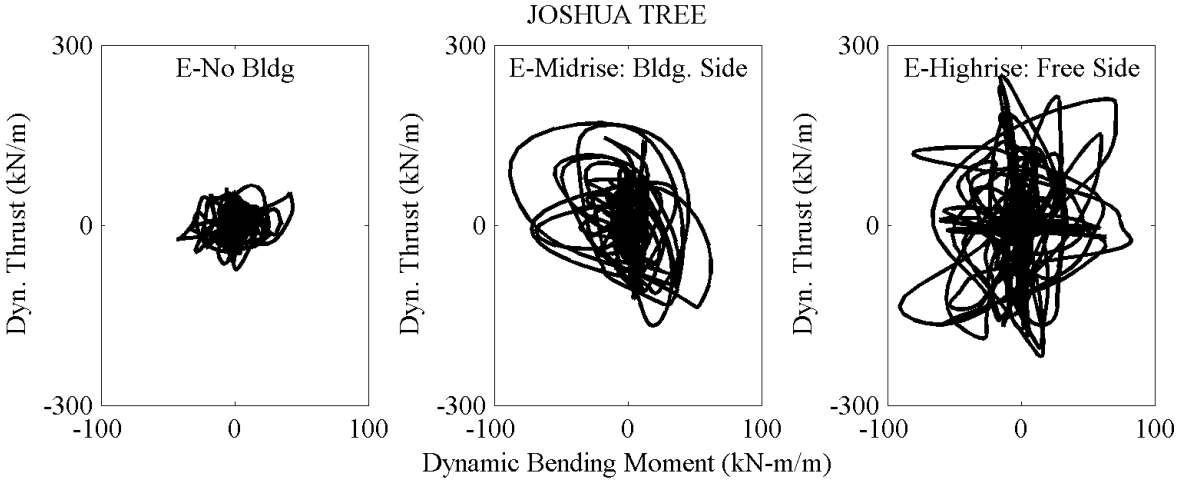

Figure 5.6-14. Dynamic thrust versus dynamic bending moment loops.

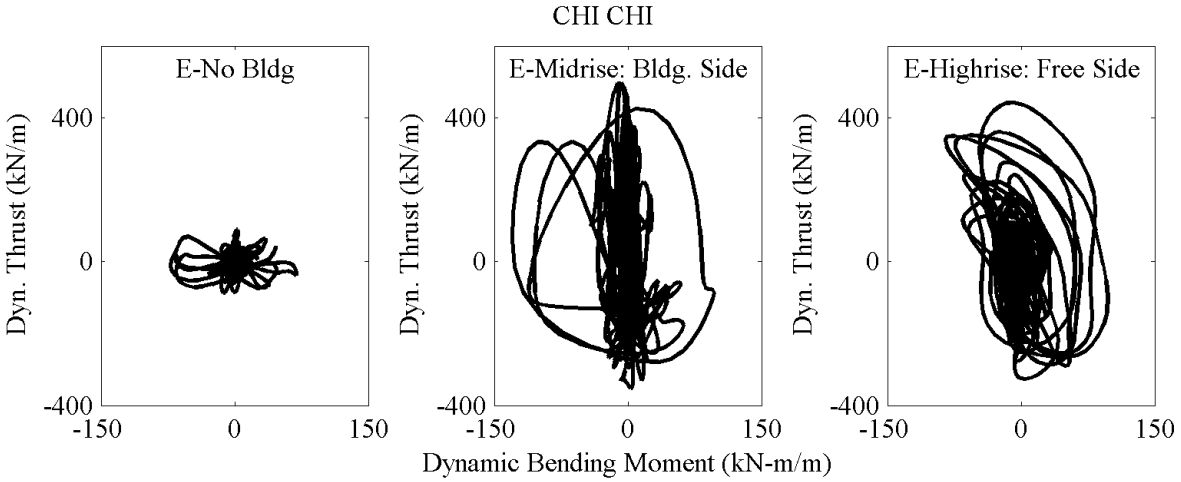

Figure 5.6-15. Dynamic thrust versus dynamic bending moment loops.

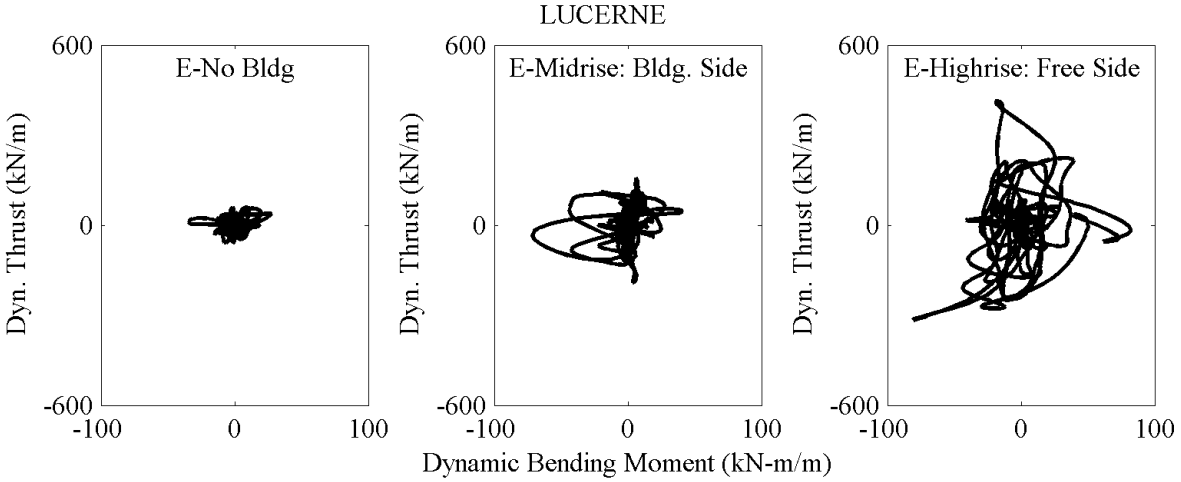

Figure 5.6-16. Dynamic thrust versus dynamic bending moment loops.

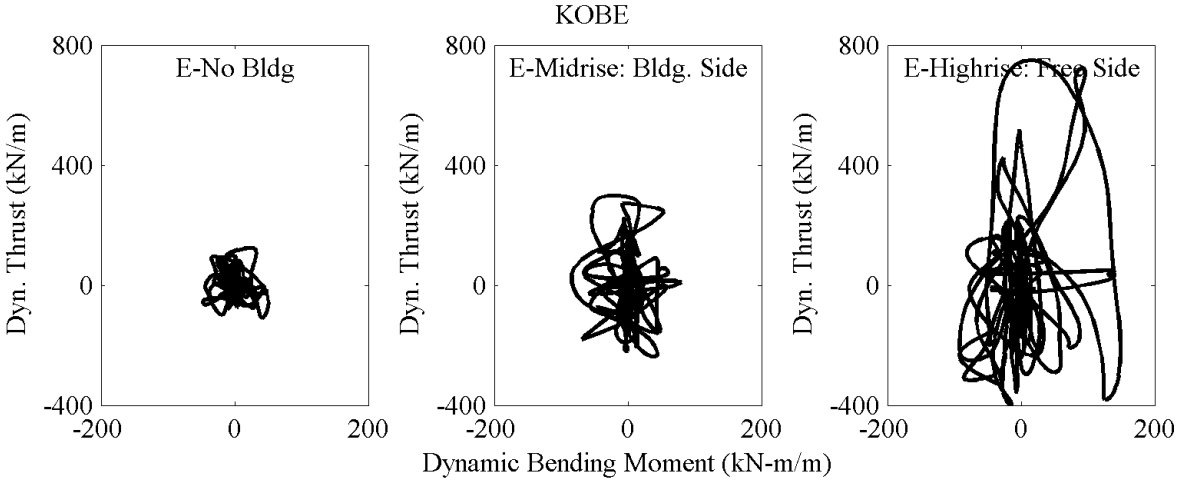

Figure 5.6-17. Dynamic thrust versus dynamic bending moment loops.

5.6.4 Summary

Tactile pressure sensor recordings showed significantly greater dynamic thrusts on both excavation walls with the addition of an adjacent midrise or highrise building. The increase in dynamic thrust seemed to correlate with the base shear of the adjacent structure in both amplitude and frequency content, which was consistent with the response of the permanent box structure. The increase in lateral earth pressures acting on the excavation walls, however, did not translate into greater racking displacements, but it did induce significantly larger bending strains and deflections along the two walls and larger axial loads on the struts. This pattern was not similar to the tunnel tests.

The tunnel walls were much stiffer than the excavation walls. The increased lateral earth pressures did not noticeably increase the deflection along the tunnel neither in terms of racking deformations nor in terms of dynamic bending strain profiles. This implies that the addition of an adjacent building did not worsen the performance of the tunnel. The increased lateral earth pressures with the presence of an adjacent building, however, significantly influenced the performance of the more flexible excavation walls in terms of bending strain profiles (more curvature induced by earthquake loading) but not in terms of racking. This implies that a simplistic deformation measure such as racking, which only considers the displacement of top of the wall with respect to base of excavation instead of the extent of deflection along the entire wall, may not be sufficient in evaluating the performance of relatively flexible temporary braced excavations. A cumulative measure of bending strains maybe more appropriate to evaluate the performance of these flexible underground structures.

Chapter 6

6 DISCUSSION ON MECHANISMS OF SOIL-STRUCTURE-UNDERGROUND STRUCTURE-INTERACTION

6.1 Introduction

Typically soil-structure-interaction (SSI) is evaluated in terms of kinematic and inertial effects separately, to better understand the underlying mechanisms of interaction. In this dissertation, a similar framework is used to organize and describe mechanisms contributing to soil-structure-underground structure-interaction (SSUSI) or the interaction between a tall building and the soil-underground structure system. This section provides a discussion of how kinematic and inertial effects near the tall building, in addition to the increased confinement, influenced the seismic performance of the adjacent underground structures.

6.2 Inertial Interaction

For many tall buildings (i.e., with a large mass and inertia), inertial interaction can have a significant influence on the seismic response of the building as well as the forces translated into the soil. "The effects of structural inertia on foundation motions tend to be concentrated near the first-mode structural frequency, so kinematic effects can be approximately evaluated across the remainder of the frequency spectrum," Stewart (1996). Hence, the impact of the inertial

response of the midrise and highrise building in the centrifuge experiments was evaluated on both accelerations and dynamic thrust near the expected fundamental frequency of the corresponding building. Both accelerations and forces experienced on the tunnel were hypothesized to be amplified near the flexible-based, fundamental frequency of the adjacent building due to its inertial interaction with the soil-underground structure system.

6.2.1 Inertial Effects on Displacements and Accelerations

Racking and total lateral displacements along the walls of the permanent and temporary box structures were previously observed to reduce slightly due to the presence of the adjacent tall building. To evaluate the impact of tall buildings' inertia on the movement of the soil-underground structure system, accelerations recorded on the baseplate and basement walls of the midrise and highrise building were compared with the near-field recordings of the T-No Bldg and E-No Bldg experiments at the same distance from the box structure. Figures 4.2.5 and 4.2.7 or Figure 6.2.1 and Figure 6.2.2, shown again here for convenience, show the elevation layout of the accelerometers used in T-No Bldg and T-Highrise, respectively.

Figure 6.2.3(a) compares the Fourier amplitude spectra of accelerations in the near-field at the surface in T-No Bldg (with no building) and at the baseplate of the midrise building in T-Midrise during the Chi Chi motion. The red lines in this figure show the transfer function of the T-Midrise top floor, middle floor, and bottom floor with respect to the baseplate acceleration, the peaks of which identify the flexible-based modal frequencies of the building during that motion. A fundamental frequency of approximately 0.28 Hz is evident for the midrise building in this case, which was lower than its fixed-based fundamental frequency of 0.33 Hz, as expected.

Figure 6.2.3(a) shows no noticeable amplification in near-field accelerations from T-No Bldg to T-Midrise near the fundamental frequency of the midrise building (around 0.28 Hz). In

fact, the near-field accelerations generally de-amplified at lower frequencies near the fundamental frequency of either the midrise or highrise building (Figure 6.2.3b). This trend was observed consistently among all of the ground motions from each experiment, and is likely the result of displacement constraints introduced by the deep basement (i.e., kinematic interaction, discussed later in more detail). The same trend was observed in the excavation experiments shown by Figure 6.2.4.

Figure 6.2.5 and Figure 6.2.6 present transfer functions (TF's) that compare the near-field accelerations in each experiment during the Chi Chi motion. In these figures, the solid lines labeled "NF" compare the acceleration response at various elevations of either the midrise or highrise basement with those at the same location when the building was not present in T-No Bldg and E-No Bldg, respectively. The dashed lines represent a direct comparison of either tunnel or excavation performance among experiments.

Transfer functions (TF) greater than 1.0 at a given frequency indicate amplified accelerations at a given location due to the presence of the structure, and vice versa. At lower frequencies (less than about 1 Hz), de-amplification of both near-field and tunnel accelerations was observed in most cases due to the addition of an adjacent building. Therefore, in this case, inertial interaction did not influence accelerations near the tall building and the adjacent underground box structure. This may be because of the low fundamental frequency of the buildings tested, which were not excited sufficiently with the applied base motions that contained little content at low frequencies.

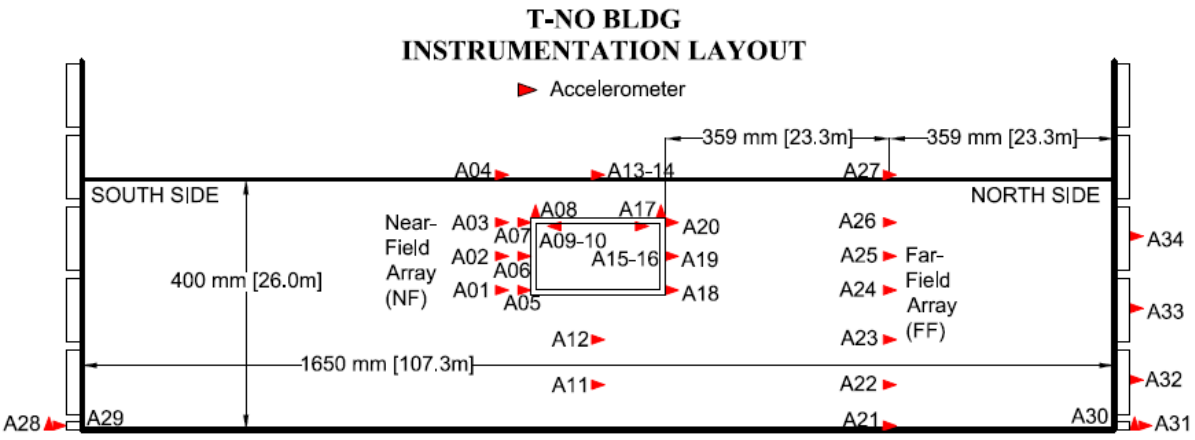

Figure 6.2.1. T-No Bldg accelerometer layout, elevation view.

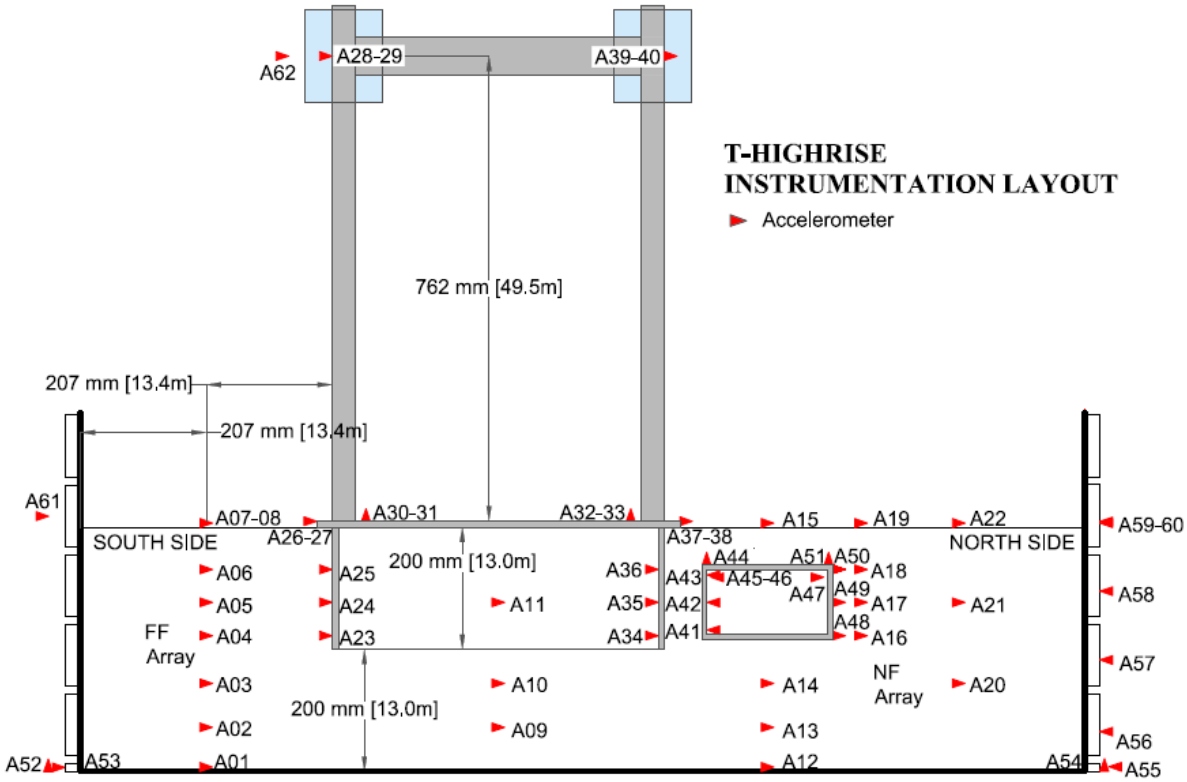

Figure 6.2.2. T-Highrise accelerometer layout, elevation view.

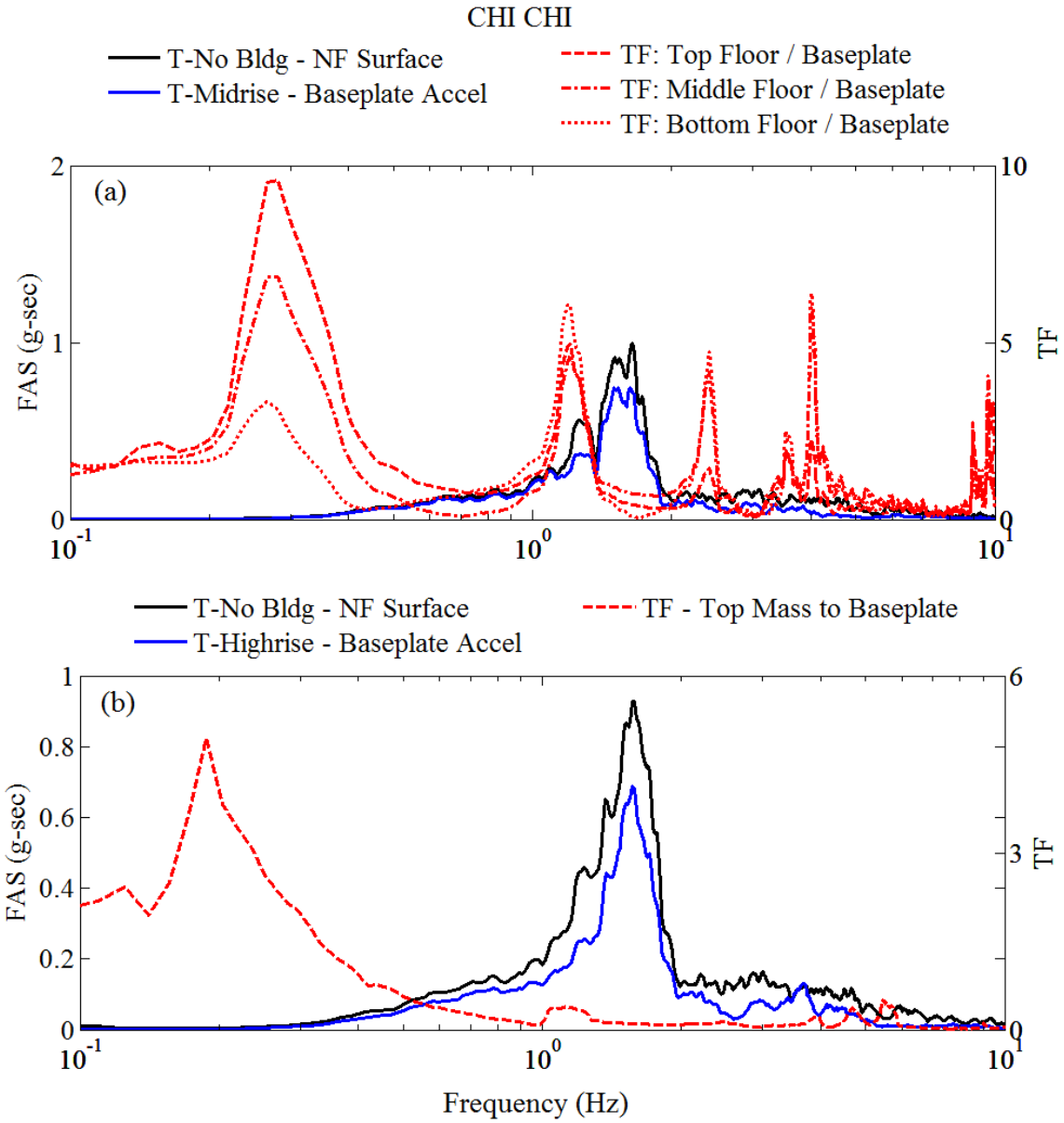

Figure 6.2.3. Comparing (a) T-Midrise; and (b) T-Highrise baseplate with T-No Bldg near-field surface acceleration during the Chi Chi ground motion.

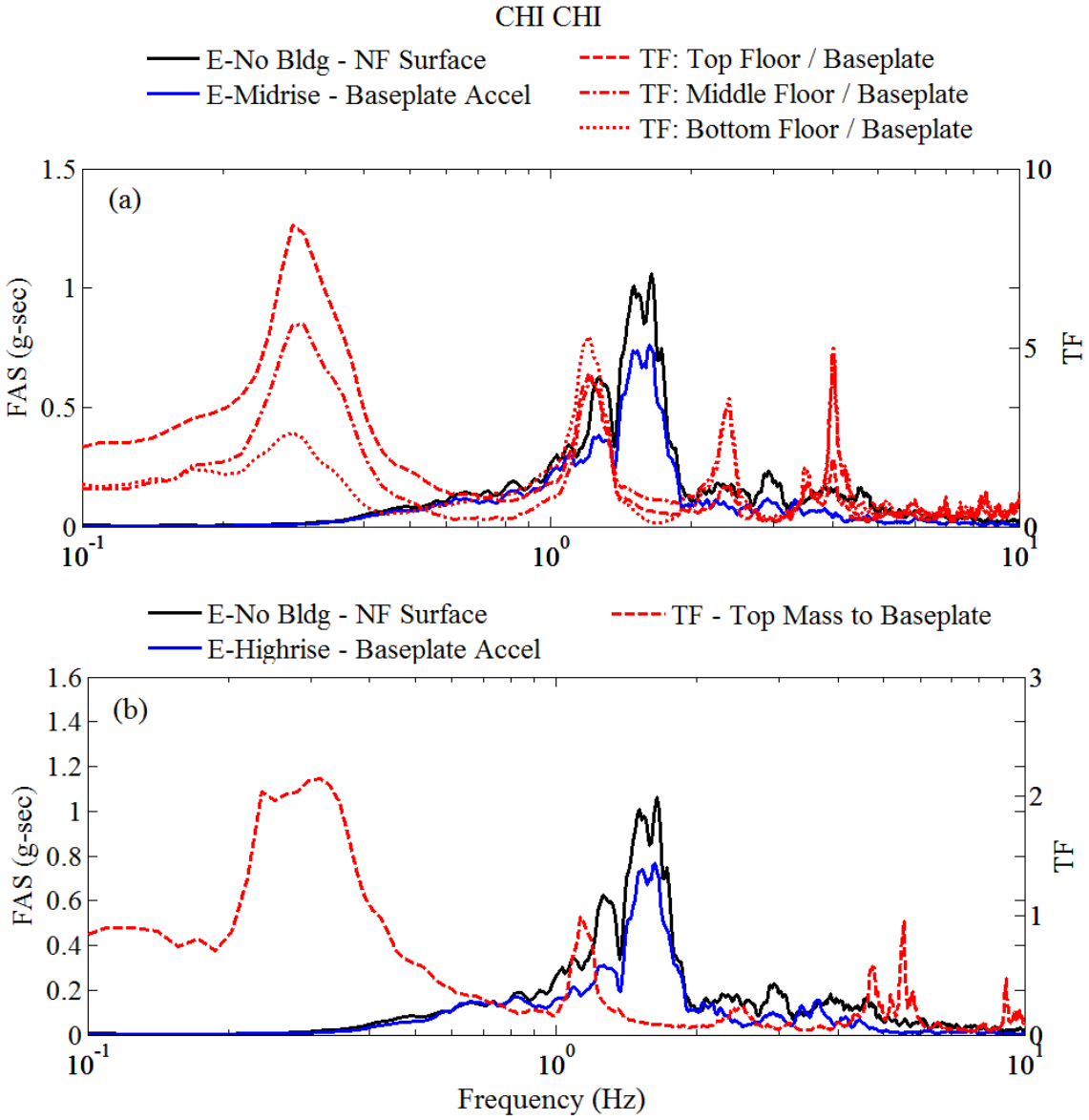

Figure 6.2.4. Comparing (a) E-Midrise and (b) E-Highrise baseplate with E-No Bldg near-field surface acceleration during the Chi Chi ground motion.

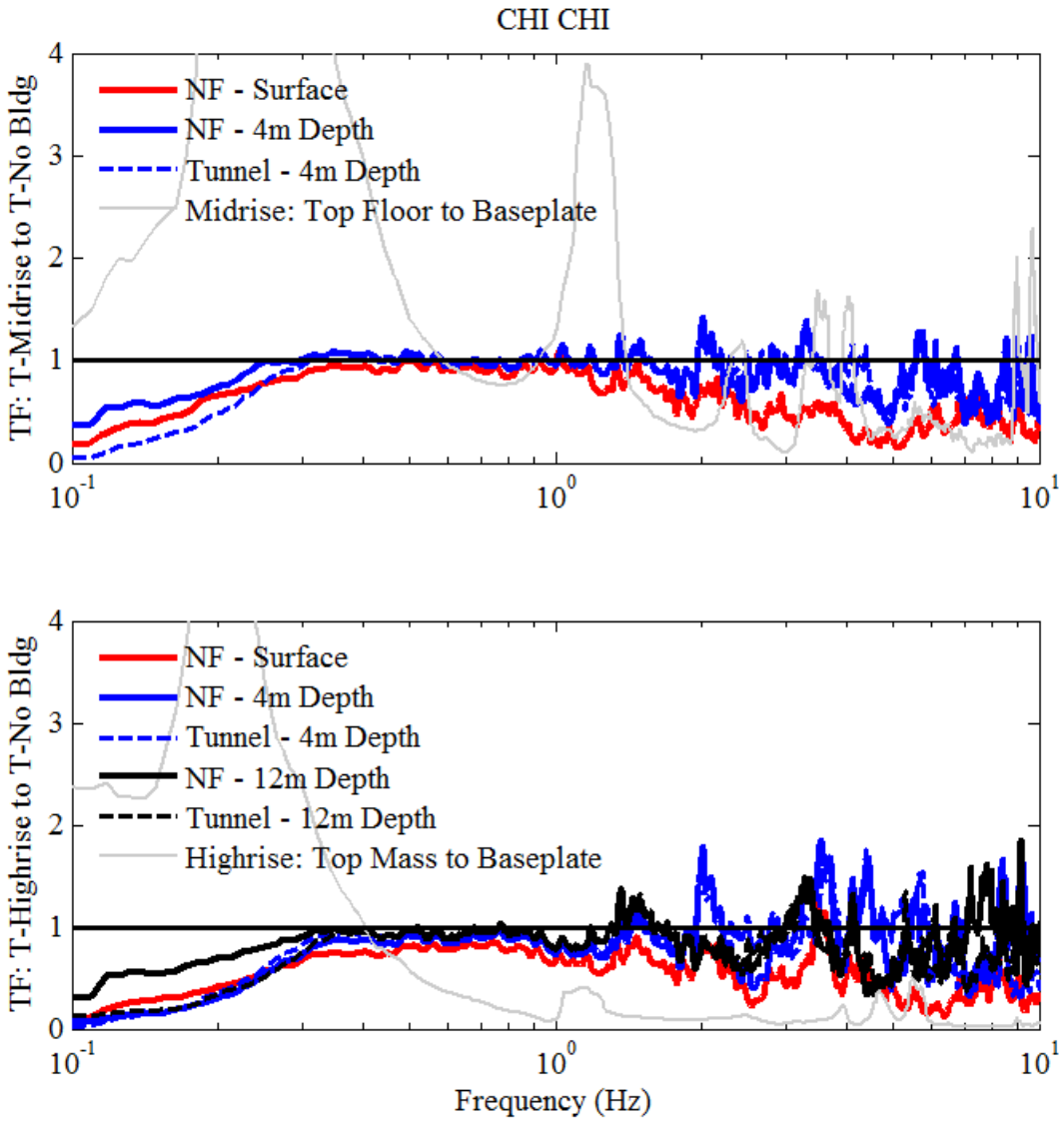

Figure 6.2.5. Transfer function comparison of near-field and funnel accelerations among the tunnel experiments.

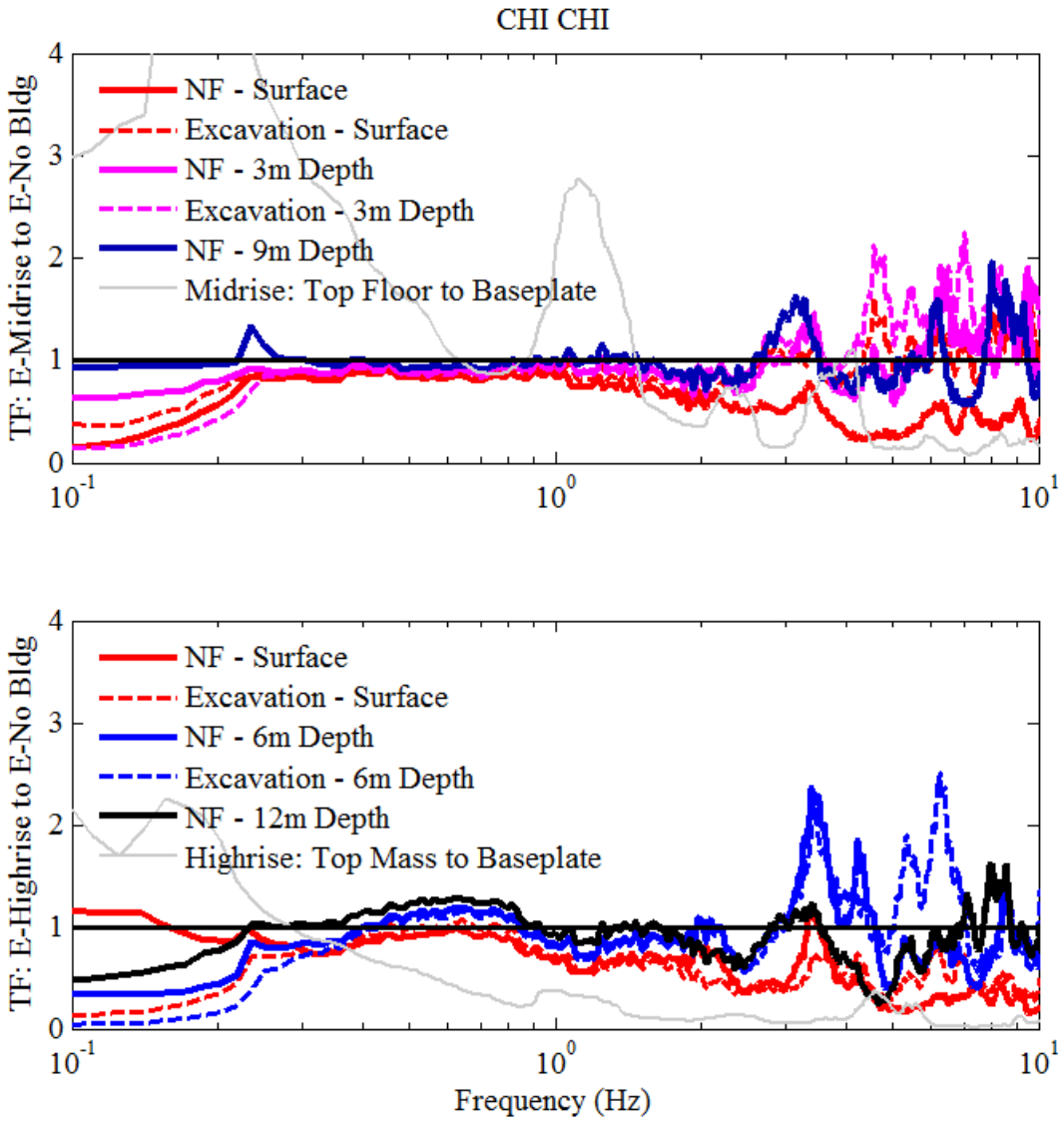

Figure 6.2.6. Transfer function comparison of near-field and excavation accelerations among the excavation experiments.

6.2.2 Inertial Effects on Dynamic Forces

Although the inertial response of the tall buildings did not seem to amplify accelerations and displacements near the building and underground structure, it was expected to amplify the dynamic thrust experienced on the box structure, because seismic lateral earth pressures were previously observed to increase with the addition of an adjacent building. More specifically, the increase in the transfer functions of T-Midrise to T-No Bldg and T-Highrise to T-No Bldg

dynamic thrust acting on the tunnel was expected to be affected by the inertial force (or base shear) of the adjacent tall building, as shown in previous sections.

Figure 6.2.7 compares transfer functions of dynamic thrust acting on the box structure with and without a building (e.g., TF values greater than 1.0 indicating amplification of dynamic thrust due to the presence of the building) together with the transfer functions of top floor (midrise) and top mass (highrise) to baseplate for both midrise and highrise buildings that identify their flexible-base modal frequencies. The Fourier amplitude spectra of both midrise and highrise base shear are also included in this figure to evaluate the building inertial forces in the frequency domain in parallel. In most cases, there was a correlation between the frequencies at which building base shear peaked, and the frequencies at which dynamic thrust on the tunnel was strongly amplified due to the presence of that building. This trend was stronger for the highrise building, and not as evident for the midrise structure, likely due to its smaller base shear contribution compared with the highrise. The highrise building was expected to have a higher inertial impact on the system than the midrise due to its greater mass.

Figure 6.2.8 through Figure 6.2.11 show in more detail the TF of dynamic thrust between T-Highrise and T-No Bldg, the TF of acceleration on the mass to baseplate, and the Fourier Amplitude Spectra (FAS) of base shear for the highrise building. These figures show that during all motions the inertial force (i.e., base shear) from the adjacent highrise building influenced the frequencies at which dynamic thrust acting on the tunnel was amplified.

Figure 6.2.12 compares transfer functions (TFs) of dynamic thrusts on the excavation walls in the experiments with a tall building to E-No Bldg, TFs of bending moments on the excavation wall at a depth of 8 m (a sensitive point), TFs of excavation strut forces on the bottom strut, and the FAS of the corresponding building base shear. TFs of top floor to baseplate

accelerations are also plotted to show the flexible-based natural frequency of each building. As was the case for the tunnel, a correlation was observed between the amplification of dynamic thrust and base shear, particularly during E-Highrise The amplification in axial strut forces was also strongly influenced by the inertial force or base shear of the adjacent building in E-Highrise. The bending moments on the excavation wall were also affected, but not as strongly as dynamic thrust and strut axial forces.

Figure 6.2.13 through Figure 6.2.18 focus on the comparison between E-Highrise and E-No Bldg, where the effect of building's inertia was more strongly felt by the adjacent excavation. The results show that the influence was consistently observed during all motions.

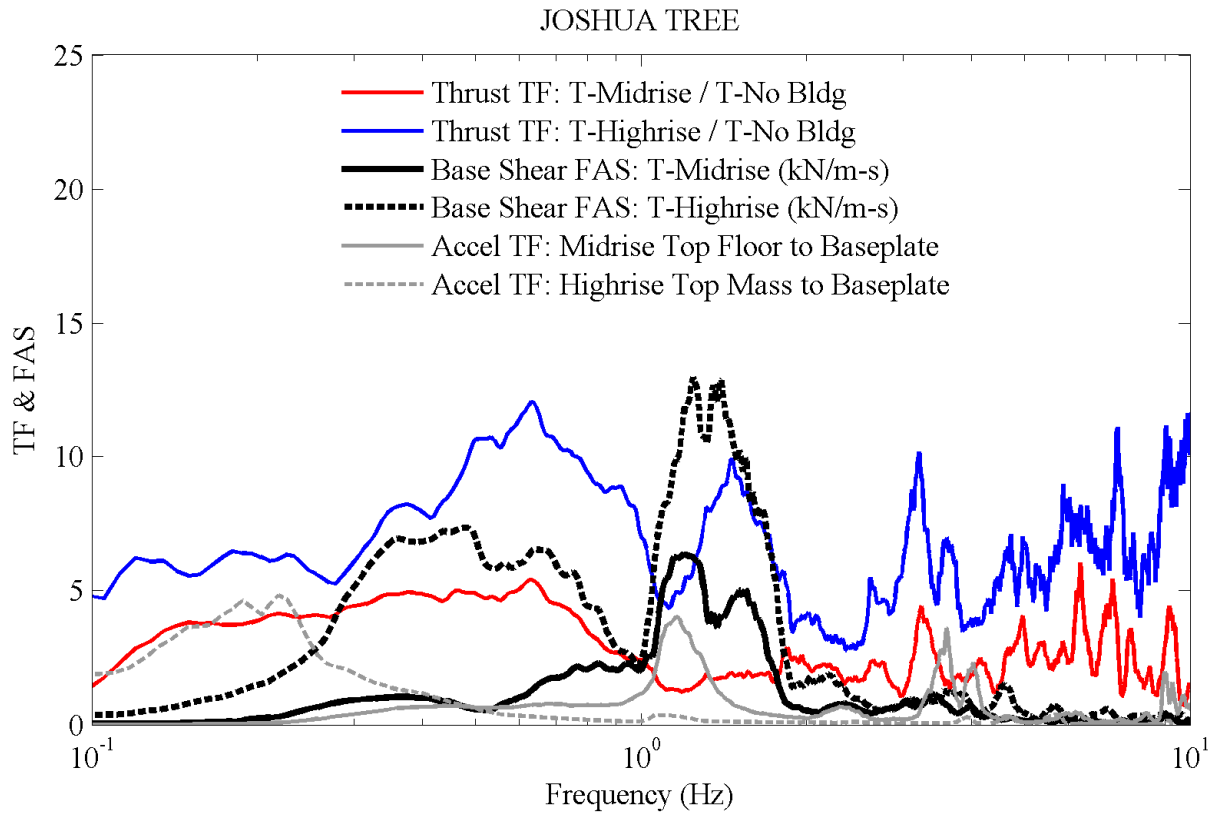

Figure 6.2.7. Transfer function of dynamic thrust on the tunnel between T-Highrise and T-No Bldg, and T-Midrise and T-No Bldg, compared with transfer function of the building's top floor/mass to baseplate, and the Fourier amplitude spectra of the building's base shear.

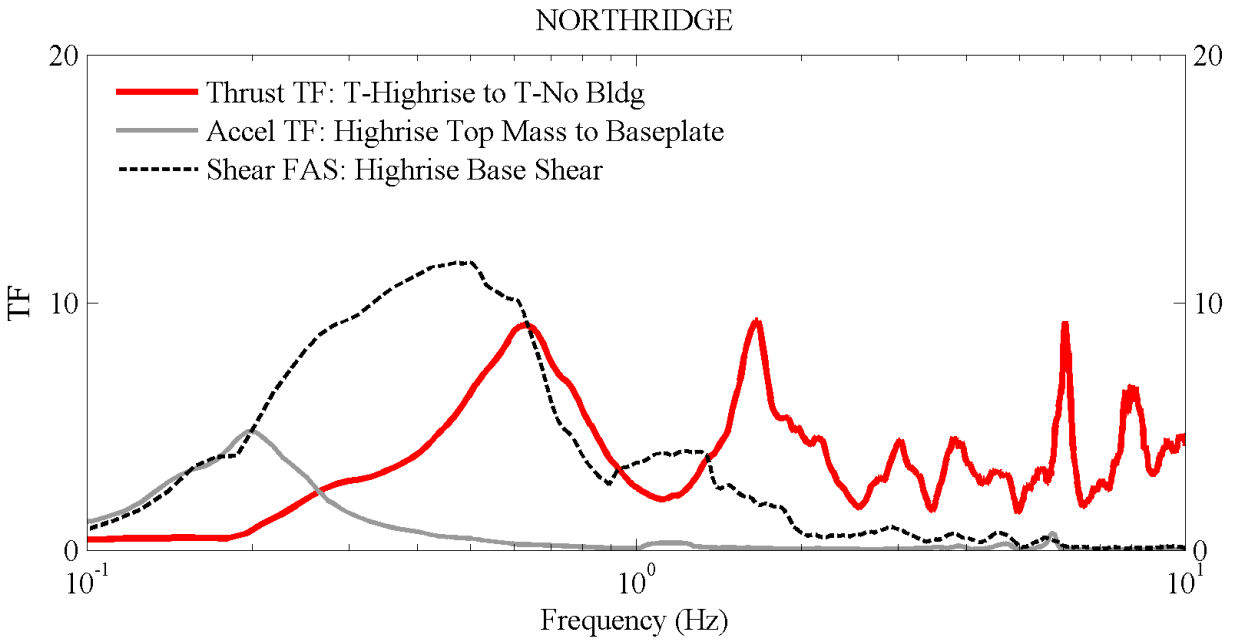

Figure 6.2.8 Transfer function of tunnel dynamic thrust (T-Highrise to T-No Bldg) compared with the TF of highrise building's top mass to baseplate and the Fourier amplitude spectra of highrise base shear during the Northridge motion.

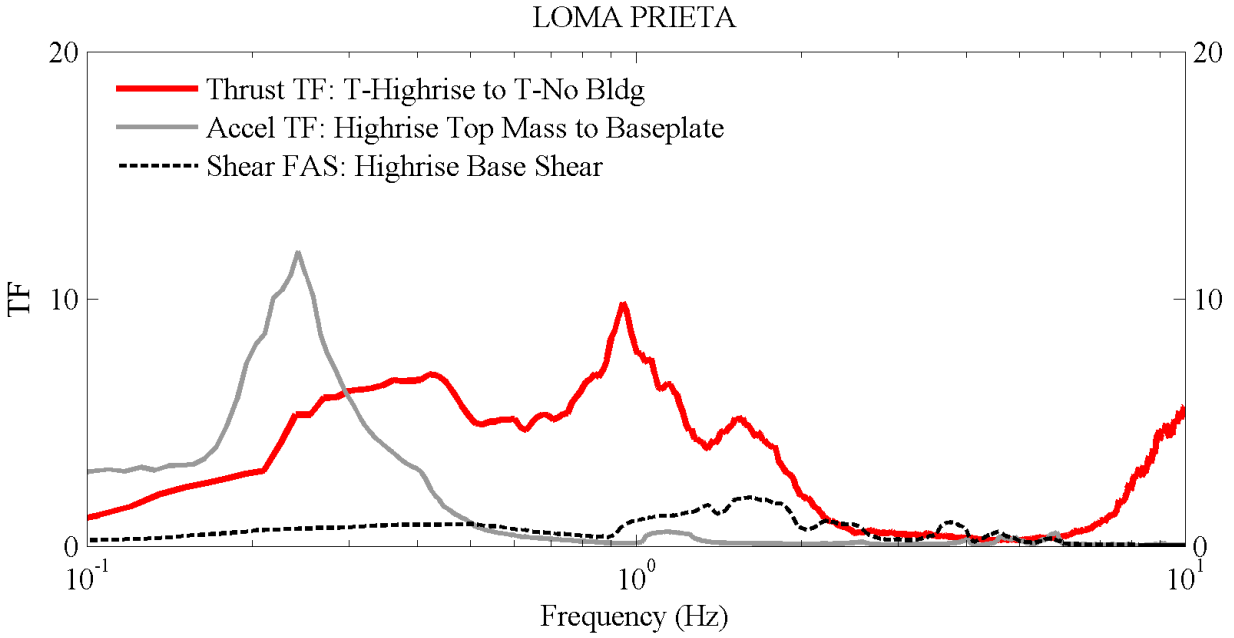

Figure 6.2.9 Transfer function of tunnel dynamic thrust (T-Highrise to T-No Bldg) compared with the TF of highrise building's top mass to baseplate and the Fourier amplitude spectra of highrise base shear during the Loma Prieta motion.

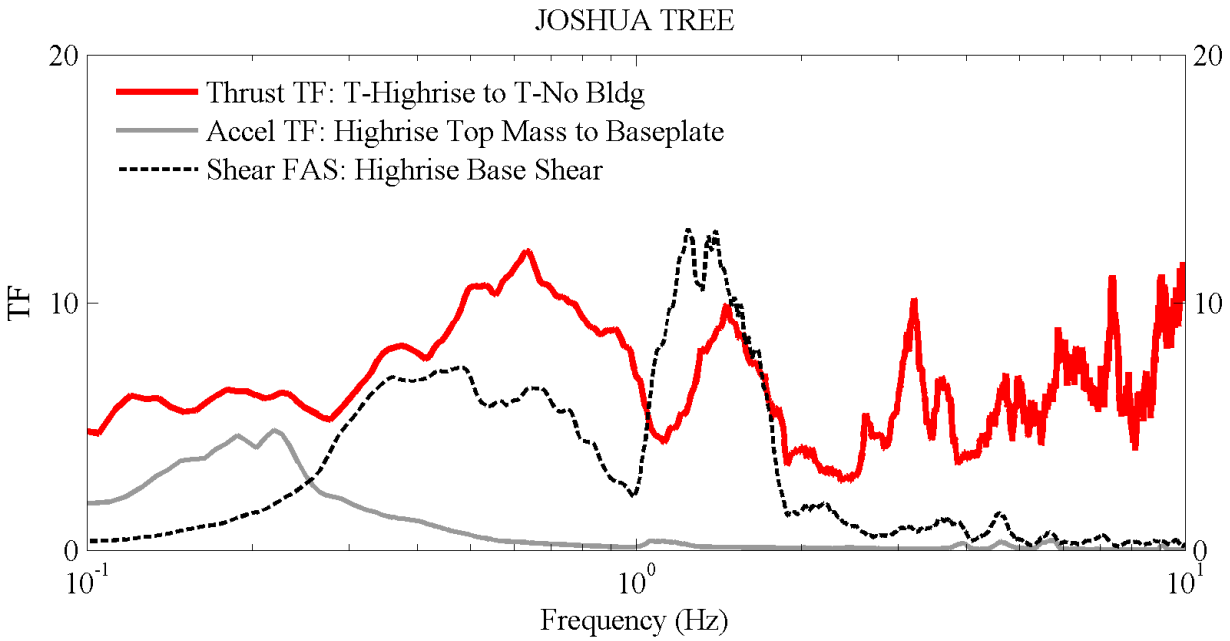

Figure 6.2.10 Transfer function of tunnel dynamic thrust (T-Highrise to T-No Bldg) compared with the TF of highrise building's top mass to baseplate and the Fourier amplitude spectra of highrise base shear during the Joshua Tree motion.

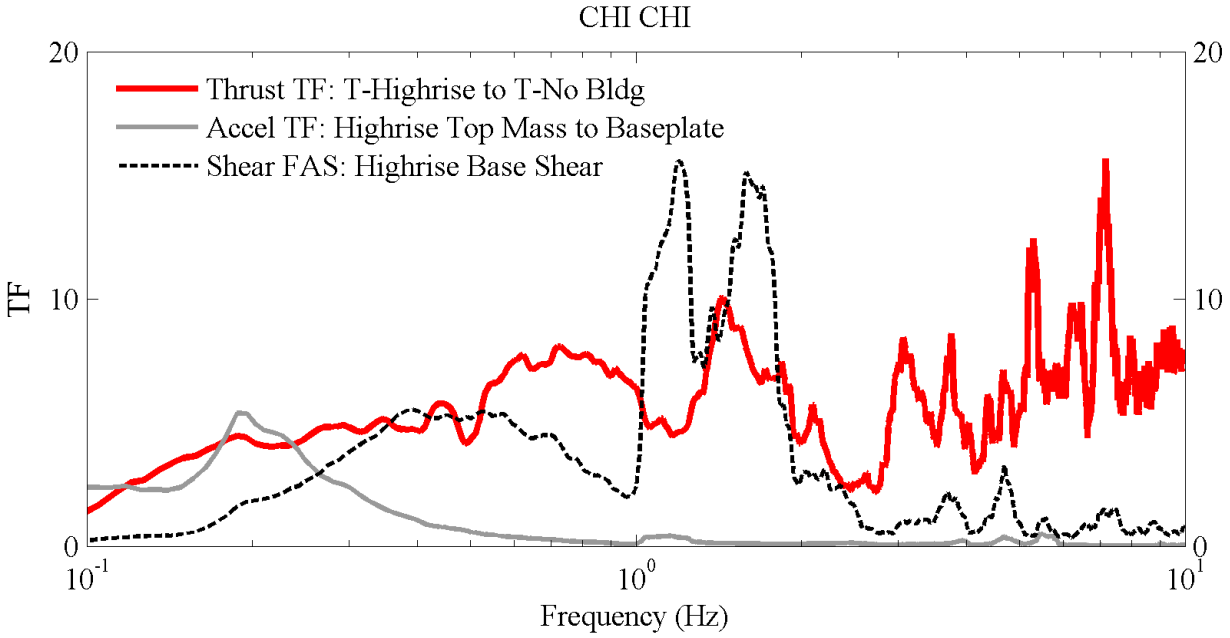

Figure 6.2.11 Transfer function of tunnel dynamic thrust (T-Highrise to T-No Bldg) compared with the TF of highrise building's top mass to baseplate and the Fourier amplitude spectra of highrise base shear during the Chi Chi motion.

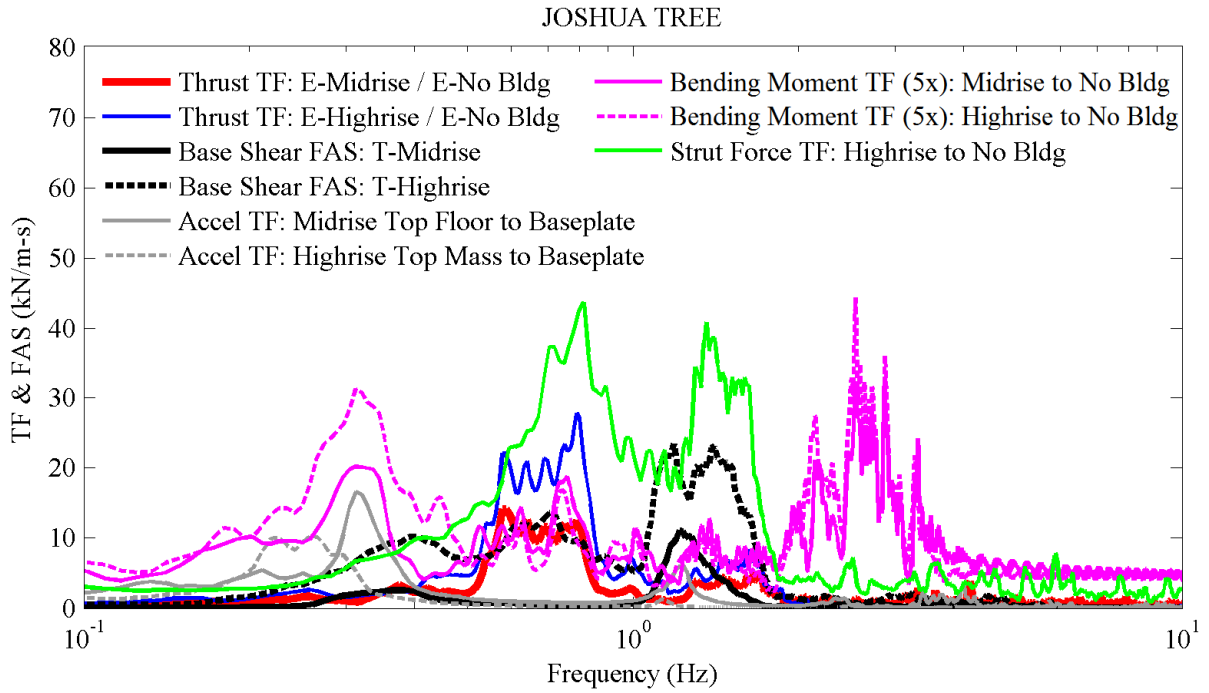

Figure 6.2.12. Transfer function (TF) of dynamic thrust on the excavation between E-Highrise and E-No Bldg, and E-Midrise and E-No Bldg, compared with TFs of the building's top floor/mass to baseplate, TFs of excavation wall bending moment, TF of strut force, and the Fourier amplitude spectra of the building's base shear.

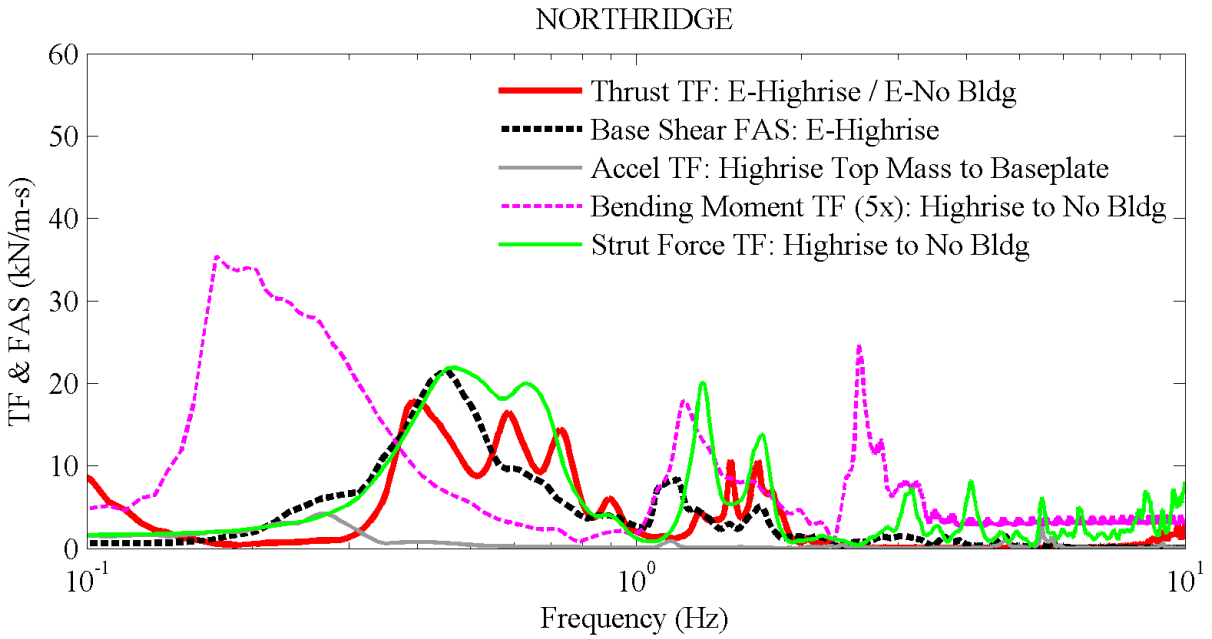

Figure 6.2.13 Transfer function (TF) of excavation dynamic thrust (E-Highrise to E-No Bldg) compared with the TF of highrise building's top mass to baseplate, TF of wall bending moment, TF of strut axial force, and the Fourier amplitude spectra of highrise base shear during the Northridge motion.

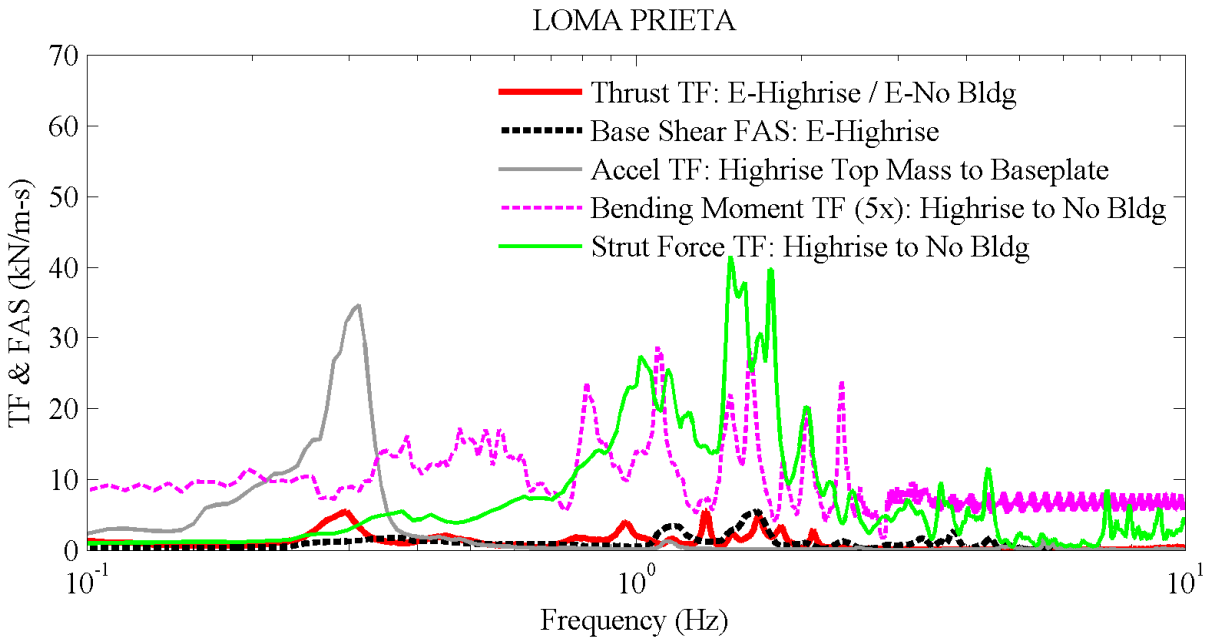

Figure 6.2.14 Transfer function (TF) of excavation dynamic thrust (E-Highrise to E-No Bldg) compared with the TF of highrise building's top mass to baseplate, TF of wall bending moment, TF of strut axial force, and the Fourier amplitude spectra of highrise base shear during the Loma Prieta motion.

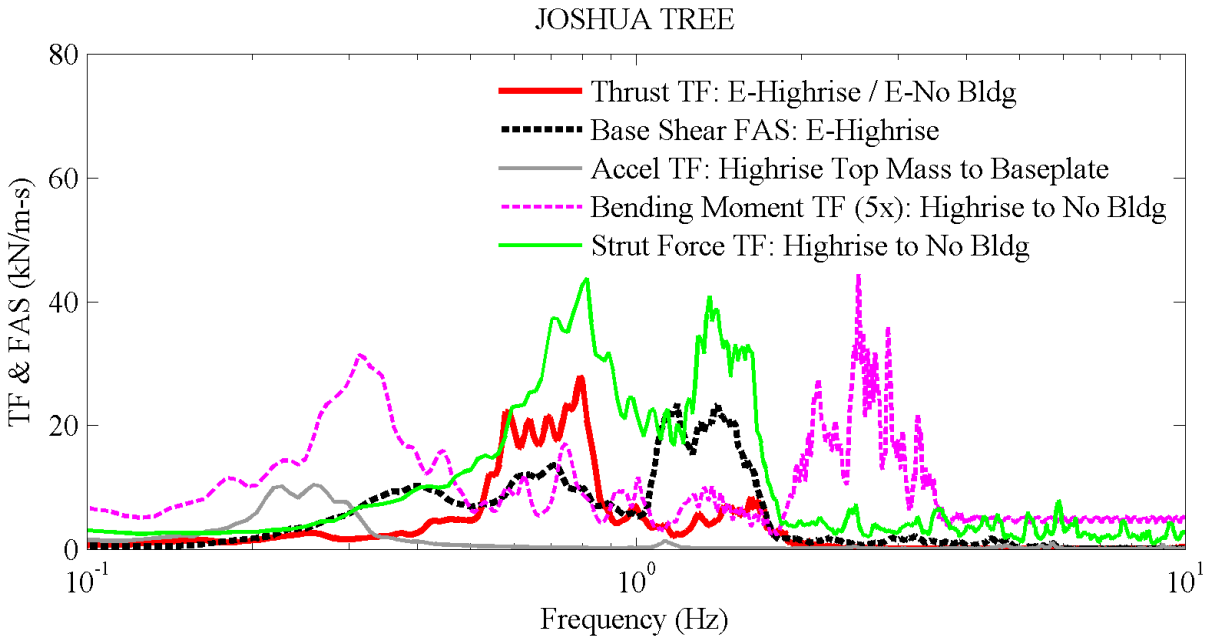

Figure 6.2.15 Transfer function (TF) of excavation dynamic thrust (E-Highrise to E-No Bldg) compared with the TF of highrise building's top mass to baseplate, TF of wall bending moment, TF of strut axial force, and the Fourier amplitude spectra of highrise base shear during the Joshua Tree motion.

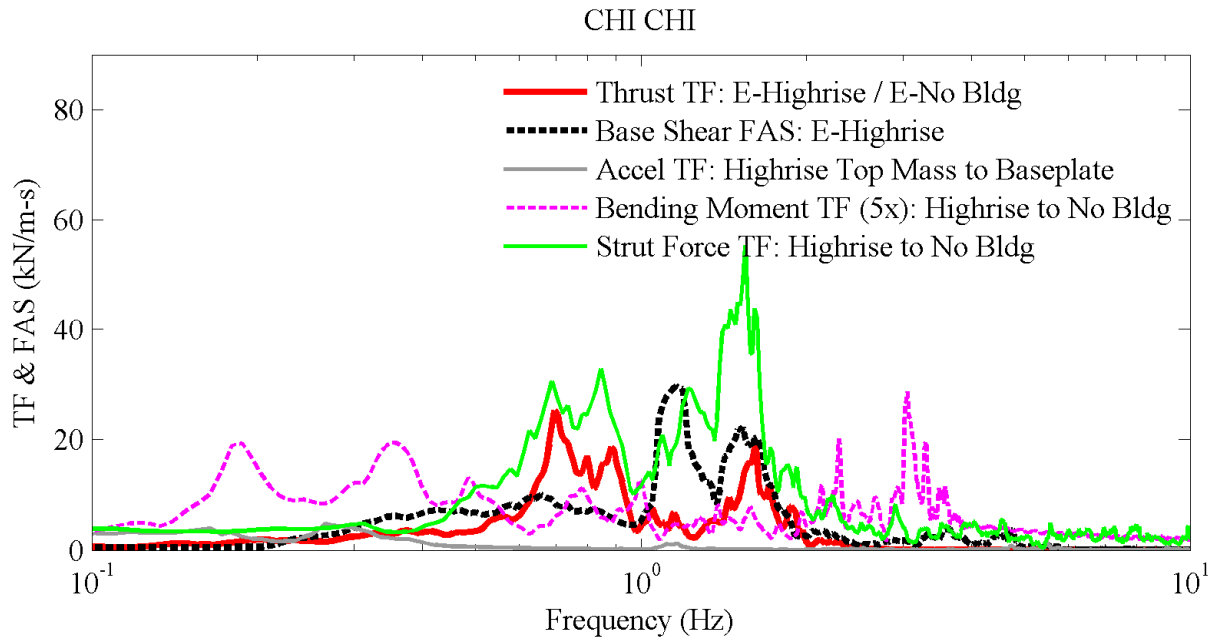

Figure 6.2.16 Transfer function (TF) of excavation dynamic thrust (E-Highrise to E-No Bldg) compared with the TF of highrise building's top mass to baseplate, TF of wall bending moment, TF of strut axial force, and the Fourier amplitude spectra of highrise base shear during the Chi Chi motion.

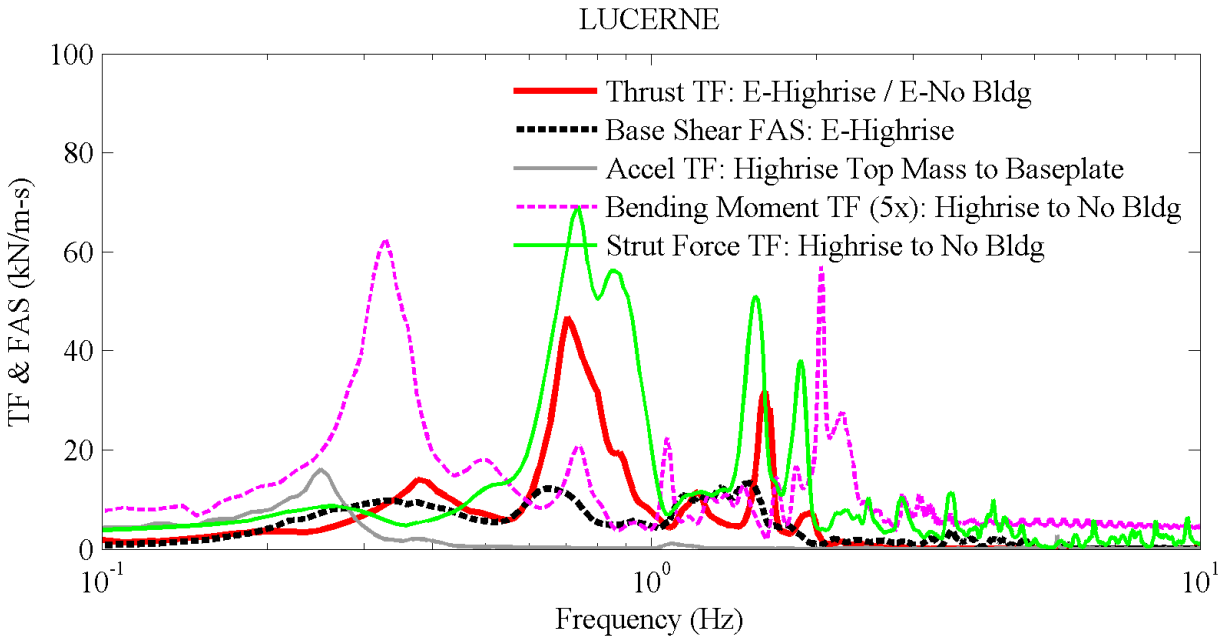

Figure 6.2.17 Transfer function (TF) of excavation dynamic thrust (E-Highrise to E-No Bldg) compared with the TF of highrise building's top mass to baseplate, TF of wall bending moment, TF of strut axial force, and the Fourier amplitude spectra of highrise base shear during the Northridge motion.

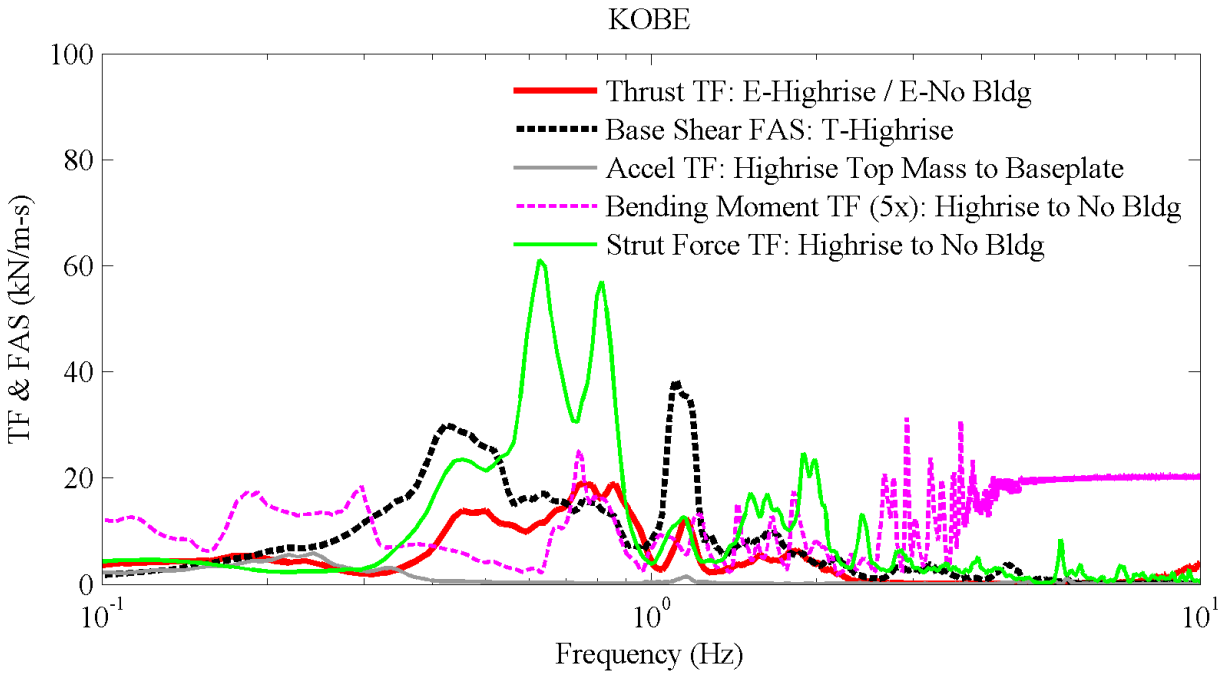

Figure 6.2.18 Transfer function (TF) of excavation dynamic thrust (E-Highrise to E-No Bldg) compared with the TF of highrise building's top mass to baseplate, TF of wall bending moment, TF of strut axial force, and the Fourier amplitude spectra of highrise base shear during the Kobe motion.

6.3 Kinematic Interaction

Kinematic interaction changes the foundation level motion on the structure relative to the free- or far-field motion, due to the presence of a foundation that is stiffer than the surrounding soil, disregarding the impact of mass and inertia. Computer simulations of kinematic SSI effects set the foundation to be massless to purely evaluate the effect from the presence of a stiff foundation. This separation of mass and stiffness (inertial and kinematic interaction) cannot be done experimentally, but their conceptual distinction is still useful for understanding the experimental results.

Kinematic effects are usually thought to affect a structure in two ways: base-slab averaging and embedment effects. Base-slab averaging describes a process when incoherent seismic waves traveling to the foundation arrive from different angles and become averaged along the

foundation. Embedment effects affect embedded structures by transmitting ground motions that are less amplified beneath the surface into the foundation. Base-slab averaging is not typically expected to play as significant a role in dynamic centrifuge experiments, in which a 1-D shake table mainly produces homogeneous, vertically propagating, horizontal shear waves that are spatially equivalent (Mason 2013). In this research, both the midrise and the highrise structures contained basements with significant embedment, but since the basements were filled with soil, the embedment effect was also expected to be minor.

Typically when investigating kinematic interaction effects, the foundation level motion of a massless structure is compared with the free-field. In this study, the response of the tall building's foundation was compared with the near-field soil at the same location without a building (similar to the previous section) to understand how the tall building's presence changed accelerations in a region that influenced the response of the soil-underground structure system (Figure 6.2.5 and Figure 6.2.6). Further, total and racking displacements of the tunnel and excavation were compared previously among experiments, another way to evaluate the influence of foundation's kinematic constraints on the displacement and distorsion of the adjacent underground structure.

The Chi Chi motion was representative of the other ground motions in the way that the soil surface generally experienced a de-amplification of accelerations at frequencies smaller than about 0.3 Hz and greater than about 1 Hz in experiments involving the tall buildings compared to the case without a building. The de-amplification of accelerations particularly at greater frequencies is likely the result of kinematic interaction near the building due to the added stiffness of the foundation and basement walls. The acceleration patterns were slightly different at greater depths, as amplification was at times observed at higher frequencies, the potential

reasons for which are discussed in the following section. Total and racking deformations on the underground structures were also previously shown to slightly decrease due to the presence of an adjacent building, likely due to the kinematic constraints introduced by the tall building with a deep basement.

6.4 Effects of Increased Confinement

The large mass of the midrise and highrise buildings was expected to have a noticeable influence on the stress conditions and hence, the stiffness and modal frequencies of the soil directly beneath and next to these tall buildings. Table 6.4.1 lists the estimated overburden pressure from the superstructure in each case. The superstructure includes all of the building components above the soil surface, including the base plate. The test soil had a unit weight of approximately 15.3 kN/m^3. At this unit weight, the additional overburden pressure contribution from the highrise building, for example, was similar to adding 20 m of soil to the surface. This large additional load was expected to increase the soil stiffness (as sand properties are pressure-dependent), which would itself act to limit the strains and importantly shift the fundamental frequency of the site to a higher value, altering the amplification patterns. The reduction in shear strains or displacements due to added shear stiffness may partially explain the previously observed reduction in accelerations at lower frequencies. The shift in the fundamental frequency of the site to a higher value may explain the amplification of accelerations observed at greater depths at higher frequencies, not explained by inertial and kinematic interaction. It must be kept in mind, however, that all mechanisms of interaction occurred simultaneously and likely affected one another, and their separation into distinct mechanisms is difficult experimentally. These hypotheses can most properly be evaluated numerically.

To confirm whether or not the presence of the structure caused a change in soil properties, results from bender elements are compared in T-Highrise and E-Highrse under the building and in the far-field. Calculating shear wave velocities from bender elements was a direct and relatively reliable way to estimate and compare small-strain properties of sand. Figure 6.4.1 shows the instrumentation layout of bender elements in T-Highrise. The location and bender element pair ID names were the same for E-Highrise. Table 6.4.2 compares the shear wave velocities measured at different locations in the T-Highrise and E-Highrise model. Pair 2 underneath the highrise, recorded the largest shear wave velocities in both experiments. Pair 3, which only worked during E-Highrise, located 8m depth beneath the baseplate recorded the largest shear wave velocities at this depth. The results clearly show that the building's overburden pressure amplified the measured shear wave velocities.

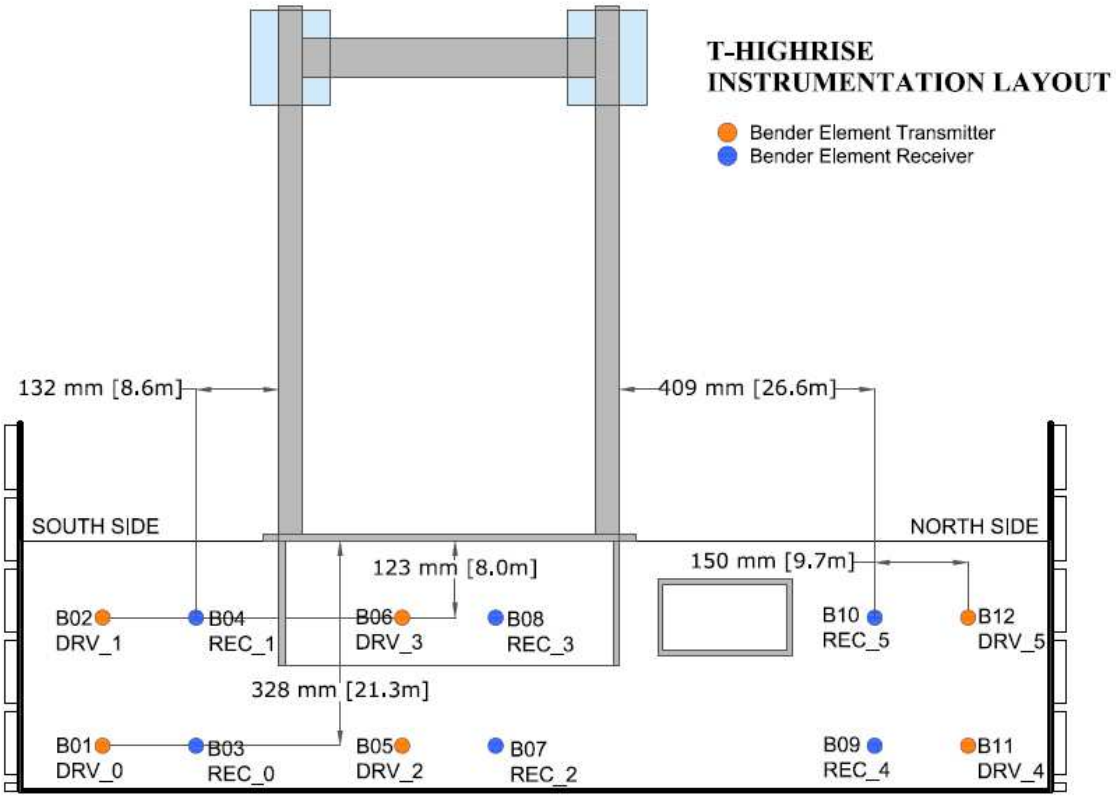

Figure 6.4.1. T-Highrise bender element layout.

Table 6.4.1. Expected overburden pressure contribution from each tall building.

Tall Building	Superstructure Weight (kN)	Baseplate Area (m^2)	Contact Pressure (kPa)
Midrise	52804	24.8 m x 40.8 m = 1010 m^2	52
Highrise	460147	38.8 m x 38.8 m = 1506 m^2	306

Table 6.4.2. Shear wave velocities at different locations of the T-Highrise and E-Highrise tests.

T-Highrise			E-Highrise		
Bender Pair	Depth (m)	V_S (m/s)	Bender Pair	Depth (m)	V_S (m/s)
Pair 0	21.3	294 - 319	Pair 0	21.3	294 – 319
Pair 1	8	224 - 254	Pair 1	8	227 – 246
Pair 2	21.3	306 - 323	Pair 2	21.3	300 - 326
Pair 4	21.3	254 - 283	Pair 3	8	246 - 268
Pair 5	8	231 - 250	Pair 4	21.3	263 – 283
			Pair 5	8	224 - 242

6.5 Summary

Experimentally evaluated mechanisms of SSUSI were conceptually broken into three effects from: 1) building's inertia, 2) foundation's kinematic constrains, and 3) building's added confinement, in order to better understand the mechanisms causing change in the seismic performance of the underground structures both in terms of seismic deformations and loads. Inertial effects from the tall buildings did not increase accelerations or displacements in their vicinity near the flexible-based, first mode frequency of the corresponding building. However, building's inertial force (or base shear) greatly influenced the increase in dynamic forces (e.g., dynamic thrust on the walls, axial forces on the struts), as the increase in dynamic forces were roughly correlated with the base shear forces of the adjacent building, particularly the highrise building with a greater inertial impact.

Kinematic interaction effects were expected to be minor in these experiments, mainly because of the application of 1-D motions (reducing base-slab averaging compared to real field conditions) and basements that were filled with sand (reducing embedment effects). However, the slight reduction in accelerations at frequencies less than about 0.3 Hz and greater than 1 Hz (not near the building's modal frequencies) were likely primarily due to kinematic interaction. Further, the slight reduction in total and racking deformations observed on the underground structures were likely due to the kinematic constraints introduced by the building's foundation and basement. Lastly, the increased overburden pressure due to the presence of tall buildings increased the stiffness and fundamental frequency of the soil in the vicinity of the building, which were expected to change the strains and amplification patterns in accelerations as well as seismic forces. The additional confining stress in soil under and near the structure increased soil's shear modulus and , which likely contributed to the reduction of shear strains and

accelerations at lower frequencies. The added confinement also increased the soil's fundamental frequency by increasing its stiffness, which in turn amplified near-field accelerations at greater frequencies compared to the case without a building. The added confinement was also observed to increase static lateral earth pressures acting on the underground structures, as expected.

Chapter 7

7 CONCLUSIONS AND RECOMMENDATIONS

7.1 Conclusions

In seismically active, dense urban environments, tall buildings and other above and belowground structures interact with one another through the soil during earthquakes. These interactions are currently not well-understood. This work aims to provide a better and more fundamental understanding of the mechanics of seismic soil-structure-underground structure-interaction (SSUSI) experimentally with relatively simple soil and structure configurations in order to validate advanced numerical tools that are used in design. In total, six large scale centrifuge tests were performed at UCD-CGM in 2012, 2013, and 2014. Three centrifuge experiments evaluated the seismic performance of an underground box structure, first in isolation and subsequently adjacent to a midrise and then a highrise building. Another three centrifuge tests evaluated the response of a temporary braced excavation in a similar manner. The midrise and highrise building models were specifically designed to replicate the key dynamic properties of a 13 and 42 story building. This dissertation summarizes the centrifuge testing plan, approximations and considerations needed to design, build, and test the key components of tall buildings and evaluate

their impact on soil and adjacent underground structures during earthquakes, instrumentation challenges, and the insight gained from experimental results and recordings.

The key conclusions made from experimental results are summarized below to enable a better understanding of the mechanics of SSUSI, as observed experimentally. It must be noted that these conclusions are preliminary and based on centrifuge experiments only. Although insightful in evaluating trends and underlying mechanisms, experiments alone are affected by instrumental uncertainties and limited by the simplified configurations employed. Parallel numerical simulations (currently under way by the research team) are needed before providing generalized conclusions and recommendations for practice. In the conclusions below, the experiments that did not have a building present are used as baseline (T-No Bldg and E-No Bldg), in order to evaluate the impact of an adjacent tall building on the seismic response of the soil-underground structure system. The response of the buildings alone or the effects of the underground structure on building performance was not the focus of this investigation.

- *Inertial* and *kinematic* interaction as well as changes in *confining stress* had different effects on displacements and forces induced on the soil-underground structure system by the adjacent building: Horizontal accelerations near the tunnel were generally de-amplified (particularly at lower frequencies) with the presence of an adjacent mid to highrise building. This de-amplification was likely caused by the *kinematic constrains* introduced by the rigid foundation and deep basement walls as well as the *increased confinement* in the soil near the buildings, increasing shear stiffness and limiting strains. The added confinement also increased the fundamental frequency of the soil near the building, slightly amplifying the motions at higher frequencies compared to the case without a building. The impact of *building inertia* on the adjacent underground structure's accelerations was negligible, as no

amplification was observed near the fundamental frequency of the adjacent building. However, the highrise building's *inertial forces* appeared to have significantly increased the dynamic earth forces (e.g., lateral earth pressures and strut axial loads) on underground structures.

- Due to the de-amplification of near-field accelerations at lower frequencies, the transient lateral displacements measured along the walls of the permanent box structure in some cases decreased slightly with the addition of an adjacent midrise or highrise building. The racking displacement of the box structure, defined as the relative transient lateral displacement of the roof with respect to the base, also decreased with the addition of a tall building (similar on the two walls). The reduction in peak tunnel racking in T-Midrise and T-Highrise compared to T-No Bldg ranged from about 28 to 40% during different motions.
- The racking displacement of the braced excavation, here defined as the relative transient lateral displacement of the top of each wall with respect to the base of the excavation, decreased with the addition of an adjacent tall building, but in an unequal manner (a larger reduction on the building-side of the wall compared to the free-side). The reduction in peak excavation racking in E-Midrise and E-Highrise compared to E-No Bldg ranged from about 20 to 40%.
- Racking versus Flexibility Ratios obtained experimentally during T-No Bldg and E-No Bldg compared well with the NCHRP 411 recommendation commonly used in design. The experimental results were, however, lower than the NCHRP guideline in the tests with an adjacent midrise or highrise building, due to the racking constraint provided by the adjacent tall building and its deep basement. It must be noted, however, that in this exercise, the flexibility ratio was simplistically obtained based on the stiffness of the underground

structure and that of the soil in the free-field (away from any underground or aboveground structure). Whereas in a setting where an adjacent tall building is present, a more proper approach may be to consider soil properties in the vicinity of the tall building, which are different due to the added confinement.

- Dynamic bending strains and moments recorded around the permanent box structure did not change significantly and reduced slightly with the addition of an adjacent tall building, which was in line with the lateral displacement and racking observations on this type of structure.
- Static and dynamic bending strains along the excavation walls and axial strains on the struts increased notably with the addition of an adjacent building. These observations are not in line with those of lateral displacement and racking. This is because of the nonlinear and S-shaped deformations observed along the excavation walls as opposed to a roughly linear deformation pattern that is assumed when computing racking.
- Dynamic lateral earth pressures and thrust increased significantly on the walls of both underground structures when an adjacent midrise or highrise building was present. The increase in dynamic thrust, however, was more substantial on the permanent box structure that did not undergo large deformations, and it was strongly affected by the building's inertial response. Dynamic earth pressures increased on both sides of the underground structures with the addition of a building on one side.
- The timing of increase in dynamic thrust was generally consistent with the timing of decreased gap between the underground structure and the adjacent basement. Further, base shear forces from the midrise and highrise buildings calculated at their foundation level was comparable in amplitude and frequency content to the measured dynamic thrust on the tunnel

and excavation walls. These trends confirmed the importance of the inertial response of the building on the dynamic earth pressures imposed on the underground structure.

- The increased dynamic earth pressures and thrust measured on the permanent box structure with the addition of an adjacent building did not translate into increased deformations, neither in terms of transient lateral displacements and racking nor in terms of dynamic bending strains. Therefore, not considering an adjacent building in their design may be reasonable within a performance-based design framework. This observation, is however, limited to the type of permanent box structure, soil condition, and ground motions considered in this study and may not be generalized.
- The increased dynamic thrust on the excavation, although smaller than the tunnel, did not change racking displacements but notably amplified bending strains along the walls and axial forces on the struts. This shows that racking, which assumes a linear displacement pattern, may be an insufficient parameter in evaluating the performance of flexible braced excavations. The observed large increase in strains along the walls and struts have potentially significant implications for the seismic design of these more flexible underground structures in dense urban environments, justifying more advanced simulations that consider SSUSI.

7.2 Future Research Needs

In a limited set of experiments, only a number of key parameters can be identified and studied systematically. Additional parameters, if found to be important, can be studied via additional tests or well calibrated numerical tools. In this fundamental study, certain properties of the tall buildings, such as their mass and fundamental frequencies were judged important, while other properties such as building height and seismic moment had to be sacrificed. Buildings with

relatively low fundamental frequencies (near 0.25 and 0.33 Hz) were selected in this study with the intention of simulating realistic fundamental frequencies for tall buildings. However, it was shown to be difficult to excite those structures with the motions achieved, given the limitation of the centrifuge shake table to produce long period (low frequency) motions. Therefore, it was difficult to maximize the impact of inertial interaction in these experiments. Simplistic and uncommon soil conditions (dry, medium dense sand) were used to evaluate the complex interactions, instead of a more realistic and complex soil profile. A series of 1-D horizontal motions were applied to the base of the container with a range of properties, yet real motions are 3-D.

In future experimental studies, it is recommended to consider heavy buildings at a range of fundamental frequencies that the shake table can excite adequately, to maximize the interaction and evaluate its effects. Other soil conditions and their influence on SSUSI must be evaluated in the future. Further, the impact of multi-dimensional loading on the nature of these complex interactions needs to be studies in the future. A growing number of centrifuge shaking tables are becoming capable of applying 2-D horizontal motions successfully in centrifuge, which is a good start. Numerical modeling tools, once validated against experiments even with simplistic conditions (such as those presented in this research), can be valuable in evaluating the interaction of tall buildings and a nearby underground structure by isolating each mechanism and varying various properties and components of the different structures. These numerical tools can then be employed in a parametric study toward developing reliable procedures and guidelines for practicing engineers for the seismic design of underground structures in dense urban environments.

REFERENCES

Abrahamson, N.A., J. F. Schneider, and J. C. Stepp (1991). "Empirical spatial coherency functions for application to soil-structure interaction analyses," Earth Retention Conference 635 *Earthquake Spectra*, Vol. 7, No. 1, 1-27.

Al Atik, L. F. (2008). "Experimental and analytical evaluation of seismic earth pressures on cantilever retaining structures," Ph.D. Dissertation, Department of Civil and Environmental Engineering, University of California, Berkeley.

Anderson, Donald G., Geoffrey R. Martin, Ignatius Lam, and J. N. Wang (2008). "Seismic analysis and design of retaining walls, buried structures, slopes and embankments," National Cooperative Highway Research Program, Transportation Research Board.

Arango, Ignacio (2008). "Earthquake engineering for tunnels and underground structures. A case history.," In: David Zeng, Majid T. Manzari, and Dennis R. Hiltunen, Eds., Geotechnical Earthquake Engineering and Soil Dynamics IV. Sacramento, CA: ASCE.

Brandenberg, Scott J., George Mylonakis, and Jonathan P. Stewart. (2015). "Kinematic framework for evaluating seismic earth pressures on retaining walls." Journal of Geotechnical and Geoenvironmental Engineering.

Darendeli, M. B. (2001). "Development of a new family of normalized modulus reduction and material damping curves," Civil Engineering. Austin: University of Texas at Austin, 395.

Dashti, S., Bray, J.D., Pestana, J.M., Riemer, M.R. and Wilson, D. (2010). "Mechanisms of seismically-induced settlement of buildings with shallow foundations on liquefiable soil," *Journal of Geotechnical and Geoenvironmental Engineering*, ASCE, Vol. 136, No. 1, 151-164.

Dashti, S., Gillis, K.M., Hashash, Y., (2012). “Sensing of lateral seismic earth pressures in geotechnical centrifuge modeling,” 15th World Conference on Earthquake Engineering. Paper No. 3552.

Ditommaso, R., M. Mucciarelli, M. R. Gallipoli, and F. C. Ponzo (2010). “Effect of a single vibrating building on free-field ground motion: numerical and experimental evidences,” Bulletin of Earthquake Engineering 8, 693-703.

Duncan Electronics, Linear potentiometers, Costa Mesa, CA

Ertugrul, O. (2014). “Seismic behavior of box-shaped culverts buried in cohesionless soils,” Pipelines 2014: pp. 2149-2160.

Gallipoli, M. R., M. Mucciarelli, F. Ponzo, M. Dolce, E. D'Alema, and M. Maistrello (2006). “Buildings as a seismic source: Analysis of a release test at Bagnoli, Italy,” Bulletin of the Seismological Society of America 96 (6), 2457-2464.

Ghayoomi, M., and Dashti, S. (2013). “Effect of ground motion characteristics on seismic soil-foundation-structure interaction,” Earthquake Spectra Journal, Earthquake Engineering Research Institute.

Gillis, K.M., (2013). “Tactile pressure sensor calibration methods and data analysis for geotechnical centrifuge modeling.” M.S. Thesis, Department of Civil, Environmental, and Architectural Engineering, University of Colorado, Boulder.

Gillis, K., Dashti, S., Hashash, Y. (2015). “Dynamic calibration of tactile sensors for measurement of soil pressures in centrifuge,” ASTM Geotechnical Testing Journal, 38(3), 1-14.

Hao, H., Oliveria, C. S. and Penzien, J. (1989). "Multiple-station ground motion progressing and simulation based on SMART-1 array data," Nuclear Engineering and Design, Vol. 111.

Hashash, Y. M. A., J.J. Hook, B Schmidt, and J. I-C. Yao (2001). "Seismic design and analysis of underground structures," *Tunneling and Underground Space Technology*, Vol. 16, 247-293.

Hibbitt, Karlsson and Sorensen Inc., ABAQUS User's Manual.

Idriss, I.M. (1990). "Influence of local site conditions on earthquake ground Motions," Proceedings of the 4th U.S. National Conference on Earthquake Engineering. Palm Springs, 55-57.

Idriss, I.M., and J.I. Sun (1992). "SHAKE91: A computer program for conducting equivalent linear seismic response analyses of horizontally layered soil deposits," Department of Civil and Environmental Engineering, University of California Davis.

Itasca Consulting Group Inc. (1992). "Universal Distinct Element Code ŽUDEC." User's Manual.

Itasca Consulting Group Inc. (1995). "FLAC3D, Version 3.3: Fast Legrangian Analysis of Continua."

Jones, C. (2015). "Interpretation of centrifuge test results of the seismic response of temporary braced excavations near tall buildings," Master's thesis, Dept. of Civil, Environmental, and Architectural Engineering, University of Colorado, Boulder.

Kawamata, Y. (2010). "Present situation of geotechnical engineering research project in NIED: E-Defense shaking table test on large-scale model underground structures in 2011," Presentation at the 8th NEES/E-Defense Planning Meeting in Kobe, Japan.

Kramer, S. L. (1996). Geotechnical earthquake engineering, Upper Saddle River, N.J.: Prentice Hall.

Kuesel, T. R. (1969). “Earthquake design criteria for subways,” Journal of the Structural Divisions, ASCE, Vol. 95, No. ST6, June

Liu, H. and Song, E. (2005). “Seismic response of large underground structures in liquefiable soils subjected to horizontal and vertical earthquake excitation,” Computers and Geotechnics, Vol. 32, 223-244.

Luu, A. (2013). Seismic earth pressures measured during a shake table experiment of underground structures, Master’s thesis, Dept. of Civil and Environmental Engineering, University of California, Irvine.

Lysmer, J., Udaka, T., Tsai, C.F., Seed, H.B., (1975). FLUSH: A computer program for approximate 3-D analysis of soil-structure interaction problems. Report no. EERC 75-30. Earthquake Engineering Research Center.

Lysmer, J., Ostadan, F., Tabatabaie, M., Tajirian, F., Vahdani, S., (1991). SASSI: A system for analysis of soil-structure interaction "User’s Manual. Geotechnical Engineering Division, Civil Engineering Department, University of California at Berkeley, and Bechtel Corporation, San Francisco, California.

Martin, G. and Lam, I.P. (2000). “Earthquake resistant design of foundation-retrofit of existing foundations,” Proceedings of GeoEngineering 2000 Conference, Melbourne, Australia.

Mason, H.B., (2011). Seismic performance assessment in dense urban environments. Ph.D. Dissertation, Dept. of Civil and Environmental Engineering, University of California, Berkeley.

Mason, H.B., Trombetta, N.W., Chen, Z., Bray, J.D., Hutchinson, T.C., Kutter, B.L. (2013). “Seismic soil-foundation-structure interaction observed in geotechnical centrifuge experiments,” Soil Dynamics and Earthquake Engineering 48, 162-174.

Matasovic, N. (1993). "Seismic response of composite horizontally-layered soil deposits," University of California, Los Angeles, pp xxix, 452 leaves. Okamoto, S., Tamura, C., Kato, K., Hamada, M., 1973. Behaviors of submerged tunnels during earthquakes. Proceedings of the Fifth World Conference on Earthquake Engineering, vol. 1. Rome, Italy, 544-553.

Mikola, R. G., (2012). "Seismic earth pressures on retaining structures and basement walls in cohesionless soils". Ph.D. Dissertation, Dept. of Civil and Environmental Engineering, University of California, Berkeley.

Mononobe, N, and Matsuo M. (1929). "On the determination of earth pressures during earthquakes," Proceedings, World Engineering Congress, Vol. 9, 179-187.

Mucciarelli, M., M. R. Gallipoli, F. Ponzo, and M. Dolce (2003). "Seismic waves generated by oscillating buildings: analysis of a release test," Soil Dynamics and Earthquake Engineering 23, 255-262.

Okabe, S., (1926). "General theory of earth pressure," *Journal of the Japanese Society of Civil Engineers*, Tokyo, Japan, Vol. 12 , No. 1,

Ostadan, F., and J. Penzien (2001). "Seismic sesign of cut-and-cover sections of the bay area rapid transit extension to San Francisco airport," Second US-Japan Soil Structure Interaction Workshop Tsukuba, Japan.

Ostadan, F. (2005). "Seismic soil pressure for building walls: An updated approach." Soil Dynamics and Earthquake Engineering, 25(7), 785-793.

Oughourlian, C.V., Powell, G.H. (1982). ANSR-III: General purpose computer program for non-linear structural analysis. Report no. UCB/EERC 82/21. Earthquake Engineering Research Center.

Owen, G. Norman, and Roger E. Scholl (1981). "Earthquake engineering of large underground structures: Report no. FHWA/RD-80/195. Federal Highway Administration and National Science Foundation.

Ozkan, M.Y., Ulgen,D., Saglam, S., (2013). "Centrifuge modeling of dynamic behavior of box shaped underground structures in sand: Final report." Seismic Engineering Research Infrastructures for European Synergies (SERIES). Project No: 227887.

Paikowsky, S.G., Parmer, C.J., Rolwes, L.E., (2006). The use of tactile sensor technology for measuring soil stress distribution, GeoCongress 2006–Geotechnical Engineering in the Information Technology Age.

Palmer, M.C., O'Rourke, T.D., Olson, N.A., Abdoun, T., Ha, D., O'Rourke, M.J. (2009). Tactile pressure sensors for soil-structure interaction assessment. Journal of Geotechnical and Geoenvironmental Engineering. 135(11), 1638–1645.

PCB Piezotronics (2010). General Operating Guide for use with Piezoelectric ICP® Accelerometers,

http://www.pcb.com/contentstore/docs/PCB_Corporate/Vibration/Products/Manuals/353B12.pdf

Pecker, A. and Pender, M. (2000). "Earthquake resistant design of foundations: new construction," Proceedings of GeoEngineering 2000 Conference, Melbourne, Australia.

Pitilakis, K., Kirtas, E., Sextos, A., Bolton, M., Madabhushi, G., and Brennan, A. (2004). "Validation by centrifuge testing of numerical simulations for soil-foundation-structure systems," Proceedings of 13th World Conf. Earthquake Engineering, Vancouver, Canada.

Romero Arduz, M.I., Hashash, Y., Dashti, S., Ghayoomi, M. (under review). "Evaluation of 1-D seismic site response modeling of sand using centrifuge experiments," Soil Dyn. and Earthquake Eng. Journal.

Seed, H.B., and Whitman, R.V. (1970). “Design of earth retaining structures for dynamic loads,” ASCE Specialty Conference, Lateral Stresses in the Ground and Design of Earth Retaining Structures, Cornell Univ., Ithaca, NY, 103–147.

Stadler A.T. (1996). “Dynamic centrifuge testing of cantilever retaining walls,” PhD Thesis, Department of Civil, Environmental, and Architectural Engineering, University of Colorado, Boulder.

Stewart, D.P., Idriss, I.M., Boulanger, R.W., Hashash, Y., Schmidt, B. (1999). “Mitigation of earthquake liquefaction hazards: a review of physical modeling studies,” Proc., 8th Australia New Zealand Conference on Geomechanics, Hobart, V. 1, 337-343.

Tekscan, Inc., 2012. I-Scan & High-Speed I-Scan User Manual v.7.5x, Tekscan Inc., Boston, MA.

Tsai, Chi-Chin, and Y.M.A. Hashash (2010). "Evaluation of two approaches to simulate spatially variable ground motions," *Journal of Earthquake Engineering*, Vol. 14, No. 2, pp. 293 - 308.

Vishay Precision Group, Precision Strain Gages, Micro-Measurements (2010).

Vucetic, Mladen, and Ricardo Dobry (1991). "Effect of soil plasticity on cyclic response," *Journal of Geotechnical Engineering*, Vol. 117, No. 1, 87-107.

Wang, J.N. (1993). "Seismic design of tunnels: a state-of-the-art approach," Monograph 7. New York, NY: Parsons Brinckerhoff Quade & Douglas, Inc.

Wood, J.H. (1973). “Earthquake induced soil pressures on structures,” PhD Thesis, California Institute of Technology, Pasadena, CA.

Wu, C. L., and J. Penzien (1994). "Seismic design of muni metro turnback project," Fifth U. S. National Conference on Earthquake Engineering. Chicago, IL, 799-808.

APPENDIX: Experimental Challenges and Recommendations for New Experimentalists

A1 Known Challenges in Model Preparation and Instrumentation

During model preparation, consistently controlling the relative density of sand with dry pluviation was challenging, particularly nearly the boundaries of the container and structures. Although every effort was made to deposit the test soil at 55% relative density throughout the container for each test, it is recognized that complete uniformity was not possible with the pluviation method employed. As detailed in Chapter 3, the model structures used in this research were the tallest models ever tested in centrifuge, introducing new challenges in their design, instrumentation, and testing which should be considered when modeling tall buildings.

A small number of instruments in each test malfunctioned for various reasons. During the first experiment, the stems of three of the four tactile pressures sensor's ripped in the centrifuge due to air moving past the bucket while spinning. This was fixed in later experiments by reinforcing the pressure sensor stems with a layer of aluminum sheet metal. However, data could not be collected on both sides of the tunnel during T-No Bldg as a result of this damage. In addition, obtaining reliable earth pressure measurements in dynamic centrifuge experiments is challenging and topic of ongoing research (e.g., Dashti et al. 2012; Gillis et al. 2015). Tactile sensors are advantageous over traditional earth pressure cells because they avoid soil arching effects. Issues related to under-sampling and a frequency-dependent response were minimized in this research by using a proper sampling rate and developing a dynamic calibration methodology, as detailed by Gillis et al. (2015). However, the recordings of these sensors should still be treated

with caution, as they can be strongly influenced by air trap inside the sensor and local in-homogeneities in the contact soil. Therefore, it is important to evaluate other measurements, such as strains, in parallel before drawing definite conclusions on the applied forces.

Strain gauges experienced a large degree of long term drift during T-Midrise and T-Highrise, making measurement of static and total strains not possible. Also, due to a mistake in the channel list, the axial strain gauges on the excavation struts in E-Midrise did not save data, which was unfortunate as these were critical measurements. The linear potentiometers (LPs) were not a reliable means of measuring transient displacements in these tests. This was partly because all LPs require a bracket to hold them in position to measure vertical or lateral displacements. In many cases, the transient measurements obtained from LPs were compromised by the independent movement of the longer brackets holding the LPs. LPs were, however, useful when measuring residual settlements and lateral displacements. Due to the motion of the LP brackets, accelerometers were often used to measure transient displacements through double integration.

Integrated Circuit-Piezoelectric (PCB) accelerometers were one of the more reliable instruments used in the centrifuge experiments. Much of the conclusions reached were done so using the accelerometer data alone. However, a number of accelerometers went out of range during strong shaking or malfunctioned. Also, cables connecting the ICP accelerometers to the DAQ system would come loose at times, compromising their measurements. Fortunately, however, in most cases there was enough redundancy to still obtain reliable measurements at key locations.

A2 Recommendations to New Centrifuge Modelers

For researchers planning to do experimental research using the geotechnical centrifuge, there are many things to become familiar with including a new setting, people, work environment, equipment, and procedures. Understanding what each centrifuge staff person's specialties are can be very helpful in building a successful experiment. Therefore, it's important to spend time with each staff person when first arriving to the centrifuge. Also, talking to professors and other graduate students who have experience with centrifuge testing can be valuable. Model construction is a physically demanding process that can take anywhere from three to six weeks, and sometimes longer depending on the type of model being constructed. It's extremely helpful to have at least one person helping with the construction of each large centrifuge test, which is often a great opportunity to mentor undergraduate and beginning graduate students. A very detailed schedule and testing plans ahead of time that was prepared and confirmed with project PI was helpful to estimate a timeline for each test and task.

For the last two centrifuge tests in this test series, our team cleaned the centrifuge container and painted the interior with a thin layer of white spray paint. This made marking key elevations where either instruments or structures would be placed in the model more organized and easy to follow. Pluviating sand into the centrifuge container at a targeted relative density is a challenge. Our team spent a worthy amount of time calibrating the sand hopper. It is critical to take the time and care during this step, as achieving the target relative density consistently is very important over the course of a centrifuge test series. When placing structures in the centrifuge container, one must check how level they are relative to the centrifuge container. Never rush model construction and always ask yourself what you are forgetting before continuing on to the next step.

It is standard practice to make sure each instrument is working and calibrated before used in the model. It's important to understand how each type of instrument works, and how output signals are translated to engineering unit output through the data acquisition (DAQ) system. Although much of the focus and time is spent on model construction, energy spent becoming familiar with the DAQ and input spreadsheets or channel lists are extremely important and can avoid difficulties or major problems during the test.

If one plans to use tactile pressure sensors or any other instrument that requires its own data acquisition (DAQ) system, it is important to synchronize the beginning of data collection with the main DAQ to the extent possible, so that synchronizing the two data sets later is not required. Time synchronization between different measurements can be important for data analysis after the experiment.

A3 Accessing Experimental Data

All experimental data and reports from each experiment are made available to the public on NEESHub at NEES.org. This data from the experimental component of this research may be found on NEESHub under a project titled "Seismic Response of Shallow Underground Structures in Dense Urban Environments" on www.nees.org.